Water Science and Technology Library

Vijay P. Singh · Shalini Yadav ·
Krishna Kumar Yadav ·
Gerald Augusto Corzo Perez ·
Francisco Munoz-Arriola ·
Ram Narayan Yadava *Editors*

Application of Remote Sensing and GIS in Natural Resources and Built Infrastructure Management

Springer

Water Science and Technology Library

Volume 105

The aim of the *Water Science and Technology Library* is to provide a forum for dissemination of the state-of-the-art of topics of current interest in the area of water science and technology. This is accomplished through publication of reference books and monographs, authored or edited. Occasionally also proceedings volumes are accepted for publication in the series. *Water Science and Technology Library* encompasses a wide range of topics dealing with science as well as socio-economic aspects of water, environment, and ecology. Both the water quantity and quality issues are relevant and are embraced by *Water Science and Technology Library*. The emphasis may be on either the scientific content, or techniques of solution, or both. There is increasing emphasis these days on processes and *Water Science and Technology Library* is committed to promoting this emphasis by publishing books emphasizing scientific discussions of physical, chemical, and/or biological aspects of water resources. Likewise, current or emerging solution techniques receive high priority. Interdisciplinary coverage is encouraged. Case studies contributing to our knowledge of water science and technology are also embraced by the series. Innovative ideas and novel techniques are of particular interest.

Comments or suggestions for future volumes are welcomed.

Vijay P. Singh, Department of Biological and Agricultural Engineering & Zachry Department of Civil and Environment Engineering, Texas A&M University, USA
Email: vsingh@tamu.edu

All contributions to an edited volume should undergo standard peer review to ensure high scientific quality, while monographs should also be reviewed by at least two experts in the field.

Manuscripts that have undergone successful review should then be prepared according to the Publisher's guidelines manuscripts: https://www.springer.com/gp/authors-editors/book-authors-editors/book-manuscript-guidelines

Vijay P. Singh · Shalini Yadav ·
Krishna Kumar Yadav ·
Gerald Augusto Corzo Perez ·
Francisco Muñoz-Arriola · Ram Narayan Yadava
Editors

Application of Remote Sensing and GIS in Natural Resources and Built Infrastructure Management

Springer

Editors
Vijay P. Singh
Department of Biological and Agricultural Engineering, Zachry Department of Civil and Environment Engineering
Texas A&M University
College Station, TX, USA

Krishna Kumar Yadav
Faculty of Science
Madhyanchal Professional University
Bhopal, India

Francisco Muñoz-Arriola
The School of Natural Resources and Department of Biological Systems Engineering
University of Nebraska-Lincoln
Lincoln, Nebraska, USA

Shalini Yadav
Department of Civil Engineering
Rabindranath Tagore University
Bhopal, Madhya Pradesh, India

Gerald Augusto Corzo Perez
IHE Delft Institute for Water Education
Delft, The Netherlands

Ram Narayan Yadava
Madhyanchal Professional University
Bhopal, India

ISSN 0921-092X ISSN 1872-4663 (electronic)
Water Science and Technology Library
ISBN 978-3-031-14095-2 ISBN 978-3-031-14096-9 (eBook)
https://doi.org/10.1007/978-3-031-14096-9

This Springer imprint is published by the registered company Springer Nature Switzerland AG
The registered company address is: Gewerbestrasse 11, 6330 Cham, Switzerland

Contents

About the Editors

Professor Vijay P. Singh Ph.D., D.Sc., D. Eng. (Hon.), Ph.D. (Hon.), P.E., P.H., Hon.D.WRE, Dist.M. ASCE, Dist.Hon. M. IWRA, Dist.F. AGGS, Hon. Member AWRA,NAE, holds the Caroline & William N. Lehrer Distinguished Chair in Water Engineering and is a Distinguished Professor and a Regents Professor, Department of Biological, and Agricultural Engineering, and Zachry Department of Civil & Environmental Engineering at Texas A&M University, USA. Professor Singh has been recognized for four decades of leadership in research, teaching and service to the hydrologic and water resources engineering profession. Singh's contribution to the state of the art has been significant in many different specialty areas, including hydrologic science and engineering, hydraulic engineering, water resources engineering, environmental engineering, irrigation science, soil and water conservation engineering, entropy-based modeling, copula-based modeling, and mathematical modeling. His extensive publications in these areas include 32 textbooks, 1432 refereed journal articles, 80 edited books, 115 book chapters, 330 conference proceedings papers, and 72 technical reports.

For his seminal contributions, Dr. Singh has been honored with more than 105national/international awards from professional organizations. As a sample, he is a recipient of the Arid Land Hydraulic Engineering Award, Ven Te Chow Award, Torrens Award, Norma Medal, Royce C. Tipton Award, Lifetime Achievement Award, Distinguished Membership, and OPAL Award, all given by ASCE. He was awarded the Ray K. Linsley Award for outstanding contributions to surface water hydrology and the Founders Award of AIH. He has been awarded three honorary doctorates. He is a fellow of ASCE, AWRA, IE, ISAE, IWRS, IASWC, and IAH; a member of AGU, IAHR, IAHS and WASER. He is member/fellow of 12 engineering/science academies, including National Academy of Engineering (NAE). Prof. Singh is licensed as a Professional Engineer (PE), a Professional Hydrologist (PH), and Honorary Diplomate, AAWRE.

Prof. Shalini Yadav is a Professor in the Dept. of Civil Engineering and Head of theCentre of Excellence in Advanced Water and Environmental Research, Rabindranath Tagore University, Bhopal, India. Her research interests include solid

and hazardous waste management, construction management, environmental quality, and water resources. She has executed a variety of research/consultancy projects in the area of environment and water science, and has got rich experience in planning, formulating, organizing, executing, and management of R&D programs. She has got to her credit guiding of 35 M.Tech. and 10 Ph.D. students.

She has published more than 90 journal articles and technical reports. She is a member of the organizing and scientific committee of several conferences and reviewer in several of international journals. Also she has published a number of edited books, namely Climate Change Impacts, Water Resources Management, Groundwater, Energy and Environment, Environmental Pollution, Hydrologic Modeling, Water Quality Management, Environmental Degradation: Challenges and Strategies for Mitigation in the Water Science and Technology Library; and Environmental Management in India: Waste to Wealth, Wastewater Assessment, Treatment, Reuse and Development in India in the Earth and Environmental Sciences Library of Springer Nature.

Dr. Krishna Kumar Yadav is working on a position of Assistant Professor in the Faculty of Science and Information Technology of the Madhyanchal Professional University, Madhya Pradesh, India. His research interest is in Defluoridation of Groundwater, Waste Management, and Bioremediation/ Phytoremediation of Heavy Metals, and Energy Recovery from the Waste. He has executed a Varity of research and consultancy projects in the area Environmental Sciences, Sustainability, Water Quality and Water and Waste Water Treatment, and Material Science. Also Dr. Krishna Kumar has got rich experience in executing, and management of R&D programs, He has earned his Master of Science in Environmental Science from V. B. S. Purvanchal University, Jaunpur, India; Master of Philosophy and Doctor of Philosophy in Environmental Science from the Bundelkhand University, Jhansi, India. Also he is recipient of Young Environmental Scientist Award in an International Conference on Agriculture, Allied and Applied Sciences held at JNU New Delhi, India in 2018.

Dr. Krishna Kumar has published more than 70 journal articles and technical reports. He is a member of the organizing and scientific committee of several conferences and reviewer of Journal of cleaner production, Journal of Hazardous Materials, Energy; and Section Editor of International Journal of Environmental Chemistry. Also he has published a number of edited books.

Dr. Gerald Augusto Corzo Perez is Associate Professor at IHE Delft institute for water education. His research work covers a full range of water resources areas applying spatiotemporal statistics, pattern recognition and machine learning techniques. Since the last four year he has been working on the analysis of global hydrological extremes, exploring responses to drought and floods. In 2012 he won the Tison award as young scientist from the IAHS association. He has worked on different international institution like Wageningen University in the Netherlands and the Technologic of Monterrey in Mexico. He has coordinated the statistics of the Climate change inventory of adaptation and mitigation actions for Latin-America,

presented at the WWF in 2012. Civil engineer by training with a strong background on computational science and an specialization on Telecommunications. He has developed methods for integrating computational intelligent algorithms and hydrological conceptual models for hydrological forecasting. During his Ph.D. he also worked in Flood Early Warning System models integrating Machine Learning models (Delft-FEWS). He developed scripts for areas of computational intelligence, optimization of water resources, online modeling and in fluid dynamics simulation in MATLAB. One of his recent projects focuses on exploring the use spatiotemporal rainfall objects as inputs for pattern recognition and tracking models. He is innovating in new paradigms in the areas of Natural Language processing and AI Chatbots for new concepts in decision support.

He have participated on research projects in different countries like China with the North China University for Water Conservancy and Electric Power in China, Colombia (CINARA), Mexico (Technologico of Monterrey), England (CEH), Norway (University of Oslo) and others. The last two years he served as chair of the session on geo-statistics at the European Geoscience Union. From 2011 to 2012 he created and leaded the LatinAqua network for water research scientist in Latin-America.

Dr. Francisco Muñoz-Arriola is an Associate Professor in "Climate Analytics, Analysis, and Synthesis" in the School of Natural Resources and the Department of Biological Systems Engineering at the University of Nebraska-Lincoln, and an Adjunct Faculty in the Department of Biosystems Engineering at Universidade do Sao Paulo. He is also a fellow of the Robert B. Daugherty Water for Food Global Institute, the University of Nebraska's Public Policy Center, and the Nebraska Governance and Technology Center. Francisco is a member of the American Meteorological Society (AMS) Water Resources Committee and co-chair of the presidential sessions on Food Security and Water Security at the 2022 AMS annual meeting. Francisco studies the predictability of hydrometeorological and climate extremes and their impacts on natural systems and infrastructure. He is member of the Climate-Resilient and Environmentally Adequate Infrastructure (CREA-I) research collective. CREA-I pursues to connect engineering with other disciplines creating adaptive planning and management strategies, information technologies, models, and theories. Some of Francisco's fundamental and applied research includes the study of the resilience of complex systems to changes in weather and climate, the predictability of regime shifts in water, agriculture, and public health, the integrated management of water quality and quantity, and the (re)design of climate-resilient infrastructure and actions. His collaborative network includes researchers from more than twenty countries in Asia, Europe, and the Americas, working on multiple disciplinary and transdisciplinary challenges. Francisco is an enthusiast mentor and advocate for a diverse, equal, inclusive, ethical, and accessible education. Francisco's Ph.D. is in Civil and Environmental Engineering from Duke University, and he has postdoctoral experiences at the University of Washington and the University of California, San Diego. His bachelor's degree is in Oceanography from the Facultad de Ciencias Marinas at the Universidad Autónoma de Baja California, México.

Prof. Ram Narayan Yadava holds position of Director of Research and International Affairs in Madhyanchal Professional University, Bhopal, (M.P.) India; and Director of Patel Group of Institutions, India. He has worked as a advisor of AISECT Group of Universities and a founding Vice Chancellor of the AISECT University, Hazaribag (Jharkhand), India. Prof. Yadava is also a founding member of Advanced Materials and Processes Research Institute (AMPRI) under the umbrella of Council of Scientific and Industrial Research (CSIR), India. His research interests include Solid Mechanics, Environmental Quality and Water Resources, Hydrologic Modeling, Environmental Sciences, and R&D Planning and Management. Dr. Yadava has executed a variety of research/consultancy projects in the area of Water Resources Planning and Management, Environment, Remote Sensing, Mathematical Modeling, Technology Forecasting, etc.

He has adequate experience in establishing institutes/organizations from scratch. In addition, he has adequate experience in planning, formulating, executing and managing of R&D programs including organizing seminars/symposia/conferences at national and international levels. He has got to his credit guiding a number of M. Tech. and Ph.D. students in the area of Mathematical Sciences and Earth Sciences. Dr. Yadava has visited and delivered invited lectures at different institutes/universities in India as well as in abroad in the various countries such as USA, Canada, UK, France, Thailand, Germany, South Korea, Malaysia, Singapore, South Africa, Costa Rica, The Netherlands, France, China, and Australia. He is Recipient of Raman Research Fellowship and other awards.

Dr. Yadava has been recognized for four decades of leadership in research and service to the hydrologic, environment and water resources profession. Dr. Yadava's contribution to the state of the art has been significant in many different specialty areas, including water resources management, environmental sciences, irrigation science, soil and water conservation engineering, and mathematical modeling. He has published more than 100 journal articles; four text books; sixteen edited reference books. He is reviewer of scientific journals and member of the scientific committee of international conferences. He also holds position of Vice President of International Association of Water, Environment, Energy and Society.

Chapter 1
Applications of Geospatial and Information Technologies Toward Achieving Sustainable Development Goals

Srabani Das, Kuntal Ganguly, Tarik Mitran, and Surya Deb Chakraborty

Abstract Sustainable development is possible by holistically prioritizing urban and rural development activities by capturing many complexities, constraints, and livelihood opportunities. In this context, United Nations (UN) designed a blueprint containing seventeen interlinked Sustainable Development Goals (SDGs) to address the global challenges, including climate change, environmental degradation, peace, poverty, inequality, and justice. The achievement of SDGs and their universality would be possible through readily available data from affordable sources such as remote sensing images and readily available sources. The spatio–temporal data analysis is crucial for assessing, monitoring, and decision-making and becomes integral in addressing SDG indicators. However, the advancement and availability of an enormous amount of earth observation data increased the need for new methods and techniques. Nowadays, the integration of geospatial technologies along with information and communication technology (ICT) like the Internet of Things (IoT), big data, machine learning (ML), artificial intelligence (AI), advanced sensor networking, and crowdsourcing has made a powerful analytic platform for Spatial Decision Support System (SDSS). This chapter comprehensively reviews and documents the scope and application of geospatial and information and communication technology and its role in action plan formulation toward achieving SDGs.

Keywords Artificial intelligence · Data analytics · Geospatial · IoT · Machine learning · Sustainable development goals (SDGs) · Sensors

S. Das · K. Ganguly
Cognizant Technology Solutions, Hyderabad 500001, India

T. Mitran (✉)
Soil and Land Resources Assessment Division, National Remote Sensing Centre, ISRO, Hyderabad, Telangana 500037, India
e-mail: tarikmitran@nrsc.gov.in

S. D. Chakraborty
Environmental System Research Institute, India, Ecospace, Kolkata 700091, India

V. P. Singh et al. (eds.), *Application of Remote Sensing and GIS in Natural Resources and Built Infrastructure Management*, Water Science and Technology Library 105,
https://doi.org/10.1007/978-3-031-14096-9_1

Abbreviations

AI	Artificial intelligence
AIS	Automatic identification system
GDP	Gross domestic product
GPS	Global positioning system
GT	Geospatial technologies
IBM	International business machines
ICT	Information and communication technology
IoT	Internet of things
IT	Information technology
LST	Land surface temperature
ML	Machine learning
MOOCs	Massive open online courses
RESAP	Regional space applications programme for sustainable development
SD	Sustainable development
SDGI	Sustainable development goals index
SDGs	Sustainable development goals
SDSN	Sustainable development solutions network
SDSS	Spatial decision support system
SIDS	Small island developing states
UN	United Nations
UNESCAP	United Nations economic and social commission for Asia and the Pacific
VGI	Volunteered geographic information
VR	Virtual reality

1.1 Introduction

Post-industrial revolution during the second half of the nineteenth century had a significant impact on environmental and social equality in Western societies. The series of economic and social crises may be the reason (Fig. 1.1). The ecologist and philosopher Garret Hardin wrote an essay in 1968 entitled "the tragedy of the commons", where he highlighted the issue that if individuals act according to their interests, then it would be going against the common interests of their societies and deplete the natural resources of this planet. In the early 1970s, the term "sustainability" was evolved to describe an economy "in equilibrium with basic ecological support systems". Ecologists have highlighted the alternative way of a "steady-state economy" to address environmental issues. The consequences of what could happen on a planet with limited resources had predicted through computer simulation by the researchers (Meadows et al. 1972, 2013). They have projected that an economic and social collapse will occur by the end of the twenty-first century if man imposes no

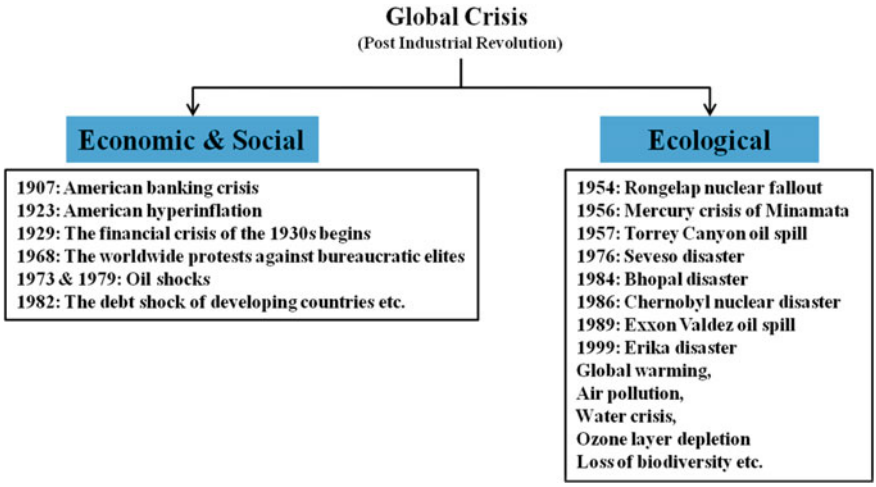

Fig. 1.1 Global economic, social, and ecological crisis after industrial revolution

limits on growth. After more than four decades, these predictions seem to be correct. The environmental degradation due to over-exploitation of limited resources and pollution and its consequences are threatening sustainable development. The idea of sustainable development (SD) was mentioned for the first time in the Brundtland Report in 1987. It was defined as the development that meets the needs of the present without compromising the ability of future generations to meet their own needs. SD is the organizing principle for meeting human development goals while simultaneously sustaining the power of natural systems to provide the natural resources and ecosystem services on which the economy and society depend.

In another way, it shows the path of systematically organizing society so it can exist in the long term considering the preservation of the environment and natural resources or social and economic equity. In 2015, United Nations (UN) set up 17 Sustainable Development Goals (SDGs) to address the various global challenges presented in Fig. 1.2. Sustainable development is possible by holistically capturing many complexities, constraints, and livelihood opportunities that they are subjected to, prioritizing urban and rural development activities. The urban development activities include food security, infrastructure, transportation, energy efficiency, waste management, etc. In rural areas, challenges are mostly related to poverty, agriculture, disasters, etc.

The spatial–temporal data analysis is the key and significant component of the sustainable development framework for the decision-making and prioritization of those activities. The advantage of using geospatial technologies has proven to be effective for achieving targets in many projects. It helps to plan and execute programs systematically and holistically because of its location-based analytics and visualization offered by earth observation technologies. National and international organizations realize the importance and effectiveness of geospatial tools and techniques in

Fig. 1.2 Seventeen SDGs proposed by the UN. Adapted from https://www.un.org

achieving the SDGs. Hence, the UN has formulated the 2030 agenda for SD, including guidelines for appropriate uses of earth observation and geospatial data to measure, monitor, report, and achieve the SDGs. Even sustainable development has included guidelines for proper use of geospatial and earth observation data. Nowadays, integrating geospatial technologies and other technologies like IoT, big data, ML, AI, advanced sensor networking, and crowdsourcing has made a powerful analytic platform for Spatial Decision Support System (SDSS). On the other hand, mobile-based services and integrated IoT networks enable person-to-object and object-to-object communication. Besides, affordable graphics processing units (GPUs) and cloud computing services ease accessibility to massive computing power. In urban areas, location analytics and advanced sensors can gather information about pollution level checking, traffic management, energy, and water usage through an intelligent building, innovative grid technology, etc. Similarly, in rural areas, geospatial analytics helps farmers take appropriate measures related to agriculture development. Besides, it helps the administration build infrastructure like schools, hospitals, banking systems, electricity distribution, and many more based upon spatial analysis. This chapter comprehensively documents geospatial data analysis and synthesis tools and methods and their role in action plan formulation toward achieving Sustainable Development Goals.

1.2 Sustainable Development Goals

1.2.1 Targets

United Nations has proposed a plan entitled "Transforming Our World: The 2030 Agenda for Sustainable Development (Agenda 2030)" to address the global issues at the UN Sustainable Development Summit in 2015. The proposal sets 17 SDGs to manage the global challenges, i.e., inequality, poverty, and the effects of climate change effects. Figure 1.2 shows all SDGs are globally recognized and adopted by many countries considering the feasibility of the plan. SDGs were set up to improve the living conditions and conservation of the environment, especially in developing countries and developed countries too. In order to reach the goal, the Sustainable Development Solutions Network (SDSN) was formed to monitor the activity of countries and regions working toward the implementation of the SDGs and also record the information related to it.

1.2.2 Sustainable Development Goals Index (SDGI) and Its Global Perspective

The effectiveness of the SDGs is determined by the SDGI. Hence, a dashboard has been set up containing a scale from 0 to 100. The "0" and "100" show the worst level of implementation and full compliance with the targets, respectively. The current status of SDGI at a global level is presented in Fig. 1.3.

The World Economic Forum has published a ranking on the performance of each country toward achieving SDGs using SDGI (World Economic Forum (2021). As per the report, countries, namely Sweden (84.5), Denmark (83.9), Norway (82.3), Finland (81), and Switzerland (80.9), have implemented SDGs more effective manner and ranked in the top five for good performance in addressing social and economic issues. However, many African countries like the Central African Republic (26.1), Liberia (30.5), the Democratic Republic of the Congo (31.3), and Niger (31.4) are in the poor performance category. The responsible aspects behind the poor performance of these countries are especially poverty, hunger, education, and peace and justice. Besides, a country like the USA is in the 25th place with 72.7points; Canada is in 13th position with 76.8 points; Australia is in 20th place with 74.5 points, and the UK is in 10th position with 78.1points.

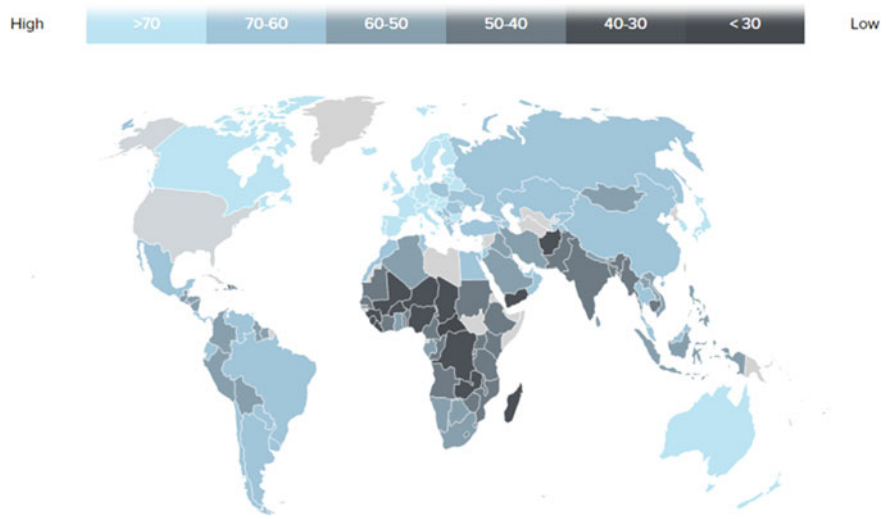

Fig. 1.3 SDGI showing status of SDGs at global level. Data source World Economic Forum (2021)

1.2.3 Impact of COVID-19 Pandemic on SDGs Implementation

The implementation of SDGs became more challenging as the COVID-19 pandemic progressed across the globe. Guillaume Lafortune from UN Sustainable Development Solutions Network Initiative has summarized the key findings of the Sustainable Development Report 2020 on June 25, 2020, and reported that COVID-19 is negatively affecting several goals such as no poverty-SDG 1; zero hunger-SDG 2; good health and well-being-SDG 3; decent work and economic growth-SDG 8; and reduced inequalities-SDG 10. The overall impact of COVID-19 on SDGs is summarized in Fig. 1.4.

1.3 Importance and Scope of Geospatial Technology on SDGs Implementation

Geospatial tools and techniques can play a vital role in achieving targets through their decision support, planning, and monitoring capabilities (Fig. 1.5). Remote sensing satellite is capable of providing a synoptic view and repetitive coverage of the earth's features. Commendable progress has been observed in the scientific world toward

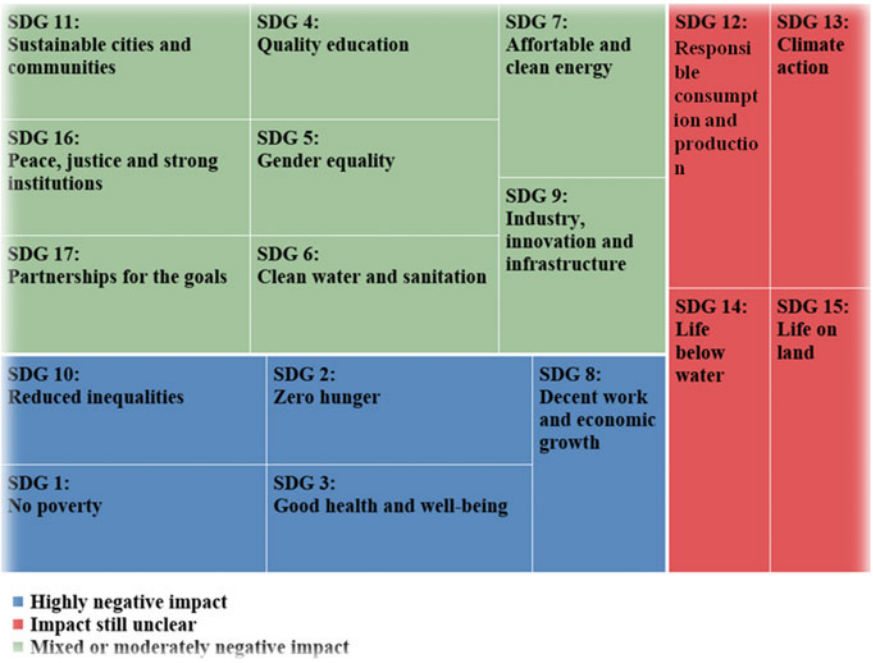

Fig. 1.4 COVID-19 impact on SDGs. Data source Sachs et al. (2020)

using geospatial data at various spectral, radiometric, temporal, and spatial resolutions enabling the usage of the data for various applications (Avtar et al. 2019; Ganguly et al. 2021; Mitran et al. 2021a, b). Hence, images provided by various satellites can be used effectively for the implementation of SDGs and monitoring of their progress.

A set of quantifiable indicators, targets, and observable data specific to each goal has been devised to monitor the progress (Hák et al. 2016). The systematic data observations at the local and community level are required for the subsequent decision-making process, which includes the collaboration of various stakeholders. The quality of data and proper data collection abilities are vital to optimally measuring various SDGs indicators. The UN has also highlighted the issues related to data collection and quality and emphasized the need for a data revolution to enhance data quality (Kharas et al. 2014). In this context, the recent advancement and availability of various geospatial data, techniques, and products could play a meaningful role.

Moreover, there are many satellite sensors, each with particular characteristics, which are essential tools for visualizing and monitoring changes at global and local scales (Avtar et al. 2019). The scientific findings obtained using geospatial approaches can provide a strong basis for policymaking to promote SD in communities at local and regional levels (Habitat 2015; United Nations 2016). Besides,

Fig. 1.5 Scope of geospatial technologies

in situ sensors can be installed to measure these variables at the local scale with a higher frequency. Hence, geospatial tools and techniques can be used very effectively for monitoring most of the SDGs (Dangermond and Artz 2010; Kuffer et al. 2018; Orimoloye et al. 2018; Tatem et al. 2017).

1.4 Application of Geospatial Techniques Toward Achieving SDGs

Geospatial tools and approaches can be used efficiently for monitoring many of the SDGs. However, geospatial data is not yet feasible for all SDGs.

The selected SDGs and geospatial tools and methods to produce appropriate data for monitoring the progress of different indicators of these goals are illustrated in Fig. 1.6. The application of geospatial technology in selected SDGs and database sources supposed to be used for that analysis is summarized and presented in Table 1.1.

1.5 Application of Information and Communication Technology Toward Achieving SDGs

Recent advancements in information and communication technology (ICT) and global interconnectedness show great potential to accelerate SD plans. The aim of using such technologies is to bridge the digital divide and to develop knowledge

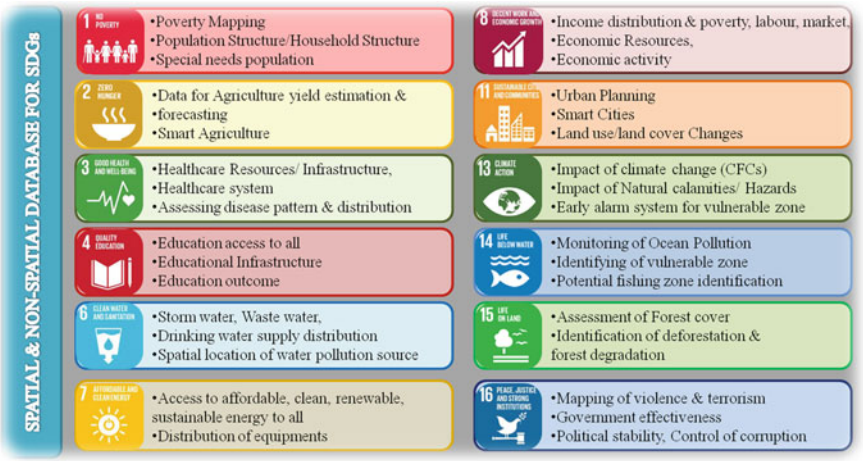

Fig. 1.6 Application of geospatial analysis in some selected SDGs

societies. Digital technology can play a crucial role in monitoring the progress of different indicators of various SDGs. The use of digital techniques could be essential to achieve the SDGs, considering the need for accelerated progress to fulfill the goals by 2030. As technology is revolutionizing, the digital transformation initiatives will radically alter agriculture, energy, manufacturing, transportation, and other industrial sectors of the economy in the next ten years. Although there are many technologies involved in such transformation, a few are especially useful in the context of SDGs. These are big data, AI/ML, and IoT.

1.5.1 Application of Big Data

There is an increasing trend in the volume of data in the world. As per a recent estimate, about 90% of this data has been created in the last two years. Moreover, there is a future projection of an annual increment in the volume of these data by 40%. A maximum share of this output is "data exhaust" or passively collected data from daily interactions with digital products or services, including social media, credit cards, mobile phones, etc. Nowadays, extensive data analysis is standard in the private sector. Several approaches such as predictive analysis, personalized services, and consumer profiling are being used for advertisement, management, and marketing purposes. Similar techniques can be adopted and used to gain real-time insights into people's well-being by targeting aid interventions to vulnerable groups.

Besides, integrating these approaches with various satellite data, geospatial techniques, and data analytics methods can enable more agile, efficient, and evidence-based decision-making if applied responsibly. It could also use to measure and monitor the progress toward achieving SDGs in a way that is both inclusive and fair.

Table 1.1 Geospatial application toward achieving different sustainable development goals

SDGs	Sources of spatial data	Sources of non-spatial data	Geospatial applications	References
SDG 1: no poverty	Satellite imageries	Census data	Poverty mapping	Asensio (1997) and Tatem et al. (2017)
			Identify inequality and spatial disparities	Kuffer et al. (2018)
	Mobile location data		Location-based credit consumption	Eagle et al. (2010) and Soto et al. (2011)
	Thematic data—slope, soil, land use type	Demographic variables, distance, travel time to public resources	Spatial pattern analysis	Okwi et al. (2007)
	Nighttime satellite data, land cover, topography	Population data	Poverty index calculated by dividing population count by the pixel brightness of nighttime images	Elvidge et al. (2009) and Tatem et al. (2017)
SDG 2: no hunger	Temporal satellite imageries		Crop yield assessment	Arroyo et al. (2017)
	Unmanned aerial vehicle (UAV)		Precision farming	Maes and Steppe (2019)
	Landsat imagery and UAV		Estimation of irrigated area	Nhamo et al. (2018)
	Climate data	Hunger population data	Hunger hotspot analysis and impact analysis of climate change	Liu et al. (2008)
SDG 3: good health	Satellite imageries	Healthcare access data	Proximity analysis of healthcare facility for primary care facilities	Rosero-Bixby (2004)
	Satellite imageries, land use and land surface temperature (LST)		Impact of urbanization and LST on health	Orimoloye et al. (2018)

(continued)

Table 1.1 (continued)

SDGs	Sources of spatial data	Sources of non-spatial data	Geospatial applications	References
	Healthcare location data	Clinical data	Epidemiology studies and GIS-based mapping to prevent future pandemics	Lüge et al. (2014) and Maude et al. (2014)
	Location data of COVID-19 infected patient	Details of patient's associated people	GIS-based contact tracing and creation of containment zones	Mishra et al. (2021)
SDG 4: quality education	Education location data	Education infrastructure data	Proximity analysis for basic education facility	Daiman and Goyal (2020)
	Enrollment data	Census data	Assessment of school enrollment and dropout students	Trinidad (2022)
SDG 6: clean water and sanitation	Satellite imagery, land cover, hydrology, geology, vegetation		Assessment of groundwater potential zone using multi-criteria analysis	Machiwal et al. (2011)
	Satellite imagery derived land cover and infrastructure data		Geographical analysis for planning of infrastructure development	Paulson (1992)
	Satellite imagery, land cover, slope, soil type	Land ownership data, weather data	Environmental impact assessment and design infrastructure facilities	Tatem et al. (2017) and Kuffer et al. (2018)
	IRS-LISS-II, DEM, and groundwater data		GIS analysis to prepare proper groundwater management plan for a hard rock terrain	Saraf and Choudhury (1998)
SDG 7: affordable and clean energy	Satellite imageries	Natural renewable energy resources data	GIS analysis for assessing access to affordable, reliable, sustainable, and modern energy	ESRI (https://learn.arcgis.com/en/paths/solve-problems-for-sustainable-development-goals)

(continued)

Table 1.1 (continued)

SDGs	Sources of spatial data	Sources of non-spatial data	Geospatial applications	References
SDG 8: decent work and economic growth	Industry location data	Industry type and category of industry	Assessing predicted economic growth and business growth by industry	ESRI (https://learn.arcgis.com/en/paths/solve-problems-for-sustainable-development-goals)
		Economic growth data	Determine how location impacts on interest rates	
SDG 11: sustainable cities and communities	Very high-resolution satellite imagery, land cover	Population	Image analysis to monitor wastewater treatment at different locations	Ulugtekin et al. (2005)
	Temporal satellite imageries		Urban growth mapping to support energy sector	Haslauer et al. (2012)
	Groundwater data, drainage data	Climate data	Water scarcity mapping and forecasting	Quinteiro et al. (2019)
	Climate data, satellite imageries	Historical disaster data	Geospatial data analysis for disaster management	Lwin et al. (2019)
	Satellite images, ground-based sensors, land use	Pollution data	Monitoring air and water pollution and forecasting future plan	Bonaiuto et al. (2015)
	Temporal satellite imageries, land use	Settlement data, socioeconomic data	Informal settlement mapping and analysis of underlying cause through GIS	Dovey (2015), El-Batran and Arandel (2005) and Karanja (2010)
SDG 13: climate action	Temporal satellite imageries, climate data	Historical events	Building geospatial framework by integrating historical and future data from different sources and merge them together in a single system using GIS	Dangermond and Artz (2010)

(continued)

Table 1.1 (continued)

SDGs	Sources of spatial data	Sources of non-spatial data	Geospatial applications	References
	Remote sensing satellite images		Ozone hole study using remote sensing data and analysis of daily global ozone concentration maps	Avtar et al. (2019)
	Remote sensing satellite images		Monitoring climate change impacts on the glacier and permafrost-related hazards which is potential threat to livelihood of population lives in mountainous areas	Kaab et al. (2006)
	Remote sensing satellite images		Monitoring sea-level changes using spatiotemporal data	Elias et al. (2020)
SDG 14: life below water	Satellite imageries	Marine ecological data	Sustainable use and management of important tropical coastal ecosystems using integrated remote sensing and GIS	Dahdouh-Guebas (2002)
	Remote sensing satellite images for marine study		Spatial monitoring of sea grasses/coastal management	Ferguson and Korfmacher (1997)
	Synthetic aperture radar (SAR) data,, Landsat-8, Sentinel-I		Detecting oil spills using microwave remote sensing images	Yu et al. (2017)
	Satellite imageries, sensor-based data		Identification of potential fishing zones by detecting sea surface height anomaly, ocean temperature, color, etc.	Saitoh et al. (2011)

(continued)

Table 1.1 (continued)

SDGs	Sources of spatial data	Sources of non-spatial data	Geospatial applications	References
SDG 15: life on land	Multi-temporal satellite imageries		Monitoring deforestation	Reddy et al. (2016)
	Global tree cover data		Forest fragmentation study	Riitters et al. (2016)
	GPS data and satellite imageries		Investigation of illegal logging operation	Kusumaningtyas et al. (2009)
	Advanced land observing satellite (ALOS) phased arrayed L-band synthetic aperture radar (PALSAR)		Monitoring above-ground forest carbon stock and carbon sequestration study due to loss of forest	Thapa et al. (2015)
SDG 16: peace, justice, and strong institutions	Satellite imageries	Institution data	GIS analysis to promote peaceful and inclusive societies, provide access to justice, and build accountable institutions	ESRI (https://learn.arcgis.com/en/paths/solve-problems-for-sustainable-development-goals)
		Public policies	Examine racial inequities in unsolved murder cases/criminal activities	
		Data collection for problem areas	Calculate environmental equity for public policy	

The integrated use of geospatial data and big data for achieving SDGs is presented in Table 1.2.

1.5.2 Application of Artificial Intelligence

Artificial intelligence is an emerging technique and has a broader impact on many sectors. It can bring about large-scale improvements and transformations in health, agriculture, and education. AI impacts these sectors by delivering government

Table 1.2 Combined use of big data and geospatial data toward achieving different SDGs

SDGs	Big data sources	Type of data	Geospatial sources	Type of data
SDG 1: no poverty	Mobile phone data	Human mobility and socioeconomic levels assessment	Satellite derive information	Poverty mapping
		Estimating poverty and wealth		
		Socioeconomic status		
	Citizen-generated data	Financial assessment		
		Disaster response		
SDG 2: no hunger	Mobile phone data	Food expenditure	Satellite data	Drought monitoring
	Online price data/scanner data/social media data	Consumer price index assessment		Crop yield assessment
SDG 3: good health and wellness	Mobile phone data	Mobility from regions of disease outbreak	Spatial information	Compilation of indicators
		Sources and sinks for diseases		
		Seasonal trends of diseases		
	Search engine data	Diseases trend assessment		
		Identification of hotspots for traffic accidents and preventive measures		
SDG 4: quality education	Mobile phone data	Low literacy zone identification	Spatial data	Compilation of data
	MOOCs data	Policymaking of education		
SDG 5: gender equality	Mobile phone data	Gender prediction	Satellite data	Gender assessment
	Social media data	Gender equality assessment		
SDG 6: clean water and sanitation	Cloud data	Service data assessment	Satellite data	Compilation of indicators
SDG 7: affordable and clean energy	Smart meter data	Determine residential electricity consumption	Satellite data	Detect nighttime luminosity

(continued)

Table 1.2 (continued)

SDGs	Big data sources	Type of data	Geospatial sources	Type of data
SDG 8: decent work and economic growth	Postal data	GDP, economic, and human development	Satellite derive information	Indicator for GDP and economic development
	Search engine data	Identifying unemployment trends and shocks in the workforce	Remote sensing data	Data compilation and assessment
	Mobile phone data	Estimation of seasonal tourism and destination of tourists and inform policies for promote sustainable tourism		
SDG 9: sustainable industrialization	Mobile phone data/GPS data/Google traffic data	Patterns of road usage, pockets of congestion, and determine mobility patterns of population, key factors in the development of infrastructure	Remote sensing data	Data compilation and assessment
SDG 10: reduce inequality	Mobile phone data	Assessing changes in the socioeconomic status of populations	Remote sensing data	Data compilation and assessment
SDG 11: sustainable cities and communities	Mobile phone data	Population hotspots	Remote sensing data	Poverty and slums mapping
		Social events and home locations	Remote sensing data	Land cover/land use changes
		Origin–destination flows	Other spatial data	Data compilation
		Geo-social radius		
		Identification of human mobility after disasters		
SDG 13: climate change	Mobile phone data	Estimation of human mobility after disasters or any climate changes	Satellite data	Changes in the water ecosystem and monitoring of other changes

(continued)

Table 1.2 (continued)

SDGs	Big data sources	Type of data	Geospatial sources	Type of data
SDG 14: life below water	Citizen generated data/cloud data	Assessment of effect of global changes	Geospatial data	Compilation for this indicator
	AIS data	Identify illegal fishing and monitoring of protected marine areas		
SDG 15: life on land	Mobile phone data	Assessment of accessibility and other factor affecting life on land	Remote sensing data	Forest mapping and changes in vegetation
	Citizen generated data	Assessing data compilation		
SDG 16: peace, justice, and strong institution	Mobile phone data/social media data	Crime prediction		
		Criminal activity zoning		

services to citizens, accelerating innovation and enterprise creation, and reducing the cost of public service and the operation of critical infrastructure.

Hence, the formulation of new methods with the inclusion of ML and AI techniques could open a pathway for effective use of the large volume of available data from satellite images and other platforms and enable us to make giant strides toward achieving SDGs.

The high-resolution temporal satellite data, advanced analytical techniques using AI and computing services, can help prevent outbreaks of diseases, map populations, provide insight into gender inequality, enable supply chain transparency, support efficient post-disaster response, and disrupt human trafficking networks. The combined applications of AI with geospatial technologies toward achieving SDGs are presented in Table 1.3. Many countries, specifically in the Middle East and Asia, have already incorporated AI as a critical component of their economic growth and development strategy. The impact of AI on achieving various SDGs (Fig. 1.7) was assessed by Vinuesa et al. (2020) and reported that AI may act as an enabler on 134 targets (79% across all SDGs) through a technological improvement, which may allow overcoming certain present limitations. However, there are 59 targets (35%, also across all SDGs) that may experience a negative impact from the development of AI.

Table 1.3 Application of AI with geospatial technology toward achieving SDGs

SDGs	Data source	Applications	References
SDG 1: no poverty	Satellite images Climate data	Predict and prevent extreme climate-related events	Decuyper et al. (2020)
SDG 3: good health	Population data Administrative map Health data	Predictive modeling to identify populations at high risk for disease	Bi et al. (2019), Dahdouh-Guebas (2002), Istepanian and Al-Anzi (2018), Topol (2019) and VoPham et al. (2018)
SDG 6: clean water and sanitation	Satellite images Local sensor data	Identifying water threats using machine learning algorithm in combination with remote sensing spectral indices	Wang et al. (2017)
SDG 11: sustainable cities and communities	Satellite images Other sensor data	AI-based algorithm to map informal settlements Predictive analysis for disaster management	Ivić (2019)
SDG 13: climate action	Satellite images Climate data	Machine learning and artificial intelligence to aid climate change research and preparedness	Huntingford et al. (2019)
SDG 15: life on land	Satellite images	Machine learning-based image classification to identify land use/land cover changes, forest cover changes	Ganguly et al. (2017)

1.5.3 Application of Internet of Things

In recent years, one of the most well-known technologies growing to new heights and creating a touchstone is the Internet of Things (IoT). The future of interaction has molded things (objects) of the natural world into smart objects (Khanna and Kaur 2020). As it is expected to grow the worldwide connected devices by this decade, it opens up an incredible opportunity to use IoT technology to aid in achieving the 2030 Agenda of SDGs. According to a study conducted in partnership with IoT research firm and IoT Analytics, 84% of existing IoT deployments can achieve the SDGs (Fig. 1.8). Surprisingly, 75% of these projects are focused on just five SDGs (World Economic Forum (2021).

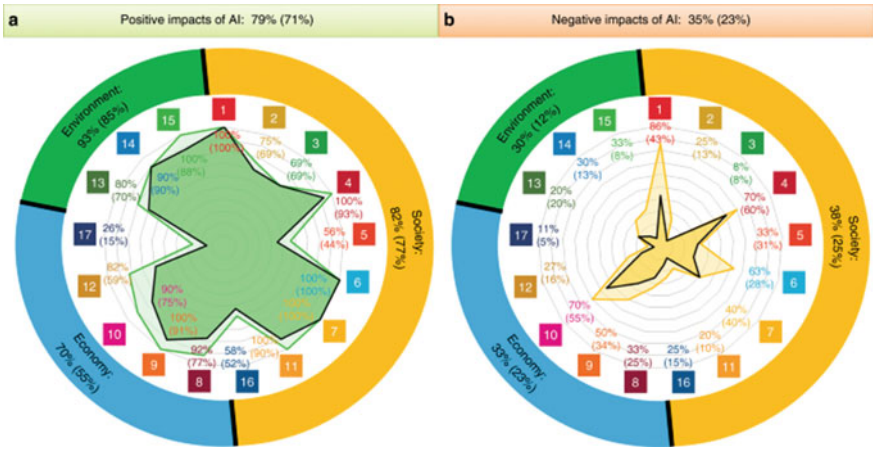

Fig. 1.7 Impact of AI on the various SDGs. Adapted from Vinuesa et al. (2020)

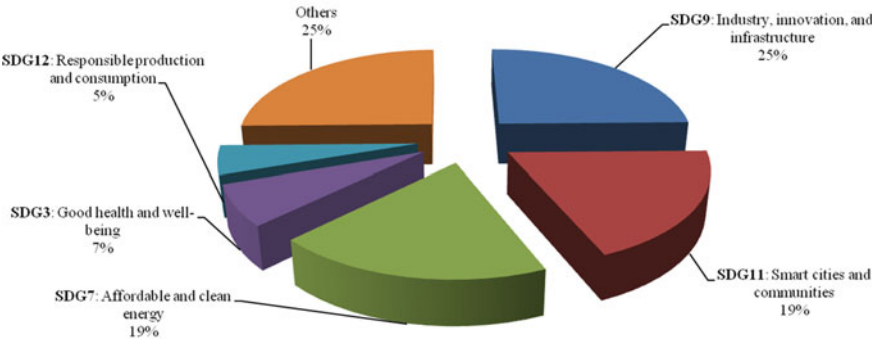

Fig. 1.8 Maximum deployment of IoT in SDGs

The Internet of Things plays a significant role in helping enterprises accomplish this goal. The combination of IoT and geospatial technology significantly improves three specific goals presented in Fig. 1.9.

1.6 Integration of Geospatial Technology with ICT and Its Significance

The advancement of cutting-edge technologies such as IoT, AI, ML, VR, Digital Twins, crowdsourcing, citizen science, VDI, and participatory sensing will alter how we work, live, and think. Geospatial technology is integrated with advanced technologies to create advanced tools for sustainable development and decision support systems at the regional level (Acharya and Lee 2019).

Fig. 1.9 Application of IoT with geospatial technology in SDGs

The challenges in geospatial data involved its acquisition, storage, transfer, sharing, searching, visualizing, and analysis of the data. The facets of big data generally refer to the three V's (i.e. Volume, Variety and Velocity) which is considered as common framework to describe big data (Laney 2001).

The remote sensing big data has numerous unique and solid characteristics; i.e., in the high-dimensional, dynamic state, the data should have nonlinearity characteristics, state, isomer, multi-scale, multi-source, isomer, and nonlinearity characteristics (Liu 2015). Figure 1.10 shows the integration of ICT with geospatial technology.

1.7 Gaps or Challenges

Integrating geospatial technology, i.e., remote sensing and geographical information system (RS and GIS) with information technology (IT), i.e., big data, AI/ML, and IoT, will change how we live, work, and the thought process. Implementing the new technology with advanced tools for sustainable development will change the method of assessment, monitoring, and decision support system. The geospatial data and big data-driven algorithm, AI/ML, and IoT will help prove high-quality, most accurate, real-time integrated, location-enabled analysis with robust decision-making tools.

Nonetheless, with the advancement of the integration of technologies, there are still some challenges and limitations. The challenges exist in various aspects; some are data-related, administration level, implementation level challenges, etc. Developed countries have enough resources, data, and awareness, but many developing countries face significant challenges due to accurate high, definition data, resources, skilled workforce, and limited understanding. Some significant challenges are identified and presented in Fig. 1.11. The challenges related to various aspects are given as follows.

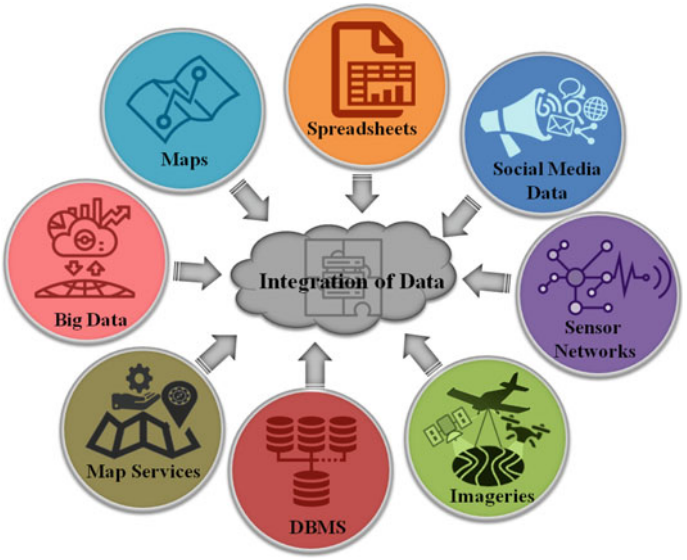

Fig. 1.10 Integration of ICT with geospatial technology

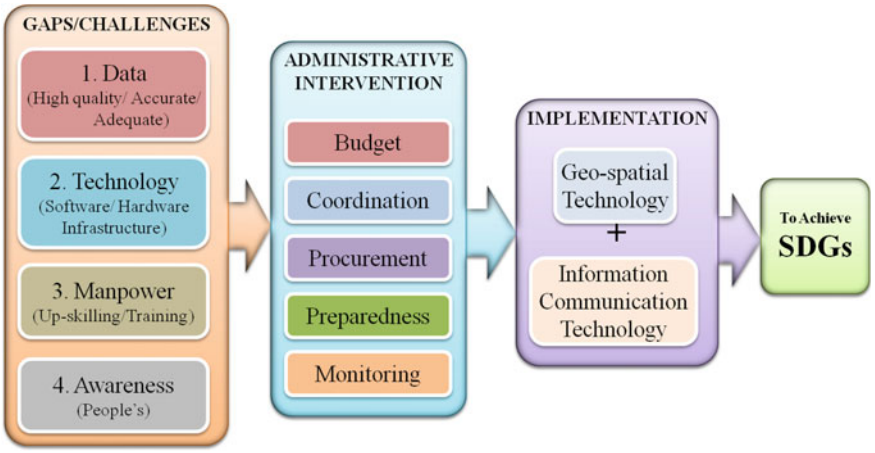

Fig. 1.11 Challenges, intervention, and implementation pattern to achieve SDGs

1.7.1 Data-Related Challenges

Various sources of data are an integral part of accurate analysis. The most critical datasets are RS data produced by many RS satellites and ground sensors. The datasets deal with calibration, quality, interoperability, data processing, visualization, etc. Other factors, i.e., image processing techniques, spectral uncertainty, and images

resolutions, affect RS data quality. Mobile phone data, cloud data, citizen generated, etc., used for big data analysis are not accessible. The availability of ground data or secondary data for the specific area will also affect the analysis. Procuring accurate data within a particular time frame is a challenging factor that needs administrative intervention.

1.7.2 Lack of Technology Infrastructure

Technologies are changing day by day with the advancement of tools and approaches. A considerable amount of data needs high data processing power hardware to process high volume data and high capacity of servers. Hence, underdeveloped countries need proper support to get those high-definition systems.

1.7.3 Skilled/Trained Manpower

Advanced technologies, including software, demand highly skilled human resources in IT sectors. Training the existing workforce using traditional analysis methods would be crucial to increasing professional human resources. More specifically, developing countries, including Small Island Developing States (SIDS), may not have sufficient experts and human resources to take advantage of these innovative technologies fully. Countries can strengthen their human resources base and build capacity through regional and international partnerships (UNESCAP 2018) and Regional Space Applications Programme for Sustainable Development (RESAP).

1.7.4 Lack of Awareness

Lack of awareness about data, technology, and new ideas is widespread in developing countries. There are fears among the traditional practitioners regarding the new geospatial and information technology that exists in developing countries, which will slow down the rate of advancement.

1.7.5 Others

Budget constraints in technology, workforce up-skilling, and data procurement are significant challenges in some developing countries. Administrative preparedness and proper coordination with technology advancement are essential to address the

significant challenges, and it should be encouraged to achieve the global Sustainable Development Goals.

1.8 Conclusions

- The current chapter shows a comprehensive review of the combined use of geospatial tools/techniques and information/communication technology to achieve SDGs.
- SDGs have been set up to address many global challenges, such as poverty, inequality, climate change, environmental degradation, peace, and justice.
- Achieving SDGs and their universality would be possible through easily available data from affordable sources such as remote sensing images and readily available sources.
- Earth observation plays a crucial role in monitoring the SDGs, given its cost-effectiveness on data acquisition on all scales and information richness.
- Advanced technology/earth observation for assessing, monitoring, and decision-making is integral in addressing the indicators associated with SDGs.
- A sustainable society would be better ensured with a proper sustainable development plan. In this context, the UN has set up seventeen SDGs to achieve the target by 2030. Hence, there will be a future need to develop new methods and techniques to process enormous earth observation data of various sizes, sources, and formats.
- The recent advancement in big data analytics, IoT, AI, etc., could play a meaningful role in reaching SDGs set up by many developed and developing countries through Spatial Decision Support Systems.

References

Acharya TD, Lee DH (2019) Remote sensing and geospatial technologies for sustainable development: a review of applications. Sens Mater 31(11):3931–3945

Arroyo JA, Gomez-Castaneda C, Ruiz E, de Cote EM, Gavi F, Sucar LE (2017) UAV technology and machine learning techniques applied to the yield improvement in precision agriculture. In: 2017 IEEE Mexican humanitarian technology conference (MHTC). IEEE, pp 137–143

Asensio S (1997) Targeting the poor-poverty indicators in a spatial context. M.Sc. thesis. ITC, The Netherlands

Avtar R, Tripathi S, Aggarwal AK, Kumar P (2019) Population–urbanization–energy nexus: a review. Resources 8(3):136

Bi WL, Hosny A, Schabath MB, Giger ML, Birkbak NJ, Mehrtash A, Allison T, Arnaout O, Abbosh C, Dunn IF (2019) Artificial intelligence in cancer imaging: clinical challenges and applications. CA Can J Clin 69:127–157

Bonaiuto M, Fornara F, Ariccio S, Cancellieri UG, Rahimi L (2015) Perceived residential environment quality indicators (PREQIs) relevance for UN-HABITAT city prosperity index (CPI). Habitat Int 45:53–63

Dahdouh-Guebas F (2002) The use of remote sensing and GIS in the sustainable management of tropical coastal ecosystems. In: Environment, development and sustainability, vol 4. https://doi.org/10.1023/A:1020887204285

Daiman A, Goyal S (2020) Geo-spatial approach based mapping using proximity analysis techniques for establishment of new higher education colleges—a case study of chambal division, Madhya Pradesh, India. Asian J Multidimension Res (AJMR) 9(2):237–246

Dangermond BJ, Artz M (2010) Climate change is a geographic problem the geographic approach to climate change. ESR I:32

Decuyper M, Chávez RO, Čufar K, Estay SA, Clevers JG, Prislan P, Sass-Klaassen U et al (2020) Spatio-temporal assessment of beech growth in relation to climate extremes in Slovenia—an integrated approach using remote sensing and tree-ring data. Agric For Meteorol 287:107925

Dovey K (2015) Sustainable informal settlements? Proc Soc Behav Sci 179:5–13. https://doi.org/10.1016/j.sbspro.2015.02.406

Eagle N, Macy M, Claxton R (2010) Network diversity and economic development. Science 328(5981):1029 LP-1021031

El-Batran M, Arandel C (2005) A shelter of their own: informal settlement expansion in greater Cairo and government responses. Environ Urban 10(1):217–232. https://doi.org/10.1630/095624798101284392

Elias P, Benekos G, Perrou T, Parcharidis I (2020) Spatio-temporal assessment of land deformation as a factor contributing to relative sea level rise in coastal urban and natural protected areas using multi-source earth observation data. Rem Sens 12(14):2296

Elvidge CD, Sutton PC, Ghosh T, Tuttle BT, Baugh KE, Bhaduri B, Bright E (2009) A global poverty map derived from satellite data. Comput Geosci 35(8):1652–1660. https://doi.org/10.1016/j.cageo.2009.01.009

ESRI. https://learn.arcgis.com/en/paths/solve-problems-for-sustainable-development-goals

Ferguson RL, Korfmacher K (1997) Remote sensing and GIS analysis of seagrass meadows in North Carolina, USA. Aquat Bot 58(3–4):241–258. https://doi.org/10.1016/S0304-3770(97)00038-7

Ganguly K, Modi M, Saxena MR, Bharadwaj R, Divya VV, Rajiv K, Shankar GR, Shankar TR, Bhanumurthy V, Murthy YVNK (2017) A multi-scale feature extraction approach to improve land use land/cover classification accuracy using IRS LISS-IV imagery. Rem Sens Land 1(1):3–17. https://doi.org/10.21523/gcj1.16010101

Ganguly K, Shabnam S, Das S, Mitran T (2021) Assessment of Urban sprawl impact on agricultural land use using geospatial techniques. In: Mitran T, Meena RS, Chakraborty A (eds) Geospatial technologies for crops and soils. Springer, Singapore. https://doi.org/10.1007/978-981-15-6864-0_14

Habitat U (2015) Governing council of the United Nations settlements programme, twenty fifth session Nairobi, 17–23 Apr 2015 item 6 of the provisional agenda

Hák T, Janoušková S, Moldan B (2016) Sustainable development goals: a need for relevant indicators. Ecol Ind 60:565–573

Haslauer E, Biberacher M, Blaschke T (2012) GIS-based backcasting: an innovative method for parameterization of sustainable spatial planning and resource management. Futures 44(4):292–302. https://doi.org/10.1016/j.futures.2011.10.012

Huntingford C, Jeffers ES, Bonsall MB, Christensen HM, Lees T, Yang H (2019) Machine learning and artificial intelligence to aid climate change research and preparedness. Rem Sens Lett 14:124007

Istepanian RSH, Al-Anzi T (2018) m-Health 2.0: new perspectives on mobile health, machine learning and big data analytics. Methods 151:34–44

Ivić M (2019) Artificial intelligence and geospatial analysis in disaster management. Int Arch Photogram Rem Sens Spat Inf Sci XLII-3/W8

Kaab A, Huggel C, Fischer L (2006) Remote sensing technologies for monitoring climate change impacts on glacier- and permafrost-related hazards. In: ECI conference on geohazards, vol 10

Karanja I (2010) An enumeration and mapping of informal settlements in Kisumu, Kenya, implemented by their inhabitants. Environ Urban 22(1):217–239. https://doi.org/10.1177/0956247809362642

Khanna A, Kaur S (2020) Internet of things (IoT), applications and challenges: a comprehensive review. Wirel Pers Commun 114:1687–1762. https://doi.org/10.1007/s11277-020-07446-4

Kharas H, Prizzon A, Rogerson A (2014) Financing the post-2015 sustainable development goals. Overseas Development Institute, London

Kuffer M, Wang J, Nagenborg M, Pfeffer K, Kohli D, Sliuzas R, Persello C (2018) The scope of earth observation to improve the consistency of the SDG slum indicator. ISPRS Int J Geo Inf 7(11):428. https://doi.org/10.3390/ijgi7110428

Kusumaningtyas R, Kobayashi S, Takeda S (2009) The impact of local community agricultural practices on livelihood security and forest degradation around the Tesso Nilo national park in Riau Province, Sumatra, Indonesia. Tropics 18(2):45–55. https://doi.org/10.3759/tropics.18.45

Laney D (2001) 3D data management: controlling data volume, velocity and variety. META Group Res Note 6(70):1

Liu J, Fritz S, Van Wesenbeeck CFA, Fuchs M, You L, Obersteiner M, Yang H (2008) A spatially explicit assessment of current and future hotspots of hunger in sub-Saharan Africa in the context of global change. Glob Planet Chang 64(3–4):222–235. https://doi.org/10.1016/j.gloplacha.2008.09.007

Liu P (2015) A survey of remote-sensing big data. Front Environ Sci 3:45. https://doi.org/10.3389/fenvs.2015.00045

Lüge T, Sudhoff RS, Lessard-Fontaine A, de la Borderie S, Soupart M (2014) GIS support for the MSF Ebola response in Guinea in 2014 case study. Médecins Sans Frontieres Operational Center, Geneva

Lwin KK, Sekimoto Y, Takeuchi W, Zettsu K (2019) City geospatial dashboard: IoT and big data analytics for geospatial solutions provider in disaster management. In: 2019 international conference on information and communication technologies for disaster management (ICT-DM). IEEE, pp 1–4

Machiwal D, Jha MK, Mal BC (2011) Assessment of groundwater potential in a semi-arid region of India using remote sensing, GIS and MCDM techniques. Water Resour Manage 25(5):1359–1386. https://doi.org/10.1007/s11269-010-9749-y

Maes WH, Steppe K (2019) Perspectives for remote sensing with unmanned aerial vehicles in precision agriculture. Trends Plant Sci 24(2):152–164

Maude RJ, Nguon C, Ly P, Bunkea T, Ngor P, Canavati De La Torre SE et al (2014) Spatial and temporal epidemiology of clinical malaria in Cambodia 2004–2013. Malar J 13(1):1–15. https://doi.org/10.1186/1475-2875-13-385

Meadows DH, Meadows DH, Randers J, Behrens WW III (1972) The limits to growth: a report to the club of Rome (1972), p 91

Meadows DH, Randers J, Meadows DL (2013) The limits to growth (1972). In: The future of nature. Yale University Press, pp 101–116

Mishra S, Singh N, Bhattacharya D (2021) Application-based COVID-19 micro-mobility solution for safe and smart navigation in pandemics. ISPRS Int J Geo Inf 10(8):571

Mitran T, Meena RS, Chakraborty A (2021a) Geospatial technologies for crops and soils: an overview. In: Geospatial technologies for crops and soils, pp 1–48

Mitran T, Meena RS, Chakraborty A (eds) (2021b) Geospatial technologies for crops and soils. Springer Nature Singapore Pte Limited

Nhamo L, Van Dijk R, Magidi J, Wiberg D, Tshikolomo K (2018) Improving the accuracy of remotely sensed irrigated areas using post-classification enhancement through UAV capability. Rem Sens 10(5):712

Okwi PO, Ndeng'e G, Kristjanson P, Arunga M, Notenbaert A, Omolo A et al (2007) Spatial determinants of poverty in rural Kenya. Proc Natl Acad Sci 104(43):16769–16774. https://doi.org/10.1073/pnas.0611107104

Orimoloye IR, Mazinyo SP, Nel W, Kalumba AM (2018) Spatiotemporal monitoring of land surface temperature and estimated radiation using remote sensing: human health implications for East London, South Africa. Environ Ear Sci 77(3):1–10. https://doi.org/10.1007/s12665-018-7252-6

Paulson B (1992) Urban applications of remote sensing and GIS analysis. In: Urban management programme

Quinteiro P, Rafael S, Vicente B, Marta-Almeida M, Rocha A, Arroja L, Dias AC (2019) Mapping green water scarcity under climate change: a case study of Portugal. Sci Total Environ 696:134024

Reddy SC, Jha CSS, Dadhwal VKK, Hari Krishna P, Vazeed Pasha S, Satish KVV et al (2016) Quantification and monitoring of deforestation in India over eight decades (1930–2013). Biodivers Conserv 25(1):93–116. https://doi.org/10.1007/s10531-015-1033-2

Riitters K, Wickham J, Costanza JKK, Vogt P (2016) A global evaluation of forest interior area dynamics using tree cover data from 2000 to 2012. Landscape Ecol 31(1):137–148. https://doi.org/10.1007/s10980-015-0270-9

Rosero-Bixby L (2004) Spatial access to health care in Costa Rica and its equity: a GIS-based study. Soc Sci Med 58(7):1271–1284. https://doi.org/10.1016/S0277-9536(03)00322-8

Sachs J, Schmidt-Traub G, Kroll C, Lafortune G, Fuller G, Woelm F (2020) The sustainable development goals and COVID-19. Sustainable Development Report. https://www.sdgindex.org/reports/sustainable-development-report-2020/

Saitoh SIS-II, Mugo R, Radiarta INN, Asaga S, Takahashi F, Hirawake T et al (2011) Some operational uses of satellite remote sensing and marine GIS for sustainable fisheries and aquaculture. ICES J Mar Sci 68(4):687–695. https://doi.org/10.1093/icesjms/fsq190

Saraf AK, Choudhury PR (1998) Integrated remote sensing and GIS for groundwater exploration and identification of artificial recharge sites. Int J Rem Sens 19(10):1825–1841. https://doi.org/10.1080/014311698215018

Soto V, Frías-Martínez E (2011) Automated land use identification using cell-phone records. In: Proceedings of the 3rd ACM international workshop on MobiArch, pp 17–22

Tatem AJJ, Bird TJJ, Bjelland J, Bengtsson L, Alegana VAA, Iqbal AMM et al (2017) Mapping poverty using mobile phone and satellite data. J R Soc Interface 14(127):20160690. https://doi.org/10.1098/rsif.2016.0690

Thapa RB, Motohka T, Watanabe M, Shimada M (2015) Time-series maps of aboveground carbon stocks in the forests of central Sumatra. Carbon Balance Manage 10(1):1–13. https://doi.org/10.1186/s13021-015-0034-5

Topol EJ (2019) High-performance medicine: the convergence of human and artificial intelligence. Nat Med 25(1):44–56

Trinidad JE (2022) Spatial analysis of high school dropout: the role of race, poverty, and outliers in New York City

Ulugtekin N, Bektas F, Dogru AO, Goksel C, Alaton IA (2005) The use of remote sensing and GIS technologies for comprehensive wastewater management. In: International symposium on remote sensing of environment, global monitoring for sustainable and security. https://www.isprs.org/proceedings/2005/isrse/html/papers/483.pdf

United Nations (2016) The sustainable development goals 2016. eSocialSciences

Vinuesa R, Azizpour H, Leite L, Balaam M, Dignum V, Domisch S, Felländer A, Langhans SD, Tegmark M, Nerini FF (2020) The role of artificial intelligence in achieving the sustainable development goals. Nat Commun 11(233). https://doi.org/10.1038/s41467-019-14108-y

VoPham T, Hart JE, Laden F, Chiang YY (2018) Emerging trends in geospatial artificial intelligence (geoAI): potential applications for environmental epidemiology. Environ Health 17(1):40

Wang X, Zhang F, Ding J (2017) Evaluation of water quality based on a machine learning algorithm and water quality index for the Ebinur Lake Watershed, China. Sci Rep 7(1):1–18
World Economic Forum (2021) IoT for sustainable development project. https://widgets.weforum.org/iot4d/index.html
Yu F, Sun W, Li J, Zhao Y, Zhang Y, Chen G (2017) An improved Otsu method for oil spill detection from SAR images. Oceanologia 59(3):311–317

Chapter 2
Comparison of Maximum Likelihood, Neural Networks, and Random Forests Algorithms in Classifying Urban Landscape

Akanksha Balha and Chander Kumar Singh

Abstract Land use land cover (LULC) is a significant component of remote sensing since it is employed in a variety of analyses, from change detection to geographic modeling. As a result, creating an accurate LULC map is critical. Three different pixel-based classification algorithms [i.e., maximum likelihood (ML), neural networks (NN) and random forests (RF)] were utilized to examine their relative performance in generating remotely sensed LULC maps in the current study. The research was carried out using high-resolution satellite images. The classification results are evaluated using accuracy measures derived from the confusion matrix. The findings suggest that it is difficult to achieve higher accuracy in classifying large urban areas using a 5 m resolution satellite dataset. The comparative results indicate that random forests have outperformed ML and NN in classifying the urban land cover using a high-resolution image. The user and producer accuracies of LULC are found to show no particular trend with any classification algorithm.

Keywords LULC · Pixel-based classification · Maximum likelihood · Neural networks · Random forests

2.1 Introduction

Land use land cover (LULC) gives a sense of landscape and has been widely used in planning for resource management using remote sensing (Gondwe et al. 2021; King 2002). The land cover is an important component that influences different aspects of the physical and human environment, affecting ecological systems (Foody 2002; Gondwe et al. 2021). The rising availability of satellite data, as well as improved knowledge of remote sensing technology's potential applications, provide the required push for monitoring land cover change. The combination of geographic information systems (GIS) and deep learning with remote sensing will give the tools

A. Balha · C. K. Singh (✉)
Department of Natural and Applied Sciences, TERI School of Advanced Studies, 10 Institutional Area, Vasant Kunj, New Delhi 110 070, India
e-mail: chander.singh@terisas.ac.in

V. P. Singh et al. (eds.), *Application of Remote Sensing and GIS in Natural Resources and Built Infrastructure Management*, Water Science and Technology Library 105,
https://doi.org/10.1007/978-3-031-14096-9_2

needed for land cover mapping (Arndt and Lunga 2021; Geneletti and Gorte 2003). Satellite image classification is critical in many remote sensing applications (Wang et al. 2021). Automated image classification is one of the simplest and most preferred methods for preparing an area's land use land cover (LULC) (Rozenstein and Karnieli 2011).

Appropriate classification algorithms are required to obtain information from satellite data (Chandra and Bedi 2021). Pixel-based classification, a conventional method of preparing LULC, relies on spectral data recorded as digital numbers (DN) in each pixel, with each pixel representing a different feature on the earth's surface. Over the last few decades, a variety of classification algorithms have been created and (Lu and Weng 2007) provide a summary of these techniques. There are two types of classifiers: basic and advanced. *K*-Means, ISODATA, MLC, and minimal distance to means are just a few of the popular categorization algorithms (Erdas Inc 1999; Lillesand and Kiefer 1999; Mather 2004). The artificial neural network (ANN) is an example of an advanced categorization system (Verbeke et al. 2004). Selecting a good classifier is important to achieve increased classification accuracy (Chandra and Bedi 2021; Lu and Weng 2007). Their findings show that the hybrid technique (73.5%) outperformed the unsupervised (70.67%) and supervised (60.83%) algorithms. (Srivastava et al. 2012) compared three pixel-based classification approaches—maximum likelihood (MLC), support vector machine (SVM), and artificial neural network (ANN)—using low-resolution Landsat TM/ETM+ pictures and found ANN to be a stronger classifier than SVM and ML. (Rozenstein and Karnieli 2011) used a low-resolution Landsat TM image to assess supervised (ML), unsupervised (ISODATA), and hybrid pixel-based categorization techniques (developed by combining spectral signatures from supervised and unsupervised classification).

Although higher resolution image contains more information than lower resolution images, pixel-based classification is a hurdle with high-resolution images (Cleve et al. 2008). Many features in a limited space in an urban region can be caught precisely in a greater spatial resolution image; however, unlike natural landscapes, this increased level of detail generates congestion in the intricacies of urban elements in the context of spectra (Arndt and Lunga 2021; Myint et al. 2011, 2006). This occurs as pixel-based classification only considers spectral data and ignores spatial data, as it is a critical characteristic in object-based classification (Benz et al. 2004; Duro et al. 2012; Myint et al. 2011; Walter 2004). "Mixed pixel problem" or "salt and pepper effect" in pixel-based categorization is produced by similar spectra from various characteristics in urban areas such as roads, rooftops, buildings, other bright surface objects, sidewalks, etc. (Cleve et al. 2008; Kelly et al. 2004; Myint et al. 2011; Ouyang et al. 2011). Consequently, spectral variability based on intra-class increases, the statistical separation between classes decreases, which leads to poor classification accuracy and misclassification (Su et al. 2004). The utilization of RF, NN, and MLC techniques for land cover mapping in the urban dominated area is investigated in this work. One can compare the performance of RF, NN, and MLC to achieve this goal.

2.2 Study Area

The study area chosen is Delhi, the capital city of India (Fig. 2.1). Delhi is situated between 28.40° and 28.88° N and 76.84° and 77.34° E.

The states of Uttar Pradesh and Haryana share a border with Delhi. The Indo-Gangetic alluvial plains run north and east of Delhi, west of the Thar Desert, and south of the Aravalli hill ranges.

Delhi covers an area of 1483 km^2. The Aravalli Range, the Yamuna River, and the alluvium plains between them make up the physiography of Delhi. Low ridges, isolated hills, and huge moderately undulating plains characterize the region's geography. At the ridge, the height ranges from 332 m above sea level to 62 m at the Yamuna (Central Ground Water Board (CGWB) 2016). The average annual rainfall in Delhi is 611.8 mm, with the monsoon season (July–September) accounting for 81 percent of the total (Central Ground Water Board (CGWB) 2016). The remainder of the annual precipitation falls as winter rain. A year is divided into four seasons based on temperature: in the cold season (November end–March mid), (ii) the hot season (March mid – June end), (iii) the monsoon season (July–September), and (iv) the fall season (October and November). The region of Delhi is heavily urbanized, with agricultural areas dominating the southwest and northwest (Central Ground Water Board (CGWB) 2016). The agricultural region is constantly changing as land is converted for various purposes. The ridge is the city's most distinguishing feature. The population of Delhi has increased from <2 million in 1901 to more than 16 million in

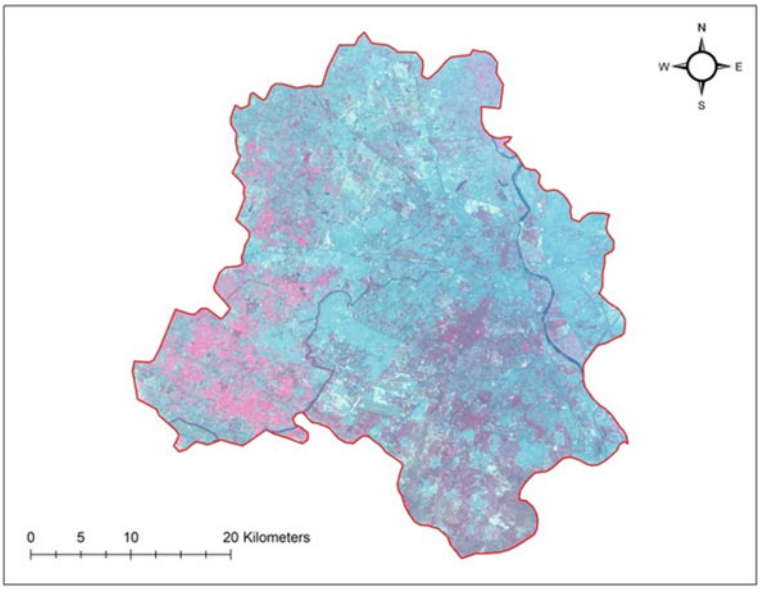

Fig. 2.1 Study area: Delhi

2011. This is due to the urbanization, which is caused mainly due to immigrating population excellent job opportunities in the city and its nearby towns of the National Capital Region (NCR) (DDA Delhi Development Authority 2017). The metropolis has a population of 29 million people and is expected to reach 36 million by 2030 (United Nations 2018).

2.3 Methodology

2.3.1 Preprocessing

For this study, we have used satellite images of LISS IV of the year 2016. The image was procured from National Remote Sensing Centre (NRSC), ISRO. The images are of a higher spatial resolution of 5 m. The image was preprocessed (haze reduction) using ERDAS 2015 (Geospatial 2016) to reduce the haze and increase the contrast of the image. Further, the preprocessed image scenes were mosaicked, and the resultant image was subset to the boundary of Delhi to obtain a high-resolution satellite image of Delhi.

2.3.2 Classification Algorithms

In this study, the performance of three classification algorithms, i.e., maximum likelihood (ML), neural network (NN), and random forest (RF) are to be compared, which are discussed below in brief.

(i) Maximum likelihood algorithm is dependent on Bayes' theorem of decision making which is expressed as Eq. (2.1). ML outperforms other parametric classification techniques when dealing with normally distributed data (Otukei and Blaschke 2010; Srivastava et al. 2012). However, it may not produce good results for non-normally statistically distributed data.

$$D = \ln(a_c) - [0.5 \ln(|\text{cov}_c|)] - [0.5(X - M_c)T(\text{cov}_c - 1)(X - M_c)] \tag{2.1}$$

where

D is the likelihood,
X is the measurement vector of the candidate pixel,
c is a particular class,
a_c is the probability percent of any candidate pixel to be a member of class c,
cov_c is a covariance matrix comprising pixels belonging to the class sample,

M_c is the mean of the sample of class c,
$|\text{cov}_c|$ is the determinant of cov_c,
ln is a natural logarithm function,
cov_c^{-1} is inverse of cov_c,
T is the transposition function.

(ii) Neural network doesn't require data of any specific statistical distribution (Srivastava et al. 2012; Shao and Lunetta 2012; Tu 1996; Zhang 2014). In the empirical and black box nature, the probability of overfitting and higher computation is regarded as the demerits of the algorithm. The logistic activation function used is expressed as Eq. (2.2)

$$o_j = 1/\left(1 + e^{-\lambda \text{net}_j}\right) \tag{2.2}$$

where λ is a gain factor and o_j is the output j;

$$\text{net}_j = \sum_i w_{ji} o_i$$

where o_i is the output of external unit i and w_{ji} is the interconnection channel weight to unit j from i.

(iii) Random forests, which are robust to hefty datasets and don't need data of any specific statistical distribution, classify based on the voting system (Hayes et al. 2014; Long et al. 2013; Puissant et al. 2014; Rodriguez-Galiano et al. 2012). The black box nature of the algorithm is its demerit. The time required for training random forests is expressed by Eq. (2.3).

$$cT\sqrt{M}N \log N \tag{2.3}$$

where T is the number of trees, M is the number of variables, c is a constant dependent on the data complexity, and N is the number of instances.

2.3.3 Image Classification

The classification of the satellite image was processed in R v. 3.3.2 (R Development Core Team 2016). For image classification in R, different add-on packages such as the "rasclass" package for ML (Wiesmann and Quinn 2011), "randomForest" package (Liaw and Wiener 2002) for RF and "nnet" package for NN (Venables and Ripley 2002) were used in R. A training dataset comprising spectral signatures from more than 2000 pixels was prepared and used for classification. The same set of training pixels was employed for all algorithms. The LULC classes identified in the image to prepare the LULC map include dense vegetation, built-up, waterbody, open land, sparse vegetation, sediment, and scrubland. To evaluate the classification results from

different algorithms, an accuracy assessment using a confusion matrix was carried out in ERDAS 2015.

2.4 Results and Discussion

Figure 2.2 depicts the LULC maps classified using all of the techniques investigated. The generated error matrix was used to assess the accuracy of all the LULC maps.

2.4.1 Comparison of Overall Accuracies

The LULC maps classified using ML, RF, and NN are shown in Fig. 2.2. The results of the accuracy assessment reveal that the overall accuracy of the LULC maps classified using ML, RF, and NN is approximately 49.4%, 56.8%, and 39.7%, respectively. Though the obtained accuracy is lower than the acceptable accuracy (Anderson et al. 1976). We aim only for the comparative performance of algorithms rather than further utilizing the maps for any assessment. To avoid any biases in the comparison, post-classification processing including filtering, recoding, or was not done. The findings derived from overall accuracy reveal that RF is found as the best classifier followed by ML. NN is found to produce the least accurate LULC.

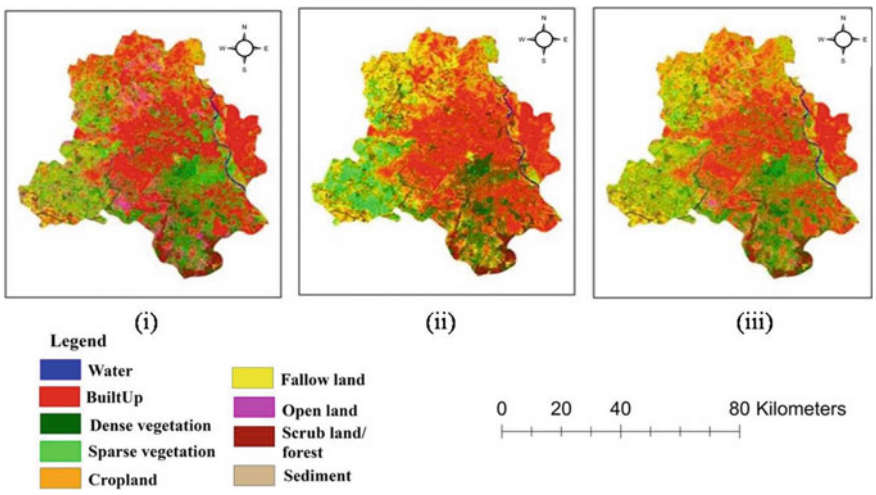

Fig. 2.2 LULC is classified using **i** maximum likelihood (ML), **ii** neural network (NN), and **iii** random forests (RF)

2.4.2 Comparison of Producer's and User's Accuracies

The producer (PA) and user accuracy (UA), as well as overall accuracy for each LULC, were calculated (Table 2.1). The producer's and user's accuracies of LULC classes do not show any particular trend with any classification algorithm. Concerning producer's accuracy (PA), RF has shown higher accuracy with water body, built-up, and scrubland; NN has shown higher accuracy with dense vegetation, fallow land; ML has shown higher accuracy with sparse vegetation, cropland, open land, and sediment.

Concerning user's accuracy (UA), RF has shown higher accuracy with cropland, dense vegetation, waterbody, open land, and built-up; ML has shown higher accuracy with sparse vegetation, fallow land, scrubland, and sediment.

Table 2.1 Accuracy assessment results of different classification algorithms

LULC classes	Accuracy	ML	NN	RF 2016
Water	PA	74.1	48.4	80.7
	UA	58.9	83.3	96.2
Built-up	PA	46.6	68.9	75.6
	UA	59.4	61.6	73.4
Dense vegetation	PA	84.3	84.4	75.0
	UA	54.0	43.6	57.1
Sparse vegetation	PA	48.3	9.9	42.9
	UA	41.9	13.0	45.4
Cropland	PA	51.6	–	48.4
	UA	74.4	–	85.7
Fallow land	PA	26.7	57.0	52.3
	UA	44.2	35.3	39.1
Open land	PA	44.4	3.2	30.2
	UA	52.8	50.0	70.4
Scrubland/ forest	PA	65.6	62.5	71.9
	UA	39.6	20.2	35.4
Sediment	PA	70.0	–	10.0
	UA	17.5	–	16.7
OA		49.4	39.7	56.8
Kappa		0.4	0.2	0.4

PA producer's accuracy and *UA* user's accuracy

2.5 Conclusion

This research work presents a comparative analysis of three popular pixel-based algorithms. Nine LULC classes consisting of built-up, waterbody, sparse vegetation, dense vegetation, sediment, open land, and scrubland are identified. The comparative performance of classification algorithms is made without post-classification processing of LULC to avoid biases in results. The assessment of the algorithms is conducted using a confusion matrix derived from overall accuracy. The results reveal that it is difficult to achieve higher overall accuracy in classifying urban areas. The reason for this is attributed to heterogeneity in the urban landscape. The RF has performed better followed by ML and NN. Hence, for pixel-based classification of an urban area using satellite images of 5 m spatial resolution, an RF algorithm is recommended. Further, the study has also attempted to evaluate the algorithms based on the producer's and user's accuracy.

References

Anderson JR, Hardy EE, Roach JT, Witmer RE (1976) A land use and land cover classification system for use with remote sensor data. In: U.S. geological survey professional paper, vol 964, p 28

Arndt J, Lunga D (2021) Large-scale classification of urban structural units from remote sensing imagery. IEEE J Sel Top Appl Ear Obs Rem Sens 14:2634–2648

Benz UC, Hofmann P, Willhauck G, Lingenfelder I, Heynen M (2004) Multiresolution, object-oriented fuzzy analysis of remote sensing data for GIS-ready information. ISPRS J Photogram Rem Sens 58(3–4):239–258

Central Ground Water Board (CGWB) (2016) Aquifer mapping and ground water management plan of NCT Delhi. Central Ground Water Board, State Unit Office, New Delhi. http://cgwb.gov.in/. Accessed 29 June 2021

Chandra MA, Bedi SS (2021) Survey on SVM and their application in image classification. Int J Inf Technol 13(5):1–11

Cleve C, Kelly M, Kearns FR, Moritz M (2008) Classification of the wildland-urban interface: a comparison of pixel-and object-based classifications using high-resolution aerial photography. Comput Environ Urban Syst 32(4):317–326

DDA Delhi Development Authority (2017) Master plan of Delhi-2021. Accessed 29 June 2021

Duro DC, Franklin SE, Dubé MG (2012) A comparison of pixel-based and object-based image analysis with selected machine learning algorithms for the classification of agricultural landscapes using SPOT-5 HRG imagery. Rem Sens Environ 118:259–272

Erdas Inc (1999) Erdas Field Guide. Erdas Inc., Atlanta, Georgia

Foody GM (2002) Status of land cover classification accuracy assessment. Rem Sens Environ 80(1):185–201

Geneletti D, Gorte BGH (2003) A method for object-oriented land cover classification combining Landsat TM data and aerial photographs. Int J Remote Sens 24(6):1273–1286

Gondwe JF, Li S, Munthali RM (2021) Analysis of land use and land cover changes in Urban areas using remote sensing: case of Blantyre City. Discrete Dynamics in Nature and Society

Hayes MM, Miller SN, Murphy MA (2014) High-resolution landcover classification using random forest. Rem Sens Lett 5(2):112–121

Hexagon Geospatial (2016) Erdas imagine 2016. Intergraph Geospatial, Huntsville

Kelly M, Shaari D, Guo Q, Liu D (2004) A comparison of standard and hybrid classifier methods for mapping hardwood mortality in areas affected by "sudden oak death." Photogram Eng Rem Sens 70(11):1229–1239

King RB (2002) Land cover mapping principles: a return to interpretation fundamentals. Int J Rem Sens 23(18):3525–3545

Liaw A, Wiener M (2002) Classification and regression by random forest. R News 2(3):18–22

Lillesand TM, Kiefer RW (1999) Remote sensing and image interpretation. Wiley, New York

Long JA, Lawrence RL, Greenwood MC, Marshall L, Miller PR (2013) Object oriented crop classification using multitemporal ETM+ SLC-off imagery and random forest. Gisci Rem Sens 50(4):418–436

Lu D, Weng Q (2007) A survey of image classification methods and techniques for improving classification performance. Int J Rem Sens 28(5):823–870

Mather PM (2004) Computer processing of remotely sensed images: an introduction. Wiley, West Sussex

Myint SW, Gober P, Brazel A, Grossman-Clarke S, Weng Q (2011) Per-pixel vs. object-based classification of urban land cover extraction using high spatial resolution imagery. Rem Sens Environ 115(5):1145–1161

Myint SW, Mesev V, Lam NSN (2006) Texture analysis and classification through a modified lacunarity analysis based on differential box counting method. Geogr Anal 38:371–390

Otukei JR, Blaschke T (2010) Land cover change assessment using decision trees, support vector machines and maximum likelihood classification algorithms. Int J Appl Earth Obs Geoinf 12:S27–S31

Ouyang ZT, Zhang MQ, Xie X, Shen Q, Guo HQ, Zhao B (2011) A comparison of pixel-based and object-oriented approaches to VHR imagery for mapping saltmarsh plants. Eco Inform 6(2):136–146

Puissant A, Rougier S, Stumpf A (2014) Object-oriented mapping of urban trees using Random Forest classifiers. Int J Appl Earth Obs Geoinf 26:235–245

R Development Core Team (2016) R: a language and environment for statistical computing, Vienna. http://www.R-project.org/. Accessed Sept 2017

Rodriguez-Galiano VF, Ghimire B, Rogan J, Chica-Olmo M, Rigol-Sanchez JP (2012) An assessment of the effectiveness of a random forest classifier for landcover classification. ISPRS J Photogram Rem Sens 67:93–104

Rozenstein O, Karnieli A (2011) Comparison of methods for land-use classification incorporating remote sensing and GIS inputs. Appl Geogr 31(2):533–544

Srivastava PK, Han D, Rico-Ramirez MA, Bray M, Islam T (2012) Selection of classification techniques for land use/land cover change investigation. Adv Space Res 50(9):1250–1265

Shao Y, Lunetta RS (2012) Comparison of support vector machine, neural network, and CART algorithms for the land-cover classification using limited training data points. ISPRS J Photogram Rem Sens 70:78–87

Su Y, Huang PS, Lin CF, Tu TM (2004) Target-cluster fusion approach for classifying high resolution IKONOS imagery. IEEE Proc vis Image Sig Process 151:241–249

Tu JV (1996) Advantages and disadvantages of using artificial neural networks versus logistic regression for predicting medical outcomes. J Clin Epidemiol 49(11):1225–1231

United Nations (2018) World urbanization prospects, The 2018 Revision. Department of Economic and Social Affairs, United Nations. https://population.un.org/. Retrieved 29 June 2021

Verbeke LPC, Vancoillie FMB, De Wulf RR (2004) Reusing back-propagation artificial neural networks for land cover classification in tropical savannahs. Int J Rem Sens 25(14):2747–2771

Venables WN, Ripley BD (2002) Modern applied statistics with S, 4th edn. Springer, New York. ISBN 0-387-95457-0

Walter V (2004) Object-based classification of remote sensing data for change detection. ISPRS J Photogram Rem Sens 58:225–238

Wang P, Fan E, Wang P (2021) Comparative analysis of image classification algorithms based on traditional machine learning and deep learning. Pattern Recogn Lett 141:61–67

Wiesmann D, Quinn D (2011) Rasclass: supervised raster image classification. R package version 0.2.1. http://cran.r-project.org/web/packages/rasclass/index.html
Zhang A (2014) Collaboration in the Australian and Chinese mobile telecommunication markets. Springer

Chapter 3
Crowd-Assisted Flood Disaster Management

S. Koswatte, K. McDougall, and X. Liu

Abstract Natural disasters, including floods, cause significant damage to people's lives and properties and, in recent years, the frequency, complexity, and severity of these events appear to be increasing. Floods, in particular, cause more devastation, death, and economic impact than any other natural disaster. Disaster reporting has now progressed from official media reporting sources to real-time on-site citizen reporters. Crowd-generated content related to disasters and other events is usually identified as Crowdsourced Data (CSD). This data is often termed geospatial CSD or Volunteered Geographic Information (VGI) when the geospatial properties are provided. With advances in technology, the opportunity for citizens to report incidents as CSD is now freely and widely available. However, the quality of CSD remains problematic as it is captured by people of different backgrounds and abilities on a variety of platforms. In general, CSD is deemed unstructured, and its consistency remains poorly described. The improvement and confirmation of quality are very important for CSD use in critical applications such as flood disaster management. This chapter discusses the background, challenges and opportunities, applications, and quality of CSD along with quality evaluation processes tested on the Ushahidi Crowdmap data of the 2011 Australian floods. CSD location availability analysis, relevancy analysis using the Geographic Information Retrieval (GIR), and credibility analysis using a naïve Bayesian network-based model are also discussed. The results of this study revealed that 59% of the ABC's 2011 Australian flood Crowdmap reports had location availability when the duplicate data were removed. They also show that GIR techniques and that naïve Bayesian models can be successfully applied to assess the CSD's relevancy and credibility. The fit-for-purpose analysis of CSD for disaster management can significantly improve CSD's precision, reliability, currency, and ability to supplement authoritative data sources by filling information gaps.

S. Koswatte (✉)
Department of RSGIS, Faculty of Geomatics, Sabaragamuwa University of Sri Lanka, Belihuloya, Sri Lanka
e-mail: sam@geo.sab.ac.lk

S. Koswatte · K. McDougall · X. Liu
Faculty of HES, School of Surveying and Built Environment, University of Southern Queensland, Toowoomba, Australia

V. P. Singh et al. (eds.), *Application of Remote Sensing and GIS in Natural Resources and Built Infrastructure Management*, Water Science and Technology Library 105,
https://doi.org/10.1007/978-3-031-14096-9_3

Keywords Floods · Crowdsourced data (CSD) · GIS · CSD quality · Disaster management

3.1 Introduction

Natural disasters such as floods, hurricanes, earthquakes, tsunamis, droughts, and wildfires have become more common and more serious in recent years. The International Federation of Red Cross and Red Crescent Societies' (IFRC) latest global disaster survey (IFRC 2020) reported that at least 410,000 people were killed during the last ten years due to extreme weather and climate-related disasters. The 2020 Australian bushfires killed at least 34 people, with 5900 buildings destroyed, and it was estimated that between 0.5 and 1.5 billion native animals were killed (van Oldenborgh et al. 2021). The Nepal earthquake on 25th April 2015 killed over 8700 people and injured more than 21,000 people. It devastated many historical sites and destroyed over 500,000 houses worth billions of dollars (OCHA 2015). Floods account for 30% of all natural disasters worldwide, causing more destruction, fatalities, and economic hardships than any other event (Degrossi et al. 2014; Helmrich et al. 2021; Songchon et al. 2021).

In responding to natural and manmade disasters, researchers and scientists are now identifying new tools and techniques for improving existing disaster management systems. In general, disaster management is challenging and cannot be handled efficiently by simply supplying more and more resources. It is impossible to accurately predict the occurrence, frequency, and severity of these natural disasters, so effective and timely management to minimize further threats to lives and properties is needed. Disaster management strategies need to be dynamic. A major flood event may develop gradually over a period of days while a cyclone may necessitate a more rapid management response. Mitigation initiatives such as the introduction of awareness campaigns, the strengthening of existing vulnerable systems, and the preparation of disaster recovery strategies will minimize human and property losses and make communities safer and more resilient (IFRC 2020).

In disaster management decision-making, having reliable and up-to-date geospatial information is critical. The uncertainty of real-time event information can cause delays or lead to incorrect disaster management decisions, while direct feedback from those who have been affected by disasters can help others save lives and properties. Readily and freely available online mapping tools and convenient modern location sensors have encouraged citizens to report these events, often in real-time with the assistance of online maps (Songchon et al. 2021). This type of citizen-reported data is often up-to-date and, hence, become a valuable source for disaster management purposes.

CSD that includes location information can be thought of as Volunteered Geographic Information (VGI) (Goodchild 2007), "crowdsourced geospatial data" (Heipke 2010), or "user-generated geographic content" (Fast and Rinner 2014) and is identified as a subset of CSD. Although there are quality and credibility problems

associated with CSD, it is more current and diverse than traditional geographic information. In some instances, when collected and managed properly, CSD outperforms official sources with respect to accuracy and context (Criscuolo et al. 2016). Current research into CSD is investigating potential quality improvement methods through numerous approaches, enabling CSD to be utilized in critical applications such as those for flood disaster management.

This chapter provides an overview of crowdsourced data and the role of the crowd in disaster management, including crowd-generated maps, with a specific focus on flood disasters. It discusses three quality aspects of CSD (location quality, credibility, and relevance) and offers a case study that analyzed crowd responses to a 2011 Australian flood disaster based on these three quality characteristics. The chapter is organized as follows. Section 3.2 explores the background of crowdsourced data, and Sect. 3.3 discusses challenges and opportunities in CSD. Section 3.4 introduces the applications of CSD, and Sect. 3.5 explores the quality and performance of CSD. Section 3.6 presents the case study on flood disaster management and, finally, Sect. 3.7 provides some conclusions regarding the utilization of fit-for-purpose CSD.

3.2 Background of Crowdsourced Data (CSD)

The technological advances in computing, information systems, positioning, and telecommunication have encouraged the community to engage in capturing disaster-related CSD (Helmrich et al. 2021; Songchon et al. 2021; Kankanamge et al. 2020). Moreover, the democratization of mapping tools and open-source initiatives have supported this trend toward geospatial CSD production. The success of crowdsourcing geospatial data is enabled by two basic technologies: (a) geo-referencing, either through global Navigational Satellite Systems (GNSS) or cellular towers; and (b) Web 2.0 development, which includes communication often made through IT platforms (Heipke 2010; Blohm et al. 2018).

Today, citizens "share and learn from their experiences through text (microblogs), photos (Flickr, Picasa, Panoramio), and maps (Google Maps, Google Earth), not only finding but also providing information" (Kankanamge et al. 2020; Spinsanti and Ostermann 2010). In this context, people engaged in CSD production range from novices to experts in particular fields; with data originating from different sources including geotagged photos, synchronous microblogging, social networking applications, sensor measurements, complete topographic maps, and other platforms (Antoniu 2016). Niu and Silva (2020) identified the key sources for CSD as (a) social media posts (b) Points of Interest (POIs) and (c) collaborative contributions through web-based forums.

Microblogs have recently become a popular service where users can broadcast short messages (generally less than 248 characters) conveniently using smartphones or similar devices. Many people use microblogging services such as Twitter and

Sina Weibo to share their information by posting short messages. Researchers have identified the opportunity of utilizing these services as social sensors for disaster-related actions including event detection through location inference.

Combining microblogging messages with locations provides the opportunity for understanding the impact of the disasters in society. A mobile device equipped with a location sensor (such as GNSS) can be used to identify geolocations. A tweet may be geotagged according to the latitude and longitude of the location by using a location sensor-enabled device. Using the geotag function can attach the latitude and longitude of the user's current location to each message as a geotag. However, most users are reluctant to enable this function because of privacy concerns. Therefore, most messages do not have geolocation information which limits their usefulness for rapid response to a sudden disaster. Researchers have begun testing mechanisms to determine the location included in a message's content.

3.3 Challenges and Opportunities in CSD

Researchers have identified several CSD concerns including crisis location inferencing issues, erroneous or fake reports, disagreements between amateur and expert opinions, false alerts in information, errors in handling duplicate reports (such as retweets), and diversity in tools and technologies used in crowdsourcing (Ogie et al. 2019).

Although CSD quality assessment is critical in crowd-supported disaster management, many researchers have identified that defining CSD quality assessment parameters is challenging. The use of conventional geospatial data quality assessment parameters is not practical due to CSD's highly unstructured nature, its varying quality, and undocumented metadata. However, Leibovici et al. (2017) suggested other than completely rejecting the International Organization for Standardization (ISO) quality measures for CSD quality assessment, it is better to decouple the Quality Assessment (QA) and Data Conflation and Data Fusion (DCDF) processes as much as possible. However, the current approaches in this regime are immature.

Disaster management decisions are typically based on the availability of current, reliable, and accurate data. It is critical to have a good understanding of the ongoing disaster before moving to make key disaster management decisions. Social media has made it easy to obtain up-to-date information during a crisis (Helmrich et al. 2021; Kankanamge et al. 2020), however, the quality of this information can be variable. From a consumer's perspective, high-quality data should be "intrinsically good" and "contextually appropriate" to the task at hand, "clearly presented" and "accessible" (Liaw et al. 2021; Wang and Strong 1996). Measuring intrinsic quality is more relevant to conventional geospatial data, and the judgment of extrinsic quality is more useful to crowdsourced type data. Generally, the refresh rate of CSD (i.e., the update frequency) is higher than conventional authoritative data, particularly when

they are associated with dynamic events. As uncertainty is a key issue related to CSD, quality assessment is vital before this data is utilized in disaster management decision-making (Koswatte et al. 2015).

The rapid detection of a particular event, such as a flood, and its accurate location is very important in disaster management. An event is identified as something that happens at a specific time and location, with all the associated circumstances and unavoidable consequences. In today's world, such events are frequently discussed and communicated via social media (Helmrich et al. 2021; Songchon et al. 2021). Researchers are currently working on emergency event detection and related studies using microblog message analysis to identify landslides (Musaev et al. 2014), floods (Shi et al. 2016), earthquakes, tsunamis (Chatfield and Brajawidagda 2012), and other burst detection (Karimi et al. 2015). In general, event detection algorithms are chosen for their ability to predict particular events rather than all possible events in a given timeframe (Paltoglou 2016).

In an emergency such as a flood, knowing the accurate location of the incident is extremely helpful in determining where to dispatch the required resources and to support victims. The identification of location data in microblog posts has inspired a wave of interest in recent years (Lingad et al. 2013). Given the usual confusion associated with non-geographic entities, identifying place names embedded in the text can also be difficult. As indicated previously, the location availability of Twitter messages (Tweets) has been described as limited. Furthermore, connecting messages from social networks and users with locations is a difficult task. Users can choose whether or not to connect to a place on services like Twitter and Facebook (Davis et al. 2011). The locations hidden in crowd-generated content such as tweets can sometimes be extracted using various Natural Language Processing (NLP) tools including Stanford NER, OpenNLP, Twitter NLP, and YahooPlaceMaker (Lingad et al. 2013).

3.4 Applications of CSD

Crises are generally first seen through the "eyes" of personal mobile phone cameras and shared in near real-time to worldwide media broadcasting organizations instead of through traditional communication channels. This allows emergency information to reach both the general public and disaster responders in a matter of minutes. The crowdsourced data may include maps generated through crowd responses that are associated with location information and becomes a valuable asset for awareness and decision-making.

Ushahidi is a crowdsourced mapping platform created to capture crowd input via cell phones and emails (Hirata et al. 2018; Pánek et al. 2017). Users can report incidents via SMS (Short Message Service), email, and the Internet, among other methods. Its popularity has grown over time, and it has been deployed successfully in a variety of disasters around the world. The most noticeable benefit is the simplicity with which mobile devices can be used to monitor events on the spot. Similar applications used in real-world disaster scenarios are "CrisisTracker" developed for tracking

Table 3.1 Characteristics of Ushahidi Crowdmaps used in three natural disasters (McDougall et al. 2012)

Characteristic	Queensland floods	Christchurch earthquake	Japanese Tsunami
Site establishment time	Approximately 48 h	12–24 h	6–12 h
Utilization	Alerts, photos, blocked roads, recovery points	Hazards, road closures, drinking water, building damage	Trapped people, dangerous areas that should be avoided, and supplies of food and clean water
Lifecycle	Active for approximately 5 weeks	Active for approximately 3 weeks	Active 8 months after the tsunami
Reported quality	99% verified reports	Unknown	6.1% verified
Availability of site	Data currently accessible	Site not available	Active
Number of reports	98,000	>100,000	>12,600

armed group activities, "CogniCity" to report urgent urban infrastructure issues, "TweetTracker" for monitoring and analyzing tweets for humanitarian and disaster relief, and "Twitcident" for manipulating crisis-related information (Ogie et al. 2019; Poblet et al. 2018).

Natural disasters appear to be becoming more common and their impact more severe. A series of devastating flash floods struck Australia (particularly Queensland) between December 2010 and February 2011. In February 2011, a magnitude 6.3 earthquake hit Christchurch in New Zealand, killing 181 people and causing over NZ $20 billion in property damage. In March 2011, Japan was struck by a massive earthquake with a magnitude of 8.9, 100 times stronger than the Christchurch earthquake, killing over 20,000 people and causing more than $300 billion in property and infrastructure damage (McDougall et al. 2012). Interestingly, in all these disasters, the Ushahidi platform was deployed successfully. Table 3.1 shows the characteristics of the Ushahidi Crowdmaps used in these three disasters.

Information required for flood disaster management can be gathered through a variety of collaborative activities such as knowledge sharing through social networks (eg., Twitter, Facebook), participatory sensing (e.g., citizen observatories), and participatory mapping (e.g., OpenStreetMap,[1] Wikimapia[2]) (Horita et al. 2015). The PetaJakarta.org[3] system is a unique example providing social media-based urban data collection facilities to "solicit, gather, sort, and map" citizens' reports related to flood situations through social media in real-time. This system was developed by the

[1] https://www.openstreetmap.org.

[2] https://wikimapia.org.

[3] https://petajakarta.org/banjir/en/index.html.

SMART Infrastructure Facility at the University of Wollongong, Australia in collaboration with the DKI Jakarta Regional Disaster Management Agency and Twitter Inc. (Ogie et al. 2019). A mobile application developed through a case study from the COBWEB[4] project enabled volunteers to report flood inundations via mobile phones (Leibovici et al. 2017). Another example of CSD applications is the AGORA-DS system developed by Horta et al. (Horita et al. 2015) which is a Spatial Decision Support System (SDSS) supporting decision-making during flood disaster management. Although there are numerous examples for collecting useful crowd inputs during disaster situations, the mechanisms for converting this information into quality spatial datasets are limited.

3.5 Quality and Performance of CSD

The technical advancements in mobile communication, positioning technology, smartphone apps, and other infrastructure innovations that support easy-to-use mobile applications, have made VGI production easier. However, its potential benefits and uses have been limited by data quality concerns including data credibility, reliability, and relevance, as well as validity, data structures, and missing metadata.

3.5.1 Credibility of Crowdsourced Data

The quality of crowdsourced data can be characterized using measures (often aligned with ISO specifications) and indicators (often dependent on biased and amateur contributions which are difficult to measure) (Antoniou and Skopeliti 2015; Senaratne et al. 2016). Basiri et al. (2019) categorized CSD quality assessment methods into: (a) comparison with authoritative data, (b) machine learning and pattern identification applied to users and their inputs, and (c) gatekeeping and weighting user inputs. They also highlighted spatial bias in crowdsourced contents and the lack of extensive analysis of these biases in CSD-related projects. In CSD, the information provided by the contributors cannot always be trusted as their skills, knowledge, and experiences vary greatly, and determining the contributors' reputations may not be practical. Volunteers in a crisis are often incredibly diverse, and their contributions are often only temporary. As a result, unlike many Twitter users with a long history of activity, profiling these contributors is difficult. Therefore, determining the credibility of the given data for potential decision-making use is a major challenge.

According to Hovland et al. (1953), credibility is defined as "the believability of a source or message," which consists of two dimensions: trustworthiness and expertise. However, the aspects of trust and expertise, as identified by Flanagin and Metzger (2008), can also be regarded as subjectively perceived as the study of credibility

[4] http://www.cobwebproject.eu.

is interdisciplinary. While the scientific community considers credibility to be an objective property of information quality, communication and social psychology researchers consider credibility to be more of a matter of perception (Flanagin and Metzger 2008; Fogg and Tseng 1999).

A Bayesian Network-based credibility assessment model developed by Kim (2013) for assessing the 2010 Haiti earthquake's CSD compared the results of the earthquake damage assessment with official information. The study showed the ability to identify microscopic effects on individual data which may be useful for understanding the quality and macroscopic variations of overall harm patterns. Moreover, the model was determined to be more appropriate for post-disaster management and hence indicates that a similar model may be applicable to CSD credibility detection for post-flood disaster management.

3.5.2 Relevance of Crowdsourced Data

Another important aspect of CSD to be tested before use in critical applications such as flood disaster management is its relevance or fitness for the purpose. As discussed previously, during a disaster event, people often use microblogs or dedicated crowdsourcing platforms such as Crowdmaps to communicate and add comments to others' posts. However, these communications are sometimes tangential to the key disaster event, and the CSD collections may contain content that is not relevant. Assessing the relevance of the CSD content for a selected purpose is important for the removal of irrelevant content.

The concept of relevance is highly cognitive and multidimensional (Borlund 2003), and it has long been explored in a variety of domains including but not limited to artificial intelligence and natural language processing, philosophy, psychology, information retrieval, and information science. Saracevic (1996) identified five types of relevance based on the relevant literature, namely (1) cognitive or topical relevance, (2) pertinence or intellectual relevance, (3) algorithmic relevance, and (4) affective or motivational relevance, and (5) situational relevance. Situational relevance, that is the "usefulness of the viewed and assessed information" considering a particular task and the information needs of the user (Andrade and Silva 2006), is more suited to determining the relevance of CSD in the context of post-flood disaster management.

3.6 Case Study: Flood Disaster Management

Floods are often caused through intense or protracted rainfall events that result in creeks and rivers overflowing their banks. Flash floods are the result of extremely heavy rainfall and are very common in Australia. Similar to other natural disasters, the risks caused by floods often develop quickly and recede over time. Disaster

management teams may be required to manage different areas of operations including search and rescue for lifesaving, infrastructure and resource management, resettlement, rehabilitation, and communication during and after a flood. Prioritizing these activities is based on the importance and level of risk at each stage of the flood.

In January 2011, the state of Queensland, Australia, "experienced its second-biggest flood since the beginning of the twentieth century" (van den Honert et al. 2011). It was caused by an extreme weather event due to the influence of a La Nina condition (a large-scale atmospheric phenomenon across the Pacific Ocean). The flood of January 2011 was Australia's first major flood since 1974 (Box et al. 2016). This severe flooding affected nearly 90 towns and 200,000 people, claiming 38 lives and costing more than AUD$ 2 billion. Citizen involvement through crisis reporting was very high in the 2011 Queensland, Australia flood disaster. More than 35,000 tweets (based on the #qldfloods hashtag) were sent during the 10–16 January 2011 period, with more than 11,600 of them on 12th January alone (Bruns et al. 2012).

During the early stages of the event, the Australian Broadcasting Corporation (ABC) deployed a customized Ushahidi-based Crowd-mapping platform (Fig. 3.1) to collect related information. Over 230,000 site visits were reported in just 24 h, indicating that the site was well-received by the public. According to ABC figures, the site received approximately 1500 reports, with almost 500 from the public and another 1000 from ABC moderators. The majority of reports were submitted via the online interface, but a small percentage were sent through email, Twitter, and SMS.

3.6.1 CSD Location Availability

The location availability of CSD is important in applications such as flood disaster management. However, not all CSD comes with clear location information as the enablement of location information is usually a deliberate action. Although location sensors are very common in today's handheld devices, the location availability of crowd-generated content such as tweets remains as low as 1–3% (Ozdikis et al. 2018; Koswatte et al. 2016) due to the location option of the application being disabled. Ushahidi Crowdmap reports are usually submitted by mobile devices with location sensors, or if the data is added by a user registered on the Crowdmap, the position can be marked graphically on the Crowdmap interface. In each case, the position is encoded in decimal degrees of latitude and longitude.

As identified by this research, 33% (704 out of 2136) of the reports submitted via the ABC's QLD flood crisis map between the 9th and 15th of January 2011 were location-enabled, while the remaining reports consisted of useful information such as a description of the event excluding location (Fig. 3.2a). Crowdsourced datasets may include many duplicate reports such as retweets, which are forwarded messages of the original posts. In the QLD flood crisis map reports, after duplicate removal, there were only 663 unique reports and 391 reports where the location was enabled. Therefore, the location availability of Crowdmap reports was 59% of the data (Fig. 3.2b).

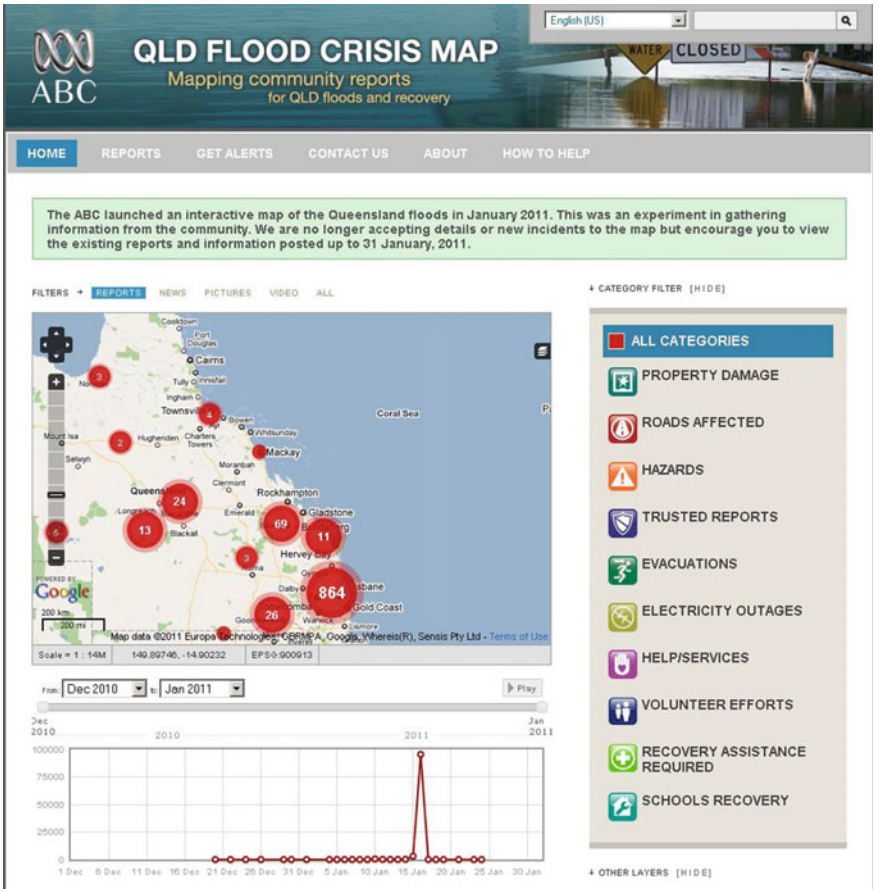

Fig. 3.1 ABC's Australian floods Ushahidi Crowdmap (Potts et al. 2011)

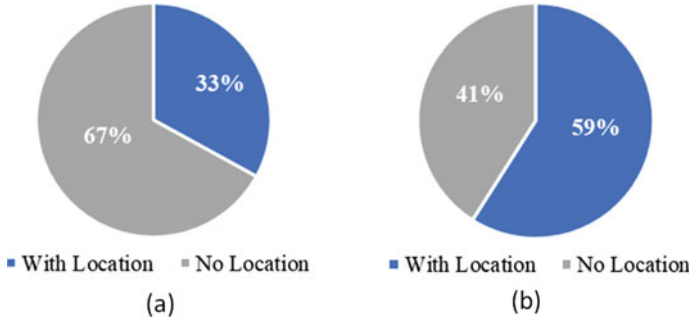

Fig. 3.2 Location availability of **a** full Crowdmap reports, **b** duplicates removed Crowdmap reports

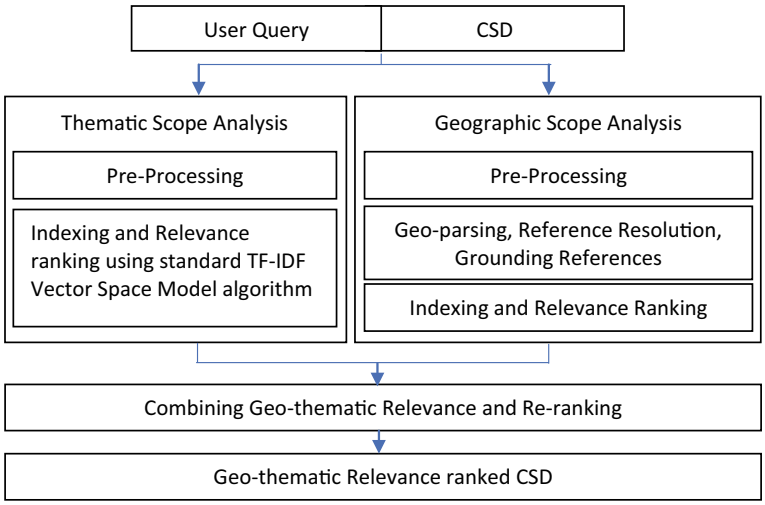

Fig. 3.3 CSD relevance detection approach adapted from Zaila and Montesi's (2015) GIR architecture

Geographic Information Retrieval (GIR) approaches can be used to analyze the CSD's relevancy. The suitability of each solution, however, is determined by the data and the task at hand.

Figure 3.3 shows the relevance analysis approach which was adopted from the Geographic Information Retrieval (GIR) architecture proposed by Zaila and Montesi (2015). In the modified architecture, the CSD was analyzed based on two key scopes: the thematic scope, and the geographic scope. In each scenario, CSD pre-processing was required to prepare the unstructured raw dataset for subsequent analysis using the steps are explained below:

1. Cleaning: removing unwanted content (e.g., numbers, units, time, date, hashtags, Twitter user accounts, and URLs)
2. Tokenization and Normalization: split the sentence into tokens, analyze and convert abbreviations and short forms commonly used in Twitter messages to normal form (e.g., B4 ≫ Before, Nxt ≫ Next, Cnr ≫ Corner)
3. Stemming and Lemmatization: adjusting to the base form (e.g., closed ≫ closing ≫ close)
4. Stop word removal: common English words (e.g., of, and, the, etc.)
5. Removal of non-words: numbers, punctuations, whitespaces (e.g., tabs, newlines, spaces).

Thematic Scope Analysis

The thematic scope relevance analysis was performed using the Lucene[5] IR system which is an open-source keyword matching information retrieval system built on

[5] http://lucene.apache.org.

the standard Term Frequency—Inverse Document Frequency Vector Space Model (TF-IDF VSM) model (Overell 2009).

The existence of relevant words in a document indicates the document's relevancy for a particular purpose. The weighting of the words can be determined by the significance of the task at hand in terms of information processing. The TF-IDF model is a widely used weighting tool (Bounabi et al. 2021). In this model, higher weights are applied to words that occur more often in a document. The more frequently a word (t) appears, the more important it is in the document (m). More commonly available words in the entire document collection (M), on the other hand, will be given a low weight.

$$\mathrm{TF}(t) = \frac{\text{Number of times the term } t \text{ occurs in a message}}{\text{Total number of terms in the message}}$$

$$\mathrm{IDF}(t) = \log_e \left[\frac{\text{Total number of messages}}{\text{Total number of messages the terms } t \text{ exists}} \right]$$

Therefore, the TF-IDF weight for term t in message m in the message collection (M) can be denoted as:

$$\text{TF-IDF}_{t,m} = \mathrm{TF}_{t,m} * \mathrm{IDF}_{t,m} \tag{3.1}$$

where

$$\mathrm{TF}_{t,m} = \frac{\sum_{i \in t} 1_{i=t}}{|m|} \tag{3.2}$$

$$\mathrm{IDF}_{t,m} = \log \frac{|M|}{\sum_{j \in M} 1_{t \in j}} \tag{3.3}$$

When the TF-IDF (Eq. 3.1) values of document terms are calculated, it represents the document in a vector space model. Each vector component represents a TF-IDF value of a term in the corpus dictionary. Thematic scope analysis was carried out utilizing Java[6] programs built on the Lucene API and its standard analyzer. One of the Java programs performed the indexing of the dataset and the other program performed the searching operations.

The quality of thematic scope analysis used the Lucene benchmark quality assessment package. According to the Lucene benchmark quality package results, the Mean Average Precision (MAP) of the quality assessment was calculated as 0.792 which is an indication of good system performance for relevance assessment as the value of 1 indicates the best performance.

[6] https://java.com.

Geographic Scope Analysis

The geographic scope analysis differs from the thematic analysis as it looks to identify the geographic scope. A natural language processing-based gazetteer lookup method was used to perform the geographic scope analysis tasks such as geo-parsing, reference resolution, and grounding references. The GATE[7] program makes these tasks much easier to complete. Pre-processing of a sample of the CSD dataset is needed to remove improper content such as duplicates. Tokenizing, stemming, and lemmatizing pre-processing operations required for thematic scope analysis cannot be undertaken during geographic scope analysis pre-processing because they will be conducted within the GATE program when a morphological analysis is performed.

Various algorithms and methods have been proposed by GIR research for indexing, relevance ranking, and merging thematic and geographic scopes. Yu and Cai (2007) suggested that it is often advantageous to consider the specificity of query scope in assessing CSD thematic relevance. This research implemented the method proposed by Yu and Cai (2007) for combining and re-ranking the CSD based on geo-thematic query specificity.

3.6.2 CSD Credibility Analysis: A Naïve Bayesian Network-Based Model for CSD Credibility Detection

The naïve Bayesian Networks are simpler BN-based probabilistic classifiers and can be used to calculate the presence of features in corpuses using their interrelations (Zamir et al. 2020).

CSD credibility can be classified using a function (f) defined as,

$$f(m,\theta) = \begin{cases} t_{\text{credible}} & \text{If } f(m,\theta) > T \text{ message classified as credible} \\ t_{\text{unreliable}} & \text{Else, the message is unreliable} \end{cases}$$

where m is a CSD post to be classified, θ is a vector of parameters, and "t_{credible}" and "$t_{\text{unreliable}}$" are status to be assigned to the CSD post based on the pre-defined threshold T to the posts.

An algorithm for the CSD credibility detection based on the naïve Bayesian Network was developed for the analysis. The Java programming language was used for coding the system within the NetBeans[8] Integrated Development Environment (IDE). The probability threshold was determined after the initial testing and was set at the 0.9 probability level (Threshold = 0.9).

Figure 3.4 depicts the key steps in the CSD credibility detection approach used in this research which was developed based on the naïve Bayesian Network and the classical "bag of words" model popular in spam email detection. The ABC's 2011 Australian Floods Crisis Map dataset (Ushahidi Crowdmap) was used as the

[7] https://gate.ac.uk/.

[8] https://netbeans.org/.

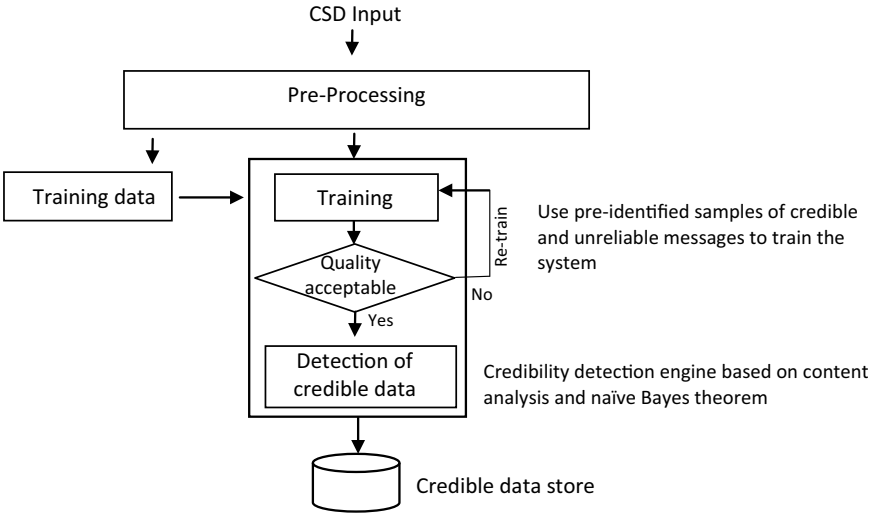

Fig. 3.4 CSD credibility detection workflow

input CSD. The whole dataset was initially pre-processed to prepare for the training, testing, and credibility detection as described above. The system was then trained and assessed in two different scenarios, unforced and forced, utilizing the testing data set to determine accuracy and performance improvements.

Once system training and testing was completed to an acceptable classification quality, a sample of 433 Ushahidi Crowdmap messages were analyzed for credibility. As Fig. 3.5a indicates, 54% (234 out of 433) of the messages were identified as credible using an unforced training classification. However, when the system was run under forced conditions, 77% (334 out of 433) of the messages were identified as credible (Fig. 3.5b). This is a more confident value than the previous result as the accuracy and precision of the credibility detection was higher.

3.7 Conclusion

Any spatial data-dependent project relies on the known quality of the spatial data. Rapid identification of appropriate and accurate spatial information is critical in disasters, such as floods, to prevent further damage, assist victims, and save lives. This work presented various CSD quality checks and improvement methods that are suitable for flood disaster management activities.

Volunteers in crises, in particular, are often extremely diverse, and their efforts are often only temporary. As a result, unlike many Twitter users with a long history of activity, profiling these contributors is difficult. Determining the credibility of CSD messages is a difficult process due to the high degree of heterogeneity in the data,

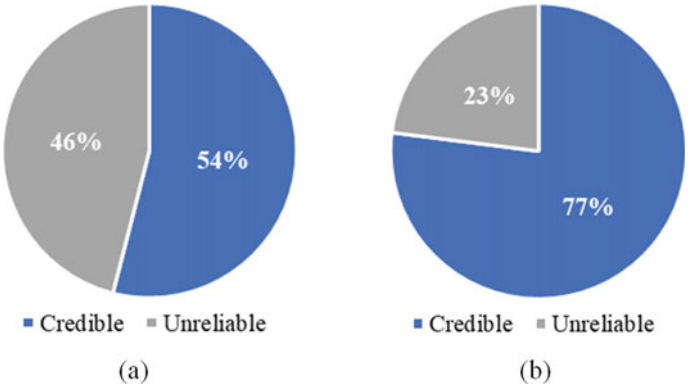

Fig. 3.5 Credibility of 2011 Australian floods Ushahidi Crowdmap data **a** under unforced environment **b** under forced environment

the lack of a standardized data structure, the diversity of the data sources, and the minimal metadata supplied. Therefore, new advances must be made to improve the quality and reliability of this data.

References

Andrade L, Silva MJ (2006) In: Proceedings of workshop on geographic information retrieval—SIGIR'06, Seattle

Antoniou V, Skopeliti A (2015) ISPRS Ann Photogram Rem Sens II-3/W5:345–351. https://doi.org/10.5194/isprsannals-II-3-W5-345-2015

Antoniu V (2016) GEOmedia 20(1)

Basiri A, Haklay M, Foody G, Mooney P (2019) Int J Geog Inf Sci 33 (8):1588–1593

Blohm I, Zogaj S, Bretschneider U, Leimeister JM (2018) Calif Manage Rev 60(2):122–149

Borlund P (2003) J Am Soc Inf Sci Technol 54(10):913–925

Bounabi M, Elmoutaouakil K, Satori K (2021) Int J Web Inf Syst 17(3):229–249. https://doi.org/10.1108/IJWIS-11-2020-0067

Box P, Bird D, Haynes K, King D (2016) Nat Hazards 81(3):1549–1568. https://doi.org/10.1007/s11069-016-2145-z

Bruns A, Burgess JE, Crawford K, Shaw F (2012) ARC centre of excellence for creative industries and innovation, Brisbane, Queensland. https://eprints.qut.edu.au/48241/1/floodsreport.pdf

Chatfield A, Brajawidagda U (2012) In: Lamp JW (ed) 23rd Australasian conference on information systems 2012 Australia. Deakin University, pp 1–10

Criscuolo L, Carrara P, Bordogna G, Pepe M, Zucca F, Seppi R, Oggioni A, Rampini A (2016) Capineri C, Haklay M, Huang H et al (eds) European handbook of crowdsourced geographic information, pp 57–74

Davis CA Jr, Pappa GL, de Oliveira DRR, de L. Arcanjo F (2011) Trans GIS 15(6):735–751

Degrossi LC, de Albuquerque JP, Fava MC, Mendiondo EM (2014) SEKE-2014, pp 570–575

Fast V, Rinner C (2014) ISPRS Int J Geoin 3(4):1278–1292

Flanagin AJ, Metzger MJ (2008) GeoJournal 72(3–4):137–148

Fogg B, Tseng H (1999) In: Proceedings of SIGCHI conference on human factors in computing systems. ACM, Pittsburgh, pp 80–87

Goodchild MF (2007) GeoJournal 69(4):211–221. https://doi.org/10.1007/s10708-007-9111-y
Heipke C (2010) ISPRS J Photogram Rem Sens 65(6):550–557. https://doi.org/10.1016/j.isprsjprs.2010.06.005
Helmrich AM, Ruddell BL, Bessem K, Chester MV, Chohan N, Doerry E, Eppinger J, Garcia M, Goodall JL, Lowry C (2021) Environ Model Softw 105124
Hirata E, Giannotti M, Larocca A, Quintanilha J (2018) J Flood Risk Manag 11:S98–S109
Horita FE, de Albuquerque JP, Degrossi LC, Mendiondo EM, Ueyama J (2015) Comput Geosci 80:84–94
Hovland CI, Janis IL, Kelley HH (1953) Yale University Press, New Haven, Connecticut, USA
IFRC (2020) Geneva, Switzerland. https://www.ifrc.org/document/world-disasters-report-2020
Kankanamge N, Yigitcanlar T, Goonetilleke A (2020) Int J Disaster Risk Reduct 48:101571
Karimi S, Yin J, Baum J (2015) Comput Linguist 41(3):539–548
Kim H (2013) M.Sc., University of Illinois at Urbana-Champaign. https://hdl.handle.net/2142/45350
Koswatte S, McDougall K, Liu X (2015) Surv Rev 47(344):307–315
Koswatte S, McDougall K, Liu X (2016) Int Arch Photogram Rem Sens 543–547
Leibovici DG, Rosser JF, Hodges C, Evans B, Jackson MJ, Higgins CI (2017) ISPRS Int J Geoin 6(3):78
Liaw ST, Guo JGN, Ansari S, Jonnagaddala J, Godinho MA, Borelli AJ,. de Lusignan S, Capurro D, Liyanage H, Bhattal N (2021) J Am Med Inform Assoc
Lingad J, Karimi S, Yin J (2013) In: Proceedings of the 22nd international conference on world wide web, pp 1017–1020
McDougall K (2012) In: Rajabifard A, Coleman D (eds) Proceedings of GSDI-2012, Quebec City, Canada, 2012. Spatially enabling Government, Industry and Citizens. GSDI Association Press, pp 201–214
Musaev A, Wang D, Pu C (2014) In: Proceedings of the 11th international ISCRAM conference University Park, Pennsylvania, USA
Niu H, Silva EA (2020) J Urban Plan Dev Div ASCE 146(2):04020007
OCHA (2015) Nepal: earthquake 2015 Situation Report. https://reliefweb.int/report/nepal/nepal-earthquake-2015-situation-report-no20-3-june-2015
Ogie RI, Clarke RJ, Forehead H, Perez P (2019) Computers. Environ Urban Syst 73:108–117
Overell SE (2009) PhD., University of London. https://citeseerx.ist.psu.edu/viewdoc/download?doi=10.1.1.157.7309&rep=rep1&type=pdf
Ozdikis O, Ramampiaro H, Nørvåg K (2018) In: European conference on information retrieval. Springer, pp 494–506
Paltoglou G (2016) J Assoc Inf Sci 67(7):1576–1587
Pánek J, Marek L, Pászto V, Valůch J (2017) Disasters 41(4):649–671
Poblet M, García-Cuesta E, Casanovas P (2018) Inf Syst Front 20(6):1363–1379
Potts M, Lo P, McGuinness R (2011) Ushahidi Queensland floods trial evaluation paper. ABC Australia
Senaratne H, Mobasheri A, Ali AL, Capineri C, Haklay M (2016) Int J Geogr Inf Sci:1–29. https://doi.org/10.1080/13658816.2016.1189556
Shi Y, Sayama T, Takara KT (2016) AGUFM 2016:NH23A-1847
Songchon C, Wright G, Beevers L, Computers, environment and urban systems 90:101690
Spinsanti L, Ostermann F (2010) Proceedings of validation of geo-information products for crisis management workshop (ValGeo 2010). JRC Ispra
van den Honert RC, McAneney J (2011) Water 3(4):1149–1173
van Oldenborgh GJ, Krikken F, Lewis S, Leach NJ, Lehner F, Saunders KR, van Weele M, Haustein K, Li S, Wallom D (2021) Nat Hazard 21(3):941–960
Wang RY, Strong DM (1996) Manag Inf Syst 12(4):5–33
Yu B, Cai G (2007) 4th ACM workshop on geographical information retrieval. Lisbon, Portugal
Zaila YL, Montesi D (2015) 9th workshop on geographic information retrieval. France, Paris

Zamir A, Khan HU, Iqbal T, Yousaf N, Aslam F, Anjum A, Hamdani M (2020) The electronic library. Emerald Publishing Limited 38(1):15. https://doi.org/10.1108/EL-05-2019-0118

Chapter 4
Geospatial Big Earth Data and Urban Data Analytics

Chitrini Mozumder and N. S. Karthikeya

Abstract Today, with the innovations and advancements of technologies and affordability of digital devices there is an explosion of huge amounts of archived and real-time digital data. This also includes the subset of the "***Big Earth Data***" which is generated using multitudinous sources viz., satellites, sensor networks, Internet of Things systems, and the hyper-connectivity of our society. It is diversified containing rich information across different geographic scales and resolutions. However, a massive challenge also exists on how this data has been exploited and explored to understand and solve problems in urban areas and cities. Furthermore, ***data analytics*** is also used for the exploration and analysis of the data sources, what the data represents, and transforming the data into information for intelligence creation. The recent evolutionary shift from Geographic Information Systems (GIS) to data analytics, including ***Urban Data Analytics*** enables us to gain insight into urban processes and answers to new and complex questions related to cities and urban areas. Based on above discussions, aims of this chapter are to provide insights on the recent trends and approaches in Geospatial Big Earth Data sources, uses, and their integration with IoT-based Big Data systems for urban studies. It also provides a review on use of machine learning and AI as state-of-the-art technologies to analyze the big urban earth data for accurate information for better decisions. Furthermore, an attempt is also made to discuss the way forward and future research areas and applications.

Keywords Big earth data · Urban data analytics · Geospatial · Big earth data processing · Society 5.0

C. Mozumder (✉) · N. S. Karthikeya
Remote Sensing and Geographic Information Systems, Information and Communication Technologies, School of Engineering and Technology, Asian Institute of Technology, Klong Luang 12120, Pathum Thani, Thailand
e-mail: chitrini@ait.asia

V. P. Singh et al. (eds.), *Application of Remote Sensing and GIS in Natural Resources and Built Infrastructure Management*, Water Science and Technology Library 105,
https://doi.org/10.1007/978-3-031-14096-9_4

4.1 Introduction

With global unprecedented increasing trends of urbanization across the world in developed, developing, and underdeveloped countries, the population is aggregating in urban areas. According to the United Nations (UN) statistics, in 1950s only 30% of the world's population lived in urban areas, which has increased to 55% in 2018. Urban areas can be categorized as cities, towns, conurbations, or suburbs based on the urban morphology. As the population increases, the needs of urban areas also increase in terms of infrastructure, facilities, utilities, goods, and materials. The planners and practitioners in urban areas eventually require a big amount of data to make informed decisions for sustainable, resilient, equitable, and livable growth.

In today's world of optimal hardware and intelligent software, systems are built to gather data. Although there is no single agreement on the "big data" definition (Mauro et al. 2015; Ward and Barker 2013), a widely accepted description of the same is the "large datasets which exceed conventional processing capabilities". Huge amounts of data are being collected in different domains such as banking, health, telecommunications, scientific observation, and simulation. A subset of this big data is the "big earth data". Although it is arguable, studies reveal that a higher percentage (~80%) of big data is the big earth data (Morais 2012; Vopham et al. 2018). It is also estimated that the size of this data is increasing by 20% every year attributing to the numerous satellites, airborne and terrestrial sensors collecting data every minute around the globe. Ever since mankind has started building the "digital earth" the society has started to feel secure as there is information on everything from weather early warnings to humanitarian assistance (Guo et al. 2020). Big data has enriched the understanding of how cities function, opening new paradigms of how social interaction and informed decision-making. One of the key advantages of big earth data is the power of location embedded.

4.2 Big Earth Data and their Characteristics

The big earth data is the digital inventory of the earth's surface collected from different platforms such as satellites, aircrafts, UAVs (Unmanned Aerial Vehicles), and other sensors. It is primarily used for data-driven analysis and interpretation, simulation, and modeling, and to make informed decisions in wide applications. In literature, synonyms of this data exist such as "big EO data", "big geospatial data", "big environmental data", or "big remote sensing data". Its main characteristics can be stated as massive, *non-homogenous, multi-source, multi-dimensional, multi-temporal, multi-scalar, highly complex, and nonstationary* (Merritt et al. 2018). Similar, to other big data, the characteristics of the big earth data can be explained with the 5 "V"s: volume, variety, velocity, veracity, and value. At the time, this chapter is being prepared, there are more Vs that are used to characterize big data such as:

Volume: It refers to the massive size of the data constantly collected by real-time sensors, location-based social media, and volunteered geographic information (VGI) sources. Satellites like the Landsat series have been collecting remotely sensed earth observation data for more than five decades archiving petabytes of data. One petabyte holds 1024 Terabytes (TB) or 1,125,899,906,842,624 bytes.

Variety: It refers to the unique types of data in big earth data such as raster (grid-based data) and vector (points, lines, polygons) data, geotagged text data, and satellite data in different resolutions and formats. The variety has an impact on the ability of the system for structured data storage and manipulation.

Velocity: It is the rate at which new data are being produced as well as the rate at which data should be processed. With frequent revisit of satellites at high resolution, continuous streaming of sensors like MODIS (Terra and Aqua), real-time GNSS, and geotagged social media, tremendous data are being generated at unimaginable speed. The requirement of storage and processing systems is increasing to match this speed of data generation.

Veracity: It refers to the degree of reliability or the quality that the data has to offer. The data quality has been influenced by the data generation process of the sensor/detector and in-sensor processing resulting in noise or abnormalities in the data. Many of the other geospatial data such as human-generated vector data, in-situ sensor collected data, social media data, and geotagged text data often contain uncertainty. Veracity can have high impact from the visualization or the presentation technique which can completely distort the actual information which can be extracted from the data (Bresciani et al. 2018).

Value: Although the fundamental characteristics of big earth data are the four already discussed above, it is realized that it is not only the size, variety, speed, or quality of the data, but also the value of the data. It relates to the concept that the data also must be worth to extract useful information as tremendous effort is put to collect, store, and process this data.

This digitally stored information can be categorized as structured, semi-structured, and unstructured data. The structured data has a unique well-defined data model and structure which follows a consistent order. This data is easily accessible and usable as it is stored in well-defined columns and databases. Inherently, most of the big earth data collected by machines (satellites/sensors) or human-generated (attribute information) are structured data. Satellite or other sensor images are raster datasets consisting of pixels and each geo-registered using a coordinate system to the ground. The pixels in raster are quantized elements in spectral space in particular bandwidth sensitive to the sensor/detector. The vector (points/line/polygons) or point clouds (LiDAR) are also structured information mapped to defined locations and associated locational attributes.

Semi-structured datasets inherit few properties of structured data but do not have formal structure of data models. In-situ data collected from fields using portable sensors such as spectrometers, air quality, or weather sensors can be considered as semi-structured data. These data have location information, however, to utilize them

for further analysis, a few preprocessing steps will be necessary. Unstructured data neither have a predefined data model nor a structure. Common examples of this kind of data are emails, word documents, social media posts, pdf, PowerPoint, etc. This type of data, e.g., geology maps, data from scientific publications, and human-generated information from social media needs extra effort to store, manipulate and extract required information for further analysis.

4.3 Big Earth Data Sources

Traditionally, the big earth datasets are categorized as land, ocean, atmosphere, hydrology, and socio-economic data collected by earth observation satellites, airborne and terrestrial sensors. However, there are newly added sources such as volunteered geographic information through social media, real-time location tracking through IoT, and in-situ observations of the urban environment. Here we broadly discuss four broad sources of big earth data.

A. Earth Observation Sensors
In the optical earth observation domain, the three major programs Landsat, Sentinel, and MODIS are the key contributors of big earth data. Due to the open data policy, data from these satellite systems are freely accessible for the entire globe. The joint USGS/NASA program provides the longest continuous space-based images of the earth. Till date, there are eight missions of Landsat, and data from7 missions (Landsat 6 failed) are available. Landsat 8 collected data for 7 years and 1.86 million images are added to the archive (Chatenoux et al. 2021). Every day, Landsat 8 is collecting approximately 700 new scenes. The Landsat 7 and 8 alone produced approximately 0.25 PB of data every year which covers the globe (Soille et al. 2018). A sharp increase in the big earth data is contributed by the Copernicus Sentinel satellites developed by the European Space Agency (ESA). Out of the six missions till date, three are responsible for monitoring land and ocean. Currently, there are two operational Sentinel-2 satellites under the present acquisition plan, which generate more than 1.7 TB of data for the 1C processing level every day (Sudmanns et al. 2018). With all Sentinel missions at full operational capacity, the data volumes are expected to exceed approximately 10 TB per day. Recently, with popularity of drone-based data collection, this is becoming an important source of big earth observation data (Athanasis et al. 2019).
B. Data from Model Simulations and Projections
With the advancement of computational models, the data derived by simulations and projections are increasing in both spatial and temporal resolutions. One key example is the Intergovernmental Panel on Climate Change (IPCC), which provides data generated from Integrated Assessment Models (IAMs), General Circulation Models, Carbon-cycle Models, and Earth System Models. The IPCC Fifth Assessment Report (AR5) generated 10 PB of simulated climatic data,

and it is estimated in the IPCC report that in the next years it is projected to generate even hundreds of petabytes (Schnase et al. 2017). One more example is the EU-funded Copernicus Climate Change Service (C3S) by ECMWF which produces petabytes of climatic data which is freely available. ERA5 is the most widely used C3S data which integrates huge volumes of historical observations into global estimates utilizing advanced modeling and data assimilation system. The ERA5 weather and climatic data are available globally from 1979, which provides over 200 variables at a spatial resolution of 31 km at every hour. The hourly ERA5 reanalysis data alone for just nine variables have a volume of about 7 TB (Wagemann 2020).

C. Internet of Things (IoT)
A new addition to the source of big data enhancing the space-based and near-earth sensors is the vast network of ground-based sensors (IoT), which collects boatload information. It is a network infrastructure of "objects" (things) that are embedded with sensors, software, and other technologies and which first collect and then transmit data to central servers (Hsu et al. 2020). In 2021, the volume of data produced by IoT applications is estimated as 847 ZB (1 ZB = 10^{21} bytes) (Cisco 2020). Unlike, Earth observation and model simulation data which are generally structured geospatial data, IoT seamlessly produces semi-structured or unstructured big earth data globally, which tends to be more heterogeneous, dynamic, and noisy (Li 2020).

D. Volunteered Geographic Information (VGI)
VGI refers to the collection and dissemination of big earth data collection which is recorded by "volunteers" through crowd-sourcing methods. One of the most successful VGI is the Open Street Map (OSM) platform where billions of contributors have created location-based data with an intention of creating a free base map for the entire world. Eventually, this is not just a base map but provides ample information not only on location but also on semantics. Another type of VGI data is created unintentionally, by people sensors through geotagging in social media platforms such as Twitter, Facebook, and Instagram. However, VGI data can be often redundant, noisy, and uncertain.

4.4 Existing Platforms for Big Earth Data Processing and Management

Big earth datasets are not only large, but this also brings complexity, therefore, conventional software, systems, and platforms are unable to handle them. This section includes some of the systems which are currently in use for working with big earth data from sources discussed above. It should be noted that there is no "one tool" which can handle all kinds of big earth data and all types of real-world complex problems (Gomes et al. 2020). In many cases, there might be combination of tools, techniques, and technologies.

A. Google Earth Engine (GEE)
GEE is one of the best and most widely used tools for big earth observation data processing and analysis. This uses a parallel processing system to carry out computation across many machines. Currently, it includes the entire EROS (NASA/USGS) Landsat scenes, selected MODIS data, Sentinel-1 datasets, precipitation data, NAIP data, sea surface temperature data, CHIRPS climate data, and elevation data (developers.google.com/earth-engine/datasets/catalog). It also has a provision for uploading user data viz., user-collected UAV and citizen sensor data for analysis. Along with petabytes of data, it also includes information and metadata of each type of data.

Earth Engine service can be connected through one of the available APIs. Currently, client libraries for JavaScript and Python are available to convert complex geospatial analyses to earth engine requests (Table 4.1). The default JavaScript code editor in GEE is an interactive environment for developing geospatial applications. The beginners are recommended to use the default panel where more than 800 functions are available for handling big earth observation data. The open-source Python library running in Google Colab can also be used which has a similar structure to the code editor. Colab or "Collaboratory" is an executable document where codes can be written, run, and share. Both the Python and JavaScript APIs access the same server-side functionality, but client-side expressions can vary because of language syntax differences. Apart from these, newly added is the REST API which can take authenticated HTTP requests and contains new and advanced features. Queries can be also issued to the earth engine REST API from Python using Google Colab.

Table 4.1 Comparison between Javascript code editor and Python API

Earth engine Javascript code editor	Earth engine Python API
• Rich documentation and tutorials available • Getting started is easier • Built-in interactive mapping functionality • Built-in authentication available • Several apps are already developed • Additional package cannot be installed	• Limited documentation and tutorials available • Language syntax are easier • Easy to share codes between scripts • Batch processing is easier (exporting images) • Executing code block by block • Numerous python packages can be linked • More plotting and visualization tools are available • Integration with open-source GIS is possible • Deep learning is possible

B. Google BigQuery GIS

BigQuery is a petabyte-scale analytics data warehouse by Google, which accepts SQL queries on large real-time and achieves datasets. This can be coupled with data visualization tools to interpret and analyze the data interactively such as trend analysis and predictions. A public dataset is also stored in BigQuery which is available for public use through the Google Cloud Public Dataset Program (cloud.google.com/solutions/datasets). Currently, this cloud includes real-time global air quality (openaq) data; over 4 million scenes from Landsat 4, 5, 7, and 8; comprehensive land, ocean, and atmospheric observation data; several datasets from NOAA including historical climatic data, operational environmental satellite data, significant earthquakes databases. This allows limited (storage of up to 10 GB of data and query up to 1 TB of data each month) access to users above which top-up can be done based on the needs.

This also has a spatial extension called BigQuery GIS. In this platform, it is possible to visualize and analyze geospatial data by utilizing geography data type and standard SQL geography functions (cloud.google.com/bigquery/docs/gis-intro). This system is proven successful in handling large vector datasets. Currently, there are limitations of this system, for example, the geography functions can be used in the standard SQL, and geography data type is supported only in the BigQuery client library for Python. Nevertheless, improvements are being made to this platform to minimize the limitations in the near future.

C. BIG Data for GeoAnalytics (ESRI ArcGIS)

The ESRI GeoAnalytics is available through ArcGIS GeoAnalytics Server (ArcGIS Enterprise Version 10.5 and more) and ArcGIS Pro (Version 2.4) to speed up batch spatial analysis and data management workflows. With GeoAnalytics Server, distributed analysis can be performed across multiple machines, while GeoAnalytics Desktop Tools use ArcGIS Pro to perform parallel analysis with local data from user machines. The GeoAnalytics Server uses distributed analytics against distributed data, with several frameworks/technologies for distributing computation. The GeoAnalytics integrated in ArcGIS Server combines technologies such as Hadoop, MapReduce, and Spark (processes distributed data in memory) on a cluster to solve analytical problems. Big earth data can be analyzed in less time by using the power of multiple machines.

The GeoAnalytics can connect to different data sources as input data, however, currently it works with mainly vector and tabular data. This data can come from IoT such as the collection of movement data (vehicles, people, storms), and VGI such as crowdsourced and social media. In addition, this also allows to use own big earth data which are in shapefiles, parquet, ORC, and delimited files (such as *.csv, *.tsv and *.txt). The outputs from the analysis can be stored in the ArcGIS Data Store. Figure 4.1 shows how data flows through GeoAnalytics Server with inputs and outputs at ArcGIS Enterprise 10.8. External storages such as Azure blob storage and data lake, Amazon S3, HDFS (Hadoop Distributed File System), Amazon S3 bucket as well as local or network file shares are available for both inputs and outputs.

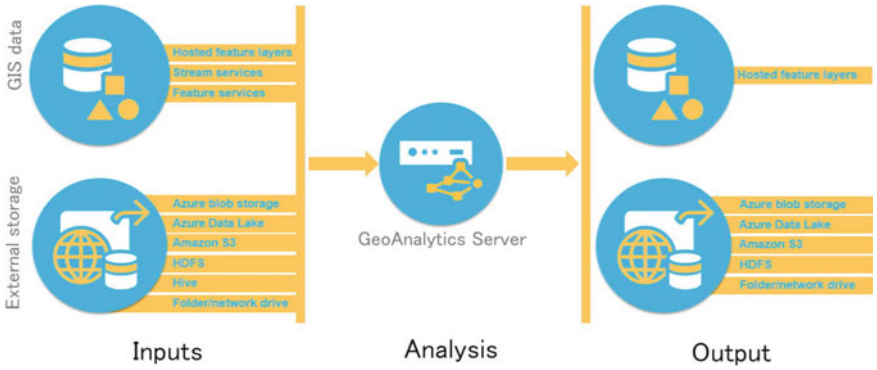

Fig. 4.1 ArcGIS Enterprise 10.8 data flows through GeoAnalytics Server (Curtis and Ambrose 2019)

D. Open Data Cube (ODC)
Another platform that allows handling, processing, and analysis of big earth observation data is Open Data Cube (ODC) (opendatacube.org). This platform is open source and is developed on GitHub. The available satellite data for analysis include Landsat, Sentinel, and MODIS. Based on the application, the ODC can be deployed on HPC, Cloud, and on local installations. Till date, the ODC can be used to catalog massive amounts of earth observation data, run python-based API for high-performance query and data access, exploratory data analysis, and already stored data processing. Currently, there is no data sharing between researchers is available on this platform (Gomes et al. 2020).

E. Open-Source Libraries and Binaries
A larger group of geospatial scientists using big data for various applications prefer to use open-source libraries and binaries. The advantage of this is that customized processes can be set up and run them programmatically inside a shell script. Regular users of big earth data generally handle them in a Linux environment rather than Windows. Python GDAL bindings are commonly used which supper both distutils and setup tools (gdal.org/api/python.html). For very large datasets, it is possible to process them into smaller batches to improve efficiency and reduce computation time.

F. Other
Other tools and technologies which are being used for different varieties of big earth data include SpatialHadoop (spatialhadoop.cs.umn.edu), AWS Athena (aws.amazon.com/athena), PostGIS (postgis.net), etc. SpatialHadoop is an open-source MapReduce extension specifically designed to handle large spatial datasets on Apache Hadoop. Athena is an interactive query service from Amazon which is serverless and facilitates analysis capabilities directly on the Amazon Simple Storage Service (Amazon S3) using standard SQL. PostGIS is a spatial database extender for PostgreSQL object-relational database. It allows location queries to be run in SQL by supporting geographic objects.

4.5 Big Earth Data Analytics

Most of the big earth data systems and platforms have been shifted to cloud computing platforms for rapid processing, analysis, visualizing, and sharing. Big earth data analytics include the process of preparation, reduction, analysis, mining, and visualization of big spatial-spectral-temporal datasets (Kempler and Mathews 2017) to uncover information such as trends, patterns, correlations, and predictions. Here, these processes we will discuss as (1) data preprocessing and (2) data analytical methods suitable for urban big earth data.

A. Big Earth Data Preprocessing
Preprocessing is necessary for any data, for big earth data due to the massive volume and rapid streaming this step is important to clean outliers, impossible data combinations and fill/ignore missing values. A consistent, complete, accurate, and smooth data should be used for further analysis or modeling, otherwise, it can be "garbage in" and "garbage out". Almost 50–80% of the time is consumed during this preprocessing phase in most of the big data analytical processes (Kempler and Mathews 2017). Yang et al. (2019) summarized five different forms of preprocessing for big earth data: extraction, transformation, evaluation, reduction, and augmentation.

Extraction: This form of preprocessing primarily involves data cleaning (missing or noisy data), outlier removal, and/or anomaly detection. Missing data is often filled by manually or estimating through mean or most probable values from the surrounding. Many times, it is ignored, to retain the original information in the dataset. Point clouds such as from LiDAR or vehicle collected data often contain noise or outliers due to environmental conditions as well as human interventions. This is often removed by several methods such as binning method, regression, and clustering. Efforts are still going on developing different noise removal methods to improve data quality (Li 2020).

Transformation and evaluation: Data transformation is necessary to standardize the data. It involves data normalization to rescale values in a specified range, format conversion, coordinate transformation to standardize projection information, discretization to replace raw values of the numeric attribute by interval or conceptual levels, and standardize data structure. The quality *evaluation* is a necessary step to choose the best quality of the data either by corrections (e.g., bias correction) or changing the data source (for example, evaluating by sensitivity analysis) (Yang et al. 2019). Evaluating spatial relationships is also required in many applications. MapReduce and Spark-based frameworks and systems, such as GeoSpark and SpatialHadoop, were designed to maximize speed in these computations.

Reduction: The data reduction is aimed at increasing storage efficiency and reducing data storage and analysis costs. It improves the storage, indexing, analysis, and visualization processes. The reduction can be done in different

ways, such as aggregation, redundancy elimination, attribute subset selection, and dimensionality reduction. Based on the purpose the type of reduction method varies. For example, data aggregation is a process where data is gathered and expressed in a statistical summary form. Again, despite the availability of numerous features, many researchers choose to reduce dimensions for further analysis. Generally, expert knowledge is combined although several algorithms exist that can perform automatically (Stromann et al. 2020).

Augmentation: In several instances, when there is not enough data within a big earth dataset to train a model, duplicate copies of each sample within the data is created. This is called data augmentation process. Yan et al. (2019) is their work has proposed a data augmentation strategy based on simulated samples to detect ships from earth observation images using deep learning methods.

B. Big Earth Data Analytics

Many researchers around the world to gather huge amounts of earth data to gather a big from the data. On the other hand, due to huge data volume, the challenges are also complex to uncover the correlations, hidden patterns, and other information. To overcome this problem, advanced recent technologies have been made to extract information efficiently and within less time. Broadly, big earth data analytics can be divided into simulation-prediction, traditional statistical methods, machine learning methods, and deep learning methods.

Simulation-Prediction

Numerical models are being utilized in simulation and prediction in various disciplines of earth sciences including land surface, solid earth, atmosphere, biosphere, and the oceans within a given period (Yang et al. 2019). A numerical simulation refers to the calculation where a mathematical model is implemented for a physical system. As big earth data gains visibility, so as the capability of numerical models to simulate and predict physical processes by combining observations with the numerical models. Traditionally, numerical models were most popular in atmospheric science and environmental modeling based on earth observation data (Binkowski and Roselle 2003; Courtier et al. 1994; Pulvirenti et al. 2020). Recently, IoT big earth data-based numerical models are also used for predictions in transportation and traffic congestion-related studies (Bernhardt 2017). Examples of numerical models used in big earth data analytics are agent-based modeling, cellular automata, etc.

Traditional Statistics

Traditional statistical tools are generally based on assumptions and are used to reveal the relationships, frequency distribution, and predictions of variables. To apply statistics on big earth data, three things need to be considered: the sampling method of the data (random/stratified), i.e., how the data was collected; data distribution, i.e., if the data is normally distributed or follows a non-normal distribution (Poisson, logistic, gamma); and the statistical estimator, based on the statistical method. Descriptive statistics such as mean, median, and skewness

are often used to understand the variables on earth. The most used inferential statistics methods are the regression models. These models help to understand relationships between variables in the earth system, such as traffic congestion and air quality. Classification (decision tree) and clustering (WaveCluster, DBSCAN) methods are used to group similar areas and differentiate variables behaving differently.

Machine Learning

It is a technique of data analytics that automates analytical model building. It also provides a set of tools to make systems learn from the data, identify patterns, and make decisions with minimal human intervention. For the successful application of machine learning, two aspects are important: (i) machine learning algorithm and (ii) training set. Once the training is completed, it is also important to validate with an independent set that was not used in the training. The performance of machine learning largely depends on the quality of the training set. The training can be done in a supervised or unsupervised manner. Supervised learning involves using labeled datasets that have inputs and expected outputs. The primary application of supervised learning is classification. Unsupervised learning used datasets with no specific structure, and the main application area is pattern analysis. With machine learning, typically three tasks are performed: Multivariate nonlinear non-parametric regression, unsupervised classification, and supervised classification (Lary et al. 2018). The data for these tasks can be from all types of sources described above. Common algorithms used to accomplish these tasks include neural networks, support vector machines, Random Forests, CART, and decision trees.

Deep Learning

It is a subset of machine learning that utilizes numerous layers of nonlinear processing units for data transformations, representations, and extract patterns by using neural networks (Bahi and Batouche 2018). Like machine learning, this also has a similar process of training, processing, and validation. Deep learning architectures are implemented through neural networks. The foundation of a neural network is the single neuron or the Perceptron, like a biological neuron. By densely connecting all the inputs of several perceptions, deep neural networks are built. These deep networks consist of multiple hidden layers, and the output of one hidden layer will be input to the next hidden layer. Some common deep learning algorithms include Convolutional Neural Networks (CNNs), Fully Convolutional Networks (FCNs), Encoder-Decoder Based Models, and Regional Convolutional Network (R-CNN) Based Models (Du et al. 2020). Some common platforms which facilitate deep learning are Tensor Flow, PyTorch, and Keras.

4.6 Big Earth Data and Urban Studies

A. Urbanization, Growth monitoring, Simulation

Urban areas attract a major portion of the population due to the abundance of opportunities, better facilities, quality of life. As a result, more than half of the world's population lives in urban areas. This is therefore of utmost importance to keep a track of the growth of urban areas to understand the urbanization process. The growth of two urban areas cannot be exactly same. Nevertheless, earth observation data is serving what it is best used for: monitoring changes. Several earth observation data are in use, one of the most popular is the Landsat data which is providing global satellite data at 30 m resolutions from 1972 till date through their different missions. Land use land cover information is extracted from these datasets to monitor short-term as well as long-term changes in urban areas. Li (2020) have used big earth observation data such as Global Human Settlement Layer (GHSL), global population grid products (Worldpop), and the global night-time light images (DMSP/OLS) to monitor urbanization in world heritage sites in China. They proposed an Urbanization Intensity Index (UII) to dynamically monitor and quantitatively assess the urbanization intensity around the world heritage sites. Identifying UHI (Urban Heat Island) and analyzing land surface temperature changes is another recently popular area. Global Surface UHI Explorer is an earth engine app that can display areas of UHI globally from 2003 to 2018.

Land use change prediction involves simulation of past changes, considering drivers of change to the desired future. The use of land use prediction in urban planning can help in making better decisions and policies. This coupled with scenarios (exploratory or normative) can give an idea of the success rate of already developed plans. Traditionally, a limited number of data was being used for simulation and prediction using methods like cellular automata (CA), Markov chain, regression models, agent-based models, etc. However, efforts have been made to use more data to improve the efficiency and accuracy of the models. In the last few years, several studies have attempted to design parallel CA algorithms on Central Processing Unit (CPU) parallel computing, Graphics Processing Unit (GPU) parallel, Message Passing Interface (MPI), GPU/CPU hybrid parallel, and MapReduce Framework to simulate urban growth (Kang et al. 2019). These methods can address the segmentation and integrity of land change simulations and predictions.

In addition to the use of huge earth observation data, VGI and IoT-based data are also being used for smarter urban planning. With the increasing trend of participatory urban planning and with an aim to reduce the gap between the local inhabitants and the goal of the government, crowdsourced maps, and mobile phone applications are being developed and used in this field. IoT-based traffic data can help decide the need of over bridges, diversion routes, and highways in areas with more traffic congestion (Thakuriah et al. 2017) also, mention about three more data types that are often combined with big earth data: private sector data, administrative data, and arts and humanities data.

B. Urban Development and City Intelligence

With the unprecedented growth of urban big data, it has become the center and core element in urban development and city intelligence. Pan et al. (2016) has enumerated three categories where big data can highly contribute to urban development: allowing web-based sharing, collaborative utilization, and integration of production factors; facilitating innovative ways of circulation and business modes for production materials, human resources, technologies, and funds; and enhancing core value and strengths of enterprises. Further, this also supports new business paradigms as well as innovative ways of administrative governance. An example is Zomato, which is a search, discovery, and delivery platform primarily connects restaurants and local inhabitants in India which came into service in 2008. It is constantly gathering data that is being used to provide services more efficiently and identify hotspot areas that need more outlet points.

In recent times, there is a race in making cities "smart" and "intelligent". "Data" is the foundation of making a city smart. The integration of IoT with artificial intelligence has made it possible to make cities smarter by providing smart governance, smart living, smart mobility, smart economy, smart environment, and of course smart people where the quality of life is at the highest level.

C. Air Quality

Urban air quality refers to how "clean" is the ambient air inside an area that is considered as urban. Generally, urban areas have more concentrated sources of pollution, but the pollutant dispersion is limited by the physical barriers than rural areas. Air pollution is considered as the greatest environmental hazard to human health and is responsible for approximately seven million deaths each year (World Health Organization 2021). Therefore, over the years several efforts have been made to develop early warnings for air pollution to reduce or control this momentous hazard. Big earth data has been used in three areas: air quality monitoring, forecasting, and traceability (Huang et al. 2021). Data from different sources are generally fused in air quality analysis methods such as weather stations, sensors mounted in vehicles (IoT), and satellite-based earth data.

Air quality monitoring is the foundation of air quality forecasting and traceability, monitoring can be done in spatial, temporal, and/or spatio-temporal manner. Along with data from monitoring stations, one of the most useful data in this analysis is the earth observation data. One of the recently popular earth observation data for air quality analysis is from the Copernicus Sentinel-5 Precursor mission which is the first Copernicus mission dedicated to monitoring the atmosphere. This mission is already contributing to the big earth observation data for ozone, methane, formaldehyde, aerosol, carbon monoxide, nitrogen oxide, and sulfur dioxide, as well as cloud characteristics. Based on this data, monitoring tropospheric NO_2 column spatial configuration in a specific period over the whole of Europe was accessed (Vîrghileanu et al. 2020).

Monitoring station data, which is also considered as the "geotagged" time series data has been long used in air quality monitoring, forecasting, as well as traceability. However, this data needs more effort in preprocessing, for cleaning outliers and approximating the missing values in absence of a dense network of a monitoring network. For this purpose, several methods can be used: statistics such as mean or median, or interpolation, Expectation Maximization (EM), matrix factorization; machine learning algorithms such as decision trees, Artificial Neural Network (ANN). Air quality forecasting traditionally is being carried out by statistical methods such as regression models and principal component analysis. These methods use large historical data to analyze the potential rules to forecast air quality to the future based on statistics (Dun et al. 2020). In the last decade, machine learning and deep learning methods are used which are based on neural networks to model and forecast big air quality data (Du et al. 2019; Zhao and Zettsu 2019). Furthermore, combining both statistics and deep learning methods for improving the accuracy of forecasting models.

D. Transportation services

IoT-based big earth data has gained tremendous popularity in recent years. On streets especially, vehicle probes collect massive trajectory data which are widely being used in evaluating traffic congestion, trip time, and traffic speed in urban areas. Several studies have used machine learning methods and deep learning models for Network Traffic Monitoring and Analysis (NTMA) applications such as traffic classification and prediction (Abbasi et al. 2021). Often, other connected device data such as smartphones are used in addition to the IoT data for these studies. NTMA techniques are mainly two types: (i) active and (ii) passive. Active techniques involve transferring a progenerated traffic probe data into a network. The "ideal" test traffic data is then compared with the real traffic to measure different network performances through metrices (e.g., network throughput, latency, packet loss ratio, and jitter). Active methods are mainly used for controlling Service Level Agreement (SLA) based services. Whereas, passive methods are primarily used for traffic monitoring, managing, and transportation planning. These uses past and real-time data to make analysis and make decisions.

In big cities, taxi and cab services play a major role in city transportation. If traffic congestion is too high, it impacts adversely to the productivity of the transportation services, resulting in the rejection of transport drivers to provide services to some destinations (Phiboonbanakit and Horanont 2021). Several studies have used this big data in different aspects such as spatial and temporal understanding of traffic congestion, taxi/cab demand prediction, algorithm, and application development for better management of transportation services. The probe systems are designed to improve the profitability of taxi companies so that the data collected in the past can help to forecast the demand in the future statistically or using machine learning. Liu et al. (2020) presented two ways for the prediction of online taxi-hailing demand based on backpropagation neural network and extreme gradient boosting. In Singapore, one of the most widely systems used by the land transport authority of Singapore is the TrafficScan

system which is an advanced transport system providing motorists real-time speed information on major roads in Singapore. They have maximized the use of technology and have innovatively used a taxi dispatch system to gather traffic data on the roads. This data is processed real-time to give traffic speed conditions on the streets, and these can be accessed online by drivers to plan their routes for a smoother journey.

E. Tourism

Urban tourism is an effective, global form of tourism, however, over the years less focus is given when it comes to linking urban studies to tourism. Therefore, there is no well-defined definition of urban definition despite its importance (Ashworth and Page 2011). Tourists visit cities in several reasons, making intensive use of many city services and facilities. But most cities are not planned or built for tourism: though cities need tourists. The cities that host the most tourists are large, multifunctional entities into which tourists can effortlessly fit, making them largely economically and physically invisible. Agapiou (2017) presented two different case studies utilizing earth observation big data in fields of archaeology and cultural heritage in urban areas. He used GEE platform to retrieve Landsat and DMSP-OLS Night-time Lights Time data to present the use of big earth data in supporting archaeological research and cultural heritage.

VGI can be beneficial in analyzing travel demand, tourism phenomenon, and tourist behavior, in an urban context (Ferreira 2019). Crowdsourced data and geotagged photosin social media such as Facebook, Twitter, and Instagram can help to identify the spatial distribution and places of concentration, in dense and complex areas. Encalada et al. (2019) used "Panoramio" (in 2007 Google acquired Panoramio and closed it down, in late 2016) and "Flickr" data to map tourists and their spatial distribution in Lisbon metropolitan area. Much effort was given to data preprocessing the unstructured data followed by spatial analysis such as global and local Moran's I, Global Getis-Ord Index, and hotspot analysis to understand the geographical patterns of the online footprints.

F. Emergency Management

In an emergency event, for example in case of a natural disaster, it is of utmost importance to send information to local people about safe places, resources such as hospitals, food sources, and road situations. For this purpose, an efficient communication network is essential which can gather and disperse such information. Nevertheless, several elements of the network such as links and nodes can get destroyed or malfunction during a disaster. Hence, a communication network that can withstand tremendous impact from disasters is critical to any emergency management system. Four critical technologies to improve communication networks resilience are demand-driven network resource management, survivable network provisioning, ad hoc networks, and delay/interruption tolerant networks (Song et al. 2020).

4.7 Big Data Urban Analytics Toward Society 5.0

Society 5.0 was initially coined in the 5th Science and Technology Basic Plan as a future aspired society of Japan. It follows Society 1.0 (hunting society), Society 2.0 (agricultural society), Society 3.0 (industrial society), and Society 4.0 (information society). Society 5.0 refers to "*A human-centered society that balances economic advancement with the resolution of social problems by a system that highly integrates cyberspace and physical space*". It is expected that in Society 5.0, people will achieve an active, enjoyable life. In this new 5.0, IoT will connect all people and things, all information and knowledge will be share and new value-added information will be derived; artificial intelligence will free humans from cumbersome work by analyzing huge data; the possibilities open to humans will expand through the use of robots, automatic car; social issues will be resolved, and humans will be free from various constraints (Deguchi et al. 2020). Although initially started in Japan, it has already reached into discussion forums of various countries.

The current digital transformation processes are driven by big data including the big earth data and data analytics which makes most of these data turning them into actionable insights (Fig. 4.2). Data Analytics is the exploration and analysis of the data sources, what the data represents, and transforming the data into information for intelligence creation. Digital transformation definitely is a means but should be utilized to build a society that focuses on human well-being, vitality, and high-level living. In the Society 5.0 concept, people, objects, and systems are all connected in cyberspace and optimal results obtained by AI exceeding the capabilities of humans are fed back to physical space. There is a need for a huge amount of big data, including the "Big Earth Data" collected by intelligent systems which converge between cyberspace and physical space. Using these insights to proactively improve efficiency is the first major step in transforming conventional communities into truly super-smart communities.

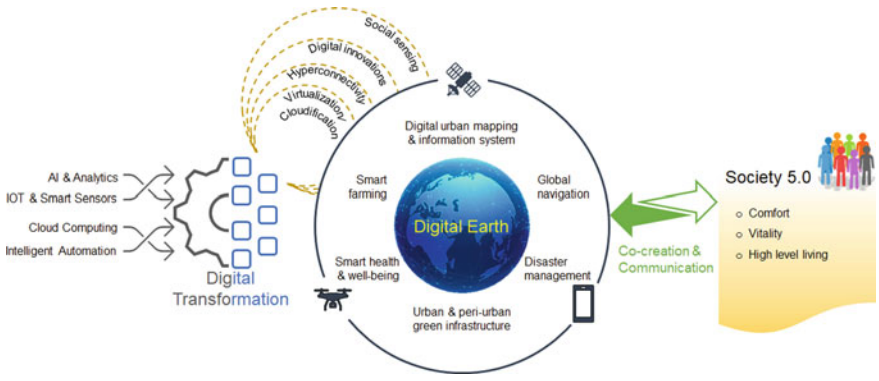

Fig. 4.2 Digital transformation—big earth data and Society 5.0 context, universe of discourse, paradigms, and enabling processes

4.8 Challenges and Way Forward

Urban areas are complex and urban planners often need to have a more comprehensive and up-to-date understanding of different aspects of the area. Big earth data despite having different challenges is increasingly used in urban studies. The big earth data from earth observation and simulations are mostly structured however can be of various formats. On the contrary, big earth data from IoT and VGI sources are semi-structured or unstructured. As the IoT and VGI-based data collection is increasing, a huge volume of data is generated every day. The success of machine learning and deep learning methods largely depends on the quality and quantity of the data. Machine learning methods work best with structured data, whereas deep learning methods are more efficient with unstructured and semi-structured datasets. IoT data such as traffic data is unstructured and unlabeled/semi-labeled. To use machine learning methods for these studies, it is a huge task in terms of money, time, and human effort to label them. Therefore, solutions should be found to integrate machine learning algorithms with deep learning, or unstructured machine learning methods for efficient modeling and analysis.

Although the cloud-based data processing platforms (distributed and parallel computing) are gaining popularity, there are new challenges coming up. For example, if the data is stored in different clouds, the data must still move for use or share if there is no standardized platform. Further, if there are issues such as power outage or poor internet connection, as well as security and privacy concerns, there will be disruption in the processing. It is also observed that even in distributed computing use of very high temporal data analysis might cost more in terms of time. This implies that the systems handling these big data must be upgraded in terms of both hardware and software to handle massive unstructured datasets, standardization of big earth data structure, and to avoid any adverse conditions.

Big earth data analytics can be hindered by lack of good programming skills, security constraints, or vendor lock-in. Cloud computing has been facilitated in several platforms, however, mainly focusing on earth observation, and simulated big earth data. There is a need of user-friendly platforms which can handle unstructured and semi-structured earth data from IoT and VGI. Further, the implementation of 3-D visualization services needs attention which can largely help to understand the relation between 2-D data with the topography. This can largely help too, for example, monitor urban growth not only horizontally, but also in a vertical manner.

References

Abbasi M, Shahraki A, Taherkordi A (2021) Deep learning for network traffic monitoring and analysis (NTMA): a survey. Comput Commun 170:19–41. https://doi.org/10.1016/j.comcom.2021.01.021

Agapiou A (2017) Remote sensing heritage in a petabyte-scale: satellite data and heritage Earth Engine© applications. Int J Digit Earth 10(1):85–102. https://doi.org/10.1080/17538947.2016.1250829

Ashworth G, Page SJ (2011) Urban tourism research: recent progress and current paradoxes. Tour Manage 32(1):1–15. https://doi.org/10.1016/j.tourman.2010.02.002

Athanasis N, Themistocleous M, Kalabokidis K, Chatzitheodorou C (2019) Big data analysis in UAV surveillance for wildfire prevention and management. In: Themistocleous M, da Cunha P (eds) Information systems. Springer International Publishing, Cham, pp 47–58

Bahi M, Batouche M (2018) Deep semi-supervised learning for virtual screening based on big data analytics. In: Tabii Y, Lazaar M, Al Achhab M, Enneya N (eds) Big data, cloud and applications, vol 872. Springer International Publishing, Cham, pp 173–184. https://doi.org/10.1007/978-3-319-96292-4_14

Bernhardt K (2017) Agent-based modeling in transportation. Artif Intell Transp 72(E-C113)

Binkowski FS, Roselle SJ (2003) Models-3 community multiscale air quality (CMAQ) model aerosol component 1. Model description. J Geophys Res Atmosp 108(D6)

Bresciani S, Eppler MJ (2018) The risks of visualization: a classification of disadvantages associated with graphic representations of information. In: Schulz PJ, Hartung U, Keller S (eds) Identität und Vielfalt der Kommunikations-wissenschaf. UVK Verlagsgesellschaft mbH, Konstanz, pp 52–65

Chatenoux B, Richard J-P, Small D, Roeoesli C, Wingate V, Poussin C, Giuliani G et al (2021) The Swiss data cube, analysis ready data archive using earth observations of Switzerland. Sci Data 8(1):295. https://doi.org/10.1038/s41597-021-01076-6

Cisco (2020) Cisco annual internet report (2018–2023) white paper. Retrieved from https://www.cisco.com/c/en/us/solutions/collateral/executive-perspectives/annual-internet-report/white-paper-c11-741490.html

Courtier P, Thépaut JN, Hollingsworth A (1994) A strategy for operational implementation of4D-Var, using an incremental approach. Quart J Roy Meteorol Soc 120(519):1367–1387

Curtis H, Ambrose S (2019) Following the flow of data in GeoAnalytics server. ArcGIS blog. Retrieved from https://www.esri.com/arcgis-blog/products/geoanalytics-server/data-management/following-the-flow-of-data-in-geoanalytics-server/

De Mauro A, Greco M, Grimaldi M (2015) What is big data? a consensual definition and a review of key research topics. AIP Conf Proc 1644(1):97–104

Deguchi A, Hirai C, Matsuoka H, Nakano T, Oshima K, Tai M, Tani S (2020) What is Society 5.0? In: Society 5.0: a people-centric super-smart society. Springer Singapore, Singapore, pp 1–23. https://doi.org/10.1007/978-981-15-2989-4_1

Du S, Li T, Yang Y, Horng S-J (2019) Deep air quality forecasting using hybrid deep learning framework. IEEE Trans Knowl Data Eng 33(6):2412–2424. https://doi.org/10.1109/tkde.2019.2954510

Du S, Li T, Yang Y, Horng S-J (2020) Multivariate time series forecasting via attention-based encoder–decoder framework. Neurocomputing 388:269–279

Dun M, Xu Z, Chen Y, Wu L (2020) Short-term air quality prediction based on fractional grey linear regression and support vector machine. Math Probl Eng 2020(2). https://doi.org/10.1155/2020/8914501

Encalada L, Ferreira CC, Boavida-Portugal I, Rocha J (2019) Mining big data for tourist hot spots: geographical patterns of online footprints. In: Koutsopoulos K, de Miguel González R, Donert K (eds) Geospatial challenges in the 21st century, key challenges in geography, pp 99–123. https://doi.org/10.1007/978-3-030-04750-4_6

Ferreira D (2019) Research on big data, VGI, and the tourism and hospitality sector: concepts, methods, and geographies. In: Sigala M, Rahimi R, Thelwall M (eds) Big data and innovation in tourism, travel, and hospitality: managerial approaches, techniques, and applications. Springer Singapore, Singapore, pp 75–85. https://doi.org/10.1007/978-981-13-6339-9_5

Gomes VCF, Queiroz GR, Ferreira KR (2020) An overview of platforms for big earth observation data management and analysis. Rem Sens 12(8):1–25. https://doi.org/10.3390/RS12081253

Guo H, Nativi S, Liang D, Craglia M, Wang L, Schade S, Annoni A et al (2020) Big earth data science: an information framework for a sustainable planet. Int J Digit Earth 13(7):743–767. https://doi.org/10.1080/17538947.2020.1743785

Hsu A, Khoo W, Goyal N, Wainstein M (2020) Next-generation digital ecosystem for climate data mining and knowledge discovery: a review of digital data collection technologies. Front Big Data 3(29). https://doi.org/10.3389/fdata.2020.00029

Huang W, Li T, Liu J, Xie P, Du S, Teng F (2021) An overview of air quality analysis by big data techniques: monitoring, forecasting, and traceability. Inf Fusion 75:28–40. https://doi.org/10.1016/j.inffus.2021.03.010

Kang J, Fang L, Li S, Wang X (2019) Parallel cellular automata markov model for land use change prediction over MapReduce framework. ISPRS Int J Geo-Information 8(10). https://doi.org/10.3390/ijgi8100454

Kempler S, Mathews T (2017) Earth science data analytics: definitions, techniques and skills. Data Sci J 16

Lary DJ, Zewdie GK, Liu X, Wu D, Levetin E, Allee RJ, Aurin D et al (2018) Machine learning applications for earth observation. In: Mathieu P-P, Aubrecht C (eds) Earth observation open science and innovation. Springer International Publishing, Cham, pp 165–218. https://doi.org/10.1007/978-3-319-65633-5_8

Li Z (2020) Geospatial big data handling with high performance computing: current approaches and future directions. In: Tang W, Wang S (eds) High performance computing for geospatial applications. Springer International Publishing, Cham, pp 53–76. https://doi.org/10.1007/978-3-030-47998-5_4

Liu Z, Chen H, Sun X, Chen H (2020) Data-driven real-time online taxi-hailing demand forecasting based on machine learning method. Appl Sci (Switz) 10(19). https://doi.org/10.3390/APP10196681

Merritt P, Bi H, Davis B, Windmill C, Xue Y (2018) Big earth data: a comprehensive analysis of visualization analytics issues. Big Earth Data 2(4):321–350. https://doi.org/10.1080/20964471.2019.1576260

Morais CD (2012) Where is the phrase "80% of data is geographic" from? Retrieved from http://www.gislounge.com/80-percent-data-is-geographic/

Pan Y, Tian Y, Liu X, Gu D, Hua G (2016) Urban big data and the development of city intelligence. Engineering 2(2):171–178. https://doi.org/10.1016/J.ENG.2016.02.003

Phiboonbanakit T, Horanont T (2021) Analyzing Bangkok city taxi ride: reforming fares for profit sustainability using big data driven model. J Big Data 8(1). https://doi.org/10.1186/s40537-020-00396-5

Pulvirenti B, Baldazzi S, Barbano F, Brattich E, Di Sabatino S (2020) Numerical simulation of air pollution mitigation by means of photocatalytic coatings in real-world street canyons. Build Environ 186:107348–107348. https://doi.org/10.1016/j.buildenv.2020.107348

Schnase JL, Duffy DQ, Tamkin GS, Nadeau D, Thompson JH, Grieg CM, Webster WP et al (2017) MERRA analytic services: meeting the big data challenges of climate science through cloud-enabled climate analytics-as-a-service. Comput Environ Urban Syst 61:198–211. https://doi.org/10.1016/j.compenvurbsys.2013.12.003

Soille P, Burger A, De Marchi D, Kempeneers P, Rodriguez D, Syrris V, Vasilev V (2018) A versatile data-intensive computing platform for information retrieval from big geospatial data. Futur Gener Comput Syst 81:30–40. https://doi.org/10.1016/j.future.2017.11.007

Song X, Zhang H, Akerkar RA, Huang H, Guo S, Zhong L, Culotta A et al (2020) Big data and emergency management: concepts, methodologies, and applications. IEEE Trans Big Data 14(8). https://doi.org/10.1109/TBDATA.2020.2972871

Stromann O, Nascetti A, Yousif O, Ban Y (2020) Dimensionality reduction and feature selection for object-based land cover classification based on sentinel-1 and sentinel-2 time series using google earth engine. Rem Sens 12(1). https://doi.org/10.3390/RS12010076

Sudmanns M, Lang S, Tiede D (2018) Big earth data: from data to information. GI For 6(1):184–193. https://doi.org/10.1553/GISCIENCE2018_01_S184

Thakuriah (Vonu) P, Tilahun NY, Zellner M (2017) Big data and urban informatics: innovations and challenges to urban planning and knowledge discovery. In: Springer geography, p 45. https://doi.org/10.1007/978-3-319-40902-3_2

Vîrghileanu M, Săvulescu I, Mihai BA, Nistor C, Dobre R (2020) Nitrogen dioxide (NO_2) pollution monitoring with sentinel-5p satellite imagery over Europe during the coronavirus pandemic outbreak. Rem Sens 12(21):1–29. https://doi.org/10.3390/rs12213575

Vopham T, Hart JE, Laden F, Chiang YY (2018) Emerging trends in geospatial artificial intelligence (geoAI): potential applications for environmental epidemiology. Environ Health Glob Access Sci Source 17(1):1–6. https://doi.org/10.1186/s12940-018-0386-x

Wagemann J (2020) ERA5 reanalysis data available in Earth engine. ECMWF Newsl. Retrieved from https://www.ecmwf.int/en/newsletter/162/news/era5-reanalysis-data-available-earth-engine

Ward JS, Barker A (2013) Undefined by data: a survey of big data definitions. School of Computer Science, University of St Andrews.https://doi.org/10.48550/arXiv.1309.5821

World Health Organization (2021) World health statistics 2021: monitoring health for the SDGs, sustainable development goals. World Health Organization, Geneva. Retrieved from https://apps.who.int/iris/handle/10665/352097

Yan Y, Tan Z, Su N (2019) A data augmentation strategy based on simulated samples for ship detection in RGB remote sensing images. ISPRS Int J Geo-Inf 8(6). https://doi.org/10.3390/ijgi8060276

Yang C, Yu M, Li Y, Hu F, Jiang Y, Liu Q, Gu J et al (2019) Big earth data analytics: a survey. Big Earth Data 3(2):83–107. https://doi.org/10.1080/20964471.2019.1611175

Zhao P, Zettsu K (2019) Convolution recurrent neural networks based dynamic transboundary air pollution predictiona. In: 2019 4th IEEE international conference on big data analytics. ICBDA 2019, pp 410–413. https://doi.org/10.1109/ICBDA.2019.8712835

Chapter 5
A Comparative Analysis of Spatiotemporal Drought Events from Remote Sensing and Standardized Precipitation Indexes in Central America Dry Corridor

Karel Aldrin Sánchez Hernández and Gerald Augusto Corzo Perez

Abstract Understanding the dynamics of the earth's surface variation patterns has been critical for climate change adaptation and mitigation. During the last decades, detecting these events through remote sensing allowed us to improve the conventional analysis toward an integrated space–time analysis. This chapter proposes a spatiotemporal exploratory analysis of the information from SPI, SPEI and links its results into remote sensing information of NDVI using computer vision algorithms for pattern recognition and tracking. This analysis was carried out in three phases. First, a 20-year analysis of vegetation-based indices (NDVI) and meteorological drought indices (SPI, SPEI), to identify and compare the water anomalies over Central America dry corridor, using ERA5 climatological information and satellite images for the period 2000–2020. These results are used to assess the spatiotemporal variations of meteorological stress and vegetation water stress. All this is analyzed considering the conditions along the phenological cycle. The implementation of the spatiotemporal drought methodology proposed by Corzo and Vitali, 2018, and its results used as input time series, through LOWESS smoothing proposed by Jong (Remote Sens Environ 115(2):692–702, 2011). The final comparison uses statistical metrics such as spatial correlation. Drought units are identified for each meteorological drought index and are compared among them, and together with the NDVI normalization, a vegetation-based drought index (vegetation condition index or VCI) is estimated. This step allows representing the phenological conditions of vegetative water stress without interferences of temporality and consistency. Finally, the VCI is classified in categorical ranges that allow the comparison of drought units to the SPI in different lags (1, 3, 6) and SPEI (1, 3, 6). By this, establishing meteorological relationships with the vegetative surface dynamics and generating the trajectories

K. A. S. Hernández (✉) · G. A. C. Perez
Department of Integrated Water Systems and Governance, IHE Delft, Delft, Netherlands
e-mail: sanchezkarel@gmail.com

V. P. Singh et al. (eds.), *Application of Remote Sensing and GIS in Natural Resources and Built Infrastructure Management*, Water Science and Technology Library 105,
https://doi.org/10.1007/978-3-031-14096-9_5

(tracking) of each drought cluster observed with the VCI. Finally, a validation of the trajectories are also compared. All validation show that his methodology allows using directly inferred drought from remote sensing as a meteorological drought index, in similar way as SPI. The spatiotemporal changes monitoring and evaluation associated with land cover and water sources, and derivation of drought index based on vegetative condition is an essential component of this chapter's contribution.

Keywords Spatiotemporal tracking · NDVI · SPI · Drought propagation · Remote sensing · Computer vision · Climate change

5.1 Introduction

Regarding the WMO (Wilhite 2006), droughts relate to water deficiency in a particular region, and their severity has potential repercussions in diverse contexts (Serda 2013). Recent studies indicate that droughts' frequency and severity appear to be increasing in some zones due to climate variability and change (Podestá et al. 2016). Also, its occurrence is cyclical and is related to the El Niño Southern Oscillation ENSO (van der Zee Arias et al. 2012), which influences both the irregularity of the precipitation cycle and the spatiotemporal magnitude of impact at scales. Regional and local, limiting the natural resilience capacity of the territory.

Relate to Diaz et al. 2020a, spatiotemporal methodologies applied to droughts have been developed. These have managed to generate a better understanding of spatiotemporal dynamics, strengthening their monitoring and impact reduction (Cai 2014). Several approaches have been proposed to describe the spatiotemporal development of drought. According to Bacanli et al. 2009; and Dracup et al. 1980, propose methodologies that apply to force a significant number of meteorological variables in the drought indexes calculation based on time series disaggregation of relating it to the spatiality of all zone, establishing a unique phenomenon in the zone.

Among the tools developed in recent decades, remote sensing has shown great promise for improving the calculation and monitoring of drought events. For this, vegetation indices and data on drought, humidity, and surface temperature derived from satellite images are used by Sahaar and Niemann (2020); Ghulam et al. 2007). Following (Tadesse et al. 2012), reported significant correlations between the normalized difference vegetation index (NDVI), obtained from MODIS images, calculated every 16 days, and drought. Tadesse et al. (2005) showed that when using NDVI, despite being an effective indicator of humidity and vegetation conditions, there is a lag between the occurrence of the drought event and the change in its values, which indicates that this index is not appropriate to monitor the drought conditions of crops, in real-time conditions (Nihoul 2005)

5.2 Case Study

Central America is one of the world's regions most exposed to the risks of natural hazards and climate variability making climate hazards the most prevalent, represented mainly by frequent droughts and severe spontaneous floods, affecting agricultural production, with greater intensity in degraded areas (Eckstein et al. 2017).

Belize, Guatemala, Honduras, Panama, El Salvador, constitutes the dry forest ecosystem corridor of Central America (Fig. 5.1). Caused by the geographic location, Central America have more probability to receive strong heat waves, also, influence of global climatic phenomena and hurricane seasons prevent a progressive recovery of its hydric condition in terms of food and environmental security (van der Zee Arias et al. 2012).

The hydrometeorological records shows that Central America had experienced an average temperature change, closing of 0.05 °C yearly, it means 0.5–1 °C of historical anomalies by temperature (Fig. 5.2) in last 40 years. Otherwise, rainfall rates have tended to decrease in 12 mm/year during the same period (Fig. 5.3).

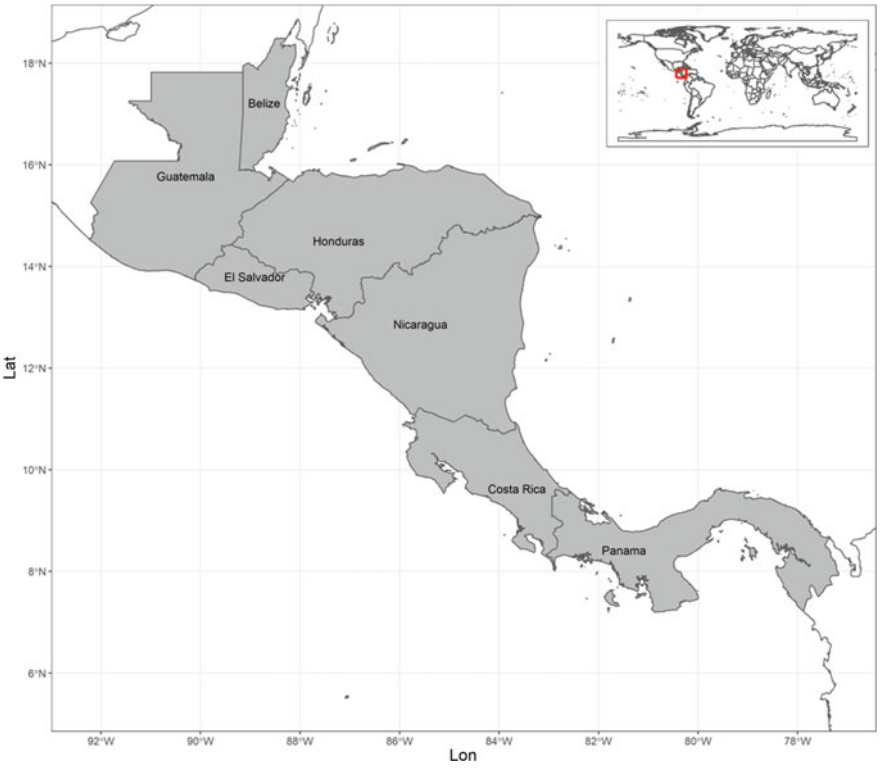

Fig. 5.1 Study area, Central America Dry Corridor

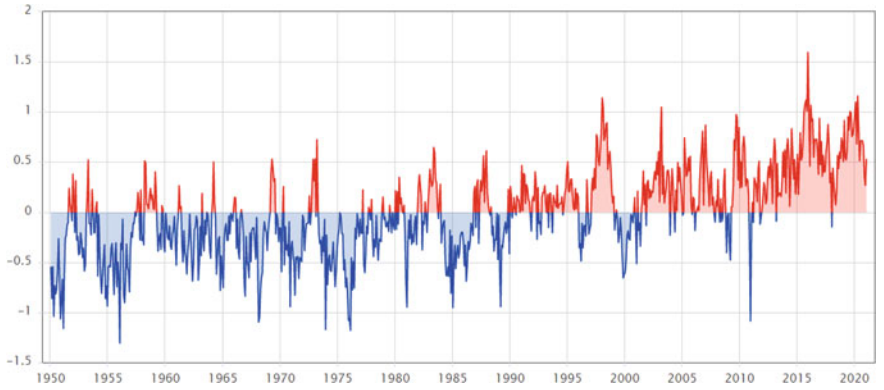

Temperature Anomaly 1950-2020

Fig. 5.2 Surface temperature anomalies and total precipitation by 1950–2020

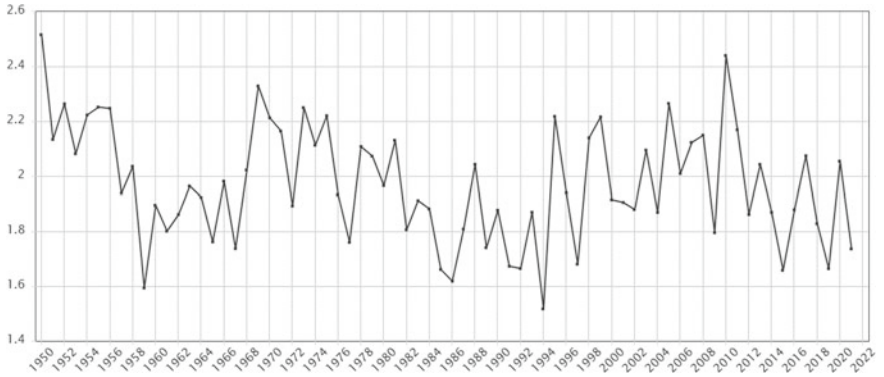

Total Precipitation 1950-2020

Fig. 5.3 Surface temperature anomalies and total precipitation by 1950–2020

According to the Intergovernmental Panel on Climate Change (IPCC), Central America is categorized as the Latin America region, with most likely to be influenced by climate change impacts and effects (Frieler et al. 2017; Anandhi et al. 2008). Which is supported by increased flooding and prolonged droughts among other adverse natural hazards (hurricanes, earthquakes).

Water supply is linked to intra-annual precipitation fluctuations as well as geographical variability. During El Niño events, annual rainfall can decrease between 38 and 42%, with extended warm periods and more extended dry spells.

High temperature seasons and the dry climate conditions have catastrophic consequences on agricultural development yield and affecting food security (Bae et al. 1981; FAO 2019). Added to the tropical storm season has damaging effects in terms of critical water levels, pollutions preventing the water system near resilience (FAO 2019).

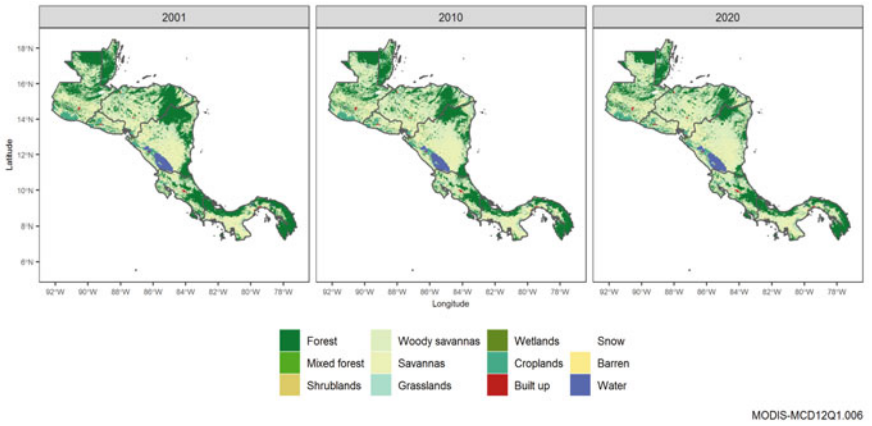

Land-cover migration over 2000 to 2020

Fig. 5.4 Land-cover migration and trends over 2000 to 2020

The hazards generated by flooding or droughts mainly, have increased in recent years. Growing food insecurity and water supply availability, increasing climatic trends, and socioeconomic stresses in the region have caused the displacement of people from their homes and communities in 1.6 millions in the last decade (Buttafuoco and Caloiero 2014).

As an example, Fig. 5.4 and 5.5 allows to understand the ecological, socio-ecological, economic, and cultural impacts of land use change on Central America, trends in land use and subsoil use change have been identified, allowing us to establish few grid cells changes mainly in forest and wetlands to woody savannas about 20% reduction of forest structures to pasture (Anderson et al. 2019; Maldonado et al. 2016). Reinforced by agricultural expansion in the region around 46% (van der Zee Arias et al. 2012). This to establish potential land cover that may be affected by drought and may cause multi-country unsustainability.

5.3 Methodology

5.3.1 Data Acquisition

Past drought events required the use of comprehensive and detailed satellite data to assess and monitor past drought events. Both hydrometeorological variables and earth observation data were used (Sexton et al. 2013). As shown in Table 5.1. Where data sets of the best available temporal and spatial resolution are used.

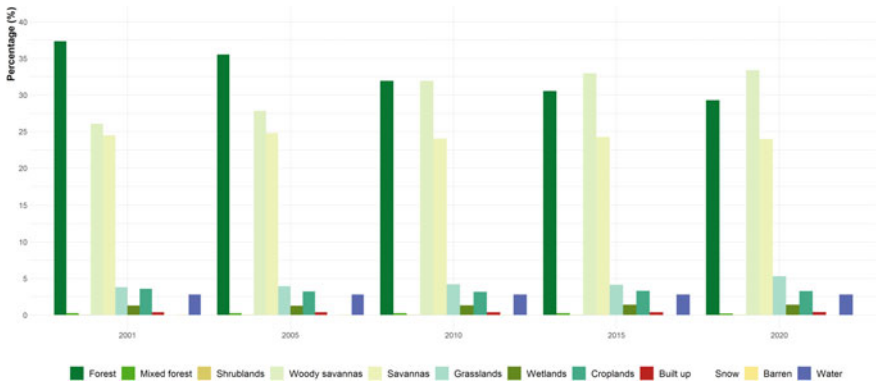

Land-cover changes from 2000 to 2020

Fig. 5.5 Land-cover migration and trends over 2000 to 2020

Table 5.1 Climatological and remote sensing data source description

Data	Source	Variable	Temporal resolution	Spatial resolution
ERA-5(Beck et al. 2017)	European Center for Medium-Range Weather Forecasting ECMWF	Precipitation	1981-present	0.25°
ERA-5(Beck et al. 2017)	European Center for Medium-Range Weather Forecasting ECMWF	Temperature	1981-present	0.25°
MODIS (Zhao et al. 2005)	NASA LP DAAC at the USGS EROS Center/GoogleEarthEngine	Satellite imagery	2000-present	500 m

5.3.2 Drought Calculation

Drought calculation needs and indicator that represents a quantitative drought condition according with the magnitude of specific variable. Drought indicator can be used to define drought (dry condition) with any variable like meteorological drought: based on precipitation condition or agricultural drought: based on water balance [P-ETP] (Van Loon 2015).

However, drought indices are not universally accepted to characterize the drought conditions (Okal et al. 2020) because depends of the driver factor and regional context. In this way, the rainfall and vegetation health are significant factors that could show the influence of drought frequency or severity for instance.

Table 5.2 NDVI drought category based on (Rokhmatullah et al. 2018)

Drought category	NDVI range
No drought	> 0.25
Moderate drought	0.1–0.25
Severe drought	0.05–0.1
Extreme drought	≤ 0.05

5.3.3 Drought Vegetation Monitoring Indexes

The analysis of surface drought conditions (vegetation response, soil moisture) based on remote sensing information involves transforming the data or bands and applying a standardized transformation as a vegetation index. MODIS datasets were used to estimate vegetation indices for the period 2000–2020. Among these indices, the most common and sensitive to vegetative dynamics are NDVI and VCI.

5.3.4 Normalized Difference Vegetation Index NDVI

The normalized difference vegetation index NDVI, is an index that measure of the phenological vegetation condition. It was computed from Terra platform with 250 m spatial resolution from MODIS server using the relation of Infrared (NIR) and Red band (RED) as its shown in (5.1).

$$\mathrm{NDVI} = \frac{\mathrm{Band}_{\mathrm{NIR}} - \mathrm{Band}_{\mathrm{RED}}}{\mathrm{Band}_{\mathrm{NIR}} + \mathrm{Band}_{\mathrm{RED}}} \tag{5.1}$$

This product was corrected using GIS techniques to correct geometrical overlapping and radiometric fluctuations and cloudy pixels were removed (Kogan 1997). Then was categorized to represent drought condition scale as (Rokhmatullah et al. 2018), that represents whether photosynthesis characteristics is above or below of average condition (Table 5.2).

5.3.5 Vegetation Condition Index VCI

Vegetation condition index VCI, is calculated from NDVI product using (5.2). VCI is a pixel-based index by considering of mean and maximum multi-annual variability (Kogan 1997).

$$\mathrm{VCI} = \frac{\mathrm{VCI}_{ijk} - \mathrm{VCI}_{i,\,\mathrm{min}}}{\mathrm{VCI}_{i,\,\mathrm{max}} - \mathrm{VCI}_{i,\,\mathrm{min}}} \times 100 \tag{5.2}$$

Table 5.3 VCI drought category based on (Rokhmatullah et al. 2018)

Drought category	VCI range
No drought	> 30
Moderate drought	20–30
Severe drought	10–20
Extreme drought	0–10

where VCI_{ijk} is the VCI value for the pixel i during month j for year k, VCI_{ijk} is the monthly, VCI value for pixel i in month j for year k. VCI, $VCI_{i,\,min}$ and $VCI_{i,\,max}$ are the multiyear minimum and maximum of VCI, respectively, for pixel i (Kogan 1997).

Then was categorized to represent drought condition scale regarding with the vegetation growing season as 30% below, as its shown below on Table 5.3 (Rokhmatullah et al. 2018).

5.3.6 Climatological Drought Indexes

Drought indices are associated numerically with the value of hydroclimatic variables that may reflect changes in their hydrological regime or quantity, such as meteorological, agricultural, and hydrological variables, representing factors that contribute to or counteract the occurrence and propagation of droughts (Habibi et al. 2020). These methodologies, mainly involve a simplification process, in which an anomaly or a normalization of the values of these driving factors is considered to influence the magnitude of other physical variables highly related to water deficits, the most used of which generalize a standardization of the driving source of water such as precipitation (SPI) and water balance (SPEI) (Depsky and Pons 2020; Belayneh et al. 2014).

5.3.6.1 Standardized Precipitation Index SPI

The SPI computation is based on the long-term precipitation records cumulated over a selected time scale. According with Husak, 2007. This methodology allows to fit this kind of data using gamma probabilistic distribution (5.3) and then standardized by normal distribution to obtain deviations from each precipitation record (Blain 2011).

$$g(x) = \frac{1}{\beta^{\alpha}\Gamma(\alpha)} x^{\alpha-1} e^{-x/\beta} \tag{5.3}$$

where, α, β are scale and shape parameters that could be obtained using L-moments method. According to the SPI, drought starts when the SPI value is equal or less than -1.0 and ends when the value becomes zero or high (Table 5.4).

Table 5.4 SPI drought category based on (Rokhmatullah et al. 2018)

Drought category	Spi range
No drought	> -1
Moderate drought	-1.5 to -1
Severe drought	-2 to -1.5
Extreme drought	≤ -2

5.3.6.2 Standardized Precipitation Evapotranspiration Index SPEI

Standardized Precipitation Evapotranspiration Index SPEI is calculated as water balance stablishing the difference between precipitation and potential evapotranspiration PET for the desired month as (5.4), then its normalized by log-logistic probabilistic distribution (5.5) to define the drought indicator (Diaz et al. 2020b), describing the water balance impacts according to the drought severity. The Thornwaite approach is widely applied to compute the PET (Bae et al. 1981).

$$\mathrm{WB}i = \mathrm{P}i - \mathrm{PET}i \tag{5.4}$$

$$f(x) = \frac{\beta}{\alpha}\left(\frac{x-\gamma}{\alpha}\right)^{\beta-1}\left[1-\left(\frac{x-\gamma}{\alpha}\right)^{\beta}\right]^{-2} \tag{5.5}$$

where, (α, β ,γ) are scale, shape and origin parameters that could be obtained using L-moments method. Then as SPI, drought scale is the same (Table 5.5).

5.3.7 Spatiotemporal Monitoring

The spatiotemporal approach is based on the methodology proposed by Corzo and Vitali, 2018. This methodology allows to perform an articulated analysis between the spatial and temporal changes of the observed drought events within the region, after the extraction of the drought extensions (areas), and its subsequent estimation of its location and temporal marks that allow evaluating its propagation and mobility in space and time, which allows addressing the problem related to its dynamics. (Diaz et al. 2020b). However, this methodology has only been applied under the use

Table 5.5 SPEI drought category based on (Rokhmatullah et al. 2018)

Drought category	SPEI range
No drought	> -1
Moderate drought	-1.5 to -1
Severe drought	-2 to -1.5
Extreme drought	≤ -2

of hydroclimatic drought indices such SPI or SPEI, so the proposed methodology proposes three stages, initially correlative analysis for the estimation of related accumulation periods (SPI-n, SPEI-n, VI-n) followed by the analysis of non-contiguous drought areas (NCDA). Finally, applying continuous drought areas (CDA) approach and tracking.

5.3.7.1 Correlation Analysis

To implement the spatiotemporal tracking methodology, it is necessary to identify the relationship between drought areas, magnitude and frequency, which are measurable between climatological and vegetation-based indices. This will allow generating a better understanding of the applicability of satellite indices in spatiotemporal drought monitoring (Jiao et al. 2016). For this purpose, Pearson's correlation test was used, between the monthly time series of SPI-n, SPEI-n, (where *n*, represents the lag-time variable) and Vegetation Indices (VI) such as VCI, and NDVI for the period 2000–2020. Considering the time series from January to December (annual cycle), and the growing season (April to September), thus establishing the periods with the highest degree of autocorrelation in different periods of accumulation and significance (Kogan 1997).

5.3.7.2 Non-Contiguous Drought Area Analysis (NCDA)

After the drought indices computation and their spatial representation verification. Threshold analysis is defined. This threshold allows to define a boundary at which the drought will be defined for its integrated analysis (in space and time) for time series and spatial grid.

That means, the threshold values below the water normal condition −1.0, was established to extract the drought true zones in the period 1981–2020 for SPI-n and SPEI-n and below 0.25 and 30% for NDVI and VCI, respectively, as shown in Fig. 5.6:

where, I indicates normal values of the drought index, II, establishes thresholder the drought categories and III represents the drought areas in a cluster.

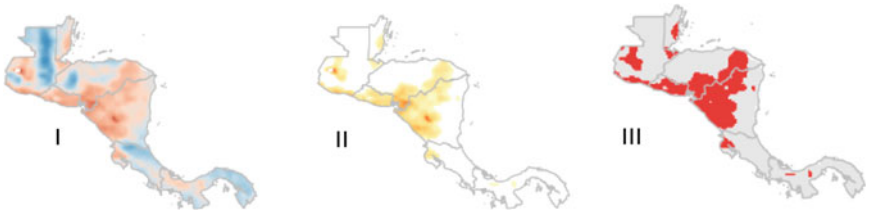

Fig. 5.6 Drought index thresholding and binarizing

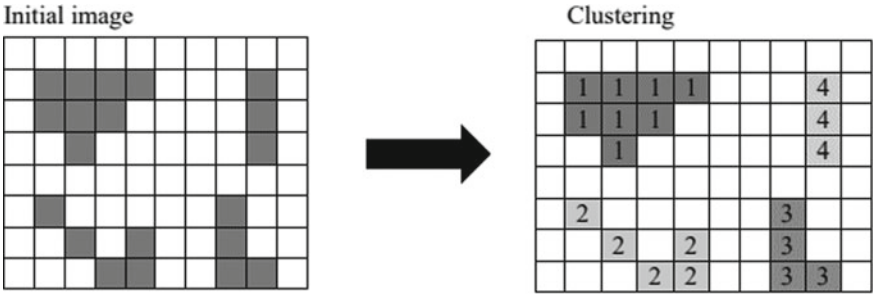

Fig. 5.7 Extracting CDA units using connected components technique

5.3.7.3 Contiguous Drought Area Analysis (CDA)

Contiguous Drought Area, is based on spatial clustering of drought adjacent cells. These drought cells are identified at each time step (Corzo 2019). If the drought indicator is lower or equal than the threshold, it is binarized between 0 and 1, where a value of 1 indicates that the cell is in drought. Otherwise, 0 is used, indicating no drought (Diaz et al. 2020b).

Image analysis approach was done using a Graphos Technique. Connected Labeling Component technique that consists of generating subgroups of patterns in an image (clusters) based on its cell value to connect it (Fig. 5.7) (Herrera-Estrada et al. 2017).

5.3.7.4 Spatiotemporal Propagation–Tracking Events

Once the contiguous areas are estimated, the largest cluster is extracted at each time step and geospatial properties such as centroid coordinates (x, y), relative area/perimeter are calculated (Diaz et al. 2020b). Then, for each largest event over time, the centroid obtained is analyzed by calculation of overlapping percentage and Euclidean distance to define the trajectory for each largest drought in time (Diaz et al. 2020a) (Fig. 5.8).

where t represents each time step (2000–2020), Ci represents the clusters, and the black spots CDA units.

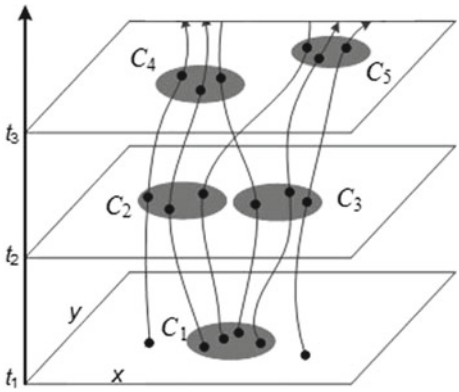

Fig. 5.8 Outlining of tracking approach based on (Blain 2011)

5.4 Results and Discussion

5.4.1 Climatological Drought Index

Based on ERA5 data, the standardized SPI-n and SPEI-n indices were calculated for accumulations of ($n = 1, 3, 6$ months) as shown in Fig. 5.9, shows the drought and non-drought values (red and blue, respectively), and their attenuation when considered as oscillations in the more attenuated time series, thus allowing to identify temporally how an event develops as a function of its magnitude in response to the water deficit.

As its shown in the Fig. 5.9, values for drought index SPI and SPEI below −1.0, reflects a moderate to extreme drought pattern, increasing in frequency over the last decade, with an average of 45–70 periods of drought-associated water deficits (Van Loon 2015; Sutanto et al. 2020; Hydrologic remote sensing: capacity building for sustainability and resilience 2007).

Temporal characteristics of interannual changes may reflect the characteristics of the long-term change in drought. SPI and SPEI variations, in other words, share similar patterns at various time scales, but the lag in the accumulation (lag-time 1, 3, 6) allows the temporal attenuation of the drought magnitude to be appreciated (lower peaks that represents extreme drought magnitude), causing its trend to increase in relative area terms (Entekhabi et al. 2010; Zhang et al. Mar. 2022; Ebrahimi et al. 2010).

On the other hand, the SPI and SPEI monthly variation characteristics clearly reflect the change in the degree of dryness and humidity in each month, especially in the last 20 years (Jiao et al. 2016; Poornima and Pushpalatha 2019; Al-Shujairy et al. 2019). However, when increasing the periods of analysis and looking in contrast at the same accumulations (SPI-6, SPEI-6), drought was more frequent in the months of March to June and October to January (Fig. 5.10), generating extensions in terms of area and deficit more frequent in meteorological drought (SPI) and more prolonged for agricultural drought (SPEI).

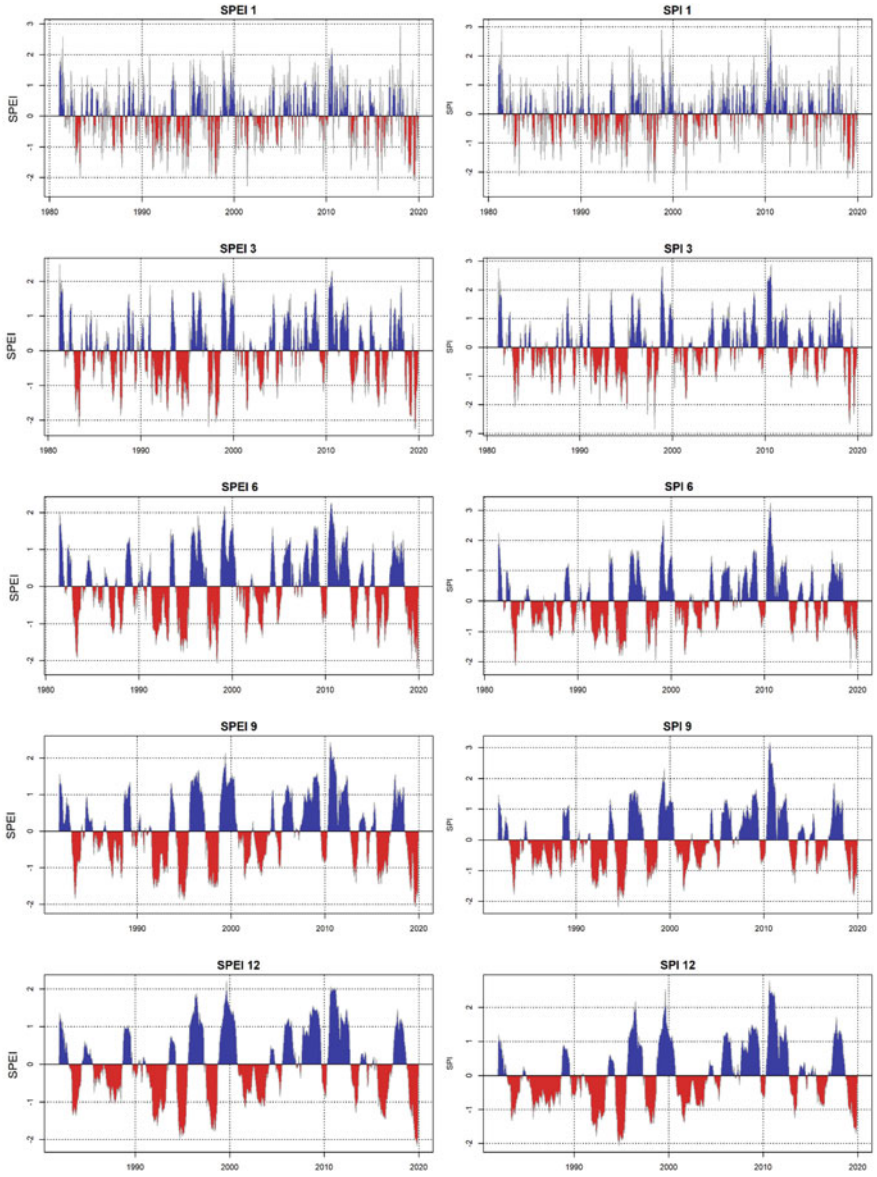

Fig. 5.9 SPEI (left), SPI (right) for (1, 3, 6, 9, 12 months lagged) time series

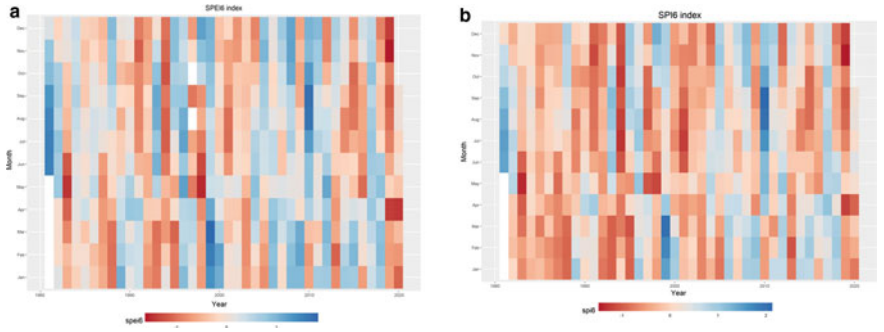

Fig. 5.10 Comparison SPEI (left -a-), SPI (right -b-) for 6 months lagged (*x*-axis years and *y*-axis month)

5.4.2 Drought Vegetation Monitoring Indexes

NDVI trends in the vegetative cycle is analyzed, considering the phenological growth as illustrated in Fig. 5.11, which allows inferring the vegetative activity as a function of temperature and water stress cycles (Colliander et al. 2017; Hafni et al. 2022). For this purpose, the monthly NDVI series corresponding to the maximum mean NDVI was selected.

For the dry corridor of Central America, a bimodal phenological pattern is observed for the periods January–May and July–October, which are directly related to rainfall patterns (Fig. 5.12). In this way, the vegetation onset depends on the meteorological conditions in the area by year, but not necessarily depends on the vegetation type or crop productivity. (Jong et al. 2011).

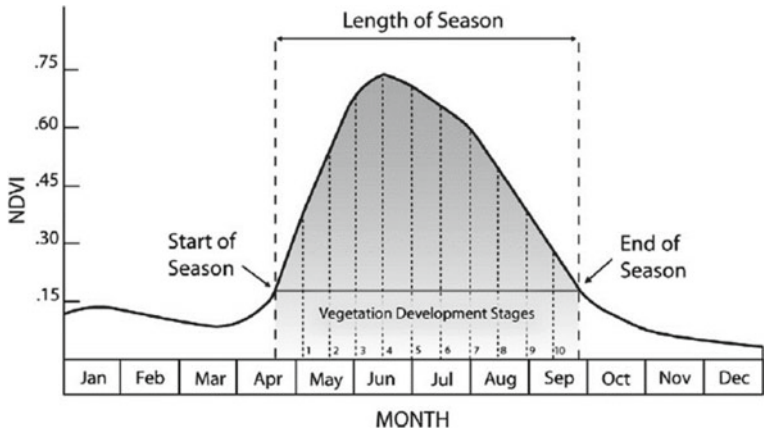

Fig. 5.11 Phenological growing season scheme, based on (Peters et al. 2002)

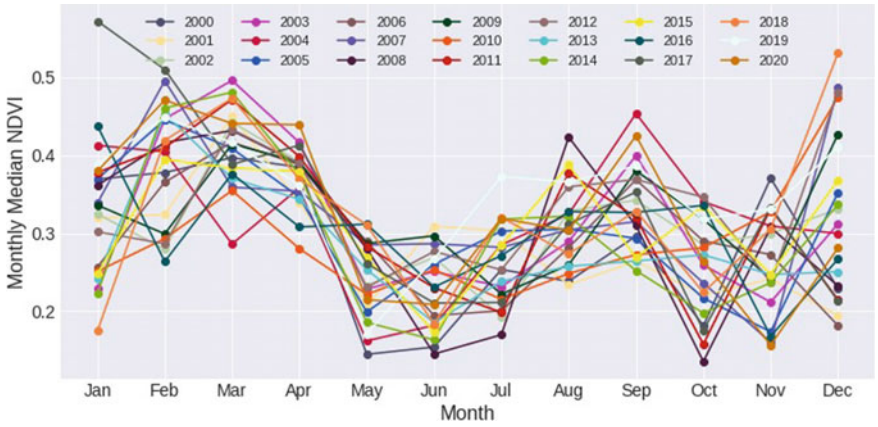

Fig. 5.12 NDVI monthly trends

However, the derivation of the VCI required a NDVI trend normalization, which is implemented by the LOWESS smoothing technique (locally weighted running line smoother) proposed by (Kogan 1997; Cai et al. 2017).

$$x = f(x) + \varepsilon_1 x_1 + \varepsilon_2 x_3 + \varepsilon_n x_n \tag{5.6}$$

$$w(x) = \{\left(1 - |x|^3\right)^3 : |x|\langle 10 : |x|\rangle 1 \tag{5.7}$$

Which, if NDVI trends (5.6) with noise ε should be adjust to a normal distribution, then each data value (x) is replaced by a combination of adjacent values of the normal series in a window $w(x)$, using a second order polynomial least squares fit (Kogan 1997). Generating a new time series normalized, (Hilda 2017; Prasetyo et al. 2019) allowing a reconstruction of the time series in which the leaf area and photosynthetic activity is easily appreciable (Murakami et al. 2016; Soudani et al. 2012; Gong 2022). This methodology is tested with 3 filters or smoothing window, in which the degree of smoothing is estimated by least squares minimization, thus allowing to reduce by attenuations sudden changes in NDVI as its shown in Fig. 5.13 (Cai et al. 2017).

5.4.3 Spatiotemporal Approach

After obtaining the drought indexes based on hydro climatological data like SPI, SPEI, and remote sensing-based like NDVI and VCI, a correlative analysis was carried out to establish those time accumulations that were related to each other to implement the spatiotemporal analysis. This correlation was generated from the binarization of each index given the threshold set out in the methodology (NCDA).

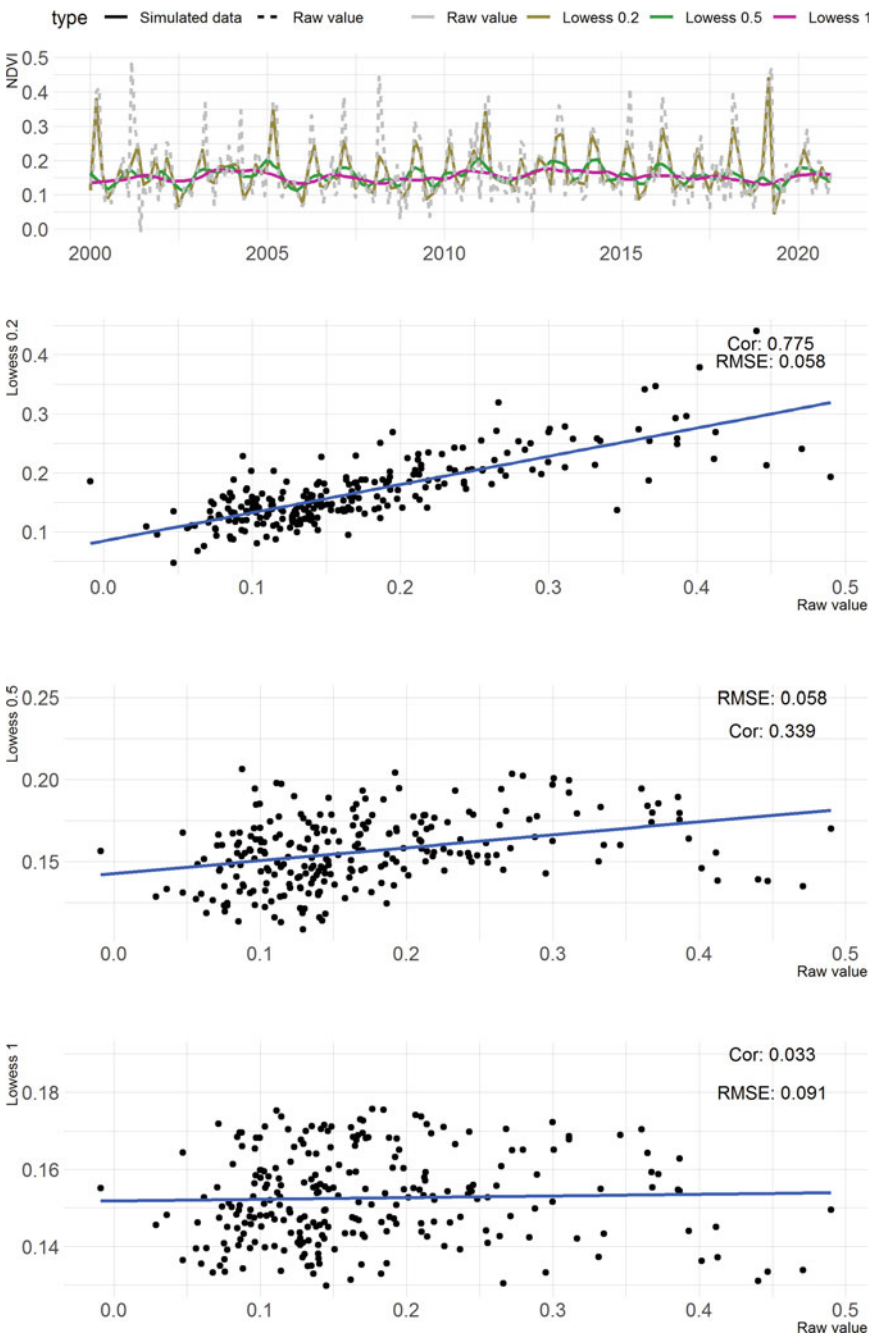

Fig. 5.13 NDVI comparison applying LOWESS smoothing

However, each drought scale proposed, in terms of magnitude varying, their spatial relationship may not fit because each index takes into account different aggregate factors, e.g., VCI standardizes NDVI in phenological response and SPI 3 standardizes precipitation as a function of three-monthly accumulation, which involves highly variable significances (−0.42 to 0.86) as shown in Figs. 5.14 and 5.15.

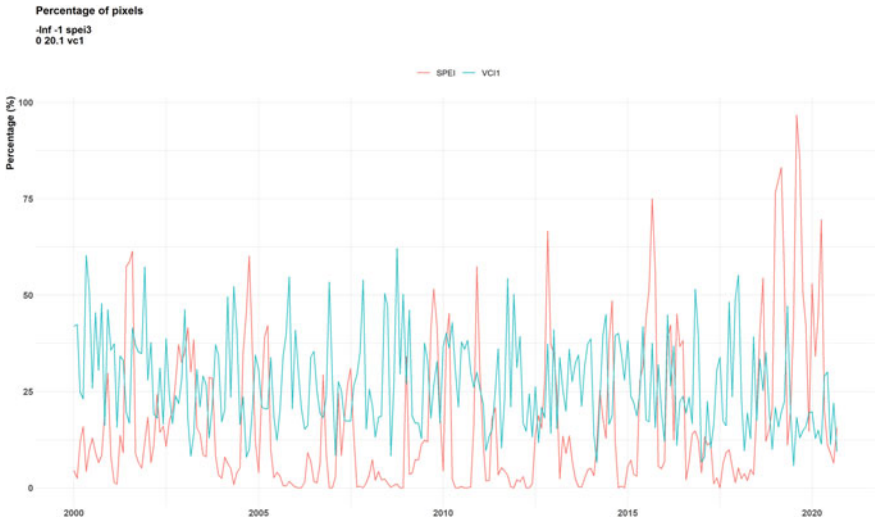

Fig. 5.14 NCDA approach correlation for SPI (−1 to inf) and VCI (0.2−1)

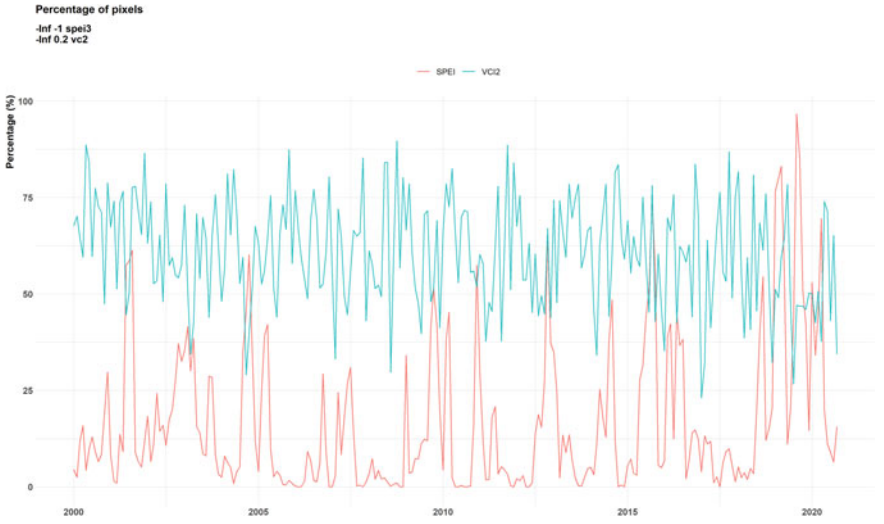

Fig. 5.15 NCDA approach correlation for SPEI 3 (−1 to inf) and VCI (0.2- inf)

Table 5.6 Drought indices general correlation

	SPI 1	SPI 3	SPI 6	SPEI 1	SPEI 3	SPEI 6
NDVI	0.3	0.418	0.7854	0.369	0.687	0.642
VCI	0.32	0.518	0.419	0.378	0.542	0.867

Therefore, equivalent drought ranges had to be established for their analysis, which implied for each category, moderate, severe, and extreme drought, to find those optimal ranges that had greater significance and representativeness in terms of the area under drought condition (NCDA).

Thus, a relationship range is found between the percentages of the area in representative drought and their spatial autocorrelation (Ghulam et al. 2007; Jiao et al. 2016; Peters et al. 2002). As shown in Table 5.6, the net correlation between climatic and remotely sensed indices varies between (0.39 and 0.89), being the combination SPI-3 (moderate drought)– VCI (extreme) and SPEI 6 (extreme)– VCI (extreme) the most significant one. These results allow validating a priori the viability of NDVI and VCI as indices for spatiotemporal drought monitoring.

Following the maximum significance criterion (Pearson coefficient > 0.6), the non-contiguous drought area percentages (NCDA) are obtained, as shown in Fig. 5.16, which comparatively compares the NCDA results for the SPEI-6-VCI combination, where there is a ratio of 2.4:1 in terms of the magnitude of the area. Locating in a temporal way, months between October to January and May to August with greater areas of drought and annually related to El Niño Southern Oscillation periods in the last two decades, like 2019, 2015, 2014, 2012, 2004, and 2003 (Sheffield et al. 2009).

Binary grids are then generated, and the connected component algorithm is used to find the largest clusters or contiguous drought units (CDA) that are most representative for subsequent monitoring as its shown in Fig. 5.17.

5.4.4 Drought Tracking

Considering, these grids that represent the largest clusters (Fig. 5.18), the characteristics of centroid location and area are extracted to evaluate whether an event t is related to an event $t + 1$. (Fig. 5.19) where shows the most representative centroids related to drought area extensions. However, as it is a dynamic phenomenon, the drought that can be visualized in a hydro climatological index is not so perceptible based on vegetation, as the phenological growth cycle only indicates for a certain crop or cover which orientation will have the water deficit. Overlap metrics were employed, excluding events that do not exceed at least 30%.

As shown below in Figs. 5.20 and 5.21, the main trajectories reported according to SPI-SPEI and VCI are presented.

Fig. 5.16 NCDA percentage of area for SPEI 6 (−1 to inf) and VCI (0.2–1)

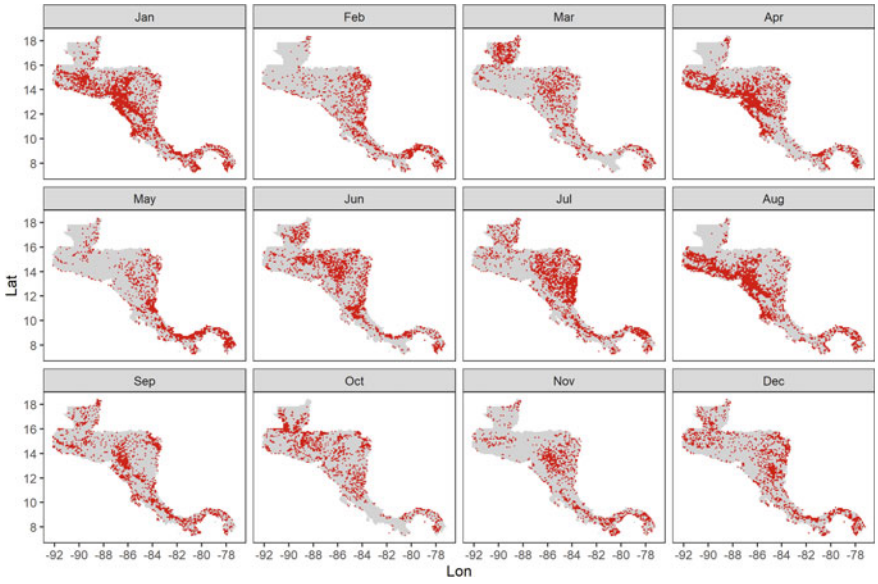

Fig. 5.17 CDA clustering for VCI index

	Picture Number	Label Id.	Centroid X	Centroid Y	Area	%Area on the image	Perimeter	Vertical longitude	Horizontal longitude
0	1	0	322	202	903	0.34	128	22	44
1	1	1	135	166	11944	4.49	535	142	129
2	2	0	366	250	966	0.36	130	24	43
3	2	1	178	214	12114	4.55	539	144	129
4	3	0	409	345	966	0.36	130	24	43
5	3	1	224	304	10977	4.13	490	119	129
6	4	0	269	341	8554	3.22	436	91	130
7	5	0	292	359	2642	0.99	257	44	87

Fig. 5.18 CDA clúster characteristics dataset

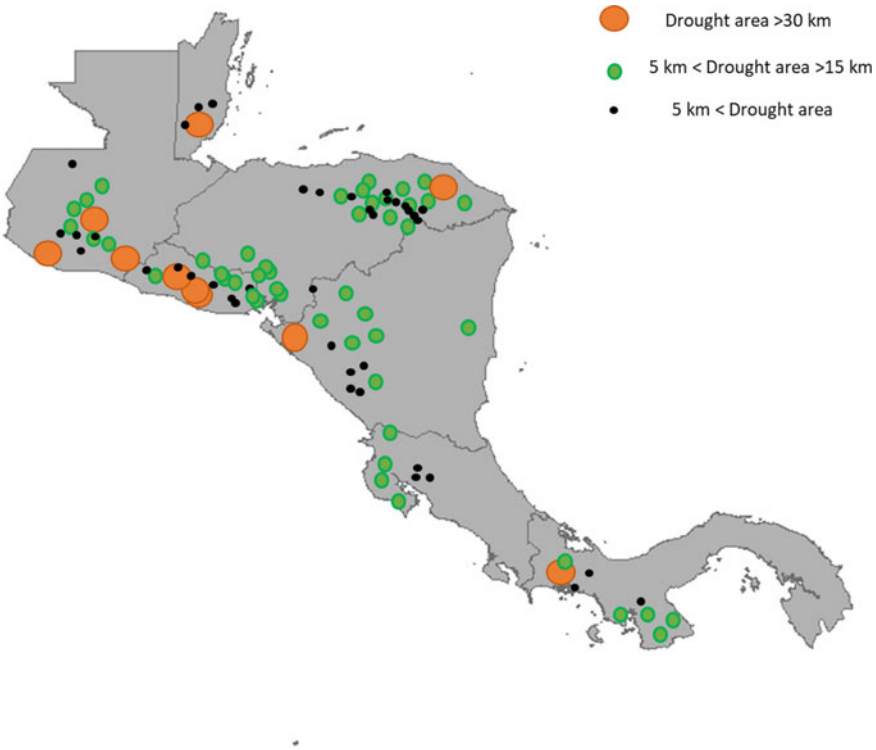

Fig. 5.19 Main centroids of highest drought events

Fig. 5.20 Main trajectories based on spatiotemporal approach driven with SPI-SPEI dataset

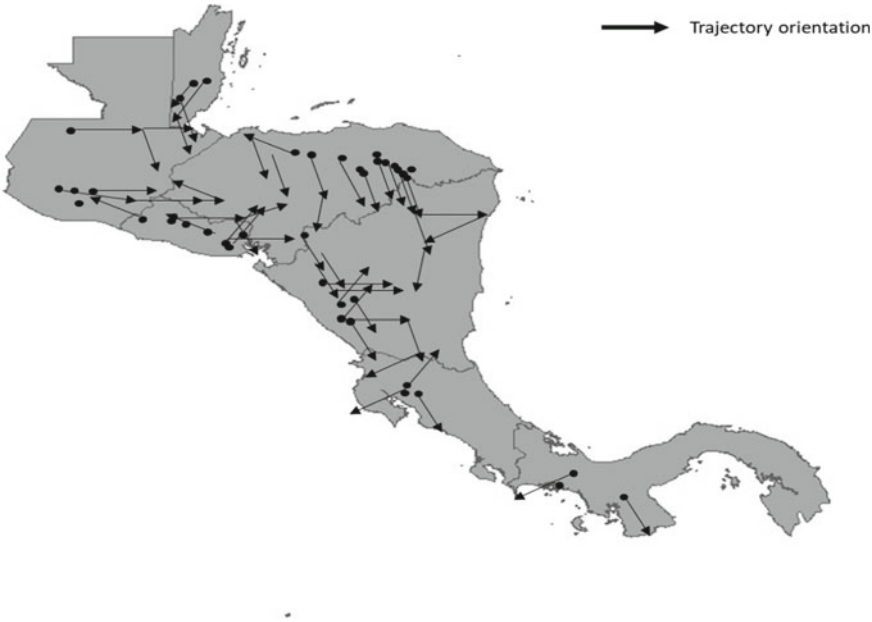

Fig. 5.21 Main trajectories directions based on spatiotemporal approach driven with VCI dataset

For SPI and SPEI, estimated trajectories emphasize that the average extend is between 8 and 13 km (Sánchez Hernández 2022). The longest drought trajectories mainly have origin in Guatemala and El Salvador, where are related to wind patterns, low atmospheric moisture, and high pressure/temperature (Cook et al. 2018; Dominguez and Magaña 2018; Aguilar et al. 2005). Orographically moderate thermal gradient phenomena in the western of the Central America dry corridor countries, allow decreasing the severity of drought and extension (Sánchez Hernández 2022).

However, the trajectories determined for the indices derived from remote information are mainly characterized by being short compared to the previous ones (average distance less than 3 km), which, although they do not allow the evaluation of cluster migration or large drought events over long distances, they do give an overview of the average direction in which they manifest themselves and their orientation allows the adoption of crop protection technologies or agricultural practices.

As can be seen in Fig. 5.21, the orientation is in a northeast position, and when contrasted with Fig. 5.20, there is a high relationship concerning regional hydro climatological aspects.

5.5 Conclusions

Central American dry corridor, drought impacts and water scarcity is increasing. Spatiotemporal analysis and validation of remote sensing information is a game-changer in this type of study requirements, becoming efficiently applicable in sectors with low data availability or early warming tool for regional monitoring (Gong 2022; Jiang et al. 2017; Zhang et al. 2019).

This study evaluated the drought dynamics using a reproducible drought vegetation index VCI using remote sensing data to 2000–2020, allow identifying the stressed vegetation spatial distribution, associated with drought conditions with cutting-edge technologies.

Some preliminary results allow using remote sensing data as NDVI as drought monitoring data source. However, remote sensing data still have some limitations that should be considered in future studies. Radiometric interferences, satellites position can affect the geometry of source, scale, for instance.

Regarding drought areas, the approximation and adaptation of the spatiotemporal analysis methodology allowed us to observe a greater concentration of drought events in regions that are directly affected by global oscillations such as ENSO, hurricanes (geographical limits with Pacific Ocean).

El Salvador, Nicaragua, Costa Rica and Guatemala for example, in the northwest, show the highest density of events per phenological cycle (January–May) and (July–October). Additionally, due to aspects such as resolution and scale of the index, it is

established that the most important migrations of water stress are highly related to the mentioned density, which allows the generation of strategies or opportunities for sustainable agriculture and improvement of drainage systems.

Central America dry corridor countries, over 20 years was found that the relationship between the SPI water deficit on short-term scales together with the VCI values increases proportionally, however, SPEI shows a stronger relationship because of the physical comparison of two observable or measurable agricultural conditions (vegetation condition, evapotranspiration) observed for SPEI 6.

For the years 2000, 2004, 2015, and 2019, longer drought durations and extensions were observed, which lead to extreme events and are highly related to the anthropic migrations of land use reported by FAO (2019); To reduce El Niño's impact on Central America's Dry Corridor, build resilience and invest in sustainable agriculture 2022; World Food Programme 2002).

5.6 Recommendations

According to the findings of this chapter, it was validated that the VCI has greater potential for agricultural drought monitoring than NDVI, and that NDVI is highly correlated with water deficit SPI in 3 months lags and SPEI in 6 months lags. However, some interferences may be associated with the scale magnitudes of the products, which is suggested to verify in detail which geo-correlation and de-scaling method allows geostatistics to have more consistent products, as well as methodologies such as Whitaker (Jiao et al. 2016) for time series smoothing.

More research is needed in case we want to apply this methodology at the crop level, which can strengthen the analysis by establishing productivity in terms of stress associated with drought, thus generating more detailed results and greater efficiency in terms of drought to the cross-border productive sector.

Finally, it is recommended the use of matching algorithms based on geostatistics to improve the performance of both satellite-based indices and their trajectory tracking, such as GWR and Multivariate Kriging, mainly (Nejadrekabi et al. 2022; Dutra et al. 2021; Baniya et al. 2019).

Acknowledgements We would like to thank the IHE-Delft and Escuela Colombiana de Ingenieria-aJulio Garavito for funding this research. Also, thanks for the support to the hydro informatics research group, Dr. Gerald Augusto Corzo Perez, especially to reviewers and editors for their valuable comments, which helped to improve the quality of this manuscript.

Data and Code Statement
Data used and Codes developed in this study are available upon request.

References

Aguilar E et al (2005) Changes in precipitation and temperature extremes in Central America and northern South America, 1961–2003. J Geophys Res Atmos 110(23):1–15. https://doi.org/10.1029/2005JD006119

Al-Shujairy QAT, Al-Hedny S, Al-Barakat H, Hao Y, Hao Z, Fu Y (2019) Drounght analysis by using standarized precipitation index (SPI) and normalized difference vegetation index (NDVI) at Bekasi Regency in 2018. IOP Conf Ser Earth Environ Sci 280(1):012002. https://doi.org/10.1088/1755-1315/280/1/012002

Anandhi A, Srinivas VV, Nanjundiah RS, Nagesh Kumar D (2008) Downscaling precipitation to river basin in India for IPCC SRES scenarios using support vector machine. Int J Climatol 28(3):401–420. https://doi.org/10.1002/joc.1529

Anderson TG, Anchukaitis KJ, Pons D, Taylor M (2019) Multiscale trends and precipitation extremes in the Central American midsummer drought. Environ Res Lett 14(12):124016. https://doi.org/10.1088/1748-9326/ab5023

Bacanli UG, Firat M, Dikbas F (2009) Adaptive neuro-fuzzy inference system for drought forecasting. Stoch Environ Res Risk Assess. https://doi.org/10.1007/s00477-008-0288-5

Bae S, Lee SH, Yoo SH, Kim T (2018) Analysis of drought intensity and trends using the modified SPEI in South Korea from 1981 to 2010. Water (Switzerland) 10(3). https://doi.org/10.3390/w10030327

Baniya B, Tang Q, Xu X, Haile GG, Chhipi-Shrestha G (2019) Spatial and temporal variation of drought based on satellite derived vegetation condition index in Nepal from 1982–2015. Sensors (Switzerland) 19(2). https://doi.org/10.3390/S19020430

Beck HE et al (2017) Global-scale evaluation of 22 precipitation datasets using gauge observations and hydrological modeling. Hydrol Earth Syst Sci 21(12):6201–6217. https://doi.org/10.5194/hess-21-6201-2017

Belayneh A, Adamowski J, Khalil B, Ozga-Zielinski B (2014) Long-term SPI drought forecasting in the Awash River Basin in Ethiopia using wavelet neural networks and wavelet support vector regression models. J Hydrol. https://doi.org/10.1016/j.jhydrol.2013.10.052

Blain GC (2011) Standardized precipitation index based on Pearson type III distribution. Rev Bras Meteorol 26(2):167–180. https://doi.org/10.1590/s0102-77862011000200001

Buttafuoco G, Caloiero T (2014) Drought events at different timescales in Southern Italy (Calabria). J Maps 10(4):529–537. https://doi.org/10.1080/17445647.2014.891267

Cai W (2014) Increasing frequency of extreme El Niño events due to greenhouse warming. Nat Clim Chang 4(2):111–116. https://doi.org/10.1038/nclimate2100

Cai Z, Jönsson P, Jin H, Eklundh L (2017) Performance of smoothing methods for reconstructing NDVI time-series and estimating vegetation phenology from MODIS data. Remote Sens 9(12). https://doi.org/10.3390/RS9121271

Colliander A et al (2017) Validation of SMAP surface soil moisture products with core validation sites. Remote Sens Environ. https://doi.org/10.1016/j.rse.2017.01.021

Cook BI, Mankin JS, Anchukaitis KJ (2018) Climate change and drought: from past to future. Curr Clim Chang Reports 4(2):164–179. https://doi.org/10.1007/S40641-018-0093-2

Corzo G (2019) Framework for spatio-temporal multi-objective optimization of preventive drought management measures. PhD research proposal

de Jong R, de Bruin S, de Wit A, Schaepman ME, Dent DL (2011) Analysis of monotonic greening and browning trends from global NDVI time-series. Remote Sens Environ 115(2):692–702. https://doi.org/10.1016/J.RSE.2010.10.011

Depsky N, Pons D (2020) Meteorological droughts are projected to worsen in Central America's Dry Corridor throughout the 21st century. Environ Res Lett 16(1):014001. https://doi.org/10.1088/1748-9326/ABC5E2

Diaz V, Corzo Perez GA, Van Lanen HAJ, Solomatine D, Varouchakis EA (2020a) Characterisation of the dynamics of past droughts. Sci Total Environ https://doi.org/10.1016/j.scitotenv.2019.134588

Diaz V, Corzo Perez GA, Van Lanen HAJ, Solomatine D, Varouchakis EA (2020b) An approach to characterise spatio-temporal drought dynamics. Adv Water Resour. https://doi.org/10.1016/j.advwatres.2020.103512

Dominguez C, Magaña V (2018) The role of tropical cyclones in precipitation over the tropical and subtropical North America. Front Earth Sci 6. https://doi.org/10.3389/FEART.2018.00019/FULL

Dracup JA, Lee KS, Paulson EG (1980) On the definition of droughts. Water Resour Res. https://doi.org/10.1029/WR016i002p00297

Dutra DJ, Elmiro MAT, Coelho CWGA, Nero MA, Temba PDC (2021) Temporal analysis of drought coverage in a watershed area using remote sensing spectral indexes. Soc Nat 33. https://doi.org/10.14393/SN-V33-2021-59505

Ebrahimi M, Matkan AA, Darvishzadeh R (2010) Remote sensing for drought assessment in Arid regions (A case study of central part of Iran, "Shirkooh-Yazd")

Eckstein D, Hutfils M-L, Winges M (2017) Germanwatch

Entekhabi D et al (2010) The soil moisture active passive (SMAP) mission. Proc IEEE. https://doi.org/10.1109/JPROC.2010.2043918

Fallah A, Rakhshandehroo GR, Berg POS, Orth R (2020) Evaluation of precipitation datasets against local observations in southwestern Iran. Int J Climatol 40(9):4102–4116. https://doi.org/10.1002/joc.6445

FAO (2019) Global report on food crises. Food Secur Inf Netw

Frieler K et al (2017) Assessing the impacts of 1.5 °C global warming—simulation protocol of the inter-sectoral impact model intercomparison project (ISIMIP2b). Geosci Model Dev 10(12):4321–4345. https://doi.org/10.5194/gmd-10-4321-2017

Ghulam A, Qin Q, Zhan Z (2007) Designing of the perpendicular drought index. Environ Geol 52(6):1045–1052. https://doi.org/10.1007/S00254-006-0544-2

Gong F et al (2022) Partitioning of three phenology rhythms in American tropical and subtropical forests using remotely sensed solar-induced chlorophyll fluorescence and field litterfall observations. Int J Appl Earth Obs Geoinf 107. https://doi.org/10.1016/j.jag.2022.102698

Habibi M, Schöner W, Babaeian I (2020) Drought monitoring using standardized precipitation index (SPI), standardized precipitation-evapotranspiration index (SPEI) and normalized-difference snow index (NDSI) with observational and ERA5 dataset, within the uremia lake basin, Iran. 11543

Hafni DAF et al (2022) Peat fire risk assessment in Central Kalimantan, Indonesia using the standardized precipitation index (SPI). IOP Conf Ser Earth Environ Sci 959(1). https://doi.org/10.1088/1755-1315/959/1/012058

Herrera-Estrada JE, Satoh Y, Sheffield J (2017) Spatiotemporal dynamics of global drought. Geophys Res Lett. https://doi.org/10.1002/2016GL071768

Hilda F (2017) Drought analysis for mitigating Peatland fires using satellite data based on geographic information systems. JOM FTEKNIK 4(2):1–9

Hydrologic remote sensing: capacity building for sustainability and resilience—Google Libros. https://books.google.com.co/books?id=jyINDgAAQBAJ&pg=PA265&lpg=PA265&dq=(Ghulam+et+al.,+2007).&source=bl&ots=-mrnulrLQ8&sig=ACfU3U3G0Xde_zS-aQuR_YAlO-_2XPg58A&hl=es-419&sa=X&ved=2ahUKEwiGjIDt2ej3AhX0SDABHf-vBAUQ6AF6BAgZEAM#v=onepage&q=(Ghulametal.%2C2007)&f=false. Accessed 18 May 2022

Jiang Y et al (2017) Analysis of relationship between meteorological and agricultural drought using standardized precipitation index and vegetation health index. IOP Conf Ser Earth Environ Sci 54(1):012008. https://doi.org/10.1088/1755-1315/54/1/012008

Jiao W, Zhang L, Chang Q, Fu D, Cen Y, Tong Q (2016) Evaluating an enhanced vegetation condition index (VCI) based on VIUPD for drought monitoring in the continental united states. Remote Sens 8(3):224. https://doi.org/10.3390/RS8030224

Kogan F (1997) Global drought watch from space. https://web.iitd.ac.in/~sagnik/C2.pdf. Accessed 23 Sep 2021

Maldonado T, Rutgersson A, Alfaro E, Amador J, Claremar B (2016) Interannual variability of the midsummer drought in Central America and the connection with sea surface temperatures. Adv Geosci. https://doi.org/10.5194/adgeo-42-35-2016

Murakami H et al (2016) Seasonal forecasts of major hurricanes and landfalling tropical cyclones using a high-resolution GFDL coupled climate model. J Clim. https://doi.org/10.1175/JCLI-D-16-0233.1

Nejadrekabi M, Eslamian S, Zareian MJ (2022) Spatial statistics techniques for SPEI and NDVI drought indices: a case study of Khuzestan Province. Int J Environ Sci Technol. https://doi.org/10.1007/S13762-021-03852-8

Nihoul JCJ (2005) Marine ecosystems and climate variation. J Mar Syst. https://doi.org/10.1016/j.jmarsys.2004.06.004

Okal HA, Ngetich FK, Okeyo JM (2020) Spatio-temporal characterisation of droughts using selected indices in Upper Tana River watershed, Kenya. Sci African 7:e00275. https://doi.org/10.1016/j.sciaf.2020.e00275

Peters A, Walter-Shea E, Ji L, Viña A, Hayes M, Svoboda M (2002) Drought Monitoring with NDVI-Based standardized vegetation index. Undefined

Podestá G, Skansi M, Herrera N, Veiga H (2016) Descripción de índices para el monitoreo de sequía meteorológica implementados por el Centro Regional del Clima para el Sur de América del Sur. Rep Técnico CRC-SAS

Poornima S, Pushpalatha M (2019) Drought prediction based on SPI and SPEI with varying timescales using LSTM recurrent neural network. Soft Comput. https://doi.org/10.1007/s00500-019-04120-1

Prasetyo Y, Bashit N, Simarsoit Y (2019) Study of correlation of residential and industrial growth pattern in Semarang city to the aquifer capacity changes in the year 2014–2017. IOP Conf Ser Earth Environ Sci 280(1). https://doi.org/10.1088/1755-1315/280/1/012001

Rokhmatullah, Hernina R, Yandi S (2018) Drounght analysis by using standarized precipitation index (SPI) and normalized difference vegetation index (NDVI) at Bekasi Regency in 2018. IOP Conf Ser Earth Environ Sci. https://doi.org/10.1088/1755-1315/280/1/012002

Sahaar SA, Niemann JD (2020) Impact of regional characteristics on the estimation of root-zone soil moisture from the evaporative index or evaporative fraction. Agric Water Manag 238. https://doi.org/10.1016/J.AGWAT.2020.106225

Sánchez Hernández KA (2021) Biblioteca Jorge Álvarez Lleras Koha › Detalles de: machine learning methods for characterising and tracking spatiotemporal drought events case study: Central America Dry Corridor . https://catalogo.escuelaing.edu.co/cgi-bin/koha/opac-detail.pl?biblionumber=22675. Accessed 18 May 2022

Serda M (2013) Synteza i aktywność biologiczna nowych analogów tiosemikarbazonowych chelatorów żelaza. Uniw śląski 343–354. https://doi.org/10.2/JQUERY.MIN.JS

Sexton JO et al (2013) Global, 30-m resolution continuous fields of tree cover: landsat-based rescaling of MODIS vegetation continuous fields with lidar-based estimates of error. Int J Digit Earth. https://doi.org/10.1080/17538947.2013.786146

Sheffield J, Andreadis KM, Wood EF, Lettenmaier DP (2009) Global and continental drought in the second half of the twentieth century: severity-area-duration analysis and temporal variability of large-scale events. J Clim. https://doi.org/10.1175/2008JCLI2722.1

Soudani K et al (2012) Ground-based Network of NDVI measurements for tracking temporal dynamics of canopy structure and vegetation phenology in different biomes. Remote Sens Environ 123:234–245. https://doi.org/10.1016/J.RSE.2012.03.012

Sutanto SJ, Wetterhall F, Van Lanen HAJ (2020) Hydrological drought forecasts outperform meteorological drought forecasts. Environ Res Lett 15(8). https://doi.org/10.1088/1748-9326/AB8B13

Tadesse T, Wardlow B, Svoboda MD, Hayes MJ (2012) Vegetation outlook (VegOut): predicting remote sensing–based seasonal greenness. Drought Mitigation Center Faculty Publications [Online]. Available: https://digitalcommons.unl.edu/droughtfacpub/102. Accessed 18 May 2022

To reduce El Niño's impact on Central America's Dry Corridor, build resilience and invest in sustainable agriculture. https://www.ifad.org/es/web/latest/-/news/to-reduce-el-nino-s-impact-on-central-america-s-dry-corridor-build-resilience-and-invest-in-sustainable-agriculture. Accessed 18 May 2022

van der Zee Arias A, van der Zee J, Meyrat A, Poveda C, Picado L (2012) Estudio de caracterización del Corredor Seco Centroamericano. p 70 [Online]. Available: https://reliefweb.int/sites/reliefweb.int/files/resources/tomo_i_corredor_seco.pdf

Van Loon AF (2015) Hydrological drought explained. Wiley Interdiscip Rev Water. https://doi.org/10.1002/wat2.1085

World Food Programme (2022) Erratic weather patterns in the Central American Dry Corridor leave 1.4 million people in urgent need of food assistance. https://www.wfp.org/news/erratic-weather-patterns-central-american-dry-corridor-leave-14-million-people-urgent-need. Accessed 18 May 2022

Wilhite D (2006) Drought monitoring and early warning: concepts, progress and future challenges. World Meteorological Organ

Zhang J et al (2022) NIRv and SIF better estimate phenology than NDVI and EVI: effects of spring and autumn phenology on ecosystem production of planted forests. Agric for Meteorol 315:108819. https://doi.org/10.1016/J.AGRFORMET.2022.108819

Zhang A, Jia G, Wang H (2019) Improving meteorological drought monitoring capability over tropical and subtropical water-limited ecosystems: evaluation and ensemble of the microwave integrated drought index. Environ Res Lett 14(4). https://doi.org/10.1088/1748-9326/AB005E

Zhao M, Heinsch FA, Nemani RR, Running SW (2005) Improvements of the MODIS terrestrial gross and net primary production global data set. Remote Sens Environ. https://doi.org/10.1016/j.rse.2004.12.011

Chapter 6
Application of GIS and Remote Sensing Tools in Assessment of Drought Using Satellite and Ground-Based Data

R. V. Galkate, Sukant Jain, R. K. Jaiswal, R. P. Pandey, A. K. Lohani, Shalini Yadav, and Ram Narayan Yadava

Abstract Satellite-based data, information, and indices have been very efficient and useful for rapid assessment of drought situations. They can be proven even more effective if tested using appropriate indicators derived from physically observed ground station-based climatic data. This chapter examines the effectiveness of satellite data in drought characterization. The MODIS Normalized Difference Vegetation Index (NDVI) data were used to monitor vegetation health and drought in the Bundelkhand region of Central India using the NDVI-based Vegetation Condition Index (VCI), and the results were compared to the Standardized Precipitation Index (SPI). Using rainfall departure analysis and SPI on a three-month time scale, long-term rainfall data from the Bundelkhand region were used to assess the extent of meteorological drought and identify the driest years. The VCI was calculated using satellite-based NDVI data from the same period. Three-month SPI was evaluated for the severe drought years identified through rainfall departure analysis and compared to VCI results. In October 2015, both SPI and VCI indicated extremely severe drought. The satellite-based indicator VCI has been found to interpret results that are consistent with the drought index SPI, which is evaluated using observed ground station-based data, indicating the utility of satellite data in quick drought monitoring.

Keywords Drought index · Standardized precipitation index · Vegetation condition index · Normalized difference vegetation index · Bundelkhand region

R. V. Galkate (✉) · S. Jain · R. K. Jaiswal
Central India Hydrology Regional Centre (CIHRC), National Institute of Hydrology, WALMI Campus, Bhopal, (M.P.), India
e-mail: galkate.nihr@gov.in

R. P. Pandey · A. K. Lohani
National Institute of Hydrology, Jal Vigyan Bhavan, Roorkee, Uttaranchal, India

S. Yadav
Department of Civil Engineering, Rabindranath Tagore University, Bhopal, (M.P.), India

R. N. Yadava
Research and International Affairs, Madhyanchal Professional University, Bhopal, (M.P.), India

V. P. Singh et al. (eds.), *Application of Remote Sensing and GIS in Natural Resources and Built Infrastructure Management*, Water Science and Technology Library 105,
https://doi.org/10.1007/978-3-031-14096-9_6

6.1 Introduction

Drought is a cyclic phenomenon that has a slow onset and terminates with a definite end. It can trigger serious damage to vegetation if it continues to evolve. Although the primary indicator of drought severity is rainfall, other factors are also needed to properly assess the severity of the situation. A comprehensive drought assessment system should also include other indicators to monitor the various aspects of drought. Some of the indicators used in a comprehensive drought assessment are temperature, streamflow, groundwater level, soil moisture, and reservoir level. Drought is a period of extremely dry weather conditions that usually affects the vegetation cover of the Earth. This condition has gained the importance of satellite data in monitoring environmental factors. Droughts are one of the most dangerous environmental disasters, causing adverse impacts on the natural ecosystem, hydrological and agricultural systems (Bond et al. 2008). Drought generally occurs due to a lack of precipitation and variability in rainfall patterns. Droughts seem like a situation of below-normal rainfall and evolve into a dangerous climatic event with significant consequences for the environment. Drought has affected about half of the global population (Kogan et al. 2019). It is one of the serious phenomena and ranks on top among all the natural hazards concerning the number of people gets affected globally (Dunn et al. 2018). Drought risks build up gradually, which often accumulate over a long period, and might last for years after the drought is over (Mishra and Singh 2010). The drought severity, onset, as well as withdrawal, are not only difficult to identify but quantify also. According to a recent Intergovernmental Panel on Climate Change (IPCC) report, maize, wheat, and rice production have decreased in various regions of Asia during the last few decades owing to global warming, water stress, a decrease in rainy days, and the frequency of El Nino occurrences (IPCC 2014).

Droughts in India are classified into three types by the National Commission on Agriculture: meteorological, hydrological, and agricultural (Mirdha 1973). A meteorological drought occurs when an area receives less than 25% of its normal precipitation. Long-term meteorological droughts cause hydrological drought which results in the drying up of rivers, streams, lakes, and reservoirs, as well as a decrease in groundwater level. Agricultural drought occurs when soil moisture is insufficient to support healthy crop growth during the growing season, resulting in crop stress and wilting. India has a total geographical area of 3.38 million km^2, of which approximately 1.08 million km^2 is subject to varying degrees of drought and water stress (Jain et al. 2009). In the last five decades, India has been one of the most vulnerable and drought-prone countries, where drought occurs almost in every three years (Miyan 2015). Droughts have caused significant agricultural and economic losses in India in the past, most prominently in 1877, 1899, 1918, 1972, 1987, and 2002 (Yadav 2009). In comparison to Northern India, the peninsular western and central parts of the country are primarily affected by drought. Droughts are causing adverse

impacts on water resources, agriculture, rural livelihoods, and the economy in Central India, particularly in the Bundelkhand region of Madhya Pradesh state (Kundu et al. 2015; Pandey et al. 2010). Drought is common in these areas due to factors such as monsoon season uncertainty, high temperatures, and unfavourable meteorological conditions.

Drought must be assessed and monitored using scientific techniques to reduce future risks and potential dangers. Traditional drought monitoring relies on ground-based observations of meteorological and hydrological data including precipitation, temperature, evapotranspiration, soil moisture, surface runoff, and groundwater levels. Several drought indicators have been developed in recent years based on this single location data such as the Standardized Precipitation Index (SPI) (Guttman 1999), Crop Moisture Index (Palmer 1968), Palmer Drought Severity Index (Palmer 1965), Soil Moisture Drought Index, Streamflow Drought Severity Index, Groundwater Drought Index. Many studies have successfully applied the SPI, which is related to the probability of occurrence of wet and dry events, many researchers efficiently for monitoring the spatial extension and intensity of droughts, at different time scales of 3, 6, 12, and 24 months (Belayneh and Adamowski 2012; Khan et al. 2008; Thomas et al. 2015). It takes longer for deficiency in precipitation to affect the streamflow, soil moisture, reservoir, and groundwater levels. SPI on 1 and 3-month time scales is associated with soil moisture and precipitation deficit; however, the hydrological drought is associated with the SPI-6 which indicates precipitation deficit for more than 6 months (Van Loon 2015). Although meteorological data from ground-based stations have a high level of accuracy and are widely utilized across the world, the density and distribution of meteorological stations are insufficient for spatial data extraction. Without an optimal network of meteorological stations throughout the study region, the geographical extent of drought cannot be accurately assessed (Vicente-Serrano and López-Moreno 2005). Even yet, the time and cost of data preparation, as well as the risk of errors, may cause a delay in drought mitigation operations. In this context, drought monitoring using satellite-based data has gained widespread acceptance in recent decades because of its low cost, ease of data acquisition, synoptic perspective, and reliability.

The conventional approaches for drought monitoring that uses ground-based data are difficult, laborious, and time-consuming. Thus, monitoring the biosphere using satellite data has gained importance in several aspects of environmental monitoring including drought monitoring. For the assessment, prediction, and monitoring of drought, remote sensing and GIS technologies are better than traditional techniques as they are capable to cover the Earth's surface (Abdulrazzaq et al. 2019). This capability was only achieved after the launch of the Advanced Very High-Resolution Radiometer (AVHRR) mission in 1979. Various studies have been conducted on the use of the National Oceanic and Atmospheric Administration (NOAA) AVHRR to study the effects of drought in depth. One example is the integration of temperature and Vegetation Condition Index data collected by the AVHRR to monitor the heatwave in India (Pal et al. 2020). They integrated the TVDI and the Regional Water

Index (RWI) to measure the drought in China's Shandong Province. AVHRR acts as an evolution for some next-generation missions like the MODIS platform. The ability to identify and monitor water vapour absorption and chlorophyll in its NIR and red bands, respectively, makes this mission more efficient for analytical applications (Chen et al. 2020).

Many drought indices are developed based on remote sensing data such as the Normalized Difference Vegetation Index (NDVI) (Tucker 1979), Land Surface Temperature (LST), Temperature Vegetation Drought Index (TVDI), Vegetation Condition Index (VCI) (Kogan 1990). VCI is more significant in drought monitoring when compared to NDVI and TVDI. VCI can distinguish between climatic and long-term biological signals, making it more capable of detecting moisture deficits. VCI can provide more precise results than other remote sensing-based indices, which is useful for monitoring and quantifying droughts in non-homogeneous areas (Hateren et al. 2020). Several studies have validated VCI's accuracy, so it is widely used in drought monitoring and analysis (Du et al. 2013; Jain et al. 2009; Liu et al. 2020; Unganai and Kogan 1998). However, only remote sensing-derived techniques are not sufficient for generating a clear picture of drought studies. It needs to be integrated into other field variables like in situ data related to hydrology, climate, biophysical, and other supporting datasets (Ahmadalipour et al. 2017). Collaboration of remote sensing data with other fields can help achieve accuracy in drought assessment and prediction.

The various remotely sensed data serve as input for the various methods, which are used for the identification, monitoring, and assessment of the drought. It is facilitated by several satellite-based indices like NDVI, VCI, SVI, NDWI, CWSI, TCI, VHI, and TVDI in visible, near-infrared, thermal infrared, and microwave regions, to target and analyse the concerned areas (Murthy 2020; Qin et al. 2021). Among these, the NDVI is also one of the popular and well-accepted remote sensing indices for agricultural drought. The "Normalized Difference Vegetation Index" (NDVI) is the most prominent vegetation index derived from remote sensing data to be used in the identification and monitoring of vegetation. The NDVI is not only used in its primary form but also used in several other forms to relate to the phenology of the vegetation cover. The mean of NDVI is used for overall greenness, maximum of NDVI for peak greenness, NDVI amplitude for real-time greenness, and multi-temporal NDVI for vegetation monitoring. The NDVI is a foundation for derivation of various other advanced remote sensing indices.

The "Vegetation Condition Index" (VCI) is a remote sensing index that is derived from the NDVI. The VCI is computed as pixel-wise normalization of the NDVI. It was first developed from AVHRR NDVI from Goddard Earth Sciences Distributed Active Archive Centre (GES-DAAC), for the control of local differences in ecosystem productivity. The VCI values can be averaged spatially and temporally to facilitate comparison with the meteorological drought indices. The condition of vegetation was thought to be supported by additional information. Temperature is one of those supporting parameters which can address drought. With the same idea, the "Temperature Condition Index" (TCI) is developed to support the VCI. It is derived from the thermal band which is converted to brightness temperature. The primary use of TCI

is to determine vegetation stress related to temperature. It is also useful in estimating stress caused by excessive wetness (Drisya and Roshni 2018). Another index was developed called as "Vegetation Health index" (VHI) from the joint information of VCI and TCI (Bento et al. 2018; Han et al. 2020). The TCI teams up along with VCI to form VHI as a substitute index characterizing vegetation health. The VHI is defined as VHI = a VCI + (1–*a*) TCI where '*a*' is the coefficient determining the contribution of the two indices. The value for VHI less than 40 represents the presence of vegetation stress and greater than 60 favours good conditions for vegetation.

The entire remote sensing-derived drought indices discussed above are more or less comparable with each other, but the service returned by them is fulfilled for the same purpose. The various indices relating to different categories are explained with their application and usage. Each index in each category has its advantages and limitations due to which their usage is limited and applied wherever the respective index is appropriate. The application of each index is defined which is taken into consideration in deducing the best index suitable for the present research work. Thus, the present study focuses on evaluating drought indicators based on the integration of meteorological and satellite-based indices in the Bundelkhand region of Madhya Pradesh, which experiences recurrent droughts.

6.2 Materials and Methodology

This section describes in detail the study area, data collection, methodology used to achieve results, and analysis performed. Rainfall-based departure analyses were used to identify the dry periods using long-term rainfall data from five stations in the Bundelkhand region falling in Madhya Pradesh state. The monthly rainfall-based index, three-month SPI, is estimated for the monsoon season of the identified severe drought years. Furthermore, satellite-based data index VCI is calculated over the area using long-term MODIS-based NDVI for the monsoon season of the same classified drought years.

6.2.1 Study Area

Madhya Pradesh is a centrally located state in India. The present study has been carried out in the Bundelkhand region located in the northern part of Madhya Pradesh state comprising five districts Sagar, Damoh, Chhatarpur, Tikamgarh, and Panna as shown in Fig. 6.1. The Bundelkhand region is located between 23.14° and 25.55° latitude and 78.05° and 80.67° longitude covering an area of 37,479 km^2. The Bundelkhand region of Madhya Pradesh state faces the problem of recurrent droughts that are unpredictable both in their occurrence and duration; hence, predictions and preparedness against droughts would be key elements for minimizing their impacts (Galkate et al. 2015). The Bundelkhand region has long been regarded as a drought-prone

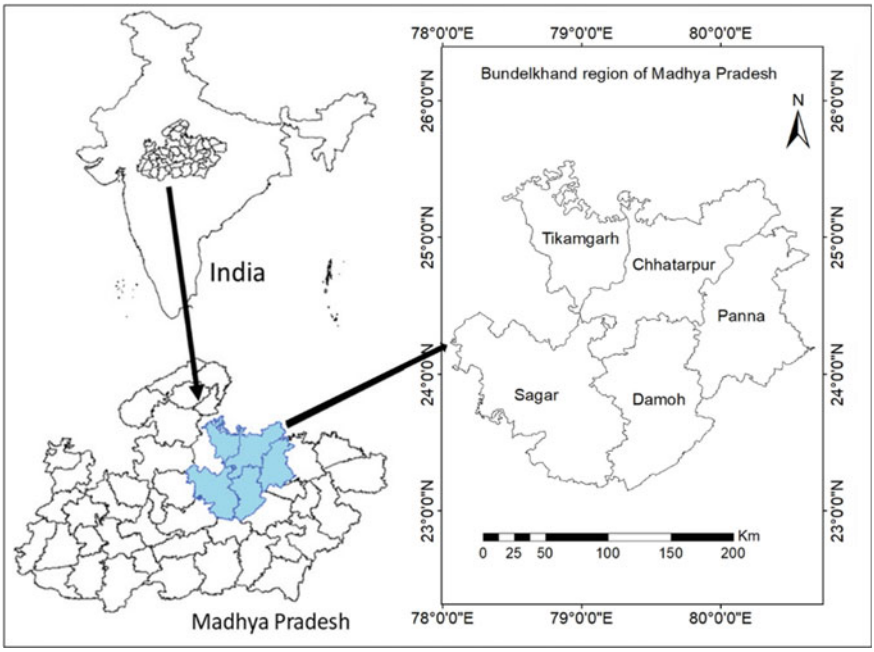

Fig. 6.1 Location of study area (Bundelkhand region of Madhya Pradesh)

region of the country, but drought frequency and severity have increased in recent decades (Gupta et al. 2014). The region receives an annual rainfall of more than 1100 mm. Around 80% of the population is directly dependent on agriculture which is mostly rain-fed and susceptible to drought. The major rivers flowing through the study area include Betwa, Sindh, Tons, and Chambal, and all are tributaries to the Ganga River. The topography of the region is undulating, with boulder-strewn plains and rocky outcrops and in a rocky landscape. Wheat and soybeans are the major crops grown in the Rabi and Kharif seasons, respectively. The major soils in this region include alluvial, black soils, and mixed red soil.

6.2.2 Statistical Analysis

The rainfall statistics of five rain gauge stations Sagar, Damoh, Panna, Tikamgarh, and Chhatarpur of the Bundelkhand region have been worked out using 38 years of rainfall data from the year 1980 to 2017. The rainfall data have been collected from India Meteorological Department and State Data Centre, Madhya Pradesh Water

Resources Department, Bhopal. The statistical analysis of annual, monsoon, non-monsoon, and monthly rainfall has been carried out to estimate average rainfall, standard deviation, and coefficient of variation of five stations and the Bundelkhand region to understand rainfall pattern and their variability.

6.2.3 Rainfall Departure Analysis

The annual rainfall departure analysis performed the determination drought years, frequency, return period, and severity in the study area. As suggested by India Meteorological Department, a year can be considered a drought year when the annual rainfall deficit is more than 25% of its long-term normal rainfall (Appa Rao, 1986). Further, the meteorological drought can be classified according to its severity level. It is considered a moderate drought when the annual rainfall deficit is between 25 and 50% and a severe drought when the annual rainfall deficit exceeds 50% of the normal. The percentage departure of the annual rainfall time series has been calculated using Eq. 6.1.

$$\text{Percentage of Departure} = \frac{\text{Annual Rainfall} - \text{Average Annual Rainfall}}{\text{Average Annual Rainfall}} \times 100 \tag{6.1}$$

6.2.4 Standardized Precipitation Index (SPI)

The Standardized Precipitation Index (SPI) assigns a numeric value to the precipitation based on the deficit severity, and it can be associated across regions with different environments. In brief, SPI is the number that represents the standard deviation of precipitation data from its long-term average for a normally distributed series. As the precipitation data is not normally distributed, a gamma distribution is fitted to the rainfall data to determine the cumulative probability which is then transformed to the standard normal random variable 'Z' with mean zero and variance one, which is the value of SPI. The SPI determines the probability of occurrence of wet and dry events at different time scales, i.e. 1–24 months which are associated with different types of droughts. The three-month SPI values are indicative of soil moisture conditions as well as meteorological drought; hence, in this study, analysis has been carried out to assess drought severity in the study area using three-month SPI values and its comparison with satellite-derived index. For this analysis, monthly rainfall time series of 38 years from the year 1980 to 2017 was used for five stations in the Bundelkhand region.

Table 6.1 SPI classification and their values

2.0 +	Extremely wet
1.5–1.99	Very wet
1.0–1.49	Moderately wet
−0.99–0.99	Near normal
−1.0–−1.49	Moderately dry
−1.5–−1.99	Severely dry
−2 and less	Extremely dry

Drought characteristics based on their severity can be assessed using an analytic method to determine the cumulative probability (McKee et al. 1993). The cumulative probability, $H(x)$, is then converted into the standard normal random variable 'Z,' which has a mean of zero and a variance of one and is the SPI value. The Z or SPI values are more easily estimated using an approximation that converts cumulative probability to the standard normal random variable Z (Abramowitz and Stegun 1965). The SPI computation for each place is based on the long-term precipitation data of the selected period. The long-term data are fitted to a probability distribution, which are then converted into a normal distribution, resulting in a mean SPI of zero for the chosen place and duration (Edwards 1997). The SPI values and their classification indicating severity range are shown in Table 6.1.

In the derived SPI series, when continuous negative values of SPI reach an intensity of −1.0 or less and then SPI remains constantly negative, a drought event has begun, which will terminate when the SPI becomes positive. As a result, each drought event has a duration that is determined by its start and end dates, as well as its intensity and severity. In the Bundelkhand region, the rainfall season comprises four to five rainy months, i.e. June, July, August, September, and October, and rainfall deficit during initial monsoon months will have cumulative impacts during later monsoon months, i.e. August, September, and October. Therefore, the analysis was especially focused on the assessment of drought severity using three-month SPI for the August, September, and October months.

6.2.5 Satellite Data

Moderate Resolution Imaging Spectroradiometer (MODIS) satellite data provide a new generation of land resources products to support natural resource management and global change research (Didan 2015). MODIS has a moderate spatial (250 m) and high temporal (1–2 days) resolution. MODIS data are lumped to produce consistent and cloudless 16 daily NDVI product optimum to use for time series analysis such as vegetation monitoring. Drought monitoring is one of the many environmental concerns for which these products are used (Bajgain et al. 2015, 2017; Gu et al. 2008). In this study, the MODIS data were accessed using Google Earth Engine (GEE), which is a cloud-based remote sensing platform. The 16-day composite (MOD13Q1)

MODIS Terra Vegetation Indices product was used to estimate NDVI-based VCI. The datasets are available for global coverage at a 250-m spatial resolution from the year 2000 onwards.

6.2.6 *Vegetation Condition Index (VCI)*

Normalized Difference Vegetation Index (NDVI) is a widely used remote sensing index that gives quantification of quantitative estimation of vegetation growth based on surface reflectance. NDVI is calculated as the ratio between the reflectance of a red band (0.6–0.7 μm) and a near-infrared (NIR) band (0.7–2.5 μm). The NDVI values range from −1 to 1, the responses of healthy vegetation in this range are towards one, while water and the built-up area will be represented as negative and near-zero values. The NDVI can be estimated using Eq. 6.2.

$$\text{NDVI} = \frac{\text{NIR} - \text{Red}}{\text{NIR} + \text{Red}} \tag{6.2}$$

To normalize current NDVI with respect to maximum and minimum NDVI over a single pixel, Kogan (1990) proposed Vegetation Condition Index (VCI). VCI compares the current vegetation index to the values observed in a similar period over a specific pixel. VCI can be estimated with Eq. 6.3

$$\text{VCI}_{ijk} = \frac{\text{NDVI}_{ijk} - \text{NDVI}_{ij\text{min}}}{\text{NDVI}_{ij\text{max}} + \text{NDVI}_{ij\text{min}}} \tag{6.3}$$

whereas VCI*ijk* is the VCI value for the pixel *i* during the month *j* for year *k*, NDVI*ijk* is the VCI value for the pixel *i* during the month *j* for year *k*, NDVI*ijk* min is the multiyear minimum NDVI for *i* pixel during the month *i,* and NDVI*ijk* max is the multiyear maximum NDVI for *i* pixel during the month *j*. The VCI value less than 0.4 indicates mild to extreme drought conditions, while VCI above 0.4 shows normal conditions as shown in Table 6.2. When compared to NDVI, this VCI normalizes NDVI responses and removes the long-term ecological indication from the short-term climatic signal, proving to be a better index for monitoring water stress conditions.

Table 6.2 VCI classification

VCI values	Category
0.0–0.1	Extreme drought
0.1–0.2	Severe drought
0.2–0.3	Moderate drought
0.3–0.4	Mild drought
0.4–1.0	No drought

6.3 Results and Discussion

The long-term rainfall data for 38 years from 1980 to 2017 were analysed to assess the average rainfall pattern and variability for five stations Sagar, Damoh, Panna, Tikamgarh, and Chhatarpur of the Bundelkhand region of Madhya Pradesh. Rainfall statistics of these stations are summarized in Table 6.3. The distribution of monthly rainfall of all five stations is shown in Fig. 6.2.

From Table 6.3, the average annual rainfall in the Bundelkhand region was observed to vary between 1202 (Sagar) and 960 (Chhatarpur) with an average of 1105 mm. The average annual monsoon and non-monsoon rainfall in the region was observed as 1008 mm and 97 mm, respectively. The region receives a major portion of rainfall during the monsoon season as shown in Fig. 6.2. The rainfall pattern in Bundelkhand has a very high temporal variation, the average standard deviation, and annual monsoon and non-monsoon rainfall that has been estimated as 336, 320, and 97 mm. The high values of the coefficient of variation for annual and monsoon rainfall 0.31 and 0.32 indicate high rainfall variation. High variation in monsoon rainfall is one of the causes of frequent and severe droughts in the Bundelkhand region.

Table 6.3 Rainfall statistics of five stations in the Bundelkhand region (data used 1980–2017)

No	Station name	Annual			Monsoon			Non-monsoon		
		Avg. (mm)	Std. dev	CV	Avg. (mm)	Std. dev	CV	Avg. (mm)	Std. dev	CV
1	Sagar	1202	390	0.32	1092	365	0.33	110	76	0.69
2	Damoh	1207	333	0.28	1114	325	0.29	92	75	0.81
3	Panna	1174	331	0.28	1074	333	0.31	100	72	0.72
4	Tikamgarh	960	309	0.32	876	295	0.34	84	84	1.00
5	Chhatarpur	984	318	0.32	884	282	0.32	100	140	1.40
	Average	1105	336	0.31	1008	320	0.32	97	89	0.92

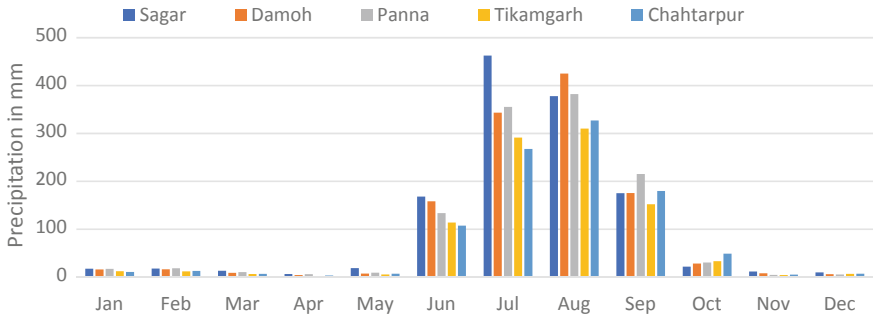

Fig. 6.2 Distribution of monthly rainfall of all stations

Table 6.4 Rainfall departure analysis using annual rainfall time series (data used 1980–2017)

Sr. no.	Station name	Frequency (%)	Return period	Drought years (deficit less than 25–50%)	Severe drought years (deficit greater than 50%)
1	Sagar	28.94	1 in 3–4 years	1986, 1988, 1989, 2002, **2007**, 2010, 2012, **2015**, **2017**	1981, 2004
2	Damoh	21.05	1 in 4–5 years	1989, 1998, 2002, 2006, **2007**, 2014, **2015**, **2017**	–
3	Panna	18.42	I in 5–6 years	1981, 1985, 2000, 2006, 2010, **2015,**	**2007**
4	Tikamgarh	23.68	1 in 4–5 years	1986, 1991, 2000, 2006, **2007**, 2010, **2015**, **2017**	1989
5	Chhatarpur	23.68	1 in 4–5 years	1995, 1998, 2000, 2006, **2007**, 2012, 2014, **2015**	**2017**

6.3.1 Rainfall Departure Analysis

Departure analyses were performed using 38 years of annual rainfall data from the year 1981 to 2017. Drought years were identified based on annual rainfall deficit, and drought years were classified based on their severity. Drought years of rainfall deficit between 25 and 50% were grouped as moderate drought years, and deficits of more than 50% were considered severe drought years as shown in Table 6.4.

From Table 6.4, it has been observed that the drought frequency is very high at all five stations; however, drought frequency was observed the highest at Sagar (29.34%), Tikamgarh (23.68%), and Chhatarpur (23.68%). Thus, the drought return period is very low at these three stations. Most of the stations in Bundelkhand experience a very low drought return period, i.e. one drought after every 4 to 5 years. Sagar station has a chance of occurring drought year after every 3 to 4 years. From the analysis, it can predominantly be seen that the years 2007, 2015, and 2017 were the most common and severe drought years at almost all stations in the Bundelkhand region. Thus, the dry event probability was typically examined for these widespread and severe drought years 2007, 2015, and 2017 for comparison of SPI and VCI.

6.3.2 Standardized Precipitation Index (SPI)

As the three-month time step SPI, i.e. SPI-3 is indicative of a meteorological drought situation, it has been used as a seasonal drought index to characterize the short-term drought and its impact on vegetation. The probability of occurrence of dry events of SPI-3 indicates the severity of drought as shown in Table 6.5.

Table 6.5 Probability of occurrence of three-month SPI in Bundelkhand

Sr. no.	Severity	Probability of occurrence of three-month SPI (%)				
		Chhatarpur	Damoh	Panna	Sagar	Tikamgarh
1	Extremely wet	1.77	2.65	3.03	4.00	2.56
2	Severely wet	5.96	4.87	4.55	3.06	5.12
3	Moderately wet	9.05	11.50	8.44	8.71	7.68
4	Near normal	74.61	71.46	70.35	70.12	78.25
5	Moderate dry	5.74	7.52	10.17	8.94	2.77
6	Severely dry	1.99	1.33	2.60	4.00	2.13
7	Extremely dry	0.88	0.66	0.87	1.18	1.49

The analysis of Table 6.5 shows the probability of occurrence of dry events of SPI-3 at all five stations of the Bundelkhand region. It is broadly seen that the probability of occurrence of moderate dry situation is high at Panna, Sagar, and Damoh with the probability of occurrence at 10.17, 8.94, and 7.52%, respectively. The probability of occurrence of severe drought events has been observed high at Sagar, Panna, and Tikamgarh. The probability of extremely dry events was also seen as high at Tikamgarh and Sagar with the probability of occurrence at 1.49 and 1.18%, respectively. From the overall analysis, it can be seen that the probability of occurrence of severe and extremely dry events is very high at Sagar and Tikamgarh stations. Though the Sagar station receives a good amount of rainfall as compared to other stations, Tikamgarh station has also shown a high probability of severe and extreme events. From the rainfall departure analysis, the years 2007, 2015, and 2017 were identified as severe dry years for which further analysis of SPI and VCI has been performed. The SPI-3 severity values of the monsoon months for severe and widespread drought years 2007, 2015, and 2017 in the Bundelkhand region are given in Table 6.6.

Table 6.6 SPI-3 values for monsoon months of drought years 2007, 2015 and 2017

Months	Sagar	Damoh	Panna	Tikamgarh	Chhatarpur
Aug-07	−1.26	−0.79	−2.05	−2.18	−2.01
Sep-07	−2.22	−0.87	−2.04	−2.28	−1.77
Oct-07	−1.31	−0.65	−1.61	−1.44	−1.15
Aug-15	−0.64	−0.78	−1.29	−0.73	−0.58
Sep-15	−0.89	−1.34	−1.69	−1.12	−1.46
Oct-15		−1.12	−1.45	−0.79	−1.79
Aug-17	−0.80	−1.41	0.15	−0.69	−1.45
Sep-17	−0.57	−1.47	−0.05	−1.43	−1.64
Oct-17	−0.78	−2.09	−0.93	−1.87	−1.80

6.3.3 Vegetation Condition Index (VCI) Analysis

To monitor drought from a long-term space-based observation, the VCI derived from NDVI is used in the study. The spatial extent and temporal change of VCI in the study area in August, September, and October for the years 2007, 2015, and 2017 are shown in Fig. 6.3. First of all, the VCI is classified into five classes from extreme drought to no drought and then the percentage of the area falling in each class in the Bundelkhand region is calculated and is given in Table 6.7.

From the analysis of Fig. 6.3 and Table 6.7, the extent and onset of drought events can be detected from the VCI maps of successive fortnights of the three driest years 2007, 2015, and 2017. Severe vegetation stress is evident all over the area during the last fortnight of October 2015. The situation was seen as normal in August 2015 in Bundelkhand, where the majority of the area was under no-drought conditions. The drought situation started worsening after the first fortnight of August 2015. By the end of October 2015, around 27.5%, 24.7%, and 13.5% area of the region were found under extreme, severe, and moderate stress conditions, respectively. A similar progression of drought situation from August to October has been seen in the years 2007 and 2017 in the whole region. Some exception was seen in the middle of September 2007, when more area was under drought as compared to October 2007 especially in the southern part of the Bundelkhand region. From the overlaying of VCI maps, it is observed that the Sagar and Tikamgarh districts of the study area are prone to water stress and severe drought. In a comparison of the dry periods identified

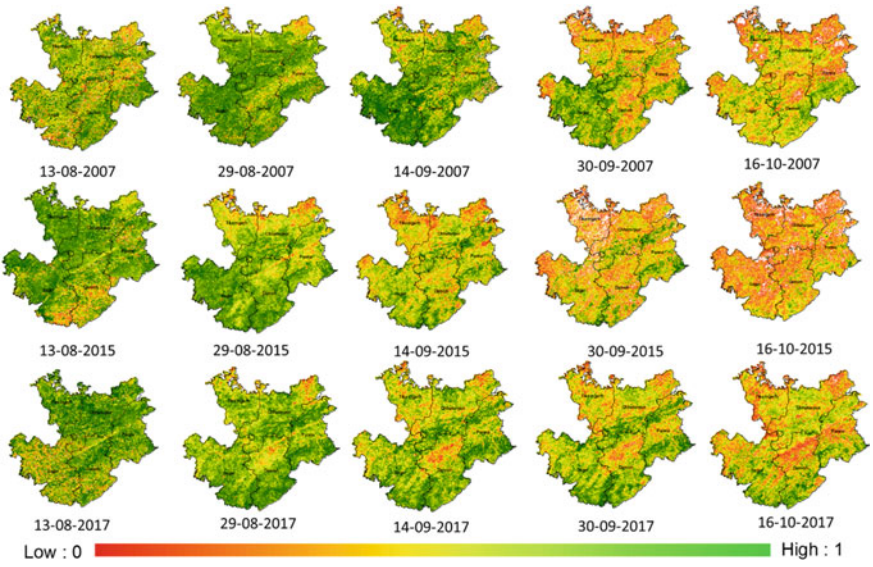

Fig. 6.3 Fortnightly spatiotemporal variation of vegetation condition index (VCI) for the years 2007, 2015, and 2017 (low VCI value indicates drought severity)

Table 6.7 Area in percentage under different VCI classes in Bundelkhand

Dates	Extreme drought	Severe drought	Moderate drought	Mild drought	No drought
13/8/2007	3.63	3.41	4.92	6.72	81.32
29/8/2007	0.20	0.36	0.72	1.46	97.26
14/9/2007	0.72	0.51	1.39	2.84	94.55
30/9/2007	7.01	9.13	11.52	11.98	60.37
16/10/2007	10.16	10.12	13.44	15.34	50.95
13/8/2015	0.91	1.32	2.14	3.20	92.43
29/8/2015	0.03	0.12	0.41	1.29	98.14
14/9/2015	0.59	2.95	6.98	11.39	78.09
30/9/2015	18.66	11.92	13.85	14.63	40.95
16/10/2015	27.52	24.86	21.74	13.55	12.33
13/8/2017	1.57	1.87	2.73	3.75	90.08
29/8/2017	0.07	0.14	0.34	0.84	98.61
14/9/2017	0.20	0.70	2.18	5.19	91.74
30/9/2017	1.16	2.97	6.32	10.64	78.91
16/102017	5.77	8.81	11.58	13.51	60.32

using SPI and water stress conditions identified using VCI, it is observed that both indices are showing droughts almost at the same period and with the same severity. VCI analysis of all the three severe drought years indicated the increase in the spatial extent of drought from August to September especially in the Sagar and Tikamgarh districts which are quite relatable and in agreement with the results derived from the SPI-3. The present study justifies the advantage of satellite-based data for identifying the spatial and temporal extent of vegetation stress and prevailing drought situation in the larger area with ease.

6.4 Conclusions

The present study examined the spatial and temporal extent of drought over five districts like Sagar, Damoh, Panna, Tikamgarh, and Chhatarpur of the Bundelkhand region in the Madhya Pradesh state of India using the annual rainfall departure analysis and a combination of station-based rainfall drought severity index (SPI) and remote sensing-based index (VCI). The annual rainfall departure analysis revealed a high frequency of droughts at most stations in the region, with one drought occurring every 4 to 5 years. Years 2007, 2015, and 2017 were identified as the severe drought years which had a wide coverage over the region and were common in all the five districts, and further analysis for comparison between SPI and VCI was carried out for those years. SPI-3 values were estimated for all five stations using the long-term

monthly rainfall data. Analysis of SPI-3 shows that, though the Sagar station receives a good amount of annual rainfall as compared to other stations, the probability of severely and extremely dry events is very high at this station. Tikamgarh station has also shown a high probability of severe and extreme events. The results of SPI-3 were further analysed for the August, September, and October months of dry years 2007, 2015, and 2017. VCI is estimated for August to October of dry years using the MODIS long-term fortnightly NDVI data. The VCI analysis during all the three severe drought years indicated an increase in the spatial extent of drought from August to October at all stations of the region and August to September especially at Sagar and Tikamgarh. Similar temporal and spatial pattern of drought severity has also been interpreted through SPI-3. The present study justifies the advantage of satellite-based data for identifying the spatial and temporal extent of vegetation stress-related drought. The study can be extended further by linking data on crop production with SPI and VCI for drought and wet years; it can be helpful to quantify the economic impact of droughts. The VCI findings may be influenced by inaccuracies in optical satellite data caused by cloud cover, which causes a shift in the real reflectance from ground objects. The remotely sensed data serve as input for the identification, monitoring, and assessment of the drought. The NDVI is one of the most useful and well-accepted remote sensing indices to assess vegetation stress conditions to be then correlated with agriculture and other droughts. Conclusively, it can be said that the onset and progression of drought can be monitored with the application of station-based and satellite-based data, which will certainly help the various stakeholders to take necessary disaster management decisions.

Acknowledgements The authors are thankful to the National Institute of Hydrology, Roorkee, for providing facilities to undertake this research work. The authors are also thankful to Indian Meteorological Department, Pune, and Madhya Pradesh Water Resources Department, Bhopal, for providing data.

References

Abdulrazzaq ZT, Hasan RH, Aziz NA (2019) Integrated TRMM data and standardized precipitation index to monitor the meteorological drought. Civ Eng J 5:1590–1598

Abramowitz M, Stegun IA (1965) Handbook of mathematical functions. Dover Publications, N Y 361

Ahmadalipour A, Moradkhani H, Yan H, Zarekarizi M (2017) Remote sensing of drought: vegetation, soil moisture, and data assimilation. In: Remote sensing of hydrological extremes. Springer, pp 121–149

Bajgain R, Xiao X, Wagle P, Basara J, Zhou Y (2015) Sensitivity analysis of vegetation indices to drought over two tallgrass prairie sites. ISPRS J Photogramm Remote Sens 108:151–160. https://doi.org/10.1016/j.isprsjprs.2015.07.004

Bajgain R, Xiao X, Basara J, Wagle P, Zhou Y, Zhang Y, Mahan H (2017) Assessing agricultural drought in summer over Oklahoma Mesonet sites using the water-related vegetation index from MODIS. Int J Biometeorol 61:377–390. https://doi.org/10.1007/s00484-016-1218-8

Belayneh A, Adamowski J (2012) Standard precipitation index drought forecasting using neural networks, wavelet neural networks, and support vector regression. Appl Comput Intell Soft Comput 2012(6):6. https://doi.org/10.1155/2012/794061

Bento VA, Trigo IF, Gouveia CM, DaCamara CC (2018) Contribution of land surface temperature (TCI) to vegetation health index: a comparative study using clear sky and all-weather climate data records. Remote Sens 10:1324

Bond NR, Lake PS, Arthington AH (2008) The impacts of drought on freshwater ecosystems: an Australian perspective. Hydrobiologia 600:3–16. https://doi.org/10.1007/s10750-008-9326-z

Change Intergovernmental Panel on Climate (2014) IPCC. Clim Change

Chen Y, Chen G, Cui C, Zhang A, Wan R, Zhou S, Wang D, Fu Y (2020) Retrieval of the vertical evolution of the cloud effective radius from the Chinese FY-4 (Feng Yun 4) next-generation geostationary satellites. Atmos Chem Phys 20:1131–1145

Didan K (2015) MOD13Q1 MODIS/Terra vegetation indices 16-Day L3 Global 250 m SIN Grid V006

Drisya J, Roshni T et al (2018) Spatiotemporal variability of soil moisture and drought estimation using a distributed hydrological model. In: Integrating disaster science and management. Elsevier, pp 451–460

Du L, Tian Q, Yu T, Meng Q, Jancso T, Udvardy P, Huang Y (2013) A comprehensive drought monitoring method integrating MODIS and TRMM data. Int J Appl Earth Obs Geoinf 23:245–253. https://doi.org/10.1016/j.jag.2012.09.010

Dunn RJH, Stanitski DM, Gobron N, Willett KM (2018) Global Climate. Bull Am Meteorol Soc 99:S5+

Edwards DC (1997) Characteristics of 20th century drought in the United States at multiple time scales. Air Force Inst of Tech Wright-Patterson AFB OH

Galkate R, Pandey R, Thomas T, Jaiswal R, Nayak T (2015) Meteorological and hydrological aspects of drought in Central India

Gu Y, Hunt E, Wardlow B, Basara JB, Brown JF, Verdin JP (2008) Evaluation of MODIS NDVI and NDWI for vegetation drought monitoring using Oklahoma Mesonet soil moisture data. Geophys Res Lett 35. https://doi.org/10.1029/2008GL035772

Gupta AK, Nair SS, Ghosh O, Singh A, Dey S (2014) Bundelkhand drought: retrospective analysis and way ahead. Natl Inst Disaster Manag New Delhi 148

Guttman NB (1999) Accepting the standardized precipitation index: a calculation algorithm. JAWRA J Am Water Resour Assoc 35:311–322. https://doi.org/10.1111/j.1752-1688.1999.tb03592.x

Han Y, Li Z, Huang C, Zhou Y, Zong S, Hao T, Niu H, Yao H (2020) Monitoring droughts in the Greater Changbai mountains using multiple remote sensing-based drought indices. Remote Sens 12:530

Jain SK, Keshri R, Goswami A, Sarkar A, Chaudhry A (2009) Identification of drought-vulnerable areas using NOAA AVHRR data. Int J Remote Sens 30:2653–2668. https://doi.org/10.1080/01431160802555788

Khan S, Gabriel HF, Rana T (2008) Standard precipitation index to track drought and assess impact of rainfall on watertables in irrigation areas. Irrig Drain Syst 22:159–177. https://doi.org/10.1007/s10795-008-9049-3

Kogan FN (1990) Remote sensing of weather impacts on vegetation in non-homogeneous areas. Int J Remote Sens 11:1405–1419. https://doi.org/10.1080/01431169008955102

Kogan F, Guo W, Yang W (2019) Drought and food security prediction from NOAA new generation of operational satellites. Geomat Nat Hazards Risk 10:651–666. https://doi.org/10.1080/19475705.2018.1541257

Kundu A, Denis D, Patel N (2015) Evaluation of the meteorological drought over the Bundelkhand region using geo-spatial techniques. Clim Change 1:418–424

Liu Q, Zhang S, Zhang H, Bai Y, Zhang J (2020) Monitoring drought using composite drought indices based on remote sensing. Sci Total Environ 711:134585. https://doi.org/10.1016/j.scitotenv.2019.134585

McKee TB, Doesken NJ, Kleist J et al (1993) The relationship of drought frequency and duration to time scales. In: Proceedings of the 8th conference on applied climatology. Boston, pp 179–183
Mirdha NRC (1973) Interim report of the national commission on agriculture on whole village development programme
Mishra AK, Singh VP (2010) A review of drought concepts. J Hydrol 391:202–216. https://doi.org/10.1016/j.jhydrol.2010.07.012
Miyan MA (2015) Droughts in Asian least developed countries: vulnerability and sustainability. Weather Clim Extrem 7:8–23. https://doi.org/10.1016/j.wace.2014.06.003
Murthy RVR (2020) Mapping spatio-temporal cropland changes due to water stress in Krishna River Basin using temporal satellite data. College of Engineering (A), Andhra University, Visakhapatnam, Ph.D.Thesis
Pal S, Chowdhury P, Talukdar S, Sarda R (2020) Modelling rabi crop health in flood plain region of India using time-series Landsat data. Geocarto Int 1–28
Palmer WC (1965) Meteorological drought. US Department of Commerce, Weather Bureau
Palmer WC (1968) Keeping track of crop moisture conditions, nationwide: the new crop moisture index
Pandey RP, Pandey A, Galkate RV, Byun H-R, Mal BC (2010) Integrating hydro-meteorological and physiographic factors for assessment of vulnerability to drought. Water Resour Manag 24:4199–4217
Qin Q, Wu Z, Zhang T, Sagan V, Zhang Z, Zhang Y, Zhang C, Ren H, Sun Y, Xu W et al (2021) Optical and thermal remote sensing for monitoring agricultural drought. Remote Sens 13:5092
Thomas T, Nayak PC, Ghosh NC (2015) Spatiotemporal analysis of drought characteristics in the Bundelkhand region of Central India using the standardized precipitation index. J Hydrol Eng 20:05015004. https://doi.org/10.1061/(ASCE)HE.1943-5584.0001189
Tucker CJ (1979) Red and photographic infrared linear combinations for monitoring vegetation. Remote Sens Environ 8:127–150. https://doi.org/10.1016/0034-4257(79)90013-0
Unganai LS, Kogan FN (1998) Drought monitoring and corn yield estimation in Southern Africa from AVHRR data. Remote Sens Environ 63:219–232. https://doi.org/10.1016/S0034-4257(97)00132-6
van Hateren TC, Chini M, Matgen P, Teuling AJ (2020) Ambiguous agricultural drought: characterizing soil moisture and vegetation droughts in Europe from earth observation. Hydrol Earth Syst Sci Discuss 1–17
Van Loon AF (2015) Hydrological drought explained. WIREs Water 2:359–392. https://doi.org/10.1002/wat2.1085
Vicente-Serrano SM, López-Moreno JI (2005) Hydrological response to different time scales of climatological drought: an evaluation of the standardized precipitation index in a mountainous Mediterranean basin. Hydrol Earth Syst Sci 9:523–533. https://doi.org/10.5194/hess-9-523-2005
Yadav RK (2009) Changes in the large-scale features associated with the Indian summer monsoon in the recent decades. Int J Climatol 29:117–133. https://doi.org/10.1002/joc.1698

Chapter 7
Determining the Yield of Rice Using the Leaf Area Index (LAI) in Iran

Hamid Rahimi, Shahnaz Karami Sorkhalije, and Hajar Marabi

Abstract Most of Iran's rice production is cultivated in the north zone of the country and also a strategic crop for Iranians. The per capita consumption of rice is 35 kg/person. Therefore, knowledge about the characteristics of rice and particularly, yield is very important. One of the most important indicators to determine the growth period and yield of rice is the leaf area index (LAI). In this study, the LAI index obtained from the MCD15A2H product of MODIS was used to border rice cultivation areas and to obtain yield estimates. According to previous studies of famous Iranian rice (Shiroodi, Kados, Hashemi and Deylamani) cultivars in relation to leaf area index (obtained from ground measurements) and the number of fertile tillers, which has been calculated significantly and positively. In this study, the equation for estimating rice yield was generated. The yield estimation equation was tested in 22,107 rice fields with an area of 90,350 ha. The estimated yield results were compared with the actual rice yield cultivars. In 2018–2019, the real average yield of rice in the country was 4539 kg/ha, and the result of the estimated yield was 4794 kg/ha. The average error in the country was 908.85 kg/ha.

Keywords LAI · Rice · Yield · Iran

H. Rahimi (✉)
Department of Surveying Engineering, Technical and Vocational University, Kermanshah, Iran
e-mail: hrahimi6767@gmail.com

S. Karami Sorkhalije
Biology Laboratory Expert, Razi University, Kermanshah, Iran

H. Marabi
GIS Institute, Miarsaghf Road & Building Company, Tehran, Iran

V. P. Singh et al. (eds.), *Application of Remote Sensing and GIS in Natural Resources and Built Infrastructure Management*, Water Science and Technology Library 105,
https://doi.org/10.1007/978-3-031-14096-9_7

7.1 Rice Cultivation in Iran

Rice is an annual plant of the cereal family that grows in warm and humid areas of equatorial or temperate climates. The appearance of rice is shown in Fig. 7.1. Cold and water scarcity are limiting factors for rice growth. In Iran, favorable areas for rice growth range from north to south in the country, but most of the cultivation area of this crop is native to the country (Mazandaran and Guilan), have a special water.

In the time of Anoushirvan, Borzoyeh Tabib brought rice to India. Rice was common in Guilan since the late Sassanids and was the predominant source of people. From the Seleucid period, especially the Parthians, in the area now called the Guilan Plain, especially in the east of Sefidrood, human settlement became embryonic and in the late Sassanid period led to the establishment of a more efficient economic system, namely agricultural production (rice cultivation). The way of life of the Guilanis until the end of the Sassani period was based on raising livestock, hunting and gathering forest products (Porhadi 2010).

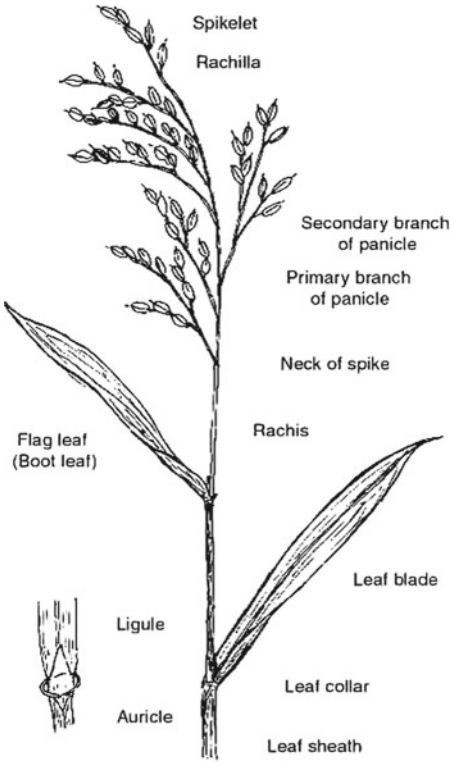

Fig. 7.1 Rice morphology (Erfanimoqada et al. 2018)

7.2 Types of Rice Cultivation in Iran

The primary center of rice cultivation in Iran has been Guilan province since ancient times. Guilani rice cultivars are about 100 species and they are classified into three categories in terms of height and shortness: Long grain group which is mainly known as "Sadri," medium grain group which is known as "anonymous" and short grain group of "Champa" species. Over the centuries, rice cultivars have changed and it is not possible to say exactly which of the remaining cultivars are the original one. The trend of these changes has accelerated since the 1940s. Today, the planting of most native cultivars that had a high area under cultivation in the past has been reduced and has been removed from the Guilani agriculture category (ISNA 2018).

From 1978 to 2013, the area under cultivation of crops in Iran has increased from 9.5 million hectares to 12.2 million hectares (National Rice Research Institute of Iran (NRRI) 2021). The amount of crops in Iran in 2019 is reported to be approximately 83 million tons. Out of a total of more than 892 thousand hectares of rice cultivation area, approximately 4.4 million tons have been harvested. Rice yield in Iran for this calculation period is 4.97 tons per hectare (Ahmadi 2019). In different parts of the Iran, rice is planted in two ways: transplanting and direct seeding. Cultivation of rice by transplanting method is more common than direct seeding method and its production is higher in Iran (Razzaghi and Abyar 2020).

7.2.1 The Method of Transplanting

In this method, seeds are first planted in a plot of land inside or outside the field, which is called a treasury. There are two types of treasuries:

I. **Traditional Treasury**: The traditional treasury has an indefinite length and width and is generally large. Due to their size, leveling and troweling, these vaults are not well maintained and as a result, it is not possible to drain water easily. Water logging causes seeds and seedlings to rot. Work with a better farmer: How to get rice in a paddy field. Due to flooding, it is attacked by houseflies and not covering with nylon led the plant to freeze due to spring frosts. Sometimes farmers have to sow twice. The amount of seeds used in the traditional treasury is more than the station treasury.
II. **Station Treasury**: It is an atmospheric reservoir and a ridge whose length varies according to the slope of the earth and its maximum length is 15 m and its width is about 1.2 m and the distance between the plots is about 30 cm. The height of the plots is about 10–15 cm above the field level. Most of the necessary moisture is provided by water leaks, which do not require irrigation and flooding. In the last days of the treasury, the treasury should be flooded to facilitate digging. These types of vaults have many advantages over traditional vaults. These advantages include lack of hydration, non-contamination of the housefly, adequate oxygen supply to the roots, ease of control and care and ease of use of nylon to cover

the nursery. To nylon the cupboard, long sticks and nails should be installed in an arched shape on both sides of the plot and then the nylon should be pulled on it. The use of nylon in the treasury is to prevent damage from the spring cold. Sowing in treasury with nylon cover in some years until early May. The nylon cover ensures that the plant does not die from the cold and continues to grow and develop. To prevent the nylon cover from overheating, some or all of the nylons are removed in the morning on hot, sunny days. The most suitable temperature for plant growth and development in the nursery at different stages of growth is:

i. Sowing for the first 5 days, maximum day temperature is 30–32 ℃ and night 20–25 ℃.
ii. From 6 to 15 days after sowing, the daytime temperature is 20–25 ℃ and at night 15–20 ℃.
iii. From 15 to 20 days after sowing, the temperature of the day is 20 ℃ and at night 12–15 ℃.

In addition, in order to adapt the plant to the atmospheric conditions at the time of transplanting, it is necessary to remove the nylon 5–7 days before transplanting so that the plant adapts to the environmental conditions and is not damaged after transplanting (Keshtiar 2020). Pictures of these three cultures can be seen in Fig. 7.2.

Fig. 7.2 (Top Left) Station treasury, (Top Right) The method of transplanting, (Bottom) Traditional treasury

7.2.2 Direct Seeding Method

Studies show that the most important issues and problems of direct cultivation are the lack of leveling of lands and overgrowth of weeds and thus control and control. Local tall cultivars are not suitable for direct cultivation because they cultivate; therefore, dwarf cultivars are suitable for direct cultivation. To succeed in direct cultivation, first of all, the lands must be completely leveled, and thus the use of dwarf cultivars, suitable herbicides and sufficient fertilizer can be a good performance.

Before sowing, water of the field should be taken out and then sowing should be done and after 5–6 h, irrigation should be done so that the seeds are well placed in the soil of the nursery. The amount of seed consumed per hectare is 70–75 kg in germination (Keshtiar 2020). Pictures of these three cultures can be seen in Fig. 7.3.

Fig. 7.3 Direct seeding method

7.3 Rice Yield Remote Estimation Indices

Many remote sensing indices have been used to estimate rice crop yield. But there is one thing in common between them all. All indicators have a local or regional application and cannot be used for throughout of the world.

Various indicators such as EVI, NDVI, LAI, DVI, SAVI, GVI, RDVI and TSAVI have been used to monitor the condition and performance of rice or any crops. But they all apply at the regional extent (Aase and Siddoway 1981; Aboelghar et al. 2011; Ahlrichs and Bauer 1983; Crist 1984; Daughtry et al. 1980; Groten 1993; Hatfield 1983; Hinzman et al. 1986; Holben et al. 1980; Nemani and Running 1989; Sharma et al. 1993; Shrestha and Naikaset 2003; Teng 1990; Tucker 1979; Wiegand and Richardson 1990; Wiegand et al. 1990). Some of these indicators are listed in Table 7.1 with their specific equations.

Most of these indicators are the result of spectral calculations of satellites and sensors such as Landsat 4, 5, 7 and 8, Sentinel 2 and 3, SPOT and MODIS. The determination of relationships is also determined by the digits R2 or the correlation coefficient.

Table 7.1 Vegetation indices used for rice yield estimation

Vegetation index	Formula	References
Normalized difference vegetation index	$\mathrm{NDVI} = \frac{\mathrm{NIR}-\mathrm{Red}}{\mathrm{NIR}+\mathrm{Red}}$	Tucker et al. (1981)
Enhanced vegetation index	$\mathrm{EVI} = 2.5 \times \frac{(\mathrm{NIR}-\mathrm{Red})}{(\mathrm{NIR}+6\times\mathrm{Red}-7.5\times\mathrm{Blue}+1)}$	Huete et al. (2002)
Leaf area index	$\mathrm{LAI} = 3.618 \times \mathrm{EVI} - 0.118$	Boegh et al. (2002)
Soil adjusted vegetation index	$\mathrm{SAVI} = \frac{1.5\times(\mathrm{NIR}-\mathrm{Red})}{(\mathrm{NIR}+\mathrm{Red}+0.5)}$	Huete (1988)
Green vegetation index	$\mathrm{GVI} = (-0.29 \times \mathrm{TM\_1}) + (-0.24 \times \mathrm{TM\_2}) + (-0.54 \times \mathrm{TM\_3}) + (-0.72 \times \mathrm{TM\_4}) + (-0.08 \times \mathrm{TM\_5}) + (-0.18 \times \mathrm{TM\_6})$	Kauth et al. (1976)
Renormalized difference vegetation index	$\mathrm{RDVI} = \frac{\mathrm{NIR}-\mathrm{Red}}{\sqrt{\mathrm{NIR}+\mathrm{Red}}}$	Roujean and Breon (1995)
Transformed soil adjusted vegetation index	$\mathrm{TSAVI} = \frac{s(\mathrm{NIR}-s*\mathrm{Red}-a)}{a*\mathrm{NIR}+\mathrm{Red}-a*s+X*(1+s2)}$ s = the soil line slope a = the soil line intercept X = an adjustment factor that is set to minimize soil noise	Baret et al. (1989)
Difference vegetation index	$\mathrm{DVI} = \mathrm{NIR} - \mathrm{Red}$	Tucker (1979)
Greenness index	$\mathrm{GI} = \frac{\mathrm{Green}-\mathrm{Red}}{\mathrm{Green}+\mathrm{Red}}$	Wiegand et al. (1989)

7.4 Leaf Area Index

The leaf area index (LAI) can be calculated in two direct ways and distance. Here are remote sensing methods. Leaf area index is an important structural property of a plant canopy. It is a bio-physical variable influencing land surface processes such as photosynthesis, transpiration and energy balance. LAI is a required input for various agricultural models. LAI is defined as the projected area of leaves per unit of ground area. The amount of leaves in the canopy is a factor in determining the amount of light intercepted by the canopy, which in turn controls photosynthetic rates. Leaves contain pores, called stomata, through which carbon dioxide and water pass between the plant and the atmosphere. So the leaf area also sets limits on transpiration and photosynthesis. For different vegetation types, LAI can vary from less than 1 for deserts to over 6–8 for rain forests. There are a variety of methods for measuring LAI.

The most straightforward, usually used in herbaceous or grassy canopies, is to simply define an area on the ground, clip off all the leaves, and measure their area. Dividing the total area of all leaves by the ground area gives LAI (Zand and Matinfar 2012).

The concept of leaf area index, which is a range of zero to generally, in this way, which is the hypothetical number of a leafed leaf in a pixel of 10 × 10 sentinel 2 satellite a completely leafy layer in that pixel makes. Similarly, the amount of 6, 6 times in the pixel of the leaves, can cover the ground (Rahimi 2021). A schematic of detecting leaf area is shown in Fig. 7.4.

There are many equations for calculating the leaf area that points to some of them. There are many equations for calculating leaf area index. By this, we mean only distance equations. Main goal is not to examine this index, but we will mention some of them. A number of common equations for this index are given in Table 7.2.

7.5 Detection of Rice Crop by Remote Sensing Method

There are two general walks to detect rice crop by remote sensing method using satellite imagery such as MODIS, Landsat 8 or Sentinel 2. One supervised and unsupervised. The most important methods are supervised by K-mean and ISODATA.

7.5.1 Unsupervised Classification

- The ISODATA algorithm has some further refinements by splitting and merging of clusters than other algorithms. Clusters are merged if either number of members in a cluster is less than a certain threshold or if centers of two clusters are closer than a certain threshold. Clusters are split into two different clusters if the cluster

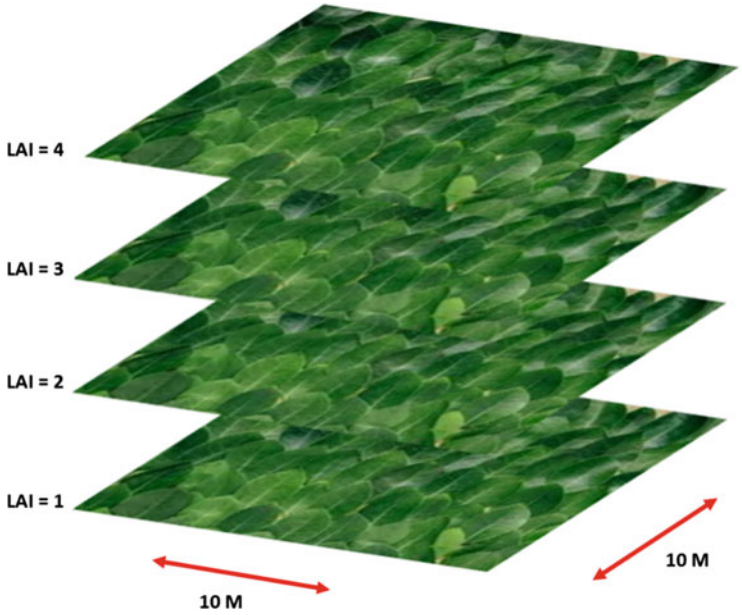

Fig. 7.4 Schematic view of the concept of leaf area index (Rahimi 2021)

Table 7.2 Some equations of the leaf area index (LAI)

Index name	Reference	Equation
Specific leaf area vegetation index	Lymburner et al. (2000)	NIR/(Red + SWIR)
Leaf area index	Boegh et al. (2002)	$3.618 \times \text{EVI} - 0.118$
Sensed leaf area index	Zand and Matinfar (2012)	$1.035 \times \text{LN}_{(\text{NDVI})} + 2.05$
Mix leaf area index	Sentinel Hub Custom Scripts (2020)	$\left(\left(\frac{\text{NIR}}{(\text{Red}+\text{SWIR}_{(1613.7)})}\right) + \left(\frac{\text{NIR}}{(\text{Red}+\text{SWIR}_{(2202.4)})}\right)\right)/2$

standard deviation exceeds a predefined value and the number of members is twice the threshold for minimum number of members. In ISODATA clustering algorithm, clusters will be merged if either the number of members in a cluster is less than a certain threshold or if the centers of two clusters are closer than a certain threshold. Meanwhile, clusters can also split into two different clusters if cluster standard deviation exceeds a predefined value and the number of members is twice the threshold for minimum number of members (Ma et al. 2011).

- K-means unsupervised classification calculates initial class means evenly distributed in the data space then iteratively clusters the pixels into the nearest class using a minimum distance technique. Each iteration recalculates class means and reclassifies pixels with respect to the new means. All pixels are classified to

the nearest class unless a standard deviation or distance threshold is specified, in which case some pixels may be unclassified if they do not meet the selected criteria. This process continues until number of pixels in each class changes by less than selected pixel change threshold or the maximum number of iterations is reached (Tou and Gonzalez 1974).

The most widely supervised methods include the following:

7.5.2 Supervised Classification

- The adaptive coherence estimator (ACE) estimates the squared cosine of the angle between a known target vector and a sample vector in a transformed coordinate space. The space is transformed according to an estimation of the background statistics, which directly effects the performance of the statistic as a target detector. ACE assumes that a target data sample can be modeled as a linear combination of a known target signature and random Gaussian noise. ACE uses an estimate of the background mean and background covariance to transform the coordinate space before comparing a known target vector to a data sample. Appropriate background estimation is very important for ACE's performance as a detection statistic. ACE assumes that background points can be modeled as a multivariate random Gaussian distribution, parameterized by a mean and covariance. In the simplest case, an entire dataset or representative subset is processed at once to generate an estimate of the mean and covariance. This estimate is then used for the entire dataset or subset that ACE is computed on (Alvey et al. 2016).
- The binary encoding classification technique encodes the data and endmember spectra into zero's and ones, based on whether a band falls below or above the spectrum mean, respectively. An exclusive or function compares each encoded reference spectrum with the encoded data spectra and produces a classification image. All pixels are classified to the endmember with the greatest number of bands that match, unless you specify a minimum match threshold, in which case some pixels may be unclassified if they do not meet the criteria (Mazer et al. 1988).
- The CEM method designs a finite-impulse response (FIR) filter that minimizes the average output energy, while constraining the response of the target to a specific value. The whole process can be considered as a convex optimization problem subject to an equality constraint. CEM can only detect one target at a time (Zhu et al. 2020).
- Mahalanobis distance is that best fits a particular measurement is based on a statistical quantity developed by Mahalanobis (1936). The dimensionless "Mahalanobis distance" is a measure of how far a particular measurement is from the centroid of a reference cluster. A particularly useful property of the Mahalanobis distance (MD) is that there is no limit to the number of variables that can be used to evaluate it (Hamill et al. 2016). Combining this method with ROIs has a very high accuracy in supervised classification.

- Maximum likelihood classification (MLC) is a supervised statistical classification approach in which class signatures are assumed to have normal distributions. The MLC pixel-based method works on the basis of multivariate probability density function of classes (Lillesand et al. 2015). Pixels are assigned to the class which has maximum likelihood, so it is important to select training samples in such a manner that each training class follows a Gaussian distribution (Mishra et al. 2017).
- In minimum distance algorithm, to find a mean value of pixels of training sets in n-dimensional space. All pixels in image classified according to the class mean to which they are closest. It is one of a simple algorithm, and the use of a training set of a class is represented as a center point based on the information about the average of all pixels of sample class. This method calculates the mean vector for each class, calculate the statistical (Euclidean) distance from each pixel to class mean vector and assign each pixel to the class it is closed. The minimum distance is calculated by using the Euclidean distance measurement. The class mean with the minimum distance with the pixel will be assigned as the class of the pixel (Abinaya and Poonkuntran 2019).
- Artificial neural network (ANN) is an empirical modeling tool that has an ability to identify underlying highly complex relationship from input/output data only (Aqil et al. 2006). ANN is tools for building models from data. Simulating the function of the human nervous system, they are essentially an applied mathematical technique, bearing a related biological terminology. They can be implemented whenever there is a vague or even unknown relationship between input and output data, though there is an adequate supply of data illustrating this relationship. Artificial neural networks are supposed to be able to handle complex multivariate relationships, non-deterministic or nonlinear problems, even enter the field of fuzzy logic. In addition, they offer fast speed of analysis, objective viewpoints, the ability to generalize and to extrapolate beyond initial data range and provide rather simple and quick update processes hidden behind complicated in most cases algorithms which undertake the role of their theoretical settings. Thus, they have already been used for forecasting as well as for other predictive and classifying tasks. This survey revises the recent use of ANNs in the environmental sector, especially for landscape applications, provides their mathematical theoretical base and derives conclusions relating to their potential as a modern land cover and land use modeling and pattern classification tool (Glezakos and Tsiligiridis 2002). Artificial neural networks have considerable potential for the classification of remotely sensed data. Multi-layer feed forward (MLFF) and radial basis function (RBF) NN classification techniques are widely used remote sensing applications. Remotely sensed images are attractive sources for extracting land cover information, where an image classification algorithm is employed to retrieve land cover information. Artificial neural network (ANN) technique has the ability to identify a relationship from given patterns and this makes it possible for ANNs to solve large-scale complex problems such as pattern recognition, nonlinear modeling, classification and association. (Ndehedehe et al. 2013).

- The idea of the orthogonal subspace projection (OSP) classifier is to eliminate all unwanted or undesired spectral signatures (background) within a pixel, then use a matched filter to extract the desired spectral signature (endmember)present in that pixel. To start with, we formulate the problem at hand. In hyperspectral image analysis, the spatial coverage of each pixel, more often than not, may encompass several different materials. Such a pixel is called a "mixed" pixel. It contains multiple spectral signatures (Ientilucci 2001). A combination of these operators into an overall OSP classification operator reduces the non-Gaussian detection and classification problem presented by mixed pixels to the solved problem of detecting an unknown constant in white noise (Harsanyi and Chang 1994).
- The parallelepiped classifier is one of the widely used supervised classification algorithms for multispectral images. The threshold of each spectral (class) signature is defined in the training data, which is to determine whether a given pixel within the class or not (Zand and Matinfar 2012). The parallelepiped classifier uses a simple decision rule, which is to find the upper and lower brightness values in each spectral dimension. Making use of the histograms of the individual spectral components in the available training data would be the most obvious solution to find these boundaries. For each class, a multidimensional box or parallel piped is formed. If an unknown pixel lies in between this box, it is assigned to that class (Walton 2015).
- Spectral angle mapper (SAM) is a physically based spectral classification that uses an n-D angle to match pixels to reference spectra. The algorithm determines the spectral similarity between two spectra by calculating the angle between the spectra and treating them as vectors in a space with dimensionality equal to the number of bands. This technique, when used on calibrated reflectance data, is relatively insensitive to illumination and albedo effects. Endmember spectra used by SAM can come from ASCII files or spectral libraries, or you can extract them directly from an image (as ROI average spectra). SAM compares the angle between the endmember spectrum vector and each pixel vector in n-D space. Smaller angles represent closer matches to the reference spectrum. Pixels further away than the specified maximum angle threshold in radians are not classified. SAM classification assumes reflectance data. However, if you use radiance data, the error is generally not significant because the origin is still near zero (Kruse et al. 1993).
- Spectral information divergence (SID) is a spectral classification method that uses a divergence measure to match pixels to reference spectra. The smaller the divergence, the more likely the pixels are similar. Pixels with a measurement greater than the specified maximum divergence threshold are not classified. Endmember spectra used by SID can come from ASCII files or spectral libraries, or you can extract them directly from an image (as ROI average spectra) (Du et al. 2004).
- The most commonly used model for analyzing satellite imagery is the support vector machine (SVM) (Kranjčić et al. 2019). SVM is based on statistical learning theory and have the aim of determining the location of decision boundaries that produce the optimal separation of classes. In the case of a two-class pattern recognition problem in which the classes are linearly separable, the SVM selects from

among the infinite number of linear decision boundaries the one that minimizes the generalization error. Thus, the selected decision boundary will be one that leaves the greatest margin between the two classes, where margin is defined as the sum of the distances to the hyperplane from the closest points of the two classes (Vapnik Vladimir 1995). Strategy for multiclass classification. SVM includes a penalty parameter that allows a certain degree of misclassification, which is particularly important for non-separable training sets. The penalty parameter controls the trade-off between allowing training errors and forcing rigid margins. It creates a soft margin that permits some misclassifications, such as it allows some training points on the wrong side of the hyperplane. Increasing the value of the penalty parameter increases the cost of misclassifying points and forces the creation of a more accurate model that may not generalize well (Chan and Lin 2001; Hsu et al. 2010; Wu et al. 2004).

But what is the difference between the unexpected and monitored method? The answer to this question is that in the unsupervised classification, the reliance on two principles of the number of classes and the statistical gap between the data.

The main difference between the two methods of monitoring and monitored classification is the use of samples. The number of these samples is more than more, and the normal spatial distribution is more classified. The satellite image can also be only one band or a combination of different gangs or all existing satellite bands. A better type of initial data that increases the work accuracy is the leaf area index. If we calculate the same leaf area index for each satellite image and combine all these layers, finally, we will have a compound layer. On the other hand, if we have a satellite image for the area, we have a total of 50–52 satellite imagery. The weekly diagram of each pixel represents the leaf area index of rice crop in throughout the year. This graph shows the initial growth process, maximum growth and rice harvest period as a curved line. The horizontal length below the curve represents the length of the growth period. In contrast, vertical growth and area below the curve represent health and the potential of rice growth. The concept of the sample and the curve of changes in leaf area index during the year are shown in Fig. 7.5.

The SVM method is one of the best methods that uses point, linear and area samples (Region Of Interest: ROI) that are among the requirements for diagnosis and classification. But there is not always a need for time coordination between satellite images and the required ROIs. In this sense, if the rice crop is detected by one-year ROIs with very high accuracy and on the other hand has a very small number and distribution in the study area, a spectral signature is obtained for the rice detection pixels. This signature is the result of the behavior of the rice crop in the confirmed cultivated pixel of rice. The ups and downs of this graph will be the LAI value on the Y axis and will show the date on the X axis. The average of thousands or even millions of pixels of a definite sample of rice is presented in the form of a validated curve called the rice spectral signature.

To determine the rice cultivation lands, 22,107 lands with an area of 90,350 ha, in all of which rice was cultivated simultaneously, were given as an ROI to the SVM model. MODIS (MCD15A2H product) and Sentinel 2 images were used to

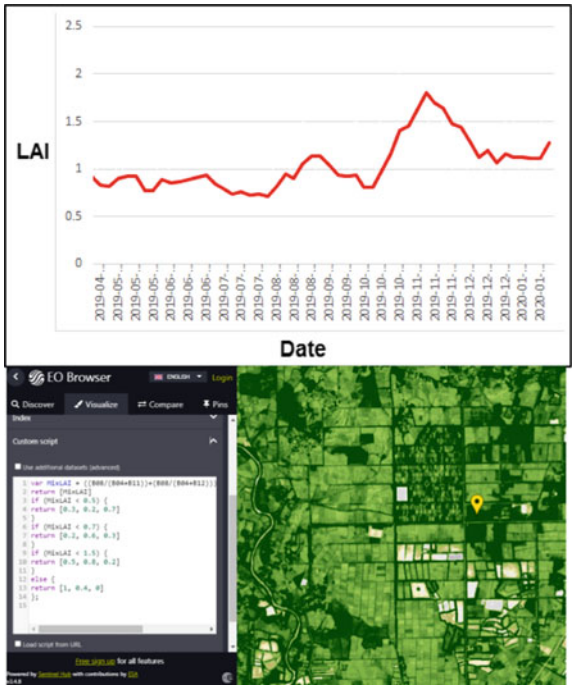

Fig. 7.5 LAI of rice crop in Someh-Sara, Guilan, Iran (2019–2020) Sentinel 2 image (Sentinel Hub EO Browser 2021)

determine LAI. In this large project, ROIs of rice crop year (from September 2018 to September 2019) were used simultaneously. The Google Earth Engine (GEE) system was used to perform routine steps such as masking, cloud removal and geometric errors. After model training for rice detection, 5000 real rice fields were used to assess the accuracy of the diagnosis. Spatial correlation 0.85 and kappa coefficient 0.9 indicate the excellent detection quality of the model in determining rice cultivated areas in Iran. The estimated rice cultivation lands obtained from the model are shown in Fig. 7.6, by provinces of Iran.

7.6 Determining Rice Yield

The default for rice yield estimation is ground measurement and monitoring of rice yield during the crop year. Rice yield estimation basis is a successful project based on rice yield estimation and monitoring based on leaf area index.

According to previous studies of famous Iranian rice (Shiroodi, Kados, Hashemi and Deylamani) cultivars in relation to leaf area index (obtained from ground measurements) and the number of fertile tillers, which has been calculated significantly and positively. Considering that the average yield of rice plant is 5579.1 kg/ha and the average tiller of this plant is 15.32 m^2. Therefore, 0.036 kg/m^2 is harvested

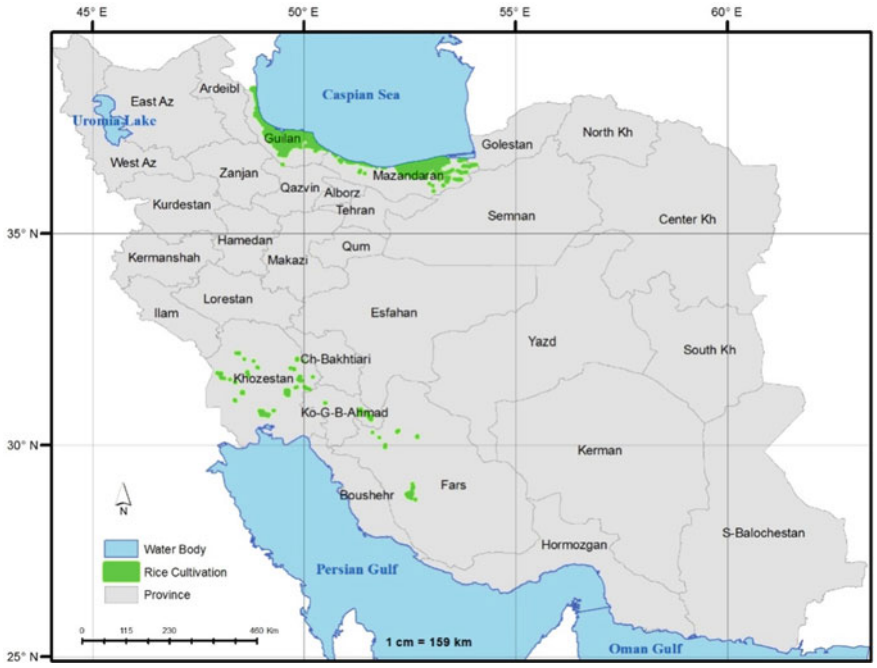

Fig. 7.6 Rice cultivation detection of Iran (2018–2019) (IAMIMC 2021)

per square meter (Mohammadi et al. 2011). This value is considered as a constant coefficient of harvest. On the other hand, the correlation coefficient of the number of tillers to the LAI is 1716.646. This coefficient is considered as a communication constant. Therefore, the final equation for estimating the yield of rice is as follows:

$$\text{Rice}_{\text{Yield}} = 1716.646 \times \text{LAI}_{\text{max}}$$

In this equation, LAI_{max} is the maximum value observed during the cultivation period. This value shows at the peak of the LAI growth curve. The final result is in kilograms per hectare (Rahimi 2021).

7.7 Results Evaluation of Rice Yield

To evaluate the accuracy of the results of this method, real return data of all provinces of Iran was received from Jihad-e-Agriculture Organization. The slight average difference between the observed data and the estimated data indicates the accuracy of the model under study. In the 2018–2019 crop year, the eight provinces of Iran cultivated rice. The actual return statistics of the provinces were compared against

Table 7.3 Evaluation of the accuracy of the estimated yield of the model against actual rice yield data in Iran (2018–2019) (National Rice Research Institute of Iran (NRRI) 2021)

Province	Actual yield	Estimate yield (Kg/H)	Absolute error (Kg/H)	RMSE	MAE
Ardebil	3465	4662	1196.863	1289.613	1000.22
Esfahan	5624	4528	1096.069	1116.809	1071.9
Khozestan	4286	4156	129.6175	191.36	119.34
Zanjan	3778	4184	406.3775	550.11	372.1
Fars	4349	5320	971.4013	1072.33	929.166
Kohgiloieh and Boierahmad	4452	3340	1112.344	1181.05	1012.01
Guilan	4481	6561	2079.181	2132.11	1981.21
Mazandaran	5879	5600	278.9772	382.5	204.31
Mean of Iran	4539.25	4793.875	908.8538	989.4853	836.282

the estimated return. This study was conducted in 814,380 ha of rice cultivated lands in Iran. The lowest average error in Mazandaran province was 279 kg/ha, and the highest error in Guilan province was 2079 kg/ha. The average error of all cultivated lands was 909 kg/ha. This is a very good number for 814,380 ha of rice cultivated land (National Rice Research Institute of Iran (NRRI) 2021). A summary of the evaluation of the results is reported in Table 7.3.

7.8 Discussion and Conclusion

For a long time, the northern region of Iran has been the origin of rice cultivation in Iran. This situation is due to the climate, soil and abundant water resources of this area. Precipitation in this area starts from 2800 mm from the west and continues up to 900 mm in the eastern. But in recent decades, rice cultivation is also cultivated in the northwestern, western and southwestern parts in Iran due to increasing consumption. But for some reason, they still do not have the popularity and quality of rice in the northern region. The good taste and aroma of rice in the northern region are very different from other parts of the country. Hashemi, Shiroodi, Tarom and smoky rice brands are widely used in restaurants and homes in Iran. But in the discussion of rice performance, Hashemi, Kadous, Shiroodi and Dilmani varieties are considered as high-yielding varieties. In the present study, the same famous varieties were used as the criterion for decision. The results of the study indicate a good relationship between leaf area index and the probable yield, but important points should be considered in this regard.

With these descriptions, it can be concluded that by accessing the library of agricultural crops, the type of plants can be determined by remote sensing for the past and future years. The cultivation classification and detection models used in satellite imagery have the ability to identify the type of plants with high accuracy. But there are important challenges along the way:

- If the number of samples is more, the accuracy of diagnosis will be higher.
- If the spatial distribution of the samples is equal and balanced, the accuracy of detection will be less error.
- If we have samples for all plants, the accuracy of diagnosis will be higher.
- If the sample area is large, the exact pixel is easily obtained.
- If the image resolution is high, we do not have the problem of reducing the pixel accuracy.
- If the image bands are more, a more accurate spectral signature is obtained.
- If we have accurate information about the time of planting and harvesting plants, the error of diagnosis will be less.
- If the time interval of the images is less, a more accurate spectral signature is drawn.
- Detection operations should be performed in homogeneous areas.
- Spectral signature of a plant is not applicable in every region.
- If the cloudiness and technical errors of satellite images are reduced, the number of images available will increase.

A summary of all the necessary steps to identify rice fields and estimate the annual yield of this product using satellite images is shown in Fig. 7.7.

Finally, it can be concluded that it can be used with almost any satellite image (any type of sensor such as MODIS, Sentinel, Landsat, etc.). High resolution is recommended. The best tool for all processes is a tool that is compatible with cloud computing capabilities. One of these tools is Google Earth Engine. This system is both free, accessible and very powerful. The biggest challenge in this mission is to have a lot of actual information from the cropland. It should never be forgotten that for the design of a spectral library of rice (or any other crop), the homogeneity of the place of cultivation should be considered. In a way, the spectral signature of an area like Mazandaran in Iran is very different from the area of Lorestan or Fars. Therefore, homogeneous parts should be considered as the border of the mask, in order to minimize the detection error of the rice crop. There are different methods for estimating rice crop yield, but in Iran, the maximum leaf area index (LAI) is very accurate. After confirming the accuracy of rice cultivation areas and land demarcation, as well as the yield of rice in the fields, from now on, the rice plant can be easily identified without the need to repeat the ground sampling operation (ROIs) for each year. The results of the project can be implemented worldwide and the main condition for the results to be correct will be only in a large number of actual samples.

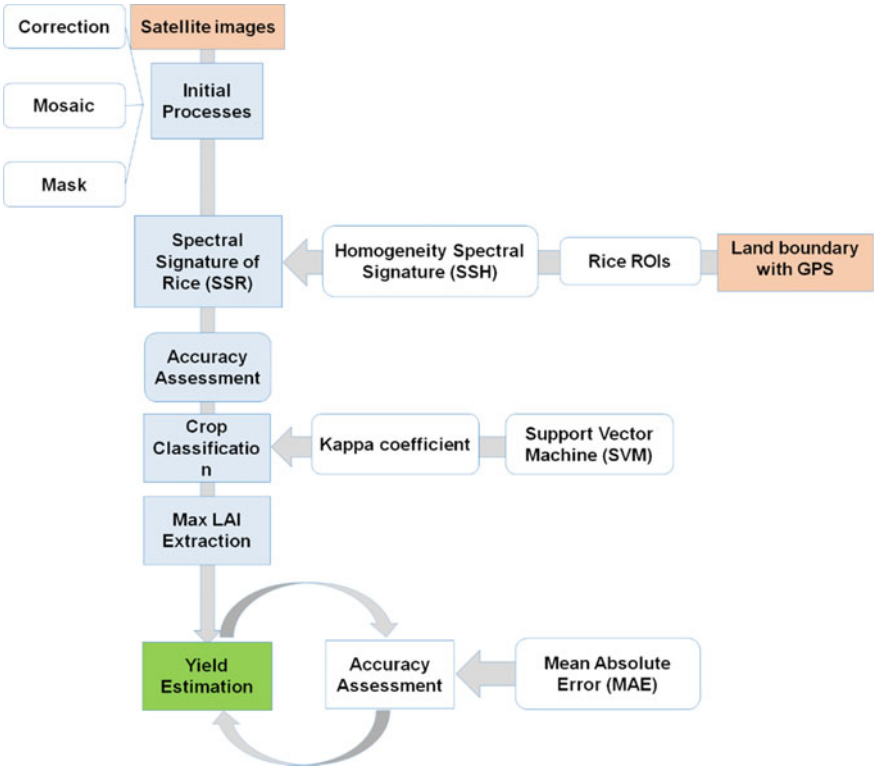

Fig. 7.7 Conceptual model of how to estimate rice yields using satellite images

References

Aase JK, Siddoway FH (1981) Spring wheat yield estimates from spectral reflectance measurements. IEEE Trans Geosci Remote Sens 2:78–84

Abinaya V, Poonkuntran S (2019) Classification of satellite image using minimum distance classification algorithm. SSRG Int J Comput Sci Eng (SSRG-IJCSE). Special Issue: 15–18.

Aboelghar M, Arafat S, Yousef MA, El-Shirbeny M, Naeem S, Massoud A, Saleh N (2011) Using SPOT data and leaf area index for rice yield estimation in Egyptian Nile delta. Egypt J Remote Sens Space Sci 14(2):81–89

Ahlrichs JS, Bauer ME (1983) Relation of agronomic and multispectral reflectance characteristics of spring wheat canopies 1. Agron J 75(6):987–993

Ahmadi K (2019) Agricultural statistics of the crop year 2018–2019. Volume One: crop products. In: Ministry of Jihad-e-agriculture: deputy for planning and economy- information and communication technology center, p 97

Alvey B, Zare A, Cook M, Ho DK (2016) Adaptive coherence estimator (ace) for explosive hazard detection using wideband electromagnetic induction (wemi). In: Detection and sensing of mines, explosive objects, and obscured targets XXI, vol 9823. SPIE, pp 58–64

Aqil M, Kita I, Yano A, Soichi N (2006) Decision support system for flood crisis management using artificial neural network. Int J Intell Technol 1(1):70–76

Baret F, Guyot G, Major DJ (1989) TSAVI: a vegetation index which minimizes soil brightness effects on LAI and APAR estimation. In: 12th Canadian symposium on remote sensing geoscience and remote sensing symposium, vol 3. IEEE, pp 1355–1358

Boegh E, Soegaard H, Broge N, Hasager CB, Jensen NO, Schelde K, Thomsen A (2002) Airborne multispectral data for quantifying leaf area index, nitrogen concentration, and photosynthetic efficiency in agriculture. Remote Sens Environ 81(2–3):179–193

Chan CC, Lin CJ (2001) LIBSVM: a library for support vector machines. Software available at http://www.csie.ntu.edu.tw/~cjlin/libsvm

Crist EP (1984) Effects of cultural and environmental factors on corn and soybean spectral development patterns. Remote Sens Environ 14(1–3):3–13

Daughtry CST, Bauer ME, Crecelius DW, Hixson MM (1980) Effects of management practices on reflectance of spring wheat canopies (No. E81-10019)

Du Y, Chang CI, Ren H, Chang CC, Jensen JO, D'Amico FM (2004) New hyperspectral discrimination measure for spectral characterization. Opt Eng 43(8):1777–1786

Erfanimoqada R, Nabipour AR, Zaman-Nori M (2018) Instructions for producing healthy rice in sustainable agricultural conditions. Publication of Agricultural Education, Iran, Karaj, p 320

Glezakos T, Tsiligiridis T (2002) Neural networks for landscape applications. In: Proceedings of the 1st conference of the Hellenic association of information and communication technology in agriculture, *Food and Environment (HAICTA)*. Athens, Greece, EU. Session 3B: pp 220–233

Groten SME (1993) NDVI—crop monitoring and early yield assessment of Burkina Faso. TitleRemote Sens 14(8):1495–1515

Hamill P, Giordano M, Ward C, Giles D, Holben B (2016) An AERONET-based aerosol classification using the Mahalanobis distance. Atmos Environ 140:213–233

Harsanyi JC, Chang CI (1994) Hyperspectral image classification and dimensionality reduction: an orthogonal subspace projection approach. IEEE Trans Geosci Remote Sens 32(4):779–785

Hatfield JL (1983) Remote sensing estimators of potential and actual crop yield. Remote Sens Environ 13(4):301–311

Hinzman LD, Bauer ME, Daughtry CST (1986) Effects of nitrogen fertilization on growth and reflectance characteristics of winter wheat. Remote Sens Environ 19(1):47–61

Holben BN, Tucker CJ, Fan CJ (1980) Spectral assessment of soybean leaf area and leaf biomass. Photogramm Eng Remote Sens 46(5):651–656

Hsu CW, Chang CC, Lin CJ (2010) A practical guide to support vector classification. Department of computer science national Taiwan university, Taipei

Huete AR (1988) A soil-adjusted vegetation index (SAVI). Remote Sens Environ 25(3):295–309

Huete A, Didan K, Miura T, Rodriguez EP, Gao X, Ferreira LG (2002) Overview of the radiometric and biophysical performance of the MODIS vegetation indices. Remote Sens Environ 83(1–2):195–213

Ientilucci E (2001) Hyperspectral image classification using orthogonal subspace projections: image simulation and noise analysis. In: Rochester institute of technology, college of science, center for imaging science, digital imaging and remote sensing laboratory. p 25

Iran Agricultural Monitoring and Intelligent Management Center (IAMIMC) (2021) Rice report

Iranian Students' News Agency (ISNA) (2018) The oldest document of the existence of rice in northern Iran. https://www.isna.ir/news/97053016257/

Kauth RJ, Thomas GS (1976) The tasselled cap--a graphic description of the spectral-temporal development of agricultural crops as seen by Landsat. In: LARS symposia, p 159

Keshtiar CO (2020) Cereals: rice user guide, keshtiar.ir

Kranjčić N, Medak D, Župan R, Rezo M (2019) Support vector machine accuracy assessment for extracting green urban areas in towns. Remote Sens 11(6):655

Kruse FA, Lefkoff AB, Boardman JW, Heidebrecht KB, Shapiro AT, Barloon PJ, Goetz AFH (1993) The spectral image processing system (SIPS)—interactive visualization and analysis of imaging spectrometer data. Remote Sens Environ 44(2–3):145–163

Lillesand T, Kiefer RW, Chipman J (2015) Remote sensing and image interpretation. Wiley, p 720

Lymburner L, Beggs PJ, Jacobson CR (2000) Estimation of canopy-average surface-specific leaf area using landsat TM data. Photogramm Eng Remote Sens 66(2):183–192
Ma Y, Tan Z, Chang G, Wang X (2011) A new P2P network routing algorithm based on ISODATA clustering topology. Procedia Eng 15:2966–2970
Mazer AS, Martin M, Lee M, Solomon JE (1988) Image processing software for imaging spectrometry data analysis. Remote Sens Environ 24(1):201–210
Mahalanobis PC (1936) On the generalized distance in statistics. Nat Inst Sci India 2:49–55
Mishra VN, Prasad R, Kumar P, Gupta DK, Srivastava PK (2017) Dual-polarimetric C-band SAR data for land use/land cover classification by incorporating textural information. Environ Earth Sci 76(1):1–16
Mohammadi S, Habibi D, Kashani A, Paknejad H, Bakhshipour F, Ardakani MR (2011) Study on physiological indices and agronomical characteristics of different rice cultivars and plant spacing in West Mazandaran Iran. J Crop Weed Ecophysiology 5(3):37–52
National Rice Research Institute of Iran (NRRI) (2021) Investigation of rice yield in Iran
Ndehedehe C, Ekpa A, Simeon O, Nse O (2013) Understanding the neural network technique for classification of remote sensing data sets. NY Sci J 6(8):26–33
Nemani RR, Running SW (1989) Testing a theoretical climate-soil-leaf area hydrologic equilibrium of forests using satellite data and ecosystem simulation. Agric Meteorol 44(3–4):245–260
Porhadi M (2010) Food culture of the people of Guilan, Iran, Tehran. 152
Rahimi H (2021) Summary of Iran's national crop monitoring project (2018–2019). Agricultural Insurance Fund (AIF), Tehran
Razzaghi MH, Abyar N (2020) Rice transplanting and direct seeding cultivation, technical and economic solution for rice production in Golestan province (on Farm). Water Manag Agric 7(1):33–44
Roujean JL, Breon FM (1995) Estimating PAR absorbed by vegetation from bidirectional reflectance measurements. Remote Sens Environ 51(3):375–384
Sentinel Hub EO Browser (2021) https://apps.sentinel-hub.com/eo-browser
Sentinel Hub Custom Scripts (2020) Sentinel 2, Mix LAI: H. Rahimi. https://custom-scripts.sentinel-hub.com/sentinel-2/mixlai/
Sharma T, Sudha KS, Ravi N, Navalgund RR, Tomar KP, Chakravarty NVK, Das DK (1993) Procedures for wheat yield prediction using landsat MSS and IRS-1 A data. Int J Remote Sens 14(13):2509–2518
Shrestha RP, Naikaset S (2003) Agro-spectral models for estimating dry season rice yield in the Bangkok Plain of Thailand. Asian J Geoinformatics 4(1):11–20
Teng WL (1990) AVHRR monitoring of US crops during the 1988 drought. Photogram Eng Remote Sens 56
Tou JT, Gonzalez RC (1974) Pattern recognition principles‖. Addison-Wesley Publishing Company Reading, Massachusetts
Tucker CJ (1979) Red and photographic infrared linear combinations for monitoring vegetation. Remote Sens Environ 8(2):127–150
Tucker CJ, Holben BN, Elgin JH Jr, McMurtrey JE III (1981) Remote sensing of total dry-matter accumulation in winter wheat. Remote Sens Environ 11:171–189
Vapnik Vladimir N (1995) The nature of statistical learning theory. 1(XV):188
Walton A (2015) Assessing the performance of different classification methods to detect inland surface water extent (Bachelor's thesis). University of Stuttgart, Geodäsie und Geoinformatik, p 56
Wiegand C, Shibayama M, Yamagata AT (1989) Spectral observations for estimating the growth and yield of rice. Jpn J Crop Sci 58:673–683
Wiegand CL, Richardson AJ (1990) Use of spectral vegetation indices to infer leaf area, evapotranspiration and yield: I Rationale. Agron J 82(3):623–629
Wiegand CL, Gerbermann AH, Gallo KP, Blad BL, Dusek D (1990) Multisite analyses of spectral-biophysical data for corn. Remote Sens Environ 33(1):1–16

Wu TF, Lin CJ, Weng RC (2004) Probability estimates for multi-class classification by pairwise coupling. J Mach Learn Res 5:975–1005

Zand F, Matinfar HR (2012) Winter wheat yield estimation base upon spectral data and ground measurement. Ann Biol Res 3(11):5169–5177

Zhu L, Wang L, Ji L, Yang W, Geng X (2020) Multiple targets inequality constrained energy minimization for multispectral imagery. Infrared Phys Technol 110:103465

Chapter 8
Soil Erosion Modeling Using Remote Sensing and GIS

Osama Mirran Hussien Al-Qaim, Vikas G. Jadhao, and Ashish Pandey

Abstract Besides a naturally occurring process, soil erosion results in a continuous loss of topsoil, ecological degradation, etc. Evaluating soil loss from watersheds is required while assessing the severity of soil erosion. The average annual soil loss from the Nathpa-Jhakri catchment has been estimated by employing the Revised Universal Soil Loss Equation (RUSLE) and Morgan-Morgan-Finney (MMF) models in the present study. The RUSLE factors and MMF parameters were calculated using meteorological data, FAO soil map, ASTER DEM map, European Space Agency (ESA) land use/cover map, and other reference studies. The model factors and parameters were integrated into the geographic information system (GIS) environment to estimate the soil loss. GIS was used in this study to generate, manipulate, and spatially organize disparate data for soil erosion modeling. The estimated average annual soil loss using the RUSLE and MMF models was 20.42 and 26.29 tons/ha/year, respectively. The coefficient of determination for sediment yield using the RUSLE and MMF models was 0.80 and 0.75, with a variation of 13.41% and 21.62%, respectively. Further, the total catchment area was categorized into the different erosion classes, viz., slight, moderate, high, very high, severe, and very severe. The RUSLE model showed that about 35.8% of the area of the Nathpa-Jhakri catchment lies in the slight to moderate, and 64.2% of the area lies in the high to very severe soil erosion classes. The soil loss estimated by MMF model showed that 13.88% of the Nathpa-Jhakri catchment area lies in the slight to moderate, and 86.12% of the area lies in the high to very severe soil erosion classes. The RUSLE model showed more precise results than the MMF model for the Nathpa-Jhakri catchment. Based on RUSLE model results, about 64.2% catchment area of the Nathpa-Jhakri needs immediate attention for proper land use management practices.

Keywords ASTER DEM · Remote sensing · GIS · MMF model · Soil erosion · RUSLE

O. M. H. Al-Qaim · V. G. Jadhao · A. Pandey (✉)
Department of Water Resources Development and Management, Indian Institute of Technology Roorkee, Roorkee, India
e-mail: ashish.pandey@wr.iitr.ac.in

V. P. Singh et al. (eds.), *Application of Remote Sensing and GIS in Natural Resources and Built Infrastructure Management*, Water Science and Technology Library 105,
https://doi.org/10.1007/978-3-031-14096-9_8

8.1 Introduction

Soil erosion is a wide-spreading and severe problem worldwide (Rodrigo-Comino 2018; Wuepper et al. 2020). It creates implications on environmental, social, economic, and political issues through on and off-site damages in developing countries (Thampapillai and Anderson 1994; Dabral et al. 2008) and leads to a change in the water quality and the storage capacity (Pandey et al. 2007). It reduces the soil depth and the natural organic content (Langdale et al. 1992) and threatens sustainable agriculture and ecosystems (Jain et al. 2010). As per (Dhruvanarayana et al. 1983), sheet erosion contributes more significantly to India's soil erosion problems. Out of 329 Mha of geographical area, about 167 Mha of the area suffers from severe water and wind erosion. The Indian Himalayan region is seriously affected by the erosion problem. As per (Raymo and Ruddiman 1992), about 5% of the Earth's land surface is contributed by the Himalayas and Tibet area, but it contributes about 25% of the dissolved sediment load of the oceans.

The erosion assessment methods predicting spatial soil loss distribution are essentially required (USDA ARS (Agricultural Research Service) 2008; Diodato and Bellocchi 2010). Remote sensing (RS) and geographic information systems (GISs) are advanced and well-known soil and water conservation methods. The use of this advanced geospatial technology was made by many researchers cited in the literature (Pandey et al. 2007, 2021; Chen et al. 2011; Demirci and Karaburun 2012; Ghosal and Bhattacharya 2020).

GIS can manipulate, store, and display spatial and non-spatial data and digitalize the catchment data (Jain et al. 2001). Soil erosion modeling can consider these complex interactions influencing soil erosion rate (Devatha et al. 2015). To represent the erosion process mathematically, soil erosion models are advanced means (Tiwari et al. 2000). Many empirical, conceptual, and physical process-based models are available to estimate soil loss (Eisazadeh et al. 2012; Singh and Panda 2017; Igwe et al. 2017). These models are designed by considering a specific set of location-specific conditions and must be tested with changes in conditions. Therefore, the soil loss estimation and categorization of the catchment area are essential for implementing soil conservation measures. Among all the models utilized for assessment of the soil loss, some most commonly used models are Universal Soil Loss Equation (USLE), Modified Universal Soil Loss Equation (MUSLE), and Revised Universal Soil Loss Equation (RUSLE) (Udayakumara et al. 2010; Wijesundara et al. 2018).

The RUSLE model assesses the soil loss for a specific site using the product of six major factors (Wischmeier and Smith 1978). The factors include rainfall erosivity (R), soil erodibility (K), slope length (L), slope steepness (S), crop management (C), and conservation practices factor (P). To enhance the accuracy of quantification in soil loss estimation, many scientists used the RUSLE model (Wischmeier and Smith 1978; Onstad et al. 1976; Risse et al. 1993; Angima et al. 2003; Pandey et al. 2008) either in the same or in the modified form. Here, (Yoder et al. 1992) modified some factors (LS and C) with a more deterministic approach for estimating the P factor incorporated in the RUSLE. According to Rapp (1994), these modifications

do not have a countable effect on the model efficiency for predictions by RUSLE on natural runoff plot data. The RUSLE model is a flexible tool and can be combined with geographic information system (GIS) adapted to the different landscapes for watershed scale (Wischmeier and Smith 1965; Sharma 2010; Ranzi et al. 2012; Prasannakumar et al. 2012; Amsalu and Mengaw 2014; Das et al. 2018). The model is used commonly in the decision support system of soil conservation and land use planning (Renard and RUSLE 1997). In the current study, the RUSLE model has been preferred to estimate the spatial distribution of soil erosion.

To estimate the soil loss from the field-sized area on the hill slopes, (Morgan et al. 1984) developed Morgan-Morgan-Finney (MMF) model. The MMF model separates the soil erosion process into two phases. One is the water phase, and another is the sediment phase. The rainfall energy for splash detachment of soil and overland flow volume is estimated in the water phase (Morgan et al. 1984). The second phase of the model considers soil particles' detachment from the soil mass. The soil erosion resulted from raindrop impact, and the transport of those particles by overland flow is estimated in this phase.

Considering all the above-narrated constraints and the need for present work, two models, namely the Revised Universal Soil Loss Equation (RUSLE) and Morgan-Morgan-Finney (MMF) model, were selected to estimate the spatial distribution of soil erosion in the present study. The recent satellite, rainfall data, and soil data were used to assign the model parameters. All these parameters were integrated into the GIS environment. The sediment delivery ratio (SDR) was used to estimate sediment yield at the catchment's outlet point. The Nathpa-Jhakri basin having a hilly catchment located in the Himalayan range of North India has been selected as the study area. The main objective of this study is to estimate the soil loss using RUSLE and MMF models by employing remote sensing and geographic information systems.

8.2 Study Area

The selected Nathpa-Jhakri catchment in the present study is located in the northern part of India, within the western zone of the Himalayan range. The areal spread of catchment is in the northeast of Himachal Pradesh state and southeast of Jammu and Kashmir states. The area lies between 31°00′ and 34°00′ N latitude and between 77°00′ and 79°00′ N longitude. Figure 8.1 shows the location map of the catchment. The Nathpa-Jhakri catchment is a part of a big watershed between China and India, with a 30% area falling inside India. Nathpa-Jhakri catchment's altitude varies between 1468 to 6751 m above MSL, covering approximately an area of 15,277.92 km^2.

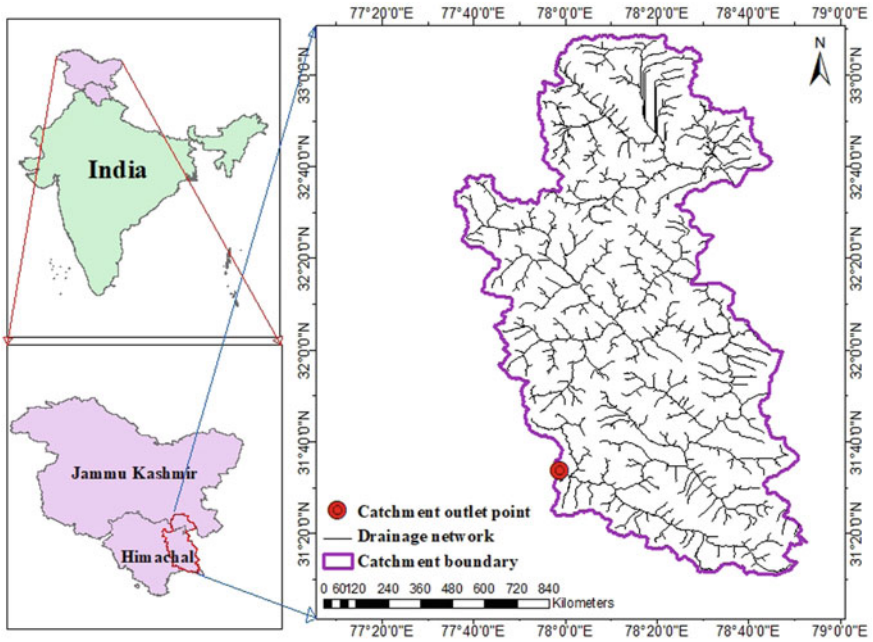

Fig. 8.1 Location map of Nathpa-Jhakri catchment

8.3 Methodology

The RUSLE and MMF models were used in the present study to estimate the spatial distribution of soil loss. The methodology adopted to extract the parameters for erosion modeling is discussed below.

8.3.1 Erosion Modeling Using RUSLE

In a grid environment using GIS, the RUSLE model helps to model the erosion process (Pandey et al. 2021). The methodology adopted for assessing the spatial distribution of soil loss using the RUSLE model is shown in Fig. 8.2.

The average annual soil loss (A, Mg ha year^{-1}) was estimated using the RUSLE model (Eq. 8.1).

$$A = R \times K \times L \times S \times C \times P \tag{8.1}$$

The measured daily rainfall data of the Indian Meteorological Department (IMD) was used in the present study to estimate R factor (Wischmeier and Smith 1978). The equation (Eq. 8.2) was developed to find the rainfall erosivity factor based on

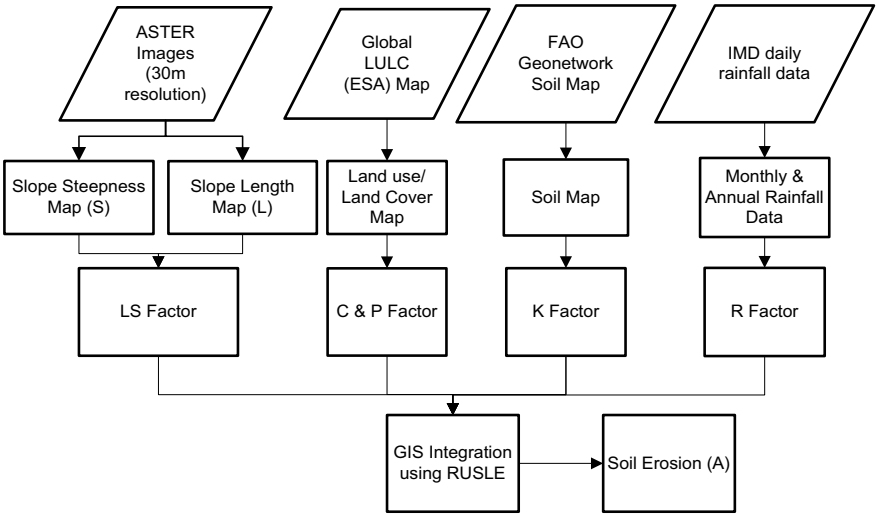

Fig. 8.2 Methodology flowchart for RUSLE

Fournier's index using the available monthly and annual rainfall data.

$$R = 1.735 \times 10^{(1.5 \times \log_{10} \sum_{1}^{12} \left(\frac{P_i^2}{P} \right) - 0.8188)} \tag{8.2}$$

P_i represents the monthly rainfall depth (mm), and P represents the annual rainfall depth (mm).

An equation developed by Wischmeier and Smith (1978) for calculating the soil erodibility factor is represented here in Eq. 8.3.

$$\mathrm{K} = 2.8 \times 10^{-7} \times M^{1.14} \times (12 - a) + 4.3 \times 10^{-3} \times (b - 2) + 3.3 \times (c - 3) \tag{8.3}$$

where M represents the soil particle size parameter and the M can be estimated as (%S + %VFS)(100-%C). S = silt, VFS = very fine sand, and C = clay. The factor a represents percent organic content. Factors b and c represent the soil structure code and the soil permeability class, respectively.

As per (Nikolakopoulos et al. 2006), soil loss is more sensitive to S-factor than L-factor. Then, (Moore and Burch 1986) proposed an equation (Eq. 8.5) for estimation of combined LS factor using GIS and used by several researchers in the study (Pandey et al. 2021, 2008; Fistikoglu and Harmancioglu 2002; Onyando et al. 2005).

$$LS = (\lambda/22.13)^m (\sin \alpha / 0.0896)^n \tag{8.5}$$

where λ = field slope length (m), α = slope gradient (°), and the value of n is taken as 1.3. As per (Wischmeier and Smith 1978), the value of m varies according to the percent slope.

For slopes > 5%	$m = 0.5$
For slopes between 3.5 and 4.5%	$m = 0.4$
For slopes between 1.0 and 3.0%	$m = 0.3$
For slopes < 1.0%	$m = 0.2$

The LS factor was estimated by using ASTER DEM available in 30 m resolutions in ESRI ARC-GIS 10.2 using bilinear interpolation techniques.

For estimation of crop management factor (C) in RUSLE, the land use and land cover classifications were carried out using satellite data from www.esa-landcover-cci.org. The land use and cover map was generated, and the C factor values for different land use/land cover classes were obtained from available literature on the C factor (Pandey et al. 2009, 2015; Biswas and Pani 2015).

The RUSLE conservation practice factor (P) values depend upon the land use and land cover (LULC) type (Pandey et al. 2015). For agricultural land, P factor is assigned as 0.28, and for bare land and other land use/cover, it is assigned as a 1.0 due to no conservation practice (Pandey et al. 2008; Mondal et al. 2016).

8.3.1.1 Spatial Inputs for RUSLE Model

Meteorological Data

The daily gridded rainfall data (0.25° × 0.25°) for 26 years (1971–1996) was collected from the IMD to calculate the monthly erosivity.

Digital Elevation Model

The Advanced Space-borne Thermal Emission and Reflection Radiometer (ASTER), Global Digital Elevation Model (GDEM) image of 30 m resolution (Fig. 8.3) was acquired from the USGS website www.earthexplorer.usgs.gov. Finally, using the flow accumulation and slope as input parameters, the topographic factor (LS) map was generated in the raster calculator of ArcGIS (Fig. 8.4).

Spatial Land Use/Land Cover Classification Map

The study area's land use/land cover classification map was developed using the European Space Agency (ESA) available on www.esa-landcover-cci.org (Fig. 8.5). Based on the classified LU/LC map, the spatial crop management and conservation practice maps were developed and presented in Figs. 8.6 and 8.7.

Soil Map

The soil erodibility factor map was developed using Food and Agriculture Organization (FAO) soil map at a scale of 1:5,000,000 available on (www.fao.org/geonetwork) and is presented in Fig. 8.8.

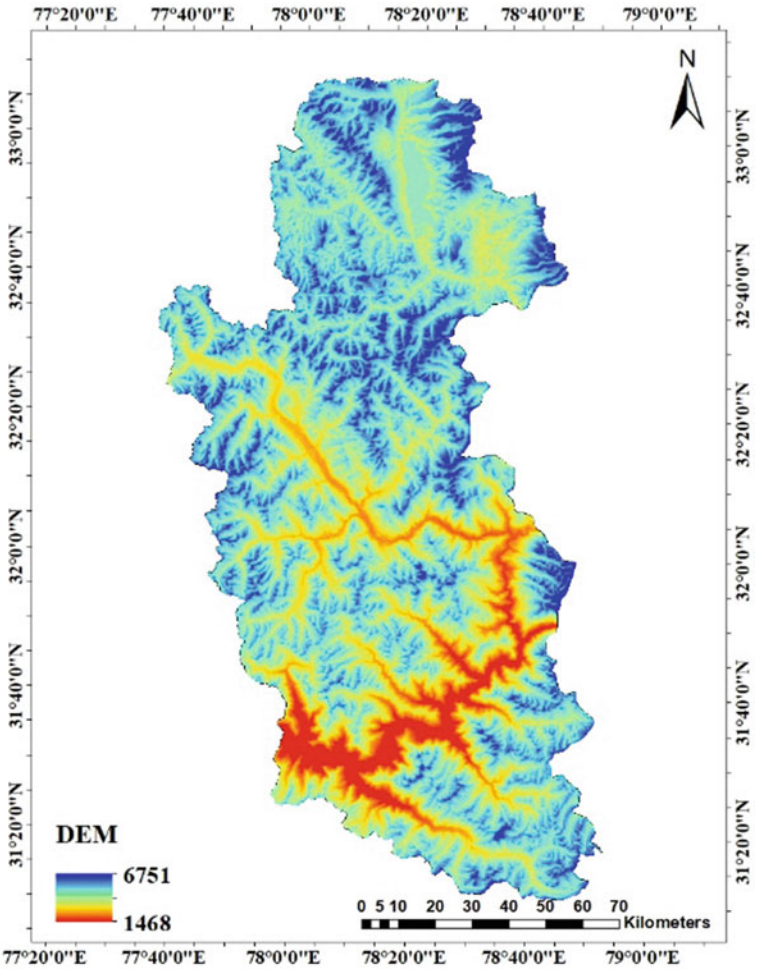

Fig. 8.3 ASTER DEM of the catchment

8.3.2 Erosion Modeling Using MMF Model

Then, (Morgan et al. 1984) developed the Morgan-Morgan-Finney (MMF) model to predict soil erosion from the field-sized areas and hilly areas. MMF model is an alternative empirical-based soil erosion mode having simple and more flexible. It requires less data in operation as compared to other process-based erosion models (Shrestha 1997; Mondal et al. 2017). The MMF model works on the physically based concept of Meyer and Wischmeier (1969), which involves separating the process of soil erosion in the water phase and sediment phase. In the water phase, the model determines the runoff volume and the available rainfall energy that is used to detach the soil particles from soil mass. In the sediment phase of the model, the soil particles'

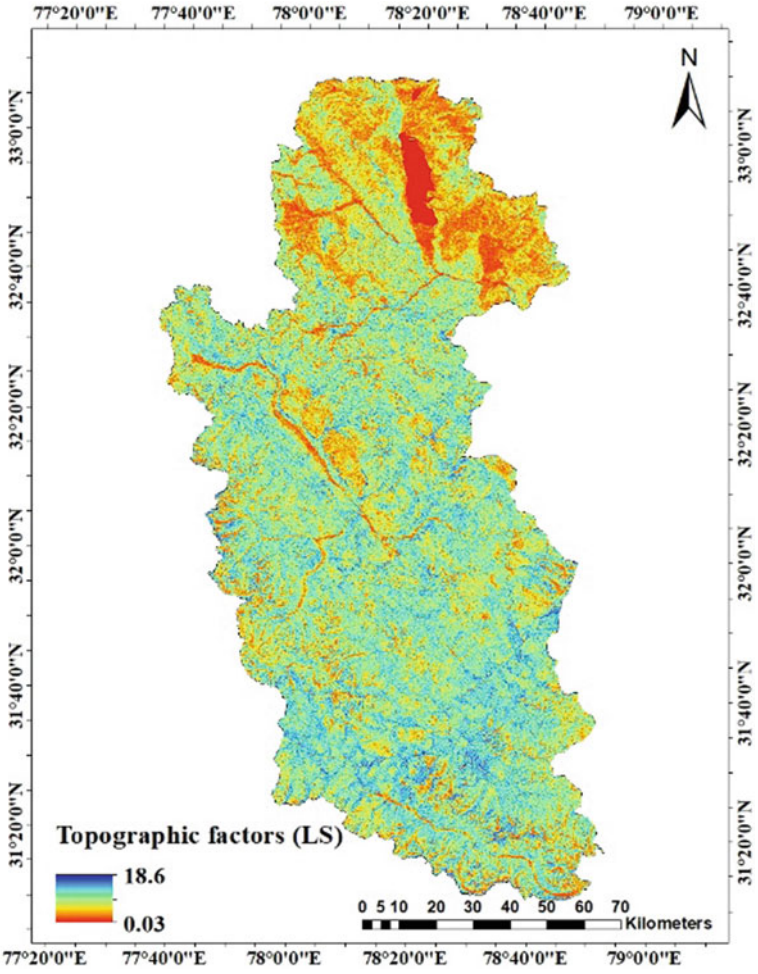

Fig. 8.4 Topographic factors map (*LS*) for Nathpa-Jhakri

detachment is taken as a function of the soil erodibility, energy of rainfall, and rainfall interception affected by vegetation. The transport capacity is computed with the overland flow volume, slope, and crop cover management.

Water Phase

The rainfall energy and runoff have to be estimated in this phase. For the estimation of rainfall kinetic energy (E, J/m^2), the annual rainfall data is used. The functional relationship between energy and rain intensity given by Wischmeier and Smith (1978) is used for modeling rainfall energy. The rainfall kinetic energy is based on the rainfall intensity, and the amount of annual rainfall depth can be estimated as

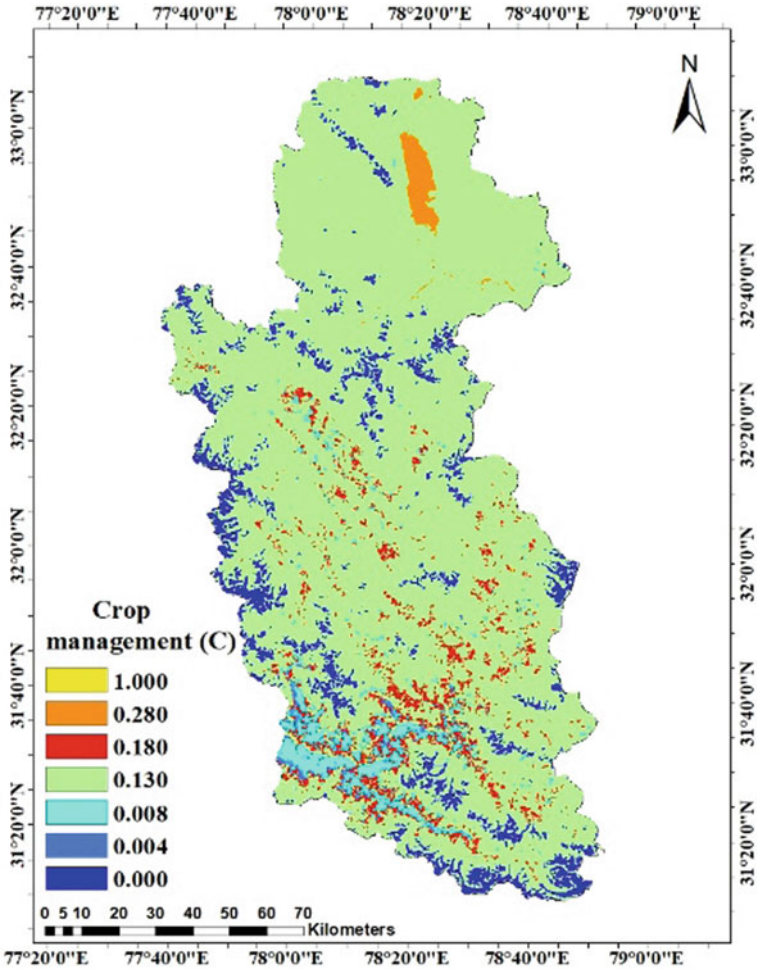

Fig. 8.5 Spatial distribution of crop management factor (*C*)

$$E = R \times \left(11.9 + 8.7 \times \log_{10} I\right) \tag{8.6}$$

R is the annual rainfall depth (mm/year), and *I* is the rainfall intensity (mm/hr). The runoff will occur when the daily rainfall exceeds the soil moisture storage capacity (Morgan et al. 1984). The annual runoff in terms of the volume of overland flow (*Q*, mm) was calculated as

$$Q = R \times \exp(-R_c/R_o) \tag{8.7}$$

where R_c = soil moisture storage capacity (mm) and R_o is the ratio of annual rainfall (R) and the number of rainy days (R_n).

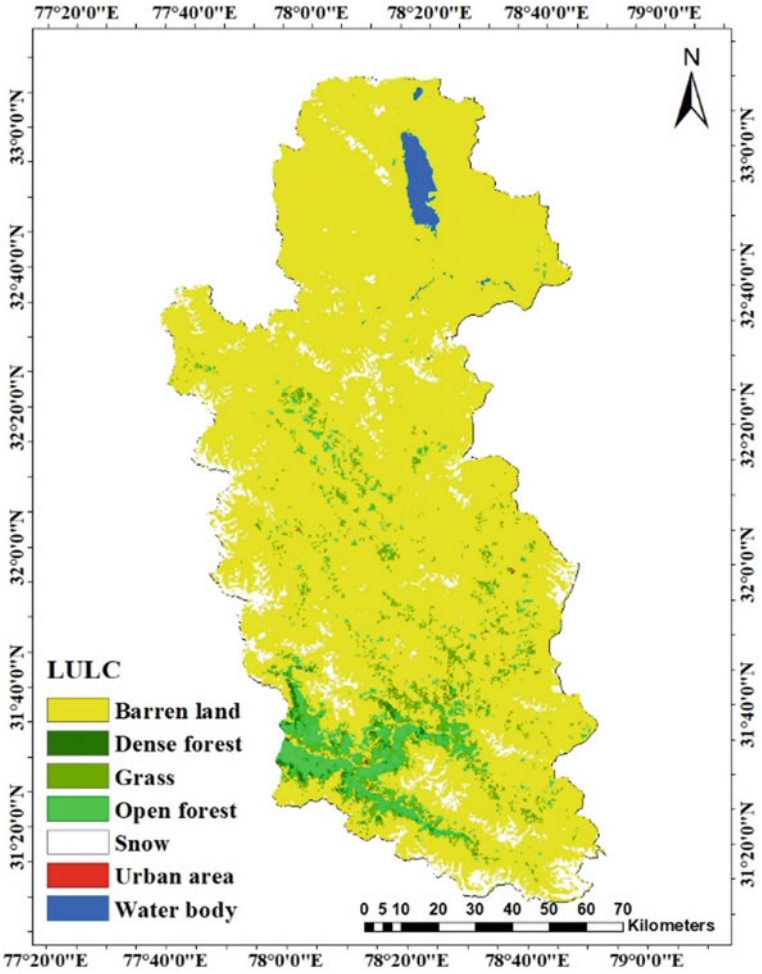

Fig. 8.6 LULC map of the catchment

Sediment Phase

The soil detachment through the splash effect of raindrops and runoff is considered in this phase. The soil detachment due to raindrop impact is considered a function of the soil detachment index (K, gm/J). Soil detachment index is the weight of detached soil from the soil mass per unit of rainfall energy. The detachment of soil by the raindrops (F, Kg/m^2) is calculated by Eq. 8.8.

$$F = K \times \left(E \times e^{-0.05 \times A}\right) \times 10^{-3} \tag{8.8}$$

where E = kinetic energy of rainfall (J/m^2) and A = permanent rainfall interception (%).

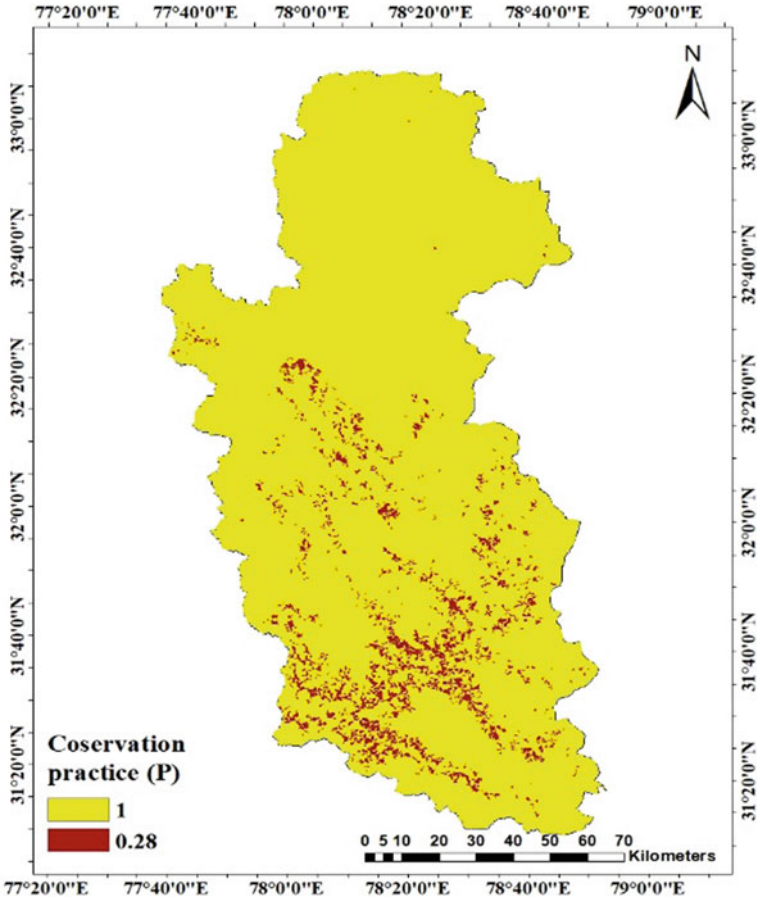

Fig. 8.7 Spatial distribution of conservation practice factor (*P*)

Some of the factors such as land slope, overland flow, crop management factors, etc., are responsible for the detachment of the soil particles by runoff (G, Kg/m^2). Thus, the soil particles' detachment by runoff is given by Eq. 8.9.

$$G = C \times Q^2 \times \sin(S) \times 10^{-3} \tag{8.9}$$

where Q = volume of the overland flow (mm), S = land slope factor (%), and C = crop management factor.

As per (Morgan et al. 1984), the model compares the predicted rate of rainfall detachment (F) with the transport capacity (G) for overland flow and equates the rate of soil loss to the lower of the two values.

Figure 8.9 shows the process flowchart of the detailed methodology adopted to estimate soil loss using the MMF model. The model compared the transport capacity

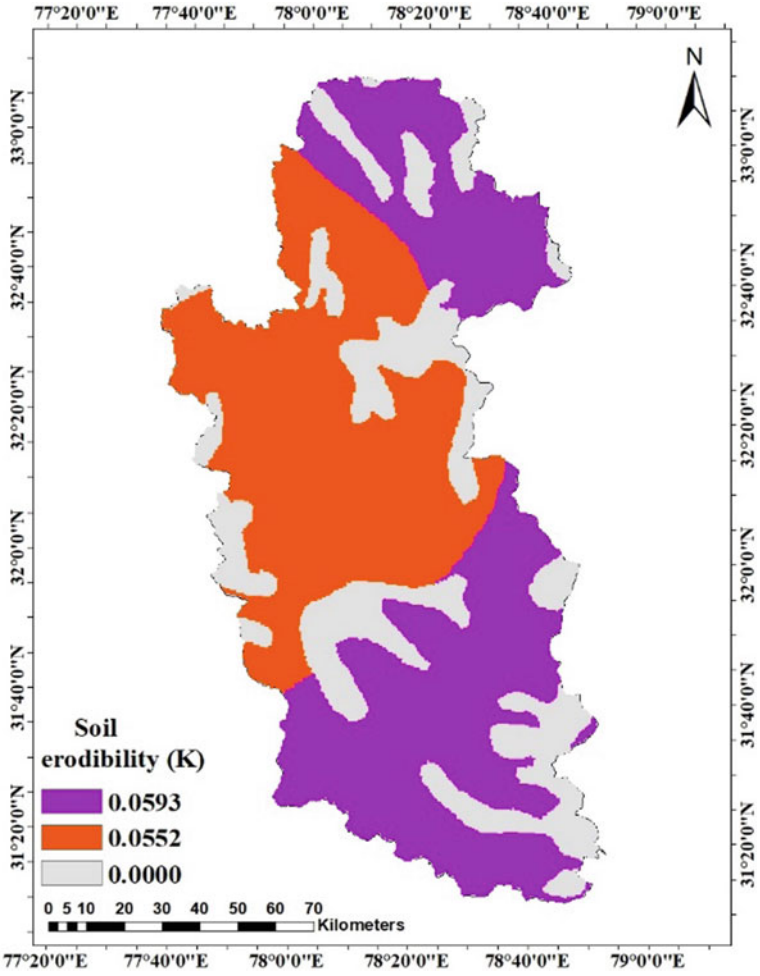

Fig. 8.8 Spatial distribution of the soil erodibility factor (K)

of the overland flow with predicted splash detachment. The lower value between transport capacity and soil detachment rate is considered as the soil loss by the model.

8.3.2.1 Spatial Inputs for MMF Model

Soil Map

The Food and Agriculture Organization (FAO) soil map available on www.fao.org/geonetwork was used to identify the soil moisture storage capacity (Fig. 8.10).

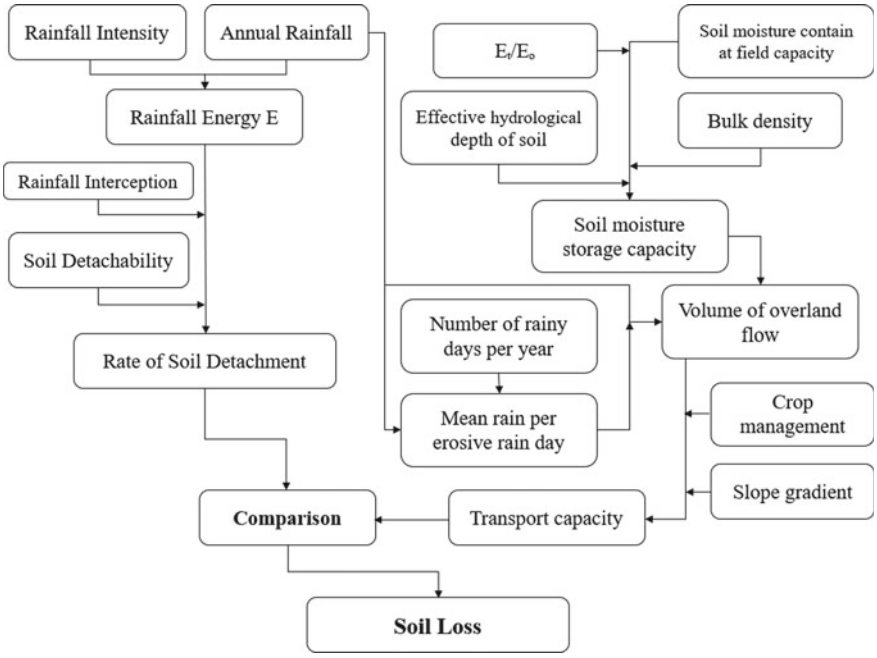

Fig. 8.9 MMF model process flowchart

Meteorological Data
The 0.25° × 0.25° gridded data obtained from IMD was used to calculate the rainfall energy. For each year, the number of rainy days is required to calculate the mean rain per erosive rain day.

Digital Elevation Model The ASTER data available on www.earthexplorer.usgs.gov was used to develop the slope gradient factor map (Fig. 8.11).

Actual (Et) to Potential Evapotranspiration (E_0) Map
The actual (Et) distribution ratio to potential evapotranspiration (E_0) for the study area was prepared using the data available on www.esa-landcover-cci.org and is shown in Fig. 8.12.

8.3.3 Sediment Delivery Ratio (SDR)

Both models helped in predicting the soil loss in terms of erosion per unit area of the catchment. Typically, the sediment transported may have numerous opportunities to be deposited between the field and point of final deposition. This may

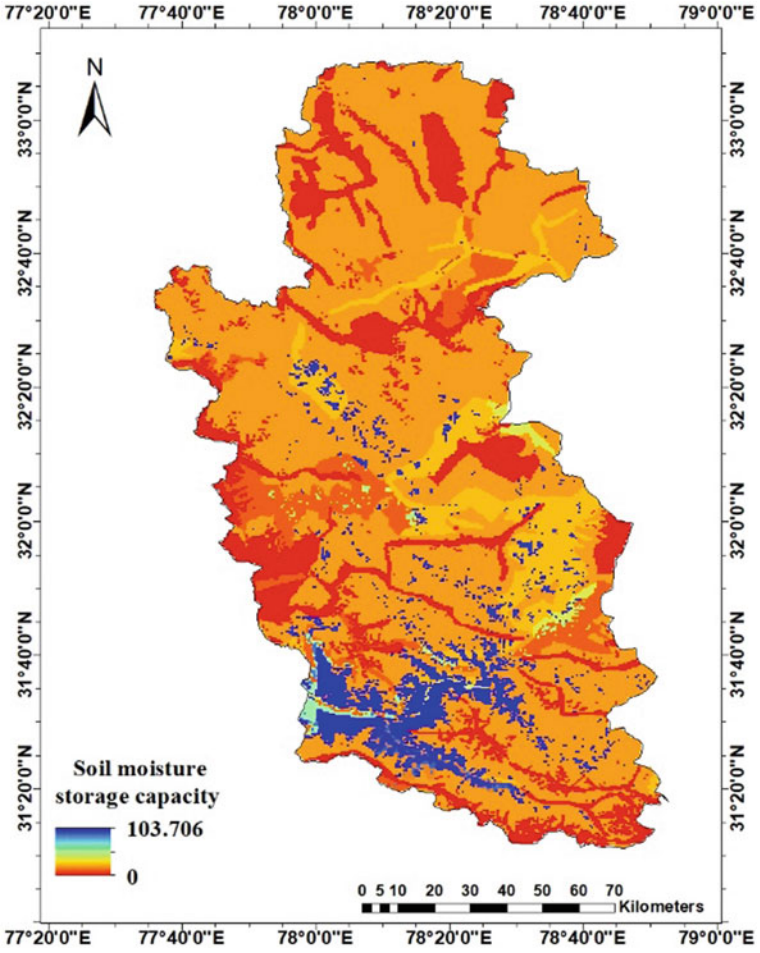

Fig. 8.10 Spatial distribution of the soil moisture storage capacity

result in reducing the sediment yield accordingly. The term sediment delivery ratio (SDR) indicates the catchment capability for storing and transporting the sediments (Gelagay and Minale 2016) and can be defined as

$$\text{SDR} = \frac{\text{Observed sediment yield}}{\text{calculated sediment rate} \times \text{area of watershed}} \tag{8.10}$$

Both the MMF models do not include procedures for evaluating deposition that occurs in overland flow before reaching concentrated flow channels. Thus, there is a need to assess the delivery ratio for both these models.

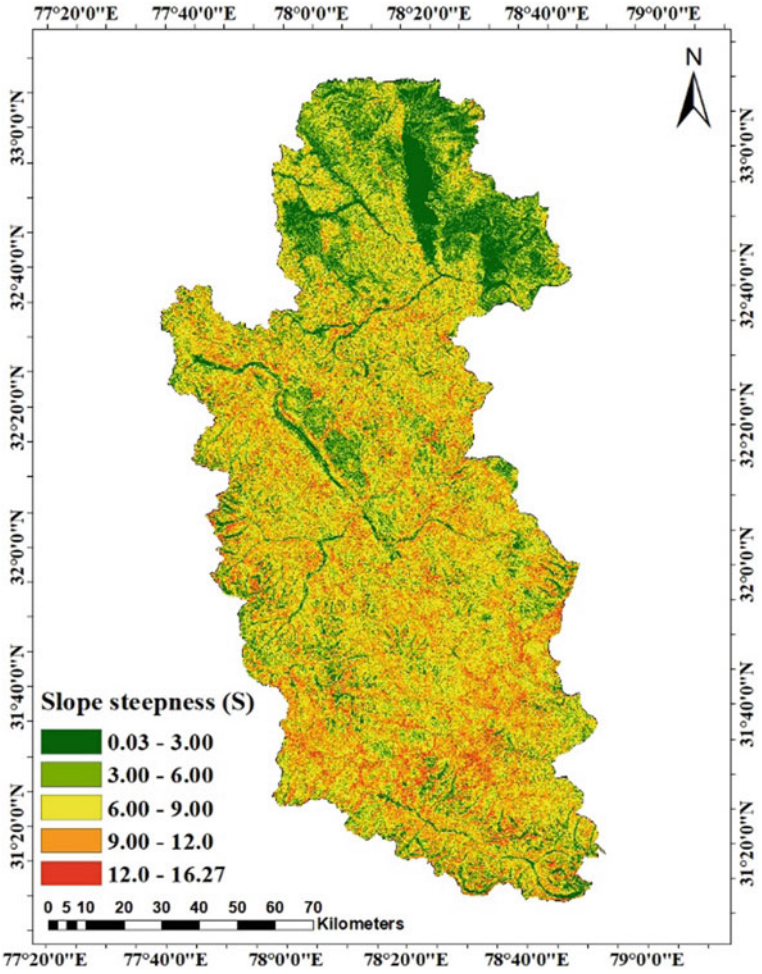

Fig. 8.11 Spatial distribution of the slope gradient factor

8.3.4 Model Validation

The output of both of the models was validated by comparing with the observed sediment yield from the catchment for a period from 1971 to 1996.

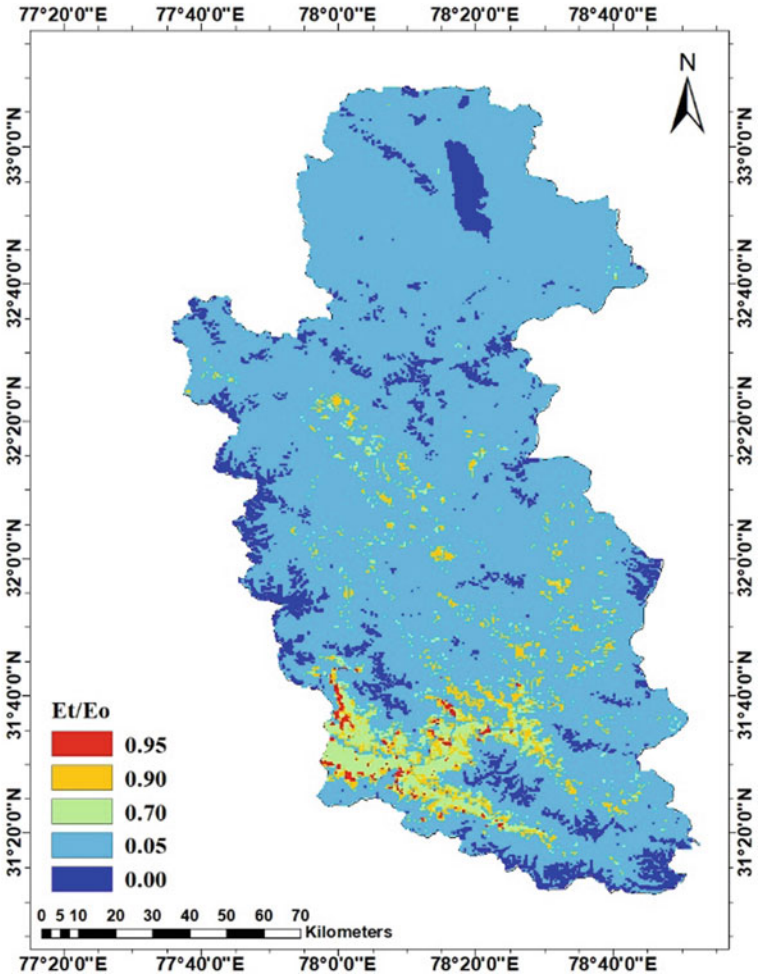

Fig. 8.12 Spatial distribution of Et/E_0 ratio

8.4 Results and Discussion

The spatial distribution of soil loss from Nathpa-Jhakri catchment obtained by RUSLE and MMF models employing spatial inputs is discussed in the following sections.

Table 8.1 LULC classes of the catchment

LULC type	Area (km^2)	Area (%)
Barren lands	12,796.506	83.705
Urban areas	5.996	0.039
Agricultural lands	693.520	4.536
Dense forest	69.463	0.454
Open forest	497.378	3.253
Snow	1062.250	6.948
Water body	162.567	1.063
Total area (km^2)	15,287.679	100.000

8.4.1 Soil Loss by RUSLE Model

The maps of RUSLE factors are assumed to be constant for all years of this study. According to the FAO geonetwork map, there are two soil classes in the Nathpa-Jhakri watershed, sandy clay loam, and loam. Thus, the values of soil erodibility factor (K) were found to be 0.05937 and 0.05524 (tons.ha.h/ha/MJ/mm), respectively. The estimated slope length (L) values for the selected catchment range from 1.055 to 1.143. The slope steepness factor (S) is ranged from 0.031 to 18.6. Seven land use/cover classes were identified in the Nathpa-Jhakri catchment (Table 8.1).

According to the LULC map of the study area, the crop management factor was assigned as 0.28 and 1 for the agricultural land and other land use, respectively. The resulted annual soil loss using the RUSLE model is shown in Table 8.2, with the average soil loss value for all 26 years of the study.

The plot between the RUSLE model results against the observed sediment yield is shown in Fig. 8.13. A linear trend line drawn between observed and RUSLE estimated sediment yield indicated a non-significant difference with a high coefficient of determination (r^2) of 0.80. This can be inferred from a straight-line plot. The differences between the predicted and observed sediment yields from the RUSLE model reinforce the erosion predictions, in general, containing a factor of error.

Areas under different soil erosion classes in the Nathpa-Jhakri catchment using the RUSLE model are presented in Table 8.3 and Fig. 8.14. According to the RUSLE model results, areas covered by slight, moderate, high, very high, severe, and severe erosion potential zones accounted for 29.6%, 6.2%, 14.3%, 34.7%, 15.13%, and 0.07%, respectively.

8.4.2 Soil Loss by MMF Model

The resulting transport capacity (G, Kg/m^2) and splash detachment by the raindrops (F, Kg/m^2) of the MMF model and the annual soil loss are given in Table 8.4 for 26 years (from 1971 to1996).

Table 8.2 Mean annual soil loss results of RUSLE model

Years	RUSLE mean soil loss (tons/ha/year)	Years	RUSLE mean soil loss (tons/ha/year)
1971	38.78	1984	12.22
1972	8.84	1985	14.44
1973	18.86	1986	17.87
1974	13.69	1987	20.46
1975	25.43	1988	28.5
1976	14.88	1989	20.77
1977	6.76	1990	21.92
1978	42.66	1991	14.15
1979	16.81	1992	17.5
1980	35.53	1993	17.65
1981	13.35	1994	11.55
1982	49.98	1995	16.91
1983	14.09	1996	17.34
Average = 20.42 (tons/ha/year)			

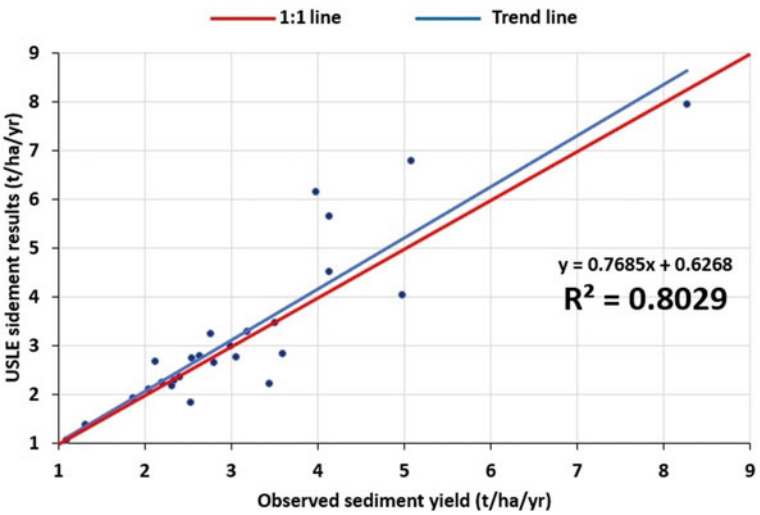

Fig. 8.13 Comaprison of RUSLE model results with the observed value

The MMF model was also validated by comparing the observed and estimated results of sediment yield, as shown in Fig. 8.15. The lower coefficient of determination (r^2) value (0.65) indicated a lower agreement of the sediment yield than the RUSLE model results.

Table 8.3 Areas under different classes of RUSLE soil loss results

Average soil loss (tons/ha/year)	Area (km^2)	Classes	Area (%)
0–5	4477.06	Slight	29.6
5–10	919.80	Moderate	6.2
10–20	2156.02	High	14.3
20–40	5141.77	Very high	34.7
40–80	2276.39	Severe	15.13
> 80	9.71	Very severe	0.07

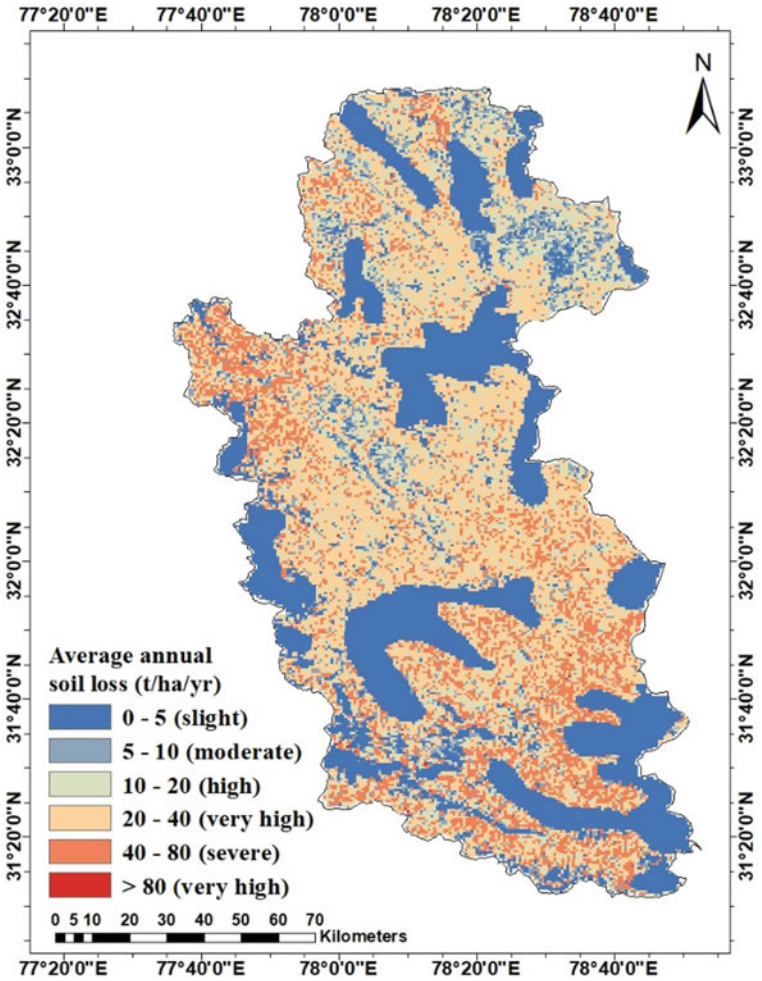

Fig. 8.14 Spatial distribution of average annual soil loss (RUSLE)

Table 8.4 Mean annual soil loss results of MMF model

Years	Transport capacity G (kg/m^2)	Splash detachment F (kg/m^2)	Annual soil loss (kg/m^2)	Years	Transport capacity G (kg/m^2)	Splash detachment F (kg/m^2)	Annual soil loss (kg/m^2)
1971	14.462	14.963	14.462	1984	4.781	10.089	4.781
1972	6.688	12.029	6.688	1985	12.342	15.232	12.342
1973	6.745	11.876	6.745	1986	20.141	18.376	18.376
1974	7.396	12.032	7.396	1987	10.873	13.973	10.873
1975	23.735	18.654	18.654	1988	33.393	19.554	19.554
1976	5.328	11.627	5.328	1989	21.947	19.582	19.582
1977	3.711	9.057	3.711	1990	14.141	16.166	14.141
1978	37.412	22.141	22.141	1991	11.944	15.053	11.944
1979	7.313	12.535	7.313	1992	12.575	15.210	12.575
1980	14.733	15.845	14.733	1993	10.267	13.621	10.267
1981	12.444	14.947	12.444	1994	8.435	14.003	8.435
1982	72.130	29.639	29.639	1995	18.448	17.016	17.016
1983	11.538	15.391	11.538	1996	18.359	18.108	18.108
Average = 13.03 (kg/m^2)							

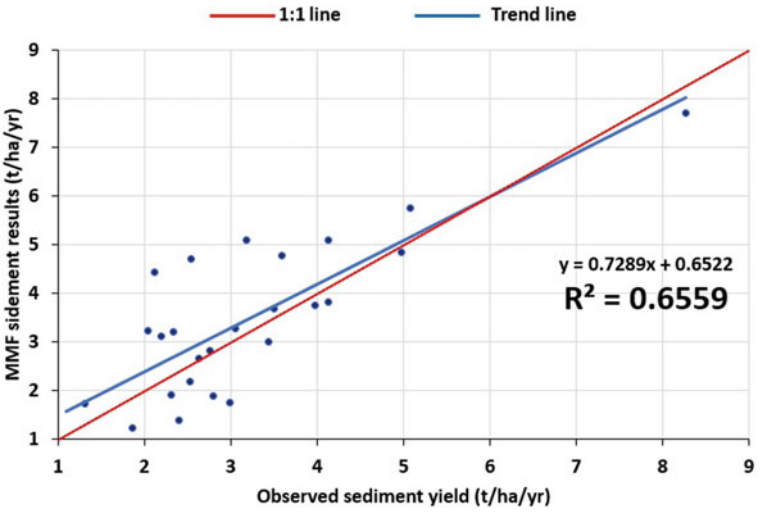

Fig. 8.15 Validation of results by MMF model

Table 8.5 Areas under different classes of MMF soil loss

Average soil loss of MMF (tons/ha/year)	Area (km^2)	Classes	Area (%)
0–5	799.66	Slight	5.36
5–10	5843.53	Moderate	39.20
10–20	5926.67	High	39.76
20–40	2019.74	Very high	13.55
40–80	311.00	Severe	2.09
> 80	5.88	Very severe	0.04

The areas under different soil erosion classes in the Nathpa-Jhakri catchment by the MMF model prediction are presented in Table 8.5 and Fig. 8.16. According to the MMF model application, the areas covered by slight erosion, moderate erosion, high erosion, very high erosion, severe erosion, and severe erosion potential zones accounted for 5.36%, 39.2%, 39.76%, 13.55%, 2.09%, and 0.04%, respectively, in the catchment.

8.5 Conclusions

The spatially distributed soil erosion was estimated by using RUSLE and MMF model. Both of the models showed the higher risk potential slope pertaining to soil erosion. Based on the study, the following conclusions are drawn.

1. The average annual soil loss by employing the RUSLE model is 20.42 tons/ha/year from the Nathpa-Jhakri catchment. The results of the RUSLE model show that 0.07% of the study area lies in the very severe class (> 80 tons/ha/year), 15.13% in the severe class (40–80 tons/ha/year), 34.7% in the very high class (20–40 tons/ha/year), 14.3% in the high class (10–20 tons/ha/year), 6.2% in the moderate class (5–10 tons/ha/year), and 29.6% in the slight class (0–5 tons/ha/year).
2. The average annual soil loss by the MMF model is 13.03 tons/ha/year from the Nathpa-Jhakri catchment. The results of the MMF model show that 0.04% of the study area lies in the very severe class (> 80 tons/ha/year), 2.09% in the severe class (40–80 tons/ha/year), 13.55% in the very high class (20–40 tons/ha/year), 39.76% in the high class (10–20 tons/ha/year), 39.2% in the moderate class (5–10 tons/ha/year), and 5.36% in the slight class (0–5 tons/ha/year).
3. A high value of the coefficient of determination and low percentage deviation using the RUSLE model as compared to the MMF model inferred that the RUSLE model results are more accurate and can be adopted in the hilly Himalayan catchments.

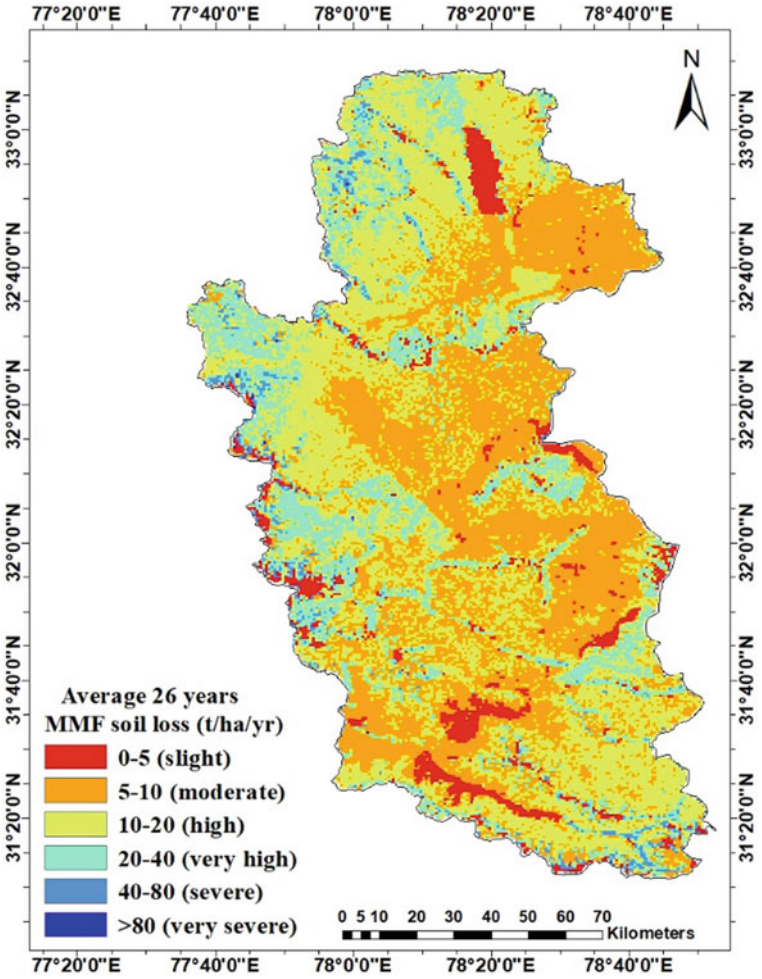

Fig. 8.16 Spatial distribution of average annual soil loss (MMF)

4. The remote sensing data and geographic information system play a significant role in generating the parameters from remote catchments for soil erosion modeling and watershed management.

Recommendations The present study was carried out to study the spatial distribution of the soil loss in the Nathpa-Jhakri catchment using RUSLE and MMF models. The results obtained by the RUSLE model show that 64.2% of the catchment area lies in high to very severe soil erosion classes. Thus, appropriate soil and water conservation measures should be adopted to minimize the soil loss from the Nathpa-Jhakri catchment.

References

Amsalu T, Mengaw A (2014) GIS-based soil loss estimation using RUSLE model: the case of jabitehinan woreda, ANRS, Ethiopia. Nat Res

Angima SD, Stott DE, O'neill MK, Ong CK, Weesies GA (2003) Soil erosion prediction using RUSLE for central Kenyan highland conditions. Agric Ecosyst Environ 97(1–3):295–308

Biswas SS, Pani P (2015) Estimation of soil erosion using RUSLE and GIS techniques: a case study of Barakar River basin, Jharkhand, India. Model Earth Syst Environ 1(4):1–13

Chen T, Niu RQ, Li PX, Zhang LP, Du B (2011) Regional soil erosion risk mapping using RUSLE, GIS, and remote sensing: a case study in Miyun Watershed, North China. Environ Earth Sci 63(3):533–541

Dabral PP, Baithuri N, Pandey A (2008) Soil erosion assessment in a hilly catchment of North Eastern India using RUSLE, GIS and remote sensing. Water Resour Manage 22(12):1783–1798

Das B, Paul A, Bordoloi R, Tripathi OP, Pandey PK (2018) Soil erosion risk assessment of hilly terrain through integrated approach of RUSLE and geospatial technology: a case study of Tirap District, Arunachal Pradesh. Model Earth Syst Envir 4(1):373–381

Demirci A, Karaburun A (2012) Estimation of soil erosion using RUSLE in a GIS framework: a case study in the Buyukcekmece Lake Watershed, Northwest Turkey. Environ Earth Sci 66(3):903–913

De Roo APJ, Jetten VG (1999) Calibrating and validating the LISEM model for two data sets from the Netherlands and South Africa. Catena 37(3–4):477–493

Devatha CP, Deshpande V, Renukaprasad MS (2015) Estimation of soil loss using RUSLE model for Kulhan Watershed, Chattisgarh—a case study. Aquat Procedia 4:1429–1436

Dhruvanarayana VV, Babu R (1983) Estimation of soil erosion in India. J Irrig Drain Eng 109(4):419–434

Diodato N, Bellocchi G (2010) MedREM, a rainfall erosivity model for the Mediterranean region. J Hydro 387(1–2):119–127

Eisazadeh L, Sokouti R, Homaee M, Pazira E (2012) Comparison of empirical models to estimate soil erosion and sediment yield in micro catchments. Eurasian J Soil Sci 1(1):28–33

Fistikoglu O, Harmancioglu NB (2002) Integration of GIS with USLE in assessment of soil erosion. Water Res Manag 16(6):447–467

Gelagay HS, Minale AS (2016) Soil loss estimation using GIS and remote sensing techniques: a case of Koga Watershed, Northwestern Ethiopia. Int Soil Water Conser Res 4(2):126–136

Ghosal K, Bhattacharya SD (2020) A review of RUSLE model. J Indian Soc Remote Sens 48(4):689–707

Griffin ML, Beasley DB, Fletcher JJ, Foster GR (1988) Estimating soil loss on topographically non-uniform field and farm units. J Soil Water Conser 43(4):326–331

Igwe PU, Onuigbo AA, Chinedu OC, Ezeaku II, Muoneke MM (2017) Soil erosion: a review of models and applications. Int J Adv Eng Res Sci 4(12):237341

Jain MK, Kothyari UC (2000). Estimation of soil erosion and sediment yield using GIS. Hydrol Sci J 45(5):771–786

Jain MK, Kumar S, Varghese J (2001) Estimation of soil erosion for a Himalayan watershed using GIS technique. Water Resour Manage 15(1):41–54

Jain MK, Mishra SK, Shah RB (2010) Estimation of sediment yield and areas vulnerable to soil erosion and deposition in a Himalayan watershed using GIS. Curr Sci 213–221

Langdale GW, West LT, Bruce RR, Miller WP, Thomas AW (1992) Restoration of eroded soil with conservation tillage. Soil Technol 5(1):81–90

McCool DK, Brown LC, Foster GR, Mutchler CK, Meyer LD (1987) Revised slope steepness factor for the Universal Soil Loss Equation. Transactions of the ASAE 30(5):1387–1396

Meyer LD, Wischmeier WH (1969) Mathematical simulation of the process of soil erosion by water. Trans ASAE 12(6):754–0758

Mondal A, Khare D, Kundu S (2016) A comparative study of soil erosion modelling by MMF, USLE and RUSLE. Geocarto Int 33(1):89–103

Mondal A, Khare D, Kundu S (2017) Uncertainty analysis of soil erosion modelling using different resolution of open-source DEMs. Geocarto Int 32(3):334–349
Moore ID, Burch GJ (1986) Physical basis of the length-slope factor in the universal soil loss equation. Soil Sci Soc Am J 50(5):1294–1298
Morgan RPC, Morgan DDV, Finney HJ (1984) A predictive model for the assessment of soil erosion risk. J Agric Eng Res 30:245–253
Nikolakopoulos KG, Kamaratakis EK, Chrysoulakis N (2006) SRTM vs ASTER elevation products. Comparison for two regions in Crete, Greece. Int J Remote Sens 27(21):4819–4838
Onstad CA, Piest RF, Saxton KE. In: 3rd Federal interagency sedimentation conference proceeding water resouces council, Washington DC, USA
Onyando JO, Kisoyan P, Chemelil MC (2005) Estimation of potential soil erosion for river perkerra catchment in Kenya. Water Res Manag 19(2):133–143
Pandey A, Chowdary VM, Mal BC (2007) Identification of critical erosion prone areas in the small agricultural watershed using RUSLE, GIS and remote sensing. Water Resour Manage 21(4):729–746
Pandey A, Chowdary VM, Mal BC, Billib M (2008) Runoff and sediment yield modeling from a small agricultural watershed in India using the WEPP model. J Hydrol 348(3–4):305–319
Pandey A, Gautam AK, Chowdary VM, Jha CS, Cerdà A (2021) Uncertainty assessment in soil erosion modelling using RUSLE, multisource and multiresolution DEMs. J Indian Soc Remote Sens 1–19
Pandey A, Mathur A, Mishra SK, Mal BC (2009) Soil erosion modelling of a Himalayan watershed using RS and GIS. Envir Earth Sci 59(2):399–410
Pandey A, Mishra SK, Gautam AK (2015) Soil erosion modelling using satellite rainfall estimates. J Water Res Hydra Eng 4(4):318–325
Prasannakumar V, Vijith H, Abinod S, Geetha NJGF (2012). Estimation of soil erosion risk within a small mountainous sub-watershed in Kerala, India, using Revised Universal Soil Loss Equation (RUSLE) and geo-information technology. Geosci Front 3(2):209–215
Ranzi R, Le TH, Rulli MC (2012) A RUSLE approach to model suspended sediment load in the Lo river (Vietnam): effects of reservoirs and land use changes. J Hydrol 422:17–29
Rapp JF (1994) Error assessment of the Revised Universal Soil Loss Equation using natural runoff plot data. M.S. thesis, University of Arizona, Tucson, Arizona. http://hdl.handle.net/10150/291699
Raymo ME, Ruddiman WF (1992) Tectonic forcing of late Cenozoic climate. Nature 359(6391):117–122
Renard KG (1997) Predicting soil erosion by water: a guide to conservation planning with the Revised Universal Soil Loss Equation (RUSLE). United States Government Printing
Risse LM, Nearing MA, Laflen JM, AD Nicks (1993) Soil Sci Soc Am J 57:3
Rodrigo-Comino J (2018) Five decades of soil erosion research in “terroir”. The State-of-the-Art. Earth-Sci Rev 179:436–447
Sharma A (2010) Integrating terrain and vegetation indices for identifying potential soil erosion risk area. Geo-Spatial Inf Sci 13(3):201–209
Shrestha DP (1997) Soil erosion modelling. ILWIS application guide
Singh G, Babu R, Narain P, Bhushan LS, Abrol IP (1992) Soil erosion rates in India. J Soil Water Conserv 47(1):97–99
Singh G, Panda RK (2017) Grid-cell based assessment of soil erosion potential for identification of critical erosion prone areas using RUSLE, GIS and remote sensing: a case study in the Kapgari watershed, India. Int Soil Water Conserv Res 5(3):202–211
Thampapillai DJ, Anderson JR (1994) A review of the socio-economic analysis of soil degradation problems for developed and developing countries. Rev Mark Agric Econ 62(430-2016-31509):291–315
Tiwari AK, Risse LM, Nearing MA (2000) Evaluation of WEPP and its comparison with RUSLE and RUSLE. Trans ASAE 43(5):1129

Udayakumara EPN, Shrestha RP, Samarakoon L, Schmidt-Vogt D (2010) People's perception and socioeconomic determinants of soil erosion: a case study of Samanalawewa watershed, Sri Lanka. Int J Sed Res 25(4):323–339

USDA ARS (Agricultural Research Service) (2008) Draft science documentation, Revised Universal Soil Loss Equation Version 2. USDA Agricultural Research Service, Washington, DC. http://www.ars.usda.gov/sp2UserFiles/Place/64080510/RUSLE/RUSLE2_Science_Doc.pdf

Wijesundara NC, Abeysingha NS, Dissanayake DMSLB (2018) GIS-based soil loss estimation using RUSLE model: a case of Kirindi Oya river basin, Sri Lanka. Model Earth Syst Environ 4(1):251–262

Williams JR, Berndt HD (1972) Sediment yield computed with universal equation. J Hydraul Div 98(12):2087–2098

Williams JR, Berndt HD (1977) Sediment yield prediction based on watershed hydrology. Trans ASAE 20(6):1100–1104

Wischmeier WH, Smith DD (1965) Predicting rainfall-erosion losses from cropland east of the Rocky Mountains: guide for selection of practices for soil and water conservation (No. 282). Agricultural Research Service, US Department of Agriculture

Wischmeier WH, Smith DD (1978) Predicting rainfall erosion losses: a guide to conservation planning (No. 537). Department of Agriculture, Science, and Education Administration

Wuepper D, Borrelli P, Finger R (2020) Countries and the global rate of soil erosion. Nat Sustain 3(1):51–55

Yoder DC, Ketchem AJ, Whittemore DA, Porter JP, Weesies GA, Renard KG (1992) RUSLE user guide. Predicion soil erosion by water: a guide to conservation planning with the Revised Universal Soil Loss Equation (RUSLE)

Chapter 9
The Mapping of the Intensity of Degradation According to the Different Land Use in Arid Regions: The Case of the Bouhamed Watershed, Southern Tunisia

Nesrine Arrak and Aziza Ghram-Messedi

Abstract The Bouhamed watershed, which is the subject of our study, belongs to an arid ecosystem characterised by an apparent fragility which is manifested by the low-vegetation cover and the spatial importance of bare soil areas. The ecosystems fragility in this region is mainly due to unfavourable climatic conditions (aridity, low rainfall, etc.). To these climatic factors are added inappropriate anthropogenic activities (overgrazing, clearing of rangelands, etc.) to the biophysical conditions of arid environments. The overexploitation of natural resources in the study region has accentuated the degradation of these environments and even their desertification. Indeed, in our case study, the implantation of olive trees at the expense of natural vegetation exposed the soil to erosion factors. In this context, this work adopts a methodology based on the combined contribution of remote sensing and GIS. Our approach consists in evaluating the state of desertification and specifying the level of sensitivity of surfaces to degradation according to the land use patterns distinguished in the study region. As a result, three radiometric indices were calculated (the soil adjusted vegetation index (SAVI), brightness index (BI), and colour index (CI)) derived from Landsat 8 Operational Land Imager (OLI) dating from 2014, whose aim is to produce a summary map that assesses the degradation intensity in the Bouhamed watershed. Based on the combination of the three indices complemented by field observations and a spatial database (land use and surface condition) integrated in a GIS, it was easy to evaluate and classify the region studied according to the intensity of degradation, from the lowest to the highest. The determination of the degradation intensity for each land use mode favours the accuracy of the level of

N. Arrak · A. Ghram-Messedi (✉)
Laboratory of Morphological Mapping of Milieus, Environments and its Dynamics (CGMED), LAGAM (Laboratoire de Géographie et d'Aménagement de Montpellier), Department of Geography, Faculty of Humanities and Social Sciences of Tunis (FSHST), University of Tunis, Tunis, Tunisia
e-mail: ghramaziza@gmail.com

V. P. Singh et al. (eds.), *Application of Remote Sensing and GIS in Natural Resources and Built Infrastructure Management*, Water Science and Technology Library 105,
https://doi.org/10.1007/978-3-031-14096-9_9

sensitivity to desertification. Thus, according to the sensitivity to the risk of desertification, agropastoral activity (rangelands, cultivated land, ploughed land) is classified from very sensitive to not sensitive to risk. The results show the dominance for the medium degradation intensity class, with 89% of the total area. This degradation class corresponds to surface conditions dominated by loamy to loamy-sandy soils with the outcrop of gypsum crust and hardpan.

Keywords Land use · Desertification · Degradation · Remote sensing · GIS

9.1 Introduction

Landscapes in the arid areas of south-eastern Tunisia are changing both as a result of the impact of anthropic actions and as response of climate fluctuations. Since the beginning of the twentieth century, these arid areas have undergone profound socio-economic changes which have marked the landscape and exposed it to a proliferation of manifestation of land degradation in view of their desertification. The study of degradation phenomena is generally related to the increase in hardpan surface, to the exposure of the soil to the appearance of outcropping gypsum crust, or to the process of wind accumulation leading to the formation of sand dunes in some places.

Our field study is located in the Northern part of the natural region of Jeffara. It is the watershed of Bouhamed, which covers an area of 567 km^2. The different biophysical environments present in this area study are in fragile equilibrium. Fragility related to an unfavourable climate, belonging to the lower arid stage, as well as to very limited natural resources. In such a way that any human activity based on the exploitation of those resources jeopardises this equilibrium and leads to the progressive degradation of natural resources, which may even harm sustainable development (Ghram Messedi 2009).

This research provides an overview of the bioclimatic context of the Bouhamed watershed, reviews on the effect of long-term environmental anthropization, presents the main lines of research aiming at assessing the intensity of degradation linked to the land use (rangelands, cultivated lands, ploughed lands), and gives an overview of the environmental sensitivity to desertification risk.

The objective of this research is to map the intensity of environmental degradation according to the different land use patterns in arid regions. In order to achieve this objective, an approach based on optical remote sensing, field observations, and the implementation of a geographic information system (GIS) was adopted. This approach is based, in the first, on the identification of soil surface states from the extraction of radiometric indicators. These are derived from index calculations (SAVI, CI, and BI) based on a *Landsat OLI* image from 2014. In a second step, the land use map was produced using satellite imagery photo interpretation and data from field observations integrated into a GIS. Finally, the GIS analysis tools helped

to produce a synthesis map that evaluates the degradation intensity in Bouhamed watershed. This map has served as a basis for segmenting the landscape according to its sensitivity to the risk of desertification.

This work contributes to a preliminary assessment of the potential risk to soil degradation that takes into account biophysical aspects. This will help us to understand the interactions between the biophysical components of the environment and the different uses of natural resources by the populations.

9.2 Study Area Exposed to Desertification Problems

9.2.1 Arid Climate and Fragile Biophysical Context

The study area, which was the subject of our work, covers 564 km^2 and encompasses the whole of Bouhamed catchment area: it corresponds to an elongated watershed with an endoreic character, which occasionally flows to sebkhat EL Maider towards the gulf of Bou-Ghrara (Fig. 9.1). From an administrative point of view, the basin is located at the boundary between the governorate of Medenine in the east and the governorate of Tataouine in the west. The study area is part of the natural region of the northern Jeffara in south-eastern Tunisia. The latter constitutes a transitional domain between semi-arid of central Tunisia and the desert Saharan South (Ben Fraj et al. 2016).

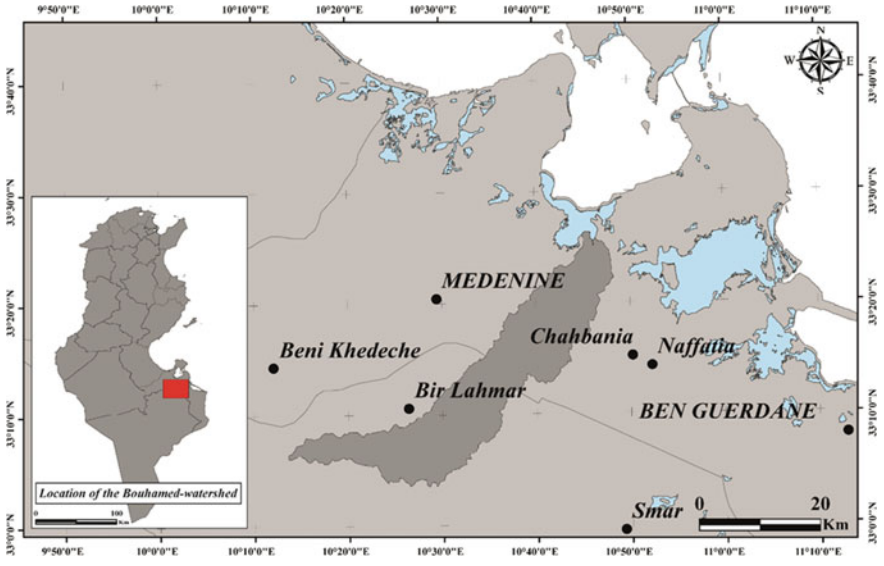

Fig. 9.1 Location of the Bouhamed watershed. *Source* administrative division of Tunisia

The Bouhamed catchment area is printed by a spatial dichotomy between the coastline and hinterland of the region: between jebel and plain is a very diverse environment, characterised by three major types of landscapes. These are ranged from limestone plateaus dominated by monoclonal structural forms of the cuesta type, to the quaternary depressions of the coast, passing through the piedmont area dominated by the alluvial fan and the plain marked by the appearance of erosion surfaces and aeolian landforms. Erosion factors and processes do not occur in the same manner across the basin. In fact, in the western part of the plateau and the piedmont, water erosion predominates, whereas wind erosion dominates in the eastern part towards the plain.

According to Emberger's classification (1955), the Bouhamed watershed is part of the lower arid stage with a temperate winter variant. The rarity, irregularity, and stormy nature of rainfall are factors that exacerbate desertification and limit the resilience of degraded environments. Indeed, the annual average is estimated at 150 mm/year. These quantities of rainfall are characterised by a torrential aspect and by an extreme variability between seasons and years (Fig. 9.2).

Thus, the succession of rainy or dry years is one of the main criteria for all arid regions of pre-Saharan Tunisia. The irregular rainfall in time and space accentuates the degradation (Khattali 1981). A succession of dry years makes ecological systems fragile, whereas a succession of rainy years does not make them regenerate (Floret and Pontanier 1976).

In addition to this irregular rainfall, there is high sunshine and temperatures, sometimes excessive (an average of 21.5 °C) which can only be a source of a very strong evapotranspiration which is often more important than the rainfall. The average values of potential evapotranspiration are very high. Indeed, for the whole of the south-east, the average PTE values oscillate between 1400 and 1700 mm/year (4–5 mm/day) (Ben Fraj et al. 2016). The winds that blowing throughout year are strong, dry, and strong. They participate in their turn to accentuate the drying of the climate.

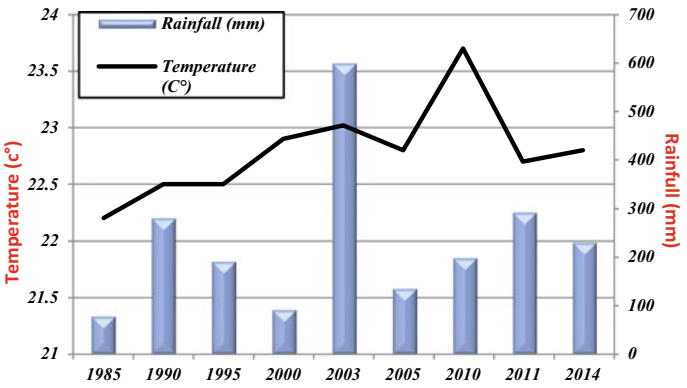

Fig. 9.2 Annual rainfall and temperatures distribution of and in Medenine resort. *Source* CRDA Medenine

The study region has a largely deficient water balance (Ben Fraj et al. 2016). Hence, water resources are relatively limited and for the mostly part, non-renewable; which is very constraining for rain-fed agriculture and explains the development of water-harvesting techniques such as the Jessour[1] in this region (Ouessar et al. 2009; Bonvallot 1979; Ben Ouezdou 2000; Calianno et al. 2020).

The water deficit has a direct repercussion on vegetal production and provides favourable conditions for the spread of wind erosion phenomena in the soil. Effectively, the soils in the study areas are fragile, vulnerable, and very sensitive to erosion processes. These soils are generally poor in organic matter and are characterised by the presence of calcareous crusts (Escadafal 1989).

The natural vegetation is essentially marked by steppe formations adapted to climatic and edaphic conditions. Therefore, the vegetation cover varies greatly between 0 and 30%: it depends on the edaphic conditions and on the human exploitation (harvesting by herds and for domestic use). It is essentially spontaneous, sparse, and predominantly Xerophilous vegetation.

For several years, the vegetation cover in arid areas has been declining and undergoing intensive regression and degradation. Indeed, the cultivation of the southern steppes, by the development of olive and cereal farming, is the cause of the desertification of natural rangelands, which, through deflation, are transformed into Rocky reg, and through the accumulations, into sand dunes (Ministère de l'Environnement 2009).

9.2.2 Ancient and Changing Human Occupation

At the same time, historical sources agree that the south-east region in general and the Jeffara, in particular, has always been an area of settlement and passage between the sea and the African continent (trade caravan) and between the north and the extreme south and the east (Mzabi 1988). Moreover, the absence of anthropic indicators of agricultural and/or pastoral activity at the beginning of the prehistoric phase underlines the weak hold of the societies of this period on the environment (Jaouadi et al. 2015).

During the present period, the pronounced increase in anthropic activities (agriculture and pastoralism) bear witness to the radical change in human–environment relations in southern Tunisia (Jaouadi et al. 2015).

Like the whole region of the Jeffara, the geographical unit of Bouhamed has been the scene, since the pre-colonial period, of a series of transformations affecting the economic and social structures and affects consequently the farming mode, the land

[1] Jessour (plural of Jesr) are ancestral hydro-agricultural systems in the Dahar plateau, and Jessour consist of small dams built across gullies and wadi thalwegs, creating a succession of terraces that partially retain the surface water and sediments required for crop growth (Calianno et al. 2020).

occupation, and the ecological environment (Abaab 1986). These transformations lead to profound changes in the landscape (Floret et al. 1989). Indeed, since the beginning of the twentieth century, the region has undergone socio-economic changes that have marked and still mark the landscape.

These changes are characterised by the passage from an extensive land occupation and its natural resources, as part of a nomadic and semi-nomadic lifestyle (collective properties and dominance of pastoralism), to a relatively intensive land occupation within the framework of a sedentary lifestyle, based on a diversification of economic activity (private properties with a limitation of transhumance areas and the extension of cereal and tree farming) (Abaab 1986; Floret and Pontanier 1982; Auclair et al. 1997). The region is marked by three main phases of change (Abaab 1986; Auclair et al. 1997; Talbi 1997): (i) *nomadic and environmental equilibrium phase of the pre-colonial era,* (ii) *semi-nomadic phase of the colonial era, and* (iii) *sedentary phase of the post-colonial era.*

During the first phase, nomadism is the general aspect that illustrates with an absence of pressure on land and physical potential (Talbi 1997). Pastoralism and episodic cereal cultivation are the main activities. Consequently, the ecological system is well balanced, with an absence of pressure on the land, and the physical potential has been preserved in these fragile areas.

Colonial intervention during the second phase has led to the beginning of a process of deconstructing lifestyles (strategy of sedentarisation, limitation of transhumance areas, privatisation of collective lands, etc.) and intensifying the land occupation and natural resources (Guillaume and Romagny 2003). This phase is characterised by the fragilisation of pastoral activities and the development of a front of agricultural colonisation towards the plain.

During the sedentary phase of the post-colonial era, the dynamics involved reached a new threshold from the 1960s and 1970s under the effect of population growth and the Tunisian State policies (Guillaume et al. 2005). This phase is characterised not only by an increasing artificialisation of the environment, but also by an accelerated development of agricultural holdings in at-risk areas and by the strategies of strong mobilisation of water resources and territorial planning implemented via the national government (Romagny and Guillaume 2004). This phase is the phase of a total breakdown of the rules that relate humans to their environment. Under these conditions, anthropic pressure is considered the main cause of desertification, and climatic conditions exacerbate the damage caused by human activity (Ouerchfani 2012). However, today's man is trying, through the means of combating desertification, to save a worrying but resilient situation. A resilience which related to new strategies[2] of adaptation to a weakened environment (Fig. 9.3).

[2] In 1962, when the first national plan for economic and social development was implemented. This plan gave particular importance to the fight against sand encroachment (Khatteli 1996; Ouessar et al. 2006).

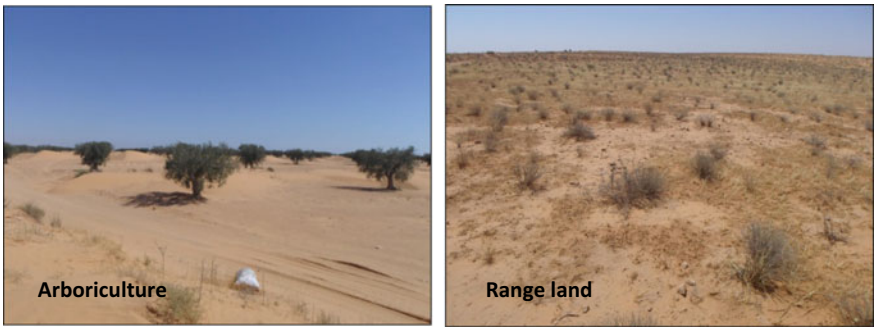

Fig. 9.3 Example of current occupation in the Bouhamed watershed. Photo shoot of Arrak N. dating from a field mission of 2014

9.3 Methodological Approach to Mapping Land Degradation Based on Remote Sensing and GIS

9.3.1 Data and Tools

The methodological approach (Fig. 9.4.) followed for the study of the degradation of arid environments according to land use patterns is essentially based on three types of data: image data (Landsat OLI images dating from 2014), field data, and existing cartographic data (topographic, geological, and thematic maps).

- *Satellite Data*:

This study was mainly based on data from a *Landsat* platform image of the *OLI* sensor dated of April 2014 (Table 9.1). This image was chosen because it was acquired close to the beginning of our field observations. Additionally, this spring date corresponds in arid regions to the vegetation peaks of a large number of natural species, as well as that of cereal species cultivated in the land plots (Ghram Messedi 2009).The image is acquired for free, on the USGS download site.[3] The image is already geo-referenced but it did not procure radiometric and atmospheric calibration. For our study, we proceeded with the radiometric correction in a first step (the conversion of digital numbers (DN) to reflectance); then, in a second step, we applied an atmospheric correction.[4]

[3] http://earthexplorer.usgs.gov/

[4] The dark object subtraction (DOS) was used in this study. The DOS method has been developed for early generation Landsat sensors (e.g. TM), over the next several years, research on the application of the DOS method in analysing Landsat 8 data deserves further examination (Gilmore and Ashty Saleem 2015).

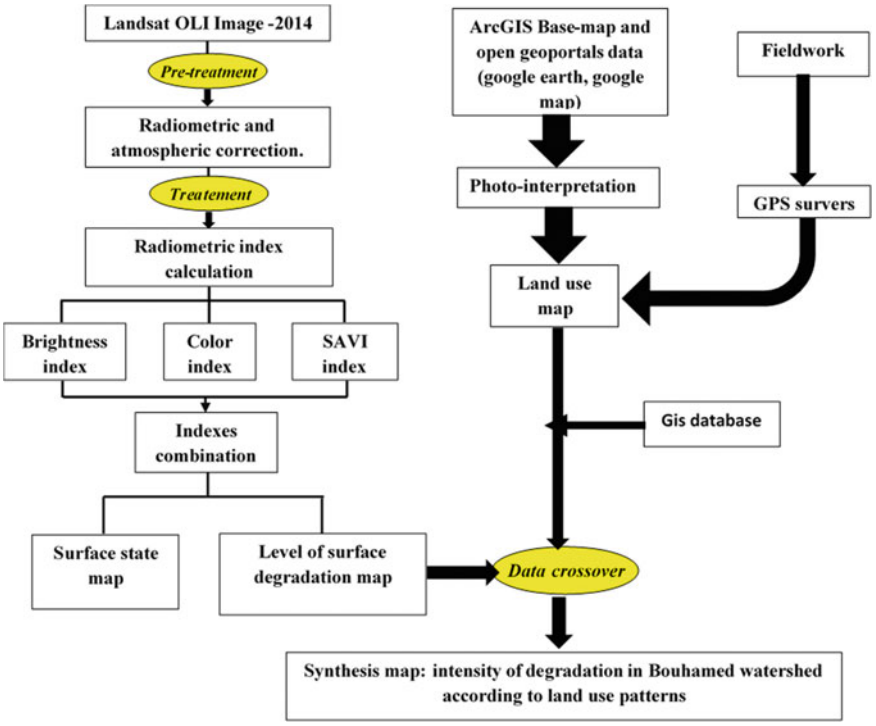

Fig. 9.4 Methodology adopted in estimating the intensity of degradation in the Bouhamed watershed

The radiometric and atmospheric correction of the image are carried out using ENVI® image processing software.

The satellite image was used as a basis for the calculation of radiometric index and the creation of neo-channels. The Google Earth image and the ArcGIS® software base map have been useful with its fine resolution to refine the visual interpretation of different types of land use.

- *Field data*:

Field data collection was based on a sampling of a set of stations using the Landsat satellite image as reference. For each station, descriptive sheets were drawn up. These sheets contain GPS surveys as well as a description of the physical environment and a characterisation of the types of human occupation. Around thirty control points throughout the watershed are being explored. These points are chosen according to their topographic position in order to present the different type of landscape.

Table 9.1 Landsat OLI image characteristics

Image	Date of acquisition	The path and the row	Type of sensor	Satellite generation	Number of bands	Spatial resolution	Radiometric resolution
Landsat	02/04/14	P: 190, R: 37	OLI-TIRS: Operational Land Imager (OLI), Thermal Infrared Sensor (TIRS)	Landsat 8	11 bands	General: 30 m PAN: 15 m THER: 60 m	B1: 0.433–0.453 µm. *Aerosols*
							B2: 0.45–0.515 µm. *B*
							B3: 0.525–0.6 µm. *G*
							B4: 0.63–0.68 µm. *R*
							B5: 0.845–0.885 µm. *NIR*
							B6: 1.650–1.660 µm. *SWIR 1*
							B7: 2.100–2.300 µm. *SWIR 2*
							B8-PAN: 0.500–0.680 µm
							B9-CIRRUS: 1.360–1.390 µm
							B10: 10.30–11.30 µm. *TIRS 1* B11: 11.50–15.50 µm. *TIRS 2*

Source https://www.nasa.gov

These surveys were integrated into the geographic information system, to be used as a support for photo interpretation of the land use map and also for the confrontation with the results obtained from the radiometric indices.

- *Existing data*:

These data concern various information (topography, hydrographic network, pedology, vegetation, climate, geology, administrative boundaries, and infrastructures). All of this data was digitised and geo-referenced and then integrated into a GIS to developpe a geodatabase of our watershed. Such a database was helped us to interpreted the phenomenon of the environmental degradation.

9.3.2 Soil Degradation Mapping Method

- Calculation of radiometric index:

Radiometric indices are new synthetic information layers that will be calculated based on statistical analysis methods and arithmetic channels combinations leading to the creation of new channels (neo-channels) (Cherel 2010). These mathematical operations are often based on the red and infrared bands because the largest differences in vegetation and soils reflectance are observed between these two bands.

The calculation of indices is used to discriminate a set of radiometric indicators that take into consideration the main physical characteristics of environment such as soil (texture, colour, roughness, moisture, etc.) and vegetation (density, biomass, etc.), in order to assess the state of degradation and distinguish between different soil surface states. Three indices were chosen to reflect vegetation, soil surface brightness, and soil colour. These indices appear to be the most suitable for the context of drylands. Indeed, studies carried out in the Tunisian arid zone (Ghram Messedi 2009; Escadafal 1989, 2007; Belghith 1997, 2003; Ghram Messedi 2007 and Delaitre 2007), have already demonstrated their effectiveness in distinguishing the different types of surface conditions. These are the soil adjusted vegetation index (SAVI), the colour index (CI), and the brightness index (BI) (Table 9.2).

Table 9.2 Characteristics of the radiometric indexes

Index	Equation	Types	Properties	Reference
SAVI	$(1 + L)\frac{(Bpir-Br)}{Bpir+Br+L}$ L is a constant equal to 0.55	Vegetation index	Minimise soil effects and introduce a fitting parameter "L" which characterises the soil and its vegetation cover	Huete 1988)
CI	$(Br - Bv)/(Br + Bv)$	Soil index	To indicate the state of soil degradation	Pouget et al. 1988)
BI	$\left(Br^2 + Bpir^2\right)\text{^}0.5$	Soil index	This index reflects the albedo of surfaces and allows vegetated cover to be separated from bare mineral areas	Escadafal and Bacha 1994)

The particular interest of SAVI index is for the calculation of the fraction of vegetation cover under sparse vegetation conditions in our study area. SAVI helps to reduce the effect of soil in areas with partial and very limited vegetation. Regarding the colour index, many studies have highlighted its interest in characterising the state of soil degradation, particularly in arid and semi-arid regions (Escadafal et al. 1994; Mougenot and Cailleu 1995; Bannari et al. 2008). In the case of the Bouhamed catchment, this index is mainly sensitive to the presence of red coloured materials in the soil, as opposed to the gypsum and limestone crust which have white–grey colour. In addition to colour, the spectral properties of a soil are intimately related to the variation in its brightness (Bannari et al. 1996). This variability makes it possible to identify the overall reflectance of a soil. The brightness index helps to distinguish between vegetated surfaces and bare soil.

The indices were calculated using ENVI®. The results obtained were exported to ARCGIS® to better interpret the radiometric values of each index.

- Construction of the GIS database:

The collection of existing maps served as the basis for a need for a data set. These data extracted from the existing map base concern a range of vector information. This information presents the set of spatial and descriptive data layers structured in a GIS (Fig. 9.5).

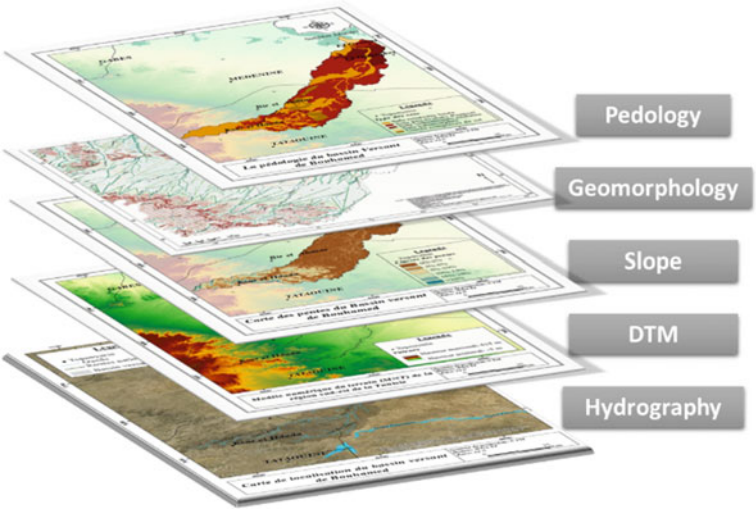

Fig. 9.5 Geodatabase GIS

Other sources were used in this study to enrich the database, such as binary raster images of the ***S*** *huttle* ***R*** *adar* ***T*** *opography* ***M*** *ission* (*SRTM*[5]). These images are used to facilitate the extraction of contour lines, wadis, and the creation of a digital terrain model. Other data sources, such as the ArcGIS base map and the open geoportals, have been exploited. In fact, Website such as Google Maps and Google Earth that provide daily updates has facilitated the updating of the study base mapping.

9.4 Study and Assessment of Degradation Intensity in the Bouhamed Watershed

9.4.1 Mapping of the Surface State by the Spectral Indices Approach

The mapping of surface states was based on the combination of the three calculated radiometric indices (Fig. 9.6). Such a combination allowed us to assemble information on both vegetation (state, density) and soil (typology, presence of crusts, and aeolian accumulations). The result was integrated into our geodatabase. The thematic interpretation, in terms of surface states, of the combination of the three indices is based on their average value and their relative comparison with the GPS surveys and the general context of the study area (the GIS database).

The combination of these three indices shows a general distinction between:

- Unvegetated surfaces with a high-brightness index (BI) and a very low-vegetation index (SAVI) value. These surfaces are either characterised by the presence of sandy accumulation or crust (gypsum or limestone) with a low CI, or with a dominance of coarse fragments (medium to high-CI value).
- The loamy-sandy surfaces have a high-colour index (CI) and a low-brightness index (BI). These surfaces are either covered by dense vegetation (high SAVI) or medium to sparse vegetation (medium to low SAVI);

The radiometric values derived from the addition of indices were classified into nine categories of the most distinguishable surface states in the Bouhamed watershed. The set of nine classes thus defined is visualised on a map. In order to determine the thematic significance of this set, we used the calculation of the average value of each index for each class (Fig. 9.7).

Finally, the different types of surface states can be described as follows:

- ***The first class*** has the lowest vegetation index values compared to other classes, and colour and brightness index values are medium to high. It is the class that groups the stony surfaces that concern mainly some wadi beds (wadi Bir El Ouelja and its tributaries). In these areas, the vegetation is almost absent, or at least has

[5] https://www2.jpl.nasa.gov/srtm/

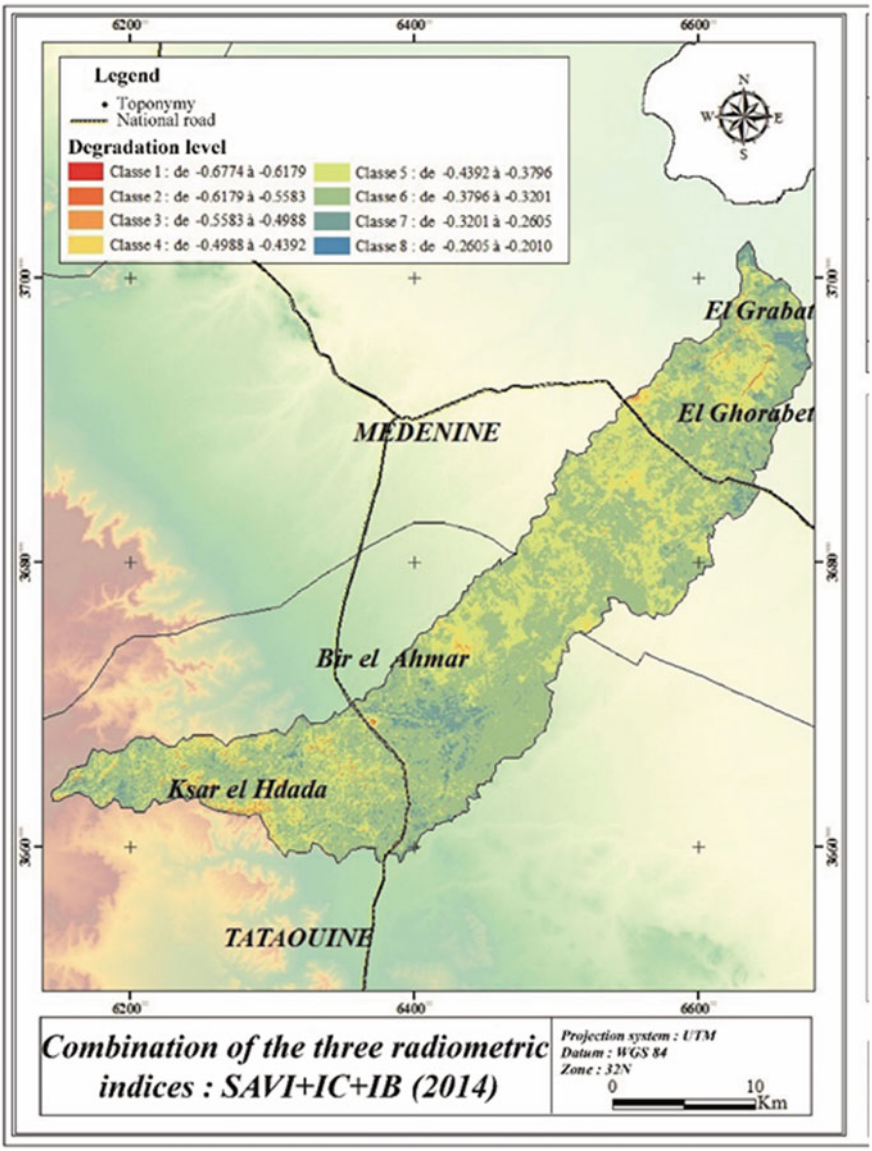

Fig. 9.6 Values of the three indices (SAVI + CI + BI) from the lowest to the highest. *Source* Landsat OLI 2014

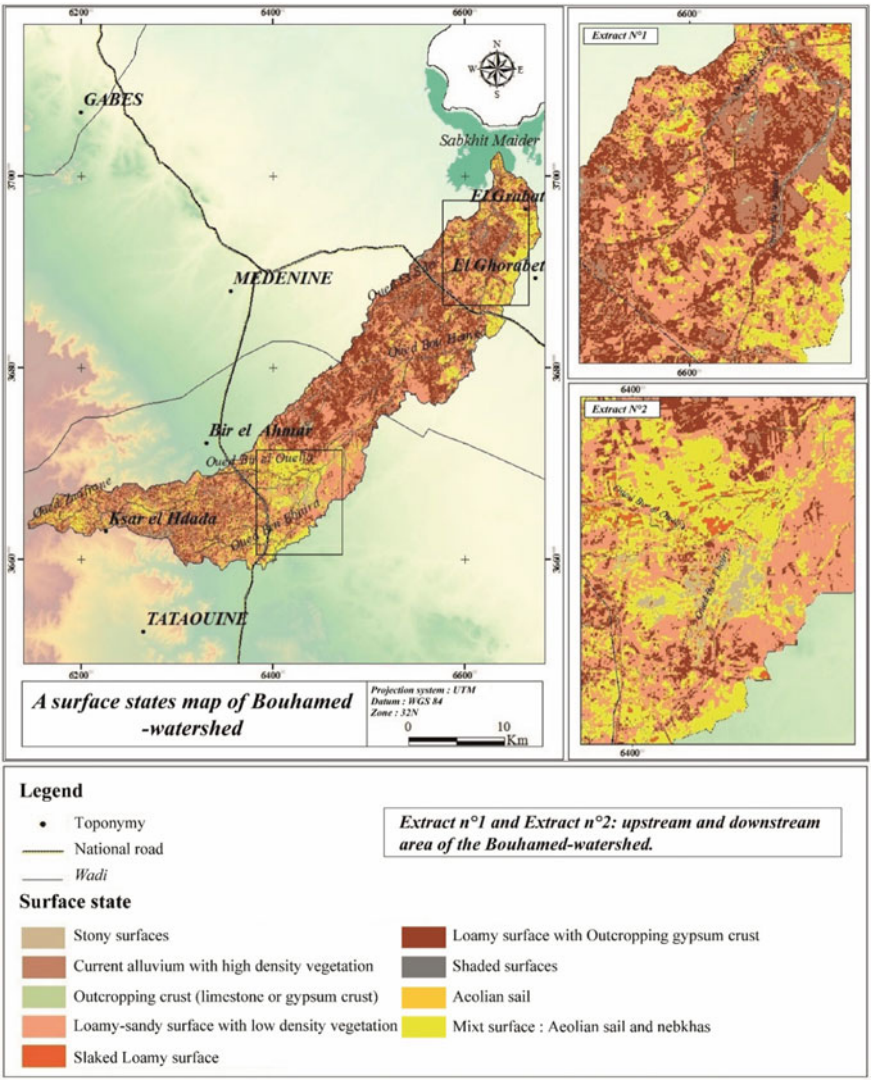

Fig. 9.7 Surface states map of Bouhamed watershed. *Source* Landsat OLI image 2014

very little chlorophyll activity. This class represents only 0.6% of the total area of the study region (Fig. 9.8).

- ***The second class*** is distinctive with high brightness, low-SAVI values, and medium to low-colour index values. This increase in reflectance is related to the presence of bright gypsum crystals (Younis et al. 1997) indicating probably the presence of gypsum crusts. The low-SAVI value reflects the absence of vegetation. The medium CI value is related to the local presence of discontinuous to

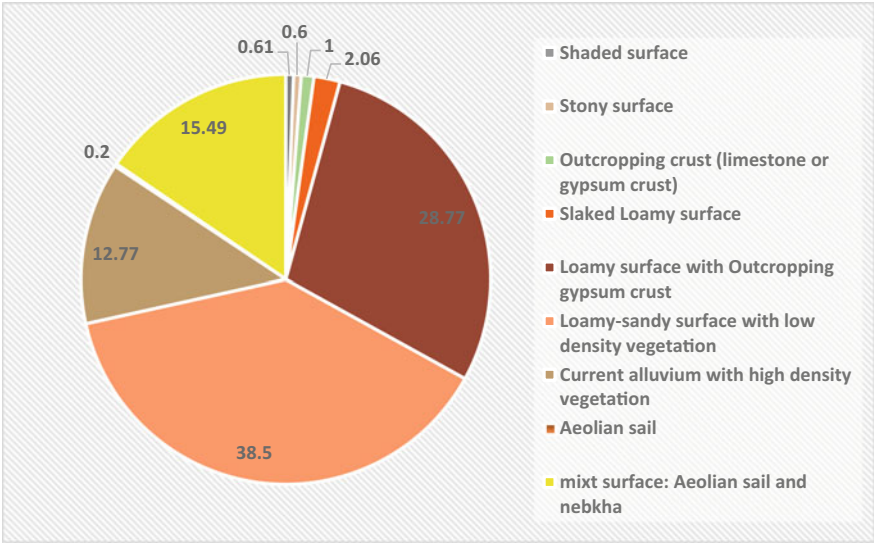

Fig. 9.8 Surface area of the different types of surface states class in the Bouhamed watershed. *Source* Surface states map

continuous silty cover and marks the absence of sand fraction. Spatially, this class of outcropping crusts covers only 1% of the overall catchment area. It is located on the middle terrace between wadi Bouhamed and wadi Es-sder.

- ***The third class*** includes slaked loamy surface. The presence of the hardpan on this surface explains the higher values of the colour index. This hardpanis an extremely unfavourable factor for the reinstallation of plant cover because of its impact on water balance, germination, and the emergence of seedlings (Floret and Pontanier 1981; Houerou 1995). This would explain the very low-SAVI values. Hardpan surface appears on the loamy or loamy-sandy soil. This class forms only 2% of the total area of the study area (Fig. 9.8).
- ***The fourth class*** is a loamy surface with outcropping gypsum crust which covers more than 28% of the total surface area of the catchment (Fig. 9.8). These surfaces characterise the middle terraces located in the low plain of the eastern part of the catchment area. In this class, the colour and brightness indices record very high values; conversely, SAVI index has a low value.
- ***The fifth class*** develops on surfaces marked by high values of brightness index and by medium values for the colour and vegetation index. Spatially, this class is the most extensive since it covers 38.5% of the general area study (Fig. 9.8). This class concerns loamy-sandy surface with low-density vegetation.
- ***The sixth class*** of current alluvium with dense vegetation and high-chlorophyll activity. This class is distinct by the highest average value of SAVI and by a relatively moderate CI and BI values. This class corresponds spatially to areas of vegetation with a relatively high-cover rate limited to areas of runoff concentration

(wadi and alluvial plain). These zones are formed on 12, 77% of the total area (Fig. 9.8).

- ***The seventh class*** is the class with the highest brightness and low-average SAVI and CI values. It is also the class with a very limited spatial extent with 0.2% (Fig. 9.8). It concerns the expanses of unvegetated aeolian sail zone in the eastern part of the study area.
- ***The eighth class*** is distinguished by a fairly high-colour index and brightness index with a slight increase in SAVI. This class covers a fairly large area of 15.49% (Fig. 9.8). It concerns the upper and the lower plain. It is a mixt surface characterises with aeolian sail and nebkha.

A class of shadow zones has been individualised. These are opaque elements with a low-radiometry variation (Ait Ahtman 2017). In our case study, these surfaces correspond to the shadow zones of reliefs with a high roughness and which extend over 0.6% of the total surface area (Fig. 9.8).

9.4.2 Mapping Human Occupation Patterns

The aim, at this level of search, is to map land use using the photo interpretation of the Landsat OLI image and the very high-resolution satellite image backgrounds integrated into ARCGIS base map, combined essentially with field observation data, and using GIS functions.

Four types of use are distinguished: a. rangeland, b. cultivated land, c. ploughed land, and d. habitat (Fig. 9.9).

- Rangelands are the dominant agropastoral activities in the catchment area. Indeed, 77% of the area is occupied by rangelands.

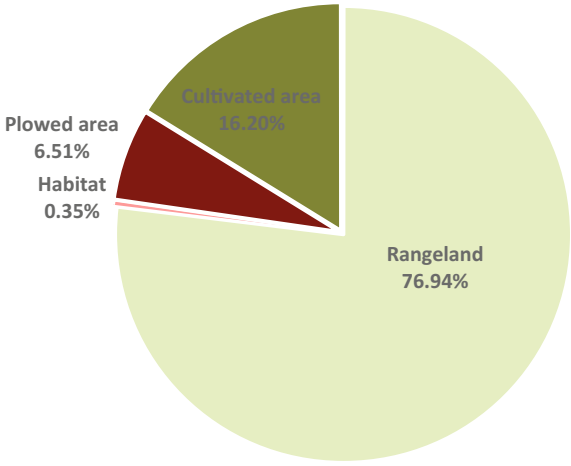

Fig. 9.9 Surface area of the different types of land use in the Bouhamed watershed

- Cultivated land represents only 16.2% of the total surface area. In the Bouhamed catchment area, approximately 92 km^2 of the land is occupied by arboriculture (mainly olive trees).
- The ploughed land is essentially prepared parcel for cereal cultivation. This mode of use is not of great spatial importance. There is 6.5% of the total area that is occupied by ploughed land. The latter are sometimes transformed into abandoned lands covered by hardpan surface or aeolian accumulations.
- Habitats are a class which has an area not exceeding 0.4% of the entire watershed.

The spatial organisation of agropastoral activities according to a topographical hierarchy closely linked to the restrictive conditions of the environment (Fig. 9.10). In the plateau and piedmont area, except for the small areas devoted to olive cultivation behind the *jessour* installed across the wadis and ravines, rangeland dominates. To the upper plain zone, a mosaic between large rangeland areas and cultivated areas which limited by topographic and edaphic constraints. In the low plain, another type of mosaic between increasingly fragmented and spatially limited rangeland areas and increasingly invasive cultivated areas. It was the extension of cereal and arboriculture to the detriment of the steppe rangelands on the loamy or sandy plains.

9.4.3 Determination of the Intensity of Degradation

The evaluation of radiometric indicators of surface helps to identify and characterise the intensity of environmental degradation. The dominant radiometric value was considered to be an essential criterion for characterising the intensity of degradation. This intensity decreases in the case of the presence of a significant vegetation cover (in case of medium or heigh SAVI index value) and increases in the case of the dominance of bare soil (in case of medium or heigh BI or CI index value). Indeed, vegetation cover and soil type have effects on increasing or decreasing forms of water or wind erosion.

The approach adopted for characterising the degradation intensity allowed the stratification of the landscape into four classes (Fig. 9.11). The interpretation of these classes has provided some spatial information about the functioning of the environment in relation to the risks of soil degradation.

An intensity scale ranging from very low to high degradation has been adopted. This scale includes four degradation classes (Table 9.3): (i) *very low degradation;* (ii) *low degradation;* (iii) *medium degradation, and* (iv) *high degradation.*

In Bouhamed watershed, the dominance was for the medium degradation intensity class, with 89% of the total area. This degradation class is characterised by a low-vegetation index and medium brightness and colour indices. It corresponds to surface conditions dominated by loamy to loamy-sandy soils with the outcrop of gypsum crust and hardpan. However, the rest of the area is occupied by classes with either low

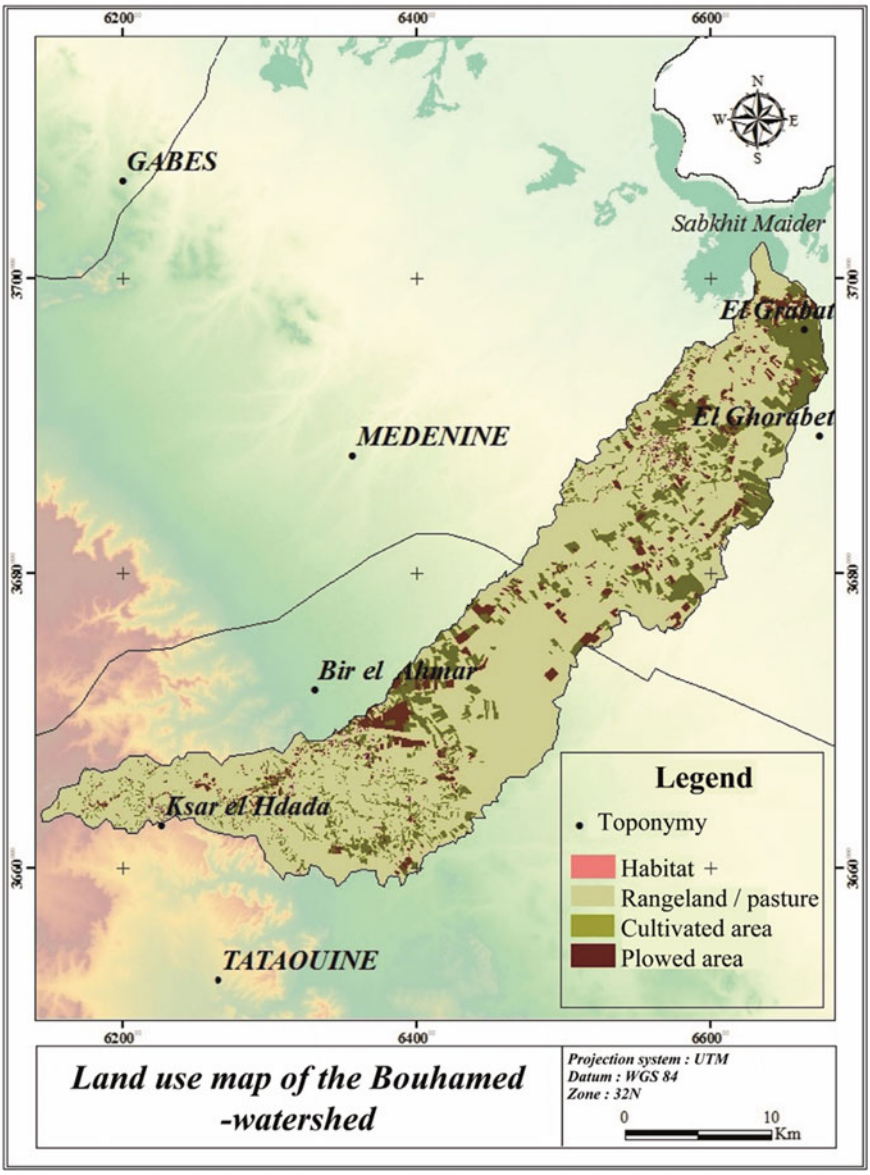

Fig. 9.10 Main modes of land use in the Bouhamed watershed

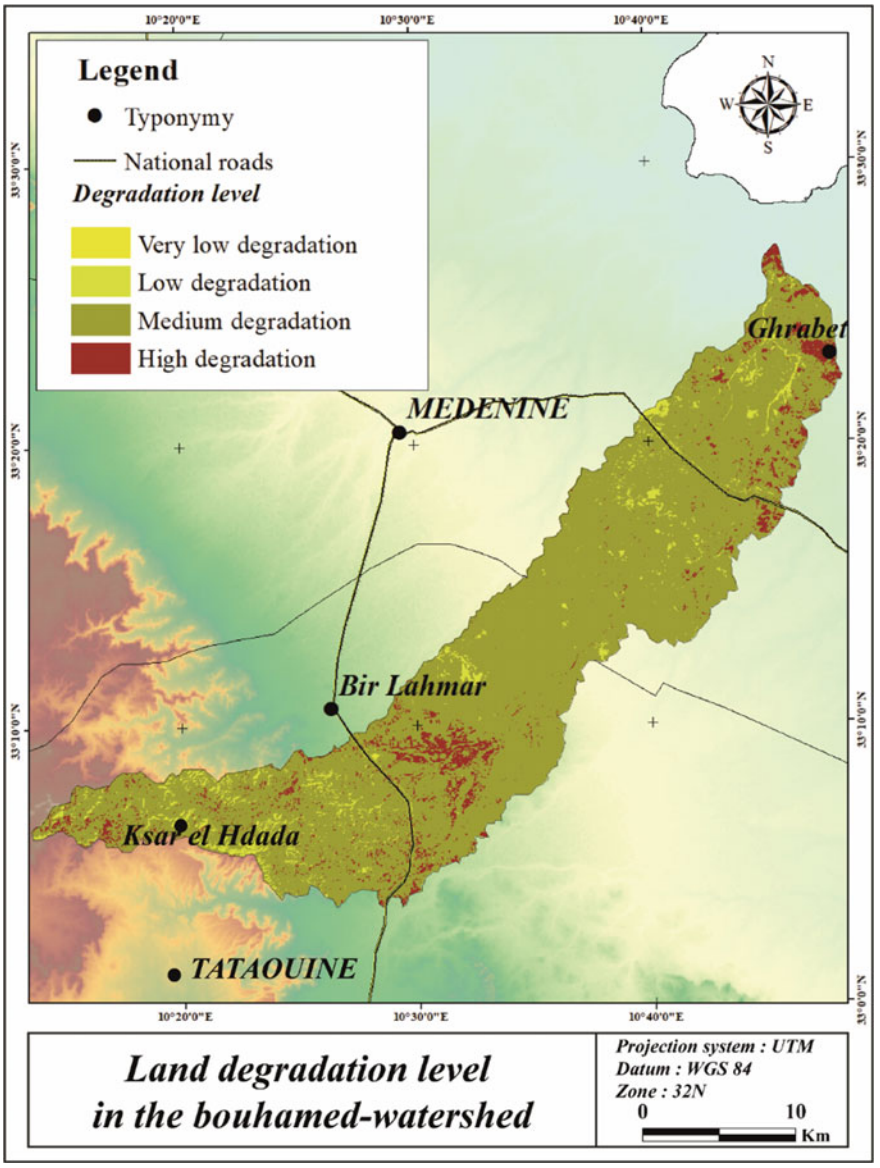

Fig. 9.11 Degradation intensity in Bouhamed watershed

to very low degradation or high degradation. In fact, the areas characterised by high to medium radiometric values for the SAVI index and in parallel low-radiometric values for the colour and brightness indices are considered as weakly degraded areas (current alluvium with dense vegetation and surfaces with sparse vegetation). On the other hand, areas with low-radiometric values for the SAVI and high-radiometric

Table 9.3 Degradation intensity and value of corresponding indices

	Degradation degree	SAVI	BI	CI
Class 1	Very low degradation	0.34–0.39	0.05–0.10	− 0.86 to − 0.77
Class 2	Low degradation	0.24–0.34	0.10–0.15	− 0.77 to − 0.69
Class 3	Medium degradation	0.14–0.244	0.15–0.18	− 0.69 to − 0.61
Class 4	High degradation	0.04–0.14	0.18–0.20	− 0.61 to − 0.56

values for the colour and brightness indices are considered to be highly degraded areas (stony or gypseous crusted surfaces and sandy surfaces).

9.4.4 Assessment of the State of Desertification by Specification of the Sensitivity Level: Summary Map

In this state of work, the synthesis map was based on a combination of the three landscape indicators developed in this research. It is a spatial cross in a GIS of maps of surface status, land use, and degradation intensity. This crossing has facilitated, in the first step, to map the degree of degradation intensity to according to each land use type (Figs. 9.12 and 9.13). In a second step, this crossing allowed us to draw up a summary table specifying for each land use category the level of degradation and the level of sensitivity to desertification by pointing to the erosion process that can be potentially responsible (Table 9.4).

This simple method of assessing land degradation related to human activities further confirms that the overall trend across the Bouhamed watershed is to medium degradation, making the region moderately sensitive to potential desertification. In$ detail, the catchment area can be divided into three main types of trends:

- ***Areas of very low to low degradation with little sensitivity to desertification***: the areas belonging to this class (4.57% of the total surface area) are generally located

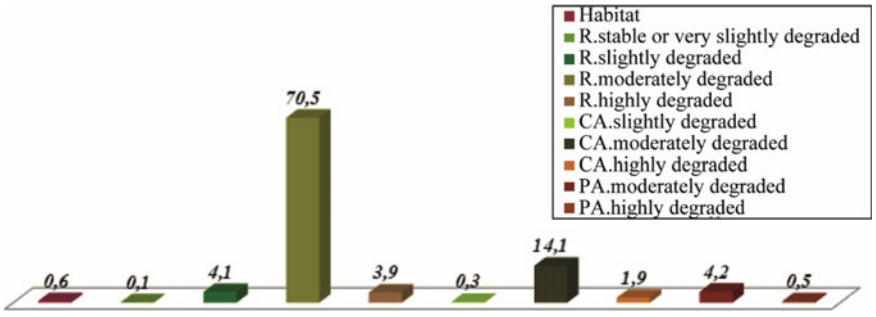

Fig. 9.12 Spatial distribution of the level of degradation according to the mode of land use in the Bouhamed watershed

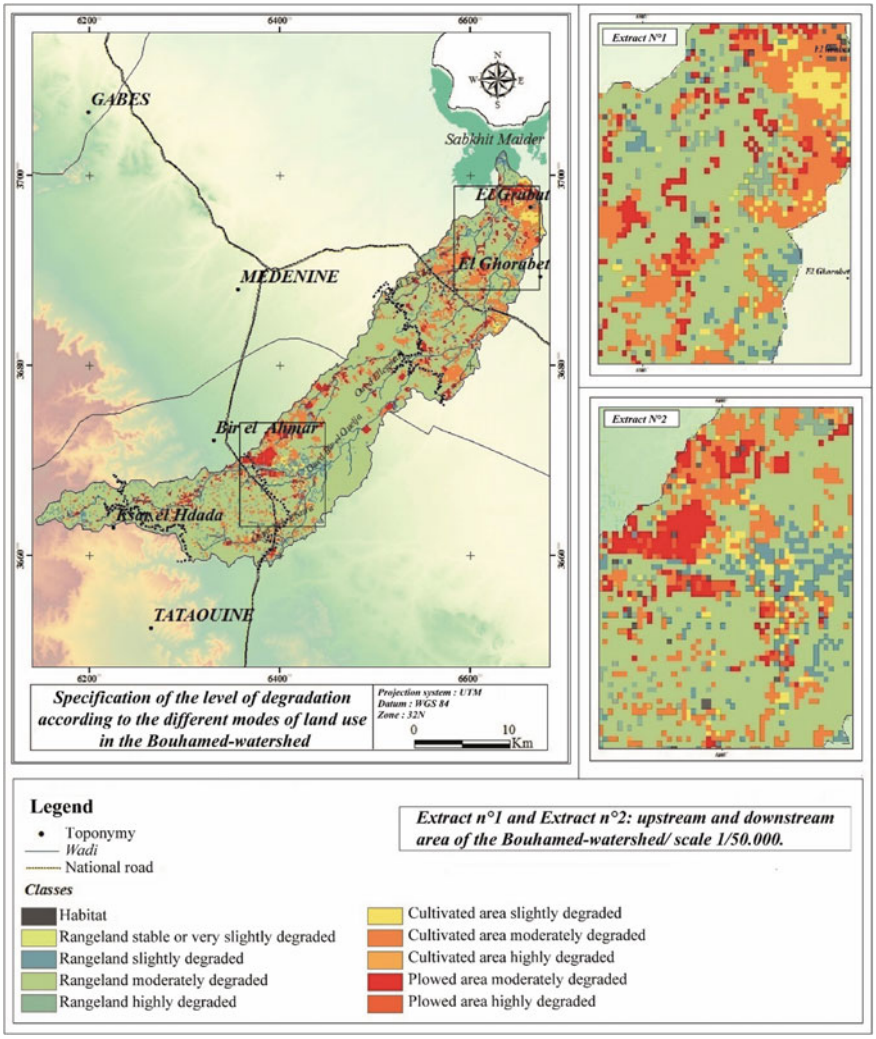

Fig. 9.13 Summary map: intensity of degradation of the Bouhamed watershed according to land use patterns

in the wadi beds (e.g. wadi Bouhamed and wadi Es-des) and in cultivated land on sandy loam soils (cultivated terraces). This low level of degradation is essentially due to the proliferation of hydric and aeolian deposited soils, which encourage the development of plant cover (natural or cultivated).

- ***Areas of medium degradation with moderately sensitive to desertification***: this class, which is the most spatially extensive, presents 88.9% of the total area, generally includes the rangelands. However, these are characterised by the presence of sparse and reduced vegetation interspersed by a silty-sandy soil, hardpan surface,

Table 9.4 Summary table of current state of degradation and potential sensitivity to desertification

Land use	Intensity of degradation according to land use patterns	Surface stat	Localisation	Level of sensibility to desertification	Degradation process
Rangeland	Relatively stable rangeland or very low degradation	Current alluvium	Area of deep water of wadi (e.g. wadi Bouhamed and wadi Es-sder)	Low sensibility	Water erosion
	Rangeland with low degradation	Current alluvium	Area of deep water of wadi (e.g. Bouhamed and Es-sder) – The left bank of wadi Es-sder (erosion surface) – Alluvial fan which extend from Jbel Ghrabaand Ali Ben Salah	Low sensibility	Water erosion
	Rangeland with medium degradation	Loamy-sandy surface	Throughout the Bouhamed watershed	Medium sensibility	Aeolian erosion
	Rangeland with high degradation	Aeolian sail, nebkha and barchans Stony surface	Area of deep water of wadi and land application areas of wadi Bir el-Ouelja The mouth of Wadi Bouhamed The fields of olive trees at El Grabat The left bank of wadi Es-sder	High sensibility	Aeolian erosion
Cultivated area	Cultivated area with low degradation	Loamy-sandy surface	The left bank of wadi Es-sder The right bank of wadi Bouhamed: alluvial terrace	Low sensibility	Aeolian and water erosion

(continued)

Table 9.4 (continued)

Land use	Intensity of degradation according to land use patterns	Surface stat	Localisation	Level of sensibility to desertification	Degradation process
	Cultivated area medium degradation	Loamy-sandy surface Loamy surface with outcropping gypsum crust	– El Grabat area – the right bank of wadi Bouhamed – The left bank of wadi Es-sder(downstreampart) – Erosion surface between Bouhamed and Es-sder (Silty deposit with calcareous concretions) – Alluvial fan near wadi Sidi Moussa	Medium sensibility	Water erosion
	Cultivated area with high degradation	Slaked Loamy surface Aeolian sail, nebkha, and barchans	– El Grabat area – Alluvium terrace – the right bank of wadi Bouhamed – Wadi Bir el-Ouelja bed	High sensibility	Aeolian erosion
Ploughed area	Ploughed area with medium degradation	Loamy-sandy surface Loamy surface with Outcropping gypsum crust (downstream part)	– El Grabat area – Area of deep water of wadi: Es-sder, Bouhamed, Ellegmeri, Bir elOuelja, elGordhab, Egrager	Medium sensibility	Aeolian erosion
	Ploughed area with high degradation	Aeolian sail, nebkha, and barkhanes Slaked Loamy surface	– ElGrabat – the right bank of wadi Bouhamed – Wadi Bir Ouelja bed	High sensibility	Aeolian erosion

and aeolian formation. This degradation is mainly due to overgrazing and the transformation of these rangelands into abandoned agricultural lands.

- ***Areas of high degradation with very sensitive to desertification***: this class presents only 6.47% of the total surface, and this type of degradation is located essentially in the downstream and intermediate part of the Bouhamed watershed. In the downstream part, the high degradation mainly affects area known as El Grabat and in the alluvial terrace on the right bank of wadi Bouhamed. In the intermediate part, a strong degradation was also identified in the land application areas of wadi Bir El Ouelja. In these areas, agriculture (arboriculture and ploughing) remains the dominant activity. The area is therefore highly sensitive to aeolian erosion and is marked by the manifestations of the seeding phenomenon.

9.5 Discussion

Along this work, we were interested in the qualitative surface state degradation. A concept of degradation which is in relation to human occupation patterns and resource availability (soil surface state and vegetation) (Ghram Messedi 2009). In fact, the soil surface state reflects the intensity of degradation in relation to water and wind erosion. In addition, a decrease in vegetation and the proliferation of gypsum crusts and hardpan surface contributes to increase runoff (Escadafal 1989, 2012; Cherel 2010). The severity of the degradation threat varies based on the type and intensity of human activity. Hence, the interest of this study and the results obtained, which show the dominance for the medium and strong degradation intensity with more than 95% of the total area, can only confirm the statements of several research on the degradation of arid and semi-arid regions in general and the Jeffara in particular (Talbi 1997, 1983, 1993; Khatteli 1996; Ouessar et al. 2006; Escadafal 2012; Omrani 1982; Abaab 1981, 1984; Nasr 1993). Such research also shows that these degradation phenomena hinder the sustainable development of often economically and socially disadvantaged regions (Pnue 1991).

In this work, we tried to account for the sensitivity of the arid environments of a region of the northern Jeffara both in their biophysical context and in relation to the agropastoral activities of the population. The detection of degraded land in the study area was based mainly on the combination of three spectral indices (SAVI, BI, and CI). The values of these indices, calculated at the pixel scale, were related to field observations and existing data.

In the light of the results obtained, we note that the combination based on the indices of colour, brightness, and vegetation significantly discriminate the different levels of soil degradation and also allows a very good-separating power between the different surface states classes considered. We can therefore conclude that soil colour, brightness levels, and vegetation are important parameters for mapping degradation intensity and desertification sensitive. However, radiometric confusions can be noticed, but the knowledge of the field and the existing database can adjust the mapping results. The above results corroborate the work of several authors

(Ghram Messedi 2009; Khatteli 1996; Mougenot and Cailleu 1995; Escadafal 2012; Kpedenou and Koumoi 2019).

Although these indices have proven their effectiveness, the possibility of adding other indices for better discrimination of the different components of the environment is welcome. In this context, we can mention the green atmospherically resistant vegetation index (GARI) which uses the apparent reflectance of the three visible channels (blue, red, and green) and the near infrared channel in order to establish a linear relationship with surface biophysical parameters, or the normalised difference water index (NDWI) which is designed to detect the presence of water in vegetation.

9.6 Conclusion

The present study mapped degraded land based on spectral indices deduced from Landsat OLI satellite imagery. The results revealed different degradation intensities unevenly distributed between very low (0.14%), low (4.44%), moderate (88.95%), and high (6.47%). Spatially, the rangeland areas are most affected by a moderate intensity of degradation. Whilst, the areas most affected by strong degradation are those under agricultural cultivation where the manifestations of the seeding phenomenon are the most pronounced. This phenomenon has already been the subject of a diachronic study conducted on the dynamics of aeolian accumulations in the Bouhamed watershed (Arrak et al. 2021).

This work is a contribution to the detection and location of degraded land and will provide local actors with a decision-making tool in the fight against desertification. However, given the importance of human pressures in South-East Tunisia, diachronic analyses are being carried out to study the extent and evolution of land degradation in order to reflect on the implementation of natural resource conservation strategies (Arrak et al. 2021). Indeed, diachronic analyses of landscape changes and their long-term monitoring will allow to indicate adaptation solutions of societies to climate and landscape change impacts.

9.7 Recommendation

Certainly, the spectral richness of the multispectral (OLI) sensors has allowed the interest and importance of integrating the red and infrared channels into the indices considered in this study to be clarified. However, it is desirable to further the analysis by testing either the power of hyperspectral remote sensing in this field of application since this technology consists of simultaneous acquisition of images in many narrow and contiguous spectral bands. Either from the coupling of radar and optics at very high-spatial resolution. The use of radar systems makes it possible to fill the gaps in the spectral range of optical imaging (microwave range).

References

Abaab A (1981) La marginalisation des techniques de la petite hydraulique familiale dans le Sud tunisien, cas des «Souanis» dans la région de Ben Gardane, thèse de 3e cycle en géographie, Université de Paris VII

Abaab A (1984) Aridité et transformations socioéconomiques dans le sud de la Jeffara tunisienne. Colloque de Géographie Maghrébine, Constantine (Algérie), pp 28–30 mai 1994, 37 p 984 (39)

Abaab A (1986) Mutations socio-économiques de la Jeffara orientale (Sud tunisien). In: Revue de l'Occident musulman et de la Méditerranée, n°41–42. Désert et montagne au Maghreb. pp 327–338. https://doi.org/10.3406/remmm.1986.2465

Ait Ahtman S (2017) Identification des surfaces artificialisées dans la région PACA, Mémoire de stage INRA ECODEVELOPPEMENT Université Fédérale de Toulouse Université Jean Jaurès – ENSAT Master 2 SIGMA. http://sigma.univ-toulouse.fr/

Arrak N, Ghram-Messedi A, Ouerchefani D (2021) Étude de la dynamique des accumulations éoliennes dans une région aride du Sud est tunisien: cas du bassin versant d'oued Bouhamed (Jeffara septentrionale). Revue Marocaine de Géomorphologie. N 5, pp 48–71. ISSN: 250.2021, ISSN: 2508-9382. http://revues.imist.ma/?journal=remageom48

Auclair L, Chaiza-Auclaire M, Delaitre E, Sandron F (1997) Dynamique sociale et désertification: le cas de Memel Habib dans le sud tunisien. Revue des régions arides, numéro spécial, Institut des régions arides, Médenine, pp 481–487

Bannari A, Huete AR, Morin D, Zagolski F (1996) Effets de la couleur et de la brillance des sols sur les indices de végétation. Int J Remote Sens 17(10):1885–1906. https://doi.org/10.1080/01431169608948745

Bannari A, ElHarti A, Haboudane D, Bachaoui M, El-Ghmari A (2008) Intégration des variables spectrales et géomorphométriques dans un SIG pour la cartographie des zones exposées à l'érosion. Revue Télédétection 7(1–4):393–404

Belghith A (1997) Etude spectroscopique, satellitaire et intégrée de la dégradation des systèmes écologiques en conditions arides (Tunisie présaharienne). Thèse de doctorat, Univ, Paris VII, p 264p

Belghith A (2003) Les indicateurs radiométriques pour l'étude de la dynamique des écosystèmes arides (région de Zougrata, Sud Est tunisien): Sécheresse. Numéro 4(14):267–74

Ben Fraj T, Abderrahman A, BenOuezdou H, Reynard E, Milano M, Calianno M, Fallot JM (2016) Les jessours dans le sud-est Tunisien : un système hydroagricole ancestral dans un milieu aride. XXIXe Colloque de l'Association Internationale de Climatologie, Lausanne—Besançon. pp 193–198

Ben Ouezdou H (2000) Les aménagements de petit hydraulique dans le Sud Tunisien, un savoir-faire traditionnel au service du développement durable. In: Proceedings of the Séminaire international, Hammamet, Tunis, 23–27 May 2000, pp 45–54

Bonvallot J (1979) Comportement des ouvrages de petit hydraulique dans la région de Médenine (Tunisie du Sud) au cours des pluies exceptionnelles de mars 1979. Cahiers ORSTOM Série Sciences Humaines 16:233–249

Calianno M, Fallot JM, Ben Fraj T, Ben Ouezdou H, Reynard E, Milano M, Abbassi M, Ghram Messedi A, Adatte T (2020) Benefits of water-harvesting systems (Jessour) on soil water retention in Southeast Tunisia. Water 12(295):21. https://doi.org/10.3390/w12010295

Cherel JP (2010) Support de cours M1 SIIG3T- Traitement d'images- Transformation d'images en télédétection [en ligne]. Disponible sur http://www.univmontp3.fr/ateliermercator/wp.content/uploads/2010/03/TRANSFO_IMAGES.pdf

Escadafal R (1989) Caractérisation de la surface des sols arides par observations de terrain et par télédétection. Applications: exemple de la région de Tataouine (Tunisie). Bondy: ORSTOM, 317p. multigr. Th.: Sci. Terre: Pédol., Paris 6

Escadafal R (2007) Les bases de la surveillance de la désertification par satellites. In: Jauffret S (dir.) Surveillance environnementale à long terme dans les zones arides et semi-arides. Sécheresse vol 18, no 4, pp 263–270. ISSN 1147-7806

Escadafal R (2012) Observation à long terme des environnements arides par satellites: retour d'expériences et perspectives. In: Requier-Desjardins M, Ben Khatra N, Nedjraoui D, Wata Sama I, Sghaier M, Briki M (eds) Surveillance environnementale et développement. Acquis et perspectives: Méditerranée, Sahara et Sahel. Montpellier: CIHEAM/OSS, 2012. pp 41–69 (Options Méditerranéennes: Série B. Etudes et Recherches ; n. 68)

Escadafal R, Bacha S (1996) Strategy for the dynamic study of desertification. Orstom, pp 19–34

Escadafal R, Belghit A, Ben-Moussa A (1994) Indices spectraux pour la télédétection de la dégradation des milieux naturels en Tunisie aride. In: Guyot G (ed) Actes du 6eme Symposium international sur les mesures physiques et signatures en télédétection, Val d'Isère (France), 17–24 Janvier 1994, pp 253–259

Floret C, Pontanier R (1976) Relation climat, sol,végétation dans quelques formations végétalesspontanées du Sud tunisien. Production végétale et bilanhydrique des sols. Document technique n 1, I.R.A., 96p

Floret, Pontanier (1982) L'aridité en Tunisie présaharienne : climat, sol, végétation et aménagement. O.R.S.T.O.M-Paris-1982, 544p

Floret C, Khatteli H, Le Floc'h E, Pontanier R (1989) Le risque de désertisation en Tunisie présaharienne: sa limitation par l'aménagement agro-pastoral. In: Eldin M, Milleville P (ed) Le risque en agriculture, Paris, ORSTOM, pp 291–307

Ghram Messedi A (2009) la dynamique des paysages en milieux arides : Apport de la télédétection et de l'observation de terrain à l'étude de la dégradation d'unités morpho-pédologiques dans la région de Menzel-Habib (Tunisie méridionale), thèse de doctorat. Univ, FSHST, Tunis, p 456p

Ghram Messedi A, Delaitre E (2007) Les états de surface en zone aride à partir d'indices radiométriqueset de classifications multi temporelles d'images Landsat TM prises sur la région de Menzel Habib (Tunisie méridionale). Revue Sécheresse, 18:305–313

Gilmore S and Ashty Saleem D (2015) Effectiveness of DOS (Dark-Object Subtraction) method and water index techniques to map wetlands in a rapidly urbanising megacity with Landsat 8 data. In: Veenendaal B, Kealy A (ed) Proceedings of Research@Locate in conjunction with the annual conference on spatial information in Australia and New Zealand, vol 1323, Mar 10–12 2015, pp 100–108. Brisbane: CEUR-WS

Guillaume H, Genin D, Nouri H (2005) Mutations agro-pastorales et recompositions socio-territoriales sur un transect montagne/plaine en Tunisie aride. Publ-Eur Assoc Anim Prod 115:39

Guillaume H, Romagny B (2003) Sociétés, dynamiques territoriales et compétitions sur les ressources naturelles dans la Jeffara tunisienne. Rapport scientifique final de l'équipe du thème 2 du programme « Jeffara », IRD-IRA, 230 p

Le Houerou HN (1995) Bioclimatologie et biogéographie des steppes arides de l'Afrique, diversité biologique, développement durable et désertification. Options méditerranéennes, série B: recherche et études, pp 1–396

Huete ARA (1988) Soil-adjusted vegetation index (SAVI). Remote Sens Environ 25(3):295–309

Jaouadi S, Lebreton V, Mannai-Tayech B, Lakhdar R, Soussi M (2015) Apport de l'analyse pollinique des sédiments de la sebkha Boujmel (Sud-Est tunisien) à la reconstitution des paléo-paysages et paléoclimats holocènes en milieu aride, Méditerranée 125:39–49. https://doi.org/10.4000/mediterranee.7891

Khattali H (1981) Recherche stationnelles sur la désertification. Dynamique de l'érosionéolienne dans la Jeffara Tunisienne. Thèse de 3ème cycle. Paris 1, 218p

Khatteli H (1996) Erosion éolienne en Tunisie aride et désertique- Analyse des processus et recherches des moyens de lutte. Thèse de doctorat Ph.D, Univ. De Gent Belgique, 180p

Kpedenou DK, Koumoi Z (2019) Cartographie et analyse spatiale de la dégradationdes terres dans le sud-est du Togo: une approche basée sur la télédétection. Annales de l'Universitéde Parakou, Série Science Naturelle et Agronomie, Université de Parakou 9(1):67–78. ffhal-02446404f

Ministère de l'Environnement (2009) Rapport national sur l'état de l'environnement, 249p
Mougenot B, Cailleu D (1995) Identification par télédétection des sols dégradés d'un domaine sahélien au Niger. Actes du Symposium International AISS (groupe de travail RS et DM), Ouagadougou, Burkina Faso, 6 au 10 février, pp 169–179
Mzabi H (1988) La Tunisie du Sud-Est : géographie d'une région fragile, marginale et dépendante. Thèse de Doctorat d'Etat. Université de Tunis I.2 tomes, 941p
Nasr N (1993) Systèmes agraires et organisationsspatiales en milieu aride : cas d'El-Ferch et duDakar de Chenini-Guermessa. Université Paul Valéry, Montpellier III, Thèse de Doctoraten Géographie, p 217
Omrani S (1982) Le territoire des Beni-Zid (sud tunisien). Modes de production etorganisation de l'espace en zone aride. Thèse de 3ème cycle en Géographie,Université Paul Valéry, Montpellier III, janv. 375p
Ouerchfani D (2012) Caractérisation et suivi des états de surfaces éolisés en Tunisie présaharienne : approches stationnelles et spatiales, thèse de doctorat. Univ, Lyon II, France, p 450p
Ouessar M, Bruggeman A, Abdelli F, Mohtar RH, Gabriels D, Cornelis WM (2009) 2009: Modelling waterharvestingsystems in the arid south of Tunisia using SWAT. Hydrol Earth Syst Sci 13:2003–2021
Ouessar M, Taâmallah H, Ouled Belgacem A (2006) Un environnement soumis à de fortes contraintes climatiques, in Entre désertification et développement: la Jeffara tunisienne: IRD; Cérès, pp 23–33, 351p. ISBN 9973-19-683-5
Pnue (1991) Rapport mondial sur le développement humain 1991, Ed. Economica, 138p
Pouget M, Le Floc'h E, Kamal S, Salem B (1988) Utilisation des données SPOT pour la cartographie des ressources renouvelables. Application à la région côtière nord-ouest de 1'Egypte, Journées télédétection - Images satellites et milieux Terrestre en régions arides tropicales. 14–17 nov., Bondy, France, Colloques. et Séminaires, Cd. Orstom, Paris, France, pp 103–12
Romagny B, Guillaume H (2004) L'accès à l'eau potable dans la Jeffara tunisienne: contradictions et nouvelles perspectives. La Houille Blanche, (1), pp 52–59. https://doi.org/10.1051/lhb:200401007
Talbi M (1983) Dégradation d'une steppe à Rhanterium suaveolens dans le sud tunisien. En collaboration avec A. El Hamrouni. Actes du séminaire IRA/UNESCO sur les problèmes d'érosion éolienne dans les zones prédésertiques, pp 103–114
Talbi M (1993) Contribution à l'étude de la désertification par télédétection dans la Jeffara (Sud-Est tunisien). Thèse de Doctorat en Géographie. Université de Tunis I, 1993: 2 tomes, 305p
Talbi M (1997) Action anthropique et dégradation de l'environnement aride: la désertification en Tunisie du Sud-Est. In: Méditerranée, tome 86, 1-2-1997. Impact anthropique en milieu méditerranéen, pp 25–31. https://doi.org/10.3406/medit.1997.2986
Younis MT, Gilabert MA, Meliaâ J, Bastida J (1997) Weathering process effects on spectral reflectance of rocks in a semi-arid environment. Int J Remote Sens 18(16):3361±3377

Chapter 10
Applicability of the Global Land Evaporation Amsterdam Model Data for Basin-Scale Spatiotemporal Drought Assessment

Ali Khoshnazar, Gerald Augusto Corzo Perez, and Vitali Diaz

Abstract Drought directly impacts the living organisms and environment, and thereby, its assessment is essential. Different drought indices require different data, which can be obtained based on models or in-situ measurements, demanding a significant amount of effort. Using remotely sensed (RS) data from satellites can facilitate this data acquisition. Nowadays, more and more satellite techniques are rising, highlighting the need to assess the accuracy of their data and the reliability of the results obtained employing them. The Wet-environment Evapotranspiration Precipitation Standardized Index (WEPSI) has shown good performance in drought monitoring and assessment, especially for agricultural purposes. This chapter employs the Global Land Evaporation Amsterdam Model (GLEAM) data to investigate its applicability in the Lempa River basin drought assessment using WEPSI. In this order, evaluated data obtained from the Water Evaluation and Planning system (WEAP) were used as the basis for comparison. Precisely, a comparison was made with GLEAM and WEAP-based data as well as WEPSI time series based on these two datasets. The results show relatively high similarity between these two datasets and calculated WEPSI drought indices. This validates the good performance of GLEAM-based data in drought monitoring and assessment based on WEPSI.

Keywords Remote sensing · GLEAM · Drought index · WEPSI · Drought assessment · Drought monitoring · Drought analysis · Agricultural drought · WEAP · Lempa River basin

A. Khoshnazar (✉) · G. A. Corzo Perez · V. Diaz
IHE Delft Institute for Water Education, Delft, The Netherlands
e-mail: ali.khoshnazaar@gmail.com

G. A. Corzo Perez
e-mail: g.corzo@un-ihe.org

V. Diaz
e-mail: v.diazmercado@tudelft.nl

V. Diaz
Water Resources Section, Delft University of Technology, Delft, The Netherlands

V. P. Singh et al. (eds.), *Application of Remote Sensing and GIS in Natural Resources and Built Infrastructure Management*, Water Science and Technology Library 105,
https://doi.org/10.1007/978-3-031-14096-9_10

10.1 Introduction

Water is the fundamental basis of biological organizations (Voeikov and Del Giudice 2009), and thereby, alterations in its availability directly impact the living organisms and environment. Drought is mostly related to the lack of water in a specific period of time, leading to a reduction in the precipitation and variation of other meteorological variables (Mishra and Singh 2010). During the past decades, the areas affected by drought are almost doubled worldwide, which has increased mortality and respiratory-related disease (Berman et al. 2021). This hazard is also one of the most important drivers of agricultural production drop and economic losses that alter human life quality (Zhang et al. 2021). Drought assessment that needs hydrometeorological data is one of the essential tasks in water planning and management (Mishra and Singh 2010). This data necessity is a concern for drought index selection. The required hydrometeorological data are usually obtained from models or in-situ measurements and requires a high deal of effort. Using remotely sensed data from satellites can facilitate this data acquisition and therefore resolve this challenge. Nowadays, more and more satellite techniques are rising, highlighting the need to assess the accuracy of their data and the reliability of the results obtained employing this data (Congalton 1991). Application of remote sensing (RS) data in drought calculation and assessment is one area that requires comprehensive attention concerning these discussed issues (Schellberg et al. 2008).

There already exist numerous drought indices in the literature. However, the application of RS-data, its accuracy, and eligibility are not widely studied in the calculation of these drought indices. Regarding the methodology for drought index calculation and identification of this phenomenon, the Palmer Drought Severity Index (PDSI) (Palmer 1965) was one of earlier attempts for agricultural purposes. Later, the Standardized Precipitation Index (SPI) (McKee et al. 1993) was introduced, which is one of the well-known drought indices working based on the precipitation data. In an attempt to address PDSI's drawback and make it a suitable index for comparing different regions, a so-called Self-Calibrated Palmer Drought Severity Index (scPDSI) (Wells et al. 2004) was developed. Additionally, for considering the role of frozen precipitation that was missed in PDSI, Shafer and Dezman (Shafer and Dezman 1982) introduced the Surface Water Supply Index (SWSI). The Standardized Precipitation Evapotranspiration Index (SPEI) (Vicente-Serrano et al. 2010) is another widely used index that incorporates the role of climate change in SPI's structure. Khoshnazar et al. (2021a) suggested the Wet-environment Evapotranspiration Precipitation Standardized Index (WEPSI) that works based on SPI's structure and suggests applying the wet evapotranspiration as the suitable water demand indicator.

Wei et al. (2021) used remotely sensed data to monitor drought dynamics in China, employing a number of drought indices, including SPI. Javed et al. (2021) used global remote sensing data to study agricultural and meteorological droughts over China by applying the Standardized Precipitation and Vegetation Water Supply

Index (SVSWI). Vicente-Serrano et al. (2018) used remote sensing data to calculate the global Standardized Evapotranspiration Deficit Index (SEDI).

It is worth noting that obtaining ET data that is present in the structure of several drought indices largely depends on modeling or other expensive attempts that may restrict its popularity. In this process of obtaining ET, RS approaches come in handy as a low-cost approach compared to traditional methods (Wen et al. 2021). Recently, a wide range of RS-based ET products [e.g., the Global Land Evaporation Amsterdam Model (GLEAM) (Martens et al. 2017)] have been developed globally and locally to complement the limited land surface coverage of the ground-based ET measurements (Wagle and Gowda 2019). RS-based ET data are used to monitor water use and assist in planning management. This ET data can be employed to simplify obtaining the values of this variable and, consequently, incorporating it in WEPSI drought index structure to improve drought monitoring accuracy compared with only precipitation-based drought indices (e.g., SPI) (Lu et al. 2019).

Khoshnazar et al. (2021a) showed that water shortage, and thereby, WEPSI could capture soil moisture status, and there is a relation between WEPSI and cereal production (Lewis et al. 1998). Hence, in this research, we have assessed droughts by applying WEPSI at the catchment scale and have used ET data calculated from a hydrological model, the Water Evaluation and Planning system (WEAP). We have further incorporated a global ET dataset, the GLEAM data, to analyze the suitability of the remotely sensed data for its use in WEPSI-based local drought assessments. This is the first attempt to use remotely sensed data in WEPSI's structure that has shown good performance in agricultural drought monitoring.

The remainder of this chapter is organized as follows. Section 10.2 describes the materials and methods that are used in this research. The next section illustrates the results and provides discussions on them. And the final section concludes the chapter.

10.2 Materials and Methods

In this section, we first explain our case study area. Then, we provide a brief description of the two models (WEAP hydrological model and GLEAM RS-based model) used to obtain the required data for WEPSI calculation. Afterward, the WEPSI calculation method is explained. The final part of this section is dedicated to the description of the experimental setup.

10.2.1 Case Study

In order to investigate the applicability of remote sensing data, we selected the Lempa River basin, which is the longest river in the Central American dry corridor (422 km). The river emanates in Guatemala, and its mouth is the Pacific Ocean in El Salvadorian territory. 85% of the Lempa River length streams in El Salvador (Hernández 2005).

A part of the river is located in Honduras as well (Fig. 10.1; Khoshnazar et al. 2021b). Around half of El Salvador's land is shared with the basin area, which is 17,790 km^2. The basin's daily average temperature, total annual precipitation, and yearly runoff are 23.5 °C, 1698 mm, and 19.21 $dm^3\ s^{-1}\ km^2$, respectively. The majority of El Salvadorian surface water and its people depend on the Lempa River basin. At the same time, the river is highly affected by droughts and other extreme events that decreased its quality and quantity (El Salvador's Ministry of Environment and Natural Resources (MARN) 2019b; Global Environment Facility 2020; Helman and Tomlinson 2018; Jennewein and Jones 2016).

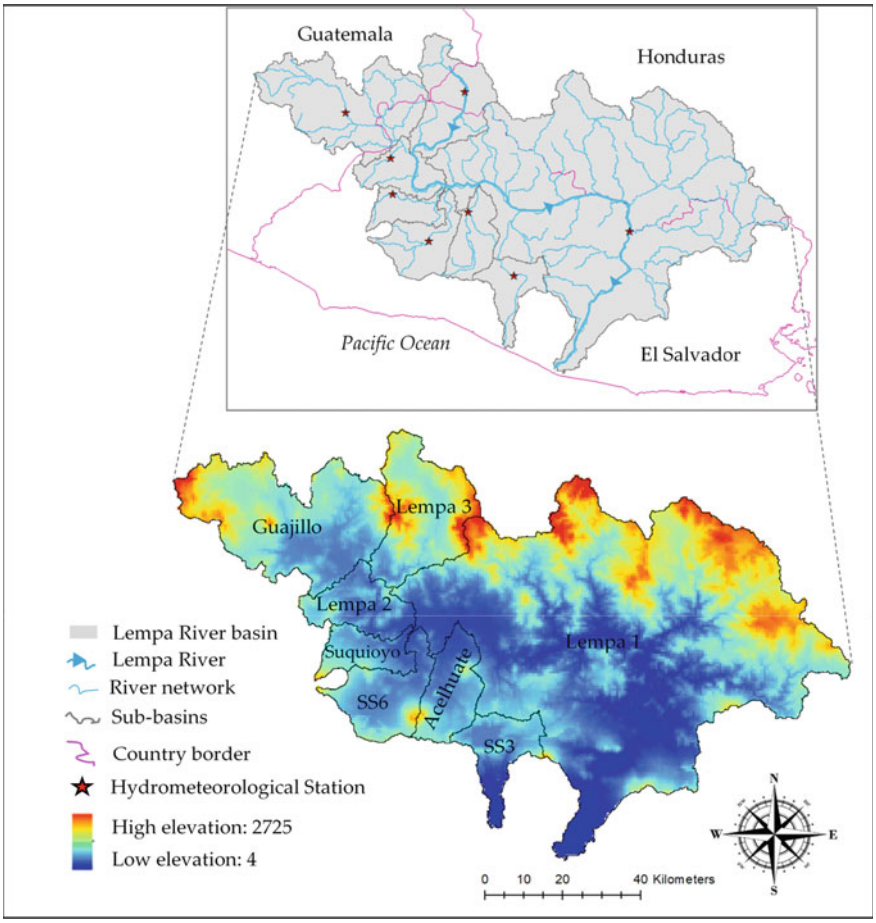

Fig. 10.1 Lempa river basin location (Khoshnazar et al. 2021b)

10.2.2 WEAP Model

The Stockholm Environment Institute's model 'the Water Evaluation And Planning system (WEAP)' (Seiber and Purkey 2015) is used to obtain essential data for WEPSI calculation between 1980 and 2010. El Salvador's Ministry of Environment and Natural Resources (MARN) (2020) data, including hydrometeorological and soil characteristics, were used as the model's inputs. The basin comprises eight sub-basins, including Lempa1, Lempa2, Lempa3, Guajillo, Suquioyo, Acelhuate, SS6, and SS3 (Fig. 10.1). The local management of the basin and its physiographic characteristics were the basis of this division.

Khoshnazar et al. (2021b) have shown that the WEAP-derived variables are reliable for drought assessment in the Lempa River basin. Our two previous papers describe more details of the validation and calibration procedure of the model (Khoshnazar et al. 2021a, 2021b). This is why we will refer to the WEAP-based WEPSI data as our actual data, hereafter called the observed data.

We selected the soil moisture method to simulate the basin processes like evapotranspiration (Fig. 10.2 shows the conceptual diagram for this method) (Seiber and Purkey 2015). In this model, the water balance is calculated by Eq. (10.1) as follows (Khoshnazar et al. 2021b; Oti et al. 2020) (assuming that the climate is steady in each sub-basin).

$$\mathrm{Rd}_j \frac{\mathrm{d}Z_{1,j}}{\mathrm{d}t} = P_\mathrm{e}(t) - \mathrm{ET_p}(t) k_{c,j}(t) \left(\frac{5Z_{1,j} - 2Z_{1,j}^2}{3} \right) - P_\mathrm{e}(t) Z_{1,j}^{\mathrm{RRF}_j} - f_j k_{s,j} Z_{1,j}^2 - \left(1 - f_j\right) k_{s,j} Z_{1,j}^2 \tag{10.1}$$

where $Z_{1,j}$ is the relative storage based on the total effective storage of the root zone. Rd_j is the soil holding capacity of the land cover fraction j (mm). $\mathrm{ET_p}$ is calculated using the modified Penman–Monteith reference crop potential evapotranspiration with the crop/plant coefficient ($k_{c,j}$). P_e is the effective precipitation, and RRF_j is the runoff resistance factor of the land cover. $P_\mathrm{e}(t) Z_{1,j}^{\mathrm{RRF}_j}$ is indicated as the surface runoff. $f_j k_{s,j} Z_{1,j}^2$ shows the interflow from the first layer, for which the term $k_{s,j}$ denotes the root zone saturated conductivity (mm/time); f_j is the partitioning coefficient that considers water horizontally and vertically, based on the soil, land cover, and topography. Finally, the term $\left(1 - f_j\right) k_{s,j} Z_{1,j}^2$ is percolation.

WEAP uses Eq. (10.2) to calculate $\mathrm{ET_a}$ (Khoshnazar et al. 2021b; Kumar et al. 2018).

$$\mathrm{ET_a} = \mathrm{ET_p} \frac{\left(5z_1 - 2z_2^2\right)}{3} \tag{10.2}$$

where z_1 and z_2 are the water depth of the top and bottom soil layers (bucket), respectively (Fig. 10.2).

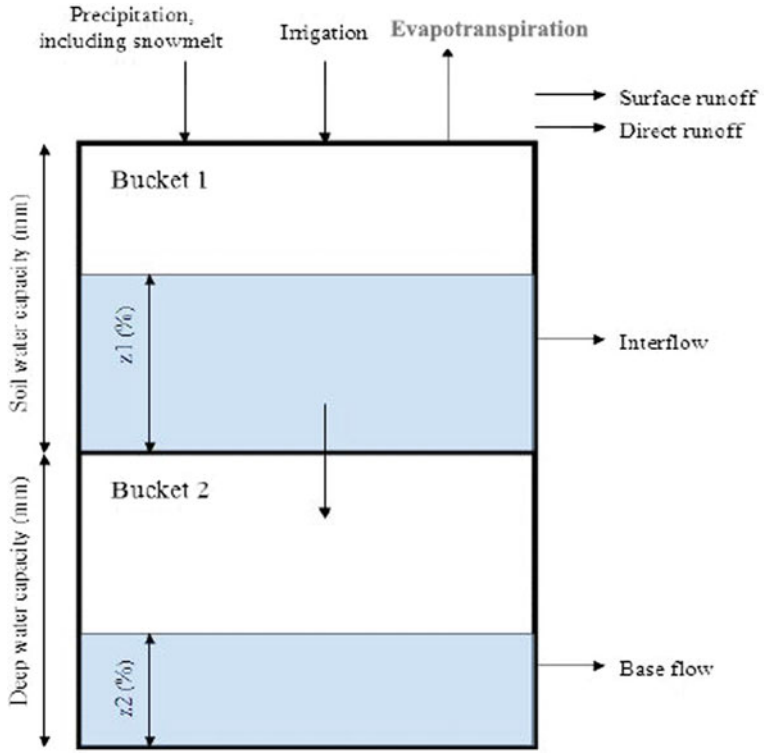

Fig. 10.2 Conceptual diagram of water balance calculation in WEAP (Seiber and Purkey 2015)

We calculated monthly ET_w with the WEAP-derived ET_p and ET_a following the procedure presented in Sect. 10.2.4.2. for each sub-basin.

10.2.3 GLEAM Data

The Global Land Evaporation Amsterdam Model (GLEAM) data provide ET_p and ET_a, among other variables (Martens et al. 2017; Miralles et al. 2011). We used the GLEAM v3.5a dataset in this research. This GLEAM version uses surface radiation and near-surface air temperature from the latest reanalysis of the European Center for Medium-Range Weather Forecasts (ECMWF)-ERA5, i.e., a combination of gauge-based reanalysis and satellite-based precipitation and vegetation optical depth. GLEAM datasets are provided within a monthly temporal.

We calculated the catchment-wide ET_p and ET_a for each sub-basin, where the actual and potential ET values of each sub-basin are obtained from the average values of all cells within the sub-basin on a monthly basis. Then, ET_w was computed with the procedure presented in Sect. 10.2.4.2.

10.2.4 The Wet-Environment Evapotranspiration and Precipitation Standardized Index (WEPSI)

10.2.4.1 WEPSI Calculation

As discussed, we have employed Wet-environment Evapotranspiration and Precipitation Standardized Index (WEPSI) for our drought assessment and monitoring. WEPSI is calculated as follows (Khoshnazar et al. 2021a): First, a long-term (at least 30 years) dataset of monthly water shortage (Eq. 10.3) is employed, and then, a time scale (aggregation period) is determined (can be 3, 6, 9, 12, 24, or 48 months). Then, the aggregated WS is fitted to a distribution function. In the next step, the cumulative probability function is equal to that of the normal distribution, for which the standardized variable with zero mean and unity standard deviation is obtained. As Khoshnazar et al. (2021a) suggest, we used the three-parameter log-logistic LL3 distribution to fit WS in WEPSI's calculation.

WS is the difference between precipitation (water supply) and wet-environment evapotranspiration (water demand) (Eq. 10.3).

$$\mathrm{WS} = P - \mathrm{ET_w} \tag{10.3}$$

Table 10.1 shows the drought categorical classification for WEPSI. This index categorizes the situation in eight classes, from extreme drought to extreme wet.

Table 10.1 Drought categorical classification using WEPSI (Khoshnazar et al. 2021a)

WEPSI value	Drought/wet category
≥2	Extreme wet
1.5 to 2	Severe wet
1 to 1.5	Moderate wet
0 to 1	Low wet
−1 to 0	Low drought
−1.5 to −1	Moderate drought
−2 to −1.5	Severe drought
≤−2	Extreme drought

10.2.4.2 ET_w Calculation

We used the methodology described by Khoshnazar et al. (2021a) for obtaining ET_w. As the reference suggested, a so-called complementary relationship (CR) is employed to relate ET_w, $ET_{p,}$ and ET_a. Kahler and Brutsaert (2006) suggested a general form for CR (Eq. 10.4).

$$(1+b)\,ET_w = bET_a + ET_p \tag{10.4}$$

where b is an empirical constant, ET_a, ET_p, and ET_w are actual, potential, and wet-environment evapotranspiration, respectively.

The symmetric CR considered by Bouchet is obtained by taking $b = 1$ in Eq. (10.4). However, the literature indicates that b generally exceeds and rarely is equal to 1, i.e., CR is asymmetric (Aminzadeh et al. 2016). Consequently, for the ET_w calculation, in addition to ET_p and ET_a, it is necessary to estimate the value of b.

Equation (10.4) can be rewritten in terms of b as follows (Aminzadeh et al. 2016).

$$b = \frac{ET_p - ET_w}{ET_w - ET_a} \tag{10.5}$$

Equation (10.5) shows that the increase of ET_p above the ET_w is proportional to the energy flux provided by surface drying and the decrease of evaporation rate. Normalizing Eq. (10.5) results in Eqs. (10.6) and (10.7) (Aminzadeh et al. 2016).

$$ET_{a+} = \frac{(1+b)\,ET_{MI}}{1+b\,ET_{MI}} \tag{10.6}$$

$$ET_{p+} = \frac{1+b}{1+b\,ET_{MI}} \tag{10.7}$$

where $ET_{a+} = \frac{ET_a}{ET_w}$, $ET_{p+} = \frac{ET_p}{ET_w}$, $ET_{MI} = \frac{ET_a}{ET_p}$, and ET_{MI} is the surface moisture index (with a maximum of 1). ET_{a+} and ET_{p+} are scaled actual and potential evapotranspiration, respectively.

To facilitate the calculation of the CR, Aminzadeh et al. (2016) suggested an atmospheric input-based equation for calculating b (Eq. 10.8).

$$b = AR_{S,net} + B \tag{10.8}$$

where $R_{S,net}$ is the net shortwave radiation flux in W m^{-2}. $R_{S,net}$ is calculated with the incoming shortwave radiation flux R_S and the surface albedo α as $R_{S,net} = (1-\alpha)R_s$.

A is a function of wind speed u_a (in m S^{-1}) (Eq. 10.9).

$$A = (3u_a + 2) \times 10^{-3} \tag{10.9}$$

Finally, the B parameter is calculated as a function of wind speed (u_a) and vapor concentration [c_a(kg m^{-3})] (Eq. 10.10).

$$B = (24.3u_a - 1.44)\left(c_a + 22 \times 10^{-3}\right) + 0.3 \tag{10.10}$$

To calculate b by Eq. (10.8), $R_{S,net}$, u_a, and c_a are required, which can be obtained from meteorological measurements, literature, or empirical equations. However, ET_w could be obtained from other sources or models. Khoshnazar et al. (2021a) proved that the mentioned methodology is more proper. As we do not confront data availability restrictions, we have followed their suggested path.

10.2.5 Experimental Setup

10.2.5.1 WEPSI Calculation at Catchment Scale

The implementation of the WEPSI drought indicator is investigated in the case study of the Lempa River basin. We estimated WEPSI for each of the river's sub-basins (Sect. 10.2.1). ET_w is calculated using Eq. (10.4). For each sub-basin, the b parameter is estimated using wind speed (u_a), net shortwave radiation $R_{S,net}$, and vapor concentration (c_a).

El Salvador's Ministry of Environment and Natural Resources (MARN) provided the meteorological data u_a, $R_{S,net}$, and c_a (El Salvador's Ministry of Environment and Natural Resources (MARN) 2019a). To calculate b, we first compute the monthly averages of u_a, $R_{S,net}$, and c_a for eight sub-basins. Then, we plug the values of each three input variables into Eq. (10.8) to get 12b values for each month and each sub-basin (Khoshnazar et al. 2021a).

We used the time series of WEAP-derived ET_p and ET_a (Sect. 10.2.2) as Eq. (10.4) inputs to determine ET_w in each sub-basin once b was calculated. Finally, we calculated WEPSI using the catchment-wide P and ET_w.

10.2.5.2 Eligibility of a Global Remotely Sensed ET Dataset for Local WEPSI Applications

In order to extend the use of WEPSI in other applications, it is necessary to have ET_w, which can be calculated through an approach similar to that presented in Sect. 10.2.2. Another option is through the use of global remotely sensed ET databases. In this sense, this part of the methodology is allocated to analyze the suitability of using global ET datasets to calculate WEPSI. The procedure involves two steps: (1) ET_w comparison and (2) the GLEAM-based WEPSI performance evaluation.

First, we extracted the catchment-wide ET_p and ET_a from the GLEAM dataset for each sub-basin. After that, we used the parameter b calculated in Sect. 10.2.4.2. to compute ET_w by Eq. (10.4). Then, we compared GLEAM- and WEAP-based ET_w by applying the following three commonly used metrics: the coefficient of determination (r^2), Kling-Gupta efficiency (KGE), and the percentage bias (PBIAS). The coefficient r^2 is calculated with Eq. (10.11).

$$r^2 = \left(\frac{\sum_{i=1}^{n}(x_i - \overline{x})(y_i - \overline{y})}{\sqrt{\sum_{i=1}^{n}(x_i - \overline{x})^2 \sum_{i=1}^{n}(y_i - \overline{y})^2}} \right)^2 \tag{10.11}$$

where x_i and y_i indicate the reference variable and the variable to compare, respectively, and $\overline{x}$ and $\overline{y}$ indicate the mean of each of them. KGE and PBIAS are obtained from Eqs. (10.12) and (10.13), respectively (Odusanya et al. 2019).

$$\mathrm{KGE} = 1 - \sqrt{(r-1)^2 + (\alpha - 1)^2 + (\beta - 1)^2} \tag{10.12}$$

$$\mathrm{PBIAS} = 100 \frac{\sum_{i=1}^{n}(x_i - y_i)}{\sum_{i=1}^{n} x_i} \tag{10.13}$$

where x_i and y_i indicate the reference variable and the variable to compare, respectively, α is the ratio between the standard deviation of the variable to compare and that of the reference variable ($\alpha = \sigma y / \sigma x$). Finally, β is the ratio between the mean of the variable to compare and that of the reference variable ($\beta = \overline{y}/\overline{x}$).

Second, after comparing ET_w, we calculated catchment-wide WEPSI with GLEAM-based ET_w. The difference between GLEAM- and WEAP-based WEPSI is the input ET_p and ET_a. With the time series of GLEAM-based WEPSI calculated in each sub-basin, we computed the time series of percentage of drought area (PDA) for the entire basin (Diaz et al. 2019). PDAs were calculated on a monthly basis as the ratio between the area of sub-basins in drought and the total area of the basin. A drought event starts once the drought index value comes below a threshold and ends as the value rises above the threshold again (Brito et al. 2018; Corzo Perez et al. 2011; Diaz et al. 2020). The threshold used in this application was drought index = −1, which is a threshold commonly employed in drought assessments (Diaz et al. 2020; Khoshnazar et al. 2021b).

10.2.5.3 Categorical Evaluation Statistics

Categorical validation techniques are vastly used for comparison or validating satellite data in the literature (Mayor et al. 2017; Sharifi et al. 2016; Yong et al. 2016). After calculating GLEAM- and WEAP-based WEPSI in the eight sub-basins, we employed three metrics using Table 10.2, as follows (Sharifi et al. 2016).

Table 10.2 Contingency table to evaluate drought occurrence by GLEAM data (Sharifi et al. 2016)

	GLEAM-based (estimated) drought			
WEAP-based (observed) drought		Yes	No	Total
	Yes	Hits (a)	Misses (c)	$a + c$
	No	False alarms (b)	Correct negative (d)	$b + d$
	Total	$a + b$	$c + d$	Total

The first applied categorical metric is the false alarm ratio (FAR), which indicates the fraction of estimated events that did not occur, and its ideal score is zero. FAR is calculated by Eq. (10.14).

$$\mathrm{FAR} = \frac{b}{a+b} \tag{10.14}$$

The second employed metric is the probability of detection (POD), which determines the fraction of the observed events correctly estimated. The best score of POD is one, and it is obtained from Eq. (10.15).

$$\mathrm{POD} = \frac{a}{a+c} \tag{10.15}$$

The third one is accuracy or fraction correct (FC), which measures the fraction of correct estimates, while its perfect score is one. FC is calculated using Eq. (10.16).

$$\mathrm{FC} = \frac{a+d}{\mathrm{total}} \tag{10.16}$$

10.3 Results and Discussion

10.3.1 WEPSI Calculation and Performance Evaluation

For the Lempa River basin, Khoshnazar et al. (2021a) have calculated parameter b in their research. They proved, compared to the symmetric CR, $b > 1$ leads to a considerable difference between the scaled evapotranspiration (ET_{a+} and ET_{p+}) as the surface dries and actual evapotranspiration decreases (Aminzadeh et al. 2016). They also highlighted the importance of using local meteorological data (net shortwave radiation, wind speed, and vapor concentration) that can lead to a better approximation of CR, and consequently, ET_w.

They also showed that WEPSI06 (i.e., WEPSI for the time step of 6 months) and SRI06 (i.e., SRI for the time step of 6 months) are most related in terms of low flows in the basin. Accordingly, they consider WEPSI06 as the representative of the

agricultural and hydrological drought conditions in the basin that means WEPSI06 reflects a realistic vision of the basin that links meteorological, agricultural, and hydrological drought. Accordingly, we employed WEPSI06 in our investigation to check the GLEAM data applicability.

10.3.2 Eligibility of a Global ET Dataset for Local WEPSI Applications

As discussed, we considered the WEAP-based data as our observed data. Figure 10.3a–c displays the r^2, KGE, and |PBIAS| between the GLEAM- and WEAP-based ET_w in the eight sub-basins of the Lempa River basin, respectively. As Fig. 10.3a shows, r^2 is more than 0.65 in the whole Lempa River basin. KGE satisfies the values larger than 0.5 all over the region, while more than 60% of the area has KGE $>$ 0.55. On the other hand, |PBIAS| is lower than 16% among the whole basin, while more than 60% of the area has a value lower than 10%.

Two sub-basins (Lempa2 and Suquioyo) have a value between 10 and 15%, and just Guajillo sub-basin has a value higher than 15% (but lower than 16%), which means the PBIAS results are acceptable (Odusanya et al. 2019).

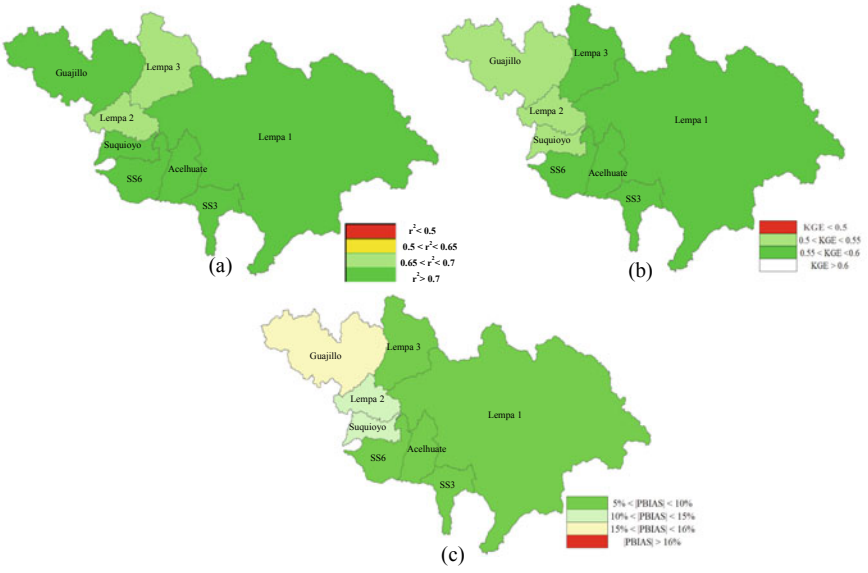

Fig. 10.3 Comparison of GLEAM- and WEAP-based ET_w in the sub-basins of Lempa River basin: **a** the coefficient of determination (r^2); **b** the Kling-Gupta efficiency (KGE); and **c** the percentage bias (PBIAS)

Generally, results depict that GLEAM-based ET_w is relatively similar to WEAP-based ET_w based on the three performance metrics, which indicates that GLEAM-based ET_w data can be used for local WEPSI applications (Odusanya et al. 2019). Results show that the GLEAM ET dataset can facilitate the global computation of WEPSI, where the lack of data is not a limitation and modeling is not required.

Figure 10.4a–h compares the time series of GLEAM- and WEAP-based WEPSI06 in the eight sub-basins of the Lempa River basin for the period 1980–2010 (31 years).

In general, the time series of both WEPSI06 are similar. Figure 10.4 concludes that for the GLEAM-based WEPSI06, the longest drought (i.e., the number of months that the value of WEPSI is below the threshold of −1) occurs in 2003, in general. The maximum drought frequency (3.54%) occurs in Guajillo, SS6, and Suquioyo sub-basins, with 13 total numbers of droughts over 31 years. The most severe drought (i.e., the aggregation of WEPSI values in sequent months at drought) occurs in Guajillo in December of 1994. These results that are obtained using the threshold of −1 as the onset of drought are similar to Khoshnazar et al. (2021a) investigation, which is based on WEAP data.

Figure 10.5 depicts WEAP- and GLEAM-based drought identification and differences between the two datasets in the eight sub-basins [a sub-basin is in drought if WEPSI06 ≤ 0 (Table 10.1)]. The employed threshold for drought onset (i.e., 0) provides more details about differences and consequently is a more suitable measure for accuracy assessment (compared to other lower thresholds, e.g., −1).

These data are used to obtain the three categorical metrics over the sub-basins (Table 10.3).

Table 10.3 contains amounts of categorical metrics as well as the mean elevation of each sub-basin. As the results suggest, Guajillo and Lempa3 have the highest values of POD and FC, respectively. These sub-basins have the highest average of elevation as well. On the other hand, Lempa2, which has the lowest mean elevation, faces the lowest values of POD and FC simultaneously.

FAR values do not show a direct relationship with the mean elevation of sub-basins. Among the eight sub-basins, Acelhuate and Lempa1 send the lowest false alarms, while SS6 and SS3 send more false alarms of drought based on GLEAM datasets.

Figure 10.6 displays the variation of drought areas through the PDAs in the Lempa River basin (whole area) for the overall 31 years based on GLEAM- and WEAP-based WEPSI06. The threshold of 0 was used to calculate drought in each WEPSI time series too.

As the figure shows, using the zero threshold as the onset of drought concludes the majority of times with the availability of drought. However, usually, the threshold of −1 is employed to this order, which provides more sensible results (Khoshnazar et al. 2021b). We have used our threshold to capture more phenomena for the comparison and therefore calculate more reliable continuous and categorical metrics for eligibility of GLEAM-based data. The result shows a correlation more significant than 0.85 between GLEAM- and WEAP-based PDA in November, February, July, August, and September. This is while March, April, and December have the lowest correlation coefficient values (all values are bigger than 0.6).

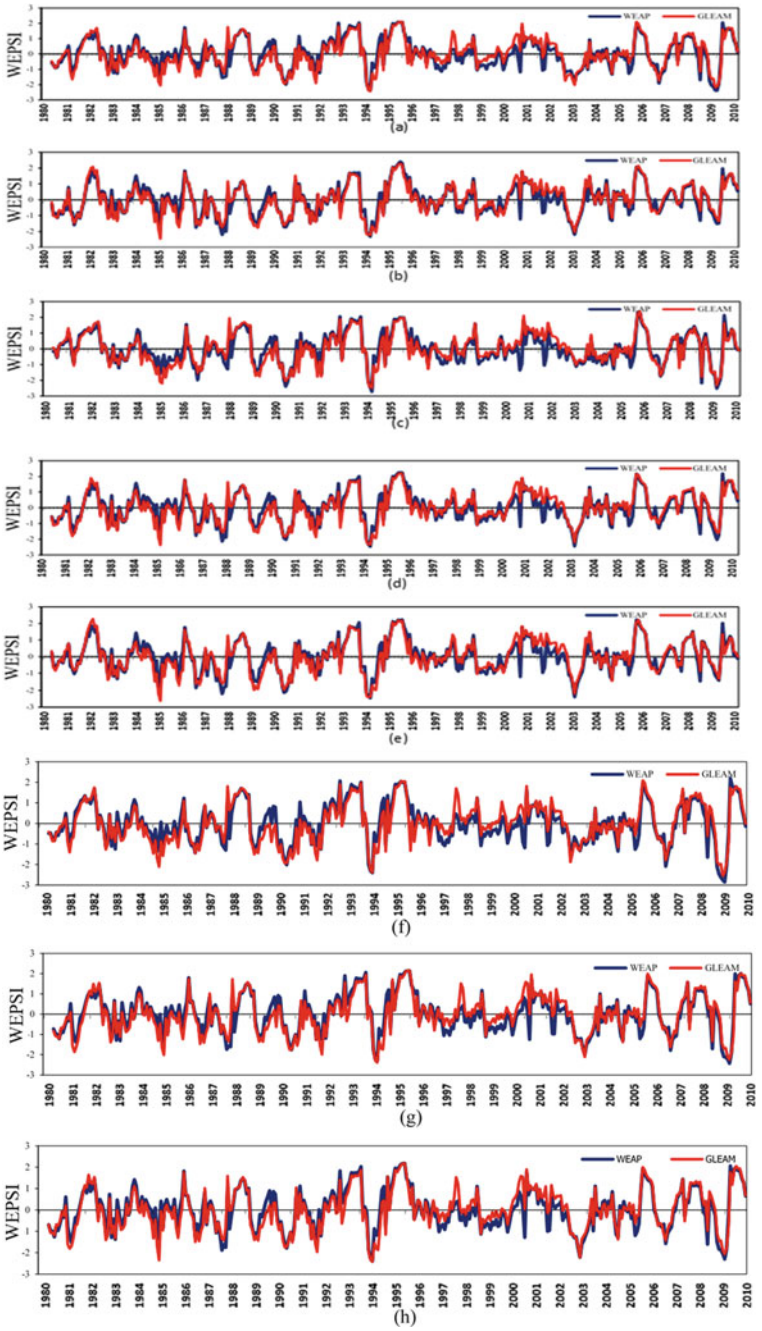

Fig. 10.4 Annual time series of GLEAM- and WEAP-based WEPSI06 in the sub-basins. **a** Acelhuate, **b** Guajillo, **c** Lempa1, **d** Lempa2, **e** Lempa3, **f** SS3, **g** SS6, and **h** Suquioyo

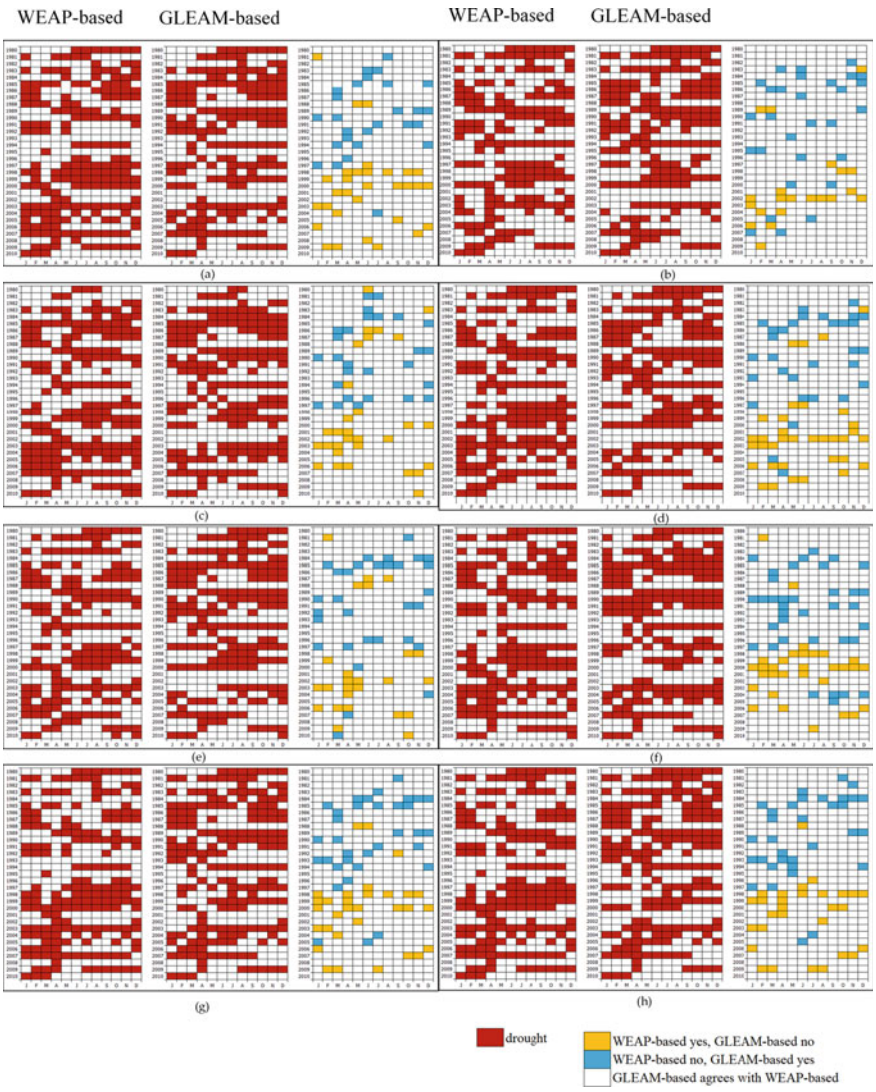

Fig. 10.5 WEAP- and GLEAM-based drought identification (i.e., WEPSI06 ≤ 0) and their differences, in the eight sub-basins: **a** Acelhuate, **b** Guajillo, **c** Lempa1, **d** Lempa2, **e** Lempa3, **f** SS3, **g** SS6, and **h** Suquioyo (The figure illustrates the situation of each sub-basin in 12 months of the year from 1980 to 2010. The situation is either white if two datasets are the same, blue if just the GLEAM-based ET_w determines a drought, or yellow if just the WEAP-based ET_w determines a drought. The red cells identify a drought)

Table 10.3 FAR, POD, and FC categorical metrics, and mean elevation of eight sub-basins

	FAR	POD	FC	Mean elevation (masl)
Acelhuate	0.15	0.84	0.84	585
Guajillo	0.16	0.88	0.86	926
Lempa1	0.15	0.84	0.84	775
Lempa2	0.17	0.81	0.82	505
Lempa3	0.17	0.86	0.85	1162
SS3	0.19	0.84	0.82	540
SS6	0.18	0.83	0.82	616
Suquioyo	0.17	0.84	0.83	574

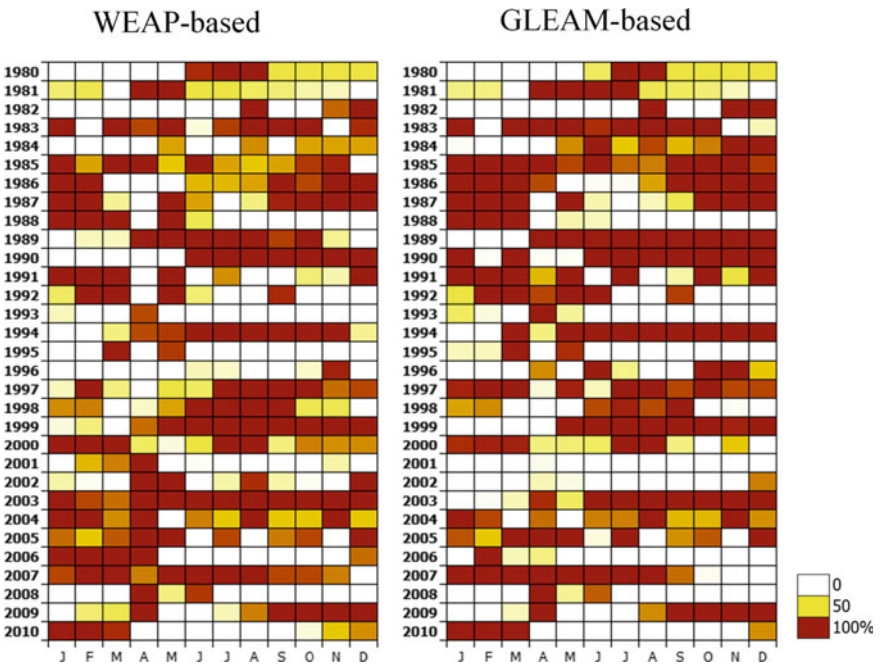

Fig. 10.6 Percentage of drought area (PDA) employing WEPSI06 based on GLEAM and WEAP data in the Lempa River basin from 1980 to 2010

August and September also have the lowest percentage of mean absolute error between the two compared PDAs (3.9 and 5.4%, respectively), while March and April face the highest percentage of mean absolute error (11.1 and 12.4%, respectively).

Obtaining evapotranspiration from classic methods or simulations is usually computationally expensive, as it needs many inputs such as hydrometeorological, soil, and vegetation data. Global RS ET datasets can resolve the challenge of retrieving ET data. Further evaluation that includes more basins and other global

ET databases is required. However, based on the results, a good performance is expected from WEPSI.

10.4 Conclusions

The Wet-environment Evapotranspiration and Precipitation Standardized Index (WEPSI) was employed in this study, which takes water shortage (WS) as its input. Precipitation (P) and wet-environment evapotranspiration (ET_w) are used to calculate WS. WEPSI was put to the test in the Lempa River basin, Central America's longest river.

For modeling with the Water Evaluation and Planning system (WEAP), the basin is divided into eight sub-basins. ET_w is calculated using WEAP's ET_p and ET_a. In order to facilitate WEPSI's application in other basins, we tested a global ET dataset for ET_w calculation. We used the Global Land Evaporation Amsterdam Model (GLEAM) ET_p and ET_a to calculate ET_w. GLEAM- and WEAP-based ET_w were compared with r^2, the Kling-Gupta efficiency (KGE), and the percentage bias (PBIAS). As the categorical metrics, we also used probability of detection (POD), false alarm ratio (FAR), and fraction correct (FC). The metrics reflect an acceptable similarity between these two datasets. Additionally, GLEAM- and WEAP-based WEPSI shows considerable similarities. These results indicate that WEPSI can be used in combination with global ET datasets for local drought assessments. Employing remotely sensed data (e.g., GLEAM), WEPSI could be calculated worldwide and under various climates and can provide a spatial and temporal depiction of drought variation.

Finally, drought events calculated with GLEAM-based WEPSI were compared. Results indicate that WEPSI that is also helpful for agricultural drought assessments (Khoshnazar et al. 2021a) could be calculated using GLEAM-based data.

This research's outcomes come in handy for the researchers and policymakers in drought calculation, monitoring, risk assessment, and forecasting. As a future research direction, we suggest using remote sensing-based WEPSI in other case studies and with other purposes.

Acknowledgements Authors thank the grant No. 2579 of the Albert II of Monaco Foundation. VD thanks the Mexican National Council for Science and Technology (CONACYT) and Alianza FiiDEM for the study grand 217776/382365.

Author Contributions A.K.: conceptualization, methodology, investigation, data processing, validation, software, writing—original draft; G.A.C.P.: conceptualization, project administration, supervision, review; V.D.: conceptualization, methodology, data processing, writing—review and editing. All authors have read and agreed to the published version of the manuscript.

References

Aminzadeh M, Roderick ML, Or D (2016) A generalized complementary relationship between actual and potential evaporation defined by a reference surface temperature. Water Resour Res 52(1):385–406

Berman JD, Ramirez MR, Bell JE, Bilotta R, Gerr F, Fethke NB (2021) The association between drought conditions and increased occupational psychosocial stress among US farmers: an occupational cohort study. Sci Total Environ 149245

Brito SSB, Cunha APM, Cunningham C, Alvalá RC, Marengo JA, Carvalho MA (2018) Frequency, duration and severity of drought in the Semiarid Northeast Brazil region. Int J Climatol 38(2):517–529

Congalton RG (1991) A review of assessing the accuracy of classifications of remotely sensed data. Remote Sens Environ 37(1):35–46

Corzo Perez G, Van Huijgevoort M, Voß F, Van Lanen H (2011) On the spatio-temporal analysis of hydrological droughts from global hydrological models. Hydrol Earth Syst Sci 15(9):2963–2978

Diaz V, Corzo G, Van Lanen HA, Solomatine DP (2019) Spatiotemporal drought analysis at country scale through the application of the STAND toolbox. In: Spatiotemporal analysis of extreme hydrological events. Elsevier, Amsterdam, pp 77–93

Diaz V, Perez GAC, Van Lanen HA, Solomatine D, Varouchakis EA (2020) An approach to characterise spatio-temporal drought dynamics. Adv Water Resour 137:103512

El Salvador's Ministry of Environment and Natural Resources (MARN). https://marn.gob.sv/. Retrieved 21 Sept 2019

El Salvador's Ministry of Environment and Natural Resources (MARN). Water resources maps. https://web.archive.org/web/20090422151648; http://snet.gob.sv/cd2/SeccionSIG/map_hi.htm. Retrieved 16 Dec 2019

El Salvador's Ministry of Environment and Natural Resources (MARN). https://marn.gob.sv/. Retrieved 14 June 2020

Global Environment Facility. https://www.thegef.org/project/fostering-water-security-trifinio-region-promoting-formulation-tdasap-its-transboundary. Retrieved 1 Sept 2020

Helman P, Tomlinson R (2018) Two centuries of climate change and climate variability, East Coast Australia. J Mar Sci Eng 6(1):3

Hernández W (2005) Nacimiento y Desarrollo del río Lempa. MARN/SNET

Javed T, Zhang J, Bhattarai N, Sha Z, Rashid S, Yun B, Ahmad S, Henchiri M, Kamran M (2021) Drought characterization across agricultural regions of China using standardized precipitation and vegetation water supply indices. J Clean Prod 127866

Jennewein JS, Jones KW (2016) Examining 'willingness to participate' in community-based water resource management in a transboundary conservation area in Central America. Water Policy 18(6):1334–1352

Kahler DM, Brutsaert W (2006) Complementary relationship between daily evaporation in the environment and pan evaporation. Water Resour Res 42(5)

Khoshnazar A, Perez GAC, Diaz V, Aminzadeh M (2021a) Wet-environment evapotranspiration and precipitation standardized index (WEPSI) for drought assessment and monitoring. Earth Space Sci Open Archive 25

Khoshnazar A, Corzo Perez GA, Diaz V (2021b) Spatiotemporal drought risk assessment considering resilience and heterogeneous vulnerability factors: Lempa transboundary river basin in the central American dry corridor. J Mar Sci Eng 9(4):386

Kumar P, Masago Y, Mishra BK, Fukushi K (2018) Evaluating future stress due to combined effect of climate change and rapid urbanization for Pasig-Marikina River, Manila. Groundw Sustain Dev 6:227–234

Lewis J, Rowland J, Nadeau A (1998) Estimating maize production in Kenya using NDVI: some statistical considerations. Int J Remote Sens 19(13):2609–2617

Lu Z, Zhao Y, Wei Y, Feng Q, Xie J (2019) Differences among evapotranspiration products affect water resources and ecosystem management in an Australian catchment. Remote Sens 11(8):958

Martens B, Miralles DG, Lievens H, Schalie RVD, De Jeu RA, Fernández-Prieto D, Beck HE, Dorigo WA, Verhoest NE (2017) GLEAM v3: satellite-based land evaporation and root-zone soil moisture. Geosci Model Dev 10(5):1903–1925

Mayor YG, Tereshchenko I, Fonseca-Hernández M, Pantoja DA, Montes JM (2017) Evaluation of error in IMERG precipitation estimates under different topographic conditions and temporal scales over Mexico. Remote Sens 9(5):503

McKee TB, Doesken NJ, Kleist J (1993) The relationship of drought frequency and duration to time scales. In: Proceedings of the 8th conference on applied climatology, Boston, pp 179–183

Miralles DG, Holmes T, De Jeu R, Gash J, Meesters A, Dolman A (2011) Global land-surface evaporation estimated from satellite-based observations. Hydrol Earth Syst Sci 15(2):453–469

Mishra AK, Singh VP (2010) A review of drought concepts. J Hydrol 391(1–2):202–216

Odusanya AE, Mehdi B, Schürz C, Oke AO, Awokola OS, Awomeso JA, Adejuwon JO, Schulz K (2019) Multi-site calibration and validation of SWAT with satellite-based evapotranspiration in a data-sparse catchment in southwestern Nigeria. Hydrol Earth Syst Sci 23(2):1113–1144

Oti JO, Kabo-Bah AT, Ofosu E (2020) Hydrologic response to climate change in the Densu River Basin in Ghana. Heliyon 6(8):e04722

Palmer WC (1965) Meteorological drought. US Department of Commerce, Weather Bureau, p 30

Schellberg J, Hill MJ, Gerhards R, Rothmund M, Braun M (2008) Precision agriculture on grassland: applications, perspectives and constraints. Eur J Agron 29(2–3):59–71

Seiber J, Purkey D (2015) WEAP—water evaluation and planning system user guide for WEAP. Stockholm Environment Institute

Shafer B, Dezman L (1982) Development of surface water supply index (SWSI) to assess the severity of drought condition in snowpack runoff areas. In: Proceeding of the western snow conference

Sharifi E, Steinacker R, Saghafian B (2016) Assessment of GPM-IMERG and other precipitation products against gauge data under different topographic and climatic conditions in Iran: preliminary results. Remote Sens 8(2):135

Vicente-Serrano SM, Beguería S, López-Moreno JI (2010) A multiscalar drought index sensitive to global warming: the standardized precipitation evapotranspiration index. J Clim 23(7):1696–1718

Vicente-Serrano SM, Miralles DG, Domínguez-Castro F, Azorin-Molina C, El Kenawy A, McVicar TR, Tomás-Burguera M, Beguería S, Maneta M, Peña-Gallardo M (2018) Global assessment of the standardized evapotranspiration deficit index (SEDI) for drought analysis and monitoring. J Clim 31(14):5371–5393

Voeikov V, Del Giudice E (2009) Water respiration-the basis of the living state. Water 1:52–75

Wagle P, Gowda PH (2019) Editorial for the special issue "Remote sensing of evapotranspiration (ET)". Multidisciplinary Digital Publishing Institute

Wei W, Zhang J, Zhou J, Zhou L, Xie B, Li C (2021) Monitoring drought dynamics in China using optimized meteorological drought index (OMDI) based on remote sensing data sets. J Environ Manag 292:112733

Wells N, Goddard S, Hayes MJ (2004) A self-calibrating Palmer drought severity index. J Clim 17(12):2335–2351

Wen W, Timmermans J, Chen Q, van Bodegom PM (2021) A review of remote sensing challenges for food security with respect to salinity and drought threats. Remote Sens 13(1):6

Yong B, Chen B, Tian Y, Yu Z, Hong Y (2016) Error-component analysis of TRMM-based multi-satellite precipitation estimates over mainland China. Remote Sens 8(5):440

Zhang A, Ji Y, Sun M, Lin C, Zhou P, Ren J, Luo D, Wang X, Ma C, Zhang X (2021) Research on the drought tolerance mechanism of Pennisetum glaucum (L.) in the root during the seedling stage. BMC Genom 22(1):1–14

Chapter 11
Remote Sensing-Based Estimation of Shallow Inland Lake Morphometry: A Case Study of Sambhar Salt Lake, Ramsar Site-464, India

Kartar Singh, Mili Ghosh Nee Lala, Shubha Rani Sharma, Ashutosh, Gaurav Chandra, and Anand Prakash

Abstract Lake morphology has been identified as a key factor for the understanding of lacustrine systems. Notably, the morphometric descriptors have been viewed as factors controlling lake productivity due to light penetration, oxygen distribution, heat balance, nature of the sediments, and littoral zone development. The overarching goal of this study is to explore the ecological knowledge of HSAS—'Hypersaline-Alkaline Shallow Lake,' through the determination of selected morphometric parameters. Despite their ubiquity and significance, however, inland HSAS lakes are generally less studied than freshwater lakes. Therefore, quantifying morphometry for these inland lakes is quite important, which has implications for their ecology and management. Lake morphology is quantified with morphometric metrics that are descriptors of the form and size of lake basins. Geospatial technology is becoming important to process and analyze morphometric metrics. To perform this analysis, spatiotemporal Landsat Multispectral Scanner System (MSS) and Operational Land Imager (OLI) Imagery have been used. These satellite images have been atmospherically corrected using Improved Dark Subtraction (IDOS) method, and based on Normalized Difference Water Indices (NDWI), the lake water surface extent was extracted

K. Singh (✉) · M. G. N. Lala
Department of Remote Sensing, Birla Institute of Technology, Mesra, Ranchi, India
e-mail: kartarbitmesra@gmail.com

S. R. Sharma
Department of Bio-Engineering, Birla Institute of Technology, Mesra, Ranchi, India

Ashutosh
Department of Earth Sciences, Banasthali Vidyapith, Tonk, India

G. Chandra
Planning, Development and Faculty Affairs, Dr. Ambedkar Institute of Technology for Handicapped, Kanpur, India

A. Prakash
Department of Biotechnology, Banasthali Vidyapith, Tonk, India

V. P. Singh et al. (eds.), *Application of Remote Sensing and GIS in Natural Resources and Built Infrastructure Management*, Water Science and Technology Library 105,
https://doi.org/10.1007/978-3-031-14096-9_11

for further analysis. For lake water depth measurements, demanding field measurements were taken using GPS receiver and other morphometric measurements were estimated using 'Håkanson morphometry' manual. This lake has been morphometrically assessed for the years 1975 and 2015. As a result, the drastic changes have been observed in its morphometrical dimensions. For the year 1975, this lake can be characterized as a shallow, convex, and intermediate type hypersaline-alkaline endorheic lake. In addition, for the year 2015, this lake behaves as an extremely shallow, concave, and small hypersaline-alkaline endorheic lake system. This analysis provides crucial knowledge in support of approaches to lake management. This study is based on only two distinct years, i.e., 1975 and 2015; if similar morphometrical analysis can be performed for a long time period, then characteristics of this lake can be defined in a more illustrative and descriptive way.

Keywords Sambhar lake · Morphometry · Geospatial · Lake management

11.1 Introduction and Background

11.1.1 Why Lake Morphometry?

Lake morphometry (LM) affects nearly all transport processes in lake systems (i.e., resuspension, sedimentation, burial, diffusion, mixing, and outflow). Thus, LM controls concentrations of contagions in water and sediments and hence ecosystem properties related to such biochemical concentrations. In general, these lake processes are obvious and applicable to all type of substances. Therefore, LM regulates the concentration of nutrient that affects the lake primary production (phytoplankton biomass) and secondary production (i.e., zooplanktons and zoobenthos). Particularly, the morphometry reflects the physical as well as biogeochemical condition of the lake under consideration. In this chapter, the values of morphometrical variables have been calculated for the years 1975 and 2015, which depict the changes occurred in the Sambhar Lake (SL) during last 40 years. In addition, this work also assesses the SL characteristics and helps to understand the lake processes with particular interest of shallow lake system research. In case of the SL, lacking of field-based reference data makes this study limited to conduct the traditional methods of wetland condition assessment in this area. The standard lake morphometric parameters have been used to assess the lake temporal condition.

11.2 Significant Literature Inferences About Importance of Lake Morphometry

Several limnological processes, including production of biomass in lake ecosystems, e.g., autotrophic and heterotrophic, are interrelated to the morphometry of an aquatic system (Fee 1979; Jenkins 1968; Olson 1979; Rawson 1955; Ryder 1965). Significantly, the foraging pattern of waterfowl's is related to the morphometric features of the inland lake system. LM affects the top surface water volume (epilimnion) and rate of resuspension or water mingling and, thus, can be have a significant impact on overall lake trophic state (Imboden and Wüest 1995; Wetzel 2001). The discrepancies in lake productivity due to the morphometry of the lake basin vary with time and geographical space. Rawson (1955) stated that the morphometric features play decisive role in determining the lacustrine biomass efficiency. Essentially, in extremely shallow inland lakes, the morphometric dimensions and microclimate affect the biomass productivity by influencing the sun light conditions. The wind-driven effects, e.g., resuspension of sediments, possibly reduce the water transparency and increase the turbidity in the lake. Nonetheless, at the same time the processes related to the lake 'microbial loop' exist that accelerate the internal regeneration of the nutrient pool. However, every morphometric parameter has its own importance, but the water surface area, mean depth, and their ratios, and shoreline development directly influence the degree of lake productivity. The morphometric properties of a lake represent the overall condition of the basin area. The regional climate and morphometry of the lake ecosystem determine the water fluctuation in the lake basin, which further regulates the nutrient loading. Notably, LM also determines the mixing of the water column, which is considered as a crucial factor for the lake metabolism.

A thorough limnological and morphometric research about the lake system is indispensable because it includes the parameters related to its genesis and hydrology and thus explains interrelation of the physical processes (Florin et al. 1993; Håkanson 1981). Additionally, the morphometry of a lake system also reflects the biogeochemistry of a lacustrine ecosystem (Trolle et al. 2010). Thienemann (1925) and Neumann (1932) stated that the basin morphometry directly affects the lake metabolism. Several pioneering studies have been conducted in the field of limnology, e.g., (Fee 1979; Kendra and Singleton 1987; Khare et al. 2008; Moses et al. 2011; Rai et al. 2006) which reflects the importance of basin morphometry into the regularization of the physical, chemical, and biological processes of the lake system. The effect on biomass productivity of the lake (Duarte and Kalff 1988; Pinel-Alloul et al. 1990; Schindler 1971), nutrient dynamics, e.g., nitrogen and phosphorous ratio (Pick and Lean 1987; Smith 1982), thermal stratification and light climate (Robertson and Ragotzkie 1990; Sterner 1990), and sediment loading (Blais and Kalff 1995; Eloranta 1986) are some of the important works related to the morphometrical analysis. The cartography, morphometry, and bathymetry play a pivotal role in wetland studies (Carpenter 1983).

The aim of this chapter is to assess the SL condition and processes using morphometrical analysis based on integrated remote sensing approach. This work helps to answer some fundamental research questions associated with the SL morphometry. These research questions are as follows:

(a) What is the need and significance of morphometric analysis of the HSAS lakes?
(b) How the morphometry influences the overall lake productivity?
(c) What spatiotemporal changes have occurred in the SL morphometry from 1975 to 2015?
(d) How the remote sensing-based morphometry analysis is important to assess the fundamental characteristics of the SL?

11.3 Material and Methods

11.3.1 Study Area—General Description

The SL is situated at 26° 58′ N, 75° 05′ E, with having nearly elliptical shape with its major axis in northeast to southwest direction (Fig. 11.1).

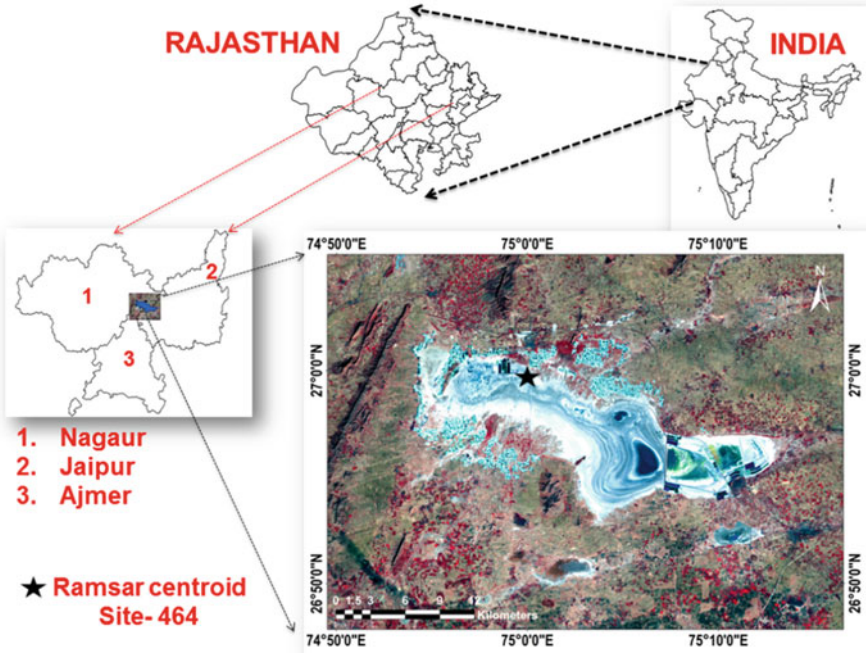

Fig. 11.1 Location of the study area

The maximum area of this lake lies within Jaipur district and remaining exists in Ajmer and Nagaur (Rajasthan, India). Remarkably, the lake catchment covers four districts of Rajasthan state (i.e., Jaipur, Nagaur, Sikar, and Ajmer), with total area of 7560 km^2. The regional population is mostly dependent upon rainfed agriculture, animal husbandry, and salt mining activities. The SL is one of the major commercial salt manufacturing sites in India with approximately two lakh tons of raw salt and 40,000 MT processed salt production every year, which is planned to increase up to 10 lakh Tons per Annum (TPA) by the end of 2019–20. This lake has a great potential for production of valuable chemical compounds (i.e., sulfate of potash, [type of substitution fertilizer]), value-added bromine (Br) derivatives, opportunities of solution mining, derivatives of magnesium chloride, production of packaged drinking water through industrial reverse osmosis, and production of β-carotene at industrial scale. In addition, The SL has possibilities for different tourism activities (i.e., heritage, rural, cultural, bird watching, religious), with aquaculture prospects.

The SL bed height varies from 360 to 365 m (a.m.s.l), and its water surface area varies from few km^2 to ~230 km^2, subjected to amount of water receiving from inlets and mean rainfall in a particular season. The SL is having ~22.5 km length and 3.5–11 km width in its geographical extent with 0.60 m and 3 m of mean to maximum water depth, respectively. Importantly, this lake is a playa depression surrounded by scattered 'Aravali' hills in its northwest and west basin area. This lake has two major lifelines named the 'Rupangarh' in the southwest and the 'Mendha' river in the northeast; unfortunately, due to extensive growth of settlements and industrial units, water flow of these ephemeral rivers has been restricted. The hypersaline-alkaline nature of this lake is a matter of geoscientific discussion, but presently it has been considered that the amount of soluble sodium salts in the lake water is due to the chemical weathering of surrounding hillocks.

In the SL region during summer, the maximum temperature ranges from 40 to 47 °C, whereas in winters, the temperature lies between 2 and 11 °C. One of the key characteristics of the SL region is the excessive temporal inconsistency in precipitation events; the meteorological records of this region show large fluctuation in rainfall, temperature, and humidity conditions. Consequently, this lake is facing scarcity of rainfall, resulting in the decline in migratory waterbirds and rapid depletion in groundwater. This playa is one of the Ramsar wetlands (Site-464) and also known as Important Bird Area (IBA, IN-RJ-16). The SL facilitates the vital breeding ground for thousands of migratory flamingos and other aquatic animals. In past years, due to degraded condition of this lake the flamingo population has declined from thousand to less than hundreds. This HSAS Lake has a rich biological diversity with variety of zoobenthos, primary producers, and waterfowls, which shows the seasonal fluctuation with changes in % salinity. In general, the SL gives dark green appearance due to rapid growth of blue-green algae (i.e., *Nostoc, Anabaenopsis, Anabaena, Dunaliella*, and *Arthrospira*) and occurrence of diatom species (i.e., *Cosmarium, Closterium*). The zooplanktons (i.e., *Brachionus, Cyclops, Moina,* and *Diaptomus*), occur in the lake during low salinity conditions. In the shoreline and catchment areas, the occurrence of typical arid and semiarid vegetation with bushes can be observed (i.e., *A.*

Table 11.1 Metadata information of the satellite images used in this study

S. No.	Type of sensor	Scene ID	Path/row	Date of acquisition
1	Landsat MSS	LM21590411975314AAA05	159/41	10/11/1975
2	L8-OLI, C1/L1	LC81480412015361LGN00	148/41	27/12/2015

indica, P. juliflora, A. senegal, A. pendula, B. serrata, A. nilotica, D. sissoo, S. persica, and *P. cineraria*).

In present work, the Landsat satellite images of the year 1975 and 2015 have been considered as reference or base image and current image for the SL morphometry analysis, respectively. The metadata information of these satellite images is provided in Table 11.1.

In the year 2015, the reservoir side of the SL is not considered for the morphometry analysis because it has been hypothesized that the anthropogenic modifications in the natural settings of the SL can significantly affect the morphometric dimensions of this lake (Fig. 11.2c).

The main lake water flow is diverted to the reservoir side, which is completely under control. Additionally, the SL consists of numerous salt production activities; hence, the area associated with these activities has not been considered for further analysis in this work. The muddy areas of the main lake also have not been considered for this study, because these areas not significantly have an impact on overall morphometry of the lake (Fig. 11.2b).

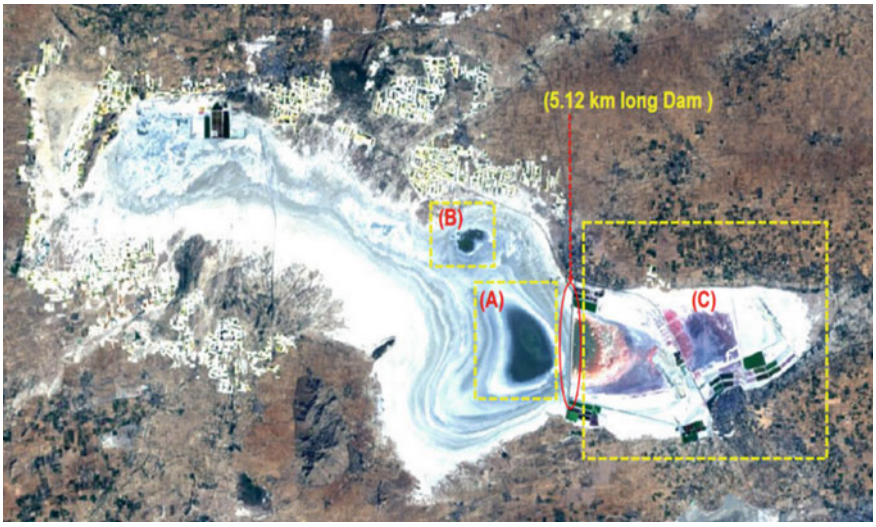

Fig. 11.2 Landsat 8 OLI imagery of the SL area of December 2015; **a** maximum depth zone; **b** part of main lake, in muddy condition; and **c** the reservoir side, which has been separated from the main lake by constructing a ~5-km-long dam

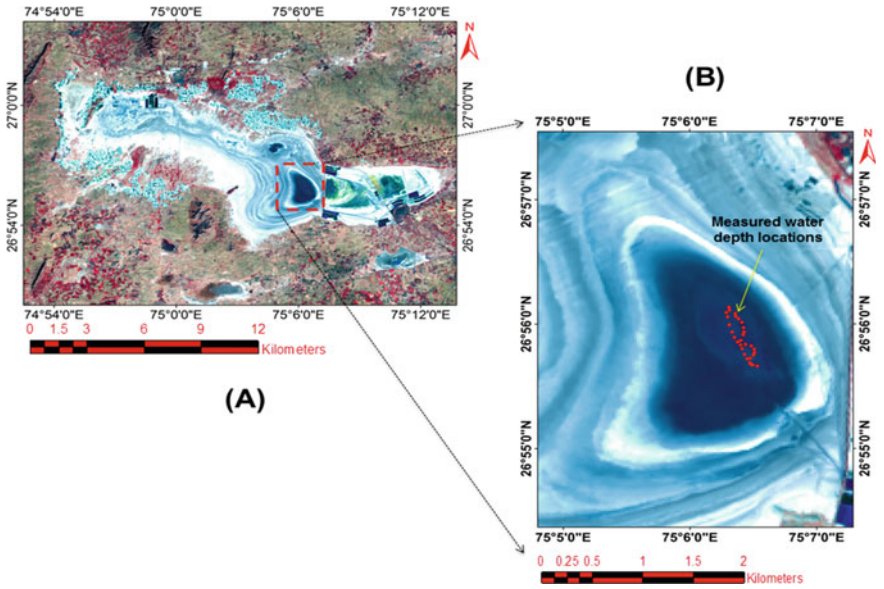

Fig. 11.3 Landsat image of the year 2015 of the SL area, **a** including reservoir side and **b** without reservoir side, and showing water depth locations measured during fieldwork

Figure 11.3 shows the actual lake area considered for the morphometric analysis for the year 2015. Similarly, for the year 1975 the reservoir side has not been taken into consideration for morphometry analysis (Fig. 11.4).

11.3.2 Image Preprocessing

The satellite data used in this study are L1T products, which provide a good geometric accuracy < 0.5 pixel by incorporating ground control points and geodetic accuracy, and further rectifications are not required for co-registration process of the Landsat images. To maintain the homogeneity of spatial scale or pixel size, the resampling process was performed on the MSS image using ERDAS Imagine software tools that changed the pixel size from 60 to 30 m. The L8-OLI and MSS images, obtained in the form of DNs, were converted to the true planetary surface reflectance ($\rho\lambda$) using the following equation.

$$\rho_\lambda = \pi[(L_{\text{sat}} - L_{\text{haze}})/E_{\text{o}} \cos \text{TZ}] \tag{11.1}$$

where $\pi = 3.14$, L_{sat} stands for sensor radiance, L_{haze} represents the atmospheric path radiance, E_{o} is the mean solar exo-atmospheric irradiance, and TZ stands for solar zenith angle.

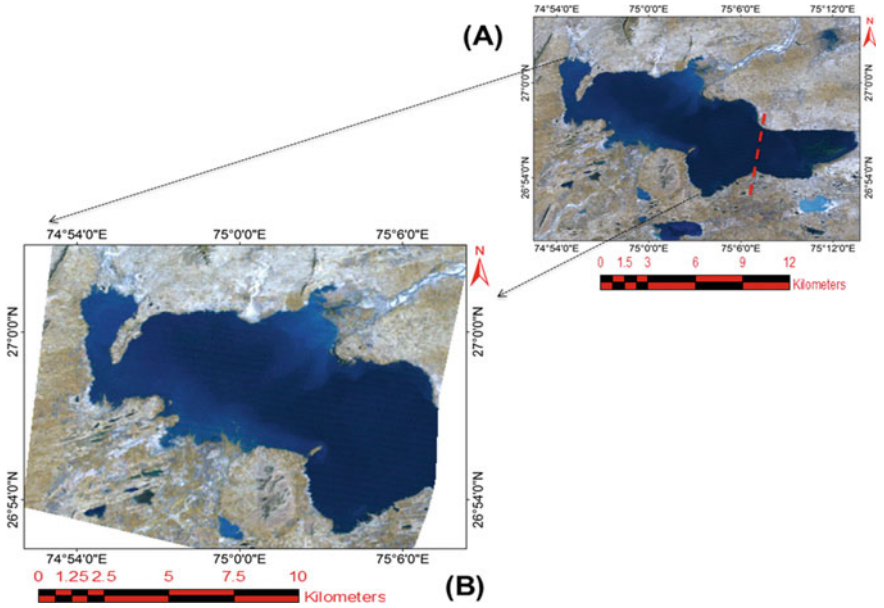

Fig. 11.4 Landsat image of the year 1975 of the SL area, **a** including reservoir side and **b** without reservoir side. Red line in **a** indicates location of dam construction, which divides the lake into two parts: main lake area and reservoir area

Accurate and reliable atmospheric correction for inland water imagery is still an unsolvable problem. The simple dark object subtraction (DOS) method assumes that the aerosol type and size distribution do not alter over the distance from which the dark pixel is selected. This assumption has been demonstrated to be applicable for various studies. Therefore, it can be concluded that the simple DOS method is very simple and feasible to be used with no fatal disadvantages. Notably, the DOS corrected the small inconsistencies of atmospheric conditions for the area under consideration.

11.3.3 Extraction of Water Surface

The Normalized Difference Water Index (NDWI) layers were generated using the modeler function in ERDAS Imagine software. The formula for NDWI is given below (McFeeters 1996).

$$\mathrm{NDWI} = \frac{\mathrm{Reflectance}_{\mathrm{green}} - \mathrm{Reflectance}_{\mathrm{nir}}}{\mathrm{Reflectance}_{\mathrm{green}} + \mathrm{Reflectance}_{\mathrm{nir}}} \tag{11.2}$$

Several methods are available that may be applied to extract open water features in satellite images with improved accuracy (i.e., emitted thermal radiation, reflected solar radiation, and active microwave emission, etc.). Simply, the use of two-band ratio (i.e., NDWI) is an effective way to delineate the lake water surface. NDWI uses the NIR band because water strongly absorbs the NIR wavelength radiation and appears as dark on remote sensing image. Conversely, dry soils and terrestrial vegetation strongly reflect the NIR radiation. In addition, the green band maximizes the light reflected in green wavelength. NDWI takes advantage of high reflectance of near infrared light from land portion and low reflectance from water surface.

11.3.4 Calculation of the Lake Morphometric Parameters

11.3.4.1 Lake Water Surface Area (a), Shoreline Length (l_0) or Perimeter (P), Maximum Length (L_{max}), Maximum Width (B_{max}), Mean Width ($\overline{B}$), Maximum Depth (D_{max}), and Mean Depth ($\overline{D}$)

The calculation of lake water surface area (LWSA) is an essential initial step for morphometry analysis. All other morphometrical parameters are well associated with LWSA. In case of SL, salt production, occurrence of migratory waterbirds, and other important management decisions are essentially based on water present in the main lake.

The significance of getting an accurate assessment of LWSA cannot be over or underestimated. An inaccurate measurement of LWSA will inevitably lead to other problems in morphometrical dimensions. Finally, NDWI-based water surface area was calculated for the respective years using ERDAS software measurement tools. The lake boundary areas were cautiously observed to decide the accuracy of NDWI layer and digitization of the SL shoreline. With the help of ERDAS digitization tools, the SL shoreline was digitized and estimated as perimeter using measurement tools. Notably, at the time of digitization, the similarity of the spatial scale was maintained for both of the satellite images (i.e., 1975 and 2015). Figures 11.5 and 11.6 depict the shoreline measurement and associated parameters for the year 1975 and 2015, respectively. D_{max} and $\overline{D}$ for the year 2015 have been determined using measured water depth during fieldwork (Fig. 11.7). For the year 1975, water depth mentioned in the peer-reviewed journal articles related to the SL has been considered for the analysis.

11.3.4.2 Lake Volume (V) and Volume Development Index or Form Factor (V_d)

Lake volume is the total water volume of the lake system under consideration. Generally, bathymetric maps and hypsographic curves are used to estimate the lake volume, but for the SL these are not available. In this study, (V) has been calculated using the

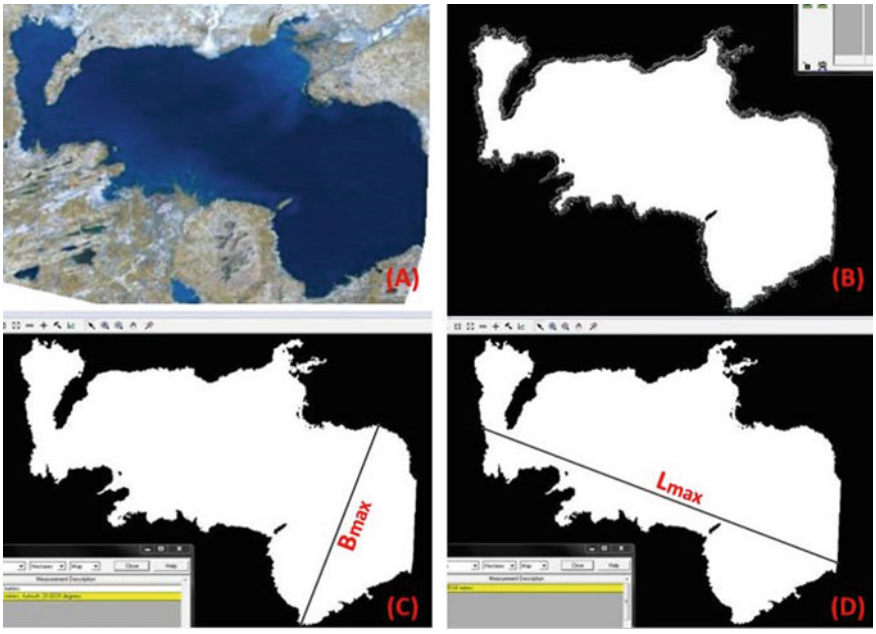

Fig. 11.5 Satellite image of the year 1975 of the SL area; **a** lake area considered for the measurement; **b** shoreline length measurement; **c** measurement of the maximum width (B_{max}); and **d** measurement of the maximum length (L_{max})

formula given below:

$$V = \overline{D} \times A \tag{11.3}$$

where $\overline{D}$ = mean depth and A or a = lake water surface area.

The V_d is a measure of departure of the shape of the lake basin from that of a cone, which has been calculated using the $\overline{D}$ and D_{max} (Håkanson 2004).

$$V_d = 3 \times \overline{D}/D_{max} \tag{11.4}$$

where $\overline{D}$ = mean depth and D_{max} = maximum depth.

Significantly, the lake volume can be highly impacted by the total lake dilution, and it can be easily assessed by the lake dilution capacity which is directly related to the sediments or particles naturally occurring from the watersheds or from anthropogenic events.

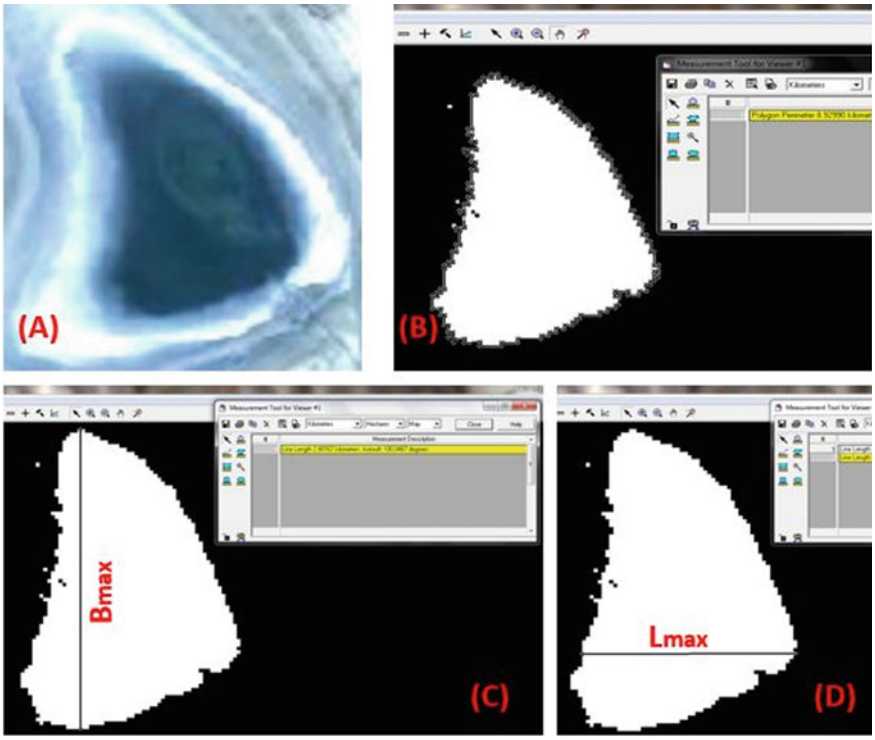

Fig. 11.6 Satellite image of the year 2015 of the SL area; **a** lake area considered for the measurement; **b** shoreline length measurement; **c** measurement of the maximum width (B_{max}); and **d** measurement of the maximum length (L_{max})

11.3.4.3 Shoreline Development Index (F)

Shoreline development index (F) or margin irregularity index is quite important in inland water systems. Generally, the shorelines having the high (F) values or more irregularities provide prey rich littoral habitats. In this study, the (F) value has been calculated using the formula given below:

$$F = \frac{P}{2 \times \sqrt{\pi a}} \tag{11.5}$$

where P or l_o = shoreline length or perimeter; $\pi = 3.14$; and a = lake water surface area.

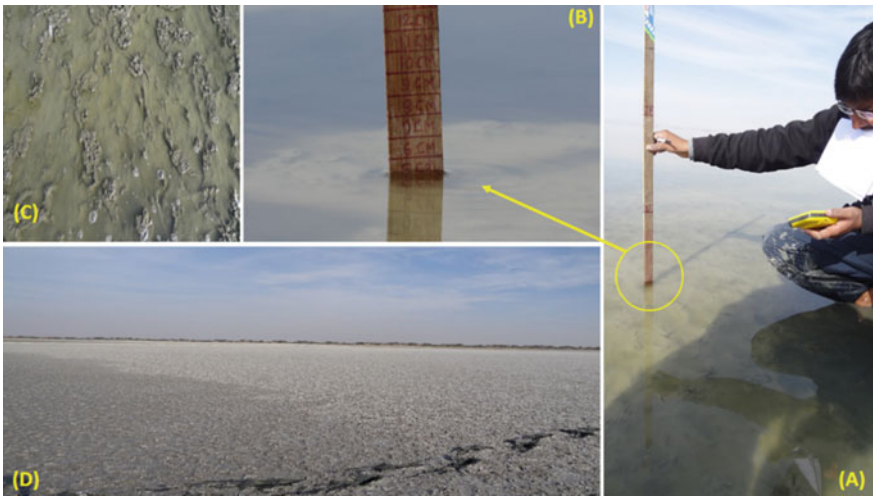

Fig. 11.7 Lake water depth measurement during fieldwork; **a** and **b** extreme shallow condition of the SL; **c** occurrence of algal scum near SL shoreline areas; and **d** dry and moist area of the lake

11.3.4.4 Dynamic Ratio (DR), Erosion-Transportation Area (ET), and Areas of Accumulation of Fine Sediments (A_0)

In shallow lakes, bottom dynamics is not very complex and influenced by prevalent wind conditions. DR determines the resuspension processes in lakes, which regulates the internal loading and sediment focusing. In this study, DR has been calculated as follows:

$$\mathrm{DR} = \sqrt{A}/\overline{D} \tag{11.6}$$

where A = lake water surface area ($A = a$) and $\overline{D}$ = mean depth.

In lake contexts, it is common to emphasize on the sediment loading because the finer materials show the highest capacity to fix the pollutants easily (Thomas et al. 1972). In analyzing the lake bottom dynamics (erosion, transportation, and accumulation), these can be defined as follows:

(A) **Areas of erosion** (E) are the areas of the water system where there is no evident deposition of fine sediment materials occur but, rather, transfer or removal of such materials.

(B) **Areas of transportation** (T) are the areas of the mixed sediments or the areas where fine sediment loads are periodically deposited. In general, these areas dominate where wind/wave action controls the lake bottom dynamics. Sometimes, it is arduous to isolate the areas of transportation from areas of erosion.

(C) **Areas of accumulation** (A_o) are the areas of the soft bottom where the fine materials are deposited constantly. These are the areas, where possibility of occurrence of the concentrations of pollutants is high.

In this study, the ET-areas have been calculated using the formula given below:

$$\mathrm{ET} = 0.25 \times \mathrm{DR} \times 41^{0.061/\mathrm{DR}} \tag{11.7}$$

where ET = the areas of the erosion and transportation and DR is the dynamic ratio.

The A_o has been calculated using the formula given below:

$$A_0 = 100 - \mathrm{ET} \tag{11.8}$$

where ET = the areas of the erosion and transportation.

11.4 Results and Discussion

11.4.1 Lake Water Surface Area (A) or (a)

In general, the lake surface area is the primary morphometric feature, which provides the first insight of the existence of the water body. LWSA is one of the significant and fundamental morphometric features. It plays an important role in lake functioning and size determination. In case of lakes, the proliferation of the biodiversity directly depends on the water surface area (Browne 1981). Thus, LWSA can be used as an indicative index for the habitat conservation in the important wetland areas. Generally, the lake storage represents the water quantity or capacity that sometimes depends on lake depth. In case of the SL, the complete lakebed is almost flat that limits the high storage capacity of this lake. Nonetheless, this lake is rich in its biomass content and physical habitats because this lake consists of extensive shoreline areas rather than deepwater conditions. However, some areas in this lake receive comparatively high volume of water that moderately changes the storage capacity of this lake. This lake has no outlet, because it receives water from closed endorheic drainage system. Solar evaporation is mainly the way of water loss in this lake. The commercial salt production activities also use the main lake water as raw material. In 1972, the process of dam construction had been started which divided the lake into two unequal parts, i.e., reservoir and main lake. In this study, the 1975 satellite imagery has been used to assess the historical condition, so reservoir area has not been included for the evaluation of the morphometry. The rationale behind not to use the reservoir area in calculations was the prominent differences in water quality due to influence of man-made structures.

In case of shallow lakes (i.e., SL), extent of water surface area may help to determine the potential impacts of wind circulations. In prevailing wind conditions, larger water surface area creates the larger waves, which positively affects the water column

Table 11.2 Lake classification based on its total water surface area (Browne 1981)

S. No.	Surface area (km^2)	Class name
1	>10,000	Very large
2	1000–10,000	Large
3	100–1000	Intermediate
4	10–100	Small
5	<10	Very small

in mixing processes. Nevertheless, in SL, the wave base height is too less, but surface waves effectively mix the lake sediments. Instead of that, LWSA also influences the dilution capacity of the lake. In 1975, this lake consists of greater water surface area, which indicates the greater dilution capacity in comparison with LWSA of the year 2015. Based on 1975 water surface area conditions, this lake can be categorized as an intermediate lake system, whereas for 2015 it comes under very small shallow lake class (Table 11.2).

11.4.2 Maximum Length (L_{max})

The straight line connecting the two most remote shoreline points of the lake defines L_{max}. Exceptionally, this line can be curved, e.g., in oxbow lakes or in irregular basins. It may cross the islands, but may not cross the land. L_{max} is significant in shallow lakes because it can influence the depth at which waves can mix water and/or bottom sediments. If a lake has no landform or island to disrupt the wind, then waves can easily mix the sediments. Generally, the larger the L_{max}, the larger is the waves and greater the potential for sediment mixing in the lake water. For mixing phenomena, the orientation of the lake is also another consideration. This morphometric parameter has limited limnological use, but it has to be considered as a descriptive measure for shallow lakes. For the SL, in 1975, L_{max} is larger than the year 2015 (Figs. 11.5 and 11.6). The corresponding numerical values are provided in Table 11.6.

11.4.3 Maximum Width (B_{max}) and Mean Width ($\overline{B}$)

In limnological context, B_{max} has an importance as a descriptive wetland measure. The straight line at the right angle to the L_{max} defines the B_{max}. This line also connects the two most remote shoreline points of the lake under consideration. It may cross the islands but not the land. The measured values of B_{max} for 1975 and 2015 are provided in Table 11.6. The $\overline{B}$ has been defined by the ratio of the lake area to the maximum length. Notably, these two morphometrical parameters have limited limnological value, but play an important role in several hydromechanical operations.

11.4.4 Lake Water Depth (Maximum Depth D_{max}) and (Mean Depth $\overline{D}$)

D_{max} is the greatest known water depth of the lake. In this study, for the year 2015, D_{max} has been determined based on field measurements (Figs. 11.7 and 11.8). For the year 1975, it has been determined based on the historical literature (Baid 1968; Jain 2005; Jakher et al. 1990; Kumar 2008; Kulshreshtha et al. 2011; Mathur and Mathur 2007; Roy and Smykatz-Kloss 2007; Roy et al. 2006; Sinha 2014; Sinha et al. 2004; Sinha and Raymahashay 2000, 2004; Sundaresan et al. 2006; Yadav 1997; Yadav and Sarin 2009a, 2009b). The lake mean depth is one the most valuable morphometric features because of its interrelationships with the overall lake productivity (Håkanson 1981). The size, shape, and depth profile of a lake are the crucial factors affecting the water mixing, instead of that the microclimate, inlet areas, and shoreline structure determine the lake functions. The occurrences of biological processes and separation of water column zones are depending on the mean depth of the lake system. The low mean depth in the SL determines that this lake has high possibility for resuspension processes by large mixing events in bottom areas due to frequent wave actions. In addition, the low mean depth in SL leads to availability of adequate nutrients in water and consequently shows the great primary and secondary productivity in the lake.

Additionally, D_{max} is vital in contexts of lake function, particularly to describe V_d of the lake. In lakes, the microbial pool can vary with variation in water depth; certainly, the biotic structure can differ in areas of D_{max} of the lake than that of

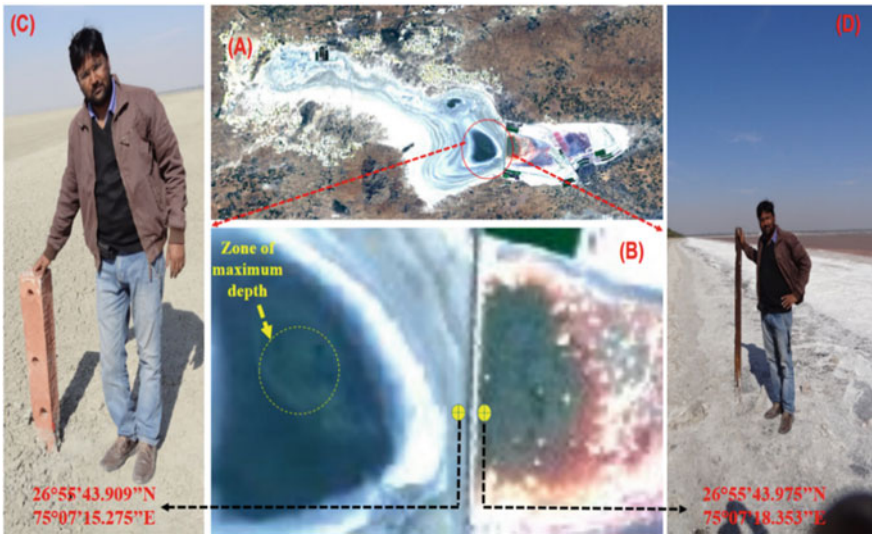

Fig. 11.8 **a** Landsat 8 OLI image of the SL (December 27, 2015); **b** showing the ~ 5-km-long dam, areas of maximum depth, and two-gauge locations; **c** gauge location for the main lake water level monitoring; **d** gauge location for reservoir water level monitoring

the shoreline areas. The dissolved oxygen content may alter with depth variation, because the oxygen consumption is the highest in deeper areas.

The SL is extremely shallow and the water is easily mixed due to prevalent wind effect; consequently, the oxygen concentration may impartially in steady condition. Conditionally, in the absence of effective wind velocity, the dissolved oxygen concentration may decline in the lake water column. The SL does not form the layers because of its poor depth profile, though some areas may stratify of deep zones of the lake. Generally, in condition of 'spring overturn' the uniform water density permits the lake water to mix entirely, which reshuffles the bottom and surface nutrient conditions. For this lake, the above process can be observed throughout the year, and this lake is not deep enough to stratify. The measured water depth values and their corresponding GPS locations are specified in Table 11.3.

11.4.5 Lake Volume (V) and Form Factor (V_d)

In limnological context, volume of the lake is an important morphometrical measure, as it can influence a lake's total dilution capacity. Evidently, lakes with high volumes of water have a greater potential to dilute the materials within its basin area. In addition, the dilution capacity must influence the nutritional concentrations of the lake microorganisms. Volume regulates the biochemistry of the lake, which leads to the formation of unique hydrobiological system for particular lake basin. In 1975, the SL conquered a high volume, which has possibly increased the dilution capacity of the lake. In 2015, the SL attains comparatively low volume that decreases the overall dilution capacity of this lake. The decreased dilution capacity of this lake also leads to more concentrated or salty water in the lake.

V_d is the ratio of volume of a lake to the volume of a cone with same water surface area and D_{max}. It is called as lake's form factor, because it illustrates the actual shape of the lake basin in terms of volume development. For most lakes, the value of V_d is > 0.33, which is the value that would be calculated for a perfect conical depression. A very low V_d occurs only for lakes with deep holes. V_d ranges from 1 to 1.5 for the lakes found in easily eroded geological conditions. For the SL in 2015, the V_d ranges > 1.33, which is exactly 2.562. In 2015, the SL forms a 'concave'-shaped basin and lies in the last morphometrical class in terms of its volume development (Table 11.4). Technically, it is possible because in 2015, the SL consists comparatively small water surface area. In 1975, this lake has a low V_d value, which is 0.6 and lies in the 'convex' shape class. Clearly, the lake depth and water surface area are the possible governing factors to form the shape of the SL basin.

Table 11.3 Measured water depth of the SL and their corresponding geographic locations (Date of measurement—December 27, 2015)

S. No.	Latitude (N)	Longitude (E)	Water depth (cm)
1	26.927713	75.10887	5.0
2	26.927846	75.108295	4.5
3	26.928171	75.107889	4.7
4	26.928749	75.107929	5.8
5	26.929175	75.108364	5.9
6	26.929516	75.108514	6.3
7	26.92998	75.108455	6.5
8	26.9304	75.108067	6.9
9	26.930621	75.107319	6.0
10	26.931139	75.106714	6.3
11	26.931887	75.107016	6.1
12	26.932274	75.107129	6.5
13	26.932849	75.107063	**7.0**
14	26.933551	75.106868	**7.0**
15	26.934037	75.106410	**7.0**
16	26.934375	75.106021	5.9
17	26.934762	75.105979	5.9
18	26.935182	75.105217	5.3
19	26.935581	75.105158	5.0
20	26.93486	75.104786	5.5
21	26.934297	75.104963	5.5
22	26.933229	75.105206	6.2
23	26.932258	75.105551	6.2
24	26.931555	75.10587	6.3
25	26.930927	75.10628	6.1
26	26.930538	75.106672	6.9
27	26.930025	75.106881	6.0
28	26.929265	75.107191	6.0
29	26.928688	75.107526	5.8
30	26.927951	75.107989	5.5

Bold represent the locations of maximum water depth have been found at the time of field visits

Table 11.4 Morphometrical classification for aquatic systems based on the form factor (V_d) (Håkanson 2004)

S. No.	Form of lake	Class name	V_d
1	Very convex	VC_x	0.05–0.33
2	Convex	C_x	0.33–0.67
3	Slightly convex	SC_x	0.67–1.00
4	Linear	L	1.00–1.33
5	Concave	C	>1.33

11.4.6 Dynamic Ratio (DR), Erosion-Transportation (ET) Areas, and Accumulation Areas (A_o)

In limnological contexts, knowledge about the condition of the bottom dynamics is one of the most valuable parameters, because it directly governs the resuspension activities and determines the wave base for lake mixing phenomena (Fig. 11.9).

In sedimentological contexts, it is important to know about the ET-areas and (A_o) areas, because the potential results and ecological effects of the sediment loading or contaminants are directly related to these areas.

DR is one of the valuable morphometrical parameters that represent the lakes' bottom dynamic conditions very efficiently (Håkanson 1982; Lindström et al. 1999). DR plays an important role in processes associated with sediment–water interface and other several wetland processes, e.g., desiccation of the lakes. In limnological context, the maximum wave base is associated with effective fetch and water surface area (Håkanson and Jansson 1983; Rowan et al. 1992). As illustrated in Fig. 11.10, a high DR value indicates a lake, which has greater bottom areas exposed to wind

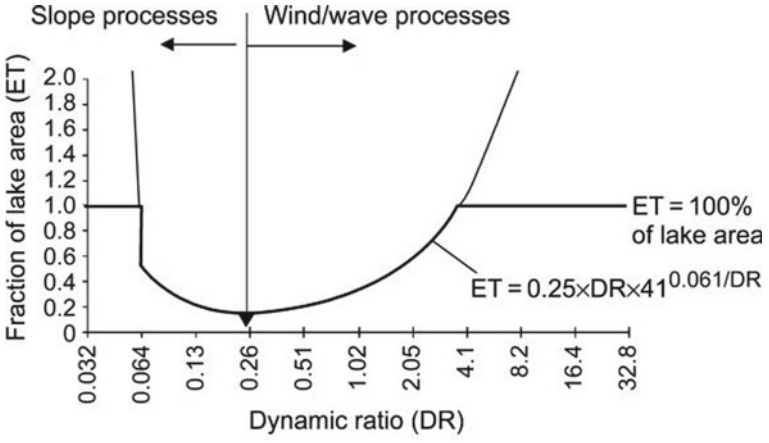

Fig. 11.9 Relationship between the lake bottom areas dominated by processes of transportation and erosion, expressed as the DR and the fraction of lake area (ET). Adapted from Håkanson (2004)

(above the wave base) than a lake with low DR. The high DR values are related to the higher degree of resuspended material (Lindström et al. 1999). In case of large and shallow lakes, the turbulence in surface water generally occurs greater (with high DR values) compared to deep and small lakes. In case of the SL, DR values (DR = 22.87 and 27.23) indicate that it has larger bottom areas exposed to wind processes or wave energy (Table 11.6). The resuspension processes related to wind/wave action generally dominate in lakes with higher dynamic ratios (DR > 0.25). Turbidity currents influenced by the slope processes are significant in lakes with low DR values (Fig. 11.10). In this study, the computed DR values show that the SL is extremely shallow inland lake system (Table 11.5).

There are two different boundary conditions for ET been given by Håkanson (2004): (1) If ET > 0.99, then ET = 0.99, and (2) if ET < 0.15, then ET = 0.15. The general illustration about ET-areas and other lake processes is shown in Fig. 11.11. In particular, the ET-areas are generally > 15% (ET = 0.15) of the total lake area, as there is always a shore zone controlled by wind/wave processes, at least for all lakes > 1 ha (Fig. 11.9) (Håkanson 2004). For functional and practical reasons, one also can generally find areas, which actually function as accumulated (A_0) areas with more or less continuous sedimentation; i.e., thus the upper limit for ET is set at ET = 0.99 (Håkanson 2004).

In this study, for the SL, ET values have been found > 0.99 for both years; therefore according to the second boundary condition, they have been considered as 0.99 (Table

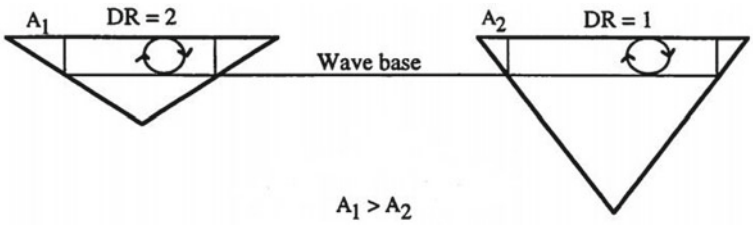

Fig. 11.10 Illustration of the DR; for two different lakes with the same area, a higher DR indicates a lake with larger areas above the wave base exposed to wind/wave energy. Adapted from Lindström et al. (1999)

Table 11.5 Classes for the dynamic ratio (Lindgren and Håkanson 2007)

S. No.	Class	DR	Description
1	Very deep	<0.064	Areas dominated by slope processes and erosion and transport processes for fine particles
2	Deep	0.064–0.25	Areas influenced by slope processes where erosion, transport, and accumulations for fine particles occur
3	Intermediate	0.25–4.1	Areas more influenced by wind and wave processes where erosion, transport, and accumulations for fine particles occur
4	Shallow	>4.1	Area dominated by wind and wave processes and erosion and transport processes for fine particles

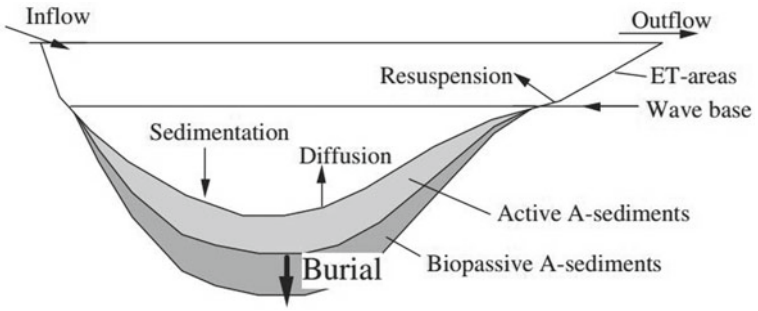

Fig. 11.11 Illustration of the lakes' fundamental and general processes. Adapted from Håkanson (2003)

Table 11.6 Computation of morphometric parameters of the SL for the years 1975 and 2015

Symbol	Formulation/method	Ref	Unit	Assessment years	
				1975	2015
(a)	Water index generation	Håkanson manual	km^2	188.351	2.6523
(l_o) or (P)	ERDAS tools		km	131.103	8.9299
(L_{max})	ERDAS tools		km	22.499	1.6465
(B_{max})	ERDAS tools		km	12.253	2.4016
($\overline{B}$)	$\overline{B} = a/L_{max}$		km	8.3715	1.6108
(D_{max})	Literature and field survey		m	3.0	0.070
($\overline{D}$)	Literature and field survey		m	0.6	0.0598
(V)	$V = \overline{D} \times a$		km^3	0.113	0.00016
(V_d)	$V_d = 3 \times \overline{D}/D_{max}$		Dimensionless	0.6	2.562
(F)	$F = \frac{P}{2\times\sqrt{\pi a}}$			2.695	1.547
DR	$DR = \sqrt{a}/\overline{D}$			22.87	27.23
ET	$ET = 0.25 \times DR \times 41^{0.061/DR}$			5.775 = 0.99	6.865 = 0.99
A_0	$A_0 = 100 - ET$ or 99			1%	1%

Note A_0 can be considered as negligible

11.6). ET-areas > 0.99 also show that the bottom areas or almost entire lakebed of the SL is exposed to the wind/wave activities, which satisfy its extreme shallowness.

11.5 Conclusion

This research work provides a partial view of the status of SL. Nonetheless, it evidently points out certain constructive inclinations showing that the work on

morphometry and condition assessment has been prolific. In limnological research, the condition assessment affects the acquaintance of the dynamics and consequences observed; limited observations may create incomplete setups about the lake investigated. Possibly, the assessment conducted about morphometric variables of the SL system might be similarly affected, demanding multifaceted ecosystem-based research. The present work enables to assess the SL basin in terms of its morphometrical dimensions.

In addition, the SL provides breeding ground for thousands of migratory waterbirds, i.e., flamingo, (Fig. 11.12). Prominently, it is possible to observe that LM does affect the number of migratory waterfowls and the abundance of other aquatic animals during winter seasons. Presently, the SL has been divided into two unequal parts, which severely affect the overall lake productivity (Fig. 11.8). Therefore, the drastic changes have been observed in its morphometrical dimensions. Based on this study, for the year 1975, this lake can be characterized as a shallow, convex, and intermediate type hypersaline-alkaline endorheic lake. In addition, for the year 2015, this lake behaves as an extremely shallow, concave, and small hypersaline-alkaline endorheic lake system. This research work is based on only two distinct years, i.e., 1975 and 2015; if similar morphometrical analysis can be performed for a long time period, then characteristics of this lake can be defined in a more illustrative and descriptive way.

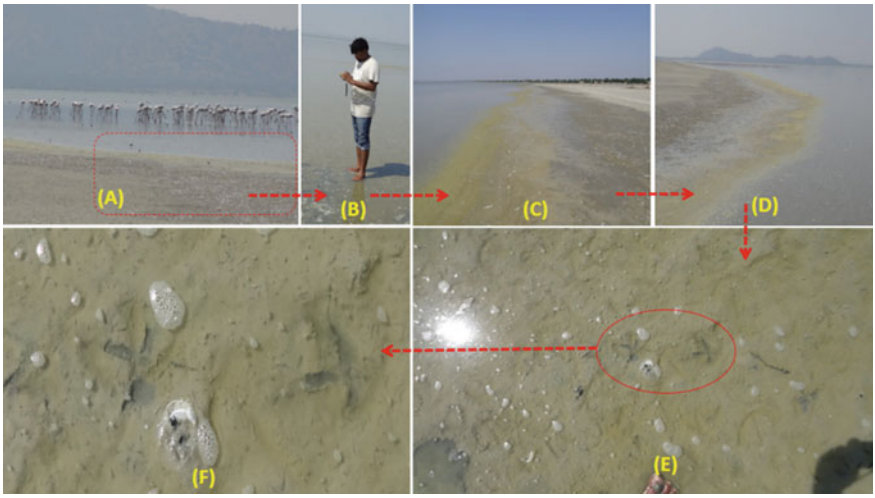

Fig. 11.12 Importance of lake shoreline areas for flamingo foraging during prevalent wind effects (Field visit date—October 03, 2014)

References

Baid IC (1968) The arthropod fauna of Sambhar Salt Lake, Rajasthan, India. Oikos 19:292–303
Blais JM, Kalff J (1995) The influence of lake morphometry on sediment focusing. Limnol Oceanogr 40:582–588
Browne RA (1981) Lakes as islands: biogeographic distribution, turnover rates, and species composition in the lakes of central New York. J Biogeogr 8:75–83
Carpenter SR (1983) Lake geometry: implications for production and sediment accretion rates. J Theor Biol 105:273–286
Duarte CM, Kalff J (1988) Influence of lake morphometry on the response of submerged macrophytes to sediment fertilization. Can J Fish Aquat Sci 45:216–221
Eloranta P (1986) Phytoplankton structure in different lake types in central Finland. Holarct Ecol 9:214–224
Fee EJ (1979) A relation between lake morphometry and primary productivity and its use in interpreting whole lake eutrophication experiments. Limnol Oceanogr 24:401–416
Florin M, Montes C, Rueda F (1993) Origin, hydrologic functioning, and morphometric characteristics of small, shallow, semiarid lakes (lagunas) in La Mancha, central Spain. Wetlands 13:247–259
Håkanson L (1981) A manual of Lake Morphometry. Springer, Berlin, p 78
Håkanson L (1982) Lake bottom dynamics and morphometry: the dynamic ratio. Water Resour Res 18:1444–1450
Håkanson L (2003) Quantifying burial, the transport of matter from the lake biosphere to the geosphere. Int Rev Hydrobiol 88:539–560
Håkanson L (2004) Lakes-form and function. New Jersey Blackburn Press, Caldwell, p 201
Håkanson L, Jansson M (1983) Principles of lake sedimentology. Springer, Berlin, p 316
Imboden DM, Wüest A (1995) Mixing mechanisms in lakes. In: Lerman A, Imboden DM, Gat JR (eds) Physics and chemistry of lakes. Springer, Berlin, pp 83–138
Jain AK (2005) Conservation planning of Sambhar Lake, Rajasthan using satellite remote sensing and GIS. M.Tech. Dissertation, Andhra University, India
Jakher GR, Bhargava SC, Sinha RK (1990) Comparative limnology of Sambhar and Didwana lakes (Rajasthan, NW India). Hydrobiologia 197:245–256
Jenkins RM (1968) The influence of some environmental factors on crop and harvest of fishes in U.S. reservoirs. In: Proceedings of the reservoir fisheries symposium, Southern Division, American Fisheries Society, Athens, GA, pp 298–321
Kendra W, Singleton L (1987) Morphometry of Lake Chelan. Ecology report no 87-1. Water Quality Investigations Section, Washington State Department of Ecology, Olympia, WA
Khare N, Chaturvedi SK, Saraswat R, Srivastava R, Raina R, Wanganeo A (2008) Some morphometric characteristics of Priyadarshini water body at Schirmacher oasis, central Dronning Maud land, Antarctica with special reference to its bathymetry. Indian J Mar Sci 37:435–438
Kulshreshtha S, Kulshreshtha M, Sharma BK (2011) Ecology and present status of flamingos at Sambhar Salt Lake, Rajasthan, India: a critical comparison with past records. Flamingo Specialist Group report, pp 24–27
Kumar S (2008) Conservation of Sambhar lake—an important waterfowl habitat and a Ramsar Site in India. In: The 12th world lake conference, pp 1509–1517
Lindgren D, Håkanson L (2007) Functional classification of coastal areas as a tool in ecosystem modeling and management. In: Mass-balance modelling and GIS-based data analysis as tools to improve coastal management. Sweden Uppsala University, Uppsala. Licentiate thesis, p 126
Lindström M, Håkanson L, Abrahamsson O, Johansson H (1999) An empirical model for prediction of lake water suspended particulate matter. Ecol Model 121:185–198
Mathur RP, Mathur LN (2007) Conservation of Sambhar wetland in Rajasthan. J Soc Policy Res Inst 2:122–129
McFeeters SK (1996) The use of normalized difference water index (NDWI) in the delineation of open water features. Int J Remote Sens 17:1425–1432

Moses SA, Janaki L, Joseph S, Justus J, Vimala SR (2011) Influence of lake morphology on water quality. Environ Monit Assess 182:443–454
Neumann E (1932) Grundzüge der regionalen Limnologie. Die Binnengewässer 11:176
Olson RA (1979) Ecology of wetland vegetation on selected strip mine ponds and stockdams in the northern Great Plains. Ph.D. Dissertation, North Dakota State University, Fargo
Pick FFA, Lean CW (1987) The role of macronutrients (C, N, P) in controlling cyanobacterial dominance in temperate lakes. NZ J Mar Freshwat Res 21:425–434
Pinel-Alloul B, Méthot G, Verrault G, Vigneault Y (1990) Phytoplankton in Quebec lakes: variation with lake morphometry, and with natural and anthropogenic acidification. Can J Fish Aquat Sci 47:1047–1057
Rai SP, Kumar V, Singh O, Kumar B, Jain SK (2006) Bathymetry, sedimentation rate and physico-chemical characteristics of Mansar lake in the Himalayan foothills, J&K, India. Geol Soc India 67:211–220
Rawson DS (1955) Morphometry as a dominant factor in the productivity of large lakes. Verhandlungen der Internationalen Vereinigung für Theoretische und Angewandte Limnologie 12:164–175
Robertson DM, Ragotzkie RA (1990) Thermal structure of a multibasin lake: influence of morphometry, inter basin exchange and groundwater. Can J Fish Aquat Sci 47:1206–1212
Rowan DJ, Kalff J, Rasmussen JB (1992) Estimating the mud deposition boundary depth in lakes from wave theory. Can J Fish Aquat Sci 49:2490–2497
Roy PD, Smykatz-Kloss W (2007) REE geochemistry of the recent playa sediments from the Thar Desert, India: an implication to playa sediment provenance. Chem Erde 67:55–68
Roy PD, Smykatz-Kloss W, Sinha R (2006) Late Holocene geochemical history inferred from Sambhar and Didwana playa sediments, Thar Desert, India: comparison and synthesis. Quatern Int 144:84–98
Ryder RA (1965) A method for estimating the potential fish production of north temperate lakes in North America. Trans Am Fish Soc 94:214–218
Schindler DW (1971) A hypothesis to explain differences and similarities among lakes in the Experimental Lakes Area, northwestern Ontario. J Fish Res Board Can 28:295–301
Sinha R (2014) The Sambhar Lake: the largest saline lake in north-western India. In: Landscapes and landforms of India, world geomorphological landscapes, pp 239–244
Sinha R, Raymahashay BC (2000) Salinity model inferred from two shallow cores at Sambhar Salt Lake, Rajasthan. J Geol Soc India 56:213–217
Sinha R, Raymahashay BC (2004) Evaporite mineralogy and geochemical evolution of the Sambhar Salt Lake, Thar Desert, Rajasthan, India. Sed Geol 166:59–71
Sinha R, Stueben D, Berner Z (2004) Palaeohydrology of the Sambhar Playa, Thar Desert, India, using geomorphological and sedimentological evidences. J Geol Soc India 64:419–430
Smith VH (1982) The nitrogen and phosphorus dependence of algal biomass in lakes: an empirical and theoretical analysis. Limnol Oceanogr 27:1101–1112
Sterner RW (1990) Lake morphometry and light in surface layer. Can J Fish Aquat Sci 47:687–692
Sundaresan S, Ponnuchamy K, Rahaman AA (2006) Biological management of Sambhar Lake Saltworks (Rajasthan, India). In: Proceedings of the 1st international conference on the ecological importance of solar saltworks (CEISSA 06), Santorini Island, Greece, 20–22 Oct 2006, pp 199–207
Thienemann A (1925) Die Binnengewässer Mitteleuropas. Die Binnengewässer 1:1–255
Thomas RL, Kemp ALW, Lewis CFM (1972) Distribution, composition and characteristics of the surficial sediments of Lake Ontario. J Sediment Petrol 42:66–84
Trolle D, Hamilton DP, Pilditch CA (2010) Evaluating the influence of lake morphology, trophic status, and diagenesis on geochemical profiles in lake sediments. Appl Geochem 25:621–632
Wetzel RG (2001) Limnology. Academic Press, San Diego
Yadav DN (1997) Oxygen isotope study of evaporating brines in Sambhar Salt Lake, Rajasthan, India. Chem Geol (Isotope Geosci) 138:109–118

Yadav DN, Sarin MM (2009a) Ra-Po-Pb isotope systematics in waters of Sambhar Salt Lake, Rajasthan (India): geochemical characterization and particulate reactivity. J Environ Radioact 100:17–22

Yadav DN, Sarin MM (2009b) Geo-chemical behavior of Uranium in the Sambhar Salt Lake, Rajasthan (India): implications to '"Source"' of salt and uranium '"Sink."' Aquat Geochem 15:529–545

Chapter 12
Remote Sensing and GIS in Spatial Monitoring of the Wetlands: A Case Study of Loktak Lake Catchment, India

Anand Vicky and Oinam Bakimchandra

Abstract Occurrence of the wetlands is characterized where the land is covered by water or the water table level is close to the land surface. Wetlands are the only ecosystems for whose conservation an international convention called Ramsar Convention was set up in the year 1971. According to Ramsar Convention, a wetland is "areas of fen, marsh, swamp, peat either artificial or natural with water which is flowing or static including areas of marine water the depth of which should not exceed six meters." As per Ramsar Convention in 2019, there are 2341 Ramsar sites listed across the world, among which Loktak Lake is one of the Ramsar sites nestled in the North-Eastern Himalayan ranges. Distinctive feature of this lake is the presence of herbaceous floating biomass (herbaceous wetlands) locally known as phumdis. In this case study land use land cover (LULC) of Loktak Lake catchment was mapped with special emphasis on wetlands and herbaceous wetlands. Based on the driving factors and past LULC for the year 2007, 2014 and 2017, the future LULC for the year 2030 was predicted by Land Change Modeller (LCM) in TerrSet using Landsat 5 and Landsat 8 multispectral satellite imageries. Artificial neural network (ANN) and Markov chain algorithms embedded in the LCM were deployed to predict the future LULC condition. ANN was trained with driving factors, namely slope and elevation, distance from built-up area and distance from roads. Results indicate that there was decrease of 28.65% and 6.08% in herbaceous wetlands and wetlands, respectively, in the year 2017 as compared to the year 2007. Similar trends were observed in the future projected LULC map of 2030 with a decrement of 6.48% and 41.56% in wetlands and herbaceous wetlands as compare to the baseline scenario of 2007. Based on the result of projected scenario, it is evident that there is a need to devise proper environment conservation policies.

Keywords Artificial neural network (ANN) · Markov chain (MC) · Land use land cover change (LULCC) · Land change modeller (LCM)

A. Vicky · O. Bakimchandra (✉)
National Institute of Technology Manipur, Imphal, India
e-mail: bakim@nitmainpur.ac.in

V. P. Singh et al. (eds.), *Application of Remote Sensing and GIS in Natural Resources and Built Infrastructure Management*, Water Science and Technology Library 105,
https://doi.org/10.1007/978-3-031-14096-9_12

12.1 Introduction

Wetlands play an important part for the survival of human. As per the ancient literature, many human civilizations have evolved near to the wetlands and riverine system. Wetlands have immense ecological, cultural, economic and social values (Ramachandra et al. 2002). They exhibit massive diversity as per their water regime, genesis, water quality, geographical location, sediment characteristics and dominant species (Space Applications Centre (SAC) 2011). With total area coverage of 12.1 million km^2 it accounts for 40.6% of the total global ecosystem services (ES) value (Ramsar Convention on Wetlands 2018). Wetlands are highly threatened by anthropogenic activities (Best 2019; Tong et al. 2017; Sieben et al. 2018; Zhang et al. 2017), and they are also recognized as critical for ecosystem services (Sieben et al. 2018; Zhang et al. 2017). Since 1970 unsustainable use and over exploitation of wetlands across globe (Rebelo et al. 2017) have resulted in 35% loss in the overall global extent of the wetlands (Ramsar Convention on Wetlands 2018). Wetland degradation and losses continue even after Ramsar Convention is rectified by 169 countries across the globe (Ramsar Convention on Wetlands 2018). In past, literature reviews have focused on wetland ecosystem services from future directions and theories (Xu et al. 2018; Liu et al. 2010), mechanisms and driving factors behind change in the wetlands (Peralta-Maraver et al. 2018; Boulton et al. 2016; Wondie 2010), policies and management, quantitative approaches (Janse et al. 2019; Barbier 2016; Langan et al. 2018), regional scale to national scale (Bassi et al. 2014; Sterner et al. 2017; Steinman et al. 2017). The studies have also concentrated on riverine wetland ecosystems (Yang et al. 2016; Dam et al. 2014), lake wetland ecosystems (Sterner et al. 2017; Steinman et al. 2017), coastal and mangroves wetlands ecosystems (Yang et al. 2016; Dam et al. 2014; Kelleway et al. 2017; Friess 2016; Zhao et al. 2016). The current study deals with spatial monitoring and projection of herbaceous wetlands using artificial intelligence (AI) analytics.

In the year 1971 an international treaty called Ramsar Convention on Wetlands was signed for national action and international cooperation for wise use of wetlands and conservation of their resources (Bassi et al. 2014). According to Ramsar Convention on Wetlands "a wetland is a area of marsh, fen, peat land or water, whether natural or artificial, permanent or temporary, with water that is static or flowing, fresh, brackish or salt, including areas of marine water the depth of which at low tide does not exceed six metres" (Ramsar Convention on Wetlands 2018). Under Ramsar Convention a total of 211 sites in North America, 1052 sites in Europe, 175 sites in South America, 289 sites in Asia, 79 sites in Oceania region and 175 sites in Africa has recognized as wetland of International Importance or the Ramsar sites (Ramsar Convention Secretariat 2013). As per the definition of Ramsar Convention most of the man-made wetlands (reservoirs, irrigated fields, ponds, gravel pits, sacred groves, canals, etc.) and natural water bodies (mangroves, rivers, coral reefs, lakes) in India make up the wetland ecosystem. Out of 289 sites in Asia 37 sites are located in India (MoEFCC 2020). Among 37 Ramsar sites in India two are located in northeastern part of India; among them one is Loktak Lake, India (MoEFCC 2020). However there

are many wetlands across India which perform potentially valuable functions that are continued to be ignored in the policy process. Due to this many wetland ecosystems are degraded and threatened due to increased economic activities, population growth, anthropogenic factors and urbanization (Central Pollution Control Board (CPCB) 2008).

Wetlands are the ecosystem that binds aquatic and terrestrial components together. The association of climate change with wetlands can be understood in two aspects: firstly, effects of change in climate on the wetlands and secondly, the capability of the wetlands to influence climate change (LDA and WISA 2010). The change in LULC has altered the hydrology, lateral and base flow, increase in landslides and floods, increase in surface runoff, decrease in groundwater recharge, increase in soil erosion, decrease in water quality, etc. in the Loktak Lake sub-catchment (Ramsar Bureau 2016). The core reason behind the issues related to the degradation of Loktak Lake catchment is the loss of vegetation. The degradation of the sub-catchment area has led to flooding in the low lying areas, increase in the siltation issues, altered hydrological regime thereby affecting the hydrological processes, decrease in the thickness of phumdis (herbaceous wetlands) and loss in the biodiversity of the peripheral zones of Loktak Lake and the Keibul Lamjao National Park (KLNP) (LDA and WISA 1999; Anand et al. 2020, 2021).

In the past decades geographic information system and remote sensing have emerged as efficient and powerful tool which has been used mapping LULC and modeling LULC for the future (Bansod and Dandekar 2018; Pozzi and Small 2002; Herold et al. 2003; Milesi et al. 2003; Peng et al. 2012; Kumar et al. 2016; Ahmed et al. 2013; Chen et al. 2017; Tan et al. 2016; Ali et al. 2018; Ahmad et al. 2009; Roy et al. 2017; Li et al. 2011; Ayele et al. 2018; Cheema and Bastiaanssen 2010). For understanding and extracting the information related to the land development processes and LULC change patterns satellite remote sensing provides economical multispectral and multi-temporal data (Li et al. 2011; Ayele et al. 2018; Cheema and Bastiaanssen 2010). In the recent times modeling tools like cellular automata, regression tree, linear regression model, Markov chain and artificial neural network are being used for the future projection of LULC (Singh et al. 2015; Yirsaw et al. 2017; Gashaw et al. 2017; Yagoub and Bizreh 2014; Liping et al. 2018; Etemadi et al. 2018; Karimi et al. 2018). Markov chain is a probabilistic approach to predict transition of one LULC class to other over a piece of land by calculating the probability of change. The change in LULC of past is applied to predict the future LULC of the region. The overriding objective of this study is to map and analyze the spatio-temporal changes in LULC of the past and predict the LULC for 2030 using Markov model embedded in LCM.

12.2 Wetlands Classifications and Distributions

12.2.1 Ramsar Classification

Wetlands can generally be classified into five basic systems, namely: Estuarine, Riverine, Marine, Palustrine and Lacustrine (Frazier 1996). These consist of deep-water habitats and complex wetlands that carve up the influence of similar biological and chemical, geomorphologic, hydrological factors (Davis 1994). The Ramsar classification of wetland types currently in use was adopted by the Conference of the Parties in 1990 and was annexed to recommendation 4.7 (Davis 1994). As per the Ramsar Convention, the wetlands can be classified in three different categories, namely: inland wetlands, coastal and marine wetlands and man-made wetlands. Further the wetlands can be reclassified into 40 different types (Davis 1994).

For the description of Ramsar sites, the Ramsar classification was developed as a simple tool. It serves as a baseline for the design of framework to provide units for comparability of terms and concept at local or national scale wetland inventory. Convention can recognize threatened wetlands across the globe and those which are under-represented in the List of Wetlands of International Importance using the broad classification system.

12.2.2 Wetlands Classifications in India

India being a vast country has diverse topographic and climatic conditions which is accountable for the high diversity of fauna and flora (Balasubramanian 2017). Wetlands are broadly distributed across India from the Himalayan ranges in the north to Deccan traps in the peninsular India. As per National Wetlands Atlas (2011) (MoEF 2011), the wetlands in India are classified in the three different levels from Level 1 to Level 3. Among the three basic levels of classification, Level 1 is further sub-divided into coastal and inland, Level 2 is sub-divided into man-made categories, and Level 3 is further sub-divided into 19 categories on the basis of topographic, vegetation and climatic conditions.

12.2.3 Distributions of Wetlands in India

In India there are 67,429 numbers of wetlands in total with area coverage of about 4.1 million hectares (MoEF 1990). Among these 2175 are natural and 65,254 are man-made wetlands. As per survey conducted by the Ministry of Environment and Forest (MoEF) in 1990, out of 4.1 million hectares of area under wetland cover, 0.45 million hectares of land is covered by mangroves, 2.6 million hectares are man-made, and 1.5 million hectares are natural wetlands. The Directory of Indian

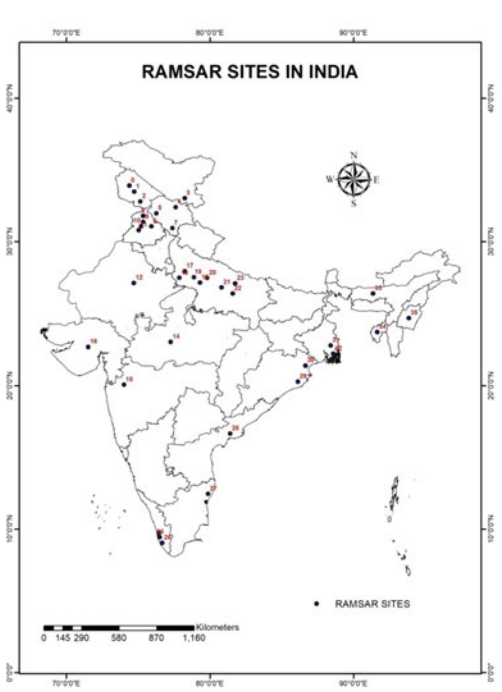

FID	Name
0	Wular Lake
1	Hokera Wetland
2	Surinsar-Mansar Lakes
3	Tsomoriri
4	Chandetal Wetland
5	Pong Dam Lake
6	Ropar
7	Nangal Wildlife Sanctuary
8	Beas Conservation Reserve
9	Hanke Lake
10	Kanjli
11	Keshopur-Miani Community Reeserve
12	Sambhar Lake
13	Keoladeo Nitional Park
14	Bhoj Wetland
15	Nandur Madhameshwar
16	Nalsarovar
17	Upper Ganga River
18	Sarsai Nawar Jheel
19	Saman Wetland Sanctuary
20	Sandi Bird Sanctuary
21	Nawabganj Bird Sanctuary
22	Samaspur Bird Sanctuary
23	Parvati Arga Bird Sanctuary
24	Astamudi Wetland
25	Sasthamkotta Lake
26	Vembanad-Kol Wetland
27	Point Calimere Wildlife and Brird Sanctuary
28	Kolleru Lake
29	Chilika Lake
30	Bhitarkanika Mangroves
31	East Calcutta Wetlands
32	Sundarban Wetland
33	Deepor Beel
34	Rudrasagar Lake
35	Loktak Lake

Fig. 12.1 Ramsar sites in India

Wetlands published by Asian Wetland Bureau records 147 sites as important and 68 as protected by the Wildlife Protection Act of 1972. There are altogether 41 Ramsar sites in India among which three of them are in NorthEastern India, i.e., Rudrasagar Lake in Tripura, Deepor Beel in Assam and Loktak Lake in Manipur (MoEFCC 2020). Location of 36 Ramsar sites in India is shown in Fig. 12.1.

12.3 Drivers for Change in Wetland Conditions

Invariable increase in population and socio-economic development in the region creates numerous drivers which cause degradation of wetlands. The driving factors for the degradation of wetlands are divided broadly into two major categories, i.e., direct drivers and indirect drivers (Van Asselen et al. 2013). Direct drivers are those anthropogenic factors or natural factors that cause biophysical changes at regional scale. In case of indirect drivers they have diffuse or disperse effect mostly related to the indirect driving factors and often relate to the cultural and demographic, socio-economic and institutional processes. Wetlands are influenced by some megatrends. Natural driving factors include volcanic eruptions, solar radiation, earthquakes, pests

and diseases and ecosystem and succession processes, whereas the human induced or anthropogenic factors consist of water abstraction, climate change, LULC change, external inputs and resource consumption. Variation in climate is natural driver, but change in climate due to anthropogenic activities is associated to greenhouse gases in the atmosphere. Drivers can have both positive and negative influence. Majority of positive drivers are human responses for mitigating change. Our perspective is hindered by the complication of the pathways from indirect drivers to wetland degradation. For example, climate change can be direct driver by affecting temperature, hydroperiods, fluctuations in the sea level, etc. (Renton et al. 2015); on the other hand it can be indirect driver, e.g., mitigation efforts can be hydropower generation. However as an element of management system of man-made wetlands many direct driving factors of natural wetlands play a significant role.

12.4 Land Use Land Cover Change (LULCC) Modeling Techniques

There are seven basic forms of modeling techniques like process-based models, data mining models, hybrid models, machine learning models and statistical models which are being used for LULC modeling. Among the several modeling techniques Cellular Automation is the most commonly used techniques. Cellular Automation is a dynamic model which was developed to simulate complex patterns (Neumann and Burks 1966). Cellular Automation can capture global patterns and local behaviors (Wolfram 1984). The basic components of Cellular Automation include: (1) grid gap which can be represented as irregular or regular cell, (2) each cell has the capability to change based on cells in its neighbors, (3) classification of data on transition rules, (4) extent of influence of neighbor cells from central cell and (5) time step. For the calibration of model to model the LULC the best set of transition rules is defined (Landis and Zhang 1998). Since the LULC patterns are complex and the numbers of variables are more, it becomes difficult to set the best combination of transition rules (Wu and Webster 1998). Generally there are two ways to model and calibrate Cellular Automation models both being dependent on time and space (Pontius et al. 2004) (Fig. 12.2). The first way is using machine learning algorithms, statistical methods (Wu 2002). The other method is by hit and try approach where the simulation result from various combinations of parameters is compared (Clarke et al. 1997). Structure of Cellular Automation (CA) model is shown in Fig. 12.3.

12.4.1 Vector-Based CA (VEC-GCA)

Using diverse functions a new vector-based CA model permits changing the size and shape of objects across time (Moreno et al. 2008, 2009). This topology is open

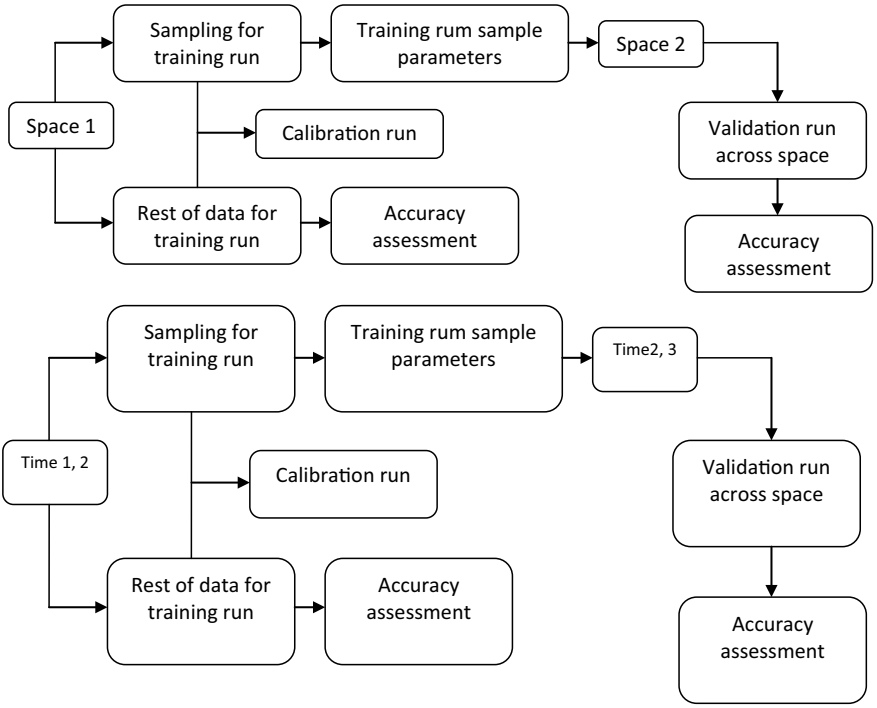

Fig. 12.2 Calibration and validation across space and time. Adopted: Amin (2013)

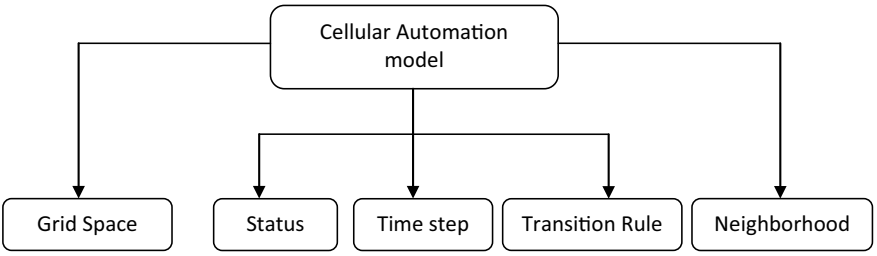

Fig. 12.3 Structure of cellular automation (CA) model

to define influence zone surrounding each object. Using dynamic neighborhood it solves the dependency on cell size of a CA model using vector data. This model is independent of number of objects between two objects. As object changes shape this model involves variety of operations making vector-based Cellular Automation model intense in computation. But the major advantage with vector-based Cellular Automation model minimizes the extensive computation time required for sensitivity analysis. The structure of vector-based Cellular Automation model is shown in Fig. 12.4.

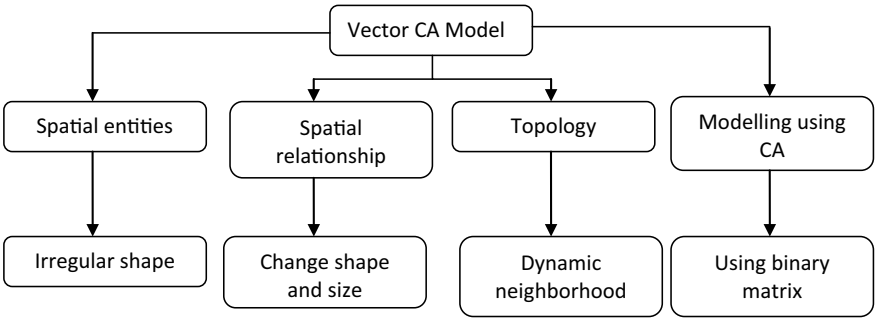

Fig. 12.4 Structure of vector-based cellular automation (CA) model. Adopted: Amin (2013)

12.4.2 CA-Support Vector Machine (SVM) (CA-SVM)

To distinguish LULC, Cellular Automation-support vector machine transition rules define linear boundaries. So it becomes important to use a model which can discover the nonlinear boundaries for the transition rules (Yang et al. 2008). Artificial neural network (ANN) can be used for the parameterization of CA; using ANN rather than global optimization it may result in local optimization. In nonlinear complexity scenario, SVM is used to define transition rules in CA to improve result (Yang et al. 2008). In order to detect the transition rule other information is combined with SVM (Fig. 12.5). Land use land cover change probability map is the final outcome which is projected based on the decision function.

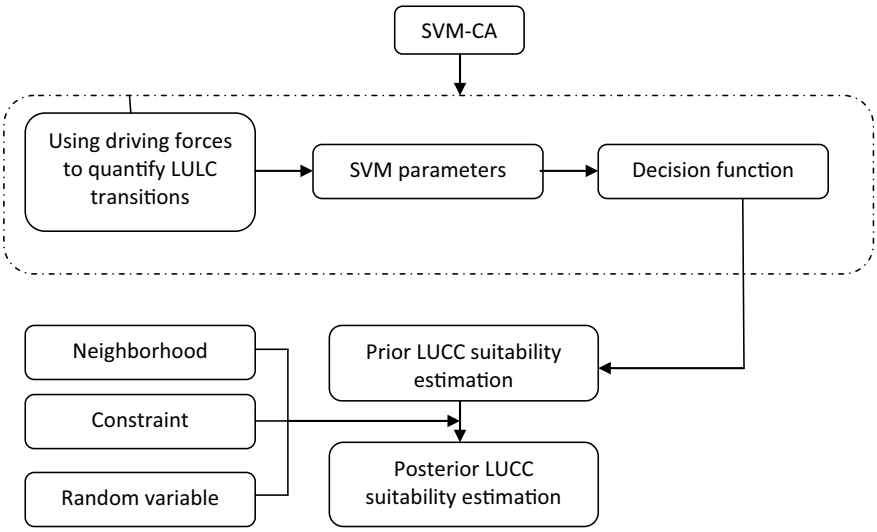

Fig. 12.5 Structure of CA-SVM model. Adopted: Yang et al. (2008)

12.4.3 CA-MCE

Based on Multiple Criteria Evaluation (MCE) CA transition rules have been set (Wu 1998). CA has been integrated with ANN for the derivation of parameters (Li and Yeh 2002). Because of ANN having the black box nature it is difficult to interpret the parameters. However interpreting the meanings of MCE weights is easy. The contribution to the land use land cover change is indicated by the smaller or the larger values of the corresponding driver.

12.5 Case Study of Herbaceous Wetlands (Phumdis) and Wetlands in Loktak Lake Catchment, Manipur, India

This case study, mapping of LULC in past for the year 2007, 2014, 2017, was carried out, and based on it LULC for the year 2030 was projected in Loktak Lake catchment, a Ramsar site in Manipur, India (Fig. 12.6). LCM embedded in the TerrSet software was used to predict the LULC map for future based on LULC map of past. Artificial neural network (ANN) and Markov chain algorithms entrenched in LCM were deployed to predict the future LULC condition. Landsat 5 C1 level-1 and Landsat 8 OLI C1 level-1 satellite data obtained from USGS earth explorer was used in this study. ANN was trained with driving factors, namely slope and elevation, distance from built-up area and distance from roads. Using obtained LULC maps for 2007 and 2014, LULC map of 2017 was predicted using LCM. Predicted LULC map of 2017 was then compared to actual LULC map of 2017 for the purpose of validation, and after obtaining good degree of agreement between observed and predicted LULC, then based on the LULC of 2007 and 2017 the LULC for the year 2030 predicted. The driving factor basic dataset, namely town plan map and road network map of Manipur, was obtained from Department of Town Planning, Govt. of Manipur and North Eastern Space Application Centre, respectively. Maximum likelihood classifier algorithm embedded in ERDAS-Imagine was used to carry out image classification. The accuracy of the classified image was assessed using historical satellite imagery obtained from Google Earth Pro and ground control point.

Markov in the LCM of TerrSet software mainly considers two techniques, first is to assess the predicted LULC based on past LULC that has provided us to develop transition probability matrix, i.e., the probability of conversion of one LULC class to other. CA-Markov was used to predict the future LULC map for 2030 based on the LULC map of 2007 and 2017 (Eastman 2015). To apply this model which is based on number of random process $T(s)$, F_T is the function of random process T, if Markov process for any time $s_1 < s_2 < s_3 \ldots\ldots < s_n < s_{n+1}$, then the random process will satisfy the Eq. (12.1) (Subedi et al. 2013)

$$F_T(T(s_{n+1}) \leq x_{n+1} | T(s_n) = x_n, T(s_{n-1}) = x_{n-1}, T(s_1)$$

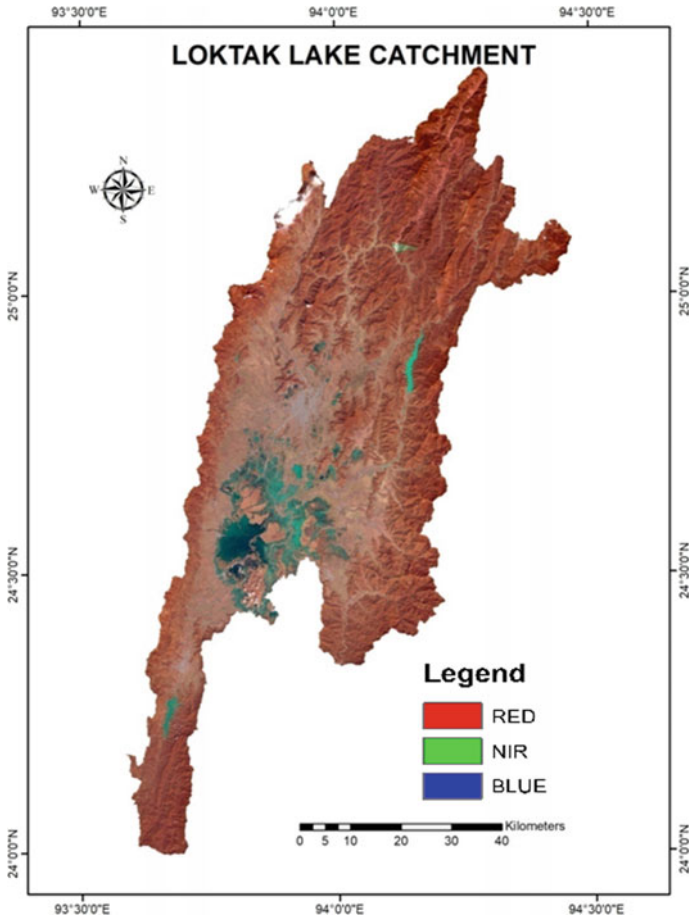

Fig. 12.6 Loktak Lake catchment area

$$= F_T(T(s_{n+1}) \leq x_{n+1}) | T(s_n) = x_n) \qquad (12.1)$$

where s_n represents present time, s_{n+1} represents any instant of time in the future, and s_1, s_2,…, s_{n-1} represents various instant of time in past.

12.6 Results

Land use land cover map produced using maximum likelihood classifier for the year 2017, 2014 and 2007 is shown in Fig. 12.7. The produced LULC map for the year 2017, 2014 and 2007 was found to be 93%, 92% and 88% accurate, respectively. The

LULC was classified in six different classes with emphasis on herbaceous wetlands and wetlands.

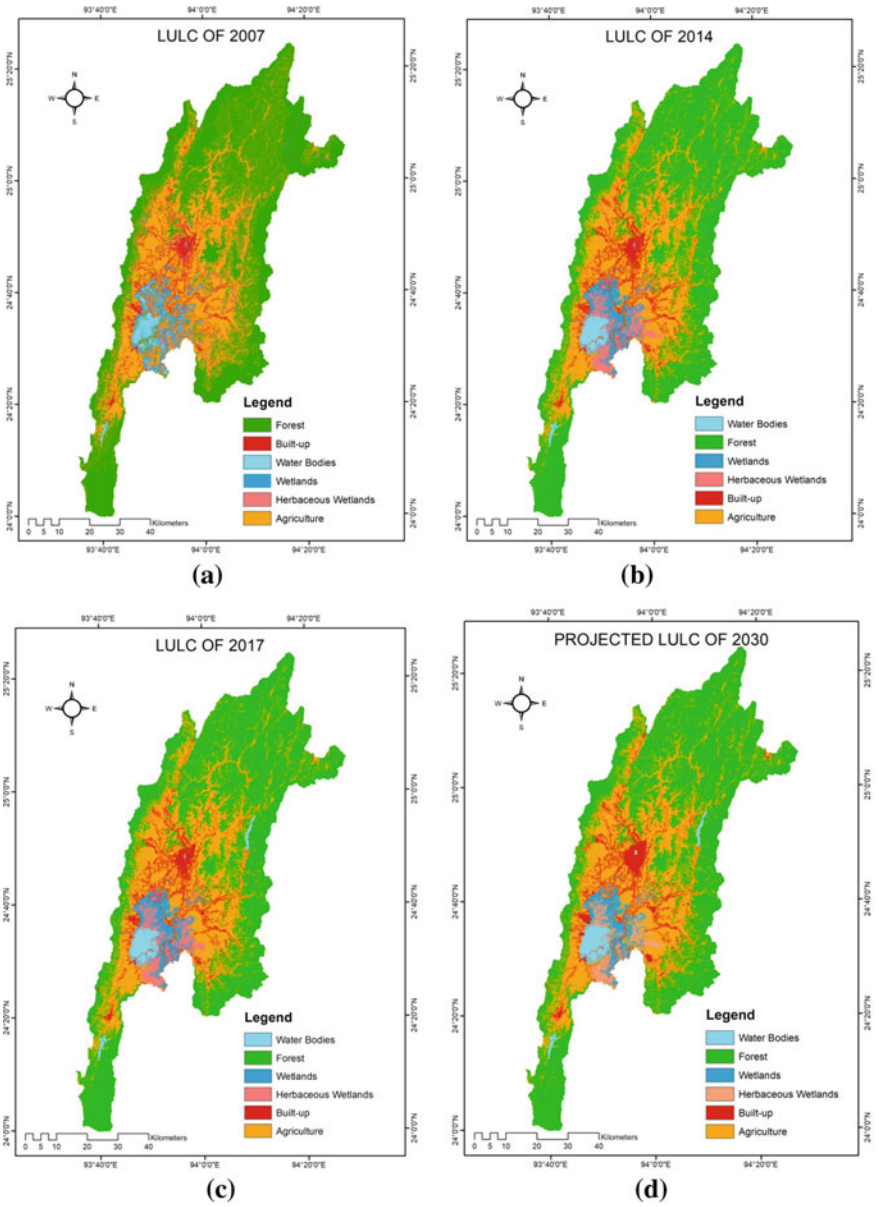

Fig. 12.7 LULC map of **a** 2007, **b** 2014 and **c** 2017, **d** projected future LULC map of 2030

Table 12.1 LULC change assessment between the year 2007 to 2030

LULC classes	Area in 2007 (km^2)	Area in 2030 (km^2)	Change in area (km^2)	Change (%)
Wetlands	158.01	148.39	−9.62	−6.48
Herbaceous wetlands	264.64	186.94	−77.7	−41.56

LULC map for the year 2007 and 2014 was used to simulate the LULC map for the year 2017 using LCM embedded in the TerrSet. Later the simulated LULC map for the year 2017 was compared with the actual LULC map of 2017 to determine the model performance. The model performance was found to be good with a model accuracy of 86%, i.e., $R^2 = 0.86$. Based on the LULC map of 2017 and 2007 the future LULC map for the year 2030 was projected using driving variables. From the mapping result it was observed that there is a decrease in herbaceous wetlands locally known as phumdis and wetlands by 22.54% and 5.99%, respectively, in the time period 2007 to 2014. The similar trends were observed between the year 2014 to 2017 with a decrease in the area coverage by 4.98% and 0.09% under herbaceous wetlands and wetland category. Comparing it to the baseline scenario of 2007, decrement of 6.08% and 28.65% in the area coverage under wetlands and herbaceous wetlands was observed for the year 2017. From the future LULC predicted by the model for the year 2030, further decrease in the area under wetlands and herbaceous wetlands by 6.48% and 41.56%, respectively, was observed (Table 12.1).

12.7 Discussions

The decrement in herbaceous wetlands and wetlands was mainly concentrated around the peripheral zone of Loktak Lake. The projected spatio-temporal change in wetlands around the peripheral zone of Loktak Lake for the year 2030 is shown in Fig. 12.8.

The decrease in the area under herbaceous wetlands was mainly because of removal of phumdis from the central core zone of Loktak Lake for the purpose of fishing (LDA and WISA 2006). The decrease in wetlands and herbaceous wetlands possesses serious threat to endangered aquatic and terrestrial species found in the Loktak Lake and peripheral zone of the Loktak Lake. The spatial change in phumdis is of serious concern to Keibul Lamjao National Park (KLNP) as the major portion of KLNP constitutes of herbaceous wetlands and possesses serious threat to the species at KLNP especially the *Rucervus eldii eldii*. For the restoration and sustainability of wetlands and herbaceous wetlands around Loktak Lake the change in LULC is of major concern. The fragile ecosystem is severely affected by the change in LULC condition surrounding the lake. Increase in population in the catchment has put immense pressure on natural resources of the lake for the livelihood of the people. Loktak Lake is currently in a deep ecological crisis, and the wetland is showing signs

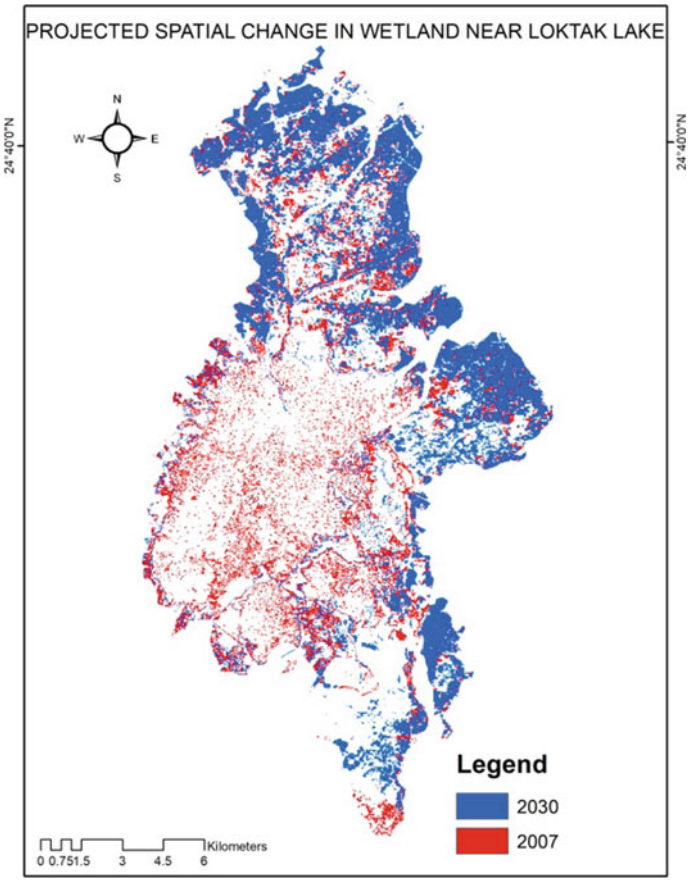

Fig. 12.8 Projected spatial change in wetlands near Loktak Lake

of near-total collapse. Loktak Lake faces a significant issue of unplanned land-use practices. Land use and land cover change is an environmental change that influences biodiversity and livelihoods and on a wide ranges of socio-economic and ecological processes. Changes in the landscape have brought considerable impacts on the environment and livelihood of the local community. Unless remedial actions are taken immediately, the whole ecosystem is headed for a major devastation.

12.8 Conclusion and Recommendation

The environmental system is seriously threatened by encroachment of herbaceous wetlands and wetlands. There is a need of proper land use planning and policies for the preservation of environment. The LULC predictive modeling techniques like

CA-Markov, ANN, SVM, vector-based CA, etc. can aid in predicting future LULC which will aid the decision- and policy-makers in building policies for environment protection and conservation. This study shows the potential remote sensing data obtained from the satellites which can aid in providing more spatial and temporal information which aid in sustainable development. There is a need to get clear understanding regarding the spatial changes in the herbaceous wetlands and wetlands in the future with high resolution datasets. To understand the phumdi dynamics, there is a need of separate study to be done on using second level of classification using high-resolution datasets. The models like LCM can aid in predicting and analyzing the future LULC for the sustainable use of resources. The modeling results show that proposed methods and remote sensing and GIS tools could be beneficial for the policy-makers to visualize, understand and future project the distribution wetlands for the sustainable use of resources.

Acknowledgements The authors gratefully acknowledge the valuable databases from Department of Town Planning (Manipur State Government), North Eastern Space Application Centre (NESAC), United States Geological Survey (USGS) and Forest Department (Manipur State Government).

References

Ahmad J, Ahmad M, Laghari A, Lohana W, Ali S, Fatima Z (2009) Public private mix model in enhancing tuberculosis case detection in District Thatta, Sindh, Pakistan. J PakMed Assoc 59(2):82

Ahmed B, Kamruzzaman M, Zhu X, Rahman MS, Choi K (2013) Simulating land cover changes and their impacts on land surface temperature in Dhaka. Bangladesh Remote Sens 5(11):5969–5998

Ali A, Khalid A, Butt MA, Mehmood R, Mahmood SA, Sami J, Ali F (2018) Towards a remote sensing and GIS-based technique to study population and urban growth: a case study of Multan. Adv Remote Sens 7(03):245–258

Amin T (2013) Simulating land use land cover change using data mining and machine learning algorithms

Anand V, Oinam B, Parida BR (2020) Uncertainty in hydrological analysis using multi-GCM predictions and multi-parameters under RCP 2.6 and 8.5 scenarios in Manipur River basin, India. J Earth Syst Sci 129:223

Anand V, Oinam B, Singh IH (2021) Predicting the current and future potential spatial distribution of endangered *Rucervus eldii eldii* (Sangai) using MaxEnt model. Environ Monit Assess 193:147. https://doi.org/10.1007/s10661-021-08950-1

Ayele GT, Tebeje AK, Demissie SS, Belete MA, Jemberrie MA, Teshome WM, Teshale EZ (2018) Time series land cover mapping and change detection analysis using geographic information system and remote sensing, Northern Ethiopia. Air Soil Water Res 11:1178622117751603

Balasubramanian A (2017) Biodiversity profile of India. http://doi.org/10.13140/RG.2.2.10664.57601

Bansod RD, Dandekar UM (2018) Evaluation of Morna river catchment with RS and GIS techniques. J Pharmacogn Phytother 7(1):1945–1948

Barbier EB (2016) The protective service of mangrove ecosystems: a review of valuation methods. Mar Pollut Bull 109:676–681

Bassi N, Kumar MD, Sharma A, Pardha-Saradhi P (2014) Status of wetlands in India: a review of extent, ecosystem benefits, threats and management strategies. J Hydrol Reg Stud 2:1–19

Best J (2019) Anthropogenic stresses on the world's big rivers. Nat Geosci 12:7–21
Boulton AJ, Ekebom J, Gislason GM (2016) Integrating ecosystem services into conservation strategies for freshwater and marine habitats: a review. Aquat Conserv Mar Freshw Ecosyst 26:963–985
Central Pollution Control Board (CPCB) (2008) Status of water quality in India 2007. Central Pollution Control Board, Ministry of Environment and Forests, Government of India New Delhi, New Delhi
Cheema MJM, Bastiaanssen WG (2010) Land use and land cover classification in the irrigated Indus Basin using growth phenology information from satellite data to support water management analysis. Agric Water Manage 97(10):1541–1552
Chen J, Theller L, Gitau MW, Engel BA, Harbor JM (2017) Urbanization impacts on surface runoff of the contiguous United States. J Environ Manag 187:470–481
Clarke KC, Hoppen S, Gaydos L (1997) A self-modifying cellular automaton model of historical urbanization in the San Francisco bay area. Environ Plan B Plan Des 24:247–261
Dam AA, Kipkemboi J, Mazvimavi D, Irvine K (2014) A synthesis of past, current and future research for protection and management of papyrus (Cyperus papyrus L.) wetlands in Africa. Wetl Ecol Manag 22:99–114
Davis TJ (1994) The Ramsar convention manual: a guide for the convention on wetlands of international importance especially as waterfowl habitat. Ramsar Convention Bureau, Gland, Switzerland, 207 p
Eastman JR (2015) TerrSet manual. TerrSet Version 15. 18, pp 1–390. https://clarklabs.org/wp-content/uploads/2016/10/Terrset-Manual.pdf
Etemadi H, Smoak JM, Karami J (2018) Land use change assessment in coastal mangrove forests of Iran utilizing satellite imagery and CA–Markov algorithms to monitor and predict future change. Environ Earth Sci 77(5):208
Frazier S (1996) An overview of the world's Ramsar sites, vol 29. Wetlands International Publishing, 58 p
Friess DA (2016) Ecosystem services and disservices of mangrove forests: insights from historical colonial observations. Forests 7:183. https://doi.org/10.3390/f7090183
Gashaw T, Tulu T, Argaw M, Worqlul AW (2017) Evaluation and prediction of land use/land cover changes in the Andassa watershed, Blue Nile Basin, Ethiopia. Environ Syst Res 6(1):17
Herold M, Goldstein MC, Clarke KC (2003) The spatiotemporal form of urban growth: measurement, analysis and modeling. Remote Sens Environ 86:286–302
Janse JH, Dam AA, Hes EMA, Klein JJM, Finlayson CM, Janssen AG, Wijk D, Mooij WM, Verhoeven JTA (2019) Towards a global model for wetlands ecosystem services. Curr Opin Environ Sustain 36:11–19
Karimi H et al (2018) Monitoring and prediction of land use/land cover changes using CA-Markov model: a case study of Ravansar County in Iran. Arab J Geosci 11(19):592
Kelleway JJ, Cavanaugh K, Rogers K, Feller IC, Ens E, Doughty C, Saintilan N (2017) Review of the ecosystem service implications of mangrove encroachment into salt marshes. Global Change Biol 23:3967–3983
Kumar K, Kumar V, Kumar D (2016) Land use and land cover change detection Ingagas river valley watershed using remote sensing and GIS. Int J Res Eng Appl Sci 6(5):31–37
Landis J, Zhang M (1998) The second generation of the California urban futures model. Part 1: model logic and theory. Environ Plan B Plan Des 30:657–666
Langan C, Farmer J, Rivington M, Smith JU (2018) Tropical wetland ecosystem service assessments in East Africa: a review of approaches and challenges. Environ Model Softw 102:260–273
LDA and WISA (1999) Loktak lake in Peril. LDA and WISA, Imphal, Manipur, India
LDA and WISA (2006) Loktak protection act 2006, Imphal, Manipur, India
LDA and WISA (2010) Loktak lake-caring for wetlands: an answer to climate change. LDA and WISA, Imphal, Manipur, India, pp 1–24
Li X, Yeh AGO (2002) Neural-network-based cellular automata for simulating multiple land use changes using GIS. Int J Geo Inf Sci 16(4):323–343

Li H, Zhang S, Sun Y, Gao J (2011) Land cover classification with multisource data using evidential reasoning approach. Chin Geogr Sci 21(3):312–321

Liping C, Yujun S, Saeed S (2018) Monitoring and predicting land use and land cover changes using remote sensing and GIS techniques—a case study of a hilly area, Jiangle, China. PLoS One 13:7

Liu S, Costanza R, Farber S, Troy A (2010) Valuing ecosystem services: theory, practice, and the need for a transdisciplinary synthesis. Ann N Y Acad Sci 1185:54–78

Milesi C, Elvidge CC, Nemani RR, Running SW (2003) Assessing the impact of urban and development on net primary productivity in the southeastern United States. Remote Sens Environ 68(3):401–410

MoEF (1990) Wetlands of India—a directory. Ministry of Environment and Forests, Govt. of India, New Delhi

MoEF (2011) National wetland atlas—an updated database of wetlands in India

MoEFCC (2020) Ramsar sites of India—factsheets. Ministry of Environment, Forest and Climate Change, Government of India

Moreno N, Ménard A, Marceau DJ (2008) VecGCA: a vector-based geographic cellular automata model allowing geometrical transformations of objects. Environ Plan B Plan Des 35:647–665

Moreno N, Wang F, Marceau DJ (2009) Implementation of a dynamic neighborhood in a land-use vector-based geographic cellular automata model. Comput Environ Urban Syst 33(1):44–54

Peng J, Liu Y, Shen H, Han Y, Pan Y (2012) Vegetation coverage change and associated driving forces in mountain areas of Northwestern Yunnan, China using RS and GIS. Environ Monit Assess 184(8):4787–4798

Peralta-Maraver I, Reiss J, Robertson AL (2018) Interplay of hydrology, community ecology and pollutant attenuation in the hyporheic zone. Sci Total Environ 610–611:267–275

Pontius RG, Huffaker, Denman K (2004) Useful techniques of validation for spatially explicit land-change models. Ecol Mod 179(4):445–461

Pozzi F, Small C (2002) Vegetation and population density in urban and suburban areas in U.S.A. In: Proceedings of the third international symposium on remote sensing of urban area, Istanbul, Turkey

Ramachandra TV, Rajashekariah K, Ahalya N (2002) Status, conservation and management of wetlands

Ramsar Bureau (2016) The list of wetlands of international importance. RAMSAR Secretariat, Gland, Switzerland, pp 1–48

Ramsar Convention on Wetlands (2018) Global wetland outlook: state of the world's wetlands and their services to people. Ramsar Convention Secretariat, Gland, Switzerland

Ramsar Convention Secretariat (2013) The Ramsar convention manual: a guide to the convention on wetlands (Ramsar, Iran, 1971), 6th edn. Ramsar Convention Secretariat, Gland

Rebelo AJ, Scheunders P, Esler KJ, Meire P (2017) Detecting mapping and classifying wetland fragments at a landscape scale. Rem Sens Appl Soc Environ 8:212–223

Renton DA, Mushet DM, DeKeyser ES (2015) Climate change and prairie pothole wetlands—mitigating water-level and hydroperiod effects through upland management. U.S. Geological Survey Scientific Investigations report 2015–5004

Roy B, Kanga S, Singh SK (2017) Assessment of land use/land cover changes using geospatial technique at Osian-Mandore, Jodhpur (Rajasthan). Int J Sci Res Comput Sci Eng Info Tech 2(5):73–81

Sieben EJJ, Khubeka SP, Sithole S, Job NM, Kotze DC (2018) The classification of wetlands: integration of top-down and bottom-up approaches and their significance for ecosystem service determination. Wetl Ecol Manag 26:441–458

Singh SK, Mustak S, Srivastava PK, Szabó S, Islam T (2015) Predicting spatial and decadal LULC changes through cellular automata Markov chain models using earth observation datasets and geo-information. Environ Process 2(1):61–78

Space Applications Centre (SAC) (2011) National wetland atlas. SAC, Indian Space Research Organisation, Ahmedabad

Steinman AD, Cardinale BJ, Munns WR, Ogdahl ME, Allan JD, Angadi T, Bartlett S, Brauman K, Byappanahalli M, Doss M, Dupont D, Johns A, Kashian D, Lupi F, McIntyre P, Miller T, Moore M, Muenich RL, Poudel R, Price J, Provencher B, Rea A, Read J, Renzetti S, Sohngen B, Washburn E (2017) Ecosystem services in the great lakes. J Great Lake Res 43:161–168

Sterner RW, Ostrom P, Ostrom NE, Klump JV, Steinman AD, Dreelin EA, Zanden MJV, Fisk AT (2017) Grand challenges for research in the Laurentian great lakes. Limnol Oceanogr 62:2510–2523

Subedi P, Subedi K, Thapa B (2013) Application of a hybrid Cellular Automaton-Markov (CA-Markov) model in land use change prediction: a case study of Saddle Creek drainage basin, Florida. Appl Ecol Environ Sci 1:126–132

Tan Y, Bai B, Mohammad MS (2016) Time series remote sensing based dynamic monitoring of land use and land cover change. In: 2016 4th international workshop on earth observation and remote sensing applications (EORSA). IEEE, pp 202–206

Tong Y, Zhang W, Wang X, Couture R, Larssen T, Zhao Y, Li J, Liang H, Liu X, Bu X, He W, Zhang Q, Lin Y (2017) Decline in Chinese lake phosphorus concentration accompanied by shift in sources since 2006. Nat Geosci 10:507–511

Van Asselen, Verburg PH, Vermaat JE, Janse JH (2013) Drivers of wetland conversion: a global meta-analysis. PLoS One 8(11):e81292

Von Neumann J, Burks AW (1966) Theory of self reproducing automata. University of Illinois Press, Urbana, Illinois

Wolfram S (1984) Computer software in science and mathematics. Scientific American, September, pp 188–203

Wondie A (2010) Improving management of shoreline and riparian wetland ecosystems: the case of Lake Tana catchment. Ecohydrol Hydrobiol 10:123–132

Wu F (1998) SimLand: a prototype to simulate land conversion through the integrated GIS and CA with AHP-derived transition rules. Int Jof Geo Inf Sci 12:63–82

Wu F (2002) Calibration of stochastic cellular automata: the application to rural-urban land conversions. Int J Geogr Info Sci 16(8):795–818

Wu F, Webster CJ (1998) Simulation of land development through the integration of cellular automata and multi-criteria evaluation. Environ Plan B Plan Des 25:103–126

Xu X, Jiang B, Tan Y, Costanza R, Yang G (2018) Lake-wetland ecosystem services modeling and valuation: progress, gaps and future directions. Ecosyst Serv 33:19–28

Yagoub MM, Bizreh AAA (2014) Prediction of land cover change using Markov and cellular automata models: case of Al-Ain, UAE, 1992–2030. J Ind Soc Rem Sen 42(3):665–671

Yang Q, Li X, Shi X (2008) Cellular automata for simulating land use changes based on support vector machines. Comput Geosci 34:592–602

Yang T, Sheng L, Zhuang J, Lv X, Cai Y (2016) Function, restoration, and ecosystem services of riverine wetlands in the temperate zone. Ecol Eng 96:1–7

Yirsaw E, Wu W, Shi X, Temesgen H, Bekele B (2017) Land use/land cover change modeling and the prediction of subsequent changes in ecosystem service values in a coastal area of China, the Su-Xi-Chang region. Sustainability 9(7):1204

Zhang Y, Jeppesen E, Liu X, Qin B, Shi K, Zhou Y, Thomaz SM, Deng J (2017) Global loss of aquatic vegetation in lakes. Earth Sci Rev 173:259–265

Zhao Q, Bai J, Huang L, Gu B, Lu Q, Gao Z (2016) A review of methodologies and success indicators for coastal wetland restoration. Ecol Indic 60:442–452

Chapter 13
Delineation of Groundwater Potential Zones in a Tropical River Basin Using Geospatial Techniques and Analytical Hierarchy Process

A. L. Achu, N. Anjali, and Girish Gopinath

Abstract The need for sustainable groundwater resource management increases with demand of clean water across the planet for industrial, agriculture, and domestic uses. In the present study, an attempt has been made to delineate the groundwater potential zones (GWPZ) in a tropical river basin, viz. Achankovil river basin (ARB), using GIS and analytical hierarchy process (AHP) techniques. For this, a total of eight geo-environmental variables such as lithology, geomorphic features, land use/land cover, soil texture, lineament density, drainage density, topographic wetness index, and mean annual rainfall were used to identify the GWPZ, and limited number dug well yield data published by the Central Ground Water Board (CGWB) is used to validate the model. The result indicates that nearly 50% of the basin is characterized by good to very good groundwater potential, whereas poor GWPZ accounts nearly 25% of the basin. Among the different thematic factors' geology, geomorphic features and slope angle have significant control over the occurrence of groundwater in the study area. The linear relation between well yield data and groundwater potential zones is assessed, and a R^2 value of 0.790 indicates that the predicted model is trustworthy and can be used for groundwater resources management in the study area. The integrated approach used in the study is reliable and can be replicated anywhere in the tropical region.

Keywords Groundwater potential · GIS · AHP · Achankovil river basin · India

A. L. Achu (✉) · N. Anjali · G. Gopinath
Department of Climate Variability and Aquatic Ecosystems, Kerala University of Fisheries and Ocean Studies (KUFOS), Kochi, Kerala 682508, India
e-mail: achu.geomatics@gmail.com

V. P. Singh et al. (eds.), *Application of Remote Sensing and GIS in Natural Resources and Built Infrastructure Management*, Water Science and Technology Library 105,
https://doi.org/10.1007/978-3-031-14096-9_13

13.1 Introduction

Among the global freshwater resources, groundwater is the second-largest reservoir, which contributes approximately 30% of the global freshwater budget (https://water.usgs.gov/edu/watercyclegwstorage.html). Groundwater serves as a major source of water for domestic, industrial, and agricultural uses and other developmental initiatives (Achu et al. 2020a; Siebert et al. 2010). Global water deficit of 40% is expected by 2030 due to increasing demand of freshwater resources in various sectors (WWAP 2012).

Overall stage of groundwater development in India is considerably less compared to recharge, which is represented by the 1034 'over-exploited' blocks (i.e., 15% of the total units), 253 'critical' units (4%), 681 'semi-critical' units (10%), and 96 'fully saline' units (1.5%) of the country (CGWB 2017). India occupies more than 30% of the global irrigated lands as per country-wise groundwater utilization list (Margat and Van der Gun 2013). Adimalla and Venkatayogi (2018) stated that in several countries, overexploitation of groundwater has become a major issue including India which consumes the highest volume of global groundwater resource. In India, over 90% of the rural population and roughly 30% of the urban population depend on groundwater to fulfill their basic needs (Reddy et al. 1996). Among the different states of India, Kerala State regularly experiences scarcity of surface water as well as groundwater resources (Achu et al. 2020a).The undulating nature of physiography often leads to increased surface runoff and low infiltration being the major reasons for water scarcity (Achu et al. 2020a; Jesiya and Gopinath 2018; Kamaraju et al. 1996). Groundwater development in Kerala has negative environmental consequences like overexploitation (Shaji et al. 2018) and decline of water levels (Hameed et al. 2015). Recent studies show that the groundwater resources of Kerala are unsafe, which are represented by 15% of the total blocks of Kerala State under over-exploited, critical, and semi-critical categories (CGWB 2017).

The primary objective of a sustainable groundwater resource utilization strategy is to delineate groundwater potential zones of the region. The conventional methods used to locate, delineate, and model the groundwater potential zones are mainly ground-based surveys using geological, geophysical, and hydrogeological techniques (Israil et al. 2006; Singh and Prakash 2002). These methods have inherent limitations such as labor intensive, extensive cost, and time consumption. However, with the introduction of geospatial technology, various authors used GIS coupled with remote sensing data for the delineation of groundwater potential zones (e.g., Achu et al. 2020a, b; Gopinath and Seralathan 2004; Kamaraju et al. 1996; Karanth and Seshubabu 1978; Krishnamurthy et al. 1996; Prasad et al. 2020; Sachdeva and Kumar 2021; Sander et al. 1996; Saraf and Choudhury 1998; Saraf and Jain 1994; Swetha et al. 2017) which are rapid and cost effective, although many authors used different machine learning techniques such as random forest (Masroor et al. 2021; Sachdeva and Kumar 2021), support vector machines (Lee et al. 2018; Naghibi et al. 2017), boosted regression tree (Prasad et al. 2020), adaptive neuro-fuzzy inference system (Moghaddam et al. 2020), artificial neural networks (Tamiru and Wagari 2021),

and statistical methods including bivariate frequency ratio (Bougharioua et al. 2021), weight of evidence (Bougharioua et al. 2021; Rane and Jayaraj 2021), index of entropy (Forootan and Seyedi 2021), and multi-criteria decision-making methods such as AHP (Achu et al. 2020a; Kaur et al. 2020; Masroor et al. 2021), fuzzy logic (Jesiya and Gopinath 2019; Singha et al. 2021), and multi-influencing factor (Mahala 2021; Rane and Jayaraj 2021). However, both machine learning and statistical models are well suited for the regions which have extensive data. MCDM methods such as AHP, fuzzy, and MIF are relying on expert opinion and are well suited for data scares regions (Achu et al. 2020a). The main aim of this study is to demarcate groundwater potential zones in Achankovil river basin of Southern Western Ghats (in Kerala) using AHP method for sustainable groundwater resources management.

13.2 Study Area

Achankovil is a major west flowing river of southern Kerala (Fig. 13.1). The Achankovil river basin (ARB) covers a total area of 1484 km^2 and a total length of 128 km^2 between Western Ghats in the east and Arabian Sea in the west, flowing parallel to the Kallada River basin in the south and Pamba river basin in the north (EMP 2012). Geographically, ARB lies between 8° 75′–9° 5′ N latitudes and 76° 25′–76° 75′ E longitudes and originates from Devermalai hill range of Western Ghats. Major tributaries of Achankovil river basin are Rishimala River, Ramakkalteri River, and Pasukidamettu River. After flowing through rouged valleys of Western Ghats, ARB enters into Kuttanad low-lying area and finally debouches into Arabian Sea through Vembanad Lake (Prasad et al. 2006). ARB exhibits rectangular, parallel, and trellis drainage patterns, and main river course is oriented in WNW-ESE direction, which follow the trend of the Achankovil shear zone. It is also noted that most of the lower-order streams of ARB are developed roughly at right angles to the main river course as structurally controlled (Manu and Anirudhan 2008) (Fig. 13.1). Geologically, ARB is located in the Southern Granulate Terrain (SGT), one of the largest granulite provinces in the world, and represents an ensemble of several crustal blocks, characterized by regionally metamorphosed rocks (Braun et al. 1998). The most dominant rock type in the study area is Precambrian crystalline rocks among which the prominent ones being charnockites and gneiss. Descending from western front of the Western Ghats, the Achankovil roughly follows the WNW-ESE trending Achankovil Shear Zone (ASZ) to the deltaic plains of the Pamba (Dhanya 2014). The 10–20-km-wide and more than 100-km-long Achankovil shear belt in southern India is a prominent lineament that has been interpreted as a major shear zone in southern Western Ghats. The major aquifer systems of the area are characterized by weathered, fissured, and fractured crystalline formations, the semi-consolidated tertiary formations, unconsolidated quaternary deposits laterite, and the alluvial formations. The potential phreatic shallow aquifer of the basin is the weathered mantle coupled with partially weathered and fractured zones in the crystalline rocks. The region experiences monsoon dominated tropical climate with two distinct rainfall seasons

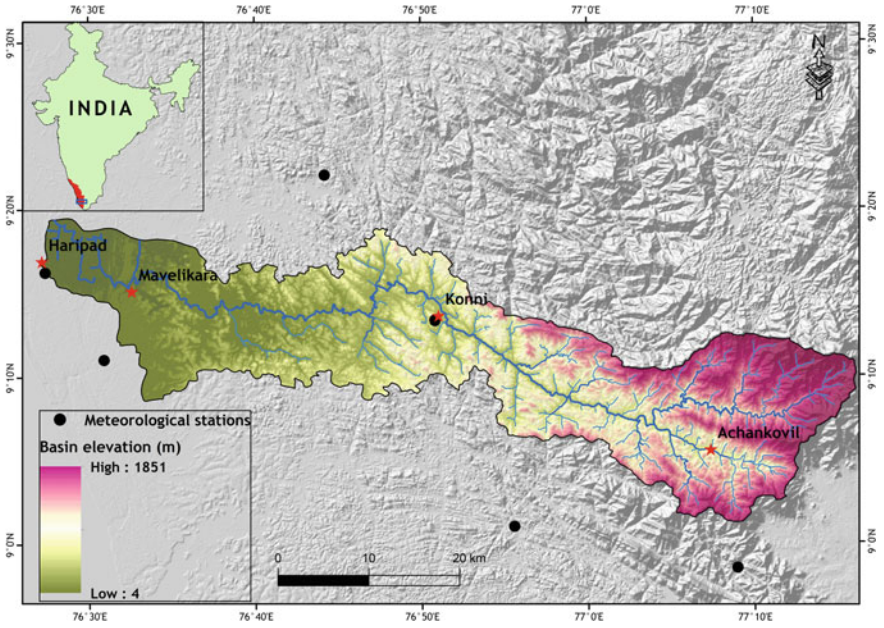

Fig. 13.1 Location map of the ARB, Kerala, India

such as southwest monsoon (June to September) and northeast monsoon (October–November). ~80% of the rainfall receiving in the study area is a contribution of southwest monsoon. ARB receives an average rainfall between 2299 and 2917 mm, having an influence of both southwest and northeast monsoon (Prasad and Ramanathan 2005).

13.3 Data and Methodology

The geo-environmental variables used for the delineation of GWPZ were lithology, geomorphic features, land use/land cover, soil texture, lineament density, drainage density, topographic wetness index, and mean annual rainfall. The district geological resources maps published by Geological Survey of India for Alappuzha and Pathanamthitta districts (the scale 1:250,000) are used to derive the lithological map of the study area. The geomorphic units of the ARB is obtained from Kerala State Remote Sensing and Environmental Centre (KSREC, scale 1:50,000). The soil series of the study area is gathered from the Soil Survey Organization, Government of Kerala. The LU/LC map of the ARB is collected from Kerala State Land Use Board (Scale 1:50,000). The photo-lineament of the ARB is extracted from Landsat 8 OLI

images with SRTM dem (30 m) and drainage lines using visual image interpretation techniques. The lineament density (Ld) of ARB was estimated by calculating the total length of lineaments in unit area (Yeh et al. 2016), using the following formula (Eq. 13.1).

$$\mathrm{Ld} = \frac{\sum_{i=1}^{i=n} \mathrm{Li}}{A} \tag{13.1}$$

where $\sum_{i=1}^{i=n} \mathrm{Li}$ is the length of the lineaments [L] and A denotes the area. Drainage lines of the ARB are generated from SOI topographical sheets with 1:50,000 scale, and subsequently, drainage density per km^2 area is computed using the following equation (Yeh et al. 2016) (13.2):

$$\mathrm{Dd} = \frac{\sum_{i=1}^{i=n} \mathrm{Si}}{A} \tag{13.2}$$

where $\sum_{i=1}^{i=n} \mathrm{Si}$ denotes the total length of drainage and A indicates unit area. The slope map of ARB is estimated from SRTM DEM (1 arc second) using ESRI's spatial analysis tool. TWI is computed from SRTM DEM using SAGA GIS package. Mean monthly rainfall of the all-available stations for last 10 year is collected from Indian Meteorological Department (IMD), and a probabilistic interpolation method (IDW) is used to generate a continuous raster surface.

The analytical hierarchy process (AHP) proposed by Saaty (1990) is the most widely used multi-criteria decision analysis tool (MCDA) (Achu et al. 2020a; Kaur et al. 2020). AHP relays on pairwise comparisons without inconstancies, for solving complex decision problems (Saaty 1990). The MCDA using AHP involves three major steps starting from (1) framing expert's knowledge about a particular phenomenon, ranking the parameters using Saaty's scale of 1–9, (2) making pairwise comparisons, and (3) finally the consistency of the judgments is estimated by consistency ratio. The relative importance of the different variables influencing GWPZs was assessed by developing a diagonal matrix, which can be expressed as Eq. 13.3.

$$A = \begin{bmatrix} 1 & a_{12} & a_{13} & \cdots & a_{1n} \\ a_{21} & 1 & a_{23} & \cdots & a_{2n} \\ a_{31} & a_{32} & \cdots & \cdots & \cdots \\ \vdots & \vdots & \vdots & \vdots & \vdots \\ a_{n1} & a_{n2} & \cdots & \cdots & 1 \end{bmatrix} \tag{13.3}$$

where $a_{ij} = \frac{\text{weight for attribute } i}{\text{weight for attribute } j}$.

The relative weightage of each variable was then computed by the estimation of the Eigen values and the corresponding normalized Eigen vectors (NEV). The consistency of the derived pairwise comparison matrix was calculated using the

consistency ratio (CR) as Eq. 13.4

$$\mathrm{CR} = \frac{\mathrm{CI}}{\mathrm{RI}} \tag{13.4}$$

in which the consistency index (CI) was calculated using Eq. 13.5, where RI is the consistency index of a random square matrix of the same order.

$$\mathrm{CI} = \frac{\lambda_{\max} - n}{n - 1} \tag{13.5}$$

where $\lambda_{\max}$ is the largest Eigen value of '*A*' and *n* is the order of the square matrix. If *A* is perfectly consistent, then $\lambda_{\max}$ will be equal to n giving a CI value of zero. As the inconsistency increases, $\lambda_{\max}$ also increases (Saaty 1990). Commission and omission of a variable depend on the value of CR, where the factors with a consistency ratio value >0.1 were omitted from the analysis. In this study, the AHP technique was implemented using R® software, and geo-environmental variables were analyzed in ArcGIS to estimate the GWPZ using Eq. 13.6:

$$\mathrm{LSI} = \sum_{i=1}^{n} W_i \times F_i \tag{13.6}$$

where W_{ji} is the ranking of various geo-environmental variables used for the computation of GWPZs and F_i is the corresponding relative weights.

13.4 Results and Discussion

The various geo-environmental factors used for modeling the GWPZs of the ARB, viz. lithology, geomorphic units, soil, lineament density, drainage density, slope, TWI and rainfall, are discussed below.

13.4.1 Lithology

Lithology is the most significant factor controlling the occurrence and movement of groundwater in a region (Dinesh Kumar et al. 2007; Kaur et al. 2020). ARB is a part of Achankovil Shear Zone (AKSZ), where ~71% of the basin are characterized by Precambrian crystalline. The dominant rock types are charnockites (area = 51%) followed by quaternary deposits of sand and silt (22%). Other significant rock types present in ARB area are acidic rocks, basic rocks, khondalite group of rocks, laterite, migmatite complex, and sandstone and clay with lignite intercalations (Fig. 13.2a).

Generally, unconsolidated sediments, viz. sand and silt and sandstone and clay, with lignite intercalations are considered as high groundwater potential.

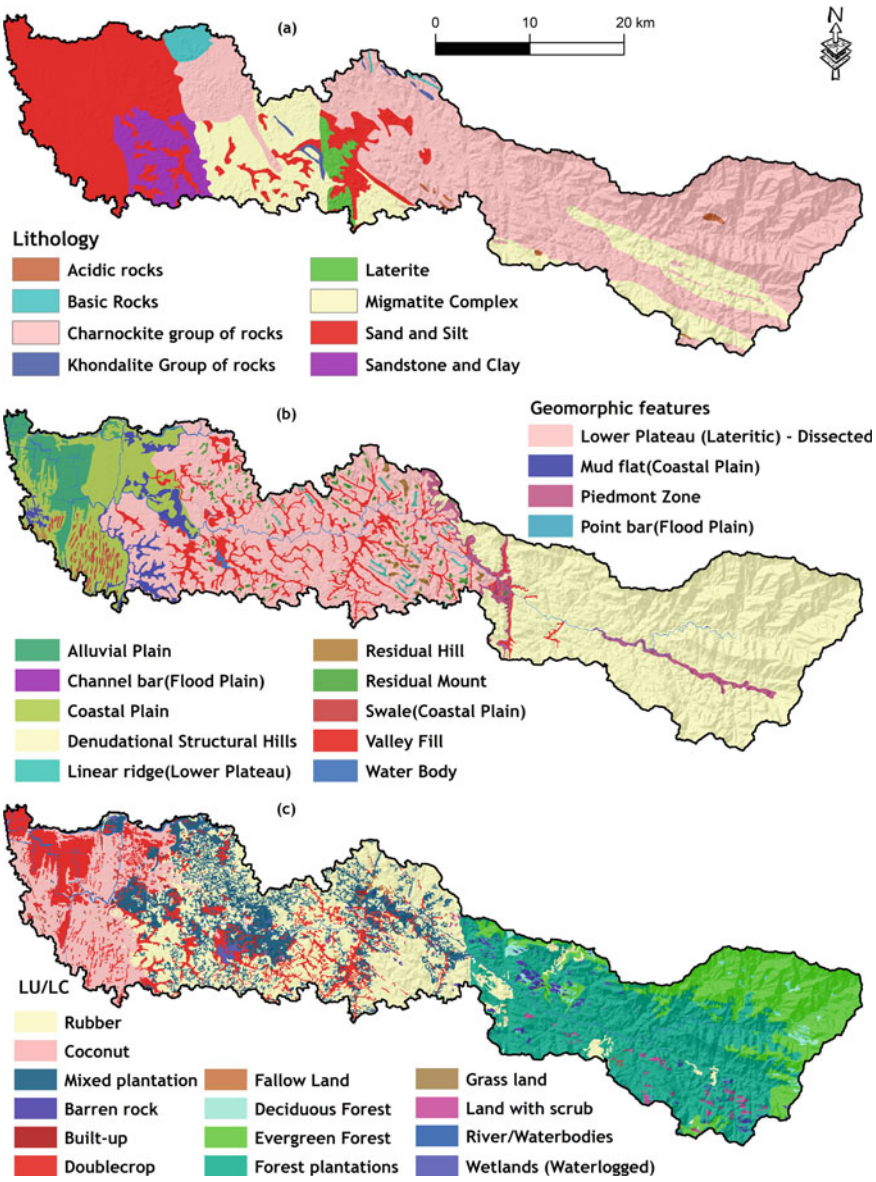

Fig. 13.2 Spatially distributed geo-environmental variables of ARB, **a** lithology of ARB, **b** geomorphology, and **c** land use/land cover

13.4.2 Geomorphological Features

Geomorphological features are the manifestations of underlying parent materials (Achu et al. 2020a). The groundwater infiltration, movement, and contamination are heterogenous in different landforms, therefore identifying hydro-geomorphic features have significant role in analyzing regional groundwater potential (Achu et al. 2020a; Aju et al. 2021; Krishnamurthy et al. 1996). The eastern portion of the ARB is characterized by Denudational Structural Hills (area = 520 km^2) with NW–SE trending ridges, narrow valleys with steep slopes, whereas in the midstream portion, it is occupied by Lower Plateau (384 km^2) and valley fills (Fig. 13.2b). Extreme downstream portion (western) area is characterized by unconsolidated sediments of alluvial plain, coastal plain, and channel bars which are generally considered as very high groundwater potentiality.

13.4.3 Land Use/Land Cover (LU/LC)

LU/LC is one of the most controlling factors of groundwater recharge process through changing the hydrologic response. The major LU/LC present in the ARB are forest plantations (area = 330.82 km^2), rubber (304 km^2), evergreen forest (169 km^2), and mixed plantation (138 km^2) (Fig. 13.2c). Other LU/LC present in the study area are rubber, coconut, double crop, deciduous forest, barren rock, mixed plantation, built up, evergreen forest, forest plantations, fallow land, land with scrub, grassland, wetlands, river, and water bodies.

13.4.4 Soil Texture

Soil permeability and porosity are the major factors controlling groundwater occurrence and movement of a region (Preeja et al. 2011). Infiltration of water is greatly dependent upon the physical characteristics of soil with the most prominent one being the grain size of soil (Preeja et al. 2011). Gravelly clay is the dominating soil texture (area = 39.26%) of ARB followed by clay, sandy, loam, and gravelly loam textures (Fig. 13.3a).

13.4.5 Lineament Density

Lineaments are curvilinear/linear features associated with faults, fractures, and joints. Groundwater storage and movements are influenced by the presence of lineaments, hence the same is considered as reliable indicator of groundwater potential (Achu

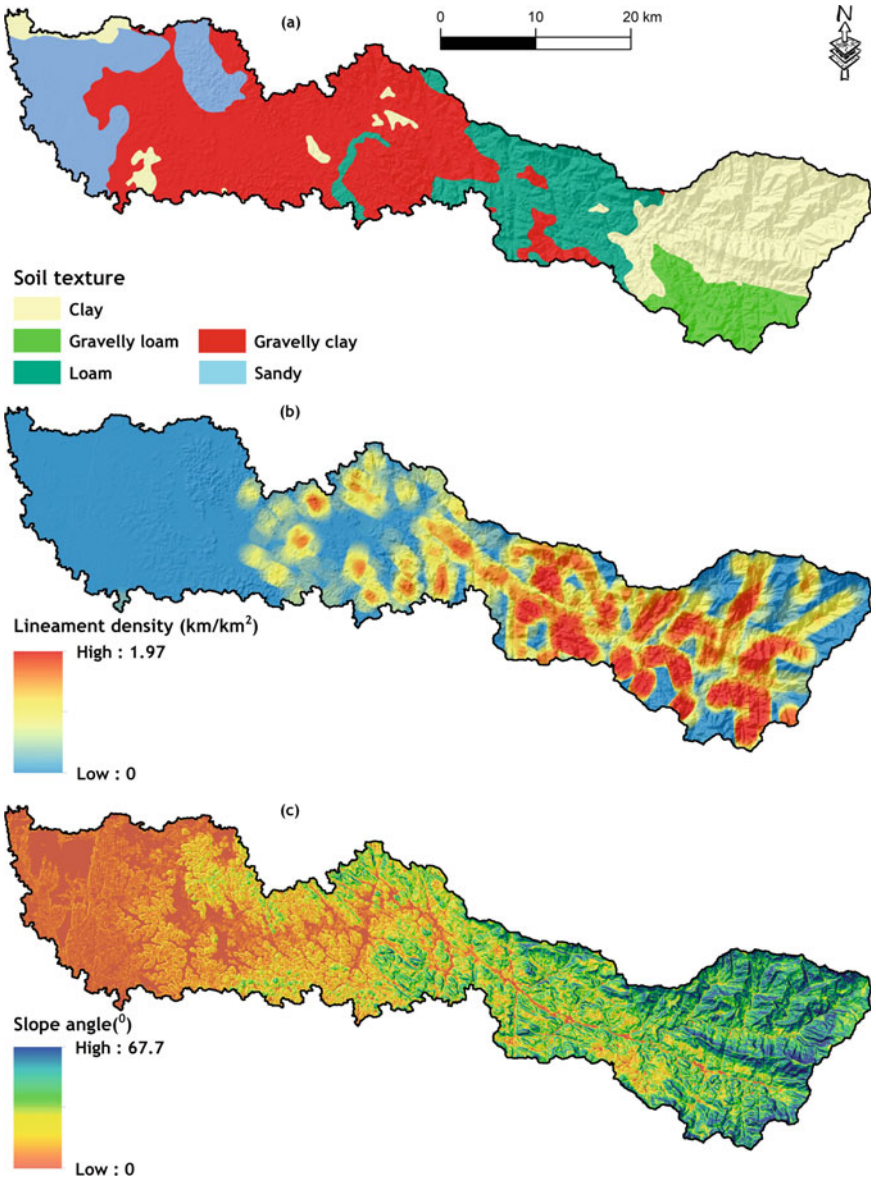

Fig. 13.3 Spatially distributed geo-environmental variables of ARB, **a** soil texture, **b** lineament density, and **c** slope angle

et al. 2020a; Florinsky 2016). The presence of lineaments indicates a permeable zone, as a result of which the groundwater occurrence of an area is indirectly revealed by the lineament density of that area (Magesh et al. 2012). In the ARB, the lineament density ranges from 0 to 1.97 km^2. It is noted that higher lineament density is observed in the eastern part of the basin (Fig. 13.3b). Generally higher the lineament density, higher the groundwater potentiality.

13.4.6 Slope Angle

Slope is major factor that controls the groundwater occurrence of a region by affecting infiltration rate and surface runoff (Dinesh Kumar et al. 2007; Sarkar et al. 2001). For instance, steep slopes are characterized by rapid surface runoff and low infiltration and vice versa. ARB is a highly undulating terrain, where slope angle ranges from 0 to 67.7°. It is noted that slope is relatively higher in eastern portion of the study area and shows a gradual decrease toward western coastal plains (Fig. 13.3c).

13.4.7 Drainage Density

Drainage density can be defined as the total length of stream channels per unit area, and it shows the distribution and spacing of drainage lines on a watershed (Yeh et al. 2016). In ARB, drainage density values range from 0 to 6.04 km/km^2 (Fig. 13.4a) which is further classified into <1 km/km^2 (poor), 1–2 km/km^2 (moderate), 2–3 km/km^2 (good), 3–4 km/km^2 (very good), and >4 km/km^2 (extreme) groundwater potentiality zones and assigned ranks, respectively (Table 13.1). It is noted that the eastern portion of the ARB shows higher drainage density and gradually decreases toward the eastern coastal pain region (Fig. 13.4a).

13.4.8 Topographic Wetness Index (TWI)

TWI is a DEM derivative used to quantify the topographical control on hydrological process (Beven and Kirkby 1979). TWI is a function of upslope contributing area and local slope which is used to determine the surface runoff concentration and soil moisture at given point. In ARB, TWI values range from 3.62 to 24.289 (Fig. 13.4b), which is further classified into five categories such as <10, 10–12, 12–14, 14–20, and >20 and assigned respective ranks (Table 13.1).

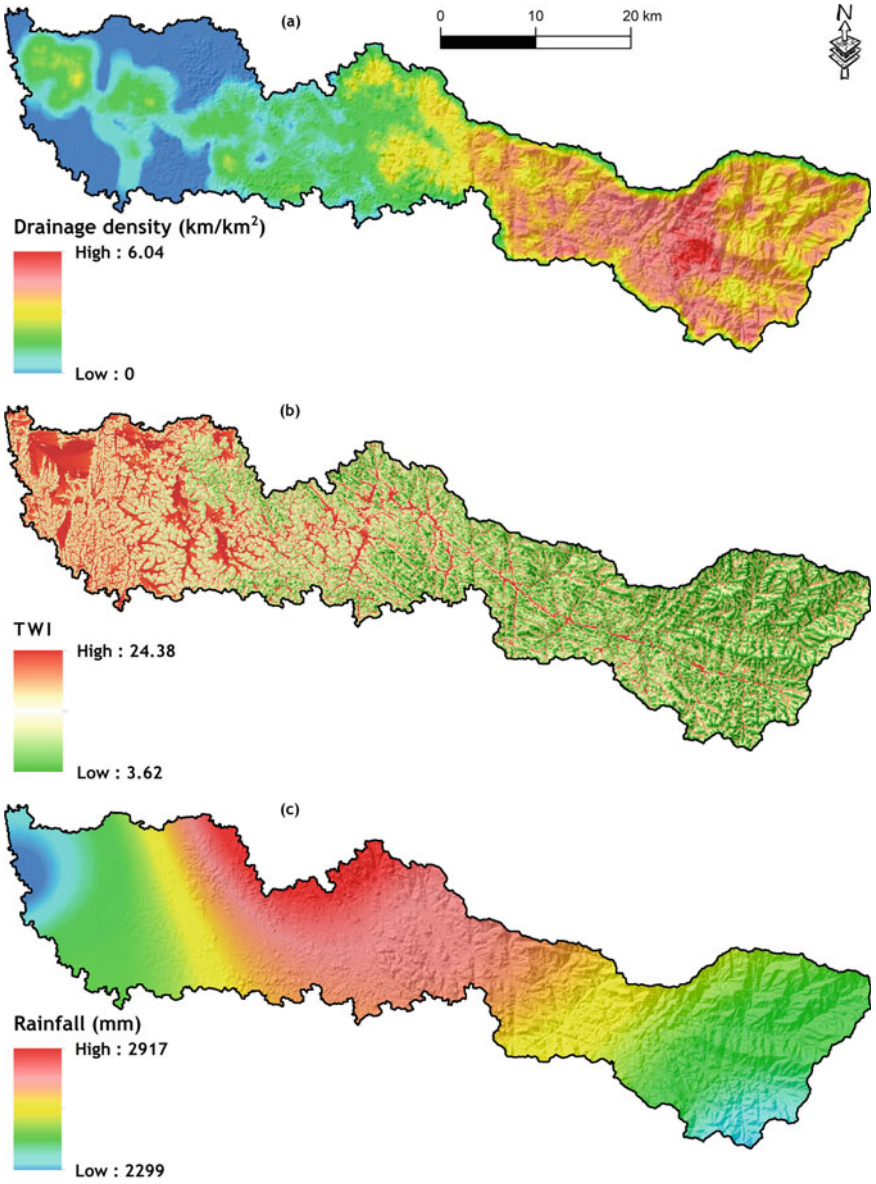

Fig. 13.4 Spatially distributed geo-environmental variables, **a** drainage density, **b** TWI, and **c** rainfall of ARB

Table 13.1 AHP weights (NEV) and CR estimated for ARB

S. No.	Theme	NEV	CR
1	**Lithology**		**1.50E−09**
	Acidic rocks	0.071	
	Basic rocks	0.071	
	Charnockite group of rocks	0.071	
	Khondalite group of rocks	0.071	
	Laterite	0.143	
	Migmatite complex	0.071	
	Sand and silt	0.286	
	Sandstone and clay	0.214	
2	**Geomorphic features**		**3.04E−11**
	Residual hill	0.012	
	Alluvial plain	0.111	
	Channel bar (flood plain)	0.086	
	Coastal plain	0.062	
	Denudational Structural Hills	0.037	
	Linear ridge (Lower Plateau)	0.025	
	Lower Plateau (Lateritic)—dissected	0.074	
	Mud flat (coastal plain)	0.099	
	Piedmont zone	0.074	
	Point bar (flood plain)	0.074	
	Residual mount (Pediment)	0.012	
	Residual mount	0.012	
	Swale (coastal plain)	0.099	
	Valley fill	0.111	
	Waterbody	0.111	
3	**LU/LC**		**3.27E−11**
	Grass land	0.018	
	Coconut	0.054	
	Agriculture plantation	0.054	
	Barren rock/stony waste/sheetrock	0.018	
	Built up	0.036	
	Double crop	0.125	
	Fallow land	0.036	
	Deciduous forest	0.071	
	Evergreen forest	0.089	
	Forest plantations	0.089	

(continued)

Table 13.1 (continued)

S. No.	Theme	NEV	CR
	Rubber	0.036	
	Land with scrub	0.054	
	River/waterbodies	0.161	
	Wetlands (waterlogged)	0.161	
4	**Soil texture**		**1.75E−09**
	Clay	0.053	
	Gravelly clay	0.105	
	Gravelly loam	0.263	
	Loam	0.211	
	Sandy	0.368	
5	**Rainfall (mm)**		**2.66E−11**
	<2400	0.067	
	2400–2500	0.133	
	2500–2600	0.200	
	2600–2700	0.267	
	>2700	0.333	
6	**TWI**		**1.48E−11**
	<10	0.059	
	10–12	0.118	
	12–14	0.176	
	14–20	0.294	
	>20	0.353	
7	**Slope angle**		**1.73E−11**
	<5	0.449	
	5–10	0.224	
	10–20	0.112	
	20–30	0.090	
	30–40	0.075	
	>40	0.050	
8	**Lineament density (km/km^2)**		**6.69E−11**
	<0.5	0.063	
	0.5–1	0.188	
	1–1.5	0.313	
	>1.5	0.438	
9	**Drainage density (km/km^2)**		**6.18E−11**
	<1	0.048	

(continued)

Table 13.1 (continued)

S. No.	Theme	NEV	CR
	1–2	0.095	
	2–3	0.190	
	3–4	0.286	
	>4	0.381	
10	**Data layers**		**1.18E−11**
	LU/LC	0.024	
	Lithology	0.214	
	Drainage density (km/km^2)	0.119	
	Soil texture	0.095	
	Rainfall (mm)	0.143	
	TWI	0.048	
	Slope angle	0.190	
	Lineament density (km/km^2)	0.167	
	Geomorphology	0.200	

13.4.9 Rainfall

Rainfall is another important factor which controlls the occurrence and movement of groundwater in a region. Intensity and duration are the two rainfall parameters which affect infiltration rate and thereby groundwater occurrence (Arulbalaji et al. 2019). ARB receives average annual rainfall between 2299 and 2917 mm and ~ 80% of the rainfall during Indian summer monsoon (Fig. 13.4c). The annual average rainfall of ARB is further classified into five categories such as <2400 mm zones, 2400–2500 mm zones, 2550–2600 mm zones, 2600–2700 mm zones, and >2700 mm zones, and ranks are assigned, respectively (Table 13.1).

13.4.10 Relative Importance of the Factors

Though numerous geo-environmental factors influence groundwater recharge, the one factor that contributes highly toward the process can be determined using AHP. Among the factors considered, the prominent one contributing toward groundwater recharge is lithology having NEV value of 0.214 followed by slope angle (0.190), lineament density (0.167), rainfall (0.143), drainage density (0.119), soil texture (0.095), and TWI (0.048) (Table 13.1). The sand and silt have relatively higher rating (0.286) in lithology, while acidic rocks, basic rocks, charnockites rocks, and khondalite rocks have the lowest weightage. The least contributing factor is land use/land cover (0.024), thereby having less influence on groundwater potential. Among the

different geomorphic unit's valley fill (NEV 0.111), Swale (coastal plain) (0.099) and channel bar (flood plain) (0.086) show higher ratings. Generally, these geomorphic units are filled with unconsolidated sediments which have good groundwater potentiality. In the case of land use/land cover, wetlands (0.161), ever green forest (0.089), and forest plantation (0.089) are considered as good groundwater potentiality, whereas grasslands are considered as poor groundwater potentiality. Among the different soil types, sandy soil shows the highest weightage (0.368) followed by gravelly loam (0.263). Clayey soil is generally considered as poor for groundwater potential (0.053), mainly due to its aquiclude nature and restricts water infiltration. In this study, the highest weightage is assigned for those areas which receive maximum rainfall >2700 mm and subsequently considered as good for groundwater potential. TWI is a function of upslope contributing area, where flow accumulation causes higher soil moisture and subsequently higher groundwater occurrence. Therefore, maximum weightage (0.353) is given in TWI category >20. Slope angle controls surface runoff and concentration and thereby a significant factor controls the occurrence of groundwater in a region. In ARB, the highest weightage is given with slope angle less than 5° and vice versa. In the case of lineament density, maximum weightage is assigned in lineament density >1.5 km/km^2 (0.438), and subsequently, minimum values are assigned in least lineament dense areas. In the case of drainage density, maximum NEV is obtained by >4 km/km^2 density class (0.381) and vice versa.

13.4.11 Groundwater Potential Zones (GWPZs)

The GWPZs of the ARB were determined based on various geo-environmental variables, viz. lithology, geomorphic features, land use/land cover, lineament density, drainage density, soil texture, slope angle, TWI, and rainfall using GIS technique and remote sensing. The GWPZ of ARB is derived from the weightages estimated using AHP techniques (Table 13.1) and reclassified into four major categories of groundwater potential, viz. poor groundwater potential zones, moderate groundwater potential zones, good groundwater potential zones, and very good groundwater potential zones (Fig. 13.5). Nearly, 25.03% of ARB belongs to poor groundwater potential zones followed by 25.22% in moderate groundwater potential zones, 25.14% in good groundwater potential zones, and 24.61% as very good groundwater potential zones. Very good groundwater potential zones are concentrated in the western part of the study area as the region has a relatively flat terrain with a greater concentration of sand and silt having low lineament density as well as drainage density, while the eastern part of the study area represents low groundwater potential zones as a result of higher slope and due to the presence of denudational structural zones.

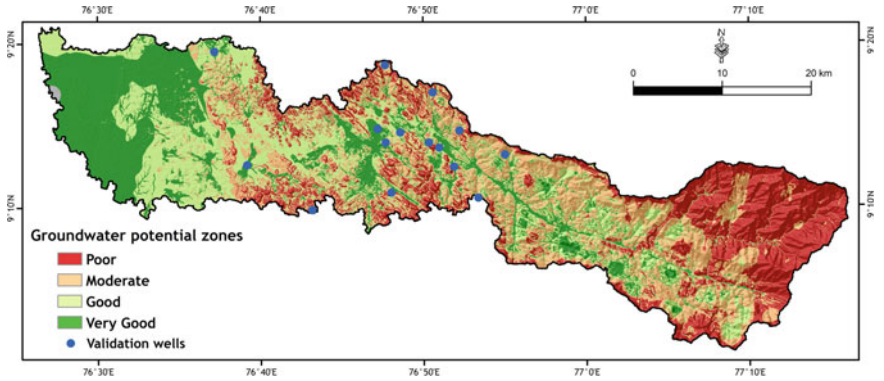

Fig. 13.5 Predicted GWPZs of ARB

The accuracy of the predicted GWPZ map of ARB is estimated by analyzing bivariate relationship between GWPZ and well yield data published by the Central Ground Water Board (CGWB) (Fig. 13.6), which shows a good fit with a R^2 value of 0.790. Therefore, the predicted model is trustworthy for future groundwater management in ARB.

13.4.12 Discussions

The result of the present study is compared with other studies carried out across the globe as well as the regional perspective. Comparison of different variables used for GWPZ in ARB with previous studies with different environmental variables shows that lithology is the major factor which controls the occurrence of groundwater (e.g., Abuzied and Alrefaee 2017; Aykut 2021; Jasrotia et al. 2016). However, Kaur et al. (2020) noticed that soil, rainfall, elevation, and slope were also significant in demarcating GWPZs. The previous studies conducted in Kerala (e.g., Achu et al. 2020a; Arulbalaji et al. 2019; Dinesh Kumar et al. 2007, Preeja et al. 2011) also reported that lithology, geomorphology, slope, and lineament density are the major factors which control the occurrence of groundwater in the region.

The delineation of GWPZS in ARB is highly useful for the implementation of a comprehensive regional sustainable groundwater resource management. Moreover, the classification scheme used in this study enables the authorities to implement site suitable management strategies in each GWPZs for groundwater development of ARB. However, the GWPZ mapping using geo-environmental variables at finer spatial resolution may provide better results.

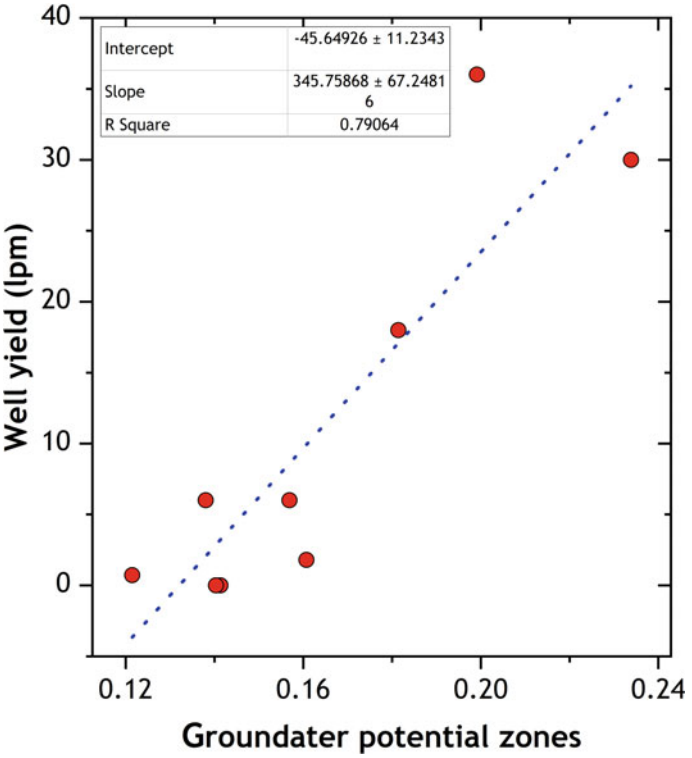

Fig. 13.6 Relationship between well yield and GWPZs

13.5 Summary and Conclusions

GIS and remote sensing are very efficent tools for determining groundwater potential zones of a river basin. The study has focused on the delineation of GWPZs in Achankovil river basin, Kerala, India, by using geospatial technique and analytical hierarchy process (AHP). Various geo-environmental factors like lithology, land use/land cover, lineament density, drainage density, soil texture, slope angle, TWI, and rainfall were used for delineation process. Lithology, geomorphic features, slope angle, lineament density, and rainfall play a critical role in the occurrence of groundwater in the study area. GWPZs of ARB are further classified into poor groundwater potential (area = 25.03%), moderate groundwater potential zones (25.22%), good groundwater potential zones (25.14%), and very good groundwater potential zones (24.61%). The predicted model is validated using the well yield data published by Central Ground Water Board. The model shows a good agreement with field (R^2 = 0.790). The study exemplifies that the knowledge about these groundwater potential zones can be useful for sustainable groundwater management as well as for proper planning for obtaining groundwater.

References

Abuzied SM, Alrefaee HA (2017) Mapping of groundwater prospective zones integrating remote sensing, geographic information systems and geophysical techniques in El-Qaà Plain area, Egypt. Hydrogeol J 25(7):2067–2088. https://doi.org/10.1007/s10040-017-1603-3

Achu AL, Reghunath R, Thomas J (2020a) Mapping of groundwater recharge potential zones and identification of suitable site-specific recharge mechanisms in a tropical river basin. Earth Syst Environ 4(1):131–145

Achu AL, Thomas J, Reghunath R (2020b) Multi-criteria decision analysis for delineation of groundwater potential zones in a tropical river basin using remote sensing, GIS and analytical hierarchy process (AHP). Groundw Sustain Dev 10:100365. https://doi.org/10.1016/j.gsd.2020.100365

Adimalla N, Venkatayogi S (2018) Geochemical characterization and evaluation of groundwater suitability for domestic and agricultural utility in semi-arid region of Basara, Telangana State, South India. Appl Water Sci 8(1):1–14. http://doi.org/10.1007/s13201-018-0682-1

Aju CD, Achu AL, Raicy MC, Reghunath R (2021) Identification of suitable sites and structures for artificial groundwater recharge for sustainable water resources management in Vamanapuram River Basin, South India. HydroResearch 4:24–37. https://doi.org/10.1016/j.hydres.2021.04.001

Arulbalaji P, Padmalal D, Sreelash K (2019) GIS and AHP techniques-based delineation of groundwater potential zones: a case study from southern Western Ghats, India. Sci Rep 9(1):1–17

Aykut T (2021) Determination of groundwater potential zones using geographical information systems (GIS) and analytic hierarchy process (AHP) between Edirne-Kalkansogut (northwestern Turkey). Groundw Sustain Dev 12:100545. https://doi.org/10.1016/j.gsd.2021.100545

Beven KJ, Kirkby MJ (1979) A physically based, variable contributing area model of basin hydrology/Un modèle à base physique de zone d'appel variable de l'hydrologie du bassin versant. Hydrol Sci J 24(1):43–69

Bougharioua E, Allouche N, Brahim FB, Nasri G, Bouri S (2021) Delineation of groundwater potentials of Sfax region, Tunisia, using fuzzy analytical hierarchy process, frequency ratio, and weights of evidence models. Environ Dev Sustain 1–26

Braun I, Montel JM, Nicollet C (1998) Electron microprobe dating of monazites from high-grade gneisses and pegmatites of the Kerala Khondalite Belt, southern India. Chem Geol 146(1–2):65–85

CGWB (2017) Dynamic groundwater resource of India (as on 31st March 2013). Central Groundwater Board, Faridabad

Dhanya V (2014) Basin asymmetry and associated tectonics: a case study of Achankovil river basin, Kerala. Transactions 36(2)

Dinesh Kumar PK, Gopinath G, Seralathan P (2007) Application of remote sensing and GIS for the demarcation of groundwater potential zones of a river basin in Kerala, southwest coast of India. Int J Remote Sens 28(24):5583–5601. https://doi.org/10.1080/01431160601086050

Florinsky I (2016) Digital terrain analysis in soil science and geology. Academic Press

Forootan E, Seyedi F (2021) GIS-based multi-criteria decision making and entropy approaches for groundwater potential zones delineation. Earth Sci Inf 14(1):333–347

Gopinath G, Seralathan P (2004) Identification of groundwater prospective zones using IRS-ID LISS III and pump test methods. J Indian Soc Remote Sens 32(4):329–342

Hameed AS, Resmi TR, Suraj S, Warrier CU, Sudheesh M, Deshpande RD (2015) Isotopic characterization and mass balance reveals groundwater recharge pattern in Chaliyar river basin, Kerala, India. J Hydrol Reg Stud 4:48–58. http://doi.org/10.1016/j.ejrh.2015.01.003

Israil M, Al-Hadithi M, Singhal DC (2006) Application of a resistivity survey and geographical information system (GIS) analysis for hydrogeological zoning of a piedmont area, Himalayan foothill region, India. Hydrogeol J 14(5):753–759

Jasrotia AS, Kumar A, Singh R (2016) Integrated remote sensing and GIS approach for delineation of groundwater potential zones using aquifer parameters in Devak and Rui watershed of Jammu and Kashmir, India. Arab J Geosci 9(4):304. https://doi.org/10.1007/s12517-016-2326-9

Jesiya NP, Gopinath G (2018) Groundwater suitability zonation with synchronized GIS and MCDM approach for urban and peri-urban phreatic aquifer ensemble of southern India. Urban Water J 15(8):801–811

Jesiya NP, Gopinath G (2019) A customized Fuzzy AHP-GIS based DRASTIC-L model for intrinsic groundwater vulnerability assessment of urban and peri urban phreatic aquifer clusters. Groundw Sustain Dev 8:654–666

Kamaraju MVV, Bhattacharya A, Reddy GS, Rao GC, Murthy GS, Rao TCM (1996) Ground-water potential evaluation of West Godavari District, Andhra Pradesh State, India—a GIS approach. Groundwater 34(2):318–325. https://doi.org/10.1111/j.1745-6584.1996.tb01891.x

Karanth KR, Seshubabu K (1978) Identification of major lineaments on satellite imagery and on aerial photographs for delineation for possible potential groundwater zones in Penukonda and Dharmavaram taluks of Anantapur district. In: Proceedings of the joint Indo-US workshop on remote sensing of water resources. National Remote Sensing Agency (NRSA), Hyderabad, India, pp 188–197

Kaur L, Rishi MS, Singh G, Thakur SN (2020) Groundwater potential assessment of an alluvial aquifer in Yamuna sub-basin (Panipat region) using remote sensing and GIS techniques in conjunction with analytical hierarchy process (AHP) and catastrophe theory (CT). Ecol Ind 110:105850. https://doi.org/10.1016/j.ecolind.2019.105850

Krishnamurthy J, Venkatesa Kumar N, Jayaraman V, Manivel M (1996) An approach to demarcate ground water potential zones through remote sensing and a geographical information system. Int J Remote Sens 17(10):1867–1884. https://doi.org/10.1080/01431169608948744

Lee S, Hong SM, Jung HS (2018) GIS-based groundwater potential mapping using artificial neural network and support vector machine models: the case of Boryeong city in Korea. Geocarto Int 33(8):847–861

Magesh NS, Chandrasekar N, Soundranayagam JP (2012) Delineation of groundwater potential zones in Theni district, Tamil Nadu, using remote sensing, GIS and MIF techniques. Geosci Front 3(2):189–196

Mahala A (2021) Delineating the status of groundwater in a plateau fringe region using multi-influencing factor (MIF) and GIS: a study of Bankura District, West Bengal, India. In: Geostatistics and geospatial technologies for groundwater resources in India, pp 215–237

Manu MS, Anirudhan S (2008) Drainage characteristics of Achankovil river basin, Kerala. J Geol Soc India 71(6):841–850 (Online archive from vol 1 to vol 78)

Margat J, Van der Gun J (2013) Groundwater around the world: a geographic synopsis. CRC Press, Boca Raton

Masroor M, Rehman S, Sajjad H, Rahaman MH, Sahana M, Ahmed R, Singh R (2021) Assessing the impact of drought conditions on groundwater potential in Godavari Middle Sub-Basin, India using analytical hierarchy process and random forest machine learning algorithm. Groundw Sustain Dev 13:100554

Moghaddam DD, Rahmati O, Panahi M, Tiefenbacher J, Darabi H, Haghizadeh A, Haghighi AT, Nalivan OA, Bui DT (2020) The effect of sample size on different machine learning models for groundwater potential mapping in mountain bedrock aquifers. CATENA 187:104421

Naghibi SA, Ahmadi K, Daneshi A (2017) Application of support vector machine, random forest, and genetic algorithm optimized random forest models in groundwater potential mapping. Water Resour Manage 31(9):2761–2775

Prasad MBK, Ramanathan AL (2005) Solute sources and processes in the Achankovil River Basin, Western Ghats, Southern India/Sources de Solutés et Processus Associés Dans le Bassin du Fleuve Achankovil, Ghats Occidentaux, Inde du Sud. Hydrol Sci J 50(2). http://doi.org/10.1623/hysj.50.2.341.61798

Prasad MBK, Ramanathan AL, Shrivastav SK, Saxena R (2006) Metal fractionation studies in surfacial and core sediments in the Achankovil river basin in India. Environ Monit Assess 121(1):77–102. http://doi.org/10.1007/s10661-005-9108-2

Prasad P, Loveson VJ, Kotha M, Yadav R (2020) Application of machine learning techniques in groundwater potential mapping along the west coast of India. Giscience Remote Sens 57(6):735–752

Preeja KR, Joseph S, Thomas J, Vijith H (2011) Identification of groundwater potential zones of a tropical river basin (Kerala, India) using remote sensing and GIS techniques. J Indian Soc Remote Sens 39(1):83–94. http://doi.org/10.1007/s12524-011-0075-5

Rane NL, Jayaraj GK (2021) Comparison of multi-influence factor, weight of evidence and frequency ratio techniques to evaluate groundwater potential zones of basaltic aquifer systems. Environ Dev Sustain 1–30

Reddy PR, Kumar KV, Seshadri K (1996) Use of IRS-1C data in groundwater studies. Curr Sci 600–605. https://www.jstor.org/stable/24097380

Saaty TL (1990) Multicriteria decision making: the analytic hierarchy process: planning, priority setting resource allocation

Sachdeva S, Kumar B (2021) Comparison of gradient boosted decision trees and random forest for groundwater potential mapping in Dholpur (Rajasthan), India. Stoch Env Res Risk Assess 35(2):287–306

Sander P, Chesley MM, Minor TB (1996) Groundwater assessment using remote sensing and GIS in a rural groundwater project in Ghana: lessons learned. Hydrogeol J 4(3):40–49. https://doi.org/10.1007/s100400050086

Saraf AK, Choudhury PR (1998) Integrated remote sensing and GIS for groundwater exploration and identification of artificial recharge sites. Int J Remote Sens 19(10):1825–1841. http://doi.org/10.1080/014311698215018

Saraf AK, Jain SK (1994) Integrated use of remote sensing and geographical information system methods for groundwater exploration in parts of Lalitpur District, UP. In: International conference on hydrology and water resources, New Delhi, 20–22 Dec 1993. Kluwer Academic Publishers, Dordrecht, The Netherlands

Sarkar BC, Deota BS, Raju PLN, Jugran DK (2001) A geographic information system approach to evaluation of groundwater potentiality of Shamri micro-watershed in the Shimla Taluk, Himachal Pradesh. J Indian Soc Remote Sens 29(3):151–164. https://doi.org/10.1007/BF02989927

Shaji E, Gómez-Alday JJ, Hussein S, Deepu TR, Anilkumar Y (2018) Salinization and deterioration of groundwater quality by nitrate and fluoride in the Chittur block, Palakkad, Kerala. J Geol Soc India 92(3):337–345. http://doi.org/10.1007/s12594-018-1017-4

Siebert S, Burke J, Faures JM, Frenken K, Hoogeveen J, Döll P, Portmann FT (2010) Groundwater use for irrigation—a global inventory. Hydrol Earth Syst Sci 14:1863–1880. https://doi.org/10.5194/hess-14-1863-2010

Singh AK, Prakash SR (2002) An integrated approach of remote sensing, geophysics and GIS to evaluation of groundwater potentiality of Ojhala sub-watershed, Mirjapur district, UP, India. In: Asian conference on GIS, GPS, aerial photography and remote sensing, Bangkok, Thailand

Singha S, Das P, Singha SS (2021) A fuzzy geospatial approach for delineation of groundwater potential zones in Raipur district, India. Groundwater Sustain Dev 12:100529

Swetha TV, Gopinath G, Thrivikramji KP, Jesiya NP (2017) Geospatial and MCDM tool mix for identification of potential groundwater prospects in a tropical river basin, Kerala. Environ Earth Sci 76(12):1–17

Tamiru H, Wagari M (2021) Comparison of ANN model and GIS tools for delineation of groundwater potential zones, Fincha Catchment, Abay Basin, Ethiopia. Geocarto Int 1–13 (just-accepted)

WWAP (2012) World Water Assessment Programme: the United Nations World Water Development report 4: managing water under uncertainty and risk

Yeh HF, Cheng YS, Lin HI, Lee CH (2016) Mapping groundwater recharge potential zone using a GIS approach in Hualian River, Taiwan. Sustain Environ Res 26(1):33–43. https://doi.org/10.1016/j.serj.2015.09.005

Chapter 14
Management of Environmentally Stressed Areas in Watershed Using Multi-criteria Decision Tool in GIS: A Noble Technique to Conserve Soil for Agriculture

Rahul Kumar Jaiswal, Shalini Yadav, and Ram Narayan Yadava

Abstract Soil erosion is a natural process that affects land productivity and is considered one of the most significant environmental hazards. The climate, landscape and land cover, and conservation practices are the factors that are accountable for the rate and quantum of erosion which varies spatially and temporally. The geographic information system (GIS) can analyze the spatial variability of different forces responsible for soil erosion and is widely used for the demarcation of hazardous areas and suitable conservation measures. Here, we have discussed the impacts of water erosion and suggested a framework to identify stressed areas using AHP and GIS-based techniques to suggest conservation measures. The scientifically developed catchment area treatment plan using multilayer information in GIS can control soil erosion up to the maximum possible extent and provide sustainable development of the area. A case study has been presented in the chapter to demonstrate the application of the suggested framework in a catchment of water resource projects.

Keyword Soil erosion · Erosion hazard parameters · Analytical hieratical process (AHP) · Catchment area treatment (CAT) plan

R. K. Jaiswal (✉)
NIH Bhopal, Bhopal, Madhya Pradesh, India
e-mail: jaiswal.nihr@gov.in

S. Yadav
Rabindranath Tagore University, Bhopal, Madhya Pradesh, India

R. N. Yadava
Madhyanchal Professional University, Bhopal, Madhya Pradesh, India

V. P. Singh et al. (eds.), *Application of Remote Sensing and GIS in Natural Resources and Built Infrastructure Management*, Water Science and Technology Library 105,
https://doi.org/10.1007/978-3-031-14096-9_14

14.1 Introduction

Soil erosion is a momentous hazard of modern times which has several harmful effects on the environment and agriculture production and is one of the principal drivers of land degradation (Perry et al. 2021; Gessesse et al. 2014; Houyou et al. 2016). The soil erosion loses top productive soil which contains important nutrients for the production of crops. Soil erosion is widely acknowledged as major problem well-being of society due to expanding population, urbanization, climate change, etc. (Issaka and Ashraf 2017). Moriasi et al. (2018) emphasized that erosion may cause disasters such as loss of capacities of reservoirs and floods during rainfall events and shifts in initial land suitability and capabilities. According to an estimate, 17% of the soils in different continents are affected by water erosion, which has emerged as an issue for conservation efforts in the twenty-first century (Suriaprasit and Shrestha 2008; Walling and Fung 2003). A broad estimate of soil erosion in India showed that the soil in the range of about 5334×10^6 tonnes is being lost with a rate of 16.35 tonnes/hectare/year (Saroba 2017), which is more than the permissible loss of 4.5–11.2 tonnes/hectare/year (Narayana and Babu 1983).

Gomiero (2016) (Singh et al. 1981) mentioned the declaration of the United Nation in its Sixty Eighth Assembly that the soil is key to the sustenance of life on earth which are essential for agriculture, ecology, and food production. The United National in its report pointed out that the increasing population exerts more pressure, and the sustenance of soils is the key to increasing the yield. Healthy soils can be ensured through sustainable management which leads to the stability and sustainability of the ecosystem and ultimately the food security of the world. Economic and social development which is possible soil management may be the key to success for poverty eradication and women's empowerment. The UN expressed an urgent need to address climate change, land degradation, water availability, climate change, and drought due to the threat on the globe.

Soil erosion has several negative consequences, and the most serious of which is nutrient loss from agricultural fields, which has a significant influence on crop productivity in poor nations (Gomiero 2016). Soil erosion has detrimental effects on the capacity of reservoirs due to sedimentation. The study of erosion from catchments is critical because sediment deposition in reservoirs diminishes reservoir capacity, limits water availability for approved uses, and may cause breaching of the river reach. Land degradation due to soil erosion affects agriculture productivity, water quality, and quantity, hydrological and environmental systems as various causing ecological imbalance and subsequent siltation and flood problems. According to an investigation by the Indian Council of Agriculture Research (ICAR), nearly 174 million ha of land in India is affected by deprivation. The fertility and productivity are mostly determined by the topsoil, which, in addition to producing biomass, serves a variety of other well-known roles.

The soil can be eroded by different agents including wind, water, and gravitation forces. The wind is the primary force of erosion of soil in arid, water in semi-arid and humid, while water and gravitational force in the mountainous region. Land uses,

land cover, and topography are the most significant aspects affecting the intensity of erosion (Belay and Mengistu 2021). The soil erosion from water starts in the progressive form from rain splash to sheet to rill to gully and lastly the bank erosion. The different forms of erosion are described below.

14.1.1 Rain Splash Erosion

Rain splash erosion is the first stage of soil erosion when raindrop strikes ware soil and disintegrates the soil aggregate due to non-cohesiveness and absence of appropriate cover. The rainfall intensity, land cover, topography and soil type, etc., are some of the primary factors that affect the disintegration due to splash erosion. Some of the studies in America have indicated that detached soil particles can move up to 0.6 m vertically and 1.5 m longitudinally due to rain splash.

14.1.2 Sheet Erosion

It is the uniform removal of soil in a tiny coat from topsoil due to the forces of raindrops and overland flow. In this erosion, the topsoil in the form of a sheet is removed and generally occurred on sloppy land causing the loss of useful nutrients for crop growth. The sheet erosion generally occurs in ploughed land where soil particles are not bonded and covered. It can spread in very large areas if left unnoticed and no conservation measures are adopted.

14.1.3 Rill Erosion

The rill erosion is an extension of sheet erosion where water concentrates and forms small channels like structures for flowing soil and water. The depth of rills may be up to 0.3 m and can be removed by normal agronomic operation.

14.1.4 Gully Erosion

When more concentrated water passes with higher velocity, the depth of the channel generally along the draining can increase by more than 0.3 m depth that moves by headward erosion. The gully erosion affects the normal agronomic operation and cannot be removed using simple agriculture equipment. It is an unembellished form of loss because it converts the land into unfertile and not suitable for agriculture.

14.1.5 Bank Erosion

It is the last form of erosion due to the water was due to flow of sediment-laden water, the banks of rivers are eroded and submerged in the river. The bank erosion causes permanent loss of land due to excessive soil erosion from upstream areas.

14.2 Soil Erosion in India

The systematic research on soil erosion in India was started in the nineties when Narayana and Rambabu (1983) (Saroba 2017) concluded that 16,400 kg of soil is being lost every year from one hectare of land amounts to 5.3×10^{12} kg. Singh et al. (1992) gave another estimate of 15,200 kg per year from one-hectare land with a total loss of 4.98×10^{12} kg each year. It was estimated about 150million ha of land was affected by soil erosion (National Commission on Agriculture 1976). The recent estimate of the National Bureau of Soil Survey and Land Use Planning indicated that 119.19 million ha of land suffered from land erosion due to water. The absence of cropping management practices, intense cultivation, tillage before the rainy season, ploughing of marginal land, and extreme climate condition is important factors for soil erosion (Lindstorm et al. 1992; Biswas et al. 2015; Colazo and Buschiazzo 2015; Ligonja and Shrestha 2015). The well-being of small and marginal farmers is affected greatly by soil erosion (Dai et al. 2015; Erkossa et al. 2015; Ochoa-Cueva et al. 2015; Taguas et al. 2015; Prosdocimi et al. 2016). Joglekar (1965) and Varsheney (1975) have suggested several enveloping curves for the prediction of sediment yield for different catchment areas in India. Correlation studies revealed that area alone does not have any significant association with sediment production rate, and hence, it calls for multivariate analysis involving several climatic and physiographic parameters (Jose et al. 1994). Misra et al. (1984) and Bundela et al. (1995) have developed statistical models on a spatial basis for small watersheds in the river Damodar. The runoff plot studies at Vasad were carried out to estimate the '*K*' factor and '*R*' factor for soil and climatic conditions and the '*C*' factor for Mung, Groundnut, and Cowpea (Nema et al. 1978). Prasad and Singh (1994) have reported soil conservation procedures in a part of Rajasthan.

Ram Babu et al. (1978) computed and presented zone-wise erosion index values based on erosion estimated from 44 stations. Singh et al. (1992) collected soil loss from 21 different places and estimated loss estimated from the universal soil loss equation from 64 places for the preparation of an iso-erosion map of India. The analysis of results suggested that mean annual soil loss due to water is lower than 2200 kg/acre for forests with a cover of more than 40%. Narain et al. (1993) have mapped erosion quantitatively in East Bengal and estimated the rate of erosion between 0.0 and 5.0 t/ha/year. A statistically significant spatial model was established by Rao et al. (1996) to estimate sediment yield in the Chenab basin using

geomorphologic, climatic, and cover parameters and revealed the high rates of sedimentation in the Chenab basin and its effect on the existing Salal dam near Jammu. Tiwari (2017) combined USLE with ILWS GIS to foresee soil loss in a part of the Narmada basin.

14.3 Assessment of Soil Erosion

The process-based WEPP was established in the nineties to examine soil erosion. In 1991, the WEPP program allowed for the simulation of soil loss from minor catchments. Many of the CREAMS model's channel routing algorithms (Knisel 1980) were implemented in WEPP and modified as needed (Ascough et al. 1995, 1997; Baffaut et al. 1997). WEAP (Lindley et al. 1995) also created a novel component to estimate sediment deposition in impoundments. WEPP is a continuous simulation tool that may drive outflow and erosion dynamics using either observed or generated climate inputs. Based on long-term weather station records and weather inputs from the CLIGEN.

The USLE model assesses the spatial distribution of loss using climatic, topographic, and management factors. The USLE model is the result of several field plot studies carried out in the USA to develop empirical equations in the multiplication of six different factors. After the invention of the USLE model, several scientists used USLE and developed many other models for the estimation of soil loss (Nearing et al. 1989; Alewell et al. 2019; Borrelli et al. 2018; D'Ambrosio et al. 2001; Diodato et al. 2017; Veihe et al. 2001).These models are mostly empirical soil erosion equations that use remote sensing to integrate soil, climate, vegetation, and topography information (Shen et al. 2003; Devatha et al. 2015).The remote sensing data can be manipulated in a GIS environment for the development of the USLE/RUSLE model to serve as an effective approach for computing soil loss from vulnerable areas in the watershed (Kayet et al. 2018; Fu et al. 2005). The GIS tool for the determination of land use from Landsat data applied to foresee the '*C* factor' of USLE is in the research done by El Jazouli et al. (2017) and Lim et al. (2005). The NDVI was found suitable for the design of the *C* factor (Fu et al. 2006; Zhang et al. 2009).

14.4 Watershed Prioritization and Design of SWC Measures

The identification of hot spots and the development of catchment area treatment plans pave the sustainable development of watersheds in the long run. In developing countries like India, it is not feasible to apply simultaneously at all places, and it is prudent to identify susceptible areas where more intensive soil conservation can be applied. Soil erosion is affected by several factors including topography, land cover,

meteorological factors, geology and geomorphology, and management practices. Regionally distributed characteristics or constraints with appropriate weights are used for the identification of degraded areas, and MCDM models are commonly regarded as quite beneficial in resolving decision-making conflicts (Ayalew et al. 2020). For the first time, Jaiswal et al. (2013) (Fathizad et al. 2014) introduced the application of Saaty's analytical hierarchical process (Khemiri et al. 2017) for the prioritization of watersheds. SAHP is the most widely applied MCDM, which uses hierarchical assemblies to portray an issue and then produces primacies for the possibilities based on the user's judgment.

An effective catchment area treatment (CAT) plan is a key factor to make water resource (WR) projects eco-friendly and sustainable. The RSdata due to their synoptic viewing, huge extent coverage, and manipulation capability in the GIS environment have immense potential in the field of prioritization, conservation, and land resource planning (Jaiswal et al. 2013; Saaty 1980; Ahmad and Pandey 2019; Kockel et al. 2020; Kushwaha et al. 2010; Pandey et al. 2007). Jaiswal et al. (2014) (Yoshino and Ishioka 2005) used a weighted overlay technique of spatially distributed thematic maps in GIS for the selection of SWC measures. Here, a case study is being presented where a decision support system has been developed for the identification of priority sub-watersheds and scientifically designed SWC measures have been suggested in a management plan for implementation under govt. funded rural employment schemes.

14.5 Application of GIS

The parameters used for the identification of environmentally stressed areas vary spatially and GIS plays the central role to depict variation in the watershed/catchment. The GIS can handle raster and vector data with their location on earth and can be manipulated to obtain desired results. The significant advantage of the GIS application is to handle remote sensing data which is helpful to give important information like land use, drainage, vegetation, etc. The DEM can be analyzed to excerpt the slope and parameters of soil loss. The geomorphological parameters can also be computed in GIS. The identification of appropriate locations and areas for different conservation measures can be made easy in GIS by the weighted overlay method. The GIS has added benefits of the availability of data readily to different users, low cost, and fewer measurement errors. Here, we are going to introduce a framework consisting of two interrelated modules that have been proposed that can be used for the scientific identification of environmentally degraded areas and suggestions for SWC measures for the catchment of the Kodar reservoir.

14.6 Case Study

14.6.1 Module-I: Prioritization

In the Kodar catchment, SAHP was utilized to select stressed sub-watersheds. In AHP, the factors that influence the choice are identified with expert consultation and field knowledge, and here we have chosen nine criteria that influence soil erodibility and dubbed them erosion hazard parameters (EHPs).The prioritization of the watershed was carried out using two steps. The first step consists of the estimation of EHPs and then applying decision support to determine the weights of these EHPs and priority sub-watersheds. The workflow of module-I has been presented in Fig. 14.1.

The erosional process depends primarily on agents of erosion and then on soil properties which are responsible for the detachment and movement of soils from their original location. The soil parameters are basic inputs in erosion models; therefore, infiltration, saturated hydraulic conductivity, texture, sp. gravity, and dry density were computed on 11 sites.

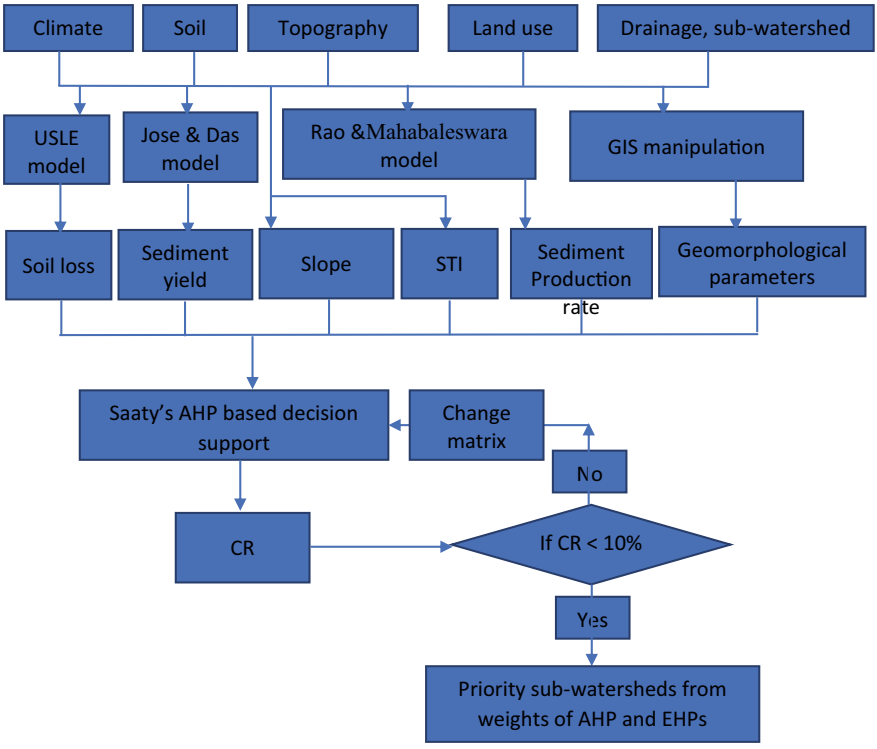

Fig. 14.1 Workflow for module-1

14.6.1.1 Erosion Hazard Parameters (EHP)

In the study, nine erosion hazard parameters have been identified and computed for Kodar catchment as per the details given below.

14.6.1.2 Soil Loss

The RUSLE model is a widely used method (Xie et al. 2022; Jaiswal et al. 2014; Renard and Freimund 1994; Malczewscki 1999; Baskan et al. 2010; Tang et al. 2014; Pan and Wen 2014; Bhandari et al. 2015) that groups landscape, rainfall, and management possible alternatives into six parameters for computation of soil loss (A in t ha^{-1} yr^{-1}).

$$\begin{aligned} A = {} & \text{Erosivity Factor}(R) * \text{Erodibility Factor}(K) * \text{Slope Length Factor}(L) \\ & * \text{Slope Steepness Factor}(S) * \text{Crop Manag. Factor}(C) \\ & * \text{Cons. Practice Factor}(P) \end{aligned} \tag{14.1}$$

14.6.1.3 Sediment Production Rate (SPR)

A sediment prediction rate (ha-m/100 km^2/year) model given by Jose and Das (1982) (Gaubi et al. 2017) was applied and represented by the following equation.

$$\begin{aligned} \text{Log(SPR)} = {} & 4919.80 + 48.64 \log(100 + \text{Form Factor}) \\ & - 1337.77 \log(100 + \text{Circulatory Ratio}) \\ & - 1165.65 \log(100 + \text{Compactness Coefficient}) \end{aligned} \tag{14.2}$$

14.6.1.4 Sediment Yield (SY)

The simple empirical model that uses rain (cm), grade, LU factor (F), and drainage density (km/km^2) to determine sediment yield (V_s in Mm^3/yr) is used for analysis and presented below (Mishra and Nagarajan 2010).

$$\begin{aligned} V_s = {} & 1.067 \times 10^{-3} * \text{Rain}^{1.384} * \text{Area}^{1.292} * \text{Drainage Density}^{0.392} \\ & * \text{Slope}^{0.129} * \text{F}^{2.51} \end{aligned} \tag{14.3}$$

The LU factor (F) can be computed using Eq. (14.4) knowing DF: dense or reserved forest, DGF: degraded forest, AG: agriculture area, PS: pasture, WL: wasteland

$$F = \frac{0.21 * \mathrm{DF} + 0.2D * \mathrm{GF} + 0.6 * \mathrm{AG} + 0.8 * \mathrm{PS} + \mathrm{WL}}{\text{Total Area}} \tag{14.4}$$

14.6.1.5 Sediment Transport Index (STI)

The STI uses the two-dimensional catchment area (A) along with slope (S) to represent overland flow and can be expressed as:

$$\mathrm{STI} = \left[\frac{A}{22.13}\right]\left[\frac{\sin(S)}{0.0896}\right]^{1.3} \tag{14.5}$$

14.6.1.6 Slope (SLP)

It is one of the most critical characteristics that has bearing on the conveyance of disconnected material. Soil erosion is more common in places with a steep slope, which can result in gullies and a loss of fertility.

14.6.1.7 Geomorphological Parameters

Geomorphology, which is commonly employed in prioritization (Jose and Das 1982; Rao and Mahabaleswara 1990; Yadav et al. 2020), is crucial to the formation of landforms and the erosion mechanism. For the selection of priority sub-watersheds, geomorphological EHPs such as drainage density (D_d: km/km^2), channel frequency (C_f: no/km^2), form factor (R_f: km^{-1}), and circulatory ratio (R_c) (Chopra et al. 2005) were utilized. Knowing the length of the ith segment (L_i in m) with total n segments, area (A in km^2), basin length (L in km), and A_p is the area of a sphere has the perimeter same as the periphery of the basin.

$$D_\mathrm{d} = \frac{\sum_{i=1}^{n} \mathrm{Li}}{A} \tag{14.6}$$

$$C_\mathrm{f} = \frac{\sum n}{A} \tag{14.7}$$

$$R_\mathrm{f} = \frac{A}{L^2} \tag{14.8}$$

$$R_\mathrm{c} = \frac{A}{A_\mathrm{p}} \tag{14.9}$$

14.6.1.8 Decision Support of the Identification of Stressed Areas/Sub-watersheds

In AHP, the comparison matrix is constructed by comparing each element with the remaining on a scale of 0 to 9 and can be seen in literature (Fathizad et al. 2014). The weight of each factor can be calculated using the eigenvector of the normalized pair-wise matrix. The consistency ratio is calculated using the following equation to determine the consistency of judgment:

$$\text{Consistancy Ratio} = \frac{\text{Consistancy Index}}{\text{Random Consistancy Index}} * 100 \tag{14.10}$$

Here, the consistency index (CI) was computed by Eq. (14.11).

$$\text{Random Consistancy Index} = \frac{\text{Primary Eigen Value}}{\text{Number} - 1} \tag{14.11}$$

The primary eigenvalue (Barman et al. 2021) can be computed approximately by calculating the product of the pair-wise comparison matrix. The unitless random consistency for different numbers of members can be taken from below given Table 14.1 (Fathizad et al. 2014).

14.6.2 Module-II: Development of CAT Plan for SWC Measures

For the CAT plan, the land use and other thematic maps (Fig. 14.2) were overlaid, and appropriate conservation strategies were identified using the criteria adopted from the literature review (Yoshino and Ishioka 2005).After crossing the slope, land use, and soil maps, an attribute table may be generated to specify various agronomic parameters for agricultural land and biological measures for the barren and open forest.

Table 14.1 Random consistency index for different numbers of members in the decision

Number	1	2	3	4	5	6	7	8	9	10
Ran. Con. index	0	0	0.58	0.90	1.12	1.24	1.32	1.41	1.45	1.49

N is the sample size and *RI* is the random consistency index

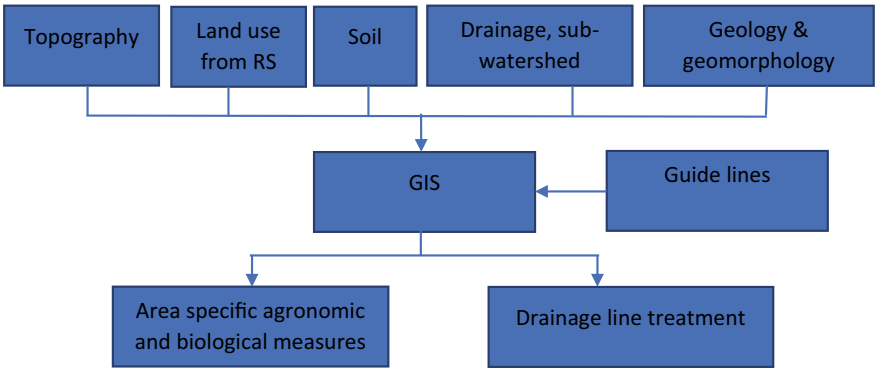

Fig. 14.2 Workflow for module-II

14.7 Study Area and Data Used

The Kodar reservoir (catchment area: 317.17 km^2), which was built over the Kodar River in Chhattisgarh has been chosen to apply the proposed framework for developing a scientific management plan including an effect assessment study. The location map of Kodar reservoir in India is presented in Fig. 14.3.

The meteorological data of Raipur from 1981 to 2008 was used in the analysis. A gauge site at Koma village was established to collect runoff and sediment data from 2010 to 2012. Various in-situ (infiltration and permeability) and laboratory (texture and densities) soil analyses were conducted in the catchment and LISS IV data were used for the detection of land use.

14.8 Results and Discussion

14.8.1 Module-I: Prioritization of Sub-watersheds

Module-1 was designed to identify priority sub-watersheds for this detailed soil investigation on eleven sites that were carried out in the basin.

14.8.1.1 Soil Investigation

On eleven sites, a detailed soil investigation was carried out for infiltration, saturated hydraulic conductivity, and texture (Fig. 14.4). The results of the analysis have been used in prioritization and input layer for the preparation of a treatment plan. The soil properties responsible for erosion at different sites in the basin are presented in Table 14.2. The soils in the catchment of Kodar reservoir are silty loam and sandy loam.

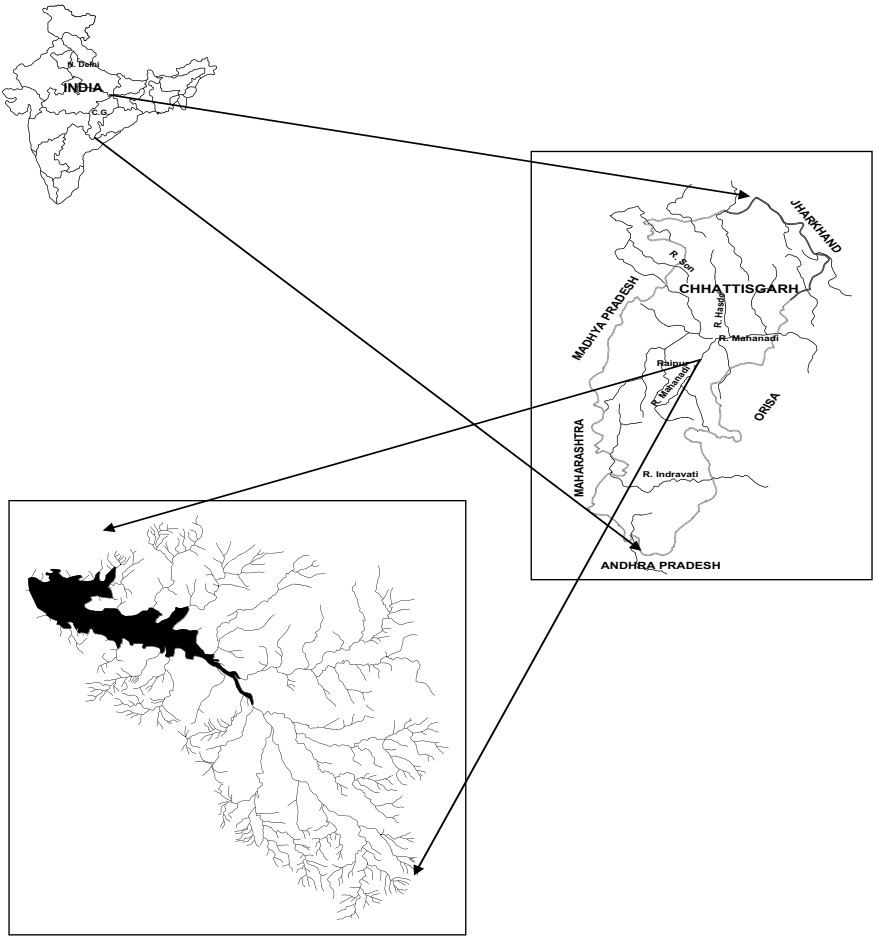

Fig. 14.3 Location map of Kodar reservoir and its catchment

14.8.1.2 Watershed Prioritization

The watershed was partitioned into 67 sub-watersheds using drainage and DEM (0.05–13.05 km^2). For all 67 sub-watersheds, the geographic distribution of all selected EHPs was computed and normalized in the range of 0 to 1.Saaty's AHP was applied to get the weights of each EHP in the decision-making. The weights of different factors are presented in Fig. 14.5. Different factors of the RUSLE model and soil loss are given in Table 14.3. The matrix and weights of different EHPs can be seen in Jaiswal et al. (2013) (Fathizad et al. 2014). The priority-wise sub-watersheds of the Kodar are presented in Fig. 14.6.

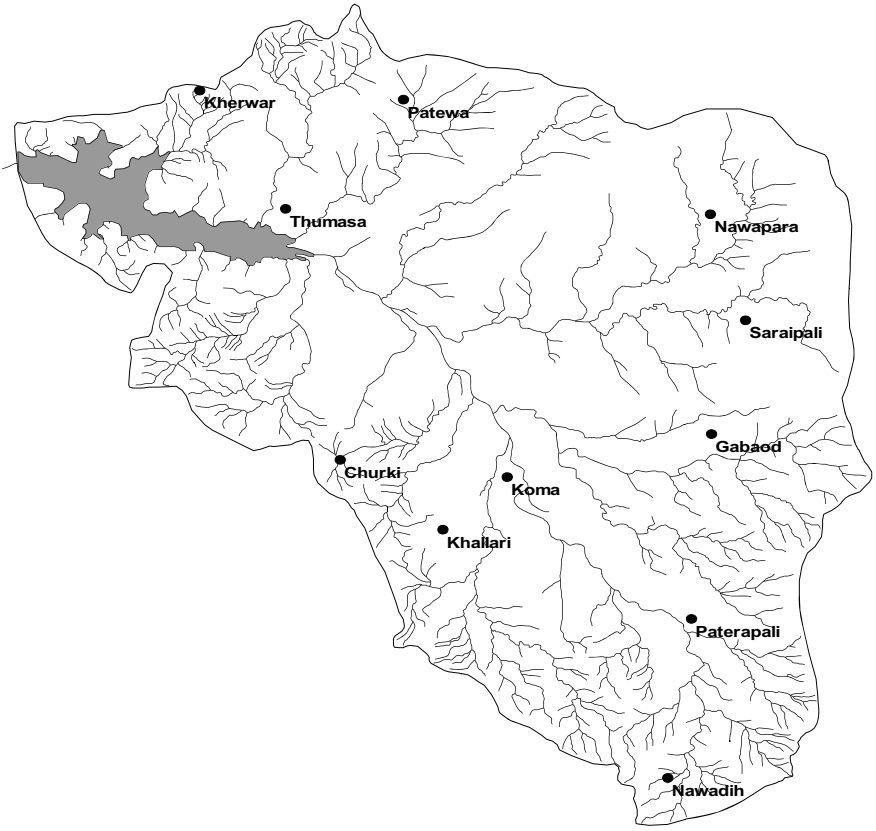

Fig. 14.4 Test sites for soil investigation

14.8.2 Module-II CAT Plan for Soil Water Conservation Measures

Land use, soil, slope, and geomorphology maps were used to create the CAT plan for the Kodar catchment. For the identification of regions amenable for agronomic and biological measures, standard criteria were employed. For the crossing map, an attribute table in ILWIS was created to select appropriate locations under different gram panchayats in the river basin. Check dams, gully plugs, Nala plugs, and boulder bunds have all been suggested as mechanical treatments in the catchment. Figure 14.7 depicts the CAT plan of the study area, which includes ideal locations for agronomic and biological soil conservation measures, as well as the positioning of mechanical measures. The CAT plan consists of the following important measures along with agronomic measures contour farming, mulching, etc., in all agriculture fields.

Table 14.2 Soil properties of soils in Kodar reservoir catchment

Site	Village	Soil type	Sat. hyd. cond. (cm/h)	Dry density (gm/cm^3)	Moisture content (%)	Bulk density (gm/cm^3)	Specific gravity
Site-1	Kherwar	Sandy loam	34.07	1.51	2.48	1.55	2.21
Site-2	Patewa	Sandy loam	7.77	1.47	3.97	1.53	2.53
Site-3	Thumsa	Sandy loam	15.38	1.51	1.08	1.52	2.52
Site-4	Nawapara	Silt loam	11.94	1.40	2.68	1.44	2.27
Site-5	Gabod	Silt loam	25.31	1.50	3.24	1.55	2.59
Site-6	Khallari	Silt loam	2.37	1.29	3.42	1.34	2.56
Site-7	Saraipali	Silt loam	7.77	1.37	4.81	1.44	2.50
Site-8	Koma	Silt loam	0.10	1.20	7.18	1.29	2.55
Site-9	Paterapali	Sandy loam	10.50	1.49	2.29	1.51	2.47
Site-10	Churki	Sandy	5.18	1.43	4.82	1.50	2.54
Site-11	Nawadih	Sandy loam	88.95	1.51	1.55	1.53	2.59

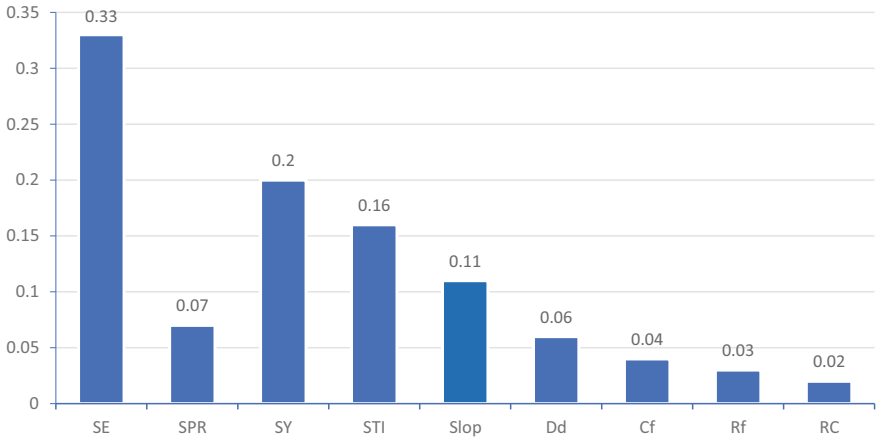

Fig. 14.5 Weights of different EHPs used in prioritization

Table 14.3 Average values of factors for different land uses in the RUSLE model

S. No.	Land use	Area (km^2)	*R*	*K*	SL	C	*P*	Loss (t/ha/yr)
1	Dense forest	48.38	426.28	0.18	2.52	0.18	0.8	27.16
2	Water body	5.81	428.60	0.18	0.29	0.28	0	0.00
3	Scrub	1.22	424.51	0.16	3.77	0.20	0.8	40.02
4	Agriculture	243.86	429.93	0.18	0.37	0.23	0.59	3.98
5	Settlement	7.88	429.32	0.18	0.23	0.22	1.00	3.93

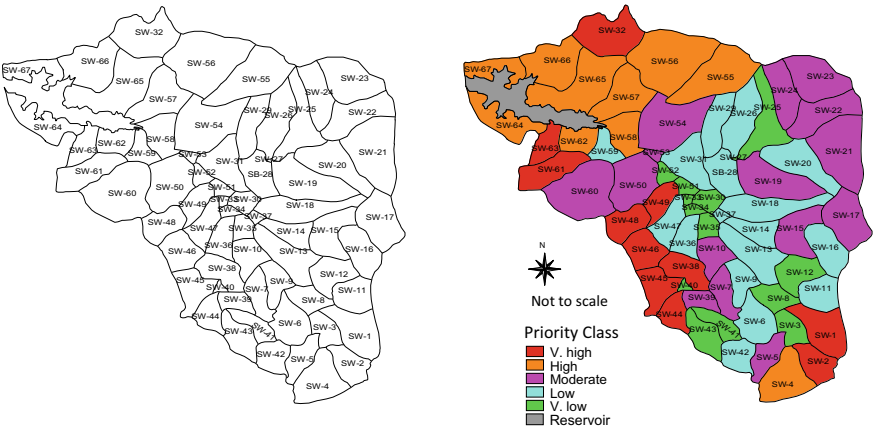

Fig. 14.6 Priority sub-watersheds in Kodar catchment

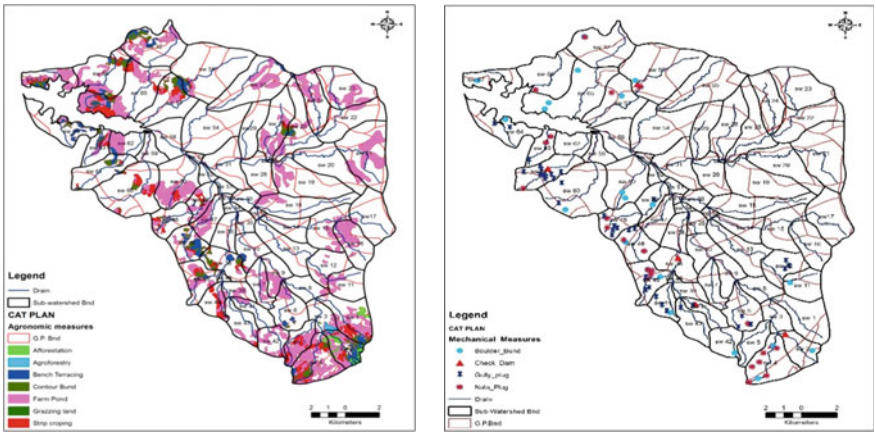

a. Agronomic measures **b. Mechanical measures**

Fig. 14.7 CAT plan for SWC measures in Kodar catchment

Afforestation: 101.61 ha,
Agroforestry: 114.86 ha,
Grazing field: 11.41 ha,
Gully plugs: 37,
Nala plugs: 22,
Boulder bunds: 21,
Check dams: 6.

14.9 Conclusions

Erosion is a serious menace due to increasing population, changes in climatic patterns, and more pressure on the natural resources for the luxury lifestyle. Based on MCDS, the current study has demonstrated a holistic framework for identifying environmentally stressed sub-watersheds and regionally dispersed soil and water conservation methods. The suggested framework has been implemented in the Kodar reservoir catchment of Chhattisgarh state of India. The catchment of Kodar reservoir is infested mainly by agriculture and has a higher erosion due to ploughing of the field just before the start of the monsoon. The detailed soil analysis on eleven sites indicated the loamy nature of soils suspectable to the high rate of erosion in the catchment. SAHP-based choice support has been used to identify priority areas where nine erosion hazard parameters were analyzed and concluded that the soil loss has a maximum impact on prioritization. According to the AHP evaluation, more than 21 sub-watersheds that cover more than 100 km^2 of the Kodar catchment have high vulnerability and need scientifically designed conservation. The proposed CAT plan, which includes the option of agroforestry, may be helpful to the rural community in terms of additional revenue and watershed environmental health. The farm pons which may be the source of catching water for dryland irrigation has been suggested in 41 km^2 areas.

Recommendations

The following are the recommendations from the study:

1. No single parameter can be found the most appropriate for the identification of environmentally stressed areas.
2. The multi-criteria decision support like the analytical hierarchal process can be used conveniently in decision support.
3. The selection of criteria for identification of stressed areas are region-specific and knowledge and geological setup, soils, slope, geomorphology, and land use should be used for the selection of appropriate environmental hazard parameters.
4. The RS and GIS can be used conveniently for the determination of the spatial distribution of different parameters and the identification of the most appropriate soil conservation measures.
5. Climate change may further aggravate soil erosion and the impact of climate variability and extreme events on soil erosion processes should be studied.

6. Soil erosion may reduce crop yield and affect reservoir performance, the identification of stressed sub-watersheds/areas is important to save the investment cost of soil conservation measures.
7. The selection of single criteria may lead to erroneous results and therefore multi-criteria decision support shall be one of the best methods to select priority sub-watersheds/areas.
8. As identification of suitable areas and site-specific soil conservation measures is a difficult task, the weighted overlay technique-based design can be used to identify appropriate soil conservation measures.

Acknowledgements The authors are thankful to the Ministry of Jal Shakti (Earlier known as MoWR, RD and GR), GOI, and Director, NIH, Roorkee (India) for support. We acknowledge the efforts of officials of the WRD (CG) for information collection, field investigation, gauging, etc.

Funding The study presented here was carried out under the Hydrology Project phase II of the Ministry of Jal Shakti (Earlier known as the Ministry of Water Resources) funded by the World Bank.

References

Ahmad N, Pandey P (2019) Role of geospatial technology in conservation, monitoring and management of biological diversity. Environ We Int J Sci Technol 14:1–12

Alewell C, Borrelli P, Meusburger K, Panagos P (2019) Using the USLE: chances, challenges and limitations of soil erosion modelling. Int Soil Water Conserv Res 7(3):203–225

Ascough JC II, Baffaut C, Nearing MA, Flanagan DC (1995) Watershed model channel hydrology and erosion processes. In: Flanagan DC, Nearing MA (eds) USDA-water erosion prediction project hillslope profile and watershed model documentation. NSERL Report No. 10, USDA-ARS National Soil Erosion Research Laboratory, West Lafayette, Indiana

Ascough JC II, Baffaut C, Nearing MA, Liu BY (1997) The WEPP watershed model: I. Hydrology and erosion. Trans Am Soc Agric Eng 40(4):921–933

Ayalew DA, Deumlich D, Šarapatka B, Doktor D (2020) Quantifying the sensitivity of NDVI-based C factor estimation and potential soil erosion prediction using spaceborne earth observation data. Remote Sens 12:1136. https://doi.org/10.3390/rs12071136

Babu R, Tejwani KG, Agarwal MC, Bhushan LS (1978) Distribution of erosion index and iso-erodent map of India. Indian J Soil Cons 6(1):1–12

Baffaut C, Nearing MA, Ascough JC, Liu BY (1997) The WEPP watershed model: II—sensitivity analysis and discretization on small watersheds. Trans Am Soc Agric Eng 40(4):935–943

Barman BK, Rao CUB, Rao KS et al (2021) Geomorphic analysis, morphometric-based prioritization and tectonic implications in Chite Lui river, Northeast India. J Geol Soc India 97:385–395. https://doi.org/10.1007/s12594-021-1696-0

Baskan O, Cebel H, Akgul S, Erpul G (2010) Conditional simulation of USLE/RUSLE soil erodibility factor by geostatistics in a Mediterranean catchment. Turk Environ Earth Sci 60(6):1179–1187

Belay T, Mengistu DA (2021) Impacts of land use/land cover and climate changes on soil erosion in Muga watershed, Upper Blue Nile basin (Abay), Ethiopia. Ecol Process 10:68. https://doi.org/10.1186/s13717-021-00339-9

Bhandari KP, Aryal J, Darnsawasdi R (2015) A geospatial approach to assessing soil erosion in a watershed by integrating socio-economic determinants and the RUSLE model. Nat Hazards 75:321–334. https://doi.org/10.1007/s11069-014-1321-2

Biswas H, Raizada A, Mandal D, Kumar S, Srinivas S, Mishra PK (2015) Identification of areas vulnerable to soil erosion risk in India using GIS methods. Solid Earth 6(4):1247–1257

Borrelli P, Meusburger K, Ballabio C et al (2018) Object-oriented soil erosion modelling: a possible paradigm shift from potential to actual risk assessments in agricultural environments. Land Degrad Dev 29(4):1270–1281

Bundela DS, Singh R, Mishra K (1995) Sediment yield modelling for small watersheds in Barkar river valley. J Inst Eng (I) 76:22–25

Chopra R, Dhiman R, Sharma PK (2005) Morphometric analysis of subwatersheds in Gurdaspur District, Punjab using remote sensing and GIS techniques. J Indian Soc Remote Sens 33(4):531–539

Colazo JC, Buschiazzo D (2015) The impact of agriculture on soil texture due to wind erosion. Land Degrad Dev 26(1):62–70. https://doi.org/10.1002/ldr.2297

Dai Q, Liu Z, Shao H, Yang Z (2015) Karst bare slope soil erosion and soil quality: a simulation case study. Solid Earth 6(3):985–995. https://doi.org/10.5194/se-6-985

D'Ambrosio D, di Gregorio S, Gabriele S, Gaudio R (2001) A cellular automata model for soil erosion by water. Phys Chem Earth Part B 26:33–39

Devatha CP, Deshpande V, Renukaprasad MS (2015) Estimation of soil loss using USLE model for Kulhan watershed Chhattisgarh—a case study. Aquatic Procedia 4:1429–1436

Diodato N, Borrelli P, Fiener P, Bellocchi G, Romano N (2017) Discovering historical rainfall erosivity with a parsimonious approach: a case study in Western Germany. J Hydrol 544

El Jazouli A, Barakat A, Ghafiri A et al (2017) Soil erosion modeled with USLE, GIS, and remote sensing: a case study of Ikkour watershed in Middle Atlas (Morocco). Geosci Lett 4(25). http://doi.org/10.1186/s40562-017-0091-6

Erkossa T, Wudneh A, Desalegn B, Taye G (2015) Linking soil erosion to on-site financial cost: lessons from watersheds in the Blue Nile basin. Solid Earth 6(2):765–774. https://doi.org/10.5194/se-6-765

Fathizad H, Karimi H, Alibakhshi SM (2014) The estimation of erosion and sediment by using the RUSLE model and RS and GIS techniques (Case study: arid and semi-arid regions of Doviraj, Ilam province, Iran). Int J Agric Crop Sci 7(6):304–314

Fu BJ, Zhao WW, Chen LD, Zhang QJ, Lu YH, Gelinck H, Poesen J (2005) Assessment of soil erosion at large watershed scale using RUSLE and GIS: a case study in the Loess Plateau of China. Land Degrad Dev 16:73–85

Fu G, Chen S, McColl DK (2006) Modelling the impacts of no-till practice on soil erosion and sediment yield with RUSLE, SEDD and arcview GIS. Soil Tillage Res 85:38–49

Gaubi I, Chaabani A, Mammu AB, Hamza MH (2017) A GIS-based soil erosion prediction using the Revised Universal Soil Loss Equation (RUSLE) (Lebna watershed, Cap Bon, Tunisia). Nat Hazards 86(1). https://doi.org/10.1007/s11069-016-2684-3

Gessesse B, Bewket W, Brauning A (2014) Model-based characterization and monitoring of runoff and soil erosion in response to land use/land cover changes in the Modjowatershed, Ethiopia. Land Degrad Dev 26(7). http://doi.org/10.1002/ldr.2276

Gomiero T (2016) Soil degradation, land scarcity and food security: reviewing a complex challenge. Sustainability 8(3). http://doi.org/10.3390/su8030281

Houyou Z, Bielders CL, Benhorama HA, Dellal A, Boutemdjet A (2016) Evidence of strong land degradation by erosion as a result of rainfed cropping in Algerian steppe: a case study of Laghouat. Land Degrad Dev 22(8). http://doi.org/10.1002/ldr.2295

Issaka S, Ashraf MA (2017) Impact of soil erosion and degradation on water quality: a review. Geol Ecol Landscape 1(1):1–11

Jaiswal RK, Thomas T, Galkate RV, Ghosh NC, Singh S (2013) Watershed prioritization using Saaty's AHP based decision support for soil conservation measures. Water Resour Manage. https://doi.org/10.1007/s11269-013-0494-x

Jaiswal RK, Thomas T, Galkate RV, Ghosh NC, Singh S (2014) Catchment area treatment (CAT) plan and crop area optimization for integrated management in a water resource project. J Inst Eng. https://doi.org/10.1007/s40030-014-0052-4
Joglekar DV (1965) Irrigation research in India. Central Board of Irrigation and Power Publication, India, No. 78, pp 1–165
Jose CS, Das DC (1982) Geomorphic prediction models for sediment production rate and Inters priorities of watersheds in Payurakshi catchment. In: Proceedings of international symposium of hydrology Asp. mountainous watersheds, Roorkee, India, vol 1, pp 115–168
Jose D, Ronald M, Arlene M, Evangelista M, Yoshida M (1994) The development of watershed management Strategies using a GIS and remote sensing: a case study. Asia Pac Remote Sens J 7(1):155–162
Kayet N, Pathak P, Chakraborty A, Sahoo S (2018) Evaluation of soil loss estimation using the RUSLE model and SCS-CN method in hillslope mining areas. Int Soil Water Conserv Res 6(1):31–42
Khemiri R, Elbedoui-Maktouf K, Grabot B, Zouari B (2017) A fuzzy multi-criteria decision-making approach for managing performance and risk in integrated procurement–production planning. Int J Prod Res 55(18):5305–5329
Knisel WG (1980) CREAMS: a field-scale model for chemicals, runoff and erosion from agricultural management systems. USDA conservation research report, vol 26, no 1, pp 36–64
Kockel A, Ban NC, Costa M et al (2020) Addressing distribution equity in spatial conservation prioritization for small-scale fisheries. PLoS ONE. https://doi.org/10.1371/journal.pone.0233339
Kushwaha SPS, Mukhopadhyay S, Hari Prasad V, Kumar S (2010) Sustainable development planning in Pathri Rao sub-watershed using geospatial techniques. Curr Sci 98(1):1479–1486
Ligonja PJ, Shrestha RP (2015) Soil erosion assessment in Kondoa eroded area in Tanzania using universal soil loss equation, geographic information systems and socioeconomic approach. Land Degrad Dev 26(4):367–379
Lim KJ, Myung Sagong M, Engel BA, Tang Z, Choi J, Kim KM (2005) GIS-based sediment assessment tool. CATENA 64:61–80
Lindley MR, Barfield BJ, Wilson BN (1995) Chapter 14—surface impoundment element model description. WEPP user summary. NSREL Report No. 11, USDA-ARSMWA, West Lafayette
Lindstorm MJ, Nebson WW, Schumacher TE (1992) Quantifying tillage erosion rates due to modifying ploughing. Soil Tillage Res 24:243–255
Malczewscki J (1999) GIS-based multicriteria decision analysis: a survey of the literature. Int J Geogr Inf Sci 20(7):703–726
Mishra S, Nagarajan R (2010) Morphometric analysis and prioritization of subwatersheds using GIS and remote sensing techniques: a case study of Odisha, India. Int J Geomatics Geosci 1(3):501–510
Misra N, Satyanarayana T, Mukherjee RK (1984) Effect of topo elements on the sediment production rate from sub-watersheds in upper Damodar valley. J Agric Eng 21(3):65–70
Moriasi DN, Steiner JL, Duke SE, Stark PJ, Verser AJ (2018) Reservoir sedimentation rates in the Little Washita river experimental watershed, Oklahoma: measurement and controlling factors. J Am Water Resour Assoc. http://doi.org/10.1111/1752-1688.12658
Narain P, Ram Babu VV, Rao RM, Sehgal JL, Datta RK, Sarkar D, Thampi CJ (1993) Soil erosion map of West Bengal. Indian J Soil Conserv 21(2):6–10
Narayana VVD, Babu R (1983) Estimation of soil erosion in India. J Irrig Drain Eng 109(4):419–434
National Commission on Agriculture (1976) Part VI-crop production, sericulture and apiculture. Ministry of Agriculture and Irrigation, Govt. of India, New Delhi
Nearing MA, Page DI, Simanton JR, Lane LJ (1989) Determining erodibility parameters from rangeland field data for a process-based erosion model. Trans Am Soc Agric Eng 32(3):919–924
Nema JP, Verma B, Patel AP (1978) Predicting universal soil loss parameters. Indian J Soil Conserv 6(2):75–79

Ochoa-Cueva P, Fries A, Montesinos P, Rodríguez-Díaz JA, Boll J (2015) Spatial estimation of soil erosion risk by land-cover change in the Andes of southern Ecuador. Land Degrad Dev 26(6):565–573

Pan J, Wen Y (2014) Estimation of soil erosion using RUSLE in Caijiamiao watershed, China. J Int Soc Prev Mitig Nat Hazards 71(3):2187–2205

Pandey A, Chowdary VM, Mal BC (2007) Identification of critical erosion-prone areas in the small agricultural watershed using USLE, GIS and remote sensing. Water Resour Manag 21:729–746

Perry LP, Lasango RG, Chartier M et al (2021) Soil erosion rates and nutrient loss in rangelands of Southern Patagonia. Earth Syst Environ Sci. https://doi.org/10.1016/B978-0-12-821139-7.00183-5

Prasad SN, Singh R (1994) Soil erosion and its control in semi-arid region of south-eastern Rajasthan. Indian J Soil Conserv 22(1 and 2):102–111

Prosdocimi M, Cerdà A, Tarolli P (2016) Soil water erosion on Mediterranean vineyards: a review. CATENA 141:1–21. https://doi.org/10.1016/j.catena.2016.02.010

Rao HSS, Mahabaleswara H (1990) Prediction of rate of sedimentation of Tungabhadra reservoir. In: Proceedings of symposium on erosion sedimentation and resources conservation, Dehradun India, vol 1, pp 12–20

Rao SVN, Rao MV, Gupa PK (1996) A study of sediment yield from Chenab river system in the western Himalayas. National Institute of Hydrology, Roorkee (India), CS(AR)-197

Renard KG, Freimund JR (1994) Using monthly precipitation data to estimate the R factor in the revised USLE. J Hydrol 157:287–306

Saaty TL (1980) The analytic hierarchy processes. McGraw-Hill, New York

Saroba J (2017) Soil erosion: causes, extent and management in India. Int J Creative Res Thoughts 5(4):1321–1330

Shen DY, Ma AN, Lin H, Nie XH, Mao SJ, Zhang B, Shi JJ (2003) A new approach for simulating water erosion on hill slopes. Int J Remote Sens 24:2819–2835

Singh G, Ram Babu, Chandra S (1981) Soil loss prediction research in India, Bulletin No. T-12/D-9. Central Soil and Water Conservation Research and Training Institute, Dehradun

Singh G, Babu R, Narain P, Bhusan LS, Abrol IP (1992) Soil erosion rates in India. J Soil Water Conserv 47(1):97–99

Suriaprasit M, Shrestha DP (2008) Deriving land use and canopy cover factor from remote sensing and field data in inaccessible mountainous terrain for use in soil erosion modelling. The International Land Development Department, Bangkok, Thailand

Taguas EV, Arroyo C, Lora A, Guzmán G, Vanderlinden K, Gómez JA (2015) Exploring the linkage between spontaneous grass cover biodiversity and soil degradation in two olive orchard micro-catchments with contrasting environmental and management conditions. Soil 1:651–664. https://doi.org/10.5194/soil-1-651

Tang Q, Xu Y, Bennett S, Li Y (2014) Assessment of soil erosion using RUSLE and GIS: a case study of the Yangon watershed in the Loess Plateau, China. Environ Earth Sci 73(4). http://doi.org/10.1007/s12665-014-3523-z

Tiwari J (2017) Integration of universal soil loss equation with geographical information system for soil erosion assessment: a case study of Banjar river watershed, M. Tech thesis, Jawaharlal Nehru Krishi Vishwa Vidyalaya, Jabalpur

Varsheney RS (1975) Engineering hydrology. Nemchand & Bros. Publication, Roorkee, pp 1–24

Veihe A, Rey J, Quinton JN, Strauss P, Sancho FM, Somarriba M (2001) Modelling of event-based soil erosion in Costa Rica, Nicaragua and Mexico: evaluation of EUROSEM model. CATENA 44:187–203

Walling DE, Fung D (2003) Recent trends in the suspended sediment loads of the world's rivers. Glob Planet Change 39(1–2):111–126

Xie Y, Xie B, Wang Z, Gupta RK, Baz M, AlZain MA, Masud M (2022) Geological resource planning and environmental impact assessments based on GIS. Sustainability. https://doi.org/10.3390/su14020906

Yadav SK, Dubey A, Singh SK, Yadav D (2020) Spatial regionalization of morphometric characteristics of mini watershed of Northern Foreland of Peninsular India. Arab J Geosci 13:1–16

Yoshino K, Ishioka Y (2005) Guidelines for soil conservation towards integrated basin management for sustainable development: a new approach based on the assessment of soil loss risk using remote sensing and GIS. Paddy Water Environ 3:235–247

Zhang Y, Degroote J, Wolter C, Sugumaran R (2009) Integration of modified universal soil loss equation (MUSLE) into a GIS framework to assess soil erosion risk. Land Degrad Dev 20(1):84–91

Chapter 15
Geospatial Technology for Estimating the Physical Vulnerability of Building Structures to Natural Hazards

K. Nakhapakorn, P. Q. Giang, A. Ussawarujikulchai, K. Tantrakarnapa, S. Jirakajohnkool, T. Weerasiri, N. Srichan, T. Maneekul, and P. PhramahaTawee

Abstract Climate change causes major effects on the environment and nature as it leads to increasing urban flood hazards. Flooding is the most frequent natural hazard that occurs in the Asia–Pacific region where an increasing number of people are choosing to live in floodplain areas. Communities living in monsoonal regions have learned to live with floods. The most important component of flood management is assessing flood vulnerability on an urban scale. This study conducted flood vulnerability assessment and analysis of physical building structures in Warin Chamrap municipality, Thailand. GIS-based method of estimating the vulnerability of buildings to floods was employed for flood vulnerability assessment. The results identified building structures in the flood-prone area that are at extreme risk. The study found that 87 households were at a moderate to extreme risk in the extreme flood vulnerability area and 130 households with structural damage. The flood vulnerability

K. Nakhapakorn (✉) · A. Ussawarujikulchai · N. Srichan · T. Maneekul
Faculty of Environment and Resource Studies, Mahidol University, Nakhon Pathom 73170, Thailand
e-mail: kanchana.nak@mahidol.ac.th

P. Q. Giang
Faculty of Environment and Office of International Cooperation and Research Management, Ha Long University, Uong Bi, Quang Ninh, Vietnam

K. Tantrakarnapa
Department of Social and Environmental Medicine, Faculty of Tropical Medicine, Mahidol University, Bangkok 10400, Thailand

S. Jirakajohnkool
Faculty of Science and Technology, Thammasat University, Khlong Luang, Pathum Thani 12121, Thailand

T. Weerasiri
Faculty of Science and Technology, The Engineering Institute of Thailand under H.M. the King's Patronage (EIT), Thammasat University, Klong Luang, Pathum Thani 12121, Thailand

P. PhramahaTawee
Mahachulalongkornrajavidyalaya University, Wang Noi, Phra Nakhon Si Ayutthaya 13170, Thailand

V. P. Singh et al. (eds.), *Application of Remote Sensing and GIS in Natural Resources and Built Infrastructure Management*, Water Science and Technology Library 105,
https://doi.org/10.1007/978-3-031-14096-9_15

index (FVI) is a powerful tool for a better understanding of community and building structures and to identify adaptations for vulnerability reduction. However, the FVI is limited by a number of factors that reduce its capacity as an accurate and practical tool for decision-makers. For future development, geospatial data visualization and GIS-based flood vulnerability assessment techniques should be considered as a method to provide a baseline to guide further study.

Keywords Geospatial technology · Flood vulnerability index · Natural hazard · Physical vulnerability

15.1 Introduction

As disaster risks from severe floods continue to increase and affect communities because of climate change, the relationship between disaster risk and human development—such as poverty reduction, affordable housing, environmental degradation, population growth and mitigation, and rapid urbanization—has become increasingly important (Booth et al. 2020; Hallegatte et al. 2020; Intergovernmental Panel on Climate Change (IPCC) 2014, 2019; Lewis 2012; Raikes et al. 2021; Schipper and Pelling 2006; Sperling and Szekely 2005; UNDP 2020; UNDRR 2019; United Nations Office for Disaster Risk Reduction (UNISDR) 2009; Wong et al. 2014; World Conference on Disaster Reduction on Behalf of the Vulnerability and Adaptation Resource Group 2005). As Cutter et al. (2003) explain, disaster vulnerability is a combination of social and physical conditions that make individuals and communities susceptible to harm. A variety of approaches defined by many researchers to evaluate vulnerability are available (Azotea et al. 2017; Balica et al. 2012; Barredo and Engelen 2010; Bizimana and Schilling 2009; Brinckerhoff 2009; Deckers et al. 2009; Kumar and Bhattacharjya 2020; Len et al. 2018; Nasiri et al. 2019; Noren et al. 2016; Papathoma-Köhle et al. 2019; Phumkokrux 2016; Phuthong 2014). Global Facility for Disaster Reduction and Recovery (2014) and UNISDR (2015) refer to vulnerability as the characteristics and circumstances of a community, system, or asset that make it susceptible to the damaging effects of a hazard. Vulnerability is one of the defining components of disaster risk. There are many aspects of vulnerability, arising from various physical, social, economic, and environmental factors. For example, poor design and construction of buildings, inadequate protection of assets, lack of public information and awareness such as weather forecasts, limited official recognition of risks and preparedness measures, and a disregard for wise environmental management.

Flooding is the most frequent hazard worldwide. It is a big problem if the flood magnitude is larger than expected. It causes loss of homes, infrastructure, and building damage in the flood-prone areas, especially in rural areas that lack flood control and protection. Hence, there is a need to decrease the vulnerability of buildings and infrastructure. Therefore, enhancing our understanding of vulnerability and developing methodologies to assess flood vulnerability is of critical importance.

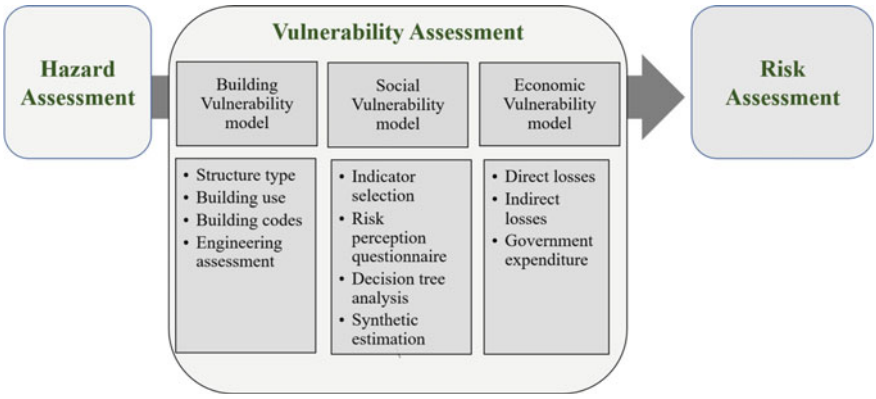

Fig. 15.1 The steps involved in performing a risk assessment. Modified from Dwyer et al. (2004)

A flood vulnerability index (FVI) enables the assessment of vulnerability to floods (Azotea et al. 2017; Balica et al. 2012; Kappes et al. 2012; Kumar and Bhattacharjya 2020; Len et al. 2018; Nasiri et al. 2019; Papathoma-Köhle et al. 2019; Xiao et al. 2020). FVI is an important approach for raising public awareness. This is because there are several factors influencing vulnerability including human settlement conditions, socio-economic patterns, infrastructure, and policy. A summary of a physical vulnerability assessment, including building vulnerability, social vulnerability, and economic vulnerability models is shown in Fig. 15.1.

Thailand is vulnerable to many natural and human-induced hazards such as floods, landslides, and storms. In the 69 years from 1951 to 2019, tropical storms including typhoons and depressions occurred 200 times in Thailand. Among the hazards, flooding is the most frequent natural hazard that occurs in Thailand, and almost 60% of the country is flooded at least 10 times per year (ADPC 2011). The most frequent cause of flooding is continued heavy rain due to tropical cyclones that sweep through the country and neighboring regions during the monsoon season. The impact of heavy rain across a wide area causing flooding and windstorm damage to properties and households has been reported (ADPC 2011; Anang and Braun 2021; Deckers et al. 2009; Department of Marine and Coastal Resources 2014; Díez-Herrero and Garrote 2020; Duriyapong and Nakhapakorn 2011; Gurukul and Nakhapakorn 2014; Kappes et al. 2012; Len et al. 2018; Nasiri and Shahmohammadi-Kalalagh 2013; Nasiri et al. 2019; Papathoma-Köhle et al. 2019; Phutthong 2011; Royal Irrigation Department (RID) 2012; Sarajit et al. 2015). Increasing rainfall will add to problems of flooding in areas not adequately designed for flood protection from rivers (Crichton and Ingleton 1999). Many of Thailand's flood defenses are antiquated and are in need of repair to reduce the flood hazards.

FVI can be aided by geoinformation technology. Geoinformation technology is widely used for data visualization and technical analysis of the environment, urban planning, recreating the past, 3D city modeling, biodiversity monitoring, access to geo-data for citizens and tourists, forest biomass mapping, public health, military,

transport network planning, and management, agriculture, meteorology, and climate change, oceanography and coupled ocean and atmosphere modeling, business location planning, architecture and, telecommunications, criminology and crime simulation, aviation, and renewable energy (Amade et al. 2018; Fuhrmann et al. 2008; Kundu et al. 2020; Kuzhelev 2013; Lemmens 2011; Levina et al. 2017; Malczewski and Rinner 2017; Morkul et al. 2018; Neussner et al. 2008; Petrescu 2007; Prasannakumar et al. 2012). According to Gomarasca (2010), "Geoinformation technology or Geomatics is defined as a systemic, multidisciplinary, integrated approach to selecting the instruments and the appropriate techniques for collecting, storing, integrating, modeling, analyzing, retrieving at will, transforming, displaying, and distributing spatially georeferenced data from different sources with well-defined accuracy characteristics and continuity in a digital format". Therefore, the objective of this research was to assess the risk and physical vulnerability of building structures to floods at the household level in a riverside communities. The study focused on the process of indicator selection and weighting based on the importance of building characteristics by using a geospatial technique. This research focused only on building vulnerability models.

15.2 The Study Area

The 2019 flooding in Thailand's northeastern province of Ubon Ratchathani is the worst in 17 years, with the level of the Moon River measured at 10.97 m, higher than the record set in 2002. The condition of riverside villages in PibunMangsaharn and Warin Chamrap districts is of serious concern which has left several communities in low-lying areas as islets surrounded by water. Warin Chamrap municipality in Ubon Ratchathani province is in the Warin Chamrap district which is located on the Mun river bank in Thailand (Fig. 15.2). There are six community zones in the Warin Chamrap municipality, classified as the commercial zone, residential zone, peri-urban, newly developed residential zone, riverside community, and old town. In 30 years from 1971 to 2000, the average yearly rainfall amount was 1581.4 mm. During the rainy season, northeast monsoons increase the frequency of flood. Ten years of collected data revealed that the Mun river is the source of Ubon Ratchathani province with the most severe flood occurring in 2019.

15.3 Methodology

The vulnerability of a building can be described by combining the geospatial data with measurable attributes relating to varying degrees of physical building vulnerability. The indicators would be sustained during floods. By characterizing these vulnerability attributes, a relationship (i.e., building vulnerability equation) is established between the buildings and the flood hazard. The building vulnerability equation

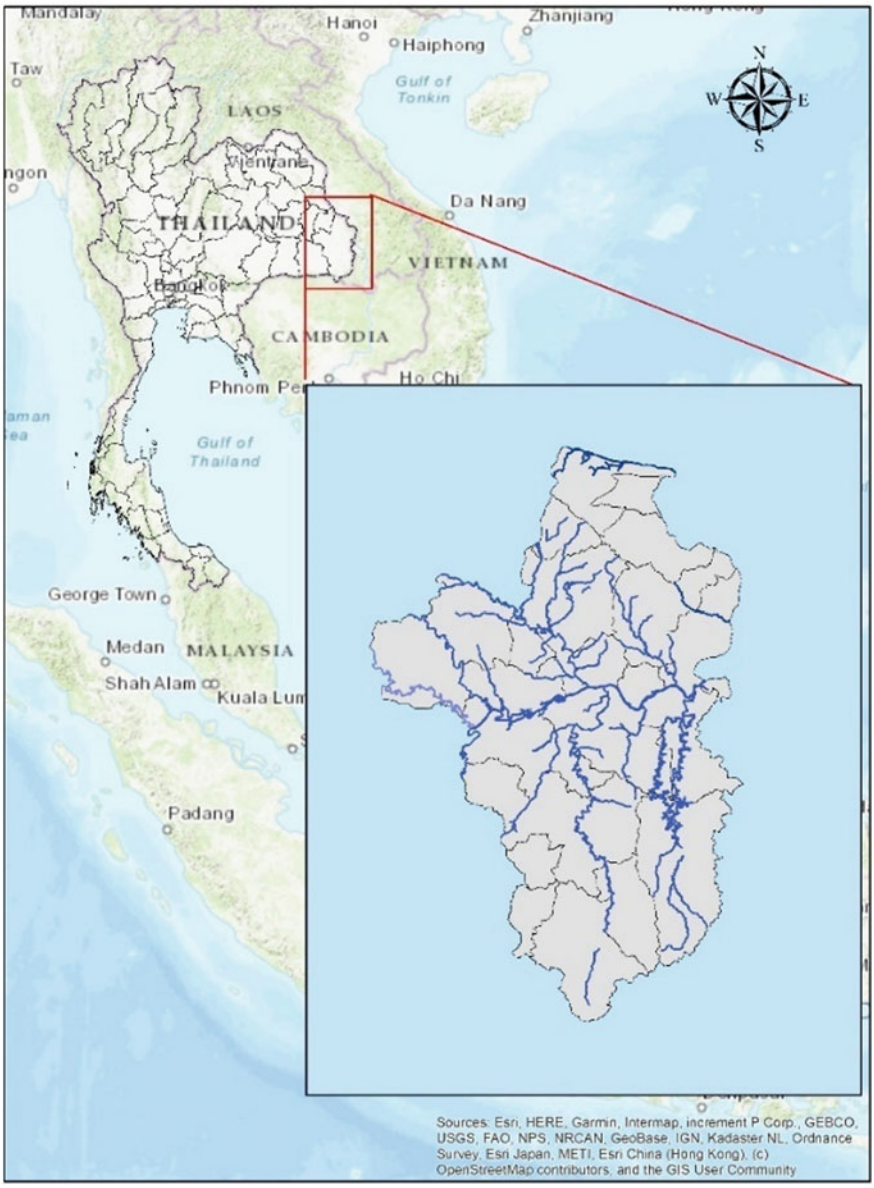

Fig. 15.2 Location map of the study area

provides the means of calculating the vulnerability score of a building. The steps are as follows: (1) Identify vulnerability attributes and grading of relevant hazards. (2) determination of physical vulnerability of the building structure and establishing the relationship between attributes. (3) Calculate vulnerability and develop maps.

15.3.1 Identification and Grading of Relevant Hazards

The flood vulnerability and risk assessment have been carried out in this chapter based on quantitative statistical techniques and geospatial technology. During a flood event, delineation maps can show flooded areas and can be compared with water depth from satellite imageries. Vulnerability assessment data was divided into two categories: primary and secondary data: (1) Primary data is data collected from field-work surveys using building location coordinates obtained from Global Navigation Satellite System (GNSS) with mobile application, (2) Secondary data was gathered from GISTDA using10 years of flood maps. After collecting data from the study area, all data was re-grouped, classified, and weighted. Many riverside communities have houses built in floodplains when flooding was less common and these communities are still allowing developments in areas at a high risk.

In an attempt to cope with this historic and ongoing problem, flood prevention and mitigation by using risk assessment methods adapted from the risk assessment process of disasters of ISO (2009). It is a process that helps people to understand the risks of natural hazards such as earthquakes and flooding. This study was interested in studying the risks and vulnerabilities, as well as the adaptation of flood-affected communities, found in Ubon Ratchathani province. Households were selected in order to identify specific damage from physical vulnerability; specifically, how such households would be affected differently by each type of disaster. For example, the difference in building material from one structure to the next has an effect on the building structure damage. In the case of floods, it is important to understand how the choice of building material impacts the vulnerability of building structure types. The Engineering Institute of Thailand under H. M. the King's Patronage (EIT) collected survey data for each household to obtain general information about each residence, such as the physical data of the house structure after major floods in order to identify valuable information about the potential need for household adaptation when faced with natural hazard.

The methodology of this research applied survey and GIS techniques to assess the vulnerability and risk of communities by gathering and analyzing spatial and non-spatial data. Geospatial data visualization and analysis was used extensively for identifying and measuring exposure accumulations and hazard data from various sources, including satellite data. In the case of floods, it is important to understand how the choice of building material impacts the vulnerability of building structures. The researcher collected survey data for each household to obtain general information about each residence, such as the physical data of the house structure before and after major floods in order to identify valuable information about the potential need for

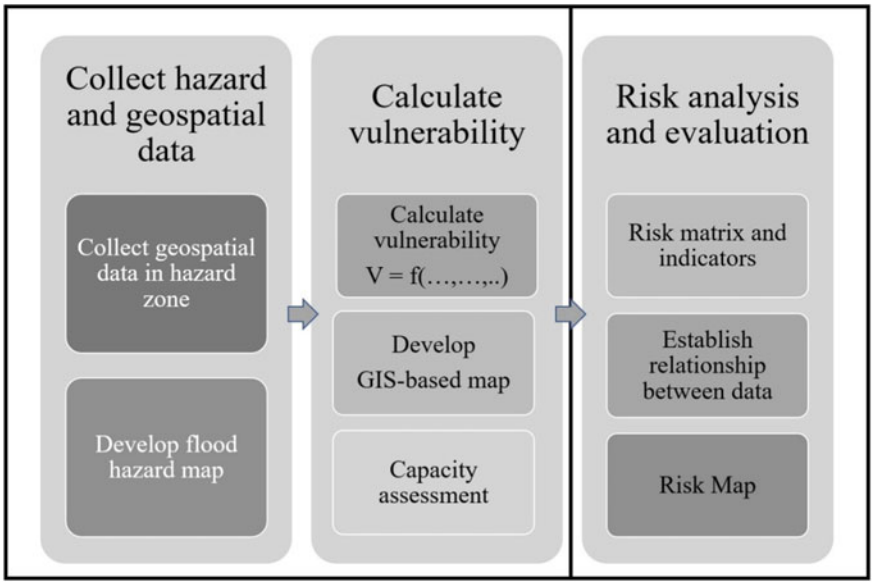

Fig. 15.3 Risk assessment conceptual framework diagram of the physical vulnerability of building structures to floods

household adaptation when faced with natural hazards. The probability and severity of natural hazards were then modeled in proper ways to establish large databases of exposure and vulnerability information.

In the final process, the research conducted a survey with GPS and GIS techniques (geospatial l data analysis and visualization) to assess vulnerability and risk for communities, including assessment of household adaptation after a severe natural disaster. Then, the risk assessment was undertaken together with a risk map of impact areas in order to analyze and reduce the negative impact associated with violence from new natural hazards as shown in Fig. 15.3.

15.3.2 Determination of Physical Vulnerability of Building Structures to Floods

It is important that the risk assessment of communities on natural hazards, such as storms, floods, and storm surges, considers the physical factors of the area as well as the social, economic, and cultural factors of the people living in the area (Andrade Pérez et al. 2010; Dwyer et al. 2004; Vahanvati 2018; Withuntat et al. 2016; Zezheng et al. 2020). The physical vulnerability assessment or building vulnerability indicators are shown in Table 15.1. Risk assessment refers to the analysis of variance in order to establish the probability of a certain outcome from an uncertain event

including the magnitude or probability of a hazard, the building material, building status, damage and crack in the structure, floor material, number of stories, foundation types, flood depth, and flood frequency. The vulnerability level can indicate the level of capacity. The effect of flood depth may be different materials and construction styles. A high score shows high vulnerability and indicates low capacity, while a low score shows low vulnerability and indicates high capacity.

Risk matrix is an uncomplicated risk analysis result that uses likelihood analysis and capacity effects of a qualitative hazard derived from the hazard likelihood and impact level. High numbers derived from matrix, indicate a high-risk level, these risk values are useful for showing or comparing risk levels. Risk evaluation is a risk comparison process between the results of risk analysis with the risk criteria as shown in Table 15.2.

Table 15.1 The physical vulnerability of building structure indicators

Indicators	Vulnerability level				
	Very low	Low	Moderate	High	Very high
	1	2	3	4	5
Building material types	Concrete	Concrete and mixed wood-concrete	Masonry	Wood	Bamboo, galvanized iron
Building status	Very good	Good	–	Bad	Very bad
Residence damage	Not damaged	Slightly damaged	Moderately damaged	Extensively damaged	Completely damaged
Cracks in structure	No	–	–	–	Yes
Floor materials	Concrete	–	–	–	Wood, bamboo
Number of stories	>2 stories	–	2 stories	–	1 stories
Flooding frequency (10 years period)	None	1–2 times	3–4 times	5–6 times	>7 times
Flood depth		<0.5 m	0.5–1 m	1–2 m	>2 m
Presence of foundation type	Yes				No

Sources Modified from Ruiter et al. (2017), Department of Disaster Prevention and Mitigation (2014), Department of Disaster Prevention and Mitigation (2015), Kappes et al. (2012), Krishnamurthy et al. (2011), Godfrey et al. (2015), Papathoma-Köhle et al. (2019), Taramelli et al. (2015), Tran et al. (2009)

Table 15.2 Level of risk assessment matrix

Frequency	Level of severity				
Likelihood	None (1)	Low (2)	Moderate (3)	High (4)	Extreme (5)
Very slightly opportunity (1) *Impossible (Risk is unlikely to occur)*	*1*	*2*	*3*	*4*	***5***
Less opportunity (2)	*2*	*4*	***6***	***8***	***10***
Moderate opportunity (3) *Possible (Risk will likely occur)*	*3*	***6***	***9***	***12***	**15**
High opportunity (4)	*4*	***8***	***12***	**16**	**20**
Very high opportunity (5) *Probable (Risk will occur)*	***5***	***10***	**15**	**20**	**25**

Extreme (score 15–25), moderate (score 5–14), low (score 1–4)
Sources ADPC (2011), IEC (2018)

15.3.3 Calculation of the Vulnerability Index (VI)

Godfrey et al. (2015) explained that the vulnerability index (VI) of each physical vulnerability of a building to floods is calculated using the normalized weights of the characteristic indicators (A_i) and the normalized weights of the observed indicator values (a_j), as shown in Eq. (15.1):

$$\mathrm{VI} = \sum_{i,j=[0,1]}^{n} A_i a_j \tag{15.1}$$

where, A_i is the normalized weight of the indicators, and a_j is the normalized weight of the indicators' observed value.

15.4 Risk Assessment for Physical Vulnerability of Building Structures to Floods

15.4.1 The Results of Hazard Assessment

Flood map data of the Ubon Ratchathani province from 2010 to 2019 was collected from Geo-Informatics and Space Technology Development Agency (GISTDA). Data was collected in GIS format, which was published online on the GISTDA website and flood map data accuracy was verified by a field survey. Then, the data was corrected and used to make a hazard map by dividing the intensity into five levels. This research was focused on the Warin Chamrap municipality, Warin Chamrap district in Ubon Ratchathani province. The analysis showed that the areas had a flood frequency

Table 15.3 Flooding frequency areas in Warin Chamrap municipality, Ubon Ratchathani province

District name	Intensity of flooding					Total (Acre)
	Level					
	Very low	Low	Moderate	High	Extreme	
	Non-flood	1–2 years flood	3–4 years flood	5–6 years flood	≥7 years flood	
Bung Mai	3699.6	1049.5	203.0	56.4	6.4	5014.9
Bung Wai	8258.2	2612.7	594.5	401.7	28.3	11,895.3
Huai Kha Yung	9933.4	1184.5	208.7	34.2	20.6	11,381.4
Kham Khwang	12,048.8	4276.7	426.6	191.8	158.7	17,102.6
Kham Nam Sap	802.4	1018.1	528.6	174.6	24.5	2548.2
Khu Mueang	6891.9	1810.6	923.2	889.7	429.9	10,945.3
Mueang Si Khai	12,723.1	1706.7	598.3	482.4	91.9	15,602.4
Non Non	4531.7	2475.4	836.5	576.8	295.4	8715.8
Non Phueng	4361.9	2179.8	658.7	523.0	124.2	7847.5
Nong Kin Phlen	3856.7	2449.3	1059.4	1414.5	1098.4	9878.3
Pho Yai	11,144.4	2581.5	1480.3	404.2	54.6	15,665.0
Sa Saming	12,964.9	1115.1	205.0	0.0	0.0	14,285.0
Saen Suk	4819.0	1814.2	342.5	50.0	0.0	7025.7
Tha Lat	5761.6	1618.8	434.1	87.6	9.9	7911.9
That	2033.1	1198.8	502.9	98.9	49.8	3883.4
Municipality	**1909.4**	**1064.4**	**229.8**	**60.7**	**4.7**	**3268.9**
Total (Acres)	105,740.0	30,156.0	9232.0	5446.4	2397.2	152,971.6

of 1–2 years for most areas, accounting for 1064.4 acres in the Warin Chamrap municipality. A flood frequency of 3–4 years was found for 229.8 acres, followed by the flood frequency of 5–6 years, which accounted for 60.7 acres. The area with flood frequency of seven or more years was the smallest, accounted for 4.7 acres. Non-flood-affected areas accounted for 1909.4 acres. These are shown in Table 15.3 and Fig. 15.4.

15.4.2 Results of the Vulnerability Assessment

Nine different indicators that influence property damage (building material, building status, residence damage, cracks in the structure, floor material, number of stories, foundation types, flood depth, and flood frequency) were assessed in 324 surveyed

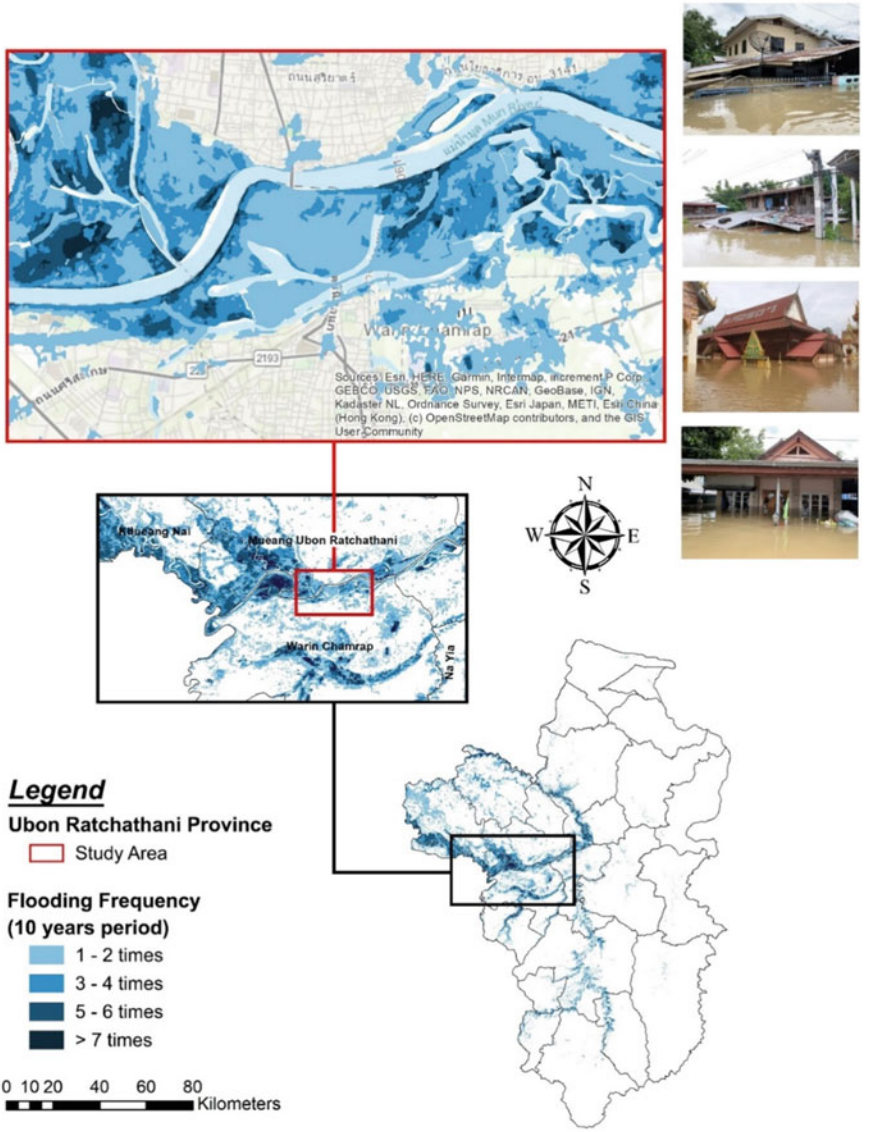

Fig. 15.4 Flooding frequency area in Warin Chamrap municipality, Ubon Ratchathani province, Thailand

households selected for this study. In the study area, 170 households were constructed from mixed wood-concrete materials. The number of households with cracks caused by flooding was 131. A total of 146 households were at very high risk during the 10 years flood period with 195 households having very high flood depths of more than 2 m as shown in Table 15.4 and Fig. 15.5. According to Ettinger et al. (2016) as well as Thouret et al. (2014) used indicators to assess the physical vulnerability indices based on indicators such as number of stories, building footprint, shape of city block, and building density as well as distance from channel.

Uncomplicated risk analysis is derived from a risk matrix, using estimates of the probability and potential effects of a qualitative hazard. There is a multiplicity

Table 15.4 The number of building in each of the hazard zones

Factors	Indicators	Rank level	Flood frequency			Total
			1–2 years	3–4 years	5–6 years	
Building material	Concrete	1	69	13	0	82
	Concrete and mixed wood-concrete	2	147	22	1	170
	Masonry	3	8	0	0	8
	Wood	4	51	6	1	58
	Bamboo	5	5	1	0	6
Crack in structure	No	1	170	21	2	193
		2	0	0	0	0
		3	0	0	0	0
		4	0	0	0	0
	Yes	5	110	21		131
Number of floors	>2 stories	1	2	0	0	2
		2	0	0	0	0
	2 stories	3	150	25	1	176
		4	0	0	0	0
	1 story	5	128	17	1	146
Foundation type	Yes	1	203	32	0	235
		2	0	0	0	0
		3	0	0	0	0
		4	0	0	0	0
	No	5	77	10	2	89
Flood depth	None	1	31	4	0	35
	<0.5 m	2	0	0	0	0
	0.5–1 m	3	0	0	0	0
	1–2 m	4	92	2	0	94
	>2 m	5	157	36	2	195

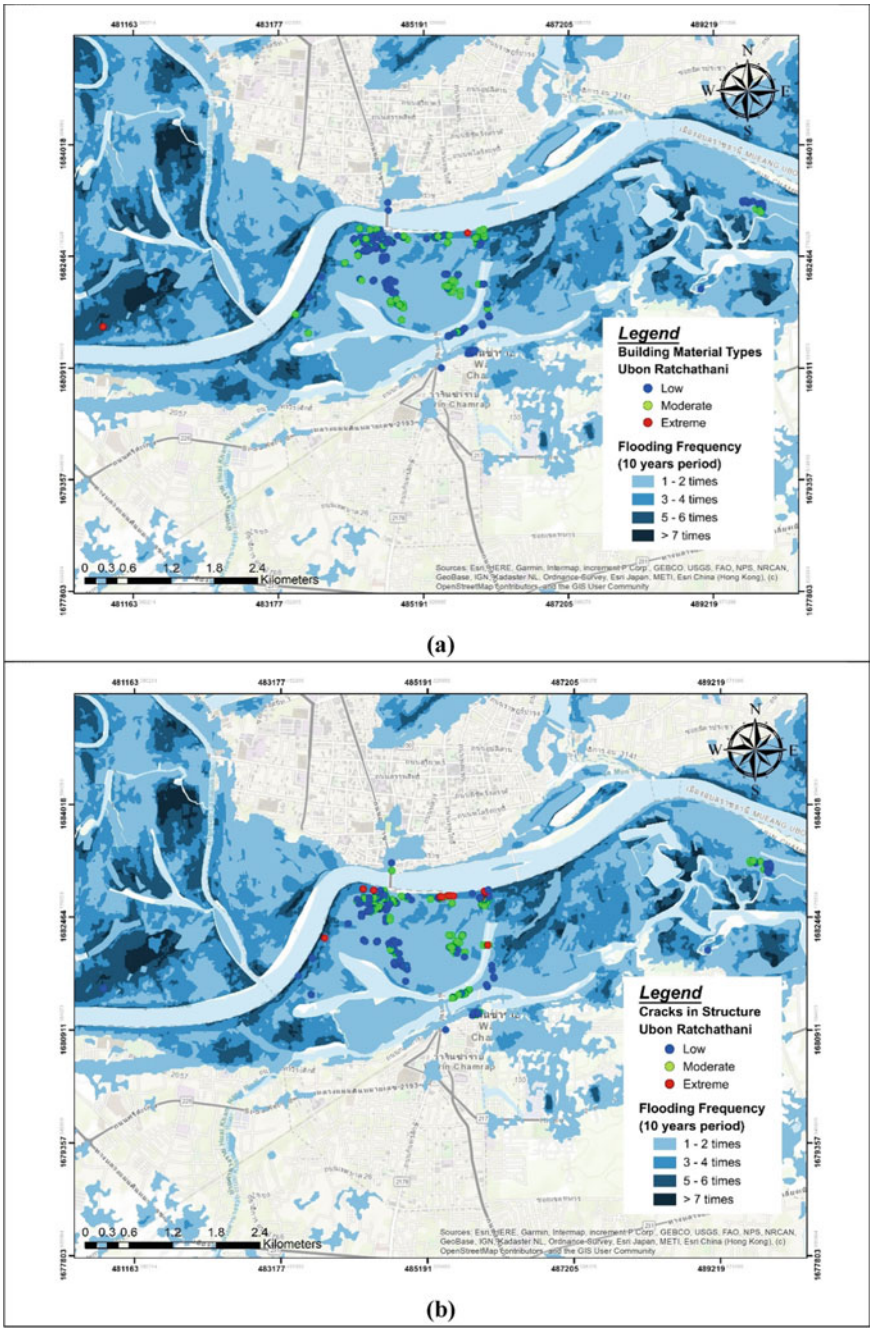

Fig. 15.5 The physical vulnerability of building structures in flood risk areas, **a** building materials, **b** crack in the structure, **c** number of stories, **d** foundation types, and **e** flood depth

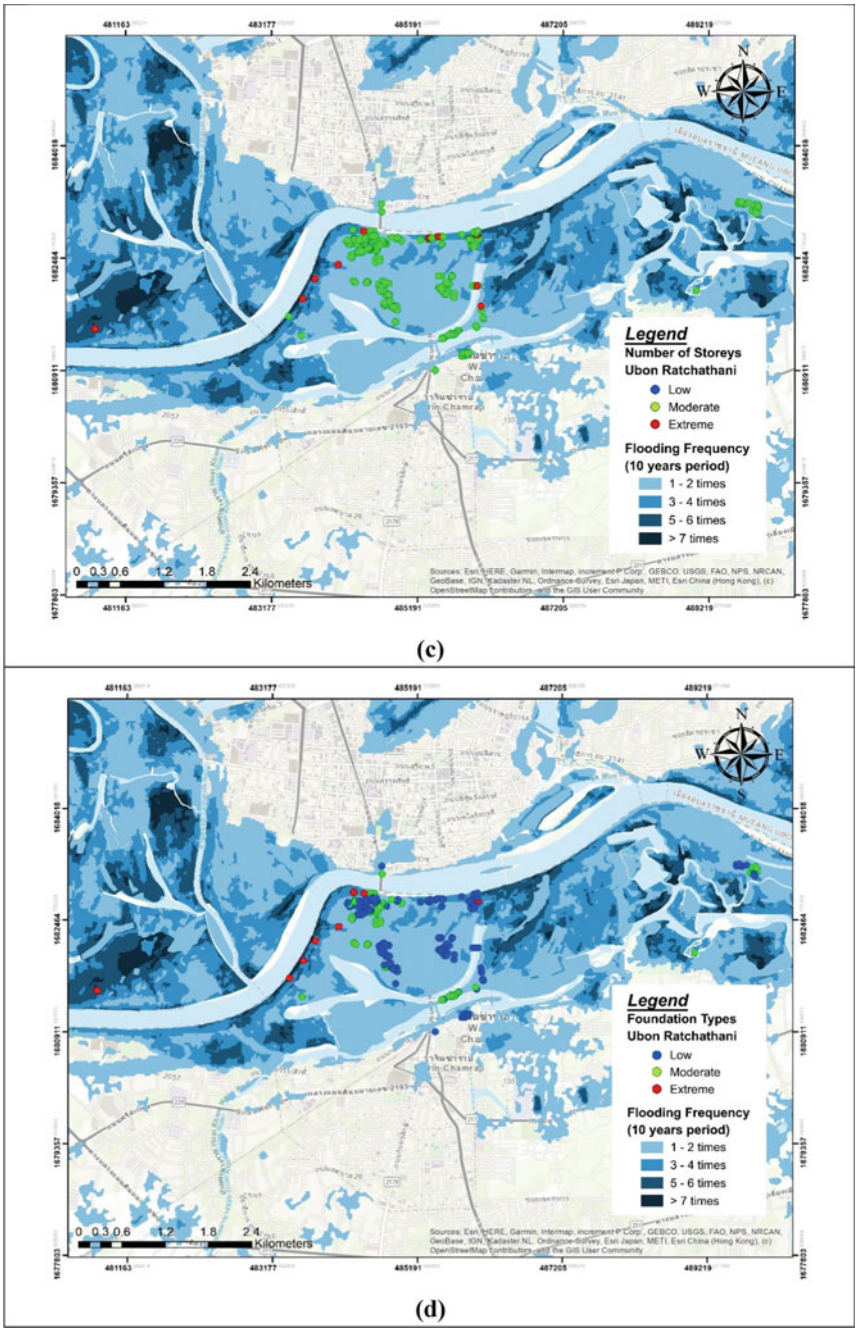

Fig. 15.5 (continued)

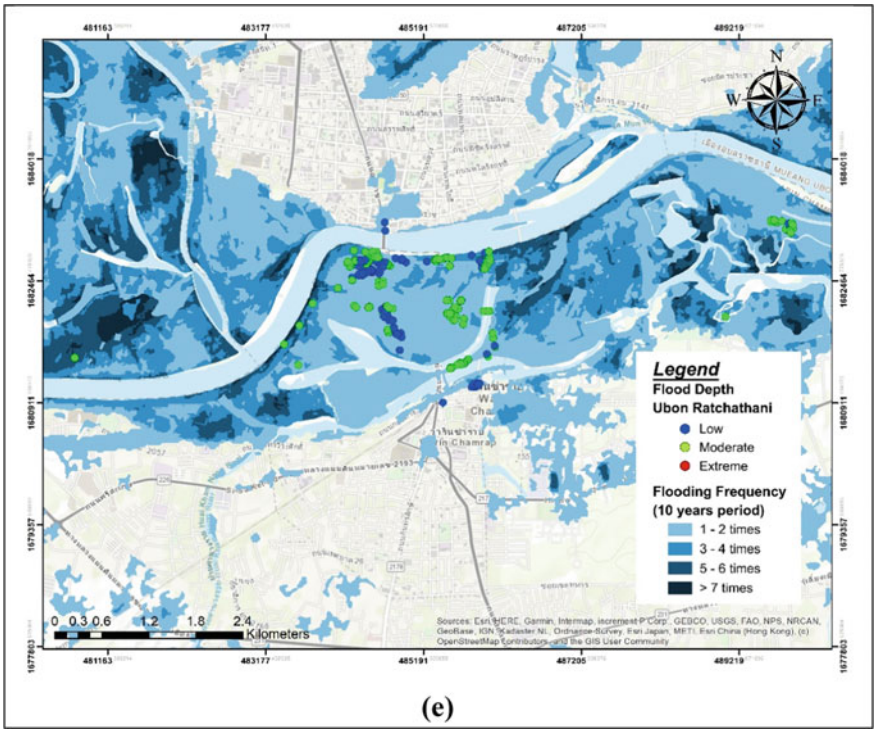

Fig. 15.5 (continued)

of possibilities of a disaster, which is derived from the assessment data. The level of impact is derived from the vulnerability analysis. As shown in Table 15.5 and Fig. 15.6, the vulnerability results are listed using classifications that are consistent with the definitions of impact on the risk matrix adapted from the ISO Risk Assessment Process (2009) (https://www.iso.org/standard/44651.html). The results in the table indicate the level of risk and indicate extreme risk levels in some areas. Each building was assigned with a score for each indicator as described in detail in Table 15.1. These risk values were useful for showing trends or comparing risk levels, as shown in Table 15.2. The levels of risk assessment matrix are: extreme (Bold), moderate (Bolditalic), and low (Italic) risk level. From Table 15.5, the results show that most households had an extreme vulnerability. Eighty-seven households had building materials at a moderate to extreme risk of damage in the extreme flood vulnerability area and 151 concrete houses were at an extreme level of flood vulnerability area. A total of 130 households in an extreme flood vulnerability area had cracks in their structure.

Table 15.5 The physical vulnerability indicators in flood risk areas (households)

Physical vulnerability indicators	Risk level	Risk level of flood vulnerability		Total (HH)
		Extreme	Moderate	
Building material	Extreme	**1**	**1**	**2**
	Moderate	86	7	93
	Low	151	78	229
Crack in structure	Extreme	21	0	21
	Moderate	109	1	110
	Low	108	85	193
Number of floors	Extreme	18	0	18
	Moderate	219	85	304
	Low	1	1	2
Foundation type	Extreme	12	0	12
	Moderate	76	1	77
	Low	150	85	235
Flood frequency	Extreme	2	0	2
	Moderate	39	3	42
	Low	197	83	280
Flood depth	Extreme	38	0	38
	Moderate	188	63	251
	Low	12	23	35

Note From Engineering Institute of Thailand under H.M. the King's Patronage (unpublished data)

15.5 Conclusion

In mapping vulnerability, consideration must be given to the issue of scale, which can be interpreted in a variety of ways. Flood vulnerability risk levels of high risk and very high risk, call for immediate action or risk management strategies. The dynamic and variable nature of human behavior and culture should be considered throughout the risk management process. Tingsanchali (2012) found that integrated urban flood disaster and risk management for developing countries are mostly in terms of reactive responses in prevailing disaster situations. Moreover, urban areas are complex and dynamic systems that are exposed to various hazards (Mebarki et al. 2012). Although the risk management process is often presented as sequential, in practice it is an interactive method. In this study, the importance of households that are single-story houses is emphasized because they are more vulnerable to flooding than houses with lifted floors. This is due to climate change and the more severe disasters, which traditional houses are not strong enough to handle. Furthermore, climate is an important factor that affects the vernacular architecture of local housing. Policies and practices for disaster risk management should be based on an understanding of

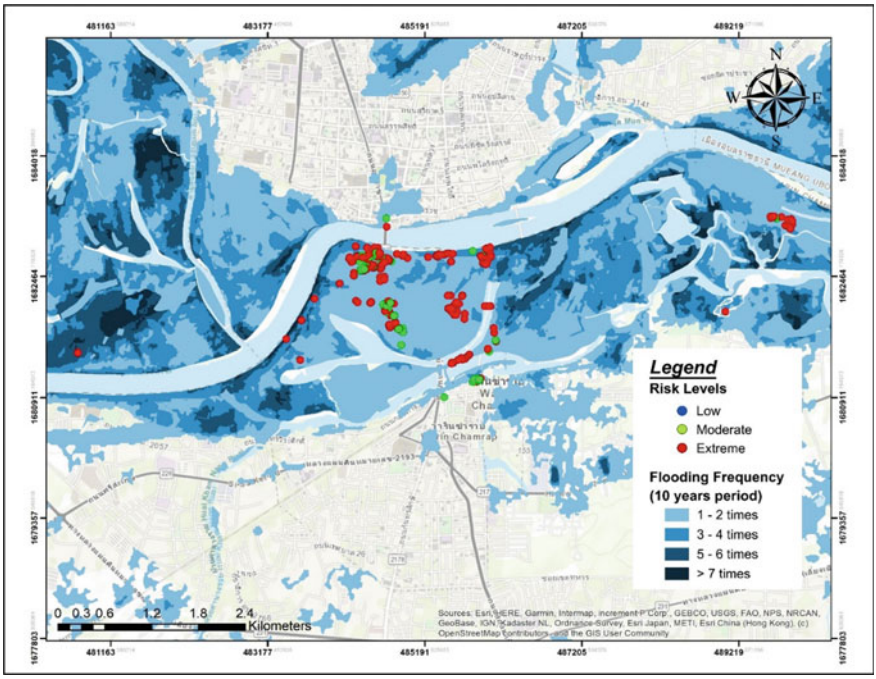

Fig. 15.6 Physical vulnerability index in flood risk area

disaster risk in all dimensions of vulnerability, coping capacity, exposure of persons and assets, hazard characteristics, and their possible effects at the relevant social and spatial scale on the ecosystem.

The local government organizations should request cooperation from government agencies with knowledge, information, and an analysis system for each type of disaster in the area. Mebarki et al. (2012) presented that beyond the damages that might be suffered due to its vulnerability, resilient territory needs adequate and efficient organization. Moreover, the risk analysis of each area requires statistical data, scientific knowledge, and technological expertise together with local wisdom. A goal for the local government organizations is to create an accurate and effective safety culture for the departments and communities in the area.

- Monitoring and assessment of the damage in all dimensions, such as the structure, economic, and agricultural, for the benefit of planning, repair, and restoration.
- Disaster assessment in order to conduct a risk analysis and measurement in the future.
- The goal of the local government organization on disaster management is to create communities of knowledge and understanding to cope with disaster; furthermore, this enables local communities to manage themselves to recover from the effects of disaster quickly.

Fig. 15.7 Rehabilitation of physical and mental health with religious leaders. *Source* Photos by Dr. Phramaha Tawee Potad, 2019

- Rehabilitation of physical and mental health with religious leaders or monks, as shown in Fig. 15.7.

Research studies can help identify areas at high risk of flooding with physical building vulnerability indicators, that would be of great benefit to the province's disaster planning and management. It is important to share data with the communities and civil society networks to raise awareness and alert communities about the risks and possible action that is needed. In addition to considering the direct impact and vulnerabilities of disasters, socio-economic risks and damage should be assessed. The analysis can be taken in the future as it improves knowledge about mitigation and preventative measures to reduce social vulnerability to flooding.

15.6 Future Directions

Nowadays, geoinformation technology and geospatial data visualization can be further strengthened in order to solve complex social, industrial, and management activities in the built environment. Furthermore, it becomes a very important technology for decision-makers across a wide range of disciplines, industries, the commercial sector, environmental agencies, local and national governments, researchers and academia, and national survey and mapping organizations, such as the Engineering Institute of Thailand or engineering volunteers, International organizations, the United Nations, emergency services, public health and epidemiology, crime mapping, transportation and infrastructure, and information technology industries. Many governmental and non-governmental agencies have started to use spatial data for managing their day-to-day activities.

This study only examines the risk and the physical flood vulnerability of housing structures, so future research should study other vulnerability indicator categories, such as economic and social vulnerability indicators, and create a flood simulation model and an evacuation map. This research presents a risk analysis method for flood areas which can be analyzed in various ways, including GIS-based analysis for assessing the physical vulnerability of building structures to floods. The produced map of flood-prone by using GIS identifies the areas and settlements at high-risk flooding. The flood vulnerability index can be used in combination with

other decision-making tools and include participatory methods with the stakeholder of identified as vulnerable areas. By considering the time and scope of the required research, future research should study several fields and may need to collaborate with other methods, such as engineering economics. Capacity assessment on the physical adaptability of household structures is based on vulnerability, with communities with a high vulnerability level having a low level of adaptability. On the other hand, communities with a low vulnerability have high adaptability. A risk map should be considered in the future to possibly develop a warning system that is effective in reducing the risk to people and property in an urgent response**.** The maps should also be used to increase the awareness of risk areas and preparedness to deal with a flood. Measuring and mapping the physical vulnerability of building structures to flood could become part of the efforts of the authority to assess flood mitigation. Knowing the local building structure vulnerability can guide decision-makers in forming mitigation and adaptation policies that help to improve the quality of life of the communities. In addition to thinking about mitigation of the risk, a strategic environmental assessment should be prepared for immediate action and plans. The national action adaptation plan focusing on this matter should be transformed from the national master plan of climate change, especially in the risk areas. The integration of Top-down and Bottom-up approaches should be considered. The basis of risk management and understanding of the flood phenomenon should be concentrated on mitigating the damage caused by unpredictable events.

Acknowledgements The authors would like to thank The Engineering Institute of Thailand under H.M. the King's Patronage (EIT), PhraUdomsittinayok (KumpholKunungkaro), Mahachulalongkornrajavidyalaya University, Dr. Phramaha Tawee Potad (Bodhimedhee) at Wat Buddhapanya and Mahachulalongkornrajavidyalaya University, for their data support. In addition, acknowledgment is given to the staffs of the Faculty of Environment and Resource Studies, Mahidol University, and other agencies that provided information for this research. Authors wish to thank Dr. Thomas Neal Stewart, Mahidol University for improvement of the manuscript.

References

ADPC (2011) Framework for mainstreaming DRR into development. Presentation for 2nd regional training course of the Regional Consultative Committee on "Mainstreaming DRR into national development processes", 6–10 June 2011, Bangkok, Thailand

Amade N, Painho M, Oliveira T (2018) Geographic information technology usage in developing countries—a case study in Mozambique. Geo-spatial Inf Sci 21(4):331–345. http://doi.org/10.1080/10095020.2018.1523995

Anang WN, Braun B (2021) Assessing the degree of tidal flood damage to salt harvesting landscape using synthetic approach and GIS—case study: Cirebon, West Java. Int J Disaster Risk Reduction 55:102099. http://doi.org/10.1016/j.ijdrr.2021.102099

Andrade Pérez A, Herrera Fernandez B, CazzollaGatti R (eds) (2010) Building resilience to climate change: ecosystem-based adaptation and lessons from the field. IUCN, Gland, Switzerland, p 164

Azotea MSB, Cheong TS, Jeong SM (2017) Comparative radial analysis of Philippines' local flood vulnerability index. J Korean Soc Hazard Mitig 17(5):291–296. https://doi.org/10.9798/KOSHAM.2017.17.5.291

Balica SF, Wright NG, van der Meulen F (2012) A flood vulnerability index for coastal cities and its use in assessing climate change impacts. Nat Hazards 64:73–105. http://doi.org/10.1007/s11069-012-0234-1

Barredo JI, Engelen G (2010) Land use scenario modeling for flood risk mitigation. Sustainability 2(5):1327–1344

Bizimana JP, Schilling M (2009) Geo-information technology for infrastructural flood risk analysis in unplanned settlements: a case study of informal settlement flood risk in the Nyabugogo Flood Plain, Kigali City, Rwanda. In: Showalter P, Lu Y (eds) Geospatial techniques in urban hazard and disaster analysis. Geotechnologies and the environment, vol 2. Springer, Dordrecht. http://doi.org/10.1007/978-90-481-2238-7_6

Booth L, Fleming K, Abad J, Schueller LA, Leone M, Scolobig A, Baills A (2020) Simulating synergies between climate change adaptation and disaster risk reduction stakeholders to improve management of transboundary disasters in Europe. Int J Disaster Risk Reduction 49:101668. http://doi.org/10.1016/j.ijdrr.2020.101668. https://www.sciencedirect.com/science/article/pii/S2212420919307927#bib1

Brinckerhoff P (2009) Flood risk assessment. Parsons Brinckerhoff Ltd., United Kingdom

Crichton D (1999) The risk triangle. In: Ingleton J (ed) Natural disaster management. Tudor Rose, London, pp 102–103

Cutter SL, Boruff BJ, Shirley WL (2003) Social vulnerability to environmental hazards. Soc Sci Q 84(2):242–261

de Ruiter MC, Ward PJ, Daniell JE, Aerts JCJH (2017) Review article: a comparison of flood and earthquake vulnerability assessment indicators. Nat Hazard 17:1231–1251. https://doi.org/10.5194/nhess-17-1231-2017

Deckers P, Kellens W, Reyns J, Vanneuville W, De Maeyer P (2009) A GIS for flood risk management in Flanders. In: Showalter P, Lu Y (eds) Geospatial techniques in urban hazard and disaster analysis. Geotechnologies and the environment, vol 2. Springer, Dordrecht. http://doi.org/10.1007/978-90-481-2238-7_4

Department of Disaster Prevention and Mitigation (2014) Mainstreaming disaster risk reduction into development. United Nations Development Program, Bangkok

Department of Disaster Prevention and Mitigation (2015) The national disaster preparedness plan. Department of Disaster Prevention and Mitigation, Bangkok

Department of Marine and Coastal Resources (2014) In: Nakhapakorn K (ed) Geo-information technology for coastal zone management. Classic Scan Press, Bangkok, 241 p. ISBN 978-616-316-190-1

Díez-Herrero A, Garrote J (2020) Flood risk assessments: applications and uncertainties. Water 12(8):2096. https://doi.org/10.3390/w12082096

Duriyapong F, Nakhapakorn K (2011) Coastal vulnerability assessment: a case study of Samut Sakhon coastal zone. Songklanakarin J Sci Technol 33(4):469–476

Dwyer A, Zoppou C, Nielsen O, Day S, Roberts S (2004) Quantifying social vulnerability: a methodology for identifying those at risk to natural hazards. Geosci Aust Rec 14

Ettinger S, Mounaud L, Magill C et al (2016) Building vulnerability to hydro-geomorphic hazards: estimating damage probability from qualitative vulnerability assessment using logistic regression. J Hydrol 541(Part A):563–581. http://doi.org/10.1016/j.jhydrol.2015.04.017

Fuhrmann S, MacEachren A, Cai G (2008) Geoinformation technologies to support collaborative emergency management. In: Chen H et al (eds) Digital government. Integrated series in information systems, vol 17. Springer, Boston, MA. http://doi.org/10.1007/978-0-387-71611-4_20

Global Facility for Disaster Reduction and Recovery (2014) Understanding risk in an evolving world: emerging best practices in natural disaster risk assessment. World Bank, Washington. Available at: https://openknowledge.worldbank.org/handle/10986/20682. License: CC BY 3.0 IGO. Retrieved 31 Jan 2021

Godfrey A, Ciurean RL, van Westen CJ, Kingma NC, Glade T (2015) Assessing vulnerability of buildings to hydro-meteorological hazards using an expert based approach—an application in

Nehoiu Valley, Romania. Int J Disaster Risk Reduction 13:229–241. https://doi.org/10.1016/j.ijdrr.2015.06.001

Gomarasca MA (2010) Basics of geomatics. Appl Geomatics 2:137–146. http://doi.org/10.1007/s12518-010-0029-6

Gurukul K, Nakhapakorn K (2014) Coastal vulnerability assessment: a case study of Samut Songkham coastal zone. Thammasat J Sci Technol 22(6):775–788

Hallegatte S, Vogt-Schilb A, Rozenberg J et al (2020) From poverty to disaster and back: a review of the literature. Econ Disasters Clim Change 4(5):223–247. https://doi.org/10.1007/s41885-020-00060-5

IEC 31010 (2018) Risk management—risk assessment techniques. https://www.iso.org/obp/ui/#iso:std:iso:31000:ed-2:v1:en. Retrieved 31 Jan 2021

Intergovernmental Panel on Climate Change (IPCC) (2014) Summary for policymakers. In: Field CB, Barros VR, Dokken DJ, Mach KJ, Mastrandrea MD, Bilir TE, Chatterjee M, Ebi KL, Estrada YO, Genova RC, Girma B, Kissel ES, Levy AN, MacCracken S, Mastrandrea PR, White LL (eds) Climate change 2014: impacts, adaptation, and vulnerability. Part A: global and sectoral aspects. Contribution of Working Group II to the fifth assessment report of the Intergovernmental Panel on Climate Change. Cambridge University Press, Cambridge, pp 1–32

Intergovernmental Panel on Climate Change (IPCC) (2019) In: Shukla PR, Skea J, Calvo Buendia E, Masson-Delmotte V, Pörtner H-O, Roberts DC, Zhai P, Slade R, Conners S, van Diemen R, Ferrat M, Haughey E, Luz S, Neogi S, Pathak M, Petzold J, Portugal Pereira J, Vyas P, Huntley E, Kissick K, Belkacemi M, Malley J (eds) Climate change and land: an IPCC special report on climate change, desertification, land degradation, sustainable land management, food security, and greenhouse gas fluxes in terrestrial ecosystems

International Organization for Standardization (ISO) (2009) ISO GUIDE 73:2009, Risk management-vocabulary. International Organization for Standardization (ISO), Vernier, Switzerland, p 15

Kappes M, Papathoma-Köhle M, Keiler M (2012) Assessing physical vulnerability for multi-hazards using an indicator-based methodology. Appl Geogr 32:577–590. https://doi.org/10.1016/j.apgeog.2011.07.002

Krishnamurthy PK, Fisher JB, Johnson C (2011) Mainstreaming local perceptions of hurricane risk into policymaking: a case study of community GIS in Mexico. Glob Environ Change 21(1):143–153. https://doi.org/10.1016/j.gloenvcha.2010.09.007

Kumar D, Bhattacharjya RK (2020) Review of different methods and techniques used for flood vulnerability analysis. Nat Hazards Earth Syst Sci [preprint]. http://doi.org/10.5194/nhess-2020-297

Kundu A, Denis DM, Patel NR, Mall RK, Dutta D (2020) Geoinformation technology for drought assessment. In: Srivastava PK, Singh SK, Mohanty UC, Murty T (eds) Techniques for disaster risk management and mitigation. Wiley, Inc. http://doi.org/10.1002/9781119359203.ch13

Kuzhelev PD (2013) Geoinformation technology for the control of transportation objects. Eur J Technol Des 2(2):97–102

Lemmens M (2011) Geo-infomation technlogies, applications and the environment. In: Geotechnologies and environment. Springer, New York, 350 p

Len NLS, Bolong N, Roslee R, Tongkul F, Bin Mirasa AK, Ayog JL (2018) Flood vulnerability index for critical infrastructure towards flood risk management. ASM Sci J 11(3):134–146

Levina EY, Masalimova AR, Kryukova NI, Grebennikov VV, Marchuk NN, Shirev DA, Renglikh KA, Shagieva RV (2017) Structure and content of e-learning information environment based on geo-information technologies. Eurasia J Math Sci Technol Educ 13(8):5019–5031. http://doi.org/10.12973/eurasia.2017.00974a

Lewis J (2012) The good, the bad and the ugly: disaster risk reduction (DRR) versus disaster risk creation. PLoS Currents 4:e4f8d4eaec6af8

Malczewski J, Rinner C (2017) Multicriteria decision analysis in geographic information science. Springer, New York, 331 p. https://doi.org/10.1007/978-3-540-74757-4

Mebarki A, Valencia N, Salagnac JL, Barroca B (2012) Flood hazards and masonry constructions: a probabilistic framework for damage, risk and resilience at urban scale. Nat Hazard 12:1799–1809. https://doi.org/10.5194/nhess-12-1799-2012

Morkul V, Semerikov S, Hryshchenko S (2018) Methods of using geoinformation technologies in mining engineers training. Cambridge Scholars Publishing, 235 p

Nasiri H, Shahmohammadi-Kalalagh S (2013) Flood vulnerability index as a knowledge base for flood risk assessment in urban area. J Novel Appl Sci 2(8):266–269

Nasiri H, Yusof MJM, Ali TAM et al (2019) District flood vulnerability index: urban decision-making tool. Int J Environ Sci Technol 16:2249–2258. https://doi.org/10.1007/s13762-018-1797-5

Neussner O, Molen A, Fischer T (2008) Using geoinformation technology for the establishment of a local flood early warning system. In: Second international conference of geoinformation technology for natural disaster management and rehablitation, 01–02 Dec 2008, Bangkok, Thailand

Noren V, Hedelin B, Nyberg L, Bishop K (2016) Flood risk assessment—practices in flood prone Swedish municipalities. Int J Disaster Risk Reduc 18:206–217. https://doi.org/10.1016/j.ijdrr.2016.07.003

Papathoma-Köhle M, Schlögl M, Fuchs S (2019) Vulnerability indicators for natural hazards: an innovative selection and weighting approach. Sci Rep 9:15026. http://doi.org/10.1038/s41598-019-50257-2

Petrescu F (2007) The use of GIS technology in cultural heritage. In: XXI international CIPA symposium, 01–06 Oct 2007, Athens, Greece

Phumkokrux S (2016) The application of GIS to analyze the risk area of flood in Nakhon Pathom Province. Geoinformation Technol Burapha Univ 1(2):41–48

Phuthong P (2014) The project to assess the potential for adaptation to natural disasters of the community in Sathing Phra Peninsula, Songkhla by local youth. Faculty of Environmental Management, Prince of Songkla University

Phutthong W (2011) Documentary notes: flood '53 water crisis from plateau to Peninsula. http://www.sarakadee.com/2011/02/26/flood53/2/. Retrieved 17 Oct 2016

Prasannakumar V, Vijith H, Abinod S, Geetha N (2012) Estimation of soil erosion risk within a small mountainous sub-watershed in Kerala, India, using Revised Universal Soil Loss Equation (RUSLE) and geo-information technology. Geosci Front 3(2):209–215. http://doi.org/10.1016/j.gsf.2011.11.003

Raikes J, Smith TF, Baldwin C, Henstra D (2021) Linking disaster risk reduction and human development. Clim Risk Manag 32:100291. http://doi.org/10.1016/j.crm.2021.100291. https://www.sciencedirect.com/science/article/pii/S2212096321000206#b0125

Royal Irrigation Department (RID) (2012) Final report: suitable study for flood problem solving, Sating-Pra Peninsula, Songkhla. Progress Technology Consultants Co., Ltd., Bangkok

Sarajit O, Nakhapakorn K, Jirakajohnkool S, Tienwong K, Pansuwan A (2015) Assessing coastal composite vulnerability indices on seasonal change in Phetchaburi, Thailand. EnvironmentAsia 8(1):115–123. http://doi.org/10.14456/ea.2015.14

Schipper L, Pelling M (2006) Disaster risk, climate change and international development: scope for, and challenges to, integration. Disasters 30:19–38

Sperling F, Szekely F (2005) Disaster risk management in a changing climate. Discussion paper prepared for the world conference on disaster reduction on behalf of the Vulnerability and Adaptation Resource Group (VARG). Reprint with addendum on conference outcomes, Washington, D.C.

Taramelli A, Valentini E, Sterlacchini S (2015) A GIS-based approach for hurricane hazard and vulnerability assessment in the Cayman Islands. Ocean Coast Manag 108:116–130. https://doi.org/10.1016/j.ocecoaman.2014.07.021

Thouret JC, Ettinger S, Guitton M et al (2014) Assessing physical vulnerability in large cities exposed to flash floods and debris flows: the case of Arequipa (Peru). Nat Hazards 73:1771–1815. https://doi.org/10.1007/s11069-014-1172-x

Tingsanchali T (2012) Urban flood disaster management. Procedia Eng 32:25–37
Tran P, Shaw R, Chantry G, Norton J (2009) GIS and local knowledge in disaster management: a case study of flood risk mapping in Vietnam. Disasters 33(1):152–169. https://doi.org/10.1111/j.1467-7717.2008.01067.x
UNDP (United Nations Development Programme) (2020) Human development report 2020. UNDP, New York
UNDRR (United Nations Office of Disaster Risk Reduction) (2019) 2019 global assessment report on disaster risk reduction. United Nations, Geneva, Switzerland
United Nations Office for Disaster Risk Reduction (UNISDR) (2009) UNISDR terminology on disaster risk reduction. United Nations International Strategy for Disaster Reduction (UNISDR), United Nations (UN), Geneva, Switzerland, p 35. https://www.undrr.org/publication/2009-unisdr-terminology-disaster-risk-reduction. Retrieved 17 Jan 2021
United Nations Office for Disaster Risk Reduction (UNISDR) (2015) Sendai framework for disaster risk reduction 2015–2030. Available at https://www.preventionweb.net/files/43291_sendaiframeworkfordrren.pdf. Retrieved 17 Jan 2021
Vahanvati M (2018) A novel framework for owner driven reconstruction projects to enhance disaster resilience in the long term. Disaster Prev Manag Int J 27(4):421–446. https://doi.org/10.1108/DPM-11-2017-0285
Withuntat S, Marqueza CR, Matthew S (2016) Disaster risk assessment guideline. United Nations Development Program Thailand, Bangkok. https://www.th.undp.org/content/dam/thailand/docs/DRAGuideline_Full_Nov2016.pdf
Wong PP, Losada IJ, Gattuso JP, Hinkel J, Khattabi A, McInnes KL, Saito Y, Sallenger A (2014) In: Field CB, Barros VR, Dokken DJ, Mach KJ, Mastrandrea MD, Bilir TE, Chatterjee M, Ebi KL, Estrada YO, Genova RC, Girma B, Kissel ES, Levy AN, MacCracken S, Mastrandrea PR, White LL (eds) Coastal systems and low-lying areas. Climate change 2014: impacts, adaptation, and vulnerability. Part A: global and sectoral aspects. Contribution of Working Group II to the fifth assessment report of the Intergovernmental Panel on Climate Change. Cambridge University Press, Cambridge, pp 361–409
World conference on disaster reduction on behalf of the Vulnerability and Adaptation Resource Group, Washington, DC, USA (2005)
Xiao L, Wang J, Zhu Y, Zhang J (2020) Quantitative risk analysis of a rainfall induced complex landslide in Wanzhou County, Three Gorges Reservoir, China. Int J Disaster Risk Sci 11(3):347–363
Zezheng Y, Hanping Z, Fangping W, Xiaoxue Z, Sida C, Xiaowen M (2020) Rapid assessment of building collapse based on sequential dynamic fusion of multi-source disaster information from news media. Int J Disaster Risk Reduction 51:101910. http://doi.org/10.1016/j.ijdrr.2020.101910

Chapter 16
Cooling Potential Simulation of Urban Green Space Using Remote Sensing and Web-Based GIS Integration in Panat Nikom Municipality, Thailand

Chanida Suwanprasit, Sakda Homhuan, and Wanpen Charoentrakulpeeti

Abstract The most important local and global change driving force is urbanization because it progressively replaces natural surfaces with built surfaces. These causes enhance the urban heat island phenomenon where the temperature in the urban area is higher than the temperature in the countryside around the city. Increasing urban green space can play an important role in reducing the urban heat island effects and providing comfort to the nearby area. It can also contribute to the United Nations Sustainable Development Goals (SDGs), especially SDG 11, which aims to make cities and human settlements inclusive, safe, resilient, and sustainable. This study aimed to develop a web-based simulation platform for examining local temperature changes from the change in the proportion of green space in the city. The Worldview-3 imagery was used for green space area extraction through NDVI and land surface temperature from Landsat 8 OLI. The relationship between surface temperature and the green area was studied with NDVI using regression analysis to develop an equation for land surface temperature calculated according to the changes in the green area. The web-based GIS platform was developed using open source with Geoserver and LeafletJS using an equation developed for exploring and simulating the cooling potential of urban green spaces through a web user interface. The temperature was more related to the NDVI, which can refer to the quality of the green area rather than the size of the green space. It was concluded that the cooling potential of such green areas is determined mainly by the quantity and quality of the green space, which is essential to increasing or decreasing the local temperature and ecological environment. Setting the target for reducing the temperature to the comfort level might require tools that allow urban policymakers to know the level of temperature in the area and the temperature drop changes by increasing green area proportion to determine how much more green space the city has needs.

Keywords Cooling potential · Urban green space · Remote sensing · Web-based GIS · Local temperature

C. Suwanprasit (✉) · S. Homhuan · W. Charoentrakulpeeti
Department of Geography, Faculty of Social Sciences, Chiang Mai University, Chiang Mai, Thailand
e-mail: Chanida.suwanprasit@cmu.ac.th

V. P. Singh et al. (eds.), *Application of Remote Sensing and GIS in Natural Resources and Built Infrastructure Management*, Water Science and Technology Library 105,
https://doi.org/10.1007/978-3-031-14096-9_16

16.1 Introduction

Green spaces play an important role in urban sustainability, recognized in the United Nations Millennium Sustainable Development Goals (UN SDGs), especially SDG 11, which aims to make cities and human settlements inclusive, safe, resilient, and sustainable. Urban green is a significant factor to support a good quality of life for people, especially in the city. In terms of ecosystem services, green space plays a significant role in controlling urban climate by utilizing cooling conditions in the city, and it has been known as the effect of urban green spaces (Fryd 2011).

Several studies have been published on the available strategies for reducing the UHI effect, including the use of vegetation cover at various scales such as trees, shrubs, and lawns, stack night ventilation, the use of water bodies, and the use of materials with high albedo ratings for pavement and other ground surfaces (Aram et al. 2019). However, the extent of its influence on the creation of cool temperatures has remained unclear. Previous research on the cooling effects is important for urban green conservation and development. However, evaluating the cooling effects on urban areas relevant to various aspects and dynamics in time and space necessitates modern ways to apply and explain the status of cooling from urban green space. Measurements (field measurements, scale models, and thermal remote sensing) and computer simulation have already demonstrated the benefit of green infrastructure in lowering urban thermal islands (Aram et al. 2019).

While green space is cooler than built-up areas, cooling varies depending on the surrounding components and location. The three primary elements that affect the cooling levels of urban green spaces are as follows. Firstly, intensive urban land use, primarily build-up areas, contributes a substantial amount of anthropogenic heat to the atmosphere, while green areas contribute cooling effects—for example, urban greening in Hong Kong helps cool the air and provides shade in the high-densely living environment (Ng et al. 2012). Secondly, the land cover with a high concentration of vegetation produces the cooling process in urban areas. It has been found that vegetation and water can alleviate the urban heat island effect (Ma et al. 2021). Lastly, the urban geometry with low-rise buildings and wide paths promotes well ventilation, enhancing the cooling process of green spaces. Therefore, the green space's spatial component plays a significant role in the cooling conditions of urban green areas.

Meanwhile, geographical location has also influenced the cooling situation of green space differently. In the tropical region, green areas will more distinctly present the effect of a cooling process than the temperate region. The cooling effect of green areas has been verified for specific places. The highest heat island intensity was in the tropical environment to a great extent. UHI in tropical was higher in a temperate climate with an intensity value exceeding 6 °C (Amorim and Dubreuil 2017). However, one area cannot be addressed for another area. The advent of remote sensing and web-based GIS pave the way to study the cooling effect for a given site. With available spatial data provided from satellite base measurement, the requirement

of various spatial data can be acquired for a given study area. Meanwhile, web-based GIS will help create correlation equations of a proportion of green areas and pertinent parameters and then apply those equations to present the results of the cooling situation in any given site with different sets of parameter data.

This chapter aims to describe the effect of urban green space on the cooling effect in Panat Nikom Municipality, Chon Buri Province, Thailand, using remote sensing and a web-based GIS. The cooling effect on urban areas will serve as an incentive for legislators to understand the value of green spaces in cities and, ideally, to decide in favor of integrating green space effects on urban growth.

16.2 Urban Climate and Green Space Relationship

Urban climate has been roughly considered at two levels: below and above roof-level morphology (Oke 1987). The former is called "the urban canopy layer (UCL)" while the latter is called "the urban boundary layer (UBL)". The UCL is governed by site-specific and the mean height of buildings and trees characteristics and operating processes at a micro-scale. The site-specific characteristics are accountable for intrinsic properties, thermal properties, moisture status, radiative capability, and the aerodynamics of urban morphology. As UCL can be separated into two scales: "micro-scale" and "local-scale," the intrinsic properties play an important role in producing micro-climate and integrating that into local climate. The UBL is controlled by the existence of the composite urban landscape: land use, land covers, and landforms, operative at a local to meso-scale. This level is a function of the land use zone, in which all land use in the entire city can be mixed and referred to as meso-scale (Arnfield 2003) (Fig. 16.1).

The urban climate was analyzed in terms of energy movement. Airflows are critical in pushing energy circulation from a UCL unit to the UBL during turbulent conditions. According to Collier (2006), the UBL is created by airflow from rural to urban areas. The micro-scale initiates energy circulation—below roof levels—as a result of the heterogeneous urban morphology's influence. These causes in energy transfer from several characteristics: urban street canyon flows, energy from individual buildings mixing with adjacent building groups, and the atmosphere above the roof. The appearance of a turbulent-wake layer above the roof level can occur at approximately 2.5–3 times the height of the buildings (Roth 2000). This layer is often termed a "roughness sub-layer" while above the roughness sub-layer is the urban surface layer or the inertial sub-layer; it is the effect of a combination of a larger part of the urban area. The turbulent flux is constant with height (Collier 2006). Meanwhile, the mixed urban layer height is set above the surface layer, with its characteristics are affected by the presence of urban surface heterogeneity, and it extends upwards to the top of the UBL during daylight periods.

According to intrinsic urban properties and urban landscape, it has produced a diverse phenomenon, the so-called urban heat island (UHI). The UHI characteristics are very different because of landscape differences. Although there are similar

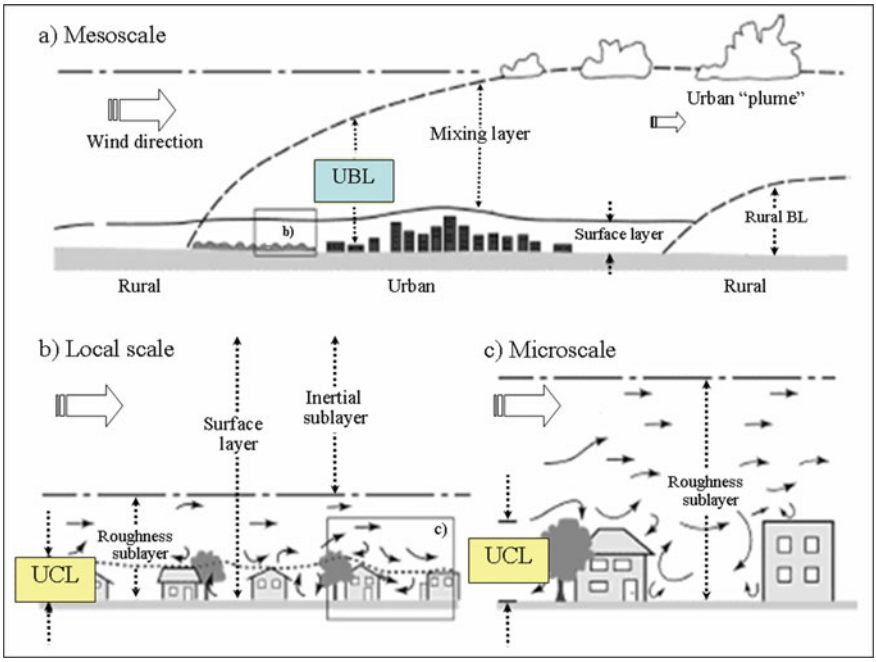

Fig. 16.1 Urban morphological scale. *Source* Oke (2002)

building heights, fewer trees, and less irrigated turf, Phoenix faces with UHI effect more than Kuwait city, with the urban heat island intensity of Phoenix (0.22 °C per decade) higher than Kuwait city (00.07–0.12 °C per decade) (Nasrallah et al. 1990). In terms of the spatial pattern, the UHI is controlled by the component of built-up areas and probably be separated by the influence of intra-urban land use in the city (Oke 1987). According to thermal properties, built-up areas, always pavement materials, play significant roles in determining the temperatures of near-surface air (Li 2016). If the near-surface temperature was considered, the industrial-commercial and high-density residential areas presented the highest land surface temperature (Uritescu 2017).

These result in the probable appearance of areas of cooling effects, such as parks, lakes, or open spaces, or areas of warming effects with consequences from various urban activities, such as high-rise buildings, shopping complexes, and industrial areas (Fig. 16.2) (Oke 1987).

According to three critical components of the landscape that influence urban climate: urban geometry, urban land use, and urban land cover; this chapter will focus on only land cover effects in terms of green space relationships. It was discovered that several intrinsic properties, including thermal admittance, moisture status, and surface albedo, play a significant role in producing urban climate.

Surfaces materials with large thermal admittance play an important role in possessing greater absorbing and re-emitting thermal radiation properties. A high

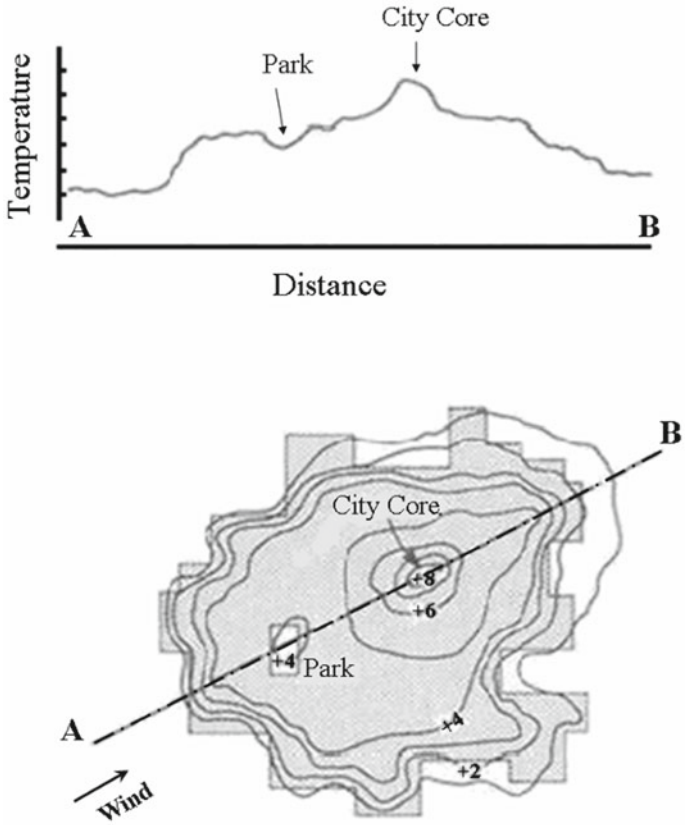

Fig. 16.2 Spatial heat island characteristics. *Source* Oke (1987)

proportion of high thermal admittance of surface materials is a key to maintaining warmer urban temperatures (Oke et al. 1991). It has been found to have a higher cooling rate in the surrounding wooded countryside than flat concrete in the city; as a result, it can be generated a heat island at approximately 8 °C (Oke 1981). While the moisture quality of the land cover is crucial, defined as the quantity of moisture accessible to the UCL's ability to store water (Oke 1982). It is a significant factor in the organization of mixed-surfaced micro-climates as surface moisture plays a crucial role in controlling turbulent heat transport in the UCL (Oke 1982). In wet areas, advection of warmer and drier air from surrounding impervious areas increases evaporation from irrigated lawns, gardens, and parks (Kanda 2007). This process contributes to mixed air in a micro-climate. In cities, the interaction of advection among impervious areas produces extra heat and makes sufficient moisture in parks or irrigated gardens. These factors can contribute to the formation of an oasis effect—the formation of a local micro-climate that is colder than the surrounding dry area as a result of evaporation or evapotranspiration of a water source or plants

life and the higher albedo of plant life than bare ground (Oke 1982, 1987). The surface may contain sufficient water to allow evaporation to exceed the potential rate in the presence of less net radiation than latent heat in the appropriate settings. This condition results in cool islands in a region of dried urban air. The surface albedo is another crucial component that influences the daylight net radiation budget, which is the energy that enters, is reflected, absorbed, and expelled by the Earth system. For a given solar input, it is regulated the surface shortwave absorption by surface albedo, materials with high albedo will absorb less solar radiation than the low ones. In general, dark surfaces will contribute to low surface albedo while bright surfaces have a high surface albedo (Taha 1997).

The studies of urban climate and green space relationship are found in remote sensing; for instance, Cao et. al. (2010) used ASTER and IKONOS satellite images to investigate the relationship between thermal temperature and cooling effect of 92 public parks in Nagoya, Japan. He found that sizes and the proportion of hardscape and soft scape areas in the parks influence the cooling effect and temperature decrease; however, the result was not shown green space areas in terms of quality. This chapter, therefore, discovers urban climate and green space in both quantity and quality by applying remote sensing.

One crucial component factor for urban planning is urban greening because of its various contribution to citizens' well-being and quality of living by minimizing the effects of local severe weather conditions and air pollution (Abutaleb et al. 2021; Evans et al. 2013). Urban green spaces may include places with "natural surfaces" or "natural settings" but may also include specific types of urban greenery, such as street trees, and may also include "blue space," which represents water elements ranging from ponds to coastal zones (World Health Organization 2013). Thermal characteristics (which enhance heat storage) and street canyon geometry (which minimizes longwave radiation loss) are equally capable of generating a heat island under conditions relevant to UHI development (Fernando 2013).

Grilo (2020) demonstrated the effect of green and gray spaces in the cooling island effect, which showed that even green spaces with reduced areas could control microclimate, alleviating temperature by 1–3 °C and increasing humidity by 2–8%, on average. Green spaces with a higher tree density generated a more significant cooling impact. The shape, aspect, and degree of exposure to solar radiation of grey surfaces were also significant features considered in the models. Green spaces affected temperature and relative humidity up to 60 m away from the parks' boundaries, but gray areas had a much smaller effect, ranging from 5 to 10 m (Fig. 16.3).

Urban green space temperature can be 1–2 °C, and sometimes 5–7 °C, cooler than their urban environments, establishing a "park cool island" (PCI) mentioned on several field-based measurements (Aram et al. 2019; Gonçalves et al. 2018; Ersoy 2019). Furthermore, several proves, such as field measurements, scale models, thermal remote sensing, and computer simulation, mentioned the effectiveness of reducing the temperature by green infrastructure (Aram et al. 2019). Aram et al. (2019) reviewed the literature related to the cooling effect of green infrastructure in different shapes and scales, including small local parks, large urban parks, urban forests, urban gardens, green roofs, green facades, and street trees. However, different

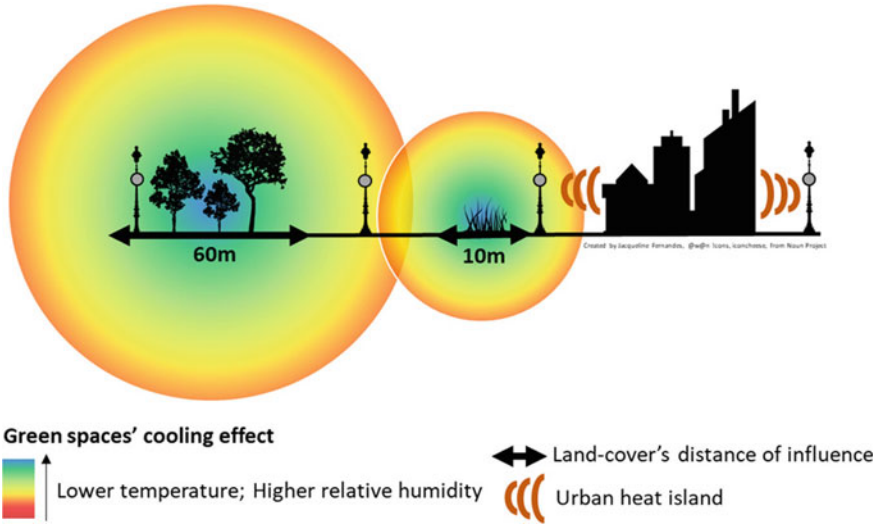

Fig. 16.3 Green spaces' cooling effect. *Source* Grilo (2020)

urban forms have been created in cities, and each of these forms has different effects on the micro-climate of the city by changing the duration of direct sunlight and the mean radiant temperature. Typically, cooling extends depending on greenspace size, with larger greenspaces commonly providing more cooling. Vaz Monteiro et al. (2016) discovered the cooling effects and suggested that the greenspaces with areas of 3–5 ha, situated 100–150 m apart, could provide a spatially comprehensive mean cooling service of about 0.7 °C across a city with a similar climate/characteristics to London. Moreover, the results showed that very small greenspaces (with areas < 0.5 ha) did not affect the air temperatures of their surrounding areas (Vaz Monteiro et al. 2016).

Urban heat island (UHI) effect has been an issue in urban areas. Due to the UHI effect, an urban area can be 1.0–6.0 °C warmer than the neighboring non-urban areas, as shown in Fig. 16.4 (Aram et al. 2019). American cities face 0.5–4.0 °C higher daytime air temperatures and 1.0–2.5 °C higher night-time air temperatures than the neighboring rural areas (Wuebbles et al. 2017). Consequently, increasing urban green space can play a critical role in reducing the urban heat island effects and providing comfort to the neighboring area. Various studies confirmed that UHI, air temperature (AT), land surface temperature (LST), and the types of land cover/use are linked (e.g. Buo et al. 2021; Shahfahad et al. 2021; Rajkumar and Elangovan 2020; Shorabeh et al. 2020; Tawfeek et al. 2020; Amindin et al. 2021; Athukorala and Murayama 2021) as well as its connection with ecosystem service value (Guha 2021; Lei and Wang 2019).

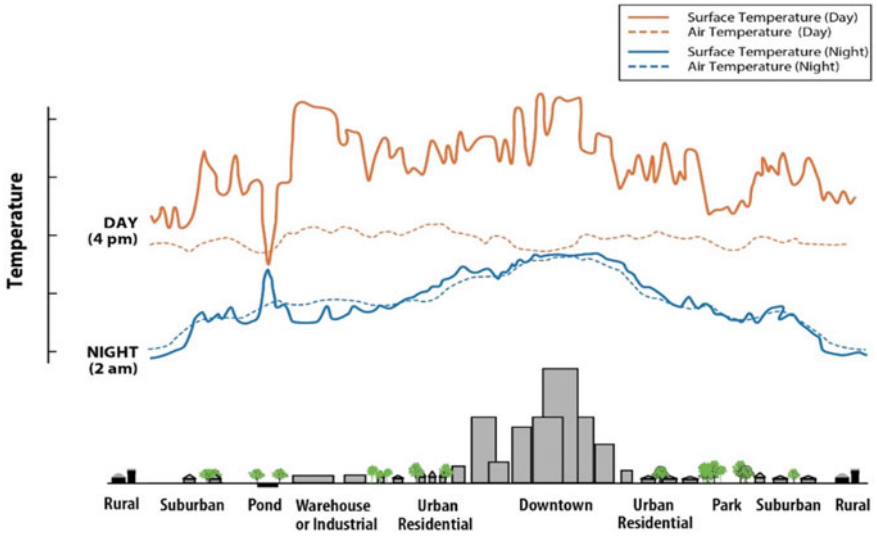

Fig. 16.4 Urban heat islands. *Source* U.S. Environmental Protection Agency (2021)

16.3 Remote Sensing for Quality of Green Space and Local Temperature

Remote sensing is a tool to obtain information about the urban context, particularly thermal field monitoring and land use/land cover (Busato et al. 2014; Silva and Torres 2021). It brings an excellent opportunity to identify the vegetation phenology in different resolutions. The proportion of greenness in urban vegetation can be assessed at the pixel level using a variety of spectral unmixing variations in order to derive area-based green space information. Remote sensing data enables the assessment of various land use and occupation characteristics, which can be noticed via the spectral response of vegetation indices or land surface temperature. The land surface temperature (LST) and normalized difference vegetation index (NDVI) have been widely used to determine surface temperature and vegetation in many contexts, including urban temperature and urban green spaces at various spatial scales (e.g. Ekwe et al. 2021; Rahaman et al. 2021; Shafizadeh-Moghadam et al. 2020).

16.3.1 Land Surface Temperature (LST)

Some studies have emphasized studying small and medium cities' built environments based on remotely acquired information. Thermal remote sensing describes the flaw observed in conventional monitoring of urban temperature, especially for detecting the urban heat island (Chen et al. 2006; Mirzaei, et al. 2020; Siddiqui et al. 2021;

Sun 2021). The cooling effect of urban greenspace is commonly analyzed using temperature and land surface temperature (LST) data (Liao et al. 2021; Yang et al. 2017). Because satellite-derived LST data are widely available on a regional–global scale, it is frequently used to estimate near-surface air temperature (Stisen et al. 2007). However, the air temperature dataset is usually not widely available, and only a limited amount of measurement sites exist in a small area, especially in a city or town. The thermal infrared remote sensor (TIRS) is broadly utilized for LST deriving to its extensive spatial coverage (Nichol and Wong 2008). LST, which is sometimes referred to as the Earth's skin temperature and is derived from remotely detected thermal infrared (TIR) data, is a critical metric for assessing and modeling the surface energy balance (Weng 2019).

Current satellite TIR data are well-suited for studying cities' thermal conditions and resolving urban environmental and health issues due to their significant geographical variability. The thermal infrared sensors on numerous satellites are listed in Table 16.1.

LST is an important component of climate and biology, impacting species and ecosystems on various sizes, from local to global. NASA and other international organizations have designated LST as one of the most critical Earth System Data Records because it measures thermal radiation emission from the land surface, where incident solar energy interacts with and heats the ground or the surface of tree canopies in vegetated areas (Hulley et al. 2019).

In this study, the LST was computed using Landsat 8 OLI/TIRS Band 10 (thermal infrared region) using formulas from the USGS web page for calculating the top of atmospheric (TOA) spectral radiance (L_λ: W/m^2 srad μm) for Landsat 8 OLI as follows:

$$L_\lambda = M_L * Q_{\text{cal}} + A_L - O_i \tag{16.1}$$

Table 16.1 Thermal infrared remote sensors

Satellite	Spectral resolution (μm)	Spatial resolution (m)	Revisit time (days)
NOAA AVHRR	10.30–11.30 11.30–12.50	1100	1
Landsat 4/5 TM	10.40–12.50	120	16
Landsat 7/ETM+	10.40–12.50	60	16
Landsat 8/ETM+	10.60–12.51	100	16
Aster	10.40–12.50	90	16
HCMM	10.50–12.50	600	1
MODIS	3.66–4.08 10.78–12.27	1000	1

Source Weng (2009)

where M_L represents the band-specific multiplicative rescaling factor, Q_{cal} is the Band 10 image, A_L is the band-specific additive rescaling factor, and O_i is the correction for Band 10.

After the digital numbers (DNs) are converted to the reflectance values, the TIRS band data should be converted from spectral radiance to brightness temperature (BT) by using the following equation:

$$\text{BT} = \frac{K_2}{\ln\left(\frac{K_1}{L_\lambda} + 1\right)} - 272.15 \tag{16.2}$$

where K_1 and K_2 stand for the band-specific thermal conversion constants from the metadata (for this study, K_1 and K_2 were 774.89 and 1321.08, respectively). The radiant temperature is converted to Celsius values by adding absolute zero (about 273.15 °C) (Avdan and Jovanovska 2016).

Numerous research has demonstrated the efficiency of a group of urban green spaces in reducing UHI and cooling the urban environment by utilizing the advantages of remote sensing in urban ecological studies. Numerous satellite imagery datasets, such as the LST map, QuickBird, IKONOS, and ASTER, are valid for analyzing the effect of green spaces on huge expanses (Aram et al. 2019).

16.3.2 Normalized Difference Vegetation Index (NDVI)

Earlier research has demonstrated that the cooling effect of the blue-green space depends on the size, shape, connectivity, and complexity (composition and configuration) of the blue-green space and the greenness of the green vegetation measured by the Normalized Difference Vegetation Index (NDVI). NDVI is not only an indicator of the greenness of the biomes but also an indicator of vegetation health based on how plants reflect specific ranges of the electromagnetic spectrum. Because the urban thermal environment is related to reducing evapotranspiration from the surface vegetation cover, NDVI is helpful to understand the relationship between surface vegetation cover and water availability (Lo et al. 1997). Over time, it has been used for vegetation change in environmental studies, agricultural monitoring, and examinations of vegetation vitality changes. Rouse et al. (1974) was the first person who proposed the NDVI, which has been widely used to express the vegetation amount in urban areas using the ability of red and near infrared (NIR) wavelengths.

Calculations of NDVI for a given pixel always result in a number that ranges from minus one (−1) to plus one (+1); however, no green leaves give a value close to zero. A zero means no vegetation, and close to +1 (0.8–0.9) indicates the highest possible density of green leaves.

$$\text{NDVI} = \frac{\rho\text{NIR} - \rho\text{R}}{\rho\text{NIR} + \rho\text{R}} \tag{16.3}$$

Table 16.2 NDVI range in each land cover type

Land cover types	NDVI range	Land cover types	NDVI range
Water	−0.28 to 0.015	Shrub and grassland	0.18–0.27
Built-up	0.015–0.14	Sparse vegetation	0.27–0.36
Barren land	0.14–0.18	Dense vegetation	0.36–0.74

Source Akbar et al. (2019)

where ρ is the surface reflectance values for the near infrared (NIR) and red (R) spectral bands. Akbar et al. (2019) reported the NDVI range for land cover classes using Landsat 8 OLI image from 2016, as shown in Table 16.2.

16.4 Web-Based GIS for Cooling Potential Simulation of Urban Green Space

A web map, or web-based geographic information system, is an interactive display of geographic data that can be used for various purposes, including data visualization, presenting real-time geographical data, querying spatial data in online catalogs, and searching tools. JavaScript is one of the most popular built-in web-based GIS (Dorman 2020). Due to the increased popularity of web-based GIS, new applications for GIS techniques in participatory spatial planning and decision making have emerged (Jelokhani-Niaraki and Malczewski 2015). The concept of a multicriteria spatial decision support system (MC-SDSS) has been offered as a useful tool for participatory/collaborative decision making and consensus building in spatial planning or decision making.

Figure 16.5 illustrates a web-based geographic information system concept. The operation of a web map consists of two important parts: server and client. The *server* serves various geospatial data services, while the client part allows the user to access the data via the web or application. The server and the client communicate via Hypertext Transfer Protocol (HTTP/HTTPS). The information communicated between the GIS server and the client is based on the Open Geospatial Consortium (OGC). Usually, servers have a different Uniform Resource Locator or URL. Users can find and access URLs on the Internet network. The function of a server is to listen to requests for information from users and send them back as requested through a communication channel based on HTTP/HTTPS protocol. The communication data formats are HTML and binary. image, Extensible Markup Language (XML), Geography Markup Language (GML), or JavaScript Object Notation (JSON).

A GIS server provides specialized software to transform geographic information such as shapefile, GeoPackage, GML, TIFF, KML, or data stored in a spatial database into the standard OGC web service format. The OGC standard specification defines some different methods for exchanging geospatial data, including Web Map Service

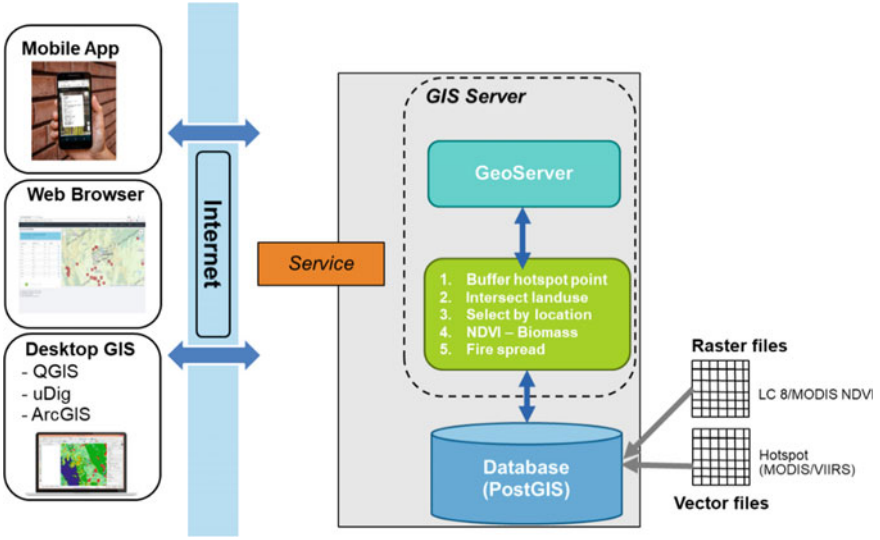

Fig. 16.5 Concept of web-based GIS. *Source* Adapted from GeoServer (2013)

(WMS), Web Feature Service (WFS), and Web Map Tile Service (WMTS) (Wu et al. 2011).

- WMS is a standard for exchanging georeferenced maps derived from geospatial databases. The GIS server sends the image data to JPEG, and PNG, which can be displayed in a browser application. Additionally, the generated image data can be configured for transparency to overlay other layers produced by other servers.
- WFS is a standard for exchanging geographic information on the Internet. The advantage of this service is that information is exchanged over a network instead of sharing geographic information at the file level. Some operators allow users to create, delete, edit and display detailed information.
- WMTS is a standard protocol for serving georeferenced map tiles where they are precomputed.

The distinction between WMS and WMTS is that WMTS transmits tiles (usually 256×256 pixel size), whereas WMS gives a single image for each request. To access geographic information in a web-based GIS, a client employs the HTTP/HTTPS protocol. This protocol makes it simple to use and supports a high number of users simultaneously. Additionally, it is cross-platform, accessible via numerous web browsers like Internet Explorer, Firefox, and Chrome, each of which supports various operating systems, including Windows, Linux, Mac OS, and iOS. APIs that are available and support OGC standards, such as Open Layers, Leaflet, Mapbox GL, ArcGIS API, and others, provide another data source (Omidipoor et al. 2019). Key technologies and tools for web GIS development include spatial database, software clients, GIS server middleware, and frontend libraries and frameworks.

The geographic database system is an essential component of web GIS development since it deals with data collecting and provides tools for retrieving, managing, and analyzing spatial data. The majority of spatial databases are relational databases that are used in conjunction with GIS. These databases provide features or additions that allow them to support various forms of spatial data. The OGC specification covers the types and functions of a standard spatial database. Vector and raster datasets with geographic indexes and spatial functions for managing and evaluating the data are examples of spatial data formats that can be stored in a database. Various database applications such as PostgreSQL/PostGIS, MySQL, Oracle Database, and others are utilized for spatial data.

In order to provide Internet network data, software clients or GIS Desktop are required to be installed on the end user's computer. Popular GIS software such as QGIS and ArcGIS are widely used because of their wide variety of capabilities for creating, managing, analyzing, and visualizing geographic data. Nowadays, GIS software is widely used. The majority of GIS programs support connection to geospatial datasets. Users can access data from the exact location, making it easier to upgrade and analyze. There are numerous benefits: Information is kept up-to-date and is less likely to be redundant.

GIS software customers include a library utility, a command-line, or a scripting machine for managing and manipulating data. Popular library utilities include GDAL/OGR and ArcPy, supporting vector, and raster spatial data. Advantages of libraries utilities are customizable for the intended purpose. It is possible to automate re-executing through a series of developed commands. The term "middleware" refers to software installed on the GIS server's side. Its purpose is to listen to user commands and respond with data. GeoServer, Mapserver, and ArcGIS are all standard software tools. GIS server middleware can connect to geospatial databases and process vector and raster spatial data. It enables users to produce, share, process, update, and publish geospatial data from various sources via an open web service standard. These OGC web services can be rendered with the help of frontend tools such as Leaflet, Mapbox, and OpenLayers. The OGC web services can be accessed using the GIS software desktop.

Frontend libraries and frameworks allow developers to bring OGC web service data to create web-based GIS on user needs. Most frontend libraries and frameworks support JavaScript development, such as Leaflet, Mapbox, and OpenLayers. However, some frontend libraries can use other programming languages, such as Folium, which uses Python to develop web maps. Frontend development is essential because it is the part that presents information to users and interacts with them. It may have a working basis: it can be displayed on various devices, determine the current location from the device (Location), and display other data layers such as administrative boundaries. For example, forest regions, elevations, streams, and transportation routes can be enhanced with survey data such as location, images, captions, and graphs.

Currently, using online web maps to display data enables more rapid analysis of complex geographical events, the recognition of trends, and the planning and allocation of resources for policy and decision making (e.g. Evans and Sabel 2012;

Duarte et al. 2021; Muenchow et al. 2019; Neene and Kabemba 2017; Farkas 2017; Olyazadeh et al. 2017).

16.5 A Case Study: Panat Nikom Municipality, Chon Buri Province, Thailand

16.5.1 Overview of Panat Nikom Municipality

Panat Nikom Municipality is a small town in Chonburi province, Thailand, located in the southeast of Bangkok. Panat Nikom is located in the middle of the manufacturers and industries region. However, in August 2015, Panat Nikom Municipality was chosen not only to be a city to promote sustainable urban development of Thailand's local cities by the National Economic and Social Development Board (NESDB) and the Japan International Cooperation Agency (JICA) but also to be a city of the Sustainable Future City (SFC) development concept and proposed the Sustainable Future City Initiative (SFCI).

16.5.2 Data and Material

Six Landsat 8 Operational Land Imager (OLI)/Thermal Infrared Sensors (TIRS) from December 2019 to April 2020 were freely downloaded from the United States Geological Survey website (https://earthexplorer.usgs.gov) to use in the study together with GIS layers collection from several sources. Table 16.3 shows the study's Landsat 8 OLI/TIRS band characteristics.

16.5.3 Methodology

Geometric correction, radiometric correction, and resampling were applied to all images. The TIR bands were used to calculate LST (Band 10). As described in the previous section, LST and NDVI were estimated using Eqs. 16.1–16.3. Green areas were created by manually digitizing Worldview-3 satellite images using QGIS as polygons features due to its higher resolution (1.24 m × 1.24 m) than Landsat 8 OLI (30 m × 30 m). According to several studies, pocket green spaces are defined as green spaces that are less than 2 ha in size and are located in urban and suburban regions (Wu et al. 2021). Green areas were defined in this study under Thailand's Office of Natural Resources and Environmental Policy and Planning definition, which included public green areas, utility green areas, row street green areas, economical green areas, natural green areas, and undeveloped green areas. The selected green

Table 16.3 Landsat 8 OLI and TIRS characteristics

Band	Wavelength (μm)	Resolution (m)
Band 1: Coastal aerosol	0.43–0.45	30
Band 2: Blue	0.45–0.51	30
Band 3: Green	0.53–0.59	30
Band 4: Red	0.64–0.67	30
Band 5: Near infrared (NIR)	0.85–0.88	30
Band 6: SWIR 1	1.57–1.65	30
Band 7: SWIR 2	2.11–2.29	30
Band 8: Panchromatic	0.50–0.68	15
Band 9: Cirrus	1.36–1.38	30
Band 10: Thermal infrared 1	10.60–11.19	100
Band 11: Thermal infrared 2	11.50–12.51	100

Source NASA (2021)

area was done by selecting the area more than 1600 m^2 (1 Rai—a Thai area unit), which can be identified in the WorldView-3 image and correspond with the Landsat Thermal image. Each shape of the green area polygon was utilized to calculate the mean value of LST and NDVI for the correlation study using zonal statistics. After that, the regression analysis was performed to create a simulation model. Then the model was used for developing the GIS web-based GUI for the mean temperature simulation. Figure 16.6 presents the research framework.

16.5.4 Results and Conclusion

In developing a model to support green space management planning decision making, a correlation analysis was conducted between LST, NDVI, and green area.

- LST and NDVI Calculation

Indicators of vegetation cover are frequently utilized in environmental applications. Several of them are primarily used to estimate plant yield, which provides excellent supporting data for describing temperature features, as demonstrated in a study. Karnieli et al. (2010) found that NDVI can be used to study temperature differences between areas with and without vegetation cover. Areas with high NDVI values are found to have lower surface temperatures, and areas with low NDVI values have high surface temperatures. For this investigation, data in the red and near infrared wavelengths with a spatial resolution of 30 * 30 m were applied for a year throughout the winter season by selecting one typical sample from November to April in 2019, as shown in Fig. 16.7 and Table 16.4.

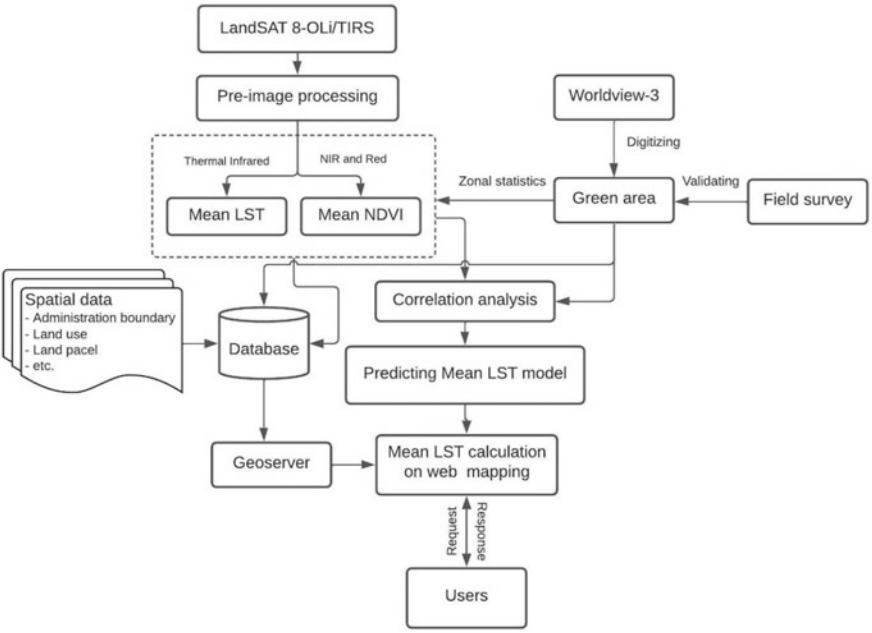

Fig. 16.6 Processing framework

- The relationship between the size of the green area surface temperature and NDVI

After calculating the LST and NDVI, the LST and NDVI values were extracted with the 109 green area sites and correlation statistics (Best 1977). The level of interpretation of the correlation coefficient is shown in Table 16.5.

The satellite images data were taken between December 2019 and April 2020. One hundred and nine of the green area sites were performed for the correlation and regression analysis. The correlation statistics are shown in Table 16.6 and Fig. 16.8, which can be seen that the size of the green area is negatively related to the mean LST and positively to the mean NDVI at a low level. For interpretation, if the green area is increased in size, the LST should dropdown. The correlations between mean LST and mean NDVI were significantly negative throughout the study period (dry season), indicating that increasing the city's quality of green space (NDVI) may decrease local temperature (mean LST). The green area's size was negatively correlated with the mean LST and positively correlated with the mean NDVI. If the green area increases, it may increase the mean NDVI.

- Linear regression analysis

From the selected data and variables for model development to support green space management planning decisions for calculating mean LST in the previous step, the size of a green area (Rai) and mean NDVI were found to be the highest value of decision coefficient analysis results from linear regression analysis (R^2) = 0.505 by

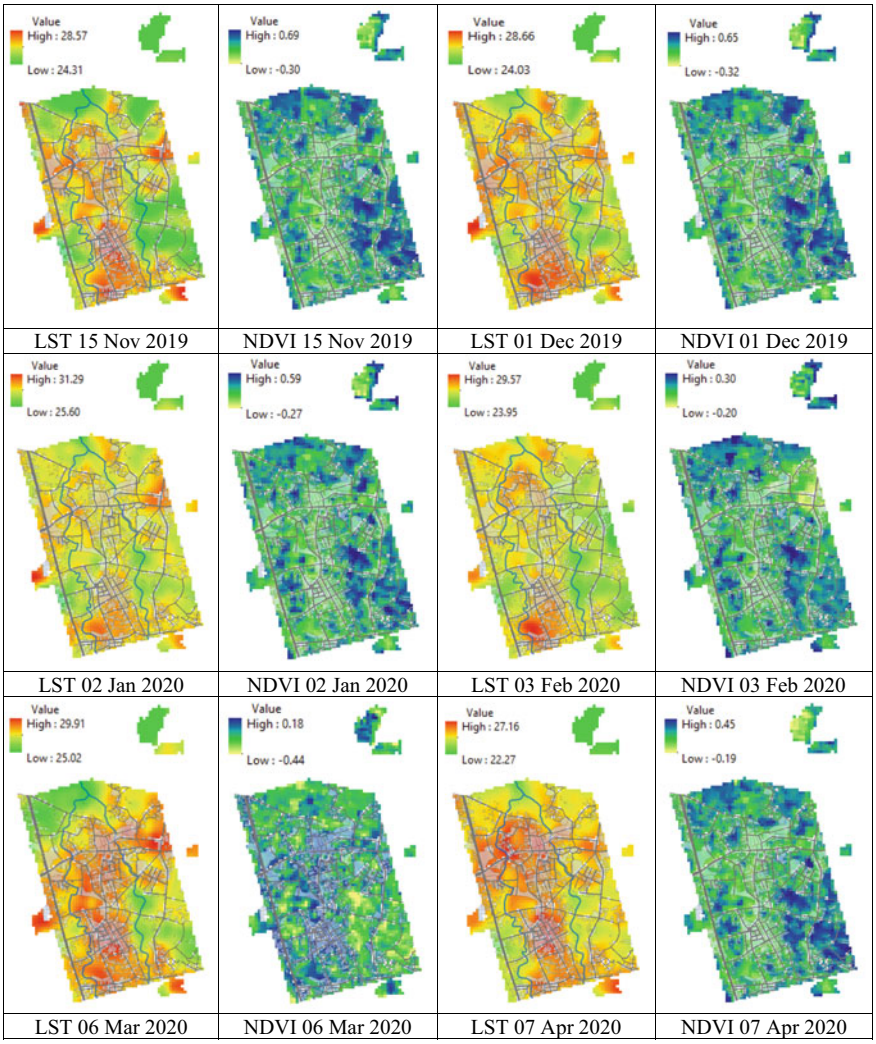

Fig. 16.7 List of LST and NDVI between November 2019 and April 2020

the model significant at p-value < 0.01, and it can be written in the form of equations as follows (Eq. 16.4):

$$\text{MEAN\_ LST} = \left(\text{Green area} * \left(-9.575 \times 10^{-6}\right)\right) - (\text{MEAN\_NDVI} * 3.507) + 28.148 \tag{16.4}$$

where

MEAN_LST is the average land surface temperature (°C).

Table 16.4 LST and NDVI statistics varies in each month

Date	LST (°C)			NDVI		
	Min	Max	Mean	Min	Max	Mean
15 Nov 2019	24.31	28.58	26.82	−0.30	0.69	0.21
01 Dec 2019	24.03	28.66	27.09	−0.32	0.65	0.18
02 Jan 2020	25.60	31.29	29.13	−0.27	0.59	0.12
03 Feb 2020	23.95	29.57	27.31	−0.20	0.30	0.01
06 Mar 2020	22.27	27.16	25.67	−0.44	0.18	−0.09
07 Apr 2020	25.02	29.91	28.28	−0.19	0.45	0.13

Table 16.5 Correlation coefficient interpretation

Coefficient (r)	Relationship
0.00–0.20	Negligible
0.20–0.40	Low
0.40–0.60	Moderate
0.60–0.80	Substantial
0.80–1.00	High to very high

Source Best and Khan (1977)

Table 16.6 Correlation coefficients of green area, mean LST, and mean NDVI

Correlation coefficients	MEAN_LST	MEAN_NDVI	Green area
MEAN_LST	1	−0.700**	−0.347**
MEAN_NDVI	−0.700**	1	0.332**
Green area	−0.347**	0.332**	1

** Correlation is significant at the 0.01 level (2-tailed). * $N = 109$

Green area is the size of the green area (Rai).
MEAN_NDVI (NDVI value range between −1 and 1).

- Development of a web-based GIS for green area management decision support system.

The web-based GIS for the green area management decision support system (Fig. 16.9) was created utilizing a website schema and Geoserver, Node.js, and PostgreSQL/PostGIS. The user can digitize by adding a new polygon of green area, and the system follows the equation mentioned above. The graphic user interface was developed to be as simple as possible for local policymakers to assist them in designing to improve green space in their area. The system will then compute and report the new lowering temperature caused by the new green area that the user has added. Figure 16.8 describes a qualitative green space planning decision support

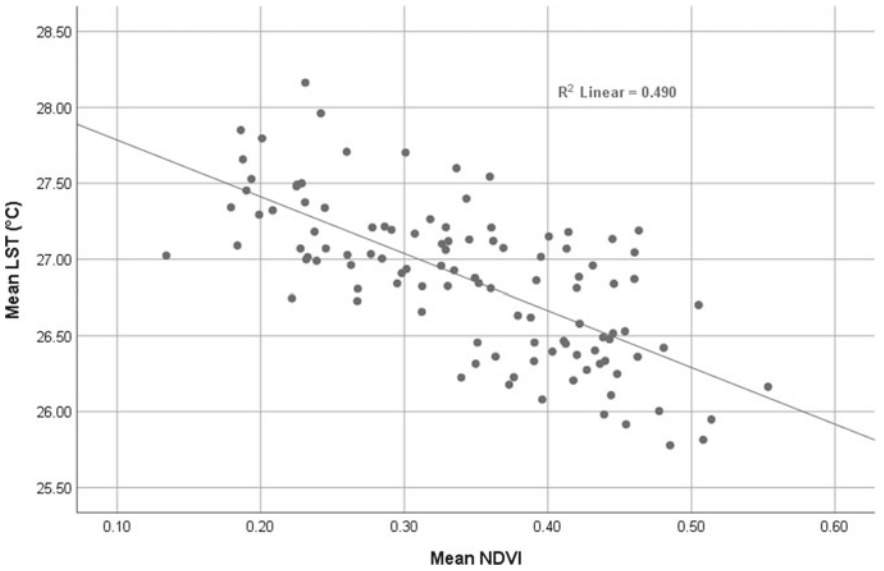

Fig. 16.8 Relationship between mean LST and mean NDVI

model in the form of a web-based GIS that can be accessed by a web browser such as Chrome, Internet Explorer, Firefox, or Safari. The mean LST simulation function will begin by digitizing the area of new green and calculating the mean NDVI at the new green area's boundary. Then both variables will be entered into Eq. 16.4, and the user will see a new mean LST value on the screen.

Overall, remote sensing methods can be applied for mapping and quantifying the cooling effects using satellite imagery. To get more precise and accurate evaluation, further study may attempt to explore the different techniques and sensors for getting a better relationship between the size of green space, quality of the green space, and land surface temperature.

16.6 Conclusion

This chapter demonstrates the integration of remote sensing and web-based GIS to describe the influence on the cooling effect of urban green space in Panat Nikom Municipality, Chon Buri Province, Thailand. It was found that the correlation between mean LST, mean NDVI, and the size of the green area was in the trend. There was a strong negative correlation between mean LST and mean NDVI. At the same time, the size of the green area was slightly negatively correlated to the mean LST and slightly positively correlated to the mean NDVI. The quality of green space (NDVI) can reduce the local temperature (LST) better than the size of green space.

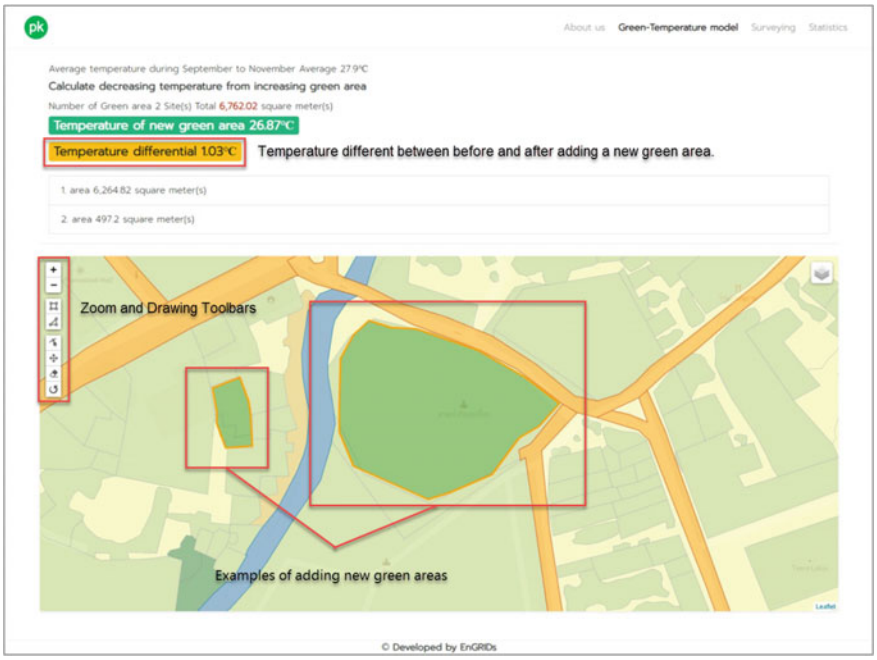

Fig. 16.9 Example of a green area management planning decision support model interface

Nonetheless, the result of this study can be a guideline for further study from a green urban planning perspective as well as the web-based GIS can be utilized as a green area management decision support system for local management in the future. The cooling effect to cool urban areas can be an incentive measure for policymakers to recognize the importance of green spaces in the city, and hopefully, they will make a decision with the integration of green space effects for urban development.

References

Abutaleb K, Freddy Mudede M, Nkongolo N, Newete SW (2021) Estimating urban greenness index using remote sensing data: a case study of an affluent vs poor suburbs in the city of Johannesburg. Egypt J Remote Sensing Space Sci 24(3, Part 1):343–351. https://doi.org/10.1016/j.ejrs.2020.07.002

Akbar TA et al (2019) Investigative spatial distribution and modelling of existing and future urban land changes and its impact on urbanization and economy. Remote Sens 11(2)

Amindin A et al (2021) Spatial and temporal analysis of urban heat island using Landsat satellite images. Environ Sci Pollut Res

Amorim MCDCT, Dubreuil V (2017) Intensity of urban heat islands in tropical and temperate climates. Climate 5(4):91

Aram F et al (2019) Urban green space cooling effect in cities. Heliyon 5(4):e01339

Arnfield AJ (2003) Two decades of urban climate research: a review of turbulence, exchanges of energy and water, and the urban heat island. Int J Climatol 23(1):1–26
Athukorala D, Murayama Y (2021) Urban heat island formation in greater Cairo: spatio-temporal analysis of daytime and nighttime land surface temperatures along the urban-rural gradient. Remote Sens 13(7)
Avdan U, Jovanovska G (2016) Algorithm for automated mapping of land surface temperature using LANDSAT 8 satellite data. J Sens 2016
Best JW (1977) Research in education, 3rd edn., vol xii. Prentice-Hall, Englewood Cliffs, 403 p
Best JW, Kahn JV (1977) Research in education. Allyn and Bacon, Boston, p 384
Buo I et al (2021) Estimating the expansion of urban areas and urban heat islands (UHI) in Ghana: a case study. Nat Hazards 105(2):1299–1321
Busato F, Lazzarin RM, Noro M (2014) Three years of study of the urban heat island in Padua: experimental results. Sustain Cities Soc 10:251–258
Cao X et al (2010) Quantifying the cool island intensity of urban parks using ASTER and IKONOS data. Landsc Urban Plan 96(4):224–231
Chen XL et al (2006) Remote sensing image-based analysis of the relationship between urban heat island and land use/cover changes. Remote Sens Environ 104(2):133–146
Collier CG (2006) The impact of urban areas on weather. Q J R Meteorol Soc 132(614):1–25
Dorman M (2020) Introduction to web mapping, 1st edn. CRC Press, Boca Raton
Duarte L et al (2021) An open source GIS application for spatial assessment of health care quality indicators. Isprs Int J Geo-Inf 10(4)
Ekwe MC et al (2021) The effect of green spaces on the urban thermal environment during a hot-dry season: a case study of Port Harcourt, Nigeria. Environ Dev Sustain 23(7):10056–10079
Ersoy E (2019) Landscape pattern and urban cooling islands. Fresenius Environ Bull 28(3):1943–1951
Evans B, Sabel CE (2012) Open-source web-based geographical information system for health exposure assessment. Int J Health Geogr 11(1):2
Evans B et al (2013) Governing sustainable cities. Routledge, London
Farkas G (2017) Applicability of open-source web mapping libraries for building massive web GIS clients. J Geogr Syst 19(3):273–295
Fernando HJS (2013) Handbook of environmental fluid dynamics. CRC Press, Taylor & Francis Group, Boca Raton, FL
Fryd O (2011) The role of urban green space and trees in relation to climate change. CAB Rev Perspect Agric Vet Sci Nutr Nat Resour 6
GeoServer (2013) GeoServer-NGA-2020-12-14.jpg. www.geosolutionsgroup.com; www.geosolutionsgroup.com
Gonçalves A et al (2018) Urban cold and heat island in the City of Bragança (Portugal). Climate 6(3):70
Grilo F et al (2020) Using green to cool the grey: modelling the cooling effect of green spaces with a high spatial resolution. Sci Total Environ 724
Guha S (2021) Dynamic seasonal analysis on LST-NDVI relationship and ecological health of Raipur City, India. Ecosyst Health Sustain 7(1)
Hulley GC et al (2019) In: Hulley GC, Ghent D (eds) 3-land surface temperature. In: Taking the temperature of the earth. Elsevier, Amsterdam, pp 57–127
Jelokhani-Niaraki M, Malczewski J (2015) Decision complexity and consensus in web-based spatial decision making: a case study of site selection problem using GIS and multicriteria analysis. Cities 45:60–70
Kanda M (2007) Progress in urban meteorology: a review. J Meteorol Soc Jpn 85B:363–383
Karnieli A et al (2010) Use of NDVI and land surface temperature for drought assessment: merits and limitations. J Clim 23(3):618–633
Lei LJ, Wang WC (2019) Analysis of urban landscape pattern and eco-environment benefit based on heat island effect-with Beijing, China as an example. Appl Ecol Environ Res 17(6):14577–14586

Li H (2016) Chapter 2—literature review on cool pavement research. In: Li H (ed) Pavement materials for heat island mitigation. Butterworth-Heinemann, Boston, pp 15–42
Liao W et al (2021) A simple and easy method to quantify the cool island intensity of urban greenspace. Urban For Urban Greening 62:127173
Lo CP, Quattrochi DA, Luvall JC (1997) Application of high-resolution thermal infrared remote sensing and GIS to assess the urban heat island effect. Int J Remote Sens 18(2):287–304
Ma Y et al (2021) Cooling effect of different land cover types: a case study in Xi'an and Xianyang, China. Sustainability 13:1099
Mirzaei M et al (2020) Urban heat island monitoring and impacts on citizen's general health status in Isfahan metropolis: a remote sensing and field survey approach. Remote Sens 12(8)
Muenchow J, Schafer S, Kruger E (2019) Reviewing qualitative GIS research—toward a wider usage of open-source GIS and reproducible research practices. Geogr Compass 13(6)
NASA (2021) Landsat 8 overview [cited 2021 16/07/2021]. Available from: https://landsat.gsfc.nasa.gov/landsat-8/landsat-8-overview
Nasrallah HA, Brazel AJ, Balling RC (1990) Analysis of the Kuwait-City urban heat-island. Int J Climatol 10(4):401–405
Neene V, Kabemba M (2017) Development of a mobile GIS property mapping application using mobile cloud computing. Int J Adv Comput Sci Appl 8(10):57–66
Ng E et al (2012) A study on the cooling effects of greening in a high-density city: an experience from Hong Kong. Build Environ 47:256–271
Nichol JE, Wong MS (2008) Spatial variability of air temperature and appropriate resolution for satellite-derived air temperature estimation. Int J Remote Sens 29(24):7213–7223
Oke TR (1981) Canyon geometry and the Nocturnal urban heat-island—comparison of scale model and field observations. J Climatol 1(3):237–0
Oke TR (1982) The energetic basis of the urban heat-island. Q J R Meteorol Soc 108(455):1–24
Oke TR (1987) Boundary layer climates, 2nd edn, vol xxiv. Methuen, London, 435 p
Oke T (2002) Urban heat island: an overview of the research and its implications. In: Urban heat island summit 2002, City of Toronto; The clean air PARNERSHIP: urban heat island summit, Metro Hall Council Chamber, Toronto, 1st–3rd May, 2002
Oke TR et al (1991) Simulation of surface urban heat islands under ideal conditions at night. 2. Diagnosis of causation. Bound Layer Meteorol 56(4):339–358
Olyazadeh R et al (2017) An offline-online web-GIS Android application for fast data acquisition of landslide hazard and risk. Nat Hazard 17(4):549–561
Omidipoor M et al (2019) A GIS-based decision support system for facilitating participatory urban renewal process. Land Use Policy 88:104150
Rahaman S et al (2021) Spatio-temporal changes of green spaces and their impact on urban environment of Mumbai, India. Environ Dev Sustain 23(4):6481–6501
Rajkumar R, Elangovan K (2020) Impact of urbanisation on formation of urban heat island in Tirupur region using geospatial technique. Indian J Geo-Mar Sci 49(9):1593–1598
Roth M (2000) Review of atmospheric turbulence over cities. Q J R Meteorol Soc 126:941–990
Rouse JW et al (1974) Monitoring vegetation systems in the Great Plains with ERTS. NASA special publication, vol 351, p 309
Shafizadeh-Moghadam H et al (2020) Modeling the spatial variation of urban land surface temperature in relation to environmental and anthropogenic factors: a case study of Tehran, Iran. GIScience Remote Sens 57(4):483–496
Shahfahad et al (2021) Modelling urban heat island (UHI) and thermal field variation and their relationship with land use indices over Delhi and Mumbai metro cities. Environ Dev Sustain
Shorabeh SN et al (2020) Modelling the intensity of surface urban heat island and predicting the emerging patterns: landsat multi-temporal images and Tehran as case study. Int J Remote Sens 41(19):7384–7410
Siddiqui A et al (2021) Bangalore: urban heating or urban cooling? Egypt J Remote Sens Space Sci 24(2):265–272

Silva AGL, Torres MCA (2021) Proposing an effective and inexpensive tool to detect urban surface temperature changes associated with urbanization processes in small cities. Build Environ 192
Stisen S et al (2007) Estimation of diurnal air temperature using MSG SEVIRI data in West Africa. Remote Sens Environ 110(2):262–274
Sun YW et al (2021) Assessing the cooling efficiency of urban parks using data envelopment analysis and remote sensing data. Theor Appl Climatol
Taha H (1997) Urban climates and heat islands: albedo, evapotranspiration, and anthropogenic heat. Energy Build 25(2):99–103
Tawfeek YQ, Jasim FH, Al-Jiboori MH (2020) A stud of canopy urban heat island of Baghdad, Iraq. Asian J Atmos Environ 14(3):280–288
Uritescu B (2017) The influences of land use on the urban heat island in Bucharest, vol 2017, pp 259–265
U.S. Environmental Protection Agency (2021) Urban heat islands. Available from: https://www.usgs.gov/media/images/urban-heat-islands
Vaz Monteiro M et al (2016) The impact of greenspace size on the extent of local nocturnal air temperature cooling in London. Urban For Urban Greening 16:160–169
Weng QH (2009) Thermal infrared remote sensing for urban climate and environmental studies: methods, applications, and trends. ISPRS J Photogramm Remote Sens 64(4):335–344
Weng Q (2019) Land surface temperature data generation. In: Techniques and methods in urban remote sensing, pp 91–127
World Health Organization (2013) Urban population growth. Global Health Observatory. Available from: http://www.who.int/gho/urban_health/situation_trends/urban_population_growth_text/en/
Wu H et al (2011) Monitoring and evaluating the quality of web map service resources for optimizing map composition over the internet to support decision making. Comput Geosci 37(4):485–494
Wu C et al (2021) Estimating the cooling effect of pocket green space in high density urban areas in Shanghai, China. http://doi.org/10.3389/fenvs.2021.657969
Wuebbles DJ et al (2017) Climate science special report: fourth national climate assessment (NCA4), vol I
Yang CB et al (2017) The cooling effect of urban parks and its monthly variations in a snow climate city. Remote Sens 9(10)

Chapter 17
Geo-spatial Modeling of Coastal Flood Exposures Due to Local Sea-Level Rise and Landscape Dynamics: A Case of Sagar Island

S. Vinay and H. A. Bharath

Abstract Coastal inundations are frequent natural events that are caused due to increase in tidal amplitudes triggered by the cyclone, storm surge, extreme rainfall, thermal expansion of oceanic waters, tectonic movements, and many other factors. Despite flooding being an essential part of the natural system, these natural events have been considered disastrous since they have a negative effect on human activities. Land use change and emissions due to anthropogenic activities have led to an increase in climatic extremes. Globally, accelerating temperatures have led to an increase in the intensity and frequency of cyclonic events and localized flooding. Inundation of coastal areas would damage agriculture yield, assets, socio-economic livelihood, natural habitats, and ecosystems. The goal of the current research is to determine the flood exposure in Sagar Island caused by storm surges, severe rainfall events, and rising sea levels. The goal was achieved by spatially overlaying two objectives, viz. (i) Land use dynamics modeling for identifying assets, houses and (ii) Flood inundation modeling. Agent-based land use change model has been used to visualize the likely change pattern for the year 2050. Zero connectivity bathtub model was used to spatially determine flood inundation exposure of the Island. Zero connectivity bathtub model assumes that all cells with elevations lesser than the threshold are subjected to flooding. Threshold in the current study was determined based on variable sea-level rise due to cyclonic storms, severe rainfall events, and topographic conditions. Population and landscapes elements that are likely to be exposed for the current and future time periods are derived based on statistical data acquired from Census of India, land use patterns, and inundation levels. The results illustrate in Sagar, the tidal height rise varies with the type of storms and quantum of local precipitation. Land use assessment indicates loss of native vegetation, increase in human-centric activities, such as housing and agriculture, resulting in increased exposure to inundation. A tide of 2 m amplitude beyond the high tide which frequently expose 32 km^2 of cultivable

S. Vinay · H. A. Bharath (✉)
RCG School of Infrastructure Design and Management, Indian Institute of Technology Kharagpur, Kharagpur, West Bengal, India
e-mail: bharath@infra.iitkgp.ac.in

S. Vinay
SR University, Warangal, Telangana, India

V. P. Singh et al. (eds.), *Application of Remote Sensing and GIS in Natural Resources and Built Infrastructure Management*, Water Science and Technology Library 105,
https://doi.org/10.1007/978-3-031-14096-9_17

landscapes (Agriculture and Horticulture), 5193 houses for the current time (2020), and by 2050 about 31 km^2 of cultivable landscapes and 10,870 houses get exposed. With tides reaching 6 m threshold, 41,632 houses and 122,712 houses are likely to be exposed in 2020 and by 2050, respectively. The current approach and findings of this study pave the way for the governing authorities and planners to prioritize mitigative measures, strategies that are region specific to reduce the impact, and risks of coastal flood inundation due to natural hazards.

Keywords Inundation · Exposure · Land use dynamics · Flooding · Cellular automata

17.1 Introduction

17.1.1 Natural Hazards

Earth's natural constructive and destructive forces such as volcanic eruptions, winds, erosion, precipitation, sedimentation, tectonic movements, glaciers, wave action, earthquake, forest fire, floods, and natural cycles (carbon, water, nutrient, etc.) have been an integral part of life, shaping earth since time immemorial (Agrawal 2018). These natural forces have paved way for the evolution of (i) life forms (diversity of flora and fauna), (ii) biotic and abiotic components (landforms, geology topography), (iii) climatic condition (micro to macro), etc. Being essential to shaping various bio-geo-physio-chemical aspect on earth, the anomalies of natural forces can be threatening on the regional and global environs causing hazards.

Natural hazards (Fig. 17.1) are defined as the result of bio-geo-physical, hydro meteorological natural events that are neither predictable nor containable, whose onset are either rapid or slow and have an impact on the environment, society (life and livelihood), asset, economy etc. (Bobrowsky 2013; Gill and Malamud 2017; Guo et al. 2008; IFRC 2020; Nelson 2018; Shi 2019). Natural disasters are the result of hazards overwhelming vulnerable community, often resulting in mortality and morbidity (Prasad and Francescutti 2017). The aftereffect of the extreme events results in loss of connectivity, damaged infrastructure, disruption of the supply chain, damage to power sources, disordered and chaotic environs (political, economic, social), increase in poverty levels, and societal inequalities (Xu et al. 2016).

In the last century, there were about 15,000 natural hazards recorded across the planet and the frequency of hazards are found to be increasing at a rate of 2–3 disasters every year (EM-DAT 2020) (Fig. 17.2). Meteorologic and hydrologic (hydrographic and oceanographic) hazards have contributed to 71% (10,995) of the natural hazards, affecting 5000 billion people, claiming over 8.5 billion lives, and damages worth 2.4 trillion US$, i.e., 68% of the total damages (EM-DAT 2020). In low income and developing countries, people are 8–12 times more vulnerable to natural hazards, suffer severe economic consequences, higher mortalities, and epidemics (Brown et al. 2018).

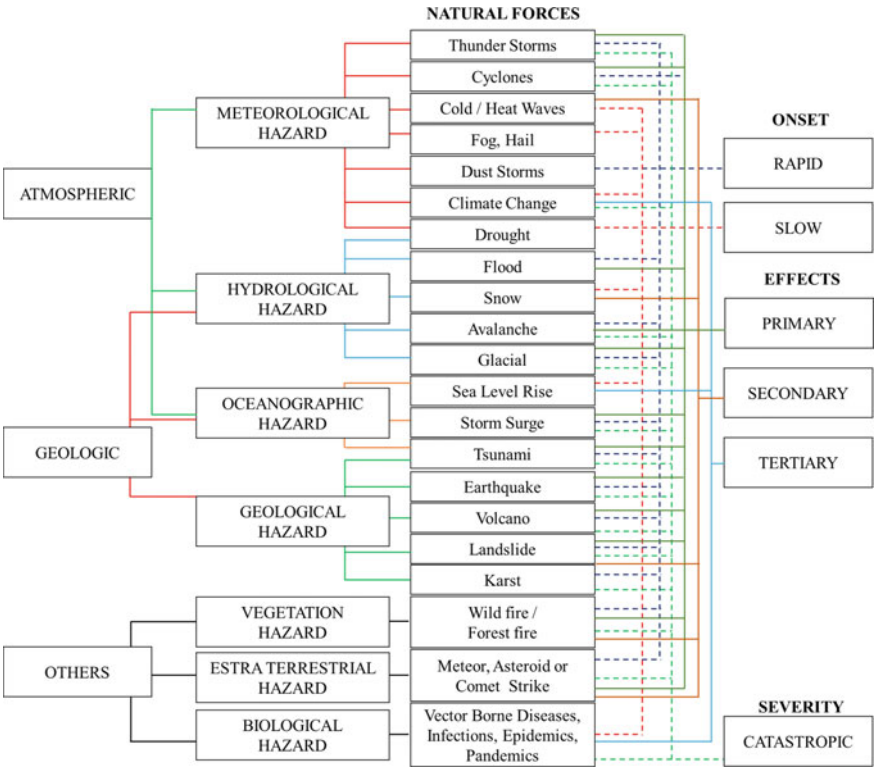

Fig. 17.1 Natural forces and hazard classification

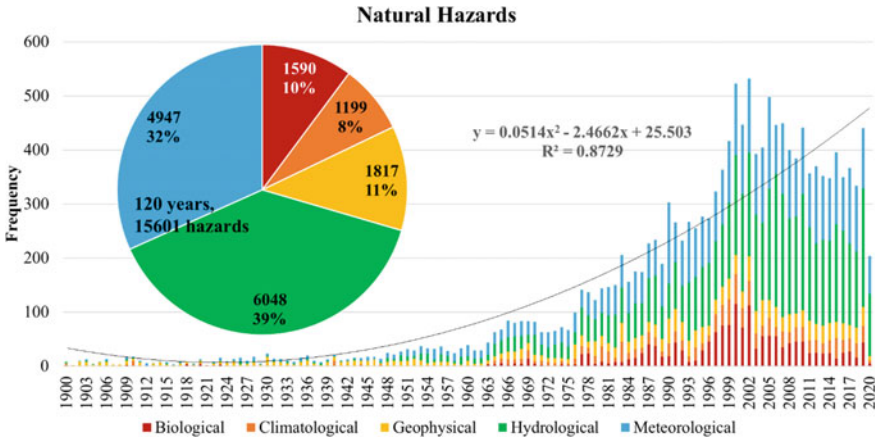

Fig. 17.2 Natural hazards and occurrences

The anthropogenic activities across the globe are creating pressures on environment, and these activities can catalyze, trigger, or induce natural hazards (Gill and Malamud 2014). The dawn of industrialization has enhanced global temperatures to 1.0 °C (IPCC 2012; Masson Delmotte et al. 2018). The increasing global temperatures have triggered changes in regional climate, enhancing natural disasters caused by climatic systems. According to the World Disasters Report 2020 (IFRC 2020), in the last decade, about 83% of the natural disasters were triggered by extreme climatic and weather conditions such as cyclonic storms, floods, heatwaves, and droughts. In addition, the rising global temperatures are melting the polar icecaps, causing thermal expansion of oceanic water, leading to rising sea levels (3.3 mm/year) (Church 2013; Rahmstorf 2010). The accelerating sea-level rise, increasing cyclonic intensity, and frequencies are significant contributors to temporary or permanent coastal inundation (CDC 2017), posing a significant threat increasing exposure levels defined by the extent of the societal elements, viz. human, assets, infrastructure, located within the flooded area.

17.1.2 Coastal Inundation

Coastal landscapes are one among the most productive and invaluable habitats in the biosphere (Walker et al. 2005). Nutrient-rich fertile soils, highly productive ecosystems (aquatic and coastal), diverse landscapes, and navigation ease (Haque and Nicholls 2018) favor human habitations, trading, and industries. Coastal areas favor population concentration and have led to the development of numerous settlements at various scales (village, towns to megacity). Globally, there are 2129 Coastal Cities and Agglomerations (CCA) (1505 small cities, 318 medium cities, 269 large cities, 22 very large cities, and 15 megacities) supporting over 53% of the global populace (Barragán and Andrés 2015). The increasing population density and CCA are vulnerable to increasing natural disasters. It is predicted by 2070, the population affected by SLR would increase by three folds and by 2050, assets exposed to coastal flooding would increase by two folds (Bukvic et al. 2020).

Coastal inundation of low-lying coastal areas is a natural phenomenon caused by increasing/high oceanic water levels because of one or a combination of the following (Muis et al. 2016; NASA 2020; Sudha Rani et al. 2015; Wang et al. 2020):

1. Storm surge–abnormal rise in seawater level caused by low-pressure systems/tropical cyclones/winds combined with high tides driving the oceanic water beyond the shorelines. One of the main causal factors for coastal flooding
2. Sea-level rise (SLR) resulted from melting polar ice caps and thermal expansion of oceanic/sea waters, and the current rate of SLR is 3.3 mm/year
3. Astronomical tides–due to the gravitational pull by the moon and sun, waves tend to reach higher amplitudes

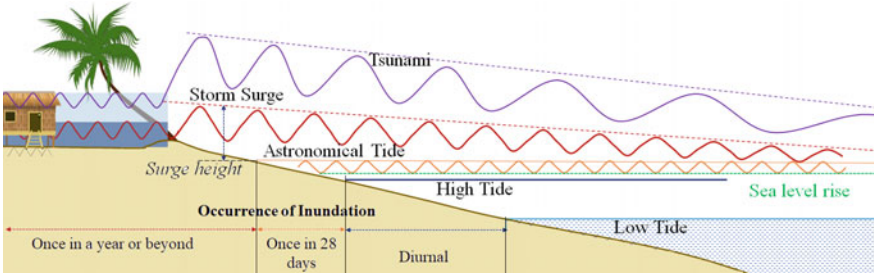

Fig. 17.3 Inundation and tidal variations

4. Tsunami–the tectonic plate movements/earthquakes below the ocean bed triggers displacement of the waterbody. The waves formed due to this would be very high (beyond 30 ft) with large wavelengths.

Figure 17.3 depicts the zone of inundation concerning various tidal conditions for a given location. Tsunamis are the ones with the highest magnitude (over 10 m), and globally there were over 30 tsunamis recorded post-1980 (ITIC 2021). Storm surges which are relatively smaller than tsunamis with amplitudes ranging up to 9 m, globally in the last century, more than 700 surges have been recorded (SURGEDAT 2021). Even though the inundations caused by surges or tsunamis are occasional and temporary, they are disastrous, causing sever damages, mortalities, etc. It takes a longer time for the local administrations and habitants to recover from the immediate and aftereffects. On the contrary, sea-level rise is not instantaneous, but inundations would be permanent, gulping the shorelines and coastal habitations. Cumulatively sea-level rise, astronomical tides, and storm surge can increase the tidal amplitudes causing extremely skewed surges (Haigh 2016) a.k.a king tides (Wright et al. 2019), subsiding coastal area and deltas (Ward et al. 2011), causing severe stresses to the coastal landscapes, society, and environment.

Globally, numerous inundation models have been developed to understand their influence on land use change, economy, society, and environment. In the recent past with the advent of spatial technologies, GIS and remote sensing are being used with hydrological and mathematical models to map coastal inundations, hazards, vulnerability, and risk at regional (local) to global scales (Batista 2018; Pattanayak et al. 2016; Rahman 2019). The attempt to use spatial or non-spatial models predicts the extent of inundation and depths by combining drivers, viz. weather, tide, flood defense, surge height, topography, bathymetry, surface material, land use, etc. (Ward et al. 2011).

Flood inundation can be modeled as planar models or hydrodynamic models (Ward et al. 2011). Planar models in general uses tidal amplitudes and distribute over terrain based on connectivity algorithms (Example: bathtub models, enhanced bathtub models, zero connectivity, four-way hydrological connectivity, and 8-way hydrological connectivity) (Williams and Lück-Vogel 2020; Yunus et al. 2016). Hydrodynamic models connect numerous parameters such as bathymetry, surface

material, wind speeds, and wind direction to describe the fluidic motion to simulate surge height and inundation (Example: NOAA SLOSH, ECMWF, LISFLOOD) (Wing et al. 2019).

Since hydrological models are data and computationally intensive, the current article, the zero connectivity planar GIS inundation model is used to understand inundation based on various tidal depths above the high tide line. This allows planners to understand the zone and level of influence where the landscapes are inundated, and society would be at in distress, thus aiding to address the local issues and reduce the influence of these hazards.

17.1.3 Land Use Dynamics

Land use defines the region's hydrological characteristics, based on the meteorological, geological, and topographical conditions. Landscape degradation, anthropogenic pressures, and climate change effects would be increasing sea-level rise, intensity, and frequency of storms, these would further enhance tidal actions, erosion patterns, sedimentations, flood risks, and changes in habitat type and distribution. The increasing sea levels and changes in land use reduce the drainage gradient, promoting coastal floods due to surge tides and severe precipitation events (Pramanik 2017).

Coastal inundations will have negative impact on society land assets, agriculture produce, housing, estuaries, and livelihood of the habitants in the region (Wang et al. 2020; Ward et al. 2011; Jones and Ahmed 2000), likewise with regards to environment, coastal flooding and sea-level rise reduce connectivity there by isolating habitats fragmenting species and ecosystems (Leonard et al. 2017). Further alteration in coastline features, landforms, coast erosion, and inundation would make the low-lying coastal areas more vulnerable in the next century, further climate change would enhance this process (Hadley 2009).

Advent in geospatial technologies along with very high-resolution remote sensing data (SAR, VIR) enables one to (i) quantify land use changes, (ii) identify extent of inundation, (iii) derive topography, and (iv) analyze the risk due to floods. Studies have been carried out globally to model and identify land use changes, shoreline line changes, using physical, mathematical, predictive models, agent-based models, regression models, rule-based models, etc. (Bharath et al. 2018; Dwarakish 2009; Kankara et al. 2015; Kermani et al. 2016; Ramachandra et al. 2021).

The technology aids understanding the mechanics of flooding, predicting extents, and potential damages which is an important issue in coastal management. Modeling and simulating land use changes help understand the influence of decisions, interventions, and policies. Besides identification of future inundation due to cumulative impact of sea-level rise and surge, the predicted maps act as a key to prevent and reduce losses, provide reliable information about flood risk, enabling better rescue and relief operations, coastal planning, and climate change adaptation.

17.1.4 Global and India Scenario

Long-term observation of the natural hazards at global scale (Table 17.1) indicates, in the last 120 years (1901–2020), there were more than 15,000 events globally, and in India, per se there were more than 700 natural hazards containing 28% of the global moralities. Of all the hazards, storms and floods are the most frequent. Globally, there were about 4349 storms and 5287 flood events accounting 43% of the total natural disasters causing 67% of the physical damages (2.3 trillion USD) and 26% global mortalities (8.3 million). In Indian scenario, 69% of the natural disasters are due to floods (307) and storms (202), causing 90% of the physical damage (112 billion US$). Coastal and inland floods contribute to 58% of the total damages and storms, causing 32% of the damages.

Increasing global temperatures (Berkeley Earth 2020) have triggered changes in regional climate, enhancing natural disasters (Fig. 17.2). According to the World Disasters Report 2020 (Guo et al. 2008), in the last decade, about 83% of the natural disasters were triggered by extreme climatic and weather conditions such as cyclonic storms, floods, heatwaves, droughts, among many. Global mean sea level (MSL) is rising at a rate of 3.3 mm per year (NASA 2020), with a decadal temperature rise (Berkeley Earth 2020) of 0.12 °C, i.e., 4.6 in./1 °C (Fig. 17.4). The accelerated rising sea levels would increase the frequency, intensity, and duration of coastal flooding (CDC 2017), posing a significant threat to the coastal areas and communities (Nauels et al. 2019).

India has been traditionally affected by natural disasters (Anandha Kumar et al. 2011), 75% of the coastline is prone to storm, and 40 million hectares in India are prone to flooding. National Disaster Management Authority (2020) emphasizes that "The rising temperatures amplify the disaster frequency and intensities." The cost

Table 17.1 Natural disasters 1901–2020 (EM-DAT 2020)

Disasters	Global			India		
	No. events	Damage million US$	Morality 1000s	No. events	Damage million US$	Morality 1000s
Drought	747	174,905	11,731	16	6541	4250
Earthquake	1515	829,871	2340	26	5342	72
Epidemic	1493		9615	70		4544
Extreme temperature	597	63,266	186	60	544	18
Flood	5287	839,295	6991	307	73,234	75
Landslide	761	10,879	67	51	55	5
Mass movement	48	209	5	2		0
Storm	4349	1,524,732	1399	202	39,536	167
Wildfire	452	107,927	4	4	2	0

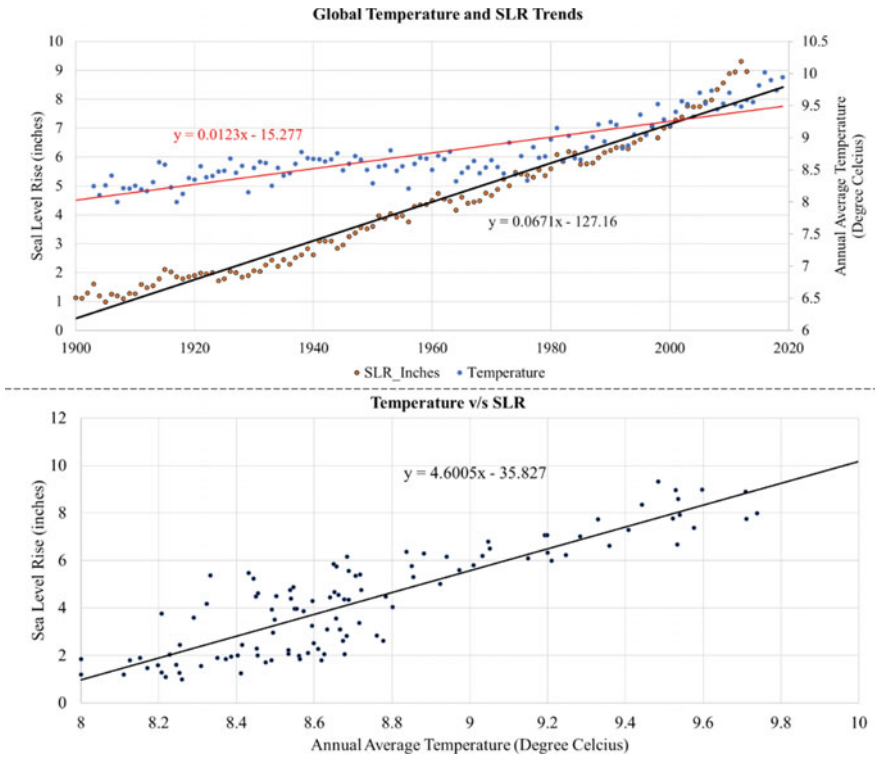

Fig. 17.4 Sea-level rise and temperature–trends and relationships

of damage prior 1996 was 18.05 billion Rs./Year that has increased to 47.45 billion Rs./Year post-1996.

India's coastline is exposed to 18% of the global tropical cyclones (Pattanayak et al. 2016). In the last century, over 265 cyclones on the east coast (95 being severe) and over 35 on the west coast (22 being severe) indicating the east coast is at least four times vulnerable than the west coast. Waves amplitudes during the extreme cyclonic events reach over 10 m (Kumar et al. 2000) inundating coastal areas, coastal islands. Ministry of Earth Sciences, Government of India, confirms increasing cyclones' events and rising sea levels (Krishnan et al. 2020). The sea-level rise rate has doubled in the last two decades from 1.75 mm/year to 3.3 m/year.

All these factors make it essential to develop a scenario-based model to understand coastal flooding and its effects on society and the local environment.

17.1.5 Objectives

It is evident that coastal India is a cyclogenesis area and is frequently exposed to coastal flooding. The goal of the current research is to model and simulate the flood exposure in Sagar Ganga Island, one of the largest habited islands in Sundarbans. The following objectives aid in achieving the said goal:

1. Land use pattern visualization and simulation
2. Simulating flood inundations based on varied tidal heights.

17.2 Data and Method

17.2.1 Data–Global and Regional Datasets

Data for flood hazard assessment were collated from various government records, portals, open databases, NRSC, PSMSL, Census of India, Survey of India, virtual earth database, and other global datasets. Table 17.2 describes the data used in the analysis.

17.2.2 Study Region and Its History with Disasters

Sagar is a coastal island located in the south of West Bengal state. The island has an area of 238.9 km^2 with 47 Mouzas (villages) (Fig. 17.5). The island has evolved from being a part of the Sundarbans mangrove forest prior to 1800 to a habited area supporting over 0.2 million people practicing agriculture, fisheries, trade, and commerce. Being located in the Bay of Bengal, the hot spot of natural disasters the Island is frequently under threat from natural disasters such as super cyclones, cyclones, heavy rains, and rising sea levels (Dilley et al. 2005; SEDAC 2006). This has been causing inundations, damaging physical property, causing mortalities (human and livestock), and disrupting the region's socio-economic activities.

In the last few decades, rising global temperatures and sea levels have inundated three villages, due to which people migrate to the main Island for their living. Earlier studies in the island have highlighted that the people in the island are vulnerable due to changing climate, sea-level rise, coastal erosion, and shoreline change (Gopinath 2010; Mondal et al. 2017; Mukherjee et al. 2019). The disaster management report of India 2011 (Anandha Kumar et al. 2011; Misra et al. 2011) and the Vulnerability Atlas of India (BMTPC 2019) emphasis the Island and its habitants are frequently exposed to water inundation due to natural hazards (Fig. 17.5). Some facts about Island and the delta are:

Table 17.2 Data used in the analysis

Data	Period	Output	Source
Resourcesat 1, 2 (5.8 m)	2012, 2020	Land use map	National Remote Sensing Centre (2020)
Cartosat 1 (2.5 m) stereo	2010	Topographic map, slope, exposure to wave action, and SLR	
Sea level data	1950–2015	Variation in sea level long term and short term	PSMSL (2020)
Cyclone data	1980–2020	Type of cyclonic event and paths	Indian Meterological Department (2020)
Tide data	1980–2019	Variation in tidal heights due to storm surges, heavy rains, and any events	Indian Meterological Department (2020)
Climate data (rainfall)	1901–2020	Rainfall anomalies in relation with tidal amplitudes	NASA (2020), Indian Meterological Department (2020)
Primary census	2011	Village-wise population	Census (2011)
Village administrative data		Village boundary (Spatial)	Mouza Information (2019)
Ancillary map	1922	Topographic map, high and low water levels	Ryder (1924)
Google earth	2012, 2020	Training data for satellite image classifications, preprocessing of data, and extraction of buildings (2012 and 2020)	Google (2020)

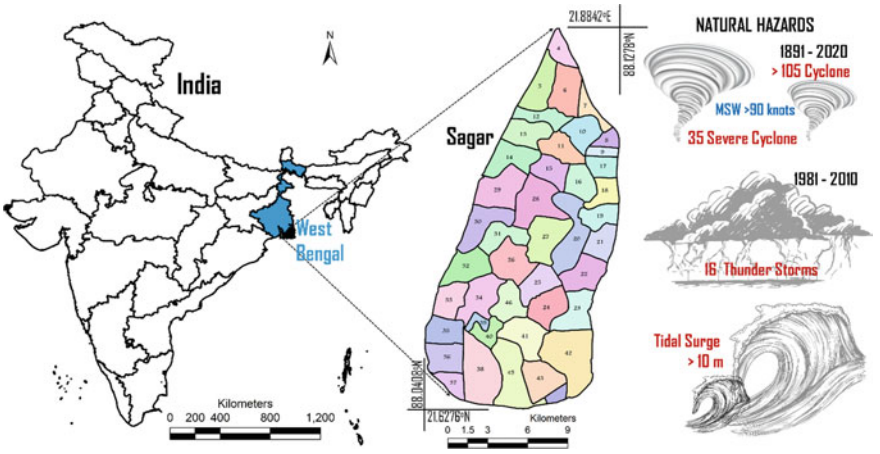

Fig. 17.5 Sagar island and natural hazards

1. Encountered more than 105 cyclonic storms with approximately 35 severe cyclonic events, with maximum sustained winds over 90 knots between 1891and 2020,
2. Seismically falls under high damage risk zone,
3. Has encountered 16 thunderstorms between 1981 and 2010,
4. Liable for floods with surge heights reaching beyond 12 m.

The presence of mangroves in the estuaries and deltas protects the Sundarbans from wave actions, storm surges, and erosion (Spalding et al. 2014). The rising sea levels in Sundarbans have been a threat to the deltas, inundating the low-lying coastal areas, and becoming a threat to mangroves and organisms. It is estimated by 2100, the rising sea levels and erosion would engulf about 10% of the deltas, mangrove areas in the Sundarbans (Rahman 2019; Payo 2016), affecting the livelihood of people and loss of habitat to the fauna. The disaster management report of West Bengal (Hazard assessment and disaster mitigation for West Bengal due to Tropical Cyclones, 2006) emphasizes these lines, i.e., Sagar Island lost about 4.8% (12.16 km^2) of area between 1969 and 2001 due to coastal erosion and flooding.

Table 17.3 depicts the history of severe flooding events in Sagar Island. In the last 2 decades, severe cyclonic events and cyclonic events are increasing in the island, leading to higher inundation conditions and hampering society's livelihood. In the last few decades, Amphan was one of the deadliest super cyclones with winds over 170 kmph causing surges of 5–6 m, and rainfall of 150 mm was observed.

Table 17.3 Chronology of floods in Sagar Island (Indian Meterological Department 2020; Bandyopadhyay 1994; Biswas 2010; Khan and Chatterjee 2018; O'Malley 1914)

Date	Name/descriptor	Cause for flood	Storm surge height (m)
1684, 1688		Cyclone	
1833	Great Gale	Cyclone, storm surge	3
1839		Torrential rain	
1864	Severe cyclone	Cyclone, storm surge	3.4
1867		Cyclone, storm surge	2
1900	Heavy rainfall for 4 days	Rainfall	
1904, 1907	Heavy rainfall	Rainfall	
1942	Public hearing	Cyclone storm	2–5
1974		Cyclone wind	
1976	Severe cyclone	Cyclone wind	3
2002	BOB 03	Cyclone	
2009	Cyclone Aila	Cyclone	4–5
2019	Severe cyclone Bulbul	Cyclone	3–4
2020	Super cyclone/very severe cyclone Amphan	Cyclone	5–6

17.2.3 Land Use Analysis and Modeling Using Agent-Based Models

17.2.3.1 Land Use Mapping

Land use planning of a region is considered a key driver in reducing the risk due to natural hazards. Land use assessment was carried out based on standard protocols using Gaussian Maximum Likelihood Classifier (GMLC) (Ramachandra et al. 2016). The process of land use classification process involves collation of satellite data, data preprocessing, image classification, and accuracy assessment (Fig. 17.6). For the current study, satellite data were acquired from IRS LISS IV FMX sensor for the year 2012 and 2020. These data are of 10-bit, 5.8 m resolution having 3 spectral bands (Green 0.52–0.59 μm, Red 0.65–0.68 μm, and IR 0.77–0.86 μm). Using virtual earth database (Google 2020), these satellite images were geometrically rectified based on ground control points such as road junctions and permanent structures. Training sites were delineated on virtual earth data as well as on the composite satellite image, covering over 15% of the Sagar Island. About 60% of the training sites were used for land use classification, while 40% were used for accuracy assessment. GMLC was used to classify the satellite data into six broad land use categories, viz. agriculture, water, horticulture, forest, urban, and others. Kappa statistics and error matrix were used to determine the accuracy of the land use classification. If the accuracy was less than 80%, additional training sites were used to classify the data.

17.2.3.2 Land Use Change Modeling

Agent-based modeling (ABM) has proved to be an individual and reliable decision-making tool to capture spatial dynamics integrating socio-economic, infrastructure, physical, and environmental factors. In the current research, cellular automata (CA)-based ABM was used to predict the likely land use dynamic for the year 2050.

ABM technique combines the foresaid factors through various concepts pertaining to Boolean algebra, fuzzy logic, analytical hierarchical process (AHP), multicriteria evaluation (MCE), cellular automata (CA), and Markov chains to simulate and predict the likely land use changes in near future (Ramachandra et al. 2021, 2019; Bharath et al. 2014).

These factors are categorized as (i) constraints—that restrict the changes in landscapes and (ii) growth factors—those which fuel the changes in landscape. The factors and their behaviors are different for different land use types. Example (i) along the shorelines, the water bodies tend to increase with rising sea levels, inundating the low-lying areas, (ii) mangrove area that is under the protection from the state forest departments would refrain themselves from changing to other land use classes, (iii) agriculture or horticulture landscapes tend to change to built-up spaces with amenities, policies, etc.

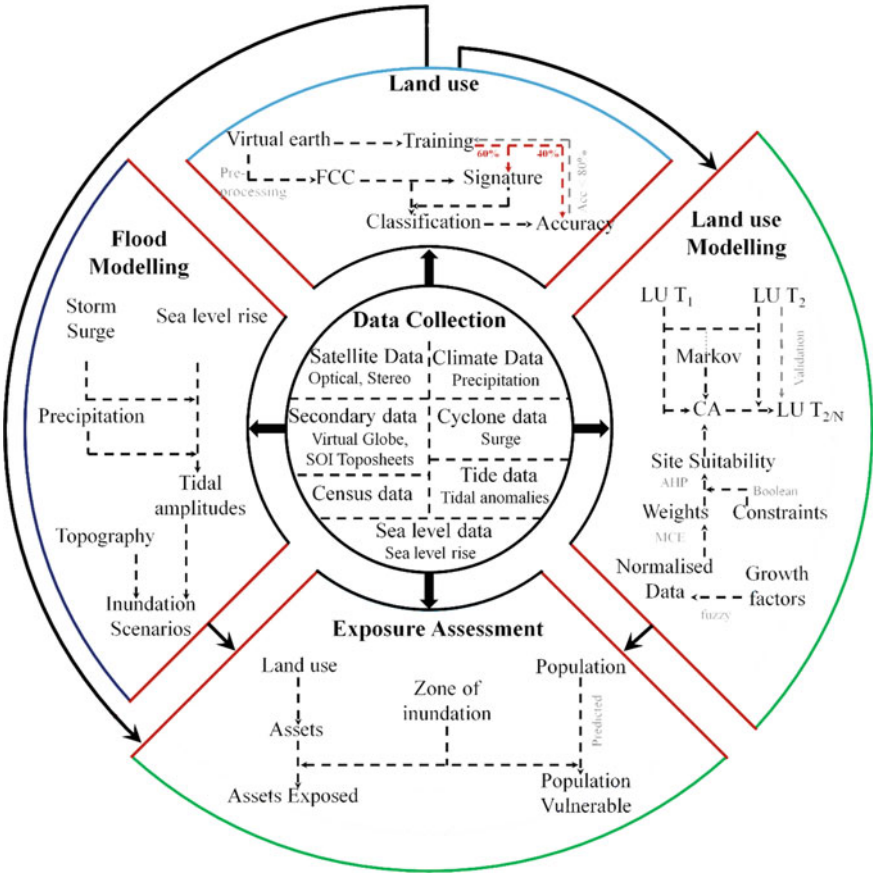

Fig. 17.6 Coastal hazard and exposure assessment

In the current study (i) Natural forests and water bodies were considered a constraint for all landscape. Boolean algebra was used indicating 0 for area under no change 1 for areas where likely land use changes could occur, (ii) factors fueling change was motorable corridors (main roads and metal roads), schools (acts as refugee in case of cyclone or similar hazards), amenities, and services (transport: bus stops; docks; banks; hospitals; police station).

The distance up to which the amenities (or policies) would alter the landscape patterns depends on the regional dynamics. For example, built-up spaces closer the proximity to these services, higher the chances of the non-built-up spaces becoming built-up. With increasing population, amenities, and services, the chances land use conversions become higher. Likewise for cultivated spaces (agriculture and horticulture), agriculture landscapes have higher tendency to change to horticulture particularly along the drainage channels, where water is comparatively abundant. The effect

of various factors is different in scale and range, due to this, normalizing the data to a common scale and range is necessary based on numerical functions, in the current study, fuzzy logic was used to normalize the data.

Further, these normalized factors were compared against each other, i.e., pair wise to evaluate the importance of one factor over the other using analytical hierarchical process (AHP). Since the comparisons would sometimes be inconsistent, consistency ratio (CR) is mathematically evaluated as a function of consistency index (CI) and random index (RI). If CR is less than 0.10, the weights obtained are used to develop site suitability maps using multicriteria evaluation and constraints maps developed based on Boolean algebra. Site suitability is generated for each of the land use class. Markov chains are used for statistically predicting likely land use changes from current state to future state based on historical changes, CA model integrates the site suitability's, probability of land use changes to define the state of each pixel.

Simulations were carried out to calibrate the ABM, changes between 2012 and 2020 were used to simulate 2020. If the simulated outcomes were comparable with actual land use 2020, the calibrated model was used to predict land use for the year 2050.

17.2.4 Coastal Hazard Exposure Assessment Framework

Tidal amplitudes vary with the factors that affect locally, inundating earth surface features. The local sea-level variations are influenced by the following (Lorie 2020):

1. Gravitational pull, rotational effect
2. Deformational effects—redistribution of mass between land, ice, and water
3. Steric effect—changes in heat and salinity distribution
4. Dynamic sea levels—winds, ocean currents, and cyclones
5. Non-climatic—glacial isostatic adjustment, tectonic movements, and sediment compaction.

With changing climate, the rising sea levels and changing land use would further add up to the areas being exposed to hazard. This has necessitated understanding tidal amplitudes, frequency of occurrences and their effects, i.e., inundation levels, area under various landscapes inundated, population exposed to flooding.

In the current study, zero connectivity planar bathtub model to derive zones prone to flood hazard based on various scenarios under variable tidal conditions. Zero connectivity model was used to derive the hazard zones with a hypothesis that the cyclone creates surges and a reason for heavy downpour that would inundate the unconnected landscape. Zero connectivity model assumes all the raster pixel that are equal to below the foresaid topographic depth gets inundated, in the presence or absence of local connectivity (Fig. 17.6). The scenarios were developed based on tidal height that is dependent upon various characteristics, viz. precipitation, cyclone, surge, etc. Figure 17.6 depicts the coastal hazard exposure assessment framework.

Long-term daily precipitation data collated from IMD were analyzed for anomalies and related to cyclonic precipitation events. This would indite the occurrences of likely rainfall events that would inundate unconnected and connected areas. Further, the surge heights during cyclones were related to the rainfall events. This interlinking would enable one to model inundation heights. These heights and the surface topography derived from very high-resolution stereo satellite data were used to develop inundation maps. Based on the precipitation and tidal surge variability, various scenarios were developed. Inundation data were overlaid on the land use for current and predicted land use 2050 to understand area inundated, assets exposed to flooding.

17.2.5 Relative Exposure Levels of Assets and Households to Coastal Floods

For every scenario, water head causing inundation varied relatively to the intensity of event. The area under inundation varies relatively to the height of flooding in the coastal areas. Based on various inundation head, the assets exposed and houses that could be affected were estimated using spatial overlay. Accordingly, the area of household and population per unit area of building was considered to estimate the population vulnerable for 2020, 2050 considering water heads.

17.3 Results and Discussions

17.3.1 Land Use Analysis

Sagar Island has witnessed large-scale erosion due to the rising sea levels in the last century, in addition, increasing anthropogenic pressures have led to reduction in the mangrove and native cover that has led to increase in flood vulnerability. Figure 17.7 depicts the changes in land use and shorelines in the last century.

Figure 17.7a depicts the changes in land use in the last 8 years, i.e., between 2012 and 2020, while Fig. 17.7b depicts the land use in 1922 and Fig. 17.7c depicts the shoreline changes in the last century.

Within the administrative area, the island which originally had 47 villages has lost 3 villages in the last century due to sea-level rise. The sinking islands have lost an area of 62.2 km^2 to oceanic water intrusions due to rising sea level. The inundation of neighboring s is one of the major reasons for alterations in the landscape of the island. The main island has undergone severe land degradation, the natural woody vegetation in the south and east that use to protect against tidal surges is lost due to the anthropogenic pressures. The woody vegetation that was about 103 km^2 is now reduced to 9 km^2, whereas the cultivated areas (agriculture, horticulture) have increased from 124 to 193 km^2.

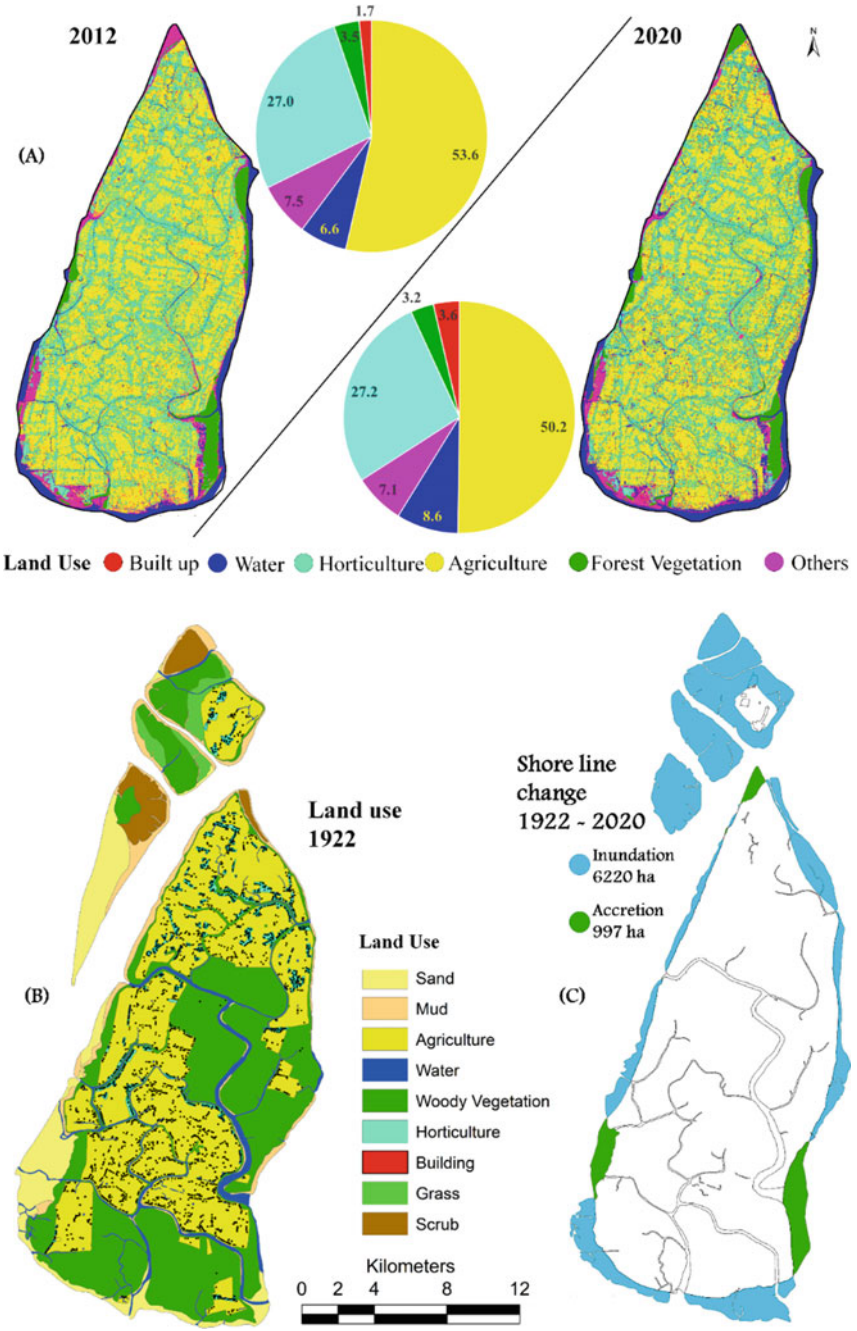

Fig. 17.7 Land use changes. **a** Land use 2012 and 2020, **b** land use 1922, **c** shoreline changes between 1922 and 2020

In the last decade, understanding the effects of coastal intrusions, afforestation activities were carried out in the sedimented areas, particularly in the north, northeast, and southeast, mostly toward the island's low-lying area. Built-up areas have increased by 2 folds, i.e., from 4.4 to 9.1 km^2 indicating rampant growth. The increasing population and changes in landscape would lead to an increase in vulnerability and exposure conditions to local levels.

According to the census of India, population of the island in 2001 was 185,644 with 31,461 houses, by 2011 population increased to 212,037, with 43,716 houses. Building extraction in Sagar Island depicts the number of houses increased to 54,375 by 2020. The population per household in the region is decreasing from 5.9 people per house in 2001 to 4.85 in 2011 and is expected to reduce to 4.07 by 2020. Accordingly, the island houses 222,772 residents in 2020.

17.3.2 Land Use Visualization

Agent-based model was used to understand the land use dynamic changes by 2050, based on (i) transitions between various land use classes between 2012 and 2020, (ii) contributing factors and constraints.

Various agents causing land use changes used in the current AHP model are proximity to motorable roads, schools, city center, transport (bus station and docks), public services (hospitals, police station, banks) as depicted in Fig. 17.8. The model was calibrated considering the changes in land use between 2012 and 2020, with 2012 as base year 2020 was simulated. The current CA-AHP model could simulate the land use for 2020 with an accuracy of 94% and kappa of 0.79. The calibrated model was then used to simulate land use for the year 2050, with land use 2020 as base year. The urban areas tend to increase from 905 to 2629 ha in the next 3 decades at the cost of agriculture, horticulture, and other spaces. The horticulture landforms would slightly reduce from 7970 to 7495 ha, while the agriculture landscapes would reduce from 11,398 to 10,254 ha between 2020 and 2050.

Beta population density, i.e., population to build up area ratio in 2020 is 246.16 person per hectare, accordingly, population by the year 2050 is expected to reach 664,103, and with 4.07 person per household, Sagar Island would be having 163,170 houses. These houses are mostly located at relatively higher altitudes, in the proximity of roads, concentrated at the north and between center to south due to various amenities in those regions.

17.3.3 Coastal Exposure Analysis

Coastal area exposure was carried using a zero connectivity bathtub planar model. Analysis of cyclone, rainfall, and surge heights shows that the cyclones are associated with heavy rainfall events and high storm surges. In the last 2 decades, there had been

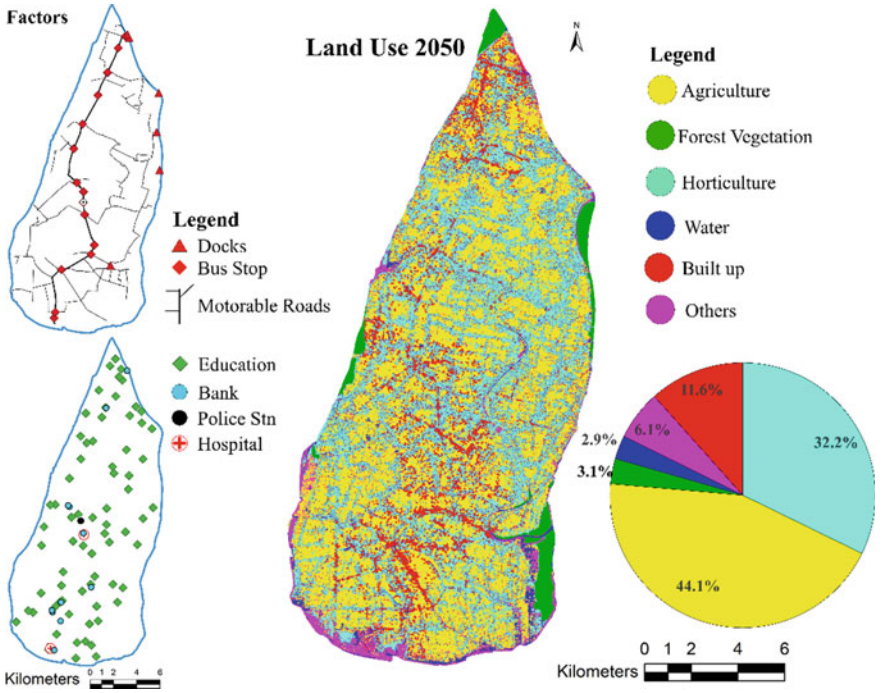

Fig. 17.8 Land use change causal factors and predicted land use 2050

three super cyclones (Table 17.4) in Sagar Island, and numerous depressions during this, the surge was over 3 m and rainfall was over 70 mm. Correlating surge and rainfall events indicate for every 10 mm rise increase in rainfall associated with storm, surge increased by 1.4 m.

Rainfall analysis: Occurrence of severe cyclones is associated with exceptionally high amounts of rainfall intensities, i.e., beyond 70 mm/day. In the last 7 decades (1951–2020), IMD data indicate that precipitation events more significant than 70 mm/day are increasing at a rate of 5 events in a century. Month-wise decadal assessment indicates during May, rainfall over 70 mm/day increasing at three events

Table 17.4 Cyclones, surges, and rainfall

Name	Cyclone type	Date	Wind speed (knots)	Surge (m)	Rainfall (mm)
Amphan	Very severe cyclonic storm	May 20, 2020	90	5–6	98.8
Bulbul	Severe cyclonic storm	November 9, 2019	60	2	71.7
Aila	Severe cyclonic storm	May 25, 2009	60	3	82.6

per century, while in the June 9 events, July 1 event, and October with two events per century, while in rest of the months, the rainfall with intensities over 70 mm/day, the trend was decreasing. In the last seven decades, in May, June, October, and November, there were more than 40 events with rainfall between 70 and 100 mm.

Correlating rainfall and inundations depths depict at 70 mm/day rainfall the surge was 2 m, while at 100 mm/day, surge was about 5.5 m, and the maximum recorded surge is just over 12 m (BMTPC 2019), accordingly, rainfall causing these surges would be over 140 mm/day.

Based on the frequency of events, various scenarios were developed (Table 17.5) to understand the exposure, and Fig. 17.9 depicts the zone of inundation under various scenarios.

Scenario 1: These severe cyclones that are frequent, rainfall in these events ranges between 70 and 80 mm with wind speeds ranging between 48 and 63 knots. The surges during these kinds of events range between 1 and 1.8 m. Considering sea-level rise of 135 mm in the next 3 decades, inundation depths of 2 m are considered to derive exposure. Figure 17.9 depicts the zone of inundations overlaid of hill shade map of Sagar Island. With a depth of 2 m getting inundated, 12.9% of the Island account to 30 km^2, particularly along the east coast.

Table 17.5 Scenarios and inundation area

Scenario	Surge height	Description	Exposed area	
			km^2	%
Scenario 1	Up to 2 m	Very frequent, associated with severe cyclonic storms and are associated with rainfall events ranging between 70 and 80 mm (Bulbul cyclone, Orissa cyclone, Fani) Sea-level rise by 2020 would be 135 mm at a rate of 4.5 mm/year	30.0	12.9
Scenario 2	<4 m	Very frequent, associated with severe cyclonic storms and are associated with rainfall events ranging between 80 and 90 mm (Aila cyclone)	87.9	37.8
Scenario 3	<6 m	Less frequent, associated with super severe cyclonic storms and rainfall ranges between 90 and 110 mm (Amphan super cyclone)	169.1	72.8
Scenario 4	<12 m	Extremely less frequent as recorded in government records (BMTPC 2019), these events are very severe and rainfall events over 140 mm	232.3	100

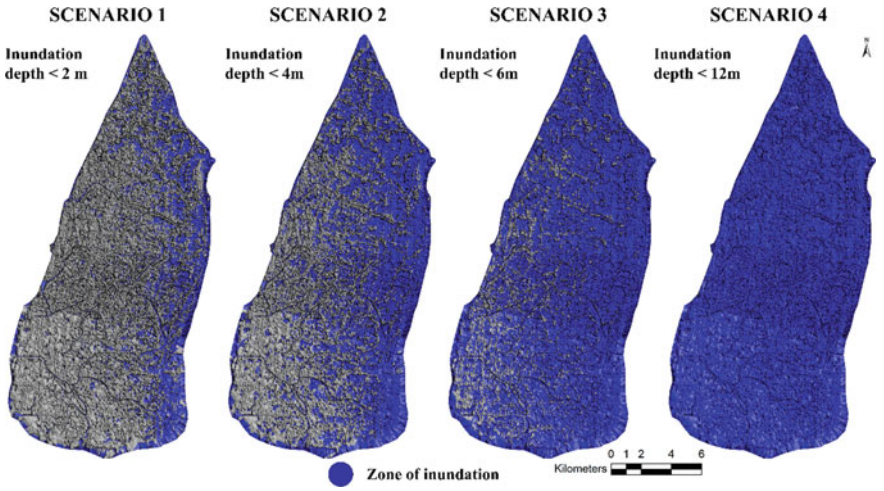

Fig. 17.9 Zone of inundation—scenario based

Scenario 2: These are also severe cyclone that are less frequent, i.e., once in 10 years, rainfall in these events ranges between 80 and 90 mm with wind speeds ranging between 48 and 63 knots. The surges during these kinds of events range between 2 and 3.5 m. Considering sea-level rise of 135 mm in the next 3 decades, inundation depths of 4 m are considered to derive exposure. Figure 17.9 depicts the zone of inundations overlaid of hill shade map of Sagar Island. With a depth of 4 m getting inundated, 37.8% of the Island account to 87.9 km^2, particularly along the coastline and traversing between the east coast and central parts of the island.

Scenario 3: These are very severe cyclone or super cyclones that are less frequent, i.e., once in 30 years (1990, 2019), rainfall in these events ranges between 90 and 110 mm with wind speeds ranging between 64 and 119 knots. The surges during these kinds of events range up to 4–6 m. Figure 17.9 depicts the zone of inundations overlaid of hill shade map of Sagar Island. With a depth of 6 m getting inundated, 72.8% of the Island accounts to 169.1 km^2, the central parts of the island to the southeastern zones (toward light house), and dry conditions prevailed. In order to compare the model's performance, we compared inundation area for Amphan super cyclone whose surge was 5.5 m above the astronomical tide. Segmentation of Sentinel 1A data dated 22 May 2020 (Fig. 17.10) indicates 144.6 km^2 area was waterlogged and according to the zero connectivity bathtub model, an area of 148.1 sq. of area was waterlogged due to Amphan. The accuracy of the bathtub model was found close to 97.5% with reference to the ground observations.

Scenario 4: BMTPC (2019) records 12 m, likewise Kumar et al. (2000) indicate a 10 m surge height in the Sundarbans belt, these tidal heights can inundate entire Island. According to this scenario, the entire island would be inundated.

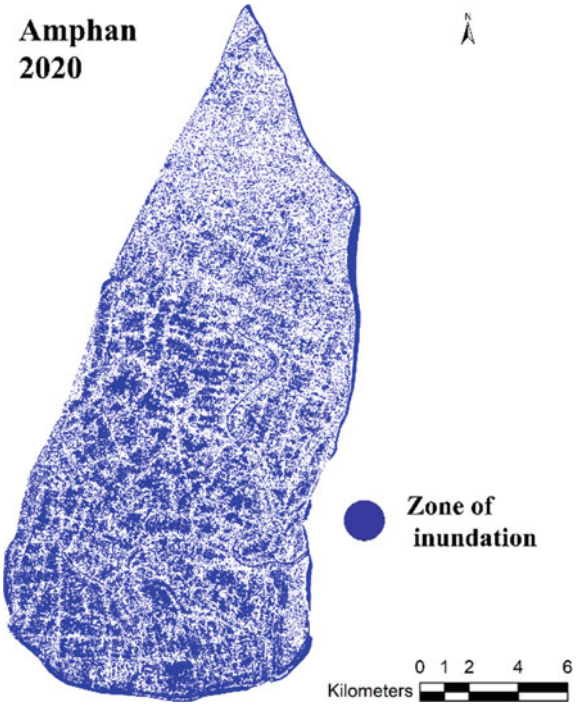

Fig. 17.10 Zone of inundation during Amphan—Sentinel 1A

17.3.4 Variable Exposure Levels Based on Land Use Change Pattern

Table 17.6 depicts the variable exposure patterns of assets and population to different inundation depths for the current and future land use scenarios. Land use assets (buildings, agriculture, and horticulture) would increase with increasing inundation depths. In the year 2020, the horticulture area exposed ranges from 7.4 to 22.9 km^2 for severe cyclonic storm events (Scenario 1 and 2). and for very severe cyclonic storm events (Scenario 3), horticulture area expose would range up to 54 km^2, in very extreme cases (Scenario 4), when the surge heights are beyond 12 m, entire area under horticulture that would be exposed to floods, i.e., about 79 km^2. With changes happening in landscape, by 2050, the area under cultivation tend to reduce with increasing habitation, and changes in cultivation patterns (agriculture to horticulture and vice versa).

In the first scenario, the area of the building that would be exposed would increase from 85.8 to 179.6 ha, at this state, the population exposed to flooding, mainly toward the east coast increase from 21 to 44 thousand from 2020 to 2050. Likewise, during very severe cyclonic storm events (Scenario 3), where the inundations are close to 6 m about 75% of the population and building assets are exposed to flooding in 2020 and 2050. The population and building assets that would be exposed to floods would

Table 17.6 Assets and population exposed

Exposure	Year	Scenario 1	Scenario 2	Scenario 3	Scenario 4
Horticulture (ha)	2020	742.3	2297.7	5417.6	7969.1
	2050	668.5	2105.8	5048.1	7493.6
Agriculture (ha)	2020	2496.2	6473.7	10,289.1	11,398.0
	2050	2495.5	6210.0	9448.5	10,253.9
Built-up (ha)	2020	85.8	319.2	687.9	904.4
	2050	179.6	838.5	2027.6	2696.1
Built-up (Numbers)	2020	5193	19,318	41,632	54,735
	2050	10,870	50,747	122,712	163,170
Population (Numbers)	2020	21,121	78,574	169,333	222,627
	2050	44,210	206,405	499,114	663,672

increase by 2.09, 2.63, 2.92, and 2.98 times between 2020 and 2050 for scenarios 1, 2, 3, and 4, respectively.

17.4 Discussion and Conclusion

With changing global climatic conditions, the number of climatic disasters occurring in India is increasing at a rate of 1 every decade. Globally, 8 out of 10 major disasters with severe mortalities and physical damages are recorded in coastal India. The east coast, particularly toward the norther part of Bay of Bengal is one of the hottest hotspots for disasters. Globally, 75% of the worlds tropical cyclones causing over 5000 mortalities are observed in Bay of Bengal cyclogenesis area. About 18–20% of the global climatic disasters are recorded in Coastal India, and 7 out of 10 oceanic and atmospheric-based disasters occur in the Bay of Bengal.

Sagar is one of the most exposed habited islands along the Sundarbans. The island is geologically very young, formed by sedimentation of particles. The island since time immemorial has witnessed several destructive natural forces. Prior to British rule, the island was pristine with mangrove forests and treated as no man's land due to these natural forces. But with anthropogenic concerns, the island has lost its native vegetation cover, making way for cultivation and human settlements. With the advent of human activities, the natural forces in the region are now termed as natural disasters since they negatively affect the human system.

GIS and remote sensing technologies have paved way to visualize long-term land use changes, map disasters and their extents, model various scenarios to visualize future landscapes, hazards, etc., enabling better planning and risk reduction.

Long-term assessment of land use using historic maps to recent very high-resolution satellite data indicates in the last century (1924–2020) the native vegetation has reduced from 103 to 7.64 km^2 in the main island, the cultivated landscape has

grown beyond 75%. Built-up area extends over 9 km^2 supporting above 0.22 million habitants in 54,735 houses. Using agent-based models for land use change prediction, the built-up area is expected to grow by 2.98 times supporting 664,103 habitants in 163,170 houses.

Analysis of tidal amplitudes (surge), rainfall events with respect to sever, and very severe cyclonic storm events in Sagar Island indicated that during severe cyclone storms, tidal surge range between 2 and 4 m with rainfall ranging between 70 and 90 mm/day, while for very severe cyclone events, rainfall intensity was closer to 100 mm/day with surges over 5.5 m. Assessment of rainfall intensity for the last 7 decades (particularly non monsoon season) indicates the number of high intensity rainfall event are increasing over time. Based on the rainfall and surge height relationships, 12-m surges that are extremely rare are expected when the rainfall is over 140 mm. These surges can inundate the entire island. Based on these characteristics, four scenarios with depths of 2 m, 4 m, 6 m, and 12 m were used to simulate and identify the zone inundation using a zero connectivity bathtub flood model. The zero connectivity bathtub model outcomes were comparable to the inundation data derived for the Amphan event using Sentinel 1A data.

In the first scenario, i.e., at inundation depth of 2 m, about 12.9% of the main island would submerge, at 4 m depths 37.8%, at 6 m depth 72.8%, and at 12 m depth 100% island would be submerged.

With varying inundation levels, the assets and people exposed to hazard vary. At inundation depths of 2 m and 4 m effectively during a severe cyclonic event, 32 km^2 and 87 km^2 of cultivable lands are likely to be exposed to floodwaters for the year 2020 and for very severe cyclone event, about 157 km^2 of cultivable lands are likely to be exposed to floods. During these events, built-up areas that are likely to be exposed are 5k, 19k, 41k, and 54k for scenarios 1, 2, 3, and 4, respectively, likewise population exposed would be 21k, 78k, 169k, and 222k, respectively. By the year 2050, population exposed would increase to 44k, 206k, 499k, and 663k for scenarios 1, 2, 3, and 4, respectively. Agriculture and horticulture land assets exposed between 2020 and 2050 would decrease between 2 and 5% for severe events (Scenario 1, 2) and by 8% for very severe event (Scenario 3, 4).

The SENDAI framework for disaster risk reduction 2015–2030 (UNDRR 2015) emphasized reducing the disaster risks caused by natural hazards through effective management for sustainable development. SENDAI framework defines seven global targets that includes (i) reducing global mortalities and people affected by disasters, (ii) reducing loss on basic infrastructure and services, economy, (iii) improving resilience through local disaster risk reduction strategies, (iv) increase availability and accessibility of multi-hazard early warning systems and disaster risk information and assessment to people.

Some of the disaster risk reduction and adaption measure include (NDMA 2020; UNDRR 2015; IPCC 2014), viz. anticipate–plan and reduce risk; reduce–exposure, vulnerability; multi-dimensional; iterative learning; protect, retreat, accommodate; protect people; habitat relocation; capacity building; hazard exposure and risk mapping; alternate livelihood and food source; introducing, conserving, restoring mangroves, marshes, sea grasses; maintaining sediment; recognizing importance and

protecting coastal ecosystems; restoration and maintenance of drainage systems, their connectivity's; providing amenities (motorable roads, health facilities).

Based on the above risk reduction strategies, in the current article, we integrate mapping inundation hazard exposures by considering oceanic effect and climatic effects. This would aid in anticipating the effects of hazards, helps the local administration and planning authorities to plan and reduce the amount of damage, mortalities due to hazard at regional scale.

Acknowledgements We are grateful to Ranbir and Chitra Gupta School of Infrastructure Design and Management for infrastructure and financial support. We also thank the National Remote Sensing Centre, India, for providing satellite data.

References

Agrawal N (2018) Natural disasters and risk management in Canada. Springer, Berlin

Anandha Kumar J, Walia A, Chaturvedi S (2012) India disaster report 2011. Available: https://nidm.gov.in/PDF/pubs/IndiaDisasterReport2011.pdf

Bandyopadhyay MK (1994) University of Calcutta. Available: https://shodhganga.inflibnet.ac.in/handle/10603/165354

Barragán JM, de Andrés M (2015) Ocean Coast Manag 114. https://doi.org/10.1016/j.ocecoaman.2015.06.004

Batista CM (2018) Encyclopedia of coastal science. Springer, Berlin. https://doi.org/10.1007/978-3-319-48657-4_356-1

Berkeley Earth (2020) Regional climate change: global data. Available: http://berkeleyearth.org/

Bharath HA, Vinay S, Ramachandra TV (2014) In: 2014 IEEE geoscience and remote sensing symposium. https://doi.org/10.1109/IGARSS.2014.6947148

Bharath HA, Chandan MC, Vinay S, Ramachandra TV (2018) Egypt J Remote Sens Sp Sci 21. https://doi.org/10.1016/j.ejrs.2017.08.002

Biswas SK (2010) University of Calcutta. Available:https://shodhganga.inflibnet.ac.in/handle/10603/156022

BMTPC (2019) Vulnerablility Atlas of India. Available: https://bmtpc.org/topics.aspx?mid=56&Mid1=180

Bobrowsky PT (ed) (2013) Encyclopedia Nat Haz. Springer, Berlin. https://doi.org/10.1007/978-1-4020-4399-4

Brown P, Daigneault AJ, Tjernström E, Zou W (2018) World Dev 104. https://doi.org/10.1016/j.worlddev.2017.12.002

Bukvic A, Rohat G, Apotsos A, de Sherbinin A (2020) Sustainability 12. https://doi.org/10.3390/su12072822

CDC (2017) Coastal flooding, climate change, and your health. Centre for Disease Control and Prevention [Online]. Available: www.cdc.gov/climateandhealth

Census (2011) District census handbook, Kolkata. Available: https://www.censusindia.gov.in/2011census/dchb/1916_PART_B_DCHB_KOLKATA.pdf

Church JA et al (2013) Sea level change. In: IPCC, 2013. Cambridge University Press, Cambridge. Available: https://www.ipcc.ch/report/ar5/wg1/sea-level-change/

Dilley M et al (2005) World Bank Disaster Risk Manag Ser. Available: https://www.preventionweb.net/files/1100_Hotspots.pdf

Dwarakish GS et al (2009) Ocean Coast Manag 52. https://doi.org/10.1016/j.ocecoaman.2009.07.007

EM-DAT (2020) CRED. https://public.emdat.be/
Gill JC, Malamud BD (2014) Rev Geophys 52. https://doi.org/10.1002/2013RG000445
Gill JC, Malamud BD (2017) Earth Sci Rev 166. https://doi.org/10.1016/j.earscirev.2017.01.002
Google, Google Earth (2020). https://www.google.com/intl/en_in/earth/
Gopinath G (2010) Environ Monit Assess 160. https://doi.org/10.1007/s10661-008-0718-3
Guo H, Hu Q, Jiang T (2008) J Hydrol 355. https://doi.org/10.1016/j.jhydrol.2008.03.020
Hadley D (2009) Land Use Policy 26. https://doi.org/10.1016/j.landusepol.2009.09.014
Haigh D et al (2016) Sci Data 3. https://doi.org/10.1038/sdata.2016.107
Haque A, Nicholls RJ (2018) Ecosystem services for well-being in deltas. Springer, Cham. https://doi.org/10.1007/978-3-319-71093-8_8
IFRC (2020) World disasters report. Available: https://media.ifrc.org/ifrc/world-disaster-report-2020
Indian Meterological Department (2020) Hydrometerological services. Available: http://www.imd.gov.in/pages/services_hydromet.php
IPCC (2012) Managing the risks of extreme events and disasters to advance climate change adaptation. https://doi.org/10.1017/cbo9781139177245
IPCC (2014) Climate change 2014: impacts, adaptation, and vulnerability. Available: http://www.ipcc.ch/report/ar5/wg2
ITIC (2021) Historical Tsunamis. Available: http://itic.ioc-unesco.org/index.php?option=com_content&view=article&id=1602&Itemid=2035
Jones G, Ahmed S (2000) J Coast Conserv 6. https://doi.org/10.1007/BF02913813
Kankara RS, Selvan SC, Markose VJ, Rajan B, Arockiaraj S (2015) Procedia Eng 116. https://doi.org/10.1016/j.proeng.2015.08.374
Kermani S, Boutiba M, Guendouz M, Guettouche MS, Khelfani D (2016) Ocean Coast Manag 132. https://doi.org/10.1016/j.ocecoaman.2016.08.010
Khan A, Chatterjee S (2018) Springer. https://doi.org/10.1007/978-3-319-69992-9
Krishnan R, Sanjay J, Gnanaseelan C, Mujumdar M, Kulkarni A, Chakraborty S (2020) E Springer. https://doi.org/10.1007/978-981-15-4327-2
Kumar BP et al (2000) Mar Geod 23. https://doi.org/10.1080/01490410050030661
Leonard PB, Sutherland RW, Baldwin RF, Fedak DA, Carnes RG, Montgomery AP (2017) Anim Conserv 20. https://doi.org/10.1111/acv.12289
Lorie et al (2020) Clim Risk Manag 29. https://doi.org/10.1016/j.crm.2020.100233
Masson Delmotte V et al (2019) In: IPCC 2018: global warming of 1.5 °C
Misra P, Kumar D, Agarwal S (2011) Disaster management in India. Available: http://sdmassam.nic.in/pdf/publication/undp/disaster_management_in_india.pdf
Mondal, Bandyopadhyay J, Dhara S (2017) Spat Inf Res 25. https://doi.org/10.1007/s41324-016-0076-0
Mouza Information, Government of West Bengal (2019). Available: https://banglarbhumi.gov.in/BanglarBhumi/Home.action
Muis S, Verlaan M, Winsemius HC, Aerts JCJH, Ward PJ (2016) Nat Commun 7. https://doi.org/10.1038/ncomms11969
Mukherjee N, Siddique G, Basak A, Roy A, Mandal MH (2019) Chin Geogr Sci. https://doi.org/10.1371/journal.pone.0105981
NASA (2020) Global climate change. Available: https://climate.nasa.gov/effects/
National Remote Sensing Centre (2020) IRS data products. Available: https://www.nrsc.gov.in/
Nauels A, Gütschow J, Mengel M, Meinshausen M, Clark PU, Schleussner C-F (2019) Proc Natl Acad Sci 116. https://doi.org/10.1073/pnas.1907461116
NDMA, Ministry of Home Affairs, Government of India (2020). Available: https://ndma.gov.in/
Nelson SA (2018) Natural disasters and assessing hazards and risk. Available: https://www.tulane.edu/~sanelson/Natural_Disasters/introduction.htm
O'Malley SS (1914) Bengal district gazetteers. Available: https://dspace.gipe.ac.in/xmlui/handle/1/38320

Pattanayak S, Mohanty UC, Dube SK (2016) Advanced numerical modeling and data assimilation techniques for tropical cyclone prediction. Springer, Dordrecht. https://doi.org/10.5822/978-94-024-0896-6_27
Payo A et al (2016) Clim Change 139. https://doi.org/10.1007/s10584-016-1769-z
Pramanik MK (2017) Environ Dev Sustain 19. https://doi.org/10.1007/s10668-016-9804-9
Prasad AS, Francescutti LH (2017) International encyclopedia of public health. Elsevier, Amsterdam. https://doi.org/10.1016/B978-0-12-803678-5.00519-1
PSMSL (2020) Data explorer. https://www.psmsl.org/
Rahman S et al (2019) J Earth Syst Sci 128. https://doi.org/10.1007/s12040-019-1184-8
Rahmstorf S (2010) Nat Clim Change 1:1004. https://doi.org/10.1038/climate.2010.29
Ramachandra TV, Gouri K, Bharath HA, Bharath S, Vinay S, Harish RB (2016) Indian Institute of Science. Available: http://wgbis.ces.iisc.ernet.in/biodiversity/pubs/ETR/ETR110/flora.html
Ramachandra TV, Sellers J, Bharath HA, Vinay S (2019) Environ Monit Assess 191. https://doi.org/10.1007/s10661-019-7701-z
Ramachandra TV, Vinay S, Bharath S (2021) Model Earth Syst Environ. https://doi.org/10.1007/s40808-021-01135-2
Ryder CHD (1924) Survey of India.
SEDAC (2006) Natural disaster hotspots. Available: https://sedac.ciesin.columbia.edu/data/collection/ndh
Shi P (2019) Disaster risk science. Springer Open. https://doi.org/10.1007/978-981-13-6689-5_1
Spalding MD, McIvor A, Tonneijck FH, Tol S, van Eijk P (2014) Wetl Int Nat Conserv. Available:https://www.nature.org/media/oceansandcoasts/mangroves-for-coastal-defence.pdf
Sudha Rani NNV, Satyanarayana ANV, Bhaskaran PK (2015) Nat Hazards 77. https://doi.org/10.1007/s11069-015-1597-x
SURGEDAT, NOAA (2021). Available: http://surge.srcc.lsu.edu/data.html
UNDRR (2015) Sendai framework for disaster risk reduction 2015–2030. Available: https://www.undrr.org/publication/sendai-framework-disaster-risk-reduction-2015-2030
Walker HJ et al (2005) Encyclopedia of coastal science. Springer, Dordrecht. https://doi.org/10.1007/1-4020-3880-1_179
Wang X, Xu L-L, Cui S-H, Wang C-H (2020) Adv Clim Change Res 11. https://doi.org/10.1016/j.accre.2020.11.010
Ward PJ, Marfai MA, Yulianto F, Hizbaron DR, Aerts JCJH (2011) Nat Hazards 56. https://doi.org/10.1007/s11069-010-9599-1
Williams LL, Lück-Vogel M (2020) J Coast Conserv 24. https://doi.org/10.1007/s11852-020-00735-x
Wing OEJ, Sampson CC, Bates PD, Quinn N, Smith AM, Neal JC (2019) J Hydrol X 4. https://doi.org/10.1016/j.hydroa.2019.100039
Wright LD, Resio DT, Nichols CR (2019) Tomorrow's coasts: complex and impermanent. Springer, Berlin. https://doi.org/10.1007/978-3-319-75453-6_7
Xu J, Wang Z, Shen F, Ouyang C, Tu Y (2016) Int J Disaster Risk Reduction 17. https://doi.org/10.1016/j.ijdrr.2016.04.001
Yunus A, Avtar R, Kraines S, Yamamuro M, Lindberg F, Grimmond C (2016) Remote Sens 8. https://doi.org/10.3390/rs8050366

Chapter 18
Three-Dimensional (3D) Noise Pollution Visualization via 3D City Modelling

Muhamad Uznir Ujang, Nurul Qahirah Dzulkefley, Suhaibah Azri, and Syahiirah Salleh

Abstract Noise pollution is an excessive sound that can affect human health and environmental quality. There is a lot of research on environmental pollution, such as air and water pollution, but little research on noise pollution. People do not realize the potential of sound to pollute the environment. This research aims to visualize and provide noise-level information that can lead to noise pollution. The output of this research is the visualization of the noise level in 3 dimension (3D). A 3D geometrical database and the noise level are modelled and processed into a 3D environment. Due to insufficient noise pollution in 2D representation, this chapter presents a 3D noise visualization approach as it offers significant insight into situations where 3D noise effects are relevant.

Keywords Noise pollution · Noise level · 3 dimension · 3D visualization

18.1 Introduction

Nowadays, many people live in urban areas because it has a lot of advantages over rural areas, having more opportunities and better living conditions. The urban area can offer access to creativity, innovation, diversity and information, improved health, higher literacy, and a better quality of life (Nasution et al. 2020). However, the interaction between humans and the environment brings a lot of environmental pollution, especially in urban areas. Several types of pollution include air pollution, light pollution, water pollution, soil pollution, and noise pollution. Noise is the most overlooked form of pollution because it is not regarded as vital to life compared to water and air; noise is hardly an annoyance to people. Environmental noise is a progressively

M. U. Ujang (✉) · S. Azri · S. Salleh
3D GIS Research Group, Universiti Teknologi Malaysia (UTM), 81310 Johor Bahru, Johor, Malaysia
e-mail: mduznir@utm.my

N. Q. Dzulkefley
Department of Geoinformation, Faculty of Built Environment and Surveying, Universiti Teknologi Malaysia (UTM), 81310 Johor Bahru, Johor, Malaysia

V. P. Singh et al. (eds.), *Application of Remote Sensing and GIS in Natural Resources and Built Infrastructure Management*, Water Science and Technology Library 105,
https://doi.org/10.1007/978-3-031-14096-9_18

common feature of urban areas that can be perceived as unwanted in non-occupational settings (King et al. 2012). Additionally, noise pollution visualization is frequently displayed in a two-dimensional (2D) format. As a result, the visual interpretation of noise pollution becomes more complicated. For instance, the noise itself moves in 3D. Thus, with the progress of 3D modelling, this issue can be overcome, and noise pollution data can be presented in a 3D environment. Nonetheless, particular processes must be developed to ensure that they are carried out appropriately.

A sound is a form of energy that the human ear can detect. Sound can travel through the air and other media such as water or steel. Noise is an unwanted sound produced by many sources, such as an operating machine tool, ambulance siren, thunderclap. Noise pollution is an excessive sound that can affect human health and environmental quality. Sound level is measured in decibels (dB). It has exposure limits derived from the World Health Organization (WHO) recommendation that sound levels below 70 dB are not damaging and are considered loud when they exceed 80 dB. Its exposure limit is 40 h per 7 days. From the national standard limit and WHO, the noise level in urban areas must not exceed 65 dBA at noon and not exceed 55 dBA at night (Ismail and Hussain 2001). Human hearing can be impacted by the loudness of the sound and how long the exposure to them is. For example, if a person is exposed to loud sounds in a concert, it could cause temporary hearing loss.

There are many effects of noise pollution on human health when continuously exposed for months or years, such as mental health. For example, people living near the airport will hear continuous noise that can increase irritation and not focus on their things (Lefèvre et al. 2020). It can affect their concentration on doing something in their daily life. Besides, noise can awaken people from sleep and be very disruptive, resulting in physical, mental, or emotional illness if they face frequent sleep disturbance. The vital point besides physical problems is psychological problems (Goines and Hagler 2007). The way to prevent and protect your hearing is by knowing where you want to go, and if you are going to be exposed to loud sound levels, make sure to use an earplug or noise-cancelling headphones. The better way is to move to a quieter area and avoid exposure to the loud sound level. After hearing the loud sound, it is advised to give your ears a break. Noise is moving in 360° which contains area and height, and we can identify where the noise is travelling with three-dimensional (3D) noise mapping, especially on a building.

In line with technological developments, the presentation of geospatial data has changed dramatically. The need for 3D models is growing and expanding rapidly in various fields (Singh et al. 2013). The 3D in geographic information system (GIS) brings z value into mapping, including elevation data. The geometry and composition of an urban environment are described using a digital 3D city model (Julin et al. 2018). The 3D city models have become crucial for various applications such as visualization for navigation, planning. The 3D city model application has become well known and continuously increases. This model can present on the web, and it has a lot of advantages that people can access everywhere and at any time. Therefore, the tools for web-based implementations of virtual globes, which allow users to navigate their data in 3D, have been available with more significant numbers of functionality (Sadidi et al. 2020; Jovanović et al. 2020; Ramlee et al. 2019). The 3D geographic

information system (GIS) applications have a good base as online virtual web globes provide it. It is essential to develop 3D noise maps that can show the influence of noise in all directions.

The purpose of the study presented in this chapter is to provide a mechanism for utilizing 3D GIS technology to visualize noise pollution in a 3D environment. Current methodologies are primarily designed to display noise pollution on a two-dimensional (2D) platform. It reduces the scattering of pollution itself, which flows naturally in 3D. Dedicated approaches are being developed to attain this goal by using 3D city modelling technologies in 3D GIS. The following section will provide some further aspects of 3D city modelling.

18.2 City Modelling

The development of 3D models as a virtual environment can also be extended further to provide a sound foundation for performing analysis, simulations, and other applications (Azri et al. 2020; Ujang et al. 2018). For instance, a digital twin of a city with a high level of detail will include road networks and buildings that can be used for visibility analysis, urban heat island detection, and air quality simulations (Beil et al. 2020). The 3D models can also be constructed to document historical structures such as windmills as part of cultural heritage conservation (Smaczyński and Horbiński 2021). This can also be extended to immersive and interactive virtual reality visualization of prehistoric artefacts (Büyüksalih et al. 2020). At a building scale, highly detailed 3D models offer support for applications for noise analysis, energy usage, and others (Lim et al. 2020). Underground infrastructure such as drainage pipes and 3D models of buildings can facilitate urban flooding simulations by including other data such as elevation, water flow, volume, and others (Shen et al. 2020). However, 3D visualization or models cannot remain as merely graphical output to implement such applications for analysis and simulations. In addition to being a digital twin, 3D models should ensure the maintenance of spatial and non-spatial attributes and geometric, semantic, and topological characteristics (Ujang et al. 2019; Salleh et al. 2020). Although virtual environments are essentially replicas of the real world, it remains a visualization open to the perception of developers or users and without standards.

To standardize 3D city modelling, CityGML was established by the Open Geospatial Consortium (OGC) as an international standard and open data model for 3D city modelling (Gerhard and Lutz 2012). The development of CityGML was targeted to be a shared definition of entities, attributes, and relationships within a 3D city model (Kolbe 2009). Similar to the compliance of the CityGML data model to ISO Standards, the schema for CityGML also complies with OGC's Geography Markup Language GML3 (GML 3.1.1) (Open Geospatial Consortium 2012). The entities in a 3D city model can also be represented in five scales or Levels-of-Detail (LoD) (Gröger and Plümer 2012). LoD0 is generally a 2.5D model of the terrain, including building footprints or roof edges. LoD1 represents buildings as blocks with smooth

and planar roofs. In LoD2, the roof of a building will be segregated from other thematically different building surfaces. LoD3 allows the definition of architectural details of wall and roof structures. LoD4 provides an interior layout for the building, including rooms, stairs, doors, and other structures. In constructing virtual 3D campus models, CityGML enables interoperability with future city models that can be used for different applications.

University campuses can be considered miniature cities with buildings within a large area. Nonetheless, campuses should also be modelled in 3D to serve as the foundation for enabling smart cities of smart campuses. A similar approach was demonstrated for transforming historical buildings into CityGML models from vector Esri Shapefiles obtained from point cloud data (Pepe et al. 2020). FME software was also utilized to convert multiple data sources to build CityGML models of detailed street systems and 3D tile files for 3D web visualization (Beil et al. 2020). Another study integrated various data sources using FME to produce a comprehensive CityGML file for managing urban flooding (Shen et al. 2020). To model a campus in 3D, various approaches to modelling buildings can be applied. One of the main differences in modelling approaches depends on the available data.

18.3 Framework of 3D Noise Pollution Modelling

To perform the 3D noise mapping, the noise-level data needs to be obtained. The noise-level data is taken in the buildings in the study area. The device used is Smart sensor AS804; as depicted in Fig. 18.1, the unit is decibel. This noise-level meter measures sound pressure and is commonly used in noise pollution studies to quantify almost any noise, especially for industrial, environmental, and aircraft noise. It is a type of sound measure level meter commonly used in noise pollution studies to quantify noise. The measuring level is 30–130 dBA (decibels).

When the noise level for the study area is obtained, the data needs to be stored in the database. The database tool used in this research is PostgreSQL. A simple database is used for this research that does not require any relation between tables. PostgreSQL comes with tools that can connect to cloud services. Figure 18.2 shows the name of the table in the database. The column of the database is shown in Fig. 18.3.

The noise level is applied to buildings in the 3D modelling. The noise characteristics are unique, and it moves in 360° directions. Thus, a 3D building model is the best model to perceive the scenario. It can show how the noise is moving in the model. Figure 18.4 shows the layer used to design the 3D buildings.

This research study area is in Universiti Teknologi Malaysia, Johor Bahru campus. The 3D model of the building is created using SketchUp 3D modelling software. OSM is used as a base for the building, and Google Maps is referred to the design of the buildings. The measurement of the buildings is followed by actual measurement in real life. For example, the height of each level is standardized into 3 m. The total number of buildings model in this research is 50 buildings with 175 levels altogether.

Fig. 18.1 Smart sensor AS804

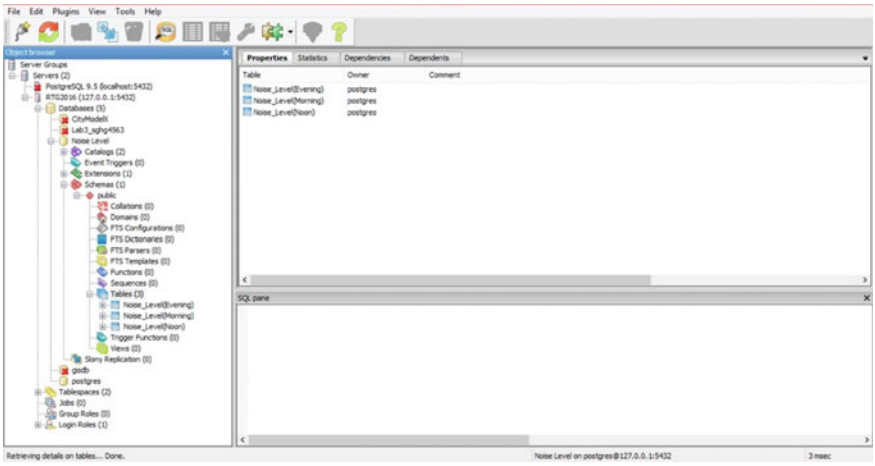

Fig. 18.2 Table names for the database

Edit Data - RTG2016 (127.0.0.1:5432) - Noise Level - public.Noise_Level(Mor...

File Edit View Tools Help

No limit

	ID [PK] integer	Building text	Level numeric	Max(dBA) text	Min(dBA) text
1	1	D01	1	79.3	53.2
2	2	D01	2	77.4	53.9
3	3	D02	1	79.4	55.3
4	4	D03	1	79.9	55.7
5	5	D04	1	79.5	55.6
6	6	D05	1	79.1	55.5
7	7	D05	2	77.4	53.4
8	8	D05	3	76.3	52.9
9	9	D05	4	72.5	49.5
10	10	D06	1	78.9	55.8
11	11	D06	2	77.1	55.1
12	12	D06	3	69.3	53.6
13	13	D06	4	62.9	52.9
14	14	D07	1	79.1	53.9
15	15	D07	2	75.8	53.3
16	16	D07	3	74.1	52.1
17	17	D07	4	66.3	51.8
18	18	D10	1	79.4	54.0
19	19	D10	2	74.8	52.8
20	20	D10	3	69.7	51.0
21	21	E01	1	79.4	55.5
22	22	E01	2	74.9	55.1
23	23	E02	1	81.3	55.7
24	24	E03	1	80.9	55.2
25	25	E04	1	76.2	56.4
26	26	E05	1	82.7	59.8
27	27	E06	1	80.3	59.9
28	28	E06	2	79.1	57.4

160 rows.

Fig. 18.3 Columns in noise-level table

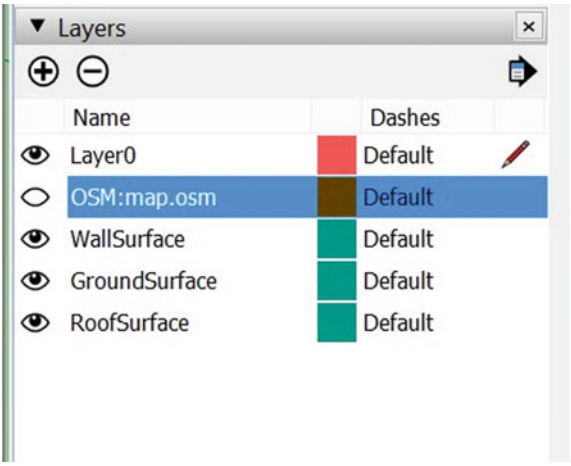

Fig. 18.4 Layers used for 3D building

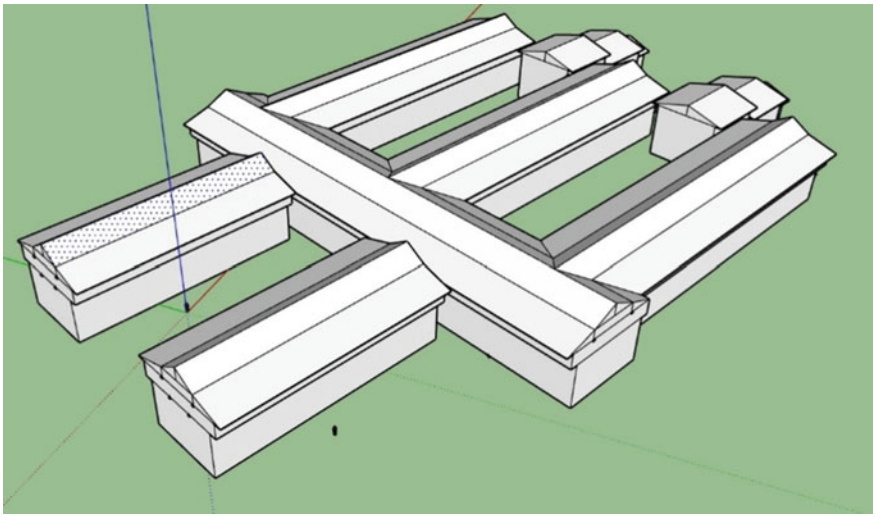

Fig. 18.5 Three-dimensional building model

The 3D model for buildings in the study area is established from OSM satellite imagery. OSM satellite imagery is exported and imported into SketchUp. The ruler in Google Maps is used to estimate the length and width of the buildings, and using street view images, the design and the structure of the building in 3D could be identified. From that, the ground surface of the building can be drawn, followed by a wall surface and roof surface. Figure 18.5 shows an example of the 3D model.

18.4 The 3D Noise Pollution Visualization

This research applies the accumulated noise-level data to the 3D buildings for every level/floor. The colour for the lowest noise level is moderate sea green, and the highest noise level is deep blue-violet. The colour contrast is intended to show the difference for each 5 dB noise level. The final 3D buildings with noise colour applied are exported into the Collada file (.dae) to be used in Cesium. These 3D buildings are in their actual geo-location to be placed precisely on the terrain. Visualizing noise mapping in Cesium helps users recognize how noise pollution affects the building. Users can perceive the buildings as it is in real life by using this approach. Figure 18.6 shows several results of 3D buildings created in this research.

The noise level is observed in 3 different phases. The phases are in the morning (7.00 am until 8.30 am), noon (12.30 pm until 1.30 pm), and evening (4.30 pm until 5.30 pm). The phases were selected based on the justification that the total number of vehicles is relatively high for the specified period in each phase. It can be considered a high number of vehicles in the morning due to staff and students coming to work

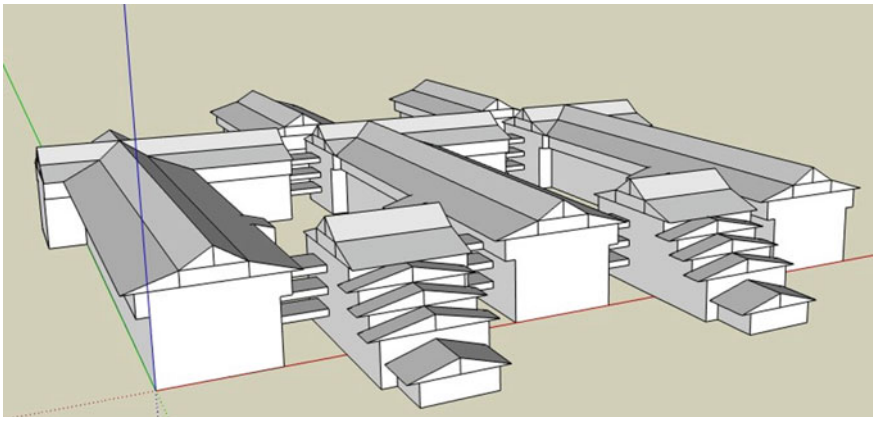

Fig. 18.6 Three-dimensional building models for Block B02, B04, B05, B07, B08, B09, and B10

and attending lectures while in the afternoon is a common break time where it is usually used for lunch or other personal matters.

Meanwhile, in the late afternoon, the high traffic flow was due to staff and students returning from campus to their respective residences. As additional information, the study area for this research is made in the university campus. Thus, the primary source of noise pollution comes from motor vehicles. However, if the study area involves other areas, such as industrial areas, then other noise pollution factors must be considered in calculating noise pollution. Figures 18.7, 18.8, and 18.9 show some snapshots of the data collected in the three phases.

In Cesium, the 3D models are visualized based on the phases observed. This information benefits the user since it helps them know exactly where the noise pollution

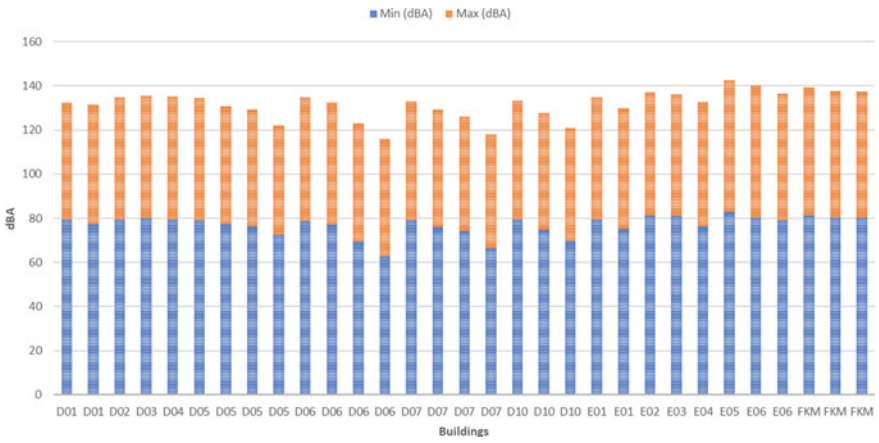

Fig. 18.7 Noise-level data for Phase 1 (7:00 am–8:30 am)

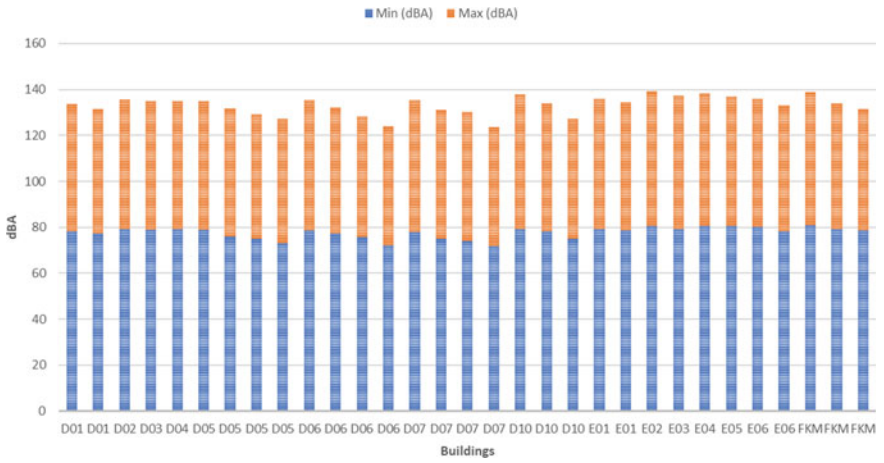

Fig. 18.8 Noise-level data for Phase 2 (12:30 pm–1:30 pm)

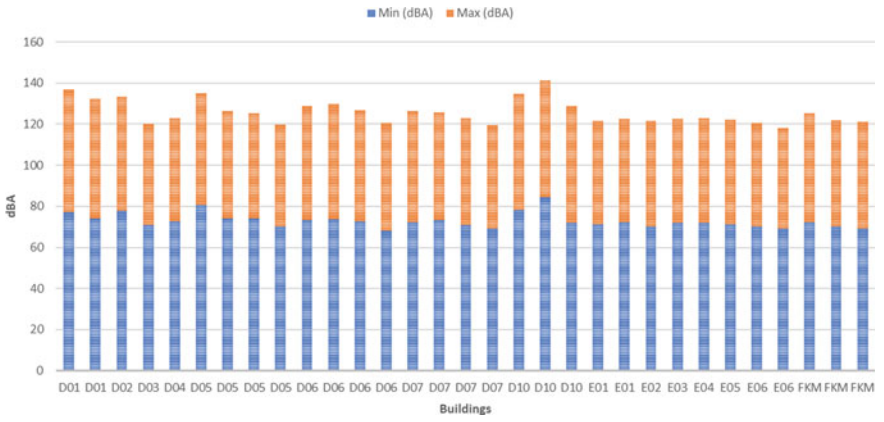

Fig. 18.9 Noise-level data for Phase 3 (4:30 pm–5:30 pm)

is around them, be more sensitive to noise pollution, and learn how to prevent it. Figures 18.10, 18.11, and 18.12 show the visualization of the noise level in Phase 1, Phase 2, and Phase 3 for the entire study area, respectively.

In this research, there are two approaches performed. First, the 3D building model built is mapped with noise pollution visualization on each building level. The colour difference shown differentiates the noise level for each level involved. As mentioned earlier, each colour difference has a different value of 5 dB. To begin, the lowest noise level is found in moderate sea green colour (35–39 dB), pale yellow (50–54 dB), brilliant tangelo (60–64 dB), brilliant red, and moderate amaranth (65–74 dB). It progresses to the highest noise level found in dark rose and deep blue-violet (75 dB and above).

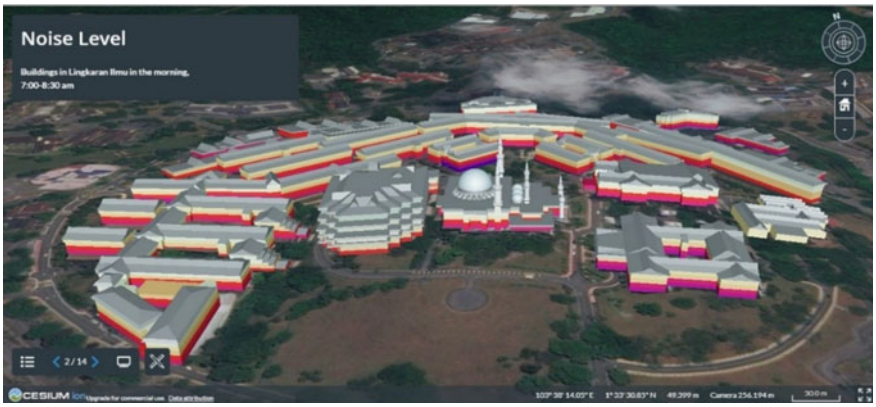

Fig. 18.10 Three-dimensional noise-level visualization for Phase 1 (7:00 am–8:30 am)

Fig. 18.11 Three-dimensional noise-level visualization for Phase 2 (12:30 pm–1:30 pm)

Fig. 18.12 Three-dimensional noise-level visualization for Phase 3 (4:30 pm–5:30 pm)

These colours describe the noise-level data observed in the three phases of data acquisition (source from motor vehicles). However, the second approach is to visualize the noise level in the building (interior). This noise may be caused by the air-conditioning system and other mechanical machine tools found in the building. The main university library building (Sultanah Zanariah Library) is used to realize this. This is because the library requires to be in a relatively quiet place compared with other academic buildings. Based on Fig. 18.12, the library building is in the model's centre and to the left of the university's mosque building. Figures 18.13 and 18.14 show the indoor and outdoor noise visualization, respectively.

The noise level in the study area surpasses the noise level recommended by the Malaysian Department of Environment (DOE). The noise level recommended for daytime in the educational area is below 50 dBA and for a library (indoor) is 40–45 dBA. It is significant to adhere to the recommended noise level to ensure the environment is conducive to academic activities. If not, it will affect the environment, and the educational activities cannot be carried out properly. The difference between

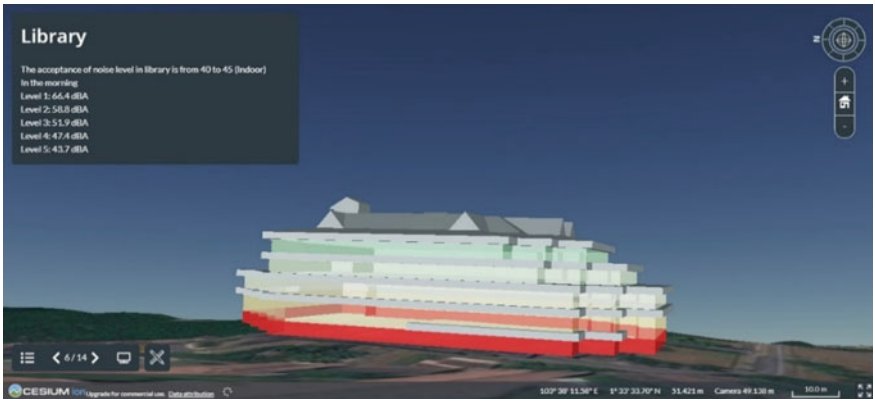

Fig. 18.13 Indoor noise level at Sultanah Zanariah Library

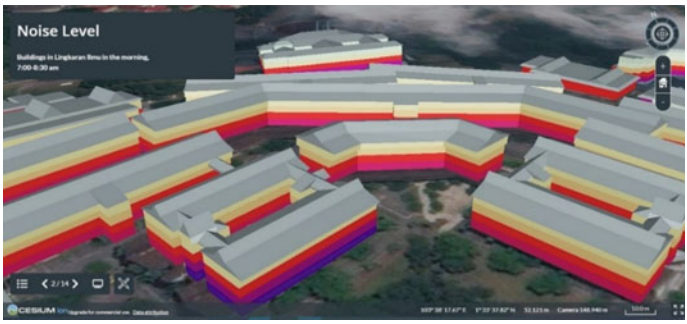

Fig. 18.14 Outdoor noise-level visualization

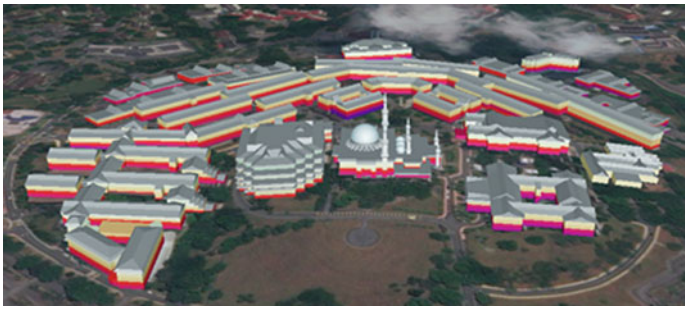

Fig. 18.15 Acquired noise-level 3D model

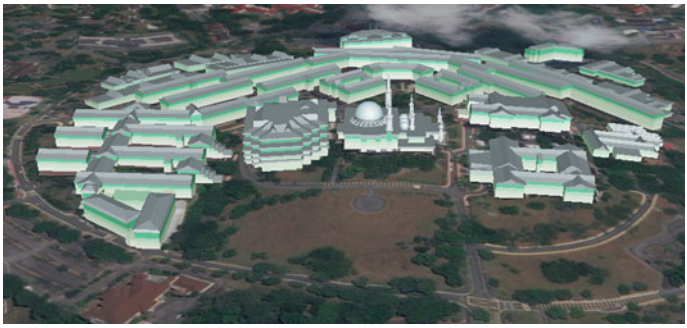

Fig. 18.16 Ideal noise-level 3D model

the ideal noise-level 3D model and the acquired noise-level 3D model in the morning for the study area is depicted in Figs. 18.15 and 18.16, respectively.

Apart from that, observations were also made on the three phases observed. Observations are made to see which building has the highest noise-level value. It aims to examine further which buildings need to be given more attention to addressing this noise control. Figures 18.17, 18.18, and 18.19 show the buildings with the highest noise pollution values for each phase observed.

18.5 Discussion

Based on noise-level mapping of the campus's buildings, it was determined that the buildings with the highest noise levels are Building C19, Building E04, and Building B12 for Phases 1 through 3. According to the observations made, it is apparent that the bottom level (ground floor) has a greater noise level than the higher floor level. Additionally, rooms or areas close to the road network have a more significant reading than those not.

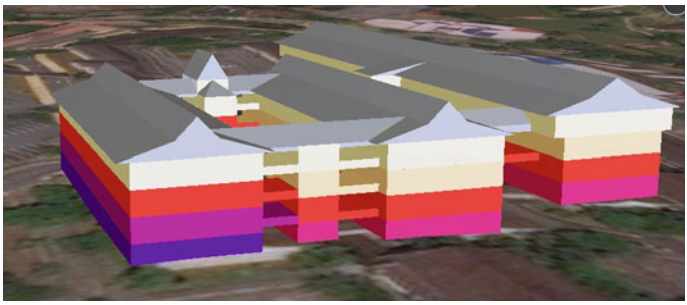

Fig. 18.17 Building with the highest noise level in Phase 1 (Building C19)

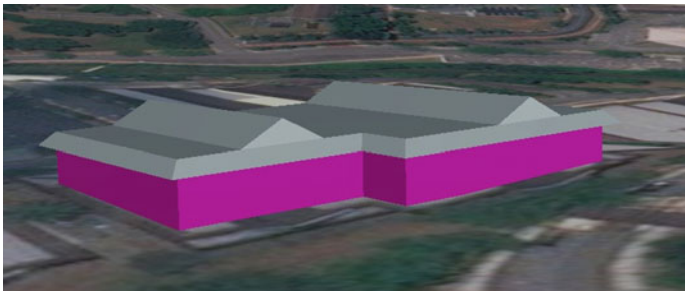

Fig. 18.18 Building with the highest noise level in Phase 2 (Building E04)

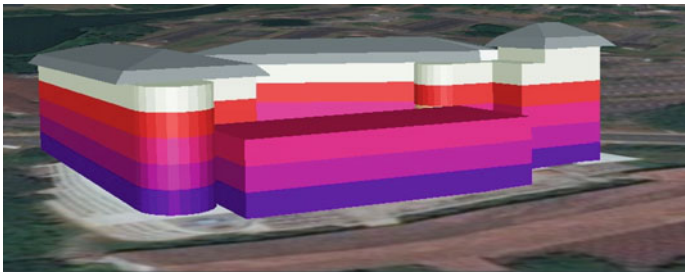

Fig. 18.19 Building with the highest noise level in Phase 3 (Building B12)

The reason why these three buildings had the highest values in each of these phases, on the other hand, remains uncertain. According to information about the campus's road network and the locations of bus stops, it was determined that these three buildings had some similarities. To begin, these buildings are situated alongside the campus's main road. Additionally, Buildings C19 and E04 are near a bus stop, where students extensively use bus services during the designated phases. The B12 building is positioned adjacent to the main campus entrance route utilized by students and the bus transporting them back to their various residential colleges. It occurs

exclusively in the afternoon, while students use alternate routes to faculty buildings during the morning (Phase 1) due to the campus's deployment of a one-way street. It explains why these areas attract users while increasing the area's noise level.

To elucidate, without the visualization developed in this research, determining the source of noise pollution or the location of the noise level is rather difficult. It is because the sound properties themselves are not visible but only audible. It cannot be accurately measured without the use of specialized instruments. Following that, the free-moving character of sound in physical space demands 3D modelling. Using 3D city modelling techniques in conjunction with noise pollution data, it is feasible to visualize noise pollution throughout the whole study area. It visually identifies the location or structure with a noise level that exceeds the specified noise level. It is possible to determine the source of pollution by combining satellite images as a base map with other information such as road networks. Additional measures can be undertaken on campus to prevent this from happening.

18.6 Conclusion

To sum up, noise pollution can occur anywhere and at any time. It is also likely that the level of human acceptance of noise pollution will oscillate throughout time. On the other hand, the World Health Organization has offered a basic guideline to prevent this noise pollution from becoming severe. Activities carried out for a place or an area can be controlled and classified using these criteria and divided into categories. Example: Industrial zones inherently require the usage of heavy machinery, which results in the indirect emission of relatively loud and disagreeable noises that are audible to members of the public. As a result, industrial zones can be classified in advance of their development, allowing for more efficient planning. Furthermore, activities or projects involving the public should not be located close to this industrial region since it is anticipated that the excessive noise will degrade the quality of life of those who live in the neighbourhood.

By utilizing the technique described in this chapter, it is possible to observe the degree of noise in a 3D environment using 3D city modelling software. This 3D visualization can aid in visualizing the effects of noise on the surrounding environment because the sound itself is unseen and moves in 360°. Additionally, more efficient and organized planning, such as development planning, is conceivable in future. For instance, an institution may impose a vehicle restriction through a specific educational area (with a high noise level).

18.7 Recommendations

The study area used in this study is based on the campus environment. The campus should have a quieter and more regulated environment. As a recommendation, this research can be further expanded to other areas such as residential, industrial, recreational, and even government administrative office areas. Other factors of noise pollution should be considered. It can help achieve a healthier life towards improving the quality of life for sustainable development.

Future research should incorporate the 3D city modelling proposed in this research with the effect of noise pollution on human health and well-being. Especially in the urban area, which is well known for its busy life, lively night atmosphere, the hustle and bustle of the city, to some extent, has undoubtedly affected the health of the city's residents. Based on the initial study in this research, the space below (ground floor) is more affected by noise than the space upstairs. It has given an early indication that noise pollution could disrupt the health levels of the city's residents. However, this matter needs to be studied further and supported by more scientific research facts. It definitely will benefit the well-being of the city's residents in future.

Acknowledgements This research was partially funded by UTM Research University Grant, VotQ.J130000.3652.02M57 and VotQ.J130000.2452.09G84.

References

Azri S, Ujang U, Abdul Rahman A (2020) Voronoi classified and clustered data constellation: a new 3D data structure for geomarketing strategies. ISPRS J Photogramm Remote Sens 162:1–16. https://doi.org/10.1016/j.isprsjprs.2020.01.022

Beil C, Ruhdorfer R, Coduro T, Kolbe TH (2020) Detailed streetspace modelling for multiple applications: discussions on the proposed CityGML 3.0 transportation model. ISPRS Int J Geo-Inf 9(10). https://doi.org/10.3390/ijgi9100603

Büyüksalih G, Kan T, Özkan GE, Meriç M, Isın L, Kersten TP (2020) Preserving the knowledge of the past through virtual visits: from 3D laser scanning to virtual reality visualisation at the Istanbul Çatalca İnceğiz Caves. PFG—J Photogramm Remote Sens Geo Sci 88(2):133–146. https://doi.org/10.1007/s41064-020-00091-3

Gerhard G, Lutz P (2012) CityGML—interoperable semantic 3D city models. ISPRS J Photogramm Remote Sens 71(0):12–33. https://doi.org/10.1016/j.isprsjprs.2012.04.004

Goines L, Hagler L (2007) Noise pollution: a modern plague. Southern Med J 100(3):287–294

Gröger G, Plümer L (2012) CityGML—interoperable semantic 3D city models. ISPRS J Photogramm Remote Sens 71:12–33. https://doi.org/10.1016/j.isprsjprs.2012.04.004

Ismail H, Hussain TPRS (2001) Perbandingan konsentrasi bunyi bising antara bandar Alor Setar (Kedah) dengan Georgetown (Pulau Pinang). Sekolah Pembangunan Sosial, Universiti Utara Malaysia

Jovanović D, Milovanov S, Ruskovski I, Govedarica M, Sladić D, Radulović A, Pajić V (2020) Building virtual 3D city model for smart cities applications: a case study on campus area of the university of Novi Sad. ISPRS Int J Geo-Inf 9(8). https://doi.org/10.3390/ijgi9080476

Julin A, Jaalama K, Virtanen J-P, Pouke M, Ylipulli J, Vaaja M, Hyyppä J, Hyyppä H (2018) Characterizing 3D city modeling projects: towards a harmonized interoperable system. ISPRS Int J Geo-Inf 7(2). https://doi.org/10.3390/ijgi7020055

King G, Roland-Mieszkowski M, Jason T, Rainham DG (2012) Noise levels associated with urban land use. J Urban Health 89(6):1017–1030. https://doi.org/10.1007/s11524-012-9721-7

Kolbe TH (2009) Representing and exchanging 3D city models with CityGML. In: 3D geo-information sciences. pp 15–31

Lefèvre M, Chaumond A, Champelovier P, Giorgis Allemand L, Lambert J, Laumon B, Evrard A-S (2020) Understanding the relationship between air traffic noise exposure and annoyance in populations living near airports in France. Environ Int 144:106058. https://doi.org/10.1016/j.envint.2020.106058

Lim J, Janssen P, Filip B (2020) Visualising detailed CityGML and ADE at the building scale. Int Arch Photogramm Remote Sens Spatial Inf Sci XLIV-4/W1-2020:83–90

Nasution AA, Nasution FN, Risanty (2020) Smart city development strategy and it's challenges for city. IOP Conf Ser Earth Environ Sci 562:012012. https://doi.org/10.1088/1755-1315/562/1/012012

Open Geospatial Consortium (2012) CityGML. Available at: https://www.ogc.org/standards/citygml

Pepe M, Costantino D, Alfio VS, Angelini MG, Restuccia Garofalo A (2020) A CityGML multiscale approach for the conservation and management of cultural heritage: the case study of the old town of Taranto (Italy). ISPRS Int J Geo-Inf 9(7). https://doi.org/10.3390/ijgi9070449

Ramlee SSS, Abd Razak N, Ujang U, Mohd Salleh S, Azri S, Choon TL (2019) Towards 3D smart campus via 3D city modelling. Int Arch Photogramm Remote Sens Spatial Inf Sci XLII-4/W16:523-526. https://doi.org/10.5194/isprs-archives-XLII-4-W16-523-2019

Sadidi J, Judaki Z, Rezayan H (2020) Designing and implementing a 3d indoor navigation web application. J Spatial Anal Environ Hazards 7(2):67–80

Salleh S, Ujang U, Azri S, Choon TL (2020) 3D topological validation of compact abstract cell complexes (CACC) data structure for buildings in CityGML. Int J Built Environ Sustain 7(2):25–32. https://doi.org/10.11113/ijbes.v7.n2.457

Shen J, Zhou J, Zhou J, Herman L, Reznik T (2020) Constructing the CityGML ADE for the multi-source data integration of urban flooding. ISPRS Int J Geo-Inf 9(6). https://doi.org/10.3390/ijgi9060359

Singh SP, Jain K, Mandla VR (2013) Virtual 3D city modeling: techniques and applications. Int Arch Photogramm Remote Sens Spatial Inf Sci XL-2/W2:73–91. https://doi.org/10.5194/isprsarchives-XL-2-W2-73-2013

Smaczyński M, Horbiński T (2021) Creating a 3D model of the existing historical topographic object based on low-level aerial imagery. KN—J Carto Geo Inf 71(1):33–43.https://doi.org/10.1007/s42489-020-00061-0

Ujang U, Azri S, Zahir M, Abdul Rahman A, Choon TL (2018) Urban heat island micro-mapping via 3D city model. Int Arch Photogramm Remote Sens Spatial Inf Sci XLII-4/W10:201–207. https://doi.org/10.5194/isprs-archives-XLII-4-W10-201-2018

Ujang U, Castro FA, Azri S (2019) Abstract topological data structure for 3D spatial objects. ISPRS Int J Geo-Inf 8(3). https://doi.org/10.3390/ijgi8030102

Chapter 19
Decadal Satellite Data Analysis for Flood Hazard Mapping: A Case Study of Eastern Uttar Pradesh

Suchita Pandey, Nilanchal Patel, and Ajay Kumar Agrawal

Abstract Flood is a natural havoc faced in many parts of India. The districts of eastern Uttar Pradesh falling under the Rapti river basin are most vulnerable to and severely affected by flood. Assessment of flood inundation and flood water stagnation has been conducted for a decade from 2008 to 2018 by using satellite datasets. Vulnerability analysis for flood-affected areas is based on the RADARSAT data available during monsoon season. The Synthetic Aperture Radar dataset has been used together with the hydrological data for estimating the period of stagnation, recurrence of flood hazards, and flood inundation. The changes in frequency of floods and its severity and the spatial extent of flood-affected areas from 2008 to 2018 have been determined from the analysis of the organized flood hazard database with spatial extent in GIS. Among the 14 districts of Rapti River basin, seven are found to be most vulnerable and heavily affected by the flood hazard viz. Gorakhpur, Shravasti, Maharajganj, Balrampur, Siddharthnagar, Deoria and Sant Kabir Nagar. Spatial intersection technique has been implemented in GIS to determine the stagnated flood water areas.

Keywords Flood hazard · Flood inundation · RADARSAT data · Rapti river basin

19.1 Introduction

Flood comes when the river overflows. Flood means havoc created by nature. It is a natural disaster that has been affecting the Indian lives and economy for last several years. Floods worldwide, beyond loss of life, also cause many millions of

S. Pandey
K. Banerjee Centre of Atmospheric and Ocean Sciences, University of Allahabad, Prayagraj, India

N. Patel (✉)
Department of Remote Sensing, Birla Institute of Technology Mesra, Ranchi, India
e-mail: npatel@bitmesra.ac.in

A. K. Agrawal
Uttar Pradesh Remote Sensing Application Centre, Lucknow, India

V. P. Singh et al. (eds.), *Application of Remote Sensing and GIS in Natural Resources and Built Infrastructure Management*, Water Science and Technology Library 105,
https://doi.org/10.1007/978-3-031-14096-9_19

dollars' worth of damage each year to crops and property. Flood inundation is a major hazard worldwide. Its prediction and prevention require considerable investment, apart from socio-economic consequences of severe flooding episodes. Better flood extent prediction is relevant to a significant percentage of the global population. Water stagnation during floods also creates many diseases spread to the surrounding area like malaria and other water-borne diseases. It is also important to raise fundamental scientific issues and challenges relating to remote sensing, distributed environmental modeling, risk analysis, and uncertainty. In recent years, remote sensing of flood plain environment has increasingly become an operational tool that may begin to solve some fundamental problems in flood conveyance estimation.

A flood-inundated area was detected using JERS-1/SAR data in the central plain of Thailand. The area is related with micro-geomorphology. It has the possibility that agricultural damage by flood can be estimated using both SAR data and geomorphologic maps (Yamada 2001). Preparation of a comprehensive flood hazard map for deltaic part of West Bengal state would be one of the most crucial steps for implementing non-structural remedial measures for floods and the study attempts to synthesize the relevant database in a spatial framework to evolve a flood hazard map for Genetic West Bengal (Sanyal and Lu 2003). The satellite rainfall product assessed was NASA's Tropical Rainfall Measuring Mission (TRMM) Multi-satellite Precipitation Analysis (TMPA) product called 3B41RT which is available in pseudo real-time with a latency of 6–10 h. Scientists observed that bias adjustment of satellite rainfall data can improve application in flood prediction to some extent with the trade-off of more false alarms in peak flow. However, a more rational and regime-based adjustment procedure needs to be identified before the use of satellite data can be institutionalized among flood modelers (Harris et al. 2007).

Flood Inundation Mapping of the Sparsely Gauged Large-Scale Brahmaputra Basin Using Remote Sensing Products was done and it was shown that the Nash Sutcliffe coefficient of the model with the uncorrected rainfall data in calibration and validation were 0.75 and 0.61, respectively whereas the similar values with the corrected rainfall data were 0.81 and 0.74. The output of the hydrological model was used as a boundary condition and lateral inflow to the hydraulic model. Modeling results obtained using uncorrected and corrected remotely sensed products of rainfall were compared with the discharge values at the basin outlet (Bahadurabad) and with altimetry data from Jason-2 satellite. The simulated flood inundation maps of the lower part of the Brahmaputra basin showed reasonably good match in terms of the probability of detection, success ratio, and critical success index (Bhattacharya et al. 2019). The fusion of remote sensing, social media, and topographic data sources developed a Bayesian statistical model to estimate the probability of flood inundation through weights-of-evidence analysis. The experiments were conducted using data collected during the 2014 UK flood event and focus on the Oxford city and surrounding areas. Using the proposed technique, predictions of inundation were evaluated against ground-truth flood extent. The results report on the quantitative accuracy of the multisource mapping process, which obtained area under receiver operating curve values of 0.95 and 0.93 for model fitting and testing, respectively (Rosser et al. 2017).

The Wavelet Transformed Classification Method provides the texture information of SAR images. This information is assigned as the component of the feature vector of a pixel. Classification using this method was successfully applied to a merged SAR image. Results indicate high classification accuracy for all the classes (Chumsamrong et al. 1998). The basin areas under Ghaghra and Rapti rivers were studied during August 2017. The thresholding and unsupervised classification technique have been used to map the inundated areas due to incessant rains. High-resolution multi-temporal Synthetic Aperture Radar (SAR) and Optical images were used to calculate the zonal statistics to find the inundated area in each district of the selected Area of Study (AOS). The obtained results are validated against the meteorological observations. From the findings, it is evident that SAR data can effectively be used for flood water mapping and flood monitoring. These findings will therefore help to minimize the flood hazard impact and aid in augmenting the flexibility in flood management (Anusha and Bharathi 2020).

There is an advanced study that reviews theories and algorithms of flood inundation mapping using SAR data, together with a discussion of their strengths and limitations, focusing on the level of automation, robustness, and accuracy. The results of the study show that the automation and robustness of non-obstructed inundation mapping have been achieved in this era of big earth observation (EO) data with acceptable accuracy, however, for the detection of beneath-vegetation flood mapping, L-band or multi-polarized (dual or fully) SAR data along with the ancillary building and topographic data are more useful (Shen et al. 2019).

In one of the studies that caused instant flooding and inundation, the scientists have used SAR data combined with the other datasets. Two hours of rain in November 2002 was enough to create total chaos in several parts of the city and its outskirts. The study area comprises Velachery and its surrounding. Their datasets comprised RADARSAT SAR of November 2002, IRS LISS III and PAN merged imagery of 2002, maps of Adyar and miscellaneous watersheds (4C2C2), Survey of India Toposheets, and Rainfall level data of November 2002 (Ramalingam and Vadivukkarasi 2005). An assessment of Maryland's vulnerability to flood damage has been done by the Maryland Department of the Environment (MDE) and the Eastern Shore Regional GIS Cooperative (ESRGC) at Salisbury University. The model was used to provide an independent analysis to collaborate some of the Department's flood hazard data and to test the usefulness of the new software. Strategies to mitigate the effects of flooding are outlined, including regulations, the State Model Floodplain Management Ordinance, local mitigation planning, the floodplain management database and repetitive loss project, mapping of risk, flood insurance, dam safety, stormwater management regulations, wetland regulations, growth management, sea level response strategy, and "no net adverse impact" watershed planning (Joyce and Scott 2005).

In another study that aimed at flood disaster resilience through composite index allows us to understand and identify the resilience capacity in eastern U.P. Secondary data is used for this study and indicators are proxy indicators that comprise five parameters viz. physical, social, economic, infrastructural, and community capacity. Districts are selected on the basis of the extent of flood-induced inundation. The results show that districts having higher composite index values are more capable of

coping with the disaster. Least resilient districts need to adopt improved mechanisms to become more resilient (Mishra and Mohapatra 2019). Another study revealed the significance of remote sensing and GIS for developing a flood inundation model to assess the flood-affected areas and number of flood-inundated villages in each district in almost real-time.

Uttar Pradesh is one of the states which faces flood problems every year. The present study indicates the significance of Remote Sensing and GIS for developing a flood inundation model to assess the flood-affected areas and numbers of flood-inundated villages in each district of Uttar Pradesh in almost real-time. This includes an attempt to take decision in near real-time on flood management for planners and decision-makers using microwave remote sensing satellite data (RADARSAT and RISAT). The model generates statistics of flood-affected areas near or in the village, affected blocks, and districts within two hours after receiving flood layers from the National Remote Sensing Center (NRSC), Disaster Management Division, Hyderabad. On the basis of this model, the relief and rescue operation may be planned in more effective manner and saving human lives and livestock (Shukla et al. 2015). In a different study the two flood-prone blocks of Ajay River Basin in West Bengal, India have been studied for flood risk assessment and hazard identification. For flood analysis, flood spread area and flood height are considered. From the result of flood prediction in Ausgram II, 13% of the block area and 17% of the block population, and in Nanoor, 21% of the block area and 28% of the population are affected (Mondal et al. 2020).

A survey study has been done by Ding et al. (2021) for flash floods by using remote sensing and GIS technique. First, a visualization analysis of the literature is performed, including a keyword co-occurrence analysis, time zone chart analysis, keyword burst analysis, and literature co-citation analysis. Then, the application of remote sensing and GIS technologies to flash flood disasters is analyzed in terms of aspects such as flash flood forecasting, flash flood disaster impact assessments, flash flood susceptibility analyses, flash flood risk assessments, and the identification of flash flood disaster risk areas. In a different study by Hong and Abdelkareem (2022) the remote sensing and GIS technique is used to indemnify the flood-prone areas and their prediction for optimum use of groundwater resources has been done. In this study, the ALOS/PALSAR and SRTM data allowed revealing geologic structures, hydromorphic characteristics, and delineated prone areas to flash flood hazards (FFHs). Multi-criteria information that controls the occurrence, movements, and infiltration capacities were combined after applying weight factors. Such information stemmed from remotely sensed and ancillary data which were used through a GIS-based method to reveal the optimum zones of water resources. The result proves that about 14.88% of studied basin considers a promising zone of groundwater probability and denotes the most likely portion for further exploration.

19.1.1 Significance of the Work

SAR images are used in the current study to extract the flood layers. The approach comprises extraction of the texturally homogeneous areas representing water surfaces on the SAR images. With this approach, flood mapping has been done on the flood layers extracted from the SAR images of the study area. Ghaghara and Rapti are the main rivers that cause floods in Uttar Pradesh. The Rapti river emerges from the higher Himalayan region in Nepal (Thapa 1997). It comprises a large catchment area in the upper Nepal region and major flood-prone catchment in the eastern Uttar Pradesh. The lower catchment of the Rapti basin receives heavy runoff from the upper catchments in Nepal. The West Rapti is a tiny river by comparison with the rivers like Kosi, Gandak, and Karnali. The average annual flows of the Kosi, Gandak, and Karnali rivers are in the range of about 1500 cumecs, whereas the average annual flow of the West Rapti river is only about 100 cumecs. The West Rapti river water is extensively used for irrigation in the Nepalese territory, as a result, this river almost dries up throughout the dry seasons. However, during the monsoon season, the damages due to the West Rapti river floods are not insignificant despite the fact that this is relatively a very small river. In recent times, almost every year widespread submersion and loss of life and property in the Indian territory due to the West Rapti river floods are reported. The rise of the West Rapti water level is exceptionally high at the time of big floods.

In the last century until 1975, the recorded highest flood water level of the West Rapti river at Birdsghet near Gorakhpur area had exceeded the warning stage level by a huge margin of over 9 ft. By comparison with the West Rapti river, the peak flood water level rises in the other rivers are relatively small. No wonder the West Rapti river's high floods devastate vast areas of land despite the fact that it is relatively a small river.

19.1.2 Purpose

The districts of Rapti basin in Uttar Pradesh that are heavily affected by flood are viz. Gorakhpur, Shrawasti, Maharajganj, Balrampur, Siddarthnagar, Deoria, St. Kabir Nagar. The flood analysis of eastern Uttar Pradesh region has been done for the following purposes:

- To delineate the main districts of the Rapti catchment in eastern U.P., which are most vulnerable to flood and are severely affected by floods during the last several years.
- To assess the damage caused by floods in the districts based on the analysis of the stagnation period of water.

Vulnerability analysis for the flood-affected villages is based on the RADARSAT data available during the monsoon season. Flood inundation mapping on the various dates provides real-time information for relief and mitigation of floods and is useful to provide control measures from flood.

19.1.3 Study Area

The study area lies in the lower sub-catchment of Rapti, distributed in the parts of Indo-Gangetic plain and contains 14 districts of eastern Uttar Pradesh viz. Bahraich, Shrawasti, Gonda, Siddarthnagar, Balrampur, Basti, Maharajgunj, Gorakhpur, Deoria, Mau, Azamgarh, Ballia, Kushinagar, and St. Kabir Nagar. The topography is almost flat, with high sediment load. The area is flood-prone and adversely affected by EL-NINO (ENSO) or southern oscillations. The study area has subtropical climate with high temperatures in summer and low in winter. The highest temperature rises up to 48 °C in summers and falls up to 8–10 °C in winter. The soils of the region are deep, excessively drained to well and moderately drained, sandy soils on gentle slopes with loamy surfaces and moderate erosion (Fig. 19.1).

19.1.4 Research Objectives

1. To perform vulnerability assessment of the flood-affected districts (eastern Uttar Pradesh) of the Rapti catchment area.
2. To perform stagnation studies for flood-affected areas.
3. To carry out flood inundation mapping using RADAR datasets.

19.1.5 Data and Software Used

1. RadarSAT-1 data of various dates in year 2008.
2. RadarSAT-2 data of various dates in year 2018.
3. Base data of the district and block boundary.
4. Software Arc GIS ver.9.1

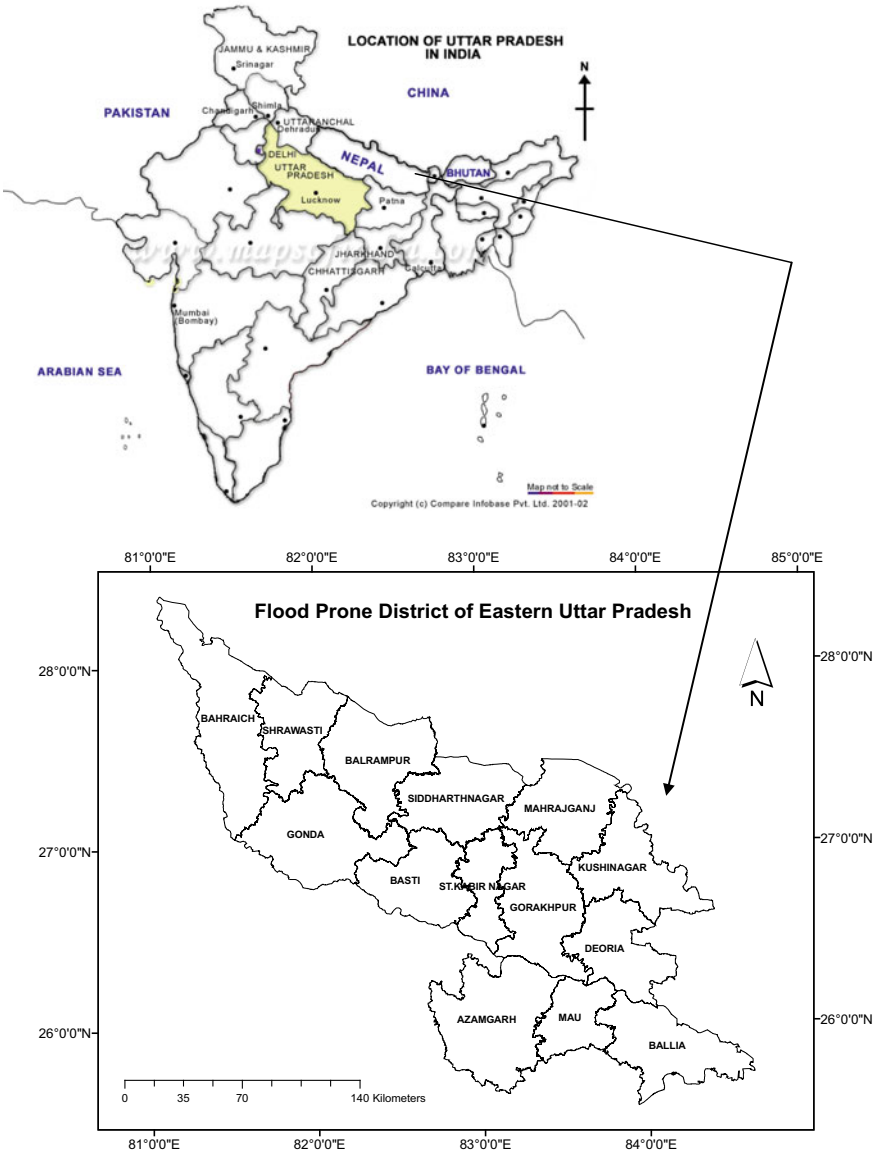

Fig. 19.1 Location map of study area

19.2 Methodology

19.2.1 Data Acquisition

The extracted flood layer and the district boundary layer are provided by the Remote Sensing Application Center, Lucknow, U.P.

19.2.2 Data Analysis

The flood-affected areas of the Rapti river cover much parts of eastern Uttar Pradesh.

The present study is focused on the inundation and stagnation mapping for flood of Rapti river during the year 2008. There is total of 14 districts lying in the study area which are heavily prone to flood.

The SAR data acquired from the NRSC (Hyderabad) is the essential component to derive the information about floods even during the cloudy days of monsoon. The extracted flood layer through the processed SAR data is used for the study (Fig. 19.2).

19.2.2.1 Flood Inundation Mapping (2008)

Spatial overlay technique is adopted for the generation of the inundation maps with the help of software Arc GIS (ver 9.1) developed by ESRI. By the spatial intersection of the flood layers of the various dates with the district layer of the study area, the corresponding flood inundation maps have been generated. The district-wise inundated areas have also been determined. The flood inundation maps of the various dates and their corresponding information about the affected areas of the district are shown in Figs. 19.3, 19.4, 19.5, 19.6, 19.7, 19.8, 19.9, 19.10 and 19.11 and in Tables 19.1, 19.2, 19.3 and 19.4, respectively.

19.2.2.2 Flood Stagnation Mapping (2008)

The multiple intersection technique is adopted for the delineation of the stagnated flood water by employing the same software. By using the flood layers of the various dates the stagnation analysis has been done for one **week, ten days, 15 days, 20 days, and one-month duration** for each district. The total stagnated area of the respective districts has been determined for all duration like from one week to one month. The stagnation maps of the various durations and their corresponding affected area of the districts are shown in Figs. 19.12, 19.13, 19.14, 19.15, 19.16, 19.17, 19.18 and 19.19 and in Tables 19.5, 19.6, 19.7, 19.8, 19.9, 19.10, 19.11, 19.12, 19.13 and 19.14, respectively.

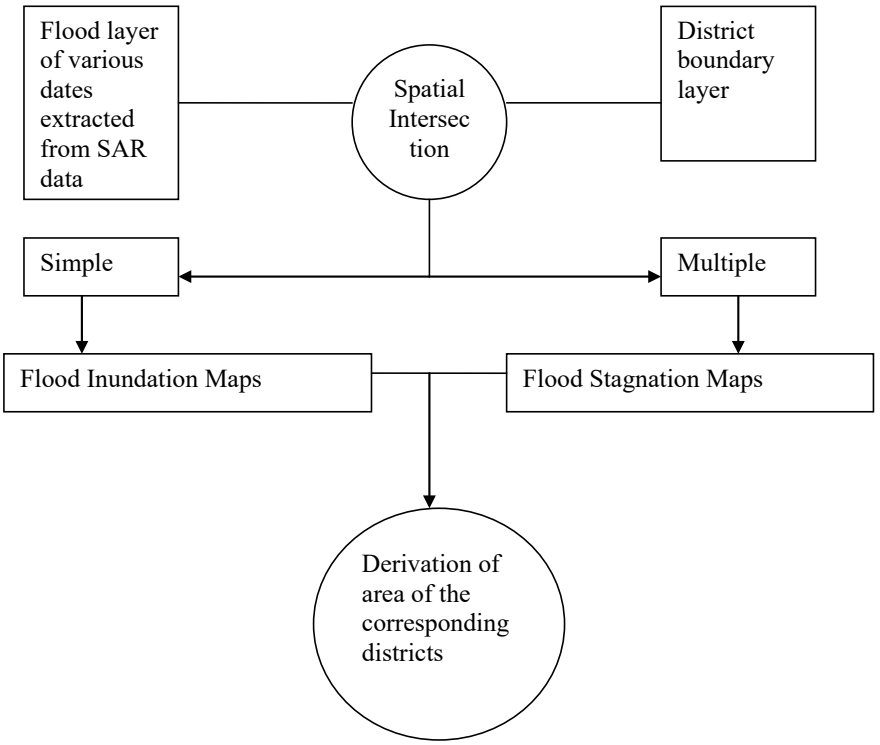

Fig. 19.2 Flow chart of methodology

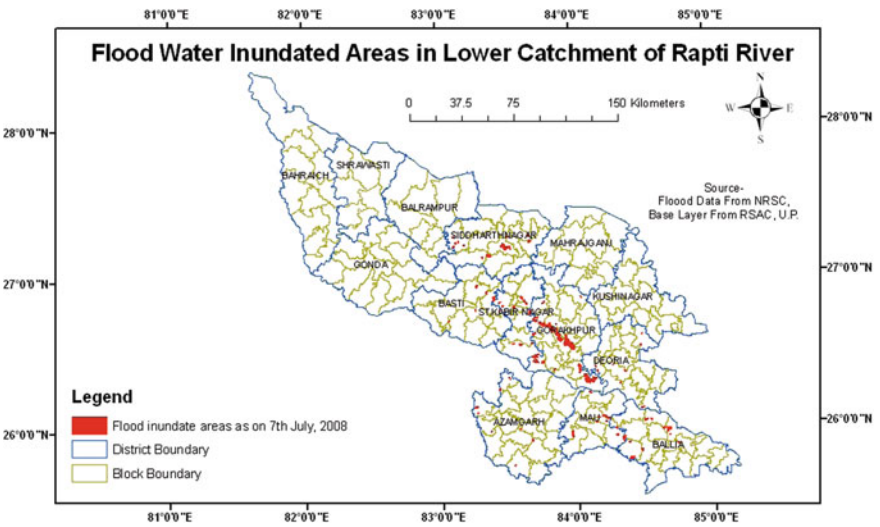

Fig. 19.3 Flood inundation on 7th July 2008

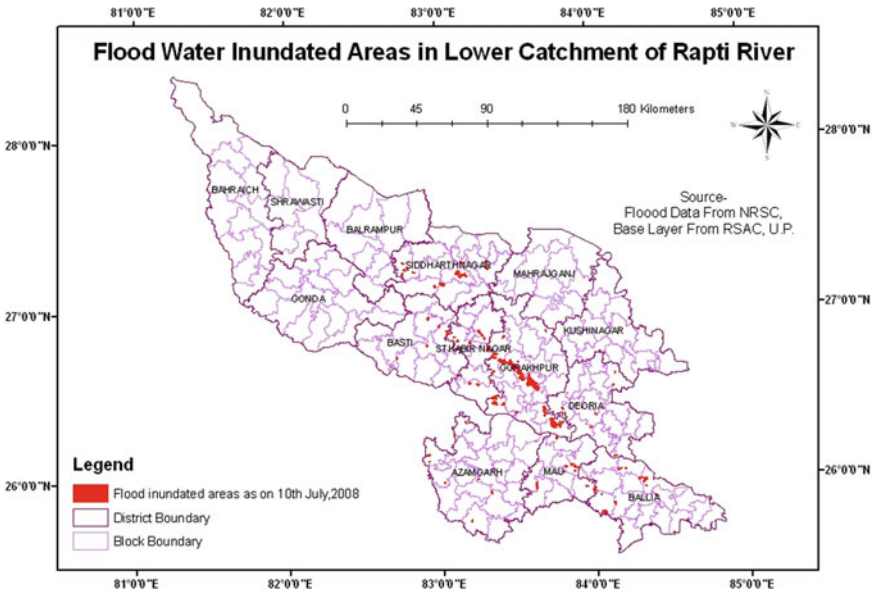

Fig. 19.4 Flood inundation on 10th July 2008

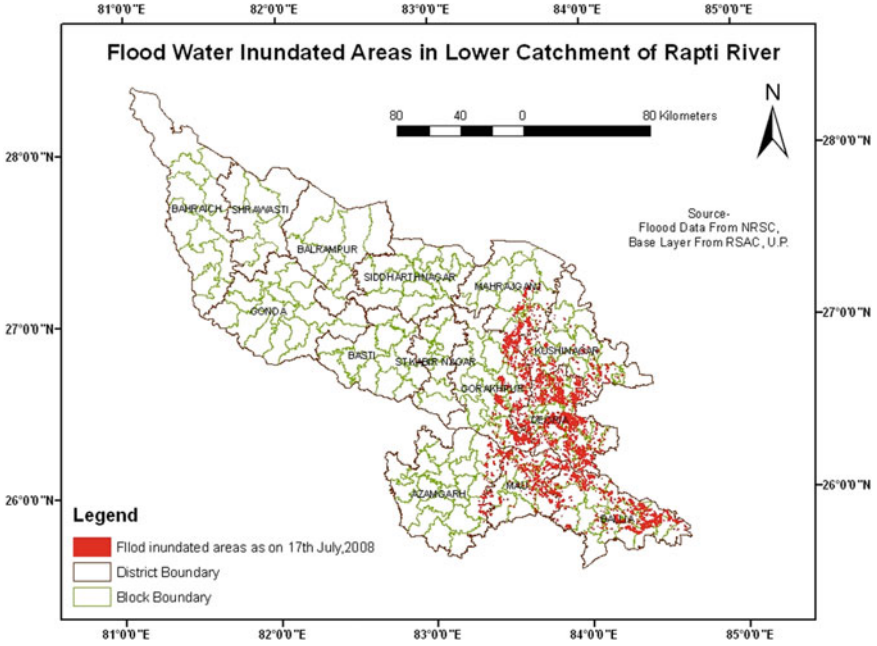

Fig. 19.5 Flood inundation on 17th July 2008

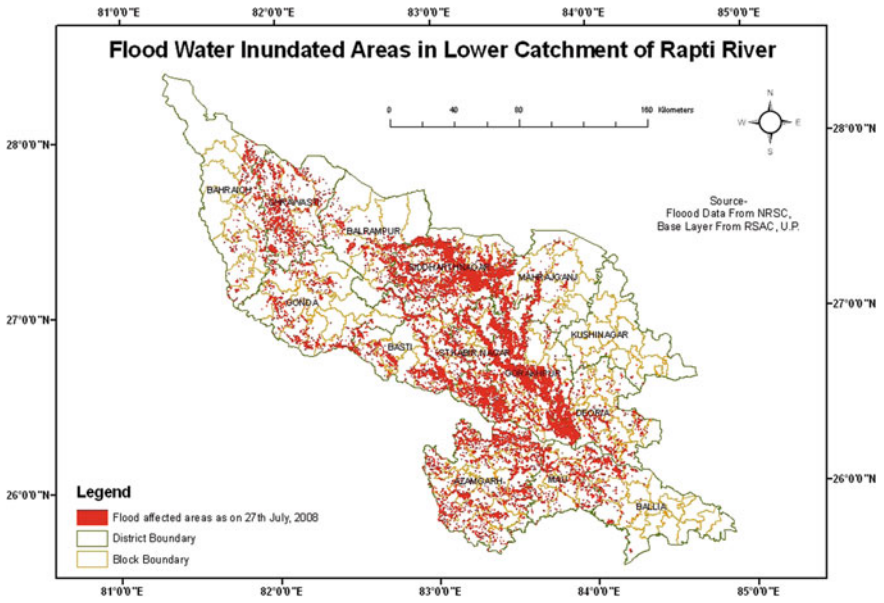

Fig. 19.6 Flood inundation on 27th July 2008

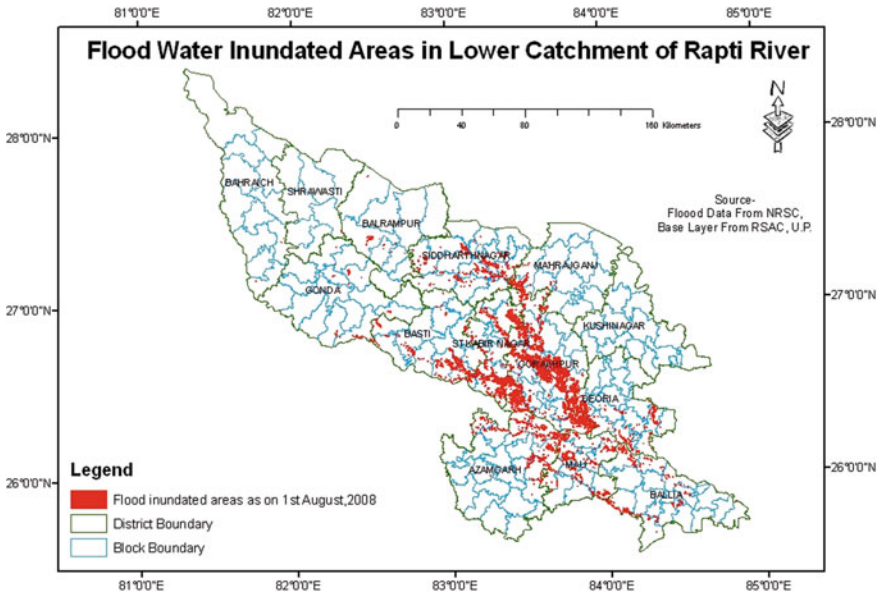

Fig. 19.7 Flood inundation on 1st August 2008

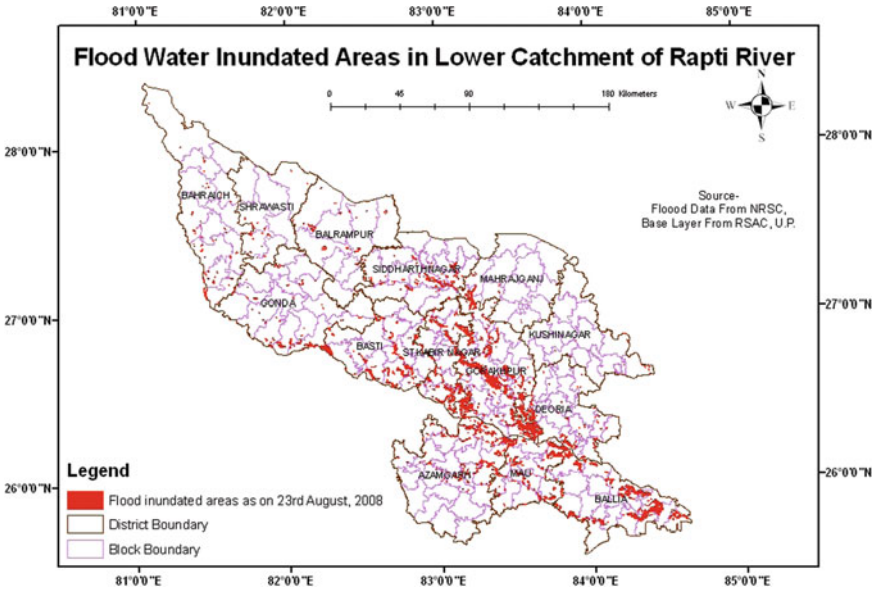

Fig. 19.8 Flood inundation on 23rd August 2008

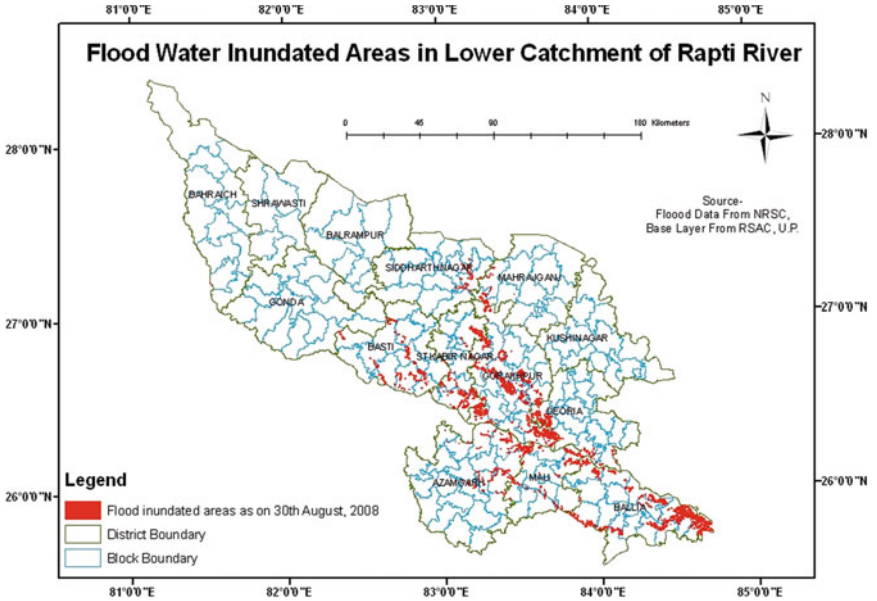

Fig. 19.9 Flood inundation on 30th August 2008

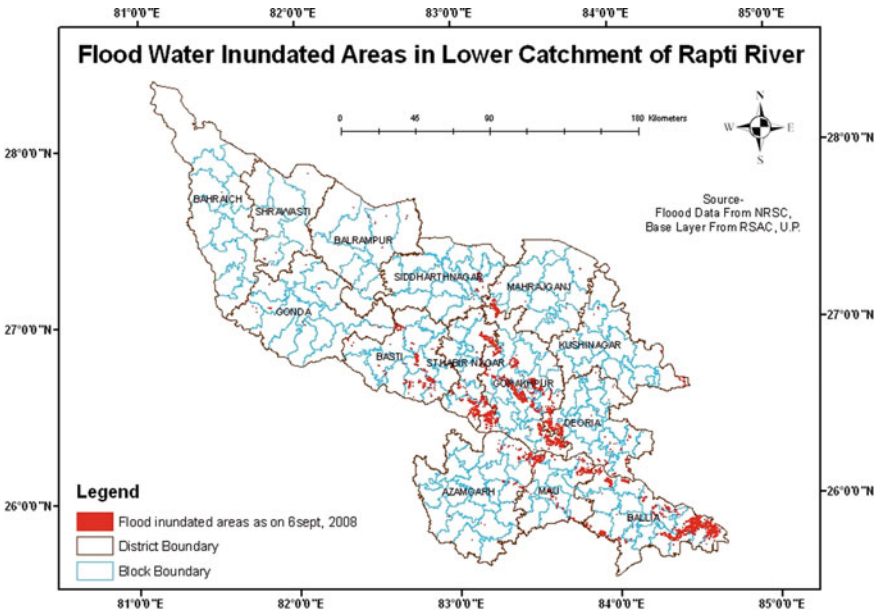

Fig. 19.10 Flood inundation on 6th September 2008

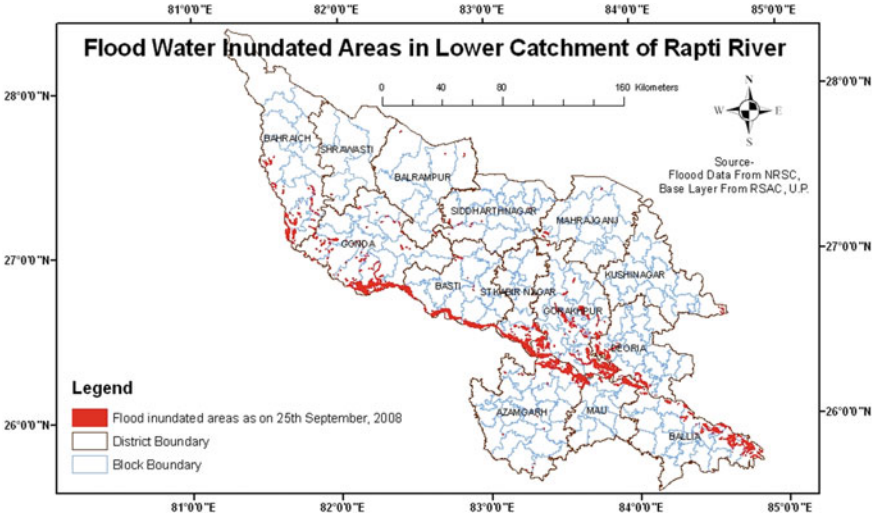

Fig. 19.11 Flood inundation on 25th September 2008

Table 19.1 Total inundated portion of the flood water over the entire study area (2008)

Total area affected by flood inundation in various dates	
Date	Affected area (km^2)
10-Jul	194.75
17-Jul	523.26
27-Jul	1605.65
1-Aug	833.74
23-Aug	718.41
30-Aug	555.75
6-Sep	285.99
25-Sep	554.68

19.2.2.3 Flood Inundation Mapping (2018)

The year 2018 is also the year of severe floods. The total area affected by flood is 2125.019 km^2 as on 16 August 2018. On this day the Siddarthnagar district was very badly affected, followed by Balrampur and Gorakhpur districts (Table 19.15; Fig. 19.20).

The total area affected by flood is 2131.847 km^2 as on 28th August 2018. Most badly affected district is Gorakhpur as on August, 28 followed by Siddarthnagar and Bahraich districts. The inundated areas of the various districts on 28th August are shown in Fig. 19.21 and Table 19.16. During 2008 on August 30, the inundated area by flood is 555.7 km^2 which is 3.8 times less than the area affected in August 2018. The most badly affected district was Deoria in 2008 followed by Gorakhpur with inundated area of 175.53 km^2 and 168.82 km^2, respectively.

The total area affected by flood is 1617.27 km^2 as on 1 September 2018. Gorakhpur is most badly affected district as on September 1 followed by Siddarthnagar and Deoria districts (Fig. 19.22 and Table 19.17).

Hence the severity of the flood and the stretch of the inundated areas become 4 to 5 times more in 2018 than in 2008. Maximum increment occurred in the flood-inundated areas in the Bahraich, Balrampur, Siddarthnagar, Gorakhpur, Deoria, Mau, Maharajganj districts in August and September months. Among them, the most severely affected district is the Gorakhpur district (Tables 19.18 and 19.19).

Table 19.2 Total flood-inundated areas in the respective districts during the month of July 2008

District	Inundated area (km^2)
District-wise flood inundation area for 10th July 2008	
Azamgarh	6.62
Ballia	16.78
Basti	8.25
Deoria	5.7
Gorakhpur (most affected)	106.29
Mau	12.51
Siddarthnagar	22.86
St. Kabir Nagar	15.74
District-wise flood inundation area for 17th July 2008	
Azamgarh	16.91
Ballia	122.51
Deoria (most affected)	165.44
Gorakhpur	106.11
Kushinagar	31.97
Maharajgung	30.48
Mau	49.84
District-wise flood inundation area for 27th July 2008	
Azamgarh	168.44
Bahraich	28.1
Ballia	26.49
Balrampur	66.97
Basti	130.81
Deoria	78.82
Gonda	62.59
Gorakhpur (most affected)	392.95
Kushinagar	0.9
Maharajgung	56
Mau	58.2
Shrawasti	64
Siddarthnagar	293.38
St. Kabir Nagar	177

Table 19.3 Flood inundation area of the respective districts in the month of August 2008

District	Inundated area (km^2)
District-wise flood inundation area for 1st August 2008	
Azamgarh	63
Bahraich	0.21
Ballia	27.49
Balrampur	4.3
Basti	53.67
Deoria	68.34
Gonda	67.7
Gorakhpur (most affected)	354.59
Mau	0.0061
Shrawasti	0.0039
Siddarthnagar	53.22
St. Kabir Nagar	127.5
District-wise flood inundation area for 23rd August 2008	
Azamgarh	58.44
Bahraich	10
Ballia	123.17
Balrampur	9.52
Basti	52.4
Deoria	54.06
Gonda	26
Gorakhpur (most affected)	218.25
Kushinagar	1.37
Maharajgung	8.72
Mau	56.54
Shrawasti	4.79
Siddarthnagar	22.29
St. Kabir Nagar	72.74
District-wise flood inundation area for 30 August 2008	
Azamgarh	35.48
Bahraich	0.14
Ballia (most affected)	175.53
Basti	36.3
Deoria	39.14
Gonda	1.22
Gorakhpur	168.82

(continued)

Table 19.3 (continued)

District	Inundated area (km^2)
Maharajgung	6.47
Mau	33
Siddarthnagar	11.06
St. Kabir Nagar	48.54

Table 19.4 Flood inundation area of the respective districts in the month of September 2008

District	Inundated area (km^2)
District-wise flood inundation area for 6th September 2008	
Azamgarh	6.95
Bahraich	0.03
Ballia	89
Balrampur	0.46
Basti	15.16
Deoria	22.2
Gonda	1.6
Gorakhpur (most affected)	96.25
Kushinagar	1.71
Maharajgung	3.29
Mau	18.17
Shrawasti	0.17
Siddarthnagar	1.68
St. Kabir Nagar	29.19
District-wise flood inundation area for 25th September 2008	
Azamgarh	66.27
Bahraich	36.19
Ballia	61.53
Balrampur	1.24
Basti	70.87
Deoria	29.63
Gonda	90.3
Gorakhpur (most affected)	117.09
Kushinagar	1.25
Maharajgung	2.26
Mau	18.41
Shrawasti	0.24
Siddarthnagar	2.16
St. Kabir Nagar	57.18

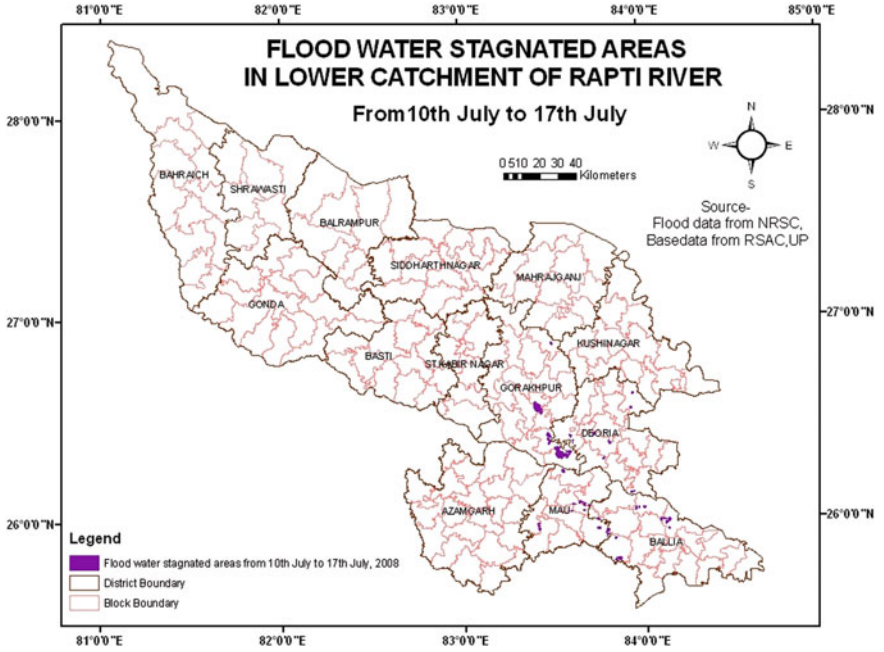

Fig. 19.12 Flood stagnation map for one-week duration

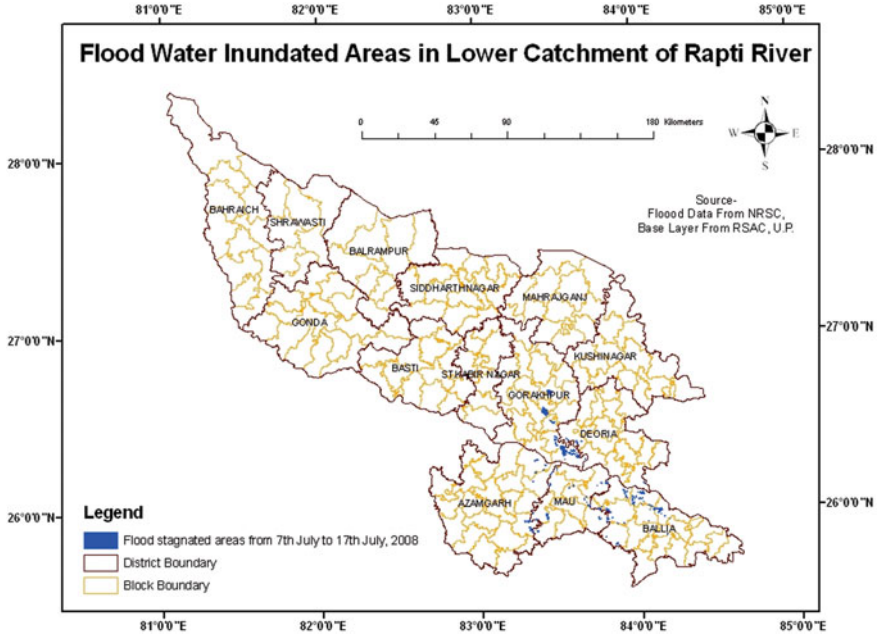

Fig. 19.13 Flood stagnation map for ten days' duration

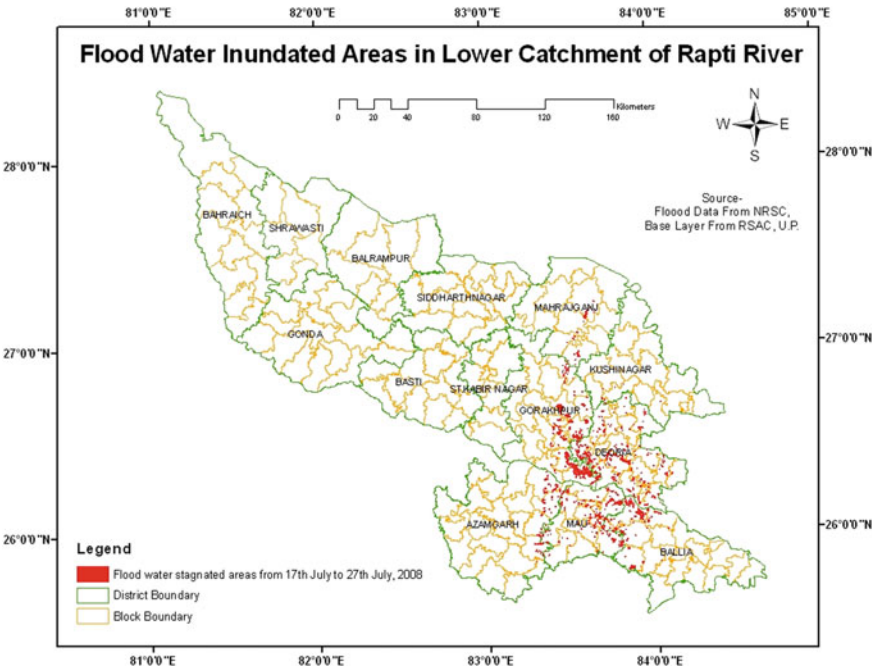

Fig. 19.14 Flood stagnation map for ten days' duration

19.3 Results and Discussions

19.3.1 Flood Inundation Studies

1. From the examination of the inundations maps vis-à-vis the area of the districts, it is found that the day of 27th July 2008 is most heavily affected by flood and flood covers almost 90% of the entire area on that day. Gorakhpur, Siddarthnagar, and the Azamgarh districts are prioritized as 1st, 2nd, and the 3rd most affected districts respectively.
2. 1st August and 23rd August also represent the days of heavy floods, which cover most part of the study area.
3. From all the inundation records pertaining to the period July 2008 to September 2008, it is inferred that Gorakhpur district is continuously and heavily affected by flood water.
4. The total area affected by flood in September 2018 is almost 5.6 times more than the area affected in 2008.
5. The inundation area is 1617.27 km^2 as on September 1, 2018 while the area inundated on September 6, 2008 was 285.86 km^2.
6. At that time most badly affected district was Gorakhpur with inundated area of 96.25 km^2 followed by St. Kabirnagar with affected area of 29.19 km^2.

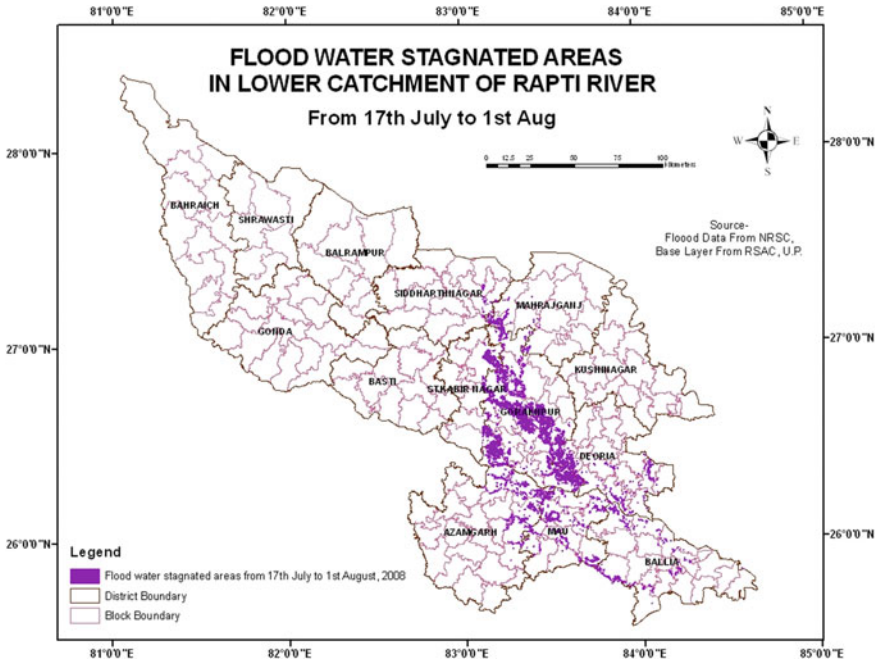

Fig. 19.15 Flood stagnation map for 15 days' duration

7. The total area affected by flood is 2131.847 km^2 as on 28 August 2018. Most badly affected district is Gorakhpur as on August, 28 followed by Siddarthnagar and Bahraich districts.
8. During 2008 on August 30, the inundated area by flood covers 555.7 km^2 which is 3.8 times less than the area affected in August 2018.
9. The most badly affected district was Deoria in 2008 followed by Gorakhpur with inundated area of 175.53 km^2 and 168.82 km^2, respectively.
10. The severity of the flood and the stretch of the inundated areas become 4–5 times greater in 2018 as compared to 2008.
11. The most affected district from 2008 to 2018 is Gorakhpur where the affected areas get incremented by almost 400 times.

19.3.2 Flood Stagnation Studies

1. Comparative analysis of the stagnation scenarios in the various time durations shows that the duration of the 15 days in the period from July 17 to August 1, 2008 exhibits the maximum areal extent of the stagnated water.
2. Under the one-week duration stagnation scenarios, Gorakhpur district is found to be covered by the maximum extent of stagnated flood water.

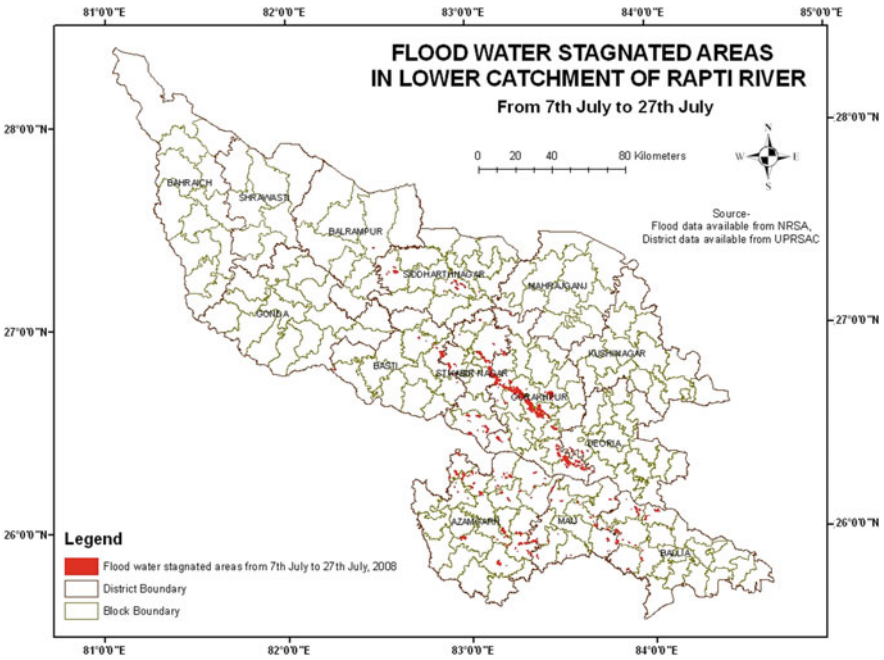

Fig. 19.16 Flood stagnation map for 20 days' duration

3. With the increment of the time duration of stagnation from one week to month, there also occurs corresponding increase in the area of stagnation.
4. Gorakhpur district exhibits the largest extent of stagnation of flood water whereas the other heavily affected districts comprise Ballia, Deoria, Mau, St. Kabirnagar, Azamgarh, Basti, Gonda, and Maharajgunj.

19.4 Key Findings

The year 2018 witnessed more severe floods than 2008. Gorakhpur and Siddarthnagar districts are most badly affected districts in the year 2018. Gorakhpur, Siddarthnagar, and the Azamgarh districts are prioritized as 1st, 2nd, and the 3rd most affected districts respectively.

19.5 Summary

Flood is a havoc created by nature. This disaster has been affecting life and economy since years. Flood inundation and stagnation studies have been done by many researchers by using remote sensing and GIS tools. The SAR data has been found to

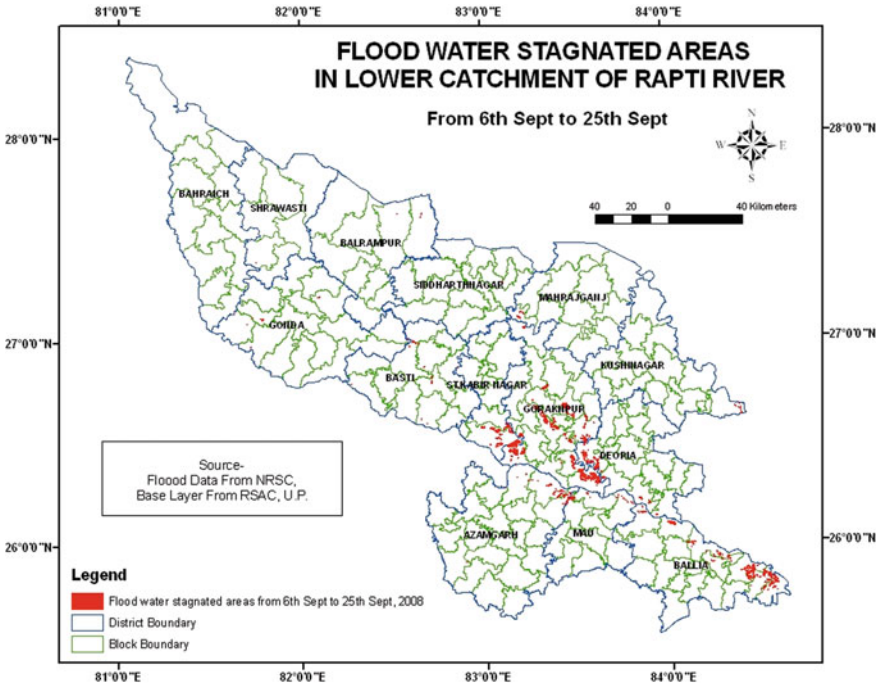

Fig. 19.17 Flood stagnation map for 20 days' duration

be the most effective for flood studies. Flood in the West Rapti river has been reported in recent times. There is widespread submersion and loss of life reported almost every year. The exceptionally high water level of the West Rapti river is reported since the last few years.

The year 2008 witnessed heavy floods in Bihar and Uttar Pradesh regions. Therefore, the flood studies have been done for year 2008 in eastern Uttar Pradesh. The data required for this study is provided by R.S.A.C., Lucknow, U.P. The main purpose of the study is to delineate flood-affected areas in the main flood-prone districts of eastern Uttar Pradesh. On the other hand, the flood water stagnation studies for the various durations in the affected districts have been also conducted. There is total of 14 districts that are affected in the study area. The main flood-prone districts are viz. Bahraich, Shrawasti, Gonda, Siddarthnagar, Balrampur, Basti, Maharajgunj, Gorakhpur, Deoria, Mau, Azamgarh, Ballia, Kushinagar, and St. Kabirnagar.

The year 2018 witnessed more severe flood than in 2008. Gorakhpur and Siddarthnagar districts are the most severely affected districts in the year 2018. By spatially intersecting the flood layers of the various dates derived from the SAR data of 2008 of monsoon season and district boundary layer in Arc GIS ver. 9.1, flood inundation maps were generated. The flood water stagnation maps were prepared through spatial intersection of the flood layers of the different dates and further with the district boundary layer. The stagnation studies of the flood water in the affected

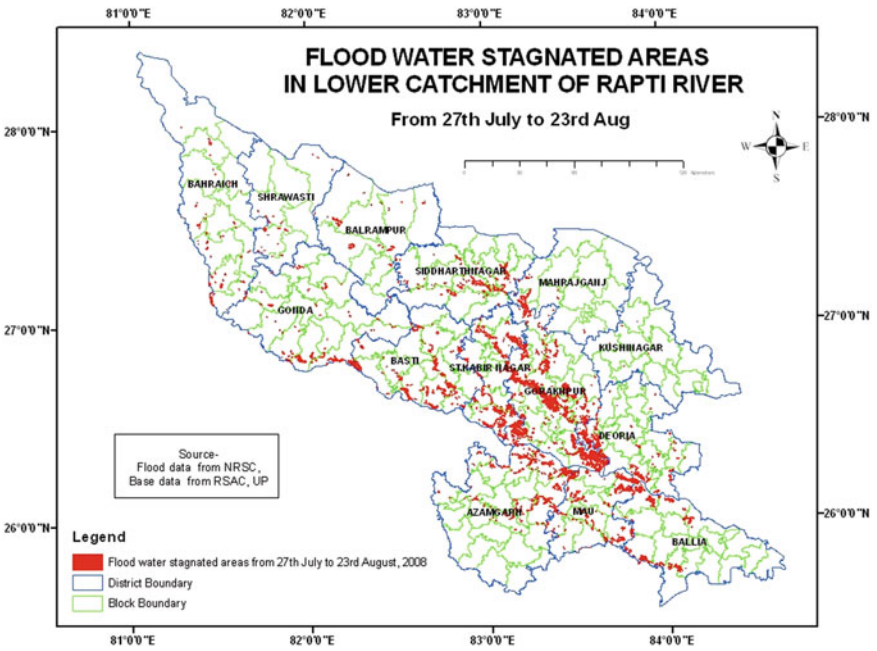

Fig. 19.18 Flood stagnation map for one-month duration

districts were conducted for one week, 10 days, 15 days, 20 days, and one-month duration, respectively.

On the basis of the various analyses performed, Gorakhpur district is found to suffer from the maximum extent of flood and is further aggravated by the most prolonged duration of water stagnation. The other districts affected with similar magnitude are viz. Siddarthnagar, Azamgarh, Ballia, Deoria, Mau, St. Kabirnagar, Basti, Gonda, and Maharajgunj respectively.

The probable causes of the increment in the flood-affected areas may be the poor drainage system and their management in the cities, extinction of water bodies, encroachment of water bodies for building infrastructure, waste disposal or other purposes, unplanned garbage disposal, and climate change. A significant increase in extreme precipitation events over central India has been reported, which can be attributed to warming of sea surface temperature (SST) over the equatorial Indian Ocean (Pai and Sridhar 2015).

The investigations demonstrated the potential of SAR images in the accurate and reliable delineation of the flooded area during the monsoon season due to its all-weather capability. In addition, it is highly recommended to undertake such studies in the flood-affected areas on a regular basis which will be significantly helpful to implement appropriate relief measures thereby ensuring minimum loss of lives and property.

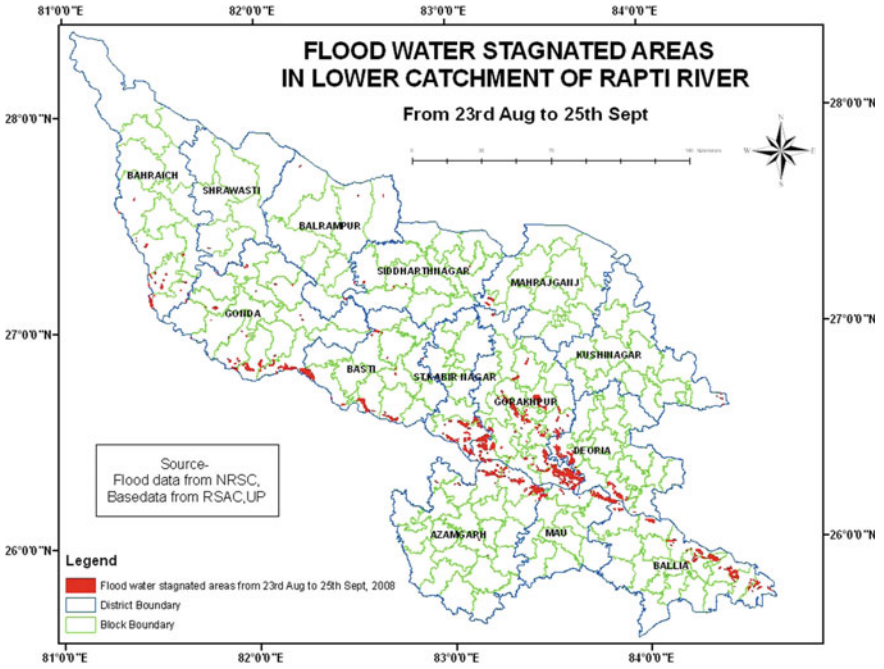

Fig. 19.19 Flood stagnation map for one-month duration

Table 19.5 Total affected area indicates the stagnated condition in the corresponding durations in the entire flood-affected area

Total stagnated area by flood water for various durations (2008)	
	Affected area (km^2)
One-week stagnation	
10–17 July	63.54
Ten days stagnation	
7–17 July	52.73
17–27 July	111.29
Fifteen days stagnation	
17 July–1 Aug	641.23
Twenty days stagnation	
7–27 July	109.52
6–25 Sept	115.49
One-month stagnation	
7 July–1 Aug	87.31
27 July–23 Aug	412.89
23 Aug–25 Sept	241.32

Table 19.6 District-wise stagnation of flood water for one-week duration (10–17 July 2008)

District	Affected area (km^2)
Ballia	10.29
Deoria	5.1
Gorakhpur (most affected)	39.83
Mau	8.31

Table 19.7 District-wise stagnation of flood water for ten days' duration (7–17 July 2008)

District	Affected area (km^2)
Azamgarh	2.86
Ballia	12.31
Deoria	1.14
Gorakhpur (most affected)	30.51
Mau	5.9

Table 19.8 District-wise stagnation of flood water for ten days' duration (17–27 July 2008)

District	Affected area (km^2)
Azamgarh	7.64
Ballia	13.2
Deoria	26.27
Gorakhpur (most affected)	41.94
Kushinagar	0.427
Maharajgung	3.66
Mau	18.2

Table 19.9 District-wise stagnation of flood water for 15 days' duration (17 July–1 August 2008)

District	Affected area (km^2)
Azamgarh	53.99
Ballia	27.48
Deoria	68.34
Gorakhpur (most affected)	354.37
Maharajgung	20.37
Mau	54.19
Siddarthnagar	6.16
St. Kabir Nagar	56.3

Table 19.10 District-wise stagnation of flood water for 20 days' duration (7–27 July 2008)

District	Affected area (km^2)
Azamgarh	17.4
Ballia	4.98
Balrampur	0.18
Basti	2.5
Deoria	1.35
Gorakhpur (most affected)	60.97
Maharajgung	0.01
Mau	4.92
Siddarthnagar	3.43
St. Kabir Nagar	13.73

Table 19.11 District-wise stagnation of flood water for 20 days' duration (6–25 September 2008)

District	Affected area (km^2)
Azamgarh	4.2
Bahraich	0.004
Ballia	25
Balrampur	0.18
Basti	1.05
Deoria	10.8
Gonda	0.97
Gorakhpur (most affected)	57.62
Kushinagar	0.64
Maharajgung	1.18
Mau	2.6
Shrawasti	0.073
Siddarthnagar	0.015
St. Kabir Nagar	11.07

19.6 Limitations

The stagnation studies could not be done for the year 2018 because of lack of data. The flood inundation mapping has also been done for August and September months because the data for all the rainfall days were not sufficient. The probable cause of increment in flood inundation and stagnation areas could not be determined because the current study has not included the other types of data.

Table 19.12 District-wise stagnation of flood water for one-month duration (7 July–1 August 2008)

District	Affected area (km^2)
Azamgarh	3.93
Ballia	2.6
Basti	1.72
Deoria	1.59
Gorakhpur (most affected)	61.1
Maharajgung	0.203
Mau	3.66
Siddarthnagar	1.4
St. Kabir Nagar	11.1

Table 19.13 District-wise stagnation of flood water for one-month duration (27 July–23 August 2008)

District	Affected area (km^2)
Azamgarh	27.99
Bahraich	1.72
Ballia	12.44
Balrampur	7.57
Basti	36.06
Deoria	31.33
Gonda	13.61
Gorakhpur (most affected)	167.49
Kushinagar	0.013
Maharajgung	5.36
Mau	23.3
Shrawasti	4.03
Siddarthnagar	19.69
St. Kabir Nagar	62.3

Table 19.14 District-wise stagnation of flood water for one-month duration (23 August–25 Sept 2008)

District	Affected area (km^2)
Azamgarh	23.62
Bahraich	6.5
Ballia	28.44
Balrampur	0.57
Basti	15.48
Deoria	20.47
Gonda	21.56
Gorakhpur (most affected)	91.15
Kushinagar	0.4
Maharajgung	1.62
Mau	9.68
Shrawasti	0.15
Siddarthnagar	0.81
St. Kabir Nagar	20.81

Table 19.15 Flood inundation for 16th August 2018, UP

District	Affected area (km^2)
Azamgarh	69.46
Ballia	157
Balrampur	268
Basti	39.15
Deoria	67.76
Gorakhpur	368.2
Maharajgung	29.72
Mau	34.24
Siddarthnagar	498.9
St. Kabir Nagar	84.84

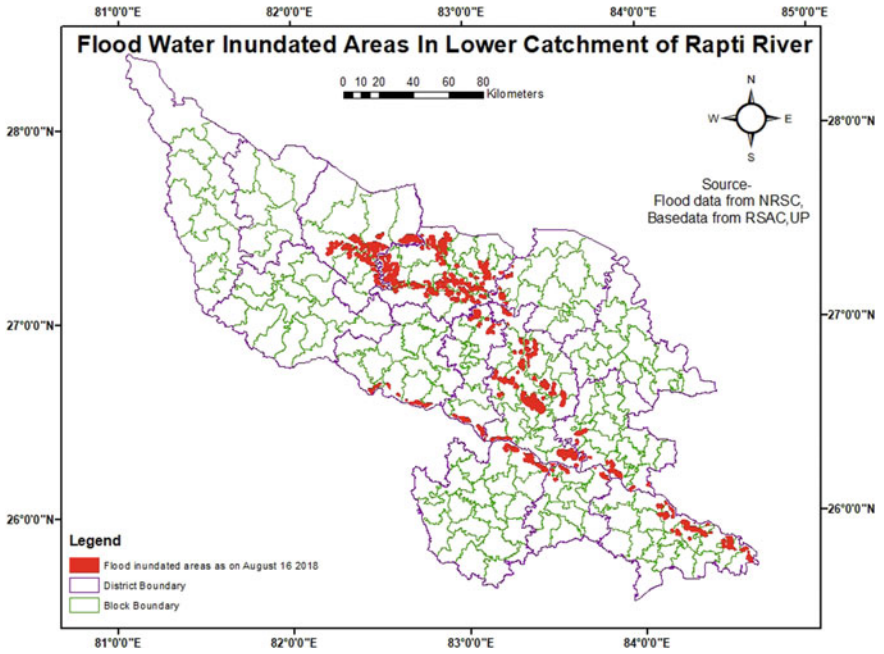

Fig. 19.20 Flood inundation map as on August 16, 2018

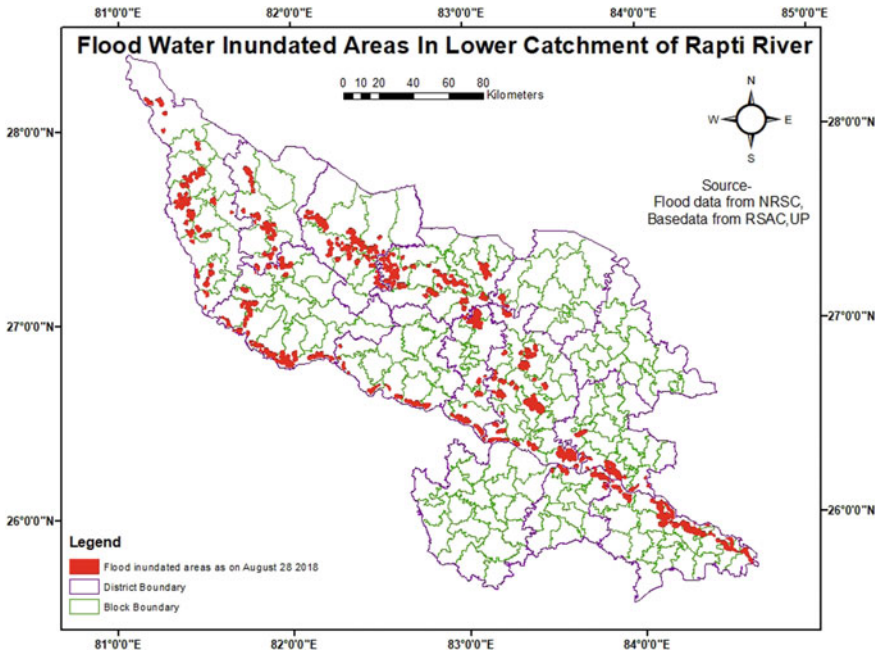

Fig. 19.21 Flood inundation map as on August 28, 2018

Table 19.16 Flood inundation for 28th August 2018, UP

District	Affected area (km^2)
Bahraich	270.29
Ballia	249.59
Balrampur	244.74
Basti	70.45
Deoria	88.30
Gonda	263.06
Gorakhpur	347.55
Maharajganj	16.73
Mau	53.47
Shravasti	128.30
Siddharthanagar	273.26
St. Kabirnagar	126.05

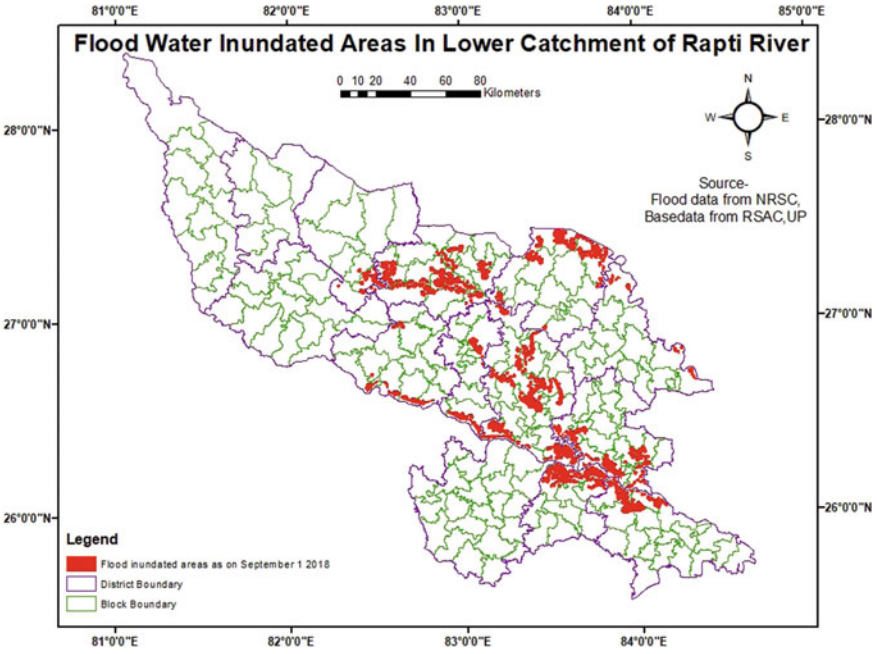

Fig. 19.22 Flood inundation map as on September 1, 2018

Table 19.17 Flood inundation for 1st September 2018, UP

District	Affected area (km^2)
Ballia	172.26
Balrampur	54.34
Basti	84.34
Deoria	249.10
Gorakhpur	529.42
Kushinagar	38.51
Maharajganj	270.0
Mau	225.26
Siddharthanagar	410.53
ST. Kabirnagar	91.20

Table 19.18 District-wise flood inundation areas for August Month, Year 2008, and 2018

District-wise flood inundation area			Variation in the affected area
Affected districts	Year 2008 (30th August)	Year 2018 (28th August)	
Azamgarh	35.48	Nil	
Bahraich	0.14	270.29	270.15
Ballia (most affected)	175.53	249.59	74.06
Balrampur	Nil	244.74	
Basti	36.3	70.45	34.15
Deoria	39.14	88.30	49.16
Gonda	1.22	263.06	261.84
Gorakhpur	168.82	347.55	178.73
Maharajgung	6.47	16.73	10.26
Mau	33	53.47	20.47
Shravasti	Nil	128.30	
Siddarthnagar	11.06	273.26	262.2
St. Kabir Nagar	48.54	126.05	77.51

Table 19.19 District-wise flood inundation areas for September Month, Year 2008, and 2018

District-wise flood inundation area			Variation in the affected area
Affected districts	Year 2008 (6th September)	Year 2018 (1st September)	
Azamgarh	6.95	Nil	
Bahraich	0.03	270.29	270.26
Ballia (most affected)	89	172.26	83.26
Balrampur	0.46	54.34	53.88
Basti	15.16	84.34	69.18
Deoria	22.2	249.10	226.9
Gonda	1.6	263.06	261.46
Gorakhpur	96.25	529.42	433.17
Kushinagar	1.71	38.51	36.8
Maharajgung	3.29	270.0	266.71
Mau	18.17	225.26	207.09
Shravasti	0.17		−0.17
Siddarthnagar	1.68	410.53	408.85
St. Kabir Nagar	29.19	91.20	62.01

References

Anusha N, Bharathi B (2020) Flood detection and flood mapping using multi-temporal synthetic aperture radar and optical data. Egypt J Remote Sens Space Sci 23:207–219

Bhattacharya B, Mazzoleni M, Ugay R (2019) Flood inundation mapping of the sparsely gauged large-scale Brahmaputra basin using remote sensing products. J Remote Sens 11(501):1–23. https://doi.org/10.3390/rs11050501

Chumsamrong W, Thitimajshima P, Rangsanseri Y (1998) Using stationary wavelet transform in the classification of Sar images. In: 19th Asian Association on remote sensing, Poster Session-1, Manila

Ding L, Ma L, Li L, Liu C, Li N, Yang Z, Yao Y, Lu H (2021) A survey of remote sensing and geographic information system applications for flash floods. J Remote Sens 13(1818):1–20. https://doi.org/10.3390/rs13091818

Harris A, Rahman S, Hossain F, Yarborough L, Bagtzoglou AC, Easson G (2007) Satellite-based flood modeling using TRMM-based rainfall products. J Sens 7:3416–3427

Hong Y, Abdelkareem M (2022) Integration of remote sensing and a GIS based method for revealing prone areas to flood hazards and predicting optimum areas of groundwater resources. Arab J Geosci 15(114):1–14

Joyce JM, Scott MS (2005) An assessment of Maryland's vulnerability to flood damage, thesis. Maryland Department of the Environment, pp 1–82

Mishra N, Mohapatra S (2019) Identification and construction of flood disaster resilience index to measure socio-economic flood resilience in Eastern Uttar Pradesh: a inter-district analysis. Int J Appl Soc Sci 6(11&12):2385–2390

Mondal KC, Saha S, Aitch P, Bhandari G (2020) Application of remote sensing and GIS in flood vulnerability assessment—a case study of lower Ajay Basin, India. In: Pal et al (eds) An inter-disciplinary approach for disaster resilience and sustainability, disaster risk reduction, Chap 10, pp 151–166. http://doi.org/10.1007/978-981-32-9527-8_10

Pai DS, Sridhar L (2015) Long term trends in extreme rainfall events over India, high-impact weather events over the SAARC region. ISBN: 978-3-319-10216-0

Ramalingam M, Vadivukkarasi M (2005) GISdevelopment.net 9(10)

Rosser JF, Leibovici DG, Jackson MJ (2017) Rapid flood inundation mapping using social media, remote sensing and topographic data. Nat Hazards 87:103–120. https://doi.org/10.1007/s11069-017-2755-0

Sanyal J, Lu XX (2003) Application of GIS in flood hazard mapping—a case study of Gangetic West Bengal, India, Map Asia. In: 2nd annual Asian conference and exhibition (poster session)

Shen X, Wang D, Mao K, Anagnostou E, Hong Y (2019) Inundation extent mapping by synthetic aperture radar: a review. J Remote Sens 11(7):879, 1–17. http://doi.org/10.3390/rs11070879

Shukla KK, Agarwal AK, Sharma P, Chaurey R (2015) Development of a model to assess flood affected areas in near real time along major rivers of Uttar Pradesh, India. Int J Innov Res Sci Eng Technol 4(7):6362–6377

Thapa PJ (1997) Water-led development in Nepal: myths, limitations and rational concerns. Water Nepal 5(1):35–57

Yamada Y (2001) Detection of flood-inundated area and relation between the area and micro-geomorphology using SAR and GIS. In: IEEE geoscience and remote sensing symposium, IGARSS 2001, vol 7, pp 3282–3284, Sydney, NSW, July 9–13. http://doi.org/10.1109/IGARSS.2001.978329